# Numerical Modelling of Shotcrete for Tunnelling

A thesis submitted to Imperial College London in partial fulfilment of the requirements for the degree of Doctor of Philosophy in the Faculty of Engineering

by

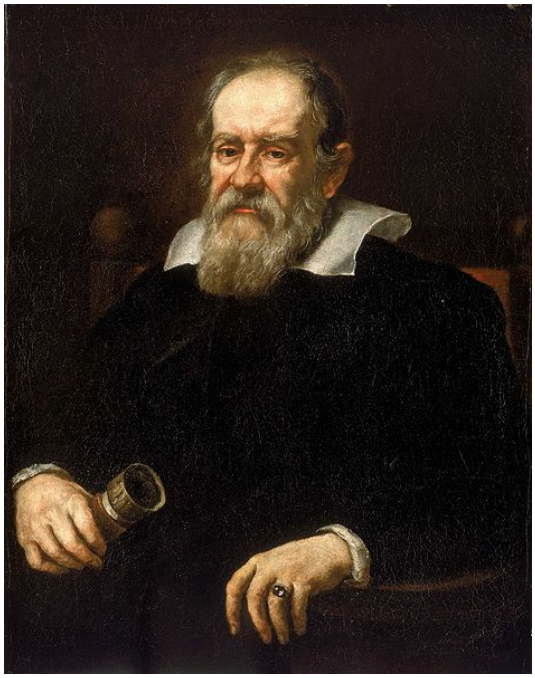
Dipl. Ing.

**Reinhard Schütz**

Department of Civil and Environmental Engineering
Imperial College London
London SW7 2AZ

February 2010

*This work is dedicated with much affection and gratitude to my beloved parents Maria and Siegfried*



Galileo Galilei (15.02.1564 - 08.01.1642)
Italian physicist, mathematician, astronomer and philosopher

*"The laws of Nature are written in the language of mathematics ... the symbols are triangles, circles and other geometrical figures, without whose help it is impossible to comprehend a single word."*

# Declaration

The work presented in this dissertation was carried out in the Department of Civil and Environmental Engineering at Imperial College London from August 2006. This thesis is the result of my own work and any quotation from, or description of the work of others is acknowledged herein by reference to the sources, whether published or unpublished.

This dissertation is not the same as any that I have submitted for any degree, diploma or other qualification at any other university. No part of this thesis has been or is being concurrently submitted for any such degree, diploma or other qualification.

This document is available on-line at www.imperial.ac.uk/geotechnics/publications, it is less than 100,000 words long, contains less than 265 figures and less than 65 tables.

Reinhard Schütz
London, 05/02/2010

# Abstract

Shotcrete is a special type of concrete which was invented at the beginning of the 20th century and is nowadays an important support element for tunnels constructed with the New Austrian Tunnelling Method (NATM). Immediately after tunnel excavation shotcrete is sprayed onto the tunnel walls at high pressure in order to provide temporary support. Unfortunately, in the past very little attention has been given to the development of sophisticated material laws for shotcrete, since its design and application was mainly based on experience. However, current design practice, such as that applied in the design of the new Crossrail tunnels, requires sophisticated modelling of shotcrete behaviour in numerical analysis of tunnel-soil interaction. Such models are not readily found in the literature, as they have been developed mainly for structural, rather than geotechnical applications.

In this thesis, a constitutive model for the time-dependent behaviour of shotcrete has been developed within the framework of elasto-plasticity. Two independent yield surfaces control the behaviour of shotcrete in multiaxial loading conditions for both compression and tension. The model formulation is based on strain hardening/softening plasticity, where the expansion and contraction of the yield surfaces are governed by normalised plastic strains. Cracking of the shotcrete is considered within the smeared crack concept. Furthermore, the proposed material law includes the time-dependency of stiffness and strength behaviour. The reducing deformability of the shotcrete during cement hydration has been taken into account. The model has been extended to account for creep, shrinkage and hydration temperature induced deformations at early shotcrete ages. After a robust implementation into the Imperial College Finite Element Program (ICFEP), model calibration and validation have been performed for shotcrete experiments taken from the literature. The developed constitutive model has then been applied to the analysis of a typical tunnel construction in London Clay, modelling the early age material properties of the shotcrete tunnel lining in detail for various excavation schemes. Finally, it has been shown that the proposed constitutive model is capable of reproducing the complex behaviour of young shotcrete at early ages and can be applied successfully to boundary value problems in geotechnical engineering.

# Acknowledgements

At first I would like to thank my supervisors Prof. D. Potts and Dr. L. Zdravković for giving me the great opportunity to do research at the Geotechnics Section of Imperial College London. Their confidence and endless support helped and motivated me to successfully carry out this challenging work. Their guidance through hard stages of my thesis is highly appreciated.

This research project was funded by the Geotechnical Consulting Group (GCG) London. Their patience and financial support is gratefully acknowledged.

I would also like to express my gratitude to the College staff for their help, support and contributions in several fruitful discussions. They showed me that science can be a very interdisciplinary field where collaboration and social skills are of high importance. Many thanks are due to all my friends and colleagues that I have made during my period of research for making the experience of staying in London an unforgettable one. I do not want to forget to thank all my friends back home in Austria, who visited me various times and therefore made our bond of friendship grow stronger despite the distance.

Finally, my last thanks go to my family in Austria for encouraging and supporting me in everything that I have done in life. Without them I would never have completed this thesis.

# Contents

**Abstract** **5**

**Acknowledgements** **6**

**Contents** **7**

**List of figures** **14**

**List of tables** **25**

**1 Introduction** **28**
1.1 General . . . 28
1.2 Tunnel collapse at Heathrow Airport . . . 29
1.3 Aims of research . . . 31
1.4 Outline of thesis . . . 31
1.5 Definition of stress and strain variables . . . 33
1.6 Terminology and symbols used in thesis . . . 39

**2 Tunnelling in urban areas** **44**
2.1 Introduction . . . 44
2.2 The New Austrian Tunnelling Method . . . 44
2.3 Typical tunnel construction process in urban areas . . . 48
2.4 The importance of monitoring in tunnelling . . . 49
2.4.1 Measuring and interpretation of displacements . . . 50
2.4.2 Measuring and interpretation of stresses in tunnel linings . . . 51
2.5 A review of tunnel lining design . . . 53
2.5.1 Empirical methods . . . 53
2.5.2 Closed-form analytical methods . . . 54
2.5.2.1 Continuum analytical methods . . . 55
2.5.2.2 Convergence-confinement method . . . 55
2.5.2.3 Bedded-beam-spring models . . . 56
2.5.3 Numerical methods . . . 57
2.5.3.1 Bearing-capacity-diagram . . . 58

2.6 Single-shell method . . . 59
2.6.1 Innovative shotcrete tunnelling . . . 61
2.7 Modelling 2D tunnel excavation in a numerical analysis . . . 63
2.7.1 Stress relief method . . . 64
2.7.2 Stiffness reduction method . . . 64
2.7.3 Gap method . . . 65
2.7.4 Volume loss control method . . . 65
2.8 Summary . . . 67

**3 The Finite Element Method 69**
3.1 Introduction . . . 69
3.2 Finite element theory for linear materials . . . 70
3.2.1 Element discretisation . . . 70
3.2.2 Approximation of primary variable . . . 70
3.2.3 Formulation of element equations . . . 72
3.2.3.1 Numerical integration . . . 74
3.2.4 Formulation of global equations . . . 75
3.2.5 Boundary conditions . . . 76
3.2.6 Solution of global equations . . . 76
3.3 Geotechnical considerations . . . 76
3.3.0.1 Undrained analysis . . . 77
3.4 Finite element theory for non-linear materials . . . 79
3.4.1 The modified Newton-Raphson method . . . 79
3.4.2 Stress point algorithm . . . 81
3.5 Summary . . . 83

**4 Shotcrete Technology 85**
4.1 Introduction . . . 85
4.2 Shotcrete as an engineering material . . . 85
4.3 Mix design . . . 88
4.3.1 Aggregates . . . 88
4.3.2 Cement . . . 89
4.3.3 Water . . . 90
4.3.4 Additives . . . 91
4.3.4.1 Silica fume . . . 91
4.3.4.2 Accelerators . . . 92
4.3.4.3 Plasticisers . . . 93
4.3.5 Fibres . . . 93
4.3.5.1 Steel fibres . . . 93
4.3.5.2 Polypropylene fibres . . . 95
4.3.5.3 Glass fibres . . . 96

4.4 Cement hydration . . . 96
4.4.1 Reaction process . . . 97
4.4.2 Degree of hydration . . . 98
4.5 Shotcrete installation . . . 98
4.5.1 Dry-mix process . . . 99
4.5.2 Wet-mix process . . . 100
4.5.3 Spraying technique . . . 101
4.5.4 Rebound behaviour . . . 102
4.6 Shotcrete testing . . . 104
4.7 Summary . . . 106

**5 Mechanical and time-dependent behaviour of concrete and shotcrete 108**
5.1 Introduction . . . 108
5.2 Uniaxial stress conditions . . . 108
5.2.1 Mechanical behaviour in compression . . . 108
5.2.2 Mechanical behaviour in tension . . . 111
5.3 Biaxial stress conditions . . . 113
5.4 Triaxial stress conditions . . . 116
5.5 Anisotropy of shotcrete . . . 116
5.6 Mechanical behaviour of steel fibre reinforced concrete and shotcrete . . . 117
5.7 Time-dependent mechanical behaviour of young shotcrete . . . 120
5.7.1 Increase in stiffness and strength . . . 121
5.7.2 Deformability at early ages . . . 132
5.7.3 Damage effects due to early-age loading . . . 136
5.8 Creep and relaxation . . . 138
5.8.1 Mechanisms behind creep . . . 140
5.8.2 Influencing factors . . . 141
5.8.3 Creep in tunnelling . . . 146
5.9 Shrinkage . . . 147
5.9.1 Mechanisms behind shrinkage . . . 148
5.9.1.1 Plastic shrinkage . . . 148
5.9.1.2 Drying shrinkage . . . 148
5.9.1.3 Autogeneous shrinkage . . . 149
5.9.1.4 Carbonation shrinkage . . . 149
5.9.2 Factors influencing shrinkage . . . 150
5.10 Temperature induced deformation . . . 153
5.11 Summary . . . 156

**6 Modelling of concrete and shotcrete 158**
6.1 Introduction . . . 158
6.2 Empirical models for concrete in compression . . . 158

6.3 Constitutive models based on elasticity . . . 163
6.3.1 Linear elastic models . . . 163
6.3.2 Non-linear elastic models . . . 164
6.4 Classical theory of elasto-plasticity . . . 165
6.4.1 Basic concepts . . . 166
6.4.2 Formulation of the elasto-plastic constitutive matrix . . . 168
6.4.3 Multi-surface plasticity . . . 169
6.5 Basic plasticity models for concrete . . . 171
6.5.1 Rankine criterion . . . 171
6.5.2 Mohr-Coulomb criterion . . . 172
6.5.3 Drucker-Prager criterion . . . 174
6.5.4 Chen & Chen criterion . . . 175
6.5.5 Further sophisticated constitutive models for concrete . . . 180
6.6 Modelling post-peak behaviour of concrete . . . 180
6.6.1 Post-peak behaviour in tension . . . 180
6.6.1.1 Discrete crack model . . . 181
6.6.1.2 Smeared crack model . . . 181
6.6.1.3 Effect of reinforcement . . . 187
6.6.1.4 Modelling steel fibre reinforced concrete (SFRC) . . . 190
6.6.2 Post-peak behaviour in compression . . . 193
6.7 Modelling of creep . . . 193
6.7.1 Basic expressions for creep . . . 194
6.7.2 Rheological units . . . 194
6.7.2.1 Kelvin model . . . 195
6.7.2.2 Maxwell model . . . 196
6.7.2.3 Burger model . . . 197
6.7.2.4 Rheological models used for modelling shotcrete behaviour . 198
6.7.3 Creep according to EC 2 (2004) . . . 203
6.7.4 Rate of flow method . . . 204
6.7.4.1 Rate of flow method after Schubert (1988) . . . 204
6.7.4.2 Rate of flow method after Golser et al. (1990) . . . 206
6.7.4.3 Rate of flow method after Aldrian (1991) . . . 206
6.8 Modelling of shrinkage . . . 207
6.8.1 Shrinkage after American Concrete Institute (ACI) . . . 207
6.8.2 Shrinkage after Bazant Model B3 . . . 208
6.8.3 Shrinkage after Gardner & Lockman (2001) . . . 209
6.9 Modelling hydration temperature in concrete structures . . . 209
6.10 A review of different constitutive models applied for tunnel lining design . . . 210
6.10.1 Hypothetical Modulus of Elasticity (HME) . . . 210
6.10.2 Non-linear beam model by Moussa (1993) . . . 212

6.10.3 Post-failure modelling of shotcrete by Hafez (1995) . . . . . 213
6.10.4 Viscoplastic material model for shotcrete by Meschke (1996) . . . . . 214
6.10.5 Shotcrete model based on chemoplasticity by Hellmich et al. (1999*a*) . 215
6.10.6 Assessment of constitutive models for shotcrete by Thomas (2003) . . 217
6.11 Summary . . . . . 218

**7 A constitutive Model for Shotcrete 221**
7.1 Introduction . . . . . 221
7.2 Formulation of the constitutive model . . . . . 222
7.2.1 Structure of the model . . . . . 222
7.2.2 Yield Function and Plastic Potential in compression . . . . . 223
7.2.3 Yield Function and Plastic Potential in tension . . . . . 224
7.3 Hardening and softening rules . . . . . 226
7.3.1 Compression . . . . . 227
7.3.2 Tension . . . . . 232
7.3.2.1 Option A - Linear softening . . . . . 233
7.3.2.2 Option B - Exponential softening . . . . . 235
7.4 Time-dependent material behaviour . . . . . 237
7.4.1 Increase in stiffness and strength with time . . . . . 237
7.4.2 Shotcrete deformability at early ages . . . . . 240
7.4.3 Creep and relaxation . . . . . 241
7.4.4 Shrinkage . . . . . 245
7.4.5 Temperature induced strains . . . . . 245
7.5 Summary of parameters . . . . . 247
7.6 Formulation of the elasto-plastic constitutive matrix for time-dependent materials . . . . . 249
7.7 Correction of the right hand side load vector . . . . . 252
7.8 Multi-surface plasticity for time-dependent materials . . . . . 253
7.9 Model implementation . . . . . 257
7.9.1 Selection of the active yield surface . . . . . 258
7.9.2 Derivatives of the stress invariants . . . . . 258
7.9.3 Partial derivatives for the compression yield surface . . . . . 259
7.9.4 Partial derivatives for the tension yield surface . . . . . 260
7.9.5 Calculation of the hardening modulus for the compression surface . . 262
7.9.6 Calculation of the hardening modulus for the tension surface . . . . . 263
7.9.7 Calculation of the elastic constitutive matrix . . . . . 265
7.9.8 Calculation of the changes in the compressive hardening parameter . . 265
7.9.9 Calculation of the changes in the tensile hardening parameter . . . . . 266
7.10 Model calibration . . . . . 267
7.10.1 Increase in stiffness and compressive strength . . . . . 267

7.10.2 Complete uniaxial compression tests at different shotcrete ages . . . . 269
7.10.3 Creep deformation in uniaxial compression . . . . . 272
7.10.4 Shrinkage . . . . . 274
7.10.5 Temperature development during cement hydration . . . . . 275
7.11 Model validation . . . . . 276
7.11.1 Increase in stiffness with time . . . . . 276
7.11.2 Uniaxial loading in compression and tension . . . . . 277
7.11.3 Biaxial loading in compression . . . . . 281
7.11.4 Creep . . . . . 282
7.11.5 Shrinkage . . . . . 284
7.11.6 Thermal strains . . . . . 285
7.12 Summary . . . . . 286

**8 Analysis of tunnel excavation in London Clay 287**
8.1 Introduction . . . . . 287
8.2 Geometry of the problem . . . . . 288
8.3 Ground conditions in London area and initial stresses . . . . . 289
8.4 Finite element model . . . . . 290
8.4.1 Mesh and boundary conditions . . . . . 290
8.4.2 Modelling of construction sequence . . . . . 294
8.4.2.1 Excavation Type 1: Full face excavation . . . . . 294
8.4.2.2 Excavation Type 2: Bench-invert excavation . . . . . 295
8.4.2.3 Excavation Type 3: Sidewall drift . . . . . 296
8.5 Adopted constitutive models and material parameters . . . . . 298
8.5.1 Tunnel lining - Shotcrete . . . . . 298
8.5.2 Soil - London Clay . . . . . 301
8.6 Tunnel analyses . . . . . 303
8.6.1 Parametric study for excavation Type 1 . . . . . 303
8.6.2 Parametric study for excavation Type 2 . . . . . 306
8.6.3 Parametric study for excavation Type 3 . . . . . 308
8.7 Discussion of results . . . . . 310
8.7.1 Surface settlements and volume loss . . . . . 312
8.7.1.1 Excavation Type 1 . . . . . 312
8.7.1.2 Excavation Type 2 . . . . . 318
8.7.1.3 Excavation Type 3 . . . . . 322
8.7.2 Hoop stress distribution and utilisation factor . . . . . 328
8.7.2.1 Excavation Type 1 . . . . . 328
8.7.2.2 Excavation Type 2 . . . . . 349
8.7.2.3 Excavation Type 3 . . . . . 360
8.7.3 Lining displacements . . . . . 371

8.7.3.1 Excavation Type 1 . . . 371
8.7.3.2 Excavation Type 2 . . . 380
8.7.3.3 Excavation Type 3 . . . 386
8.7.4 Soil stresses . . . 392
8.8 Summary . . . 405

**9 Summary and conclusions** **407**
9.1 Introduction . . . 407
9.2 General remarks . . . 407
9.3 A constitutive model for shotcrete . . . 410
9.4 Conclusions from tunnel analyses . . . 411
9.5 Recommendations for future research . . . 414

**Appendix** **417**

**References** **419**

# List of Figures


1.1 CTA concourse tunnel eye after the collapse (from HSE, 2000) . . . . . 30
1.2 a) Principal stress space and b) deviatoric plane (from Potts & Zdravković, 1999) . . . . . 36

2.1 New design philosophy for tunnels according to NATM (from Müller & Fecker, 1978) . . . . . 45
2.2 Simplified definition of principles and effects of NATM (from Sauer, 1988) . . 46
2.3 Different excavation sequences for NATM tunnel construction . . . . . 48
2.4 Longitudinal tunnel section showing excavation rounds for a bench-invert construction scheme (from ICE, 2004) . . . . . 49
2.5 Typical arrangement of convergence targets for tunnel lining (from Jones et al., 2008) . . . . . 50
2.6 Deformation examples of a roof lining (from Rokahr et al., 2005) . . . . . 51
2.7 Radial and tangential pressure cells (from Clayton et al., 2002 and Jones et al., 2005) . . . . . 52
2.8 Plane strain continuum model and charactersitic distribution of radial displacements $u$, radial stresses on the lining $\sigma_r$, hoop forces $N$ and bending moments $M$ (from Duddeck & Erdmann, 1982) . . . . . 55
2.9 The convergence-confinement method (after Oreste, 2003) . . . . . 56
2.10 Bedded ring model without bedding near the tunnel crown (from Duddeck & Erdmann, 1982) . . . . . 57
2.11 Bearing-capacity-diagram for tunnel lining (from Hoek, 2007) . . . . . 59
2.12 Composition of tunnel lining with the single-shell method (from Kusterle & Lukas, 1993) . . . . . 61
2.13 The LaserShell™ method (from Jones et al., 2008) . . . . . 62
2.14 TunnelBeamer™ system integration (from Eddie & Neumann, 2003) . . . . . 63
2.15 Principle of the stress relief method (from Potts & Zdravković, 2001) . . . . . 64
2.16 Principle of the stiffness reduction method (from Potts & Zdravković, 2001) . 65
2.17 Principle of the gap method (from Potts & Zdravković, 2001) . . . . . 65
2.18 Principle of the volume loss control method (from Potts & Zdravković, 2001) 66

3.1 8-noded isoparametric element used in ICFEP (from Potts & Zdravković, 1999) 71

3.2 Location of Gauss points for 2 x 2 and 3 x 3 integration order (from Potts & Zdravković, 1999) . . . 75
3.3 Basic principle of the modified Newton-Raphson scheme (after Potts & Zdravković, 1999) . . . 80
3.4 Basic principle of the substepping approach (from Potts & Zdravković, 1999) 81

4.1 Carl Akeley and his first cement-gun . . . 86
4.2 Recommended aggregate gradation zone from EFNARC (1996) . . . 89
4.3 Recommended cement content of shotcrete mix before installation depending on maximum aggregate size (from Aldrian, 1991) . . . 90
4.4 Relationship between compressive strength and water-cement ratio for concrete (from Karrer, 1986) . . . 91
4.5 Time dependent influence of accelerator dosage on compressive strength (from Kusterle, 1985) . . . 92
4.6 Different types of steel fibres used in sprayed concretes (from Banthia et al., 1992) . . . 94
4.7 Polypropylene fibres used in wet-mix sprayed concrete (from Austin & Robins, 1995) . . . 95
4.8 Schematic representation of the cement hydration (after Labahn, 1982) . . . 97
4.9 Process of dry-mix technology for sprayed concrete (from Austin & Robins, 1995) . . . 99
4.10 Process of wet-mix technology for sprayed concrete (from Austin & Robins, 1995) . . . 100
4.11 Different types of conveying systems for shotcrete (from Girmscheid, 2000) . 101
4.12 Preferred application procedure for sprayed concrete (from Girmscheid, 2000) 102
4.13 Effect of layer thickness on material rebound (from Parker et al., 1977) . . . 103
4.14 Effect of surface orientation on material rebound (from Girmscheid, 2000) . . 104
4.15 Test methods for compressive strength of young shotcrete according to ASCCT (2004) . . . 105
4.16 Proposed test method for uniaxial compressive strength and Young's modulus by Chang (1994) . . . 106

5.1 Typical plots of stress-strain curves for uniaxial compression (from Chen, 1982) ($f'_c = f_{cp}$) . . . 109
5.2 Influence of specimen length on post peak behaviour in uniaxial compression (from CEB-FIP Model Code, 1990) . . . 110
5.3 Relation between stress level and Poisson's ratio $\mu$ (from Chen, 1982) ($f'_c = f_{cp}$) 111
5.4 Stress-strain curves in tension for different concrete types (from Chen, 1982) . 111
5.5 Relation between uniaxial tensile and compressive strength (from Byfors, 1980) ($f_{ct} = f_{tp}$, $f_{cube} = f_{cp}$) . . . 112

5.6 Stress-strain relationships for concrete under biaxial compression (from Chen, 1982) ($f'_c = f_{cp}$) . . . 114
5.7 Biaxial failure envelope (from Kupfer & Gerstle, 1973) ($\beta_p = f_{cp}$) . . . 115
5.8 Triaxial yield and failure surface for concrete (from Chen, 1982) . . . 116
5.9 Spraying direction and loading conditions in a real tunnel lining . . . 117
5.10 Failure mechanism for steel fibre renforced shotcrete and concrete (from Ding & Kusterle, 2000) . . . 118
5.11 Uniaxial stress-deformation characteristics of fibre reinforced concrete (from Thomée, 2005) . . . 118
5.12 Compressive stress-strain curves for fibre reinforced concrete (from Strack, 2007) 119
5.13 Stress-strain curves for plain concrete and steel fibre reinforced concrete with 60 kg/m$^3$ at an age of 9 h (from Ding & Kusterle, 2000) . . . 120
5.14 Stress-strain curves in compression at different shotcrete ages (from Sezaki et al., 1989) . . . 121
5.15 Development of Young's modulus $E$ with shotcrete age obtained from various tests (from Chang, 1994) . . . 122
5.16 Relationship between stiffness and strength (from Byfors, 1980) ($E_{cc} = E$, $f_{cc} = f_{cp}$) . . . 124
5.17 Increase in stiffness with time according to various equations from the literature 125
5.18 Variation of Poisson's ratio with time (from Aydan et al., 1992) ($\nu = \mu$) . . . 126
5.19 Relation between Poisson's ratio and compressive strength (from Byfors, 1980) ($f_{cc} = f_{cp}$, $\nu_{cc} = \mu$) . . . 126
5.20 Development of uniaxial compressive strength, $f_{cp}$, with shotcrete age obtained from various tests (from Chang, 1994) . . . 127
5.21 Development of uniaxial compressive strength with time according to various equations from the literature . . . 129
5.22 Early-age strength classes for young shotcrete (after ASCCT, 2004) . . . 130
5.23 Ratio between tensile and compressive strength at early concrete ages (from Kasai et al., 1971) ($F_t = f_{tp}$, $F_c = f_{cp}$) . . . 131
5.24 Development of compressive strains at peak strength with uniaxial compressive strength and time (from Sezaki et al., 1989 and Thomas, 2003) . . . 133
5.25 Development of compressive peak strains with shotcrete age (from Wierig, 1971) 133
5.26 Development of tensile peak strains with shotcrete age (from Kusterle & Lukas, 1990) . . . 135
5.27 Ratio between tensile and compressive peak strain with compressive strength (from Byfors, 1980) ($f_{cc} = f_{cp}$, $\varepsilon_{cto} = \varepsilon_{tp}$, $\varepsilon_{cco} = \varepsilon_{cp}$) . . . 136
5.28 Reduction in gain of uniaxial compressive strength due to preloading (from Moussa, 1993) . . . 137
5.29 General form of strain development with time due to creep (from Neville, 1970) 138
5.30 Creep recovery at unloading (from Bosnjak, 2000) . . . 139

5.31 Possible values of creep Poisson's ratio $\mu_{cr}$ under uniaxial stress (from Neville, 1970) . . . 140
5.32 Factors influencing creep (from Byfors, 1980) . . . 142
5.33 Relative creep with age at loading (from Byfors, 1980) . . . 143
5.34 Creep for different stress levels (from Neville, 1970) . . . 144
5.35 Creep for different relative humidity (from Neville, 1981) . . . 145
5.36 Development of lining stresses during tunnel advance (from Pöttler, 1993) . . 146
5.37 Creep and relaxation during tunnel advance (from Rokahr & Lux, 1987) . . . 147
5.38 Concept of shrinkage induced stresses (from Malmgrem et al., 2005) . . . 148
5.39 Influence of water content on absolute values of shrinkage (from Neville, 1981) 150
5.40 Shrinkage of shotcrete (from Neubert & Manns, 1993) . . . 151
5.41 Influence of aggregate content in concrete on the ratio of shrinkage of concrete to the shrinkage of neat cement paste (from Neville, 1981) . . . 152
5.42 Influence of relative humidity on absolute values for shrinkage (from Neville, 1981) . . . 153
5.43 Temperature development in hardening concrete (from Mehta & Monteiro, 1985) 154
5.44 Age dependency for the coefficient of thermal expansion $\alpha_t$ (-/°C)(from Byfors, 1980) . . . 156

6.1 Stress-strain diagram for uniaxial compression (from CEB-FIP Model Code, 1990) . . . 159
6.2 Uniaxial compressive stress strain curves for concrete (from Desayi & Krishnan, 1964) . . . 161
6.3 Compressive stress-strain curves for different lateral confining pressures (from Attard & Setunge, 1996) . . . 162
6.4 Uniaxial compressive stress-strain curves for a) non-linear structural analysis and b) for the design of cross-sections (after EC 2, 2004) . . . 162
6.5 Variation of bulk and shear moduli with $\sigma_{oct}$ and $\tau_{oct}$ (from Kotsovos & Newman, 1978) . . . 165
6.6 Yield surface and stress states for elastic and elasto-plastic material behaviour 166
6.7 Rankine criterion in *J-p* (left) and principal stress space (right) . . . 172
6.8 Mohr-Coulomb failure criterion . . . 172
6.9 Mohr-Coulomb criterion in *J-p* (left) and principal stress space (right) . . . 174
6.10 Drucker-Prager criterion in *J-p* (left) and principal stress space (right) . . . 174
6.11 Yield and failure surfaces of Chen & Chen criterion in the principal (left) and biaxial stress space (right) (from Chen, 1982) . . . 175
6.12 Zoning of the stress state (from Chen, 1982) ($f'_c = f_{cp}$, $f'_t = f_{tp}$) . . . 178
6.13 Idealised uniaxial stress-strain curve for concrete (from Chen, 1982) ($f_c = f_{cy}$, $f'_c = f_{cp}$, $f_t = f_{ty}$, $f'_t = f_{tp}$) . . . 179
6.14 Early discrete crack modelling (from De Borst et al., 2004) . . . 181

6.15 Deformation characteristics of tensile post-peak behaviour . . . . . 182
6.16 Intrinsic material function for fracture energy (from Lackner & Mang, 2004) . 184
6.17 Stress-strain and stress-crack-opening diagram for uniaxial tension (from CEB-FIP Model Code, 1990) . . . . . 185
6.18 Some proposed stress-crack-opening relations (from Moussa, 1993) . . . . . 186
6.19 Models for reinforcement . . . . . 187
6.20 Principal effect of tension-stiffening on post-peak behaviour of concrete . . . 188
6.21 Stress-strain diagram for reinforced concrete in tension (from Gilbert & Warner, 1978) . . . . . 189
6.22 Material function for $\gamma$ depending on degree of hydration $\xi$ (from Lackner & Mang, 2003) . . . . . 190
6.23 Different stress-crack-opening relations for steel fibre reinforced concrete (from Thomée, 2005) . . . . . 191
6.24 Uniaxial tensile stress-crack-opening relation (from Thomée, 2005) . . . . . 192
6.25 Increase in fracture energy with fibre content (from Kazemi et al., 2007) . . . 193
6.26 Kelvin body . . . . . 195
6.27 Deformation response of Kelvin model . . . . . 196
6.28 Maxwell body . . . . . 196
6.29 Deformation response of Maxwell model . . . . . 197
6.30 Burger body . . . . . 197
6.31 Deformation response of Burger model . . . . . 198
6.32 Non-linear Kelvin model after Rokahr & Lux (1987) (from Hesser, 2000) . . . 199
6.33 Constitutive behaviour of shotcrete after Zheng (1989) (from Hesser, 2000) . 200
6.34 Non-linear Burger model (from Hauggaard et al., 1997) . . . . . 202
6.35 Functions for viscosity and stiffness in non-linear Burger model (from Hauggaard et al., 1997) . . . . . 202
6.36 Deformation history with time(from England & Illston, 1965) . . . . . 204
6.37 Deformation components for young shotcrete (from Schubert, 1988) . . . . . 205
6.38 Development of shrinkage strains with time (after ACI, 1992) . . . . . 208
6.39 Typical shrinkage curves given by Model B3 (from Bažant & Baweja, 1995) . 208
6.40 Principle of the HME-approach (from Karakus & Fowell, 2003) . . . . . 211
6.41 Stress-strain behaviour of young and old shotcrete (from Watson et al., 1999) 212
6.42 Proposed model for stress-strain history of shotcrete (from Moussa, 1993) . . 213
6.43 Loading surfaces of the viscoplastic material model for shotcrete (from Meschke et al., 1996) . . . . . 214
6.44 Intrinsic material functions of shotcrete (from Lackner et al., 2002) . . . . . 216
6.45 Yield surfaces and hardening law for chemoplasticity model for shotcrete (from Lackner et al., 2006) . . . . . 217

7.1 Compression and tension yield surfaces in a) the biaxial stress space and b) the $J$-$p$ space . . . 224
7.2 Apex rounding for tension surface in a) the biaxial stress space and b) the $J$-$p$ space . . . 225
7.3 Tip tolerance for apex region of tension surface . . . 226
7.4 Strain hardening concept for time-dependent matrials . . . 227
7.5 Normalised stress-strain curve for shotcrete in compression . . . 228
7.6 Fracture energy concept for shotcrete in compression . . . 230
7.7 a) Snap back behaviour for total stress-strain curve, b) Limited ultimate plastic compressive strain . . . 231
7.8 Critical value of the ultimate compressive strength for hardened concrete at 28 days . . . 231
7.9 Normalised hardening and softening curve in tension for option A . . . 233
7.10 Fracture energy concept for shotcrete in tension with linear softening . . . 234
7.11 Normalised hardening and softening curve in tension for option B . . . 235
7.12 Fracture energy concept for shotcrete in tension with exponential softening . . . 236
7.13 Increase in stiffness with time for various values of cement parameter $s$ . . . 238
7.14 Qualitative increase in compressive yield, peak, failure and ultimate strength with time . . . 239
7.15 Development of plastic uniaxial compressive peak strains with time . . . 240
7.16 Time-dependent rheological body for creep . . . 241
7.17 Development of creep strains with time upon loading at time $t_o$ . . . 242
7.18 Increase in shotcrete viscosity with time . . . 242
7.19 Creep potential surfaces and incremental creep strain vectors following a creep flow rule . . . 244
7.20 Adopted shrinkage model and the influence of parameter $B$ . . . 245
7.21 Development of $\Delta T$ with time . . . 246
7.22 Parameter fitting for increase in stiffness with time (after Huber, 1991) . . . 268
7.23 Parameter fitting for increase in compressive strength with time (after Huber, 1991) . . . 268
7.24 Parameter fitting for increase in stiffness with time (after Sezaki et al., 1989) 270
7.25 Parameter fitting for increase in compressive strength with time (after Sezaki et al., 1989) . . . 270
7.26 Parameter fitting for development of total peak and failure strains (after Sezaki et al., 1989) . . . 271
7.27 Parameter fitting for complete stress strain curves in compression for shotcrete at various ages (after Sezaki et al., 1989) . . . 272
7.28 Parameter fitting for development of creep deformation at various stages of hydration (after Kusterle, 1999) . . . 273
7.29 Parameter fitting for development of shrinkage deformation . . . 274

7.30 Parameter fitting for development of hydration temperature with time (from Huber, 1991) . . . 275
7.31 Comparison of model predictions with analytical solutions for increase in stiffness with time . . . 277
7.32 Comparison of model predictions with analytical solutions for stress-strain curves at different shotcrete ages . . . 278
7.33 Comparison of model predictions with analytical solutions for complete stress-strain curves at two different shotcrete ages . . . 279
7.34 Comparison of model predictions with analytical solutions for stress-strain curves in tension for various shotcrete ages (Option A) . . . 280
7.35 Comparison of model predictions with analytical solutions for stress-strain curves in tension for various shotcrete ages (Option B) . . . 280
7.36 Comparison of model predictions with analytical solutions for uniaxial and biaxial compressive loading at a shotcrete age of 6 h and 28 d . . . 281
7.37 Comparison of model predictions with analytical solutions for creep deformation ($n = 0.98$) . . . 283
7.38 Comparison of model predictions with analytical solutions for creep deformation with $n > 1$ . . . 283
7.39 Comparison of model predictions with analytical solutions for shrinkage deformation . . . 284
7.40 Comparison of model predictions with analytical solutions for hydration temperature induced strains . . . 285

8.1 Layout of tunnel geometry and ground conditions . . . 288
8.2 Three different excavation sequences for tunnel analyses . . . 289
8.3 Adopted $K_o$-profiles for performed analyses . . . 290
8.4 General layout of the 2D finite element mesh (without inner core) . . . 291
8.5 Two types of blocks forming the finite element mesh . . . 291
8.6 Zoom of mesh 1 for excavation Type 1: full face excavation . . . 292
8.7 Zoom of mesh 2 for excavation Type 2: bench-invert excavation . . . 293
8.8 Zoom of mesh 3 for excavation Type 3: sidewall drift . . . 293
8.9 Graphical representation of construction sequence for excavation Type 1 . . . 295
8.10 Graphical representation of construction sequence for excavation Type 2 . . . 296
8.11 Graphical representation of construction sequence for excavation Type 3 . . . 297
8.12 Development of total uniaxial compressive peak strains with time . . . 300
8.13 Variation of the shear and bulk moduli with strain level (from Potts & Zdravković, 1999) . . . 302
8.14 Variation of the compressive peak strains with time . . . 306
8.15 Analysed cross sections of tunnel lining for all three excavation sequences . . . 310

8.16 Zoom into connection point of temporary invert with tunnel lining for excavation Type 2 . . . . . 311
8.17 Investigated lining displacements for all three excavation sequences . . . . . 311
8.18 Surface settlements at end of tunnel excavation (Excavation Type 1, $K_o = 0.5$) 312
8.19 Surface settlements at end of tunnel excavation (Excavation Type 1, $K_o = 1.5$) 313
8.20 Predicted volume loss for both $K_o$-profiles adopting different shotcrete ages at the end of tunnel excavation (Excavation Type 1) . . . . . 314
8.21 Surface settlements for different developments of stiffness and strength of shotcrete with time (Excavation Type 1, $K_o = 0.5$) . . . . . 315
8.22 Surface settlements for different developments of stiffness and strength of shotcrete with time (Excavation Type 1, $K_o = 1.5$) . . . . . 315
8.23 Surface settlements for different shotcrete deformabilities (Excavation Type 1, $K_o = 0.5$) . . . . . 316
8.24 Surface settlements for analysis of creep, shrinkage and hydration temperature of shotcrete (Excavation Type 1, $K_o = 0.5$) . . . . . 317
8.25 Surface settlements for analysis of creep, shrinkage and hydration temperature of shotcrete (Excavation Type 1, $K_o = 1.5$) . . . . . 317
8.26 Surface settlements for various time-runs at the end of bench excavation (Inc 12, top) and end of invert excavation (Inc 25, bottom) . . . . . 319
8.27 Surface settlements after complete excavation for runs TPM 1 to 4 . . . . . 320
8.28 Surface settlements after complete excavation for various developments in stiffness and strength . . . . . 321
8.29 Surface settlements after complete excavation for various shotcrete deformabilities . . . . . 321
8.30 Surface settlements for various time-runs at the end of excavation of the left side gallery (Inc 12, top) and end of complete excavation (Inc 25, bottom) for excavation Type 3 . . . . . 324
8.31 Surface settlements after complete excavation for various developments of stiffness and strength for excavation Type 3 . . . . . 325
8.32 Surface settlements after complete excavation for various shotcrete deformabilities for excavation Type 3 . . . . . 326
8.33 Horizontal hoop stress distribution for crown at end of excavation (Inc 10) for $K_o = 0.5$ . . . . . 329
8.34 Horizontal hoop stress distribution for crown at end of loading (Inc 50) for $K_o = 0.5$ . . . . . 331
8.35 Vertical hoop stress distribution in right sidewall at end of excavation (Inc 10) for various developments of stiffness and strength adopting $K_o = 0.5$ . . . . . 332
8.36 Horizontal hoop stress distribution in invert at end of loading (Inc 50) for various developments of stiffness and strength adopting $K_o = 0.5$ . . . . . 333

8.37 Horizontal hoop stress distribution in crown at end of loading (Inc 50) for various developments of shotcrete deformability adopting $K_o = 0.5$ . . . . . 334
8.38 Vertical hoop stress distribution in right tunnel sidewall for analysis of creep, shrinkage and hydration temperature adopting $K_o = 0.5$ . . . . . 335
8.39 Horizontal hoop stress distribution in tunnel crown for analysis of creep, shrinkage and hydration temperature adopting $K_o = 0.5$ . . . . . 335
8.40 Vertical hoop stress distribution for right sidewall at end of excavation (Inc 10) for $K_o = 1.5$ . . . . . 337
8.41 Change in bending direction of tunnel lining due to tunnel excavation with initial stresses for $K_o = 1.5$ and surface loading . . . . . 338
8.42 Vertical hoop stress distribution for right sidewall at end of loading (Inc 50) for $K_o = 1.5$ . . . . . 339
8.43 Vertical hoop stress distribution in right sidewall at end of excavation (Inc 10) for various developments of stiffness and strength adopting $K_o = 1.5$ . . . . . 340
8.44 Horizontal hoop stress distribution in invert at end of loading (Inc 50) for various developments of stiffness and strength adopting $K_o = 1.5$ . . . . . 341
8.45 Horizontal hoop stress distribution in crown at end of loading (Inc 50) for various developments of shotcrete deformability $K_o = 1.5$ . . . . . 342
8.46 Vertical hoop stress distribution in right tunnel sidewall for analysis of creep, shrinkage and hydration temperature adopting $K_o = 1.5$ (Inc 100) . . . . . 343
8.47 Horizontal hoop stress distribution in tunnel crown for analysis of creep, shrinkage and hydration temperature adopting $K_o = 1.5$ (Inc 100) . . . . . 344
8.48 Stress level for different shotcrete ages at intrados of tunnel crown for both $K_o$-profiles . . . . . 345
8.49 Stress level for different shotcrete ages at intrados of tunnel sidewall for both $K_o$-profiles . . . . . 346
8.50 Stress level for different shotcrete ages at intrados of tunnel invert for both $K_o$-profiles . . . . . 347
8.51 Horizontal hoop stresses in tunnel invert for various time-runs at the end of invert excavation (Inc 25, top) and end of surface loading (Inc 65, bottom) . 351
8.52 Horizontal hoop stresses in temporary invert for various time-runs at the end of bench excavation (Inc 12) . . . . . 352
8.53 Horizontal hoop stresses in tunnel crown for time-runs TPM 1 to 4 at the end of invert excavation (Inc 25) . . . . . 353
8.54 Horizontal hoop stresses in tunnel crown for time-runs TPM 5 to 8 at the end of invert excavation (Inc 25) . . . . . 353
8.55 Horizontal hoop stresses in tunnel crown for time-runs TPM 9 to 12 at the end of invert excavation (Inc 25) . . . . . 354
8.56 Horizontal hoop stresses in tunnel invert for various developments of stiffness and strength at the end of surface loading (Inc 65) . . . . . 355

8.57 Horizontal hoop stresses in tunnel crown for various shotcrete deformabilty at the end of surface loading (Inc 65) . . . 356
8.58 Horizontal hoop stresses in tunnel crown for analysis of creep, shrinkage and hydration temperature . . . 357
8.59 Horizontal hoop stresses in tunnel invert for analysis of creep, shrinkage and hydration temperature . . . 358
8.60 Vertical hoop stresses in left sidewall for time-runs TPM 1 to 4 at the end of surface loading (Inc 65) . . . 361
8.61 Vertical hoop stresses in left sidewall for time-runs TPM 5 to 8 at the end of surface loading (Inc 65) . . . 362
8.62 Vertical hoop stresses in left sidewall for time-runs TPM 9 to 12 at the end of surface loading (Inc 65) . . . 363
8.63 Vertical hoop stresses in temporary sidewall at the end of excavation of the left side gallery (Inc 12) . . . 364
8.64 Vertical hoop stresses in right tunnel sidewall at the end of tunnel excavation (Inc 25) . . . 365
8.65 Vertical hoop stresses in right tunnel sidewall at the end of surface loading (Inc 65) . . . 365
8.66 Vertical hoop stresses in right sidewall at the end of surface loading (Inc 65) for various developments of stiffness and strength . . . 366
8.67 Vertical hoop stresses in left sidewall at the end of surface loading (Inc 25) for various shotcrete deformabilities . . . 367
8.68 Vertical hoop stresses in left tunnel sidewall for analysis of creep, shrinkage and hydration temperature (Inc 100) . . . 368
8.69 Vertical hoop stresses in right tunnel sidewall for analysis of creep, shrinkage and hydration temperature (Inc 100) . . . 369
8.70 Vertical crown displacement for various time runs adopting $K_o = 0.5$ (Excavation Type 1) . . . 373
8.71 Vertical invert displacement for variation in development of stiffness and strength with $K_o = 0.5$ . . . 374
8.72 Vertical crown displacement for variation in shotcrete deformability with $K_o = 0.5$ . . . 375
8.73 Horizontal displacement of right tunnel sidewall for various time runs adopting $K_o = 1.5$ . . . 377
8.74 Horizontal sidewall displacement for variation in development of stiffness and strength with $K_o = 1.5$ . . . 378
8.75 Vertical invert displacement for variation in shotcrete deformability with $K_o = 1.5$ . . . 379
8.76 Comparison of vertical crown displacements $v$ and horizontal sidewall displacements $u$ for both $K_o$-profiles for time run TPM 6 . . . 380

8.77 Vertical crown displacement for various time runs adopting $K_o = 1.5$ . . . . . 381
8.78 Vertical crown displacement for runs TPM 1 to 4 adopting $K_o = 1.5$ . . . . . 382
8.79 Horizontal displacement at the intersection of temporary invert with tunnel lining for various time runs adopting $K_o = 1.5$ . . . . . 383
8.80 Horizontal sidewall displacement for runs TPM 1 to 4 adopting $K_o = 1.5$ . . . 383
8.81 Vertical crown displacement for various developments of stiffness and strength adopting $K_o = 1.5$ . . . . . 384
8.82 Horizontal displacements of left sidewall . . . . . 387
8.83 Horizontal displacements of right sidewall . . . . . 388
8.84 Vertical displacement of intersection point of temporary sidewall with tunnel lining . . . . . 389
8.85 Vertical displacement of intersection point of temporary sidewall with tunnel lining for variousn developments of stiffness and strength . . . . . 390
8.86 Horizontal displacement of left sidewall for various shotcrete deformabilities . 391
8.87 Effective horizontal stresses in ground after excavation of tunnel (Inc 10) for linear elastic model (top) and run TPM 1 (bottom) adopting $K_o = 0.5$ . . . . 394
8.88 Effective vertical stresses in ground after excavation of tunnel (Inc 10) for linear elastic model LE (top) and run TPM 1 (bottom) adopting $K_o = 0.5$ . . 396
8.89 Sub-accumulated pore water pressures in ground after excavation of tunnel (Inc 10) for linear elastic model (top) and run TPM 1 (bottom) adopting $K_o = 0.5$ 398
8.90 Effective horizontal stresses in ground after excavation of tunnel (Inc 10) for linear elastic model (top) and run TPM 1 (bottom) adopting $K_o = 1.5$ . . . . 400
8.91 Effective vertical stresses in ground after excavation of tunnel (Inc 10) for linear elastic model LE (top) and run TPM 1 (bottom) adopting $K_o = 1.5$ . . 402
8.92 Sub-accumulated pore water pressures in ground after excavation of tunnel (Inc 10) for linear elastic model (top) and run TPM 1 (bottom) adopting $K_o = 1.5$ 404

# List of Tables


4.1 Influencing factors on rebound behaviour . . . . . 103

5.1 Parameters $a$ and $c$ for increase in Young's modulus $E$ with time (after Weber, 1979) . . . . . 122
5.2 Parameters $a$ and $b$ for development of Poisson's ratio $\mu$ (after Byfors, 1980 . 127
5.3 Parameters $a$ and $c$ for increase in uniaxial compressive strength, $f_{cp}$, with time (after Weber, 1979) . . . . . 128
5.4 Parameters $a$ and $b$ for development of peak strains with uniaxial compressive strength (after Byfors, 1980) . . . . . 135
5.5 Absolute values for plastic shrinkage (Relative humidity 50 %, Temperature 20 °C) (from Neville, 1981) . . . . . 149
5.6 Drying shrinkage after Hills, 1982 . . . . . 151
5.7 Maximum temperature rise as a function of layer thickness (after Kusterle & Lukas, 1993) . . . . . 154

6.1 $E_{ci}$, $E_{c1}$ and $\varepsilon_{c,lim}$ for various concrete grades after CEB-FIP Model Code (1990) 160
6.2 Material parameters for concrete taken from EC 2 (2004) . . . . . 163
6.3 Base values of fracture energy $G_{fo}$ from CEB-FIP Model Code (1990) . . . . 183
6.4 Coefficient $\alpha_f$ to estimate $w_c$ (from CEB-FIP Model Code, 1990) . . . . . 186

7.1 Summary of parameters for time-dependent plasticity model (all the strength and strain parameters are uniaxial parameters) . . . . . 248
7.2 Summary of model parameters for creep, shrinkage and thermal strains . . . 249
7.3 Summary of parameters for time-dependent elasticity model . . . . . 249
7.4 Mix design for tested shotcrete (from Huber, 1991) . . . . . 267
7.5 Cement parameter for increase in stiffness and strength fitted to test data from Huber (1991) . . . . . 269
7.6 Mix design for tested shotcrete (from Sezaki et al., 1989) . . . . . 269
7.7 Fitted stiffness and strength parameters . . . . . 272
7.8 Test series performed by Kusterle (1999) . . . . . 273
7.9 Fitted model parameters for predicting creep deformation . . . . . 274
7.10 Fitted model parameters for shrinkage deformation . . . . . 275
7.11 Fitted model parameters for temperature history . . . . . 276

7.12 Adopted model parameters for tensile behaviour . . . . . 279
7.13 Initial shotcrete ages for performed creep tests . . . . . 282
7.14 Model parameters for second test series of temperature history . . . . . 285

8.1 Summary for mesh 1, 2 and 3 . . . . . 294
8.2 Construction sequence for excavation Type 1 . . . . . 294
8.3 Construction sequence for excavation Type 2 . . . . . 295
8.4 Construction sequence for excavation Type 3 . . . . . 297
8.5 Basic strength parameters for shotcrete . . . . . 298
8.6 Numerical parameters for tension yield surface . . . . . 299
8.7 Basic deformability parameters for shotcrete . . . . . 299
8.8 Basic stiffness parameters for shotcrete . . . . . 300
8.9 Basic material parameters for creep, shrinkage and hydration temperature . . 301
8.10 Strength parameters for London Clay . . . . . 302
8.11 Stiffness parameters for London Clay . . . . . 302
8.12 Shotcrete ages for different time-runs for excavation Type 1 . . . . . 304
8.13 Tunnel runs simulating variation in stiffness and strength . . . . . 305
8.14 Tunnel runs simulating the variation in the development of shotcrete deformability with time . . . . . 305
8.15 Tunnel runs simulating creep, shrinkage and hydration temperature . . . . . 306
8.16 Shotcrete ages for different time-runs for excavation Type 2 . . . . . 307
8.17 Tunnel runs simulating the variation of increase in stiffness and strength and shotcrete deformability with time . . . . . 308
8.18 Tunnel runs simulating creep, shrinkage and hydration temperature for excavation Type 2 . . . . . 308
8.19 Shotcrete ages for different time-runs for excavation Type 3 . . . . . 309
8.20 Volume loss and maximum surface settlement for various time-runs at completion of tunnel excavation (Inc 25) for excavation Type 2 . . . . . 322
8.21 Volume loss and maximum surface settlement for various time-runs at completion of tunnel excavation (Inc 25) for excavation Type 3 . . . . . 327
8.22 Utilisation factor for variation in development of stiffness and strength for excavation Type 1 at end of surface loading ($K_o = 0.5$) . . . . . 348
8.23 Utilisation factor for variation in development of stiffness and strength for excavation Type 1 at end of surface loading ($K_o = 1.5$) . . . . . 348
8.24 Utilisation factor for variation in shotcrete deformability for excavation Type 1 at end of surface loading ($K_o = 0.5$) . . . . . 349
8.25 Utilisation factor for variation in shotcrete deformability for excavation Type 1 at end of surface loading ($K_o = 1.5$) . . . . . 349
8.26 Minimum and maximum principal stresses occurring in the intersection of the temporary invert with the tunnel lining at end of bench excavation (Inc 12) . 359

8.27 Utilisation factor of lining intrados at tunnel crown and invert for excavation Type 2 ($K_o = 1.5$) . . . . . 360
8.28 Minimum and maximum principal stresses occurring in the top intersection of the temporary sidewall with the tunnel lining at end of left side gallery excavation (Inc 12) . . . . . 370
8.29 Utilisation factor of lining intrados at left and right tunnel sidewall for excavation Type 3 ($K_o = 1.5$) . . . . . 371
8.30 Lining displacements of performed analyses for creep, shrinkage and hydration temperature adopting $K_o = 0.5$ . . . . . 375
8.31 Lining displacements of performed analyses for creep, shrinkage and hydration temperature adopting $K_o = 1.5$ . . . . . 379
8.32 Lining displacements of performed analyses for creep, shrinkage and hydration temperature . . . . . 385
8.33 Maximum vertical displacement $v$ of temporary invert at the end of bench excavation (Inc 12) . . . . . 386
8.34 Lining displacements of performed analyses for creep, shrinkage and hydration temperature . . . . . 391
8.35 Maximum horizontal displacement $u$ at the centre of the temporary sidewall at the end of the left side gallery excavation (Inc 12) . . . . . 392

# Chapter 1

# Introduction

## 1.1 General

Nowadays, major cities around the world are faced with an ever increasing amount of traffic. However, their relatively old infrastructure systems are often not capable of dealing with this problem due to limited space. Therefore, the construction of new underground infrastructure projects provides a possible solution and is becoming more important in urban planning, where the design of new tunnels plays a key role. One of the tunnelling techniques that has been applied successfully around the world is the New Austrian Tunnelling Method, usually abbreviated as NATM. The basic principle of this method is a sequent tunnel advance characterised by excavation and installation of supporting elements in order to stabilise the ground. One of the main support elements of NATM is sprayed concrete, often called shotcrete. Tunnel construction in an urban environment requires a safe and economic design, where the accurate calculation of stresses and ground movements that occur around geotechnical structures is of crucial importance. Often engineers are not only interested in the stresses and movements at failure, but also in the mechanical behaviour of the tunnel at different stages of construction and under working loads. Another big concern is the impact of a tunnel advance on existing structures either near to the ground surface or in the subsurface vicinity of the tunnel.

The finite element method as a particular type of numerical analysis is a technique, which is capable of dealing with complex soil-structure interaction problems and has been increasingly used in engineering practice over the last twenty years. However, although numerical analysis is a very powerful tool to analyse geotechnical structures such as tunnels, the interpretation of the results depends on the knowledge and experience of the user and the adopted constitutive laws for modelling the involved materials. For the simulation of soil behaviour significant advances have been made recently and sophisticated models exist that are able to reproduce the non-linear soil behaviour reasonably well. In the open literature it was observed that the situation seems to be completely different for modelling the behaviour of the tunnel lining. In most of the cases a tunnel shell made of cast concrete or shotcrete is

modelled as a linear elastic material, sometimes coupled with a step-wise increase in stiffness with time, which is basically a very crude assumption. In particular shotcrete shows a highly non-linear stress-strain behaviour at all stages of the hardening process during cement hydration.

Important developments have been made over the last decade in shotcrete technology by improving the quality of the constituent materials and the equipment used for installation. However, in the past the design of a shotcrete tunnel lining was mainly based on the experience of tunnel engineers - an approach which appeared to work well for deep tunnels excavated in rocks. When considering tunnel construction in soft ground conditions such as London Clay, a safe design of the whole structure can only be achieved by a realistic simulation of all the materials involved. Some elaborate sprayed concrete models have been developed recently, but a consistent framework for modelling shotcrete behaviour at early ages does not exist and there is a need for further developments including mathematical formulations and specific laboratory testing to validate models and fully understand the time-dependent material response of this special type of concrete.

## 1.2 Tunnel collapse at Heathrow Airport

Worldwide there have been a number of collapses and failures of NATM tunnels that led to serious damage to public buildings and infrastructure and even to human fatalities. One of the worst civil engineering disasters in the United Kingdom happened during the night of $20^{th}$ to the $21^{st}$ October 1994 (HSE, 2000). During this nightshift several tunnels undergoing construction beneath Heathrow Airport´s Central Terminal Area (CTA) collapsed completely. This incident caused severe damage to neighbouring buildings and structures, but luckily no one was injured. As a consequence all construction work came to a stop and some major short-term disruption to the airport followed. The tunnels were part of the Heathrow Express Rail Link Project, which is a high speed passenger service from central London (Paddington) directly to Heathrow Airport. Tunnel construction was being carried out according to the principles of the New Austrian Tunnelling Method (NATM) and compensation grouting had been used as additional ground treatment.

Extensive investigations were carried after the tunnel collapse by the Health and Safety Executive (UK) and their complete report can be found in HSE (2000). It was concluded that the direct cause of the incident was a chain of events which involved the following principal aspects:

- Poor design and planning
- Lack of quality during construction
- Lack of engineering control

- Lack of safety management

Kolymbas (1998) states, that a successful tunnel advance according to NATM requires the installation of a highly complex construction material, which is shotcrete. It was found that, in some parts of the collapsed tunnels at Heathrow Airport, the required material quality of the shotcrete lining was not achieved, mainly due to inexperienced and not properly trained workmen. Panels of the tunnel lining that were removed after the incident showed that the poor construction quality of the invert panels including joints was one of the key factors leading to failure. Fig. 1.1 shows the CTA concourse tunnel eye after the collapse. The complete lining has dropped leading to large settlements of the tunnel crown. Furthermore, the broken invert has rotated almost 90° and parts stand on end.



Figure 1.1: CTA concourse tunnel eye after the collapse (from HSE, 2000)

Visual inspection of the investigated panels provided evidence of some severe problems regarding the material quality of the shotcrete, which involved:

- Exposed reinforcement mesh in the surface of the shotcrete
- Thin sections of shotcrete where the design thickness of the lining was not achieved
- Inclusion of rebound material in the structure

After the failure, the question as to whether NATM and the use of shotcrete is a safe and proper construction method for tunnels in soft ground conditions beneath highly populated areas such as central London was debated at length. In HSE (2000) some lessons to be learned from this tunnel collapse are mentioned. However, the main conclusion is that all the parties involved in such a huge infrastructure project have to ensure that they have in place the culture, commitment, competence and health and saftey management systems to secure the risk control and the safe completion of the construction work (HSE, 2000; Kolymbas, 1998).

## 1.3 Aims of research

Following the discussion from the tunnel collapse at Heathrow Airport, the aim of this thesis was to get a better insight into the behaviour of shotcrete when used for tunnel construction in urban areas by applying the finite element method. To achieve this, the following steps have been involved:

- To perform an extensive literature review on the mechanical and time-dependent behaviour of concrete and in particular on young shotcrete at early ages. Furthermore, to get an overview of different approaches for simulating concrete and shotcrete behaviour in a numerical analysis and detect the key aspects that have to be considered when modelling such a material.
- Development of a sophisticated constitutive model for shotcrete that is capable of reproducing the main characteristics of sprayed concrete particularly at early ages. This includes a robust numerical implementation into a finite element code in order to apply the model to complex boundary value problems.
- Numerical investigation of the mechanical behaviour of shotcrete in tunnelling for various types of tunnel construction, with a particular focus on the lining behaviour.

## 1.4 Outline of thesis

The outline of the work presented in this thesis is the following:

The remaining part of this chapter aims to introduce the definitions of stress and strain variables used within this thesis. Furthermore, the applied terminology and a list of symbols are given to enable the reader to fully understand the presented theoretical background in Chapters 2 to 9.

In Chapter 2 the main principles of the New Austrian Tunnelling Method (NATM) are presented with a particular focus on tunnel construction in soft ground conditions. An overview about different tunnel lining design methods should enable the reader to understand the difficulties in achieving a safe design. Furthermore, some innovative tunnelling techniques using fibre-reinforced shotcrete are highlighted.

Chapter 3 presents a basic introduction into the finite element method applied for geotechnical engineering and describes the numerical algorithms that are used for the implementation of a constitutive model into the Imperial College Finite Element Program (ICFEP).

Chapter 4 deals with shotcrete technology and important topics regarding the appropriate mix design of sprayed concrete are presented. The components of this particular type of concrete are discussed individually with a reference to national standards and recommendations

that are available in the open literature. The impact of each of the concrete constituents on the mechanical behaviour of shotcrete is highlighted. A key point for describing the behaviour of shotcrete is to understand the process of cement hydration during the hardening phase of the material, which is explained briefly. Two existing methods of shotcrete installation are introduced (wet- and dry-mix techniques) with a particular focus on the use of sprayed concrete in tunnelling. Finally, the chapter gives a brief overview of different testing procedures of shotcrete at early ages in order to estimate values of the material properties needed for the design of shotcrete structures.

In Chapter 5 the main topic is the mechanical and time-dependent behaviour of concrete and shotcrete. Starting with simple uniaxial stress conditions both in compression and tension, it is then further explained, how the material behaves under biaxial and triaxial loading conditions, leading to smooth and convex failure surfaces in the principal stress space. Of great interest for designing a shotcrete tunnel lining is the mechanical behaviour of sprayed concrete at early ages. It is shown that with curing time a transition from a very ductile and plastic material at early ages to a relatively brittle material response of hardened shotcrete after 28 days can be expected. This transition is controlled by the increase in stiffness and strength and a reduction in material deformability with time. Furthermore, the chapter deals with important aspects related to time such as creep, shrinkage and hydration temperature induced deformation. The origin of the mechanisms for creep and shrinkage is believed to lie within the cement paste of the shotcrete and the influencing factors are discussed in detail. From the information available in the literature it can be expected that creep, shrinkage and thermal deformations can have an important impact on the mechanical behaviour of a shotcrete lining during tunnel advance. In particular, it is highlighted that young shotcrete is a very creep active medium, a fact which can lead to relatively low stresses within the tunnel lining.

Chapter 6 aims to introduce the reader to the numerical modelling of a quasi-brittle material such as concrete or shotcrete. At the beginning, a couple of mathematical functions for uniaxial stress-strain curves in compression fitted to experimental data are given. After a brief introduction into the theoretical background of elasto-plasticity, some simple constitutive models that are commonly used for modelling concrete in a finite element analysis are presented. One of these models is the Chen & Chen (1975) concrete model, which serves later in Chapter 7 as a starting point for the development of a constitutive model for shotcrete. Furthermore, it is discussed how to incorporate steel reinforcement in a numerical analysis and the so called "tension-stiffening effect" describing the interaction of concrete and steel is explained. The problems associated with modelling of cracking of concrete under tensile stresses are emphasized and an elegant fracture energy based approach to capture the post-peak behaviour is suggested. This chapter also deals with the modelling of creep, shrinkage and hydration temperature induced deformations. Some rheological models that are commonly used for describing creep effects are presented including complex viscosity functions

to realistically describe the creep behaviour of young shotcrete at early ages. However, it is shown that up to now no consistent framework exists for a simple extension of these uniaxial creep laws into 3D. Finally, a literature review about different constitutive models for shotcrete and their application to tunnelling available in the literature concludes this chapter.

In Chapter 7 a new sophisticated constitutive model for the behaviour of shotcrete that has been developed in this research project is presented. The model is based on an advanced elasto-plasticity model for hardened concrete, the so called Chen & Chen (1975) concrete model, and includes some important modifications in order to achieve a more realistic description of the material behaviour of young shotcrete. A detailed formulation of the model is given, discussing the involved independent yield functions for compression and tension, plastic potentials, hardening and softening rules and material parameters needed. Furthermore, it is shown that it is possible to calibrate this developed constitutive model for sprayed concrete against experimental data available in the literature in order to reproduce the main features of shotcrete behaviour at early ages. The necessary equations for a robust numerical implementation into ICFEP are given in this chapter and the model is validated through single element runs.

In Chapter 8 the above constitutive model for shotcrete is applied to a boundary value problem simulating a typical tunnel construction in London Clay. The results for three sets of analyses modelling different excavation sequences, i.e. full face, bench-invert and sidewall drift, are presented. Within this thesis the focus is mainly on the mechanical performance of the tunnel lining and through an extensive parametric study it has been possible to establish the main influencing parameters during tunnel construction. The presented results include surface settlements, stresses in the tunnel lining, displacements of selected points at the lining intrados and the utilisation factor (= stress level) within the shotcrete shell.

Finally, Chapter 9 provides a summary of the whole research project and the conclusions reached from the numerical work carried out in this thesis. It is complemented by some recommendations for future work to be done on the topic of shotcrete used for tunnelling.

## 1.5 Definition of stress and strain variables

In this part of the thesis the definitions of stress and strain variables and their notation are given. They are used for the presentation of the theoretical background of the different constitutive models for concrete and shotcrete in Chapter 6 and 7. It should be noted that throughout this work a tension positive sign convention has been applied.

Stress is a second order tensor, which is defined by six components and is given by the

following equation:

$$\sigma_{ij} = \begin{bmatrix} \sigma_x & \tau_{xy} & \tau_{xz} \\ \tau_{yx} & \sigma_y & \tau_{yz} \\ \tau_{zx} & \tau_{zy} & \sigma_z \end{bmatrix} \tag{1.1}$$

In this equation $\sigma$ represents a normal component of stress and $\tau$ a shearing component, where $\tau_{xy} = \tau_{yx}$, $\tau_{xz} = \tau_{zx}$ and $\tau_{zy} = \tau_{yz}$. The stress tensor can be divided into a volumetric and a deviatoric component:

$$\sigma_{ij} = \begin{bmatrix} \sigma_x & \tau_{xy} & \tau_{xz} \\ \tau_{yx} & \sigma_y & \tau_{yz} \\ \tau_{zx} & \tau_{zy} & \sigma_z \end{bmatrix} = \underbrace{\begin{bmatrix} p & 0 & 0 \\ 0 & p & 0 \\ 0 & 0 & p \end{bmatrix}}_{\text{Volumetric component}} + \underbrace{\begin{bmatrix} \sigma_x - p & \tau_{xy} & \tau_{xz} \\ \tau_{yx} & \sigma_y - p & \tau_{yz} \\ \tau_{zx} & \tau_{zy} & \sigma_z - p \end{bmatrix}}_{\text{Deviatoric component}} \tag{1.2}$$

In this equation $p$ is the mean stress given as:

$$p = \frac{1}{3}\left(\sigma_x + \sigma_y + \sigma_z\right) \tag{1.3}$$

Equation 1.2 can be rewritten in a compact form as:

$$\sigma_{ij} = p\,\delta_{ij} + s_{ij} \tag{1.4}$$

where $\delta_{ij} = \delta_{ji}$ is the Kronecker delta, which is defined as being equal to $+1$ if $i$ and $j$ are the same numbers and 0 otherwise. The deviatoric stress tensor $s_{ij}$ represents a state of pure shear and is expressed as:

$$s_{ij} = \begin{bmatrix} \sigma_x - p & \tau_{xy} & \tau_{xz} \\ \tau_{yx} & \sigma_y - p & \tau_{yz} \\ \tau_{zx} & \tau_{zy} & \sigma_z - p \end{bmatrix} \tag{1.5}$$

For materials which undergo isotropic behaviour, i.e. whose material properties are the same in all directions, it is often convenient to work with stress invariants, which are combinations of the different stress components. In geotechnical engineering one of these stress invariants is the mean stress $p$, which has already been introduced in equation 1.3. Furthermore, the following two stress invariants are commonly in use. The deviatoric stress invariant $J$ is given as:

$$J = \sqrt{\frac{1}{2}\left[\left(\sigma_x - p\right)^2 + \left(\sigma_y - p\right)^2 + \left(\sigma_z - p\right)^2 + 2\tau_{xy}^2 + 2\tau_{yz}^2 + 2\tau_{zx}^2\right]} \tag{1.6}$$

The Lode's angle $\theta$ is:

$$\theta = -\frac{1}{3}\sin^{-1}\left[\frac{3\sqrt{3}}{2}\frac{det(s_{ij})}{\left(\frac{1}{2}\left(s_{ij}s_{ij}\right)\right)^{\frac{3}{2}}}\right] \tag{1.7}$$

where $det(s_{ij})$ is the determinant of the deviatoric stress tensor and is obtained as:

$$det\,(s_{ij}) = \begin{vmatrix} \sigma_x - p & \tau_{xy} & \tau_{xz} \\ \tau_{yx} & \sigma_y - p & \tau_{yz} \\ \tau_{zx} & \tau_{zy} & \sigma_z - p \end{vmatrix} \tag{1.8}$$

If the coordinate axes are chosen to coincide with the principal stress axes, the stress tensor reduces to:

$$\sigma_{ij} = \begin{bmatrix} \sigma_1 & 0 & 0 \\ 0 & \sigma_2 & 0 \\ 0 & 0 & \sigma_3 \end{bmatrix} \tag{1.9}$$

and the three invariants are given as:

$$p = \frac{1}{3}(\sigma_1 + \sigma_2 + \sigma_3) \tag{1.10}$$

$$J = \frac{1}{\sqrt{6}}\sqrt{(\sigma_1 - \sigma_2)^2 + (\sigma_2 - \sigma_3)^2 + (\sigma_3 - \sigma_1)^2} \tag{1.11}$$

$$\theta = \tan^{-1}\left[\frac{1}{\sqrt{3}}\left(2\,\frac{(\sigma_2 - \sigma_3)}{(\sigma_1 - \sigma_3)} - 1\right)\right] \tag{1.12}$$

The geometrical significance of these stress invariants $p$, $J$ and $\theta$, is illustrated for the principal stress space in Fig. 1.2. Furthermore, the space diagonal ($\sigma_1 = \sigma_2 = \sigma_3$) and a deviatoric plane, defined as any plane perpendicular to the space diagonal, are indicated. It can be seen that the mean stress $p$ is a measure of the distance of the current deviatoric plane from the origin along the space diagonal. The deviatoric stress invariant $J$ measures the distance of the current stress state from the space diagonal in the deviatoric plane. Finally, the Lode's angle $\theta$ defines the orientation of the stress state within the deviatoric plane. It varies between +30°, which corresponds to triaxial extension ($\sigma_1 = \sigma_2 \geq \sigma_3$), and -30° for triaxial compression ($\sigma_1 \geq \sigma_2 = \sigma_3$).

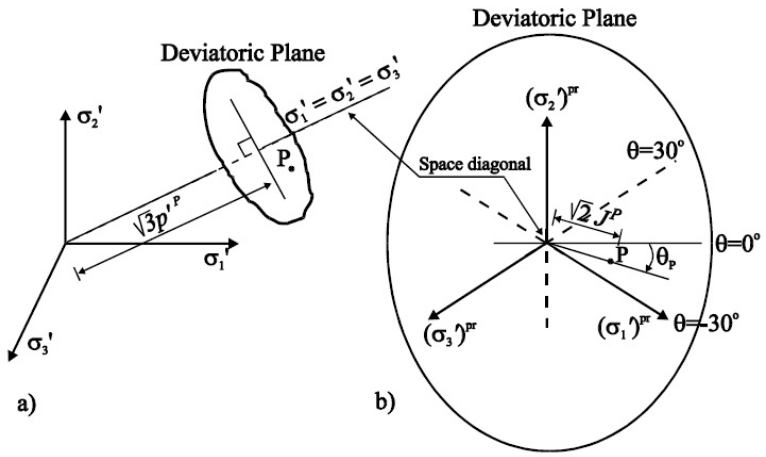



Figure 1.2: a) Principal stress space and b) deviatoric plane (from Potts & Zdravković, 1999)

It should be noted, that usually, when dealing with soil modelling the above introduced stresses and invariants are given as effective stresses in order to consider the pore water pressure $u$ by:

$$\sigma_{ij} = \sigma'_{ij} + \sigma_f \tag{1.13}$$

where $\sigma_{ij}$ is the total stress tensor, $\sigma'_{ij}$ the effective stress tensor and $\sigma_f$ is the vector of pore fluid (water) pressure given as:

$$\sigma_f = (u \quad u \quad u \quad 0 \quad 0 \quad 0 \quad )^T \tag{1.14}$$

In structural engineering a different set of stress invariants can often be encountered (Chen, 1982). For the general case the three invariants of the stress tensor can be written as:

$$I_1 = \sigma_x + \sigma_y + \sigma_z \tag{1.15}$$

$$I_2 = (\sigma_x\sigma_y + \sigma_y\sigma_z + \sigma_z\sigma_x) - {\tau_{xy}}^2 - {\tau_{yz}}^2 - {\tau_{zx}}^2 \tag{1.16}$$

$$I_3 = det\,(\sigma_{ij}) = \begin{vmatrix} \sigma_x & \tau_{xy} & \tau_{xz} \\ \tau_{yx} & \sigma_y & \tau_{yz} \\ \tau_{zx} & \tau_{zy} & \sigma_z \end{vmatrix} \tag{1.17}$$

which take the following form for the principal stress space

$$I_1 = \sigma_1 + \sigma_2 + \sigma_3 \tag{1.18}$$

$$I_2 = (\sigma_1\sigma_2 + \sigma_2\sigma_3 + \sigma_3\sigma_1) \tag{1.19}$$

$$I_3 = \sigma_1\sigma_2\sigma_3 \tag{1.20}$$

In a similar way, the invariants of the deviatoric stress tensor $s_{ij}$ can be derived as:

$$J_1 = s_{ii} = s_x + s_y + s_z = 0 \tag{1.21}$$

$$J_2 = \frac{1}{6}\left[(\sigma_x - \sigma_y)^2 + (\sigma_y - \sigma_z)^2 + (\sigma_z - \sigma_x)^2\right] + {\tau_{xy}}^2 + {\tau_{yz}}^2 + {\tau_{zx}}^2 \tag{1.22}$$

$$J_3 = det\,(s_{ij}) = \begin{vmatrix} s_x & \tau_{xy} & \tau_{xz} \\ \tau_{yx} & s_y & \tau_{yz} \\ \tau_{zx} & \tau_{zy} & s_z \end{vmatrix} \tag{1.23}$$

If the cartesian coordinate axes $x$, $y$ and $z$ coincide with the principal directions, the deviatoric invariants can be written as follows:

$$J_1 = s_1 + s_2 + s_3 \tag{1.24}$$

$$J_2 = \frac{1}{2}\left(s_1^2 + s_2^2 + s_3^2\right) = \frac{1}{6}\left[(\sigma_1 - \sigma_2)^2 + (\sigma_2 - \sigma_3)^2 + (\sigma_3 - \sigma_1)^2\right] \tag{1.25}$$

$$J_3 = \frac{1}{3}\left(s_1^3 + s_2^3 + s_3^3\right) = s_1 s_2 s_3 \tag{1.26}$$

From these invariants the Lode's angle used in structural engineering can be obtained as:

$$\theta_{st} = \frac{1}{3}\arccos\left(\frac{3\sqrt{3}}{2}\frac{J_3}{(\sqrt{J_2})^3}\right) \tag{1.27}$$

For the mathematical description of a failure criterion for concrete, special attention is usually given to the three independent invariants $I_1$, $J_2$ and $J_3$ (or $\theta_{st}$), which are of first, second and third degree in stress, respectively.

Kotsovos & Newman (1978) used in the formulation of their non-linear constitutive model for concrete (see Chapter 6) octahedral stresses which are defined as follows:

$$\sigma_{oct} = \frac{1}{3}(\sigma_1 + \sigma_2 + \sigma_3) \tag{1.28}$$

and

$$\tau_{oct}^2 = \frac{1}{9}\left[(\sigma_1 - \sigma_2)^2 + (\sigma_2 - \sigma_3)^2 + (\sigma_3 - \sigma_1)^2\right] \tag{1.29}$$

From the above definitions for the different stress invariants it can be summarized that:

$$p = \sigma_{oct} = \frac{1}{3}I_1 \tag{1.30}$$

and

$$J = \sqrt{\frac{3}{2}}\tau_{oct} = \sqrt{J_2} \tag{1.31}$$

Strain is like stress a second order tensor defined as well by six components:

$$\varepsilon_{ij} = \begin{bmatrix} \varepsilon_x & \frac{1}{2}\gamma_{xy} & \frac{1}{2}\gamma_{xz} \\ \frac{1}{2}\gamma_{yx} & \varepsilon_y & \frac{1}{2}\gamma_{yz} \\ \frac{1}{2}\gamma_{zx} & \frac{1}{2}\gamma_{zy} & \varepsilon_z \end{bmatrix} \tag{1.32}$$

where $\gamma_{xy} = \gamma_{yx}$, $\gamma_{xz} = \gamma_{zx}$ and $\gamma_{yz} = \gamma_{zy}$. The strain tensor can be divided into two components. The volumetric and the deviatoric components are given in the following equation:

$$\varepsilon_{ij} = \begin{bmatrix} \varepsilon_x & \frac{1}{2}\gamma_{xy} & \frac{1}{2}\gamma_{xz} \\ \frac{1}{2}\gamma_{yx} & \varepsilon_y & \frac{1}{2}\gamma_{yz} \\ \frac{1}{2}\gamma_{zx} & \frac{1}{2}\gamma_{zy} & \varepsilon_z \end{bmatrix} = \underbrace{\begin{bmatrix} e_v & 0 & 0 \\ 0 & e_v & 0 \\ 0 & 0 & e_v \end{bmatrix}}_{\text{Volumetric component}} + \underbrace{\begin{bmatrix} \varepsilon_x - e_v & \frac{1}{2}\gamma_{xy} & \frac{1}{2}\gamma_{xz} \\ \frac{1}{2}\gamma_{yx} & \varepsilon_y - e_v & \frac{1}{2}\gamma_{yz} \\ \frac{1}{2}\gamma_{zx} & \frac{1}{2}\gamma_{zy} & \varepsilon_z - e_v \end{bmatrix}}_{\text{Deviatoric component}} \tag{1.33}$$

In the above equation $e_v$ is equal to:

$$e_v = \frac{1}{3}(\varepsilon_x + \varepsilon_y + \varepsilon_z) = \frac{1}{3}\varepsilon_{vol} \tag{1.34}$$

with $\varepsilon_{vol}$ being the volumetric strain. Equation 1.33 can expressed in a different form as:

$$\varepsilon_{ij} = \frac{1}{3}\varepsilon_{vol}\delta_{ij} + e_{ij} \tag{1.35}$$

where $e_{ij}$ is the deviatoric strain tensor. It equals:

$$e_{ij} = \begin{bmatrix} \varepsilon_x - e_v & \frac{1}{2}\gamma_{xy} & \frac{1}{2}\gamma_{xz} \\ \frac{1}{2}\gamma_{yx} & \varepsilon_y - e_v & \frac{1}{2}\gamma_{yz} \\ \frac{1}{2}\gamma_{zx} & \frac{1}{2}\gamma_{zy} & \varepsilon_z - e_v \end{bmatrix} \tag{1.36}$$

The correspondent strain invariants to the earlier introduced stress invariants are the volumetric strain $\varepsilon_{vol}$, presented in equation 1.34, and the deviatoric strain $E_d$, which is given as:

$$E_d = \sqrt{2\left[(\varepsilon_x - e_v)^2 + (\varepsilon_y - e_v)^2 + (\varepsilon_z - e_v)^2 + \frac{1}{2}\gamma_{xy}^2 + \frac{1}{2}\gamma_{yz}^2 + \frac{1}{2}\gamma_{zx}^2\right]} \tag{1.37}$$

In terms of principal strains $\varepsilon_1$, $\varepsilon_2$ and $\varepsilon_3$ the strain invariants are given as follows:

$$\varepsilon_{vol} = \varepsilon_1 + \varepsilon_2 + \varepsilon_3 \tag{1.38}$$

and

$$E_d = \frac{2}{\sqrt{6}}\sqrt{(\varepsilon_1 - \varepsilon_2)^2 + (\varepsilon_2 - \varepsilon_3)^2 + (\varepsilon_3 - \varepsilon_1)^2} \tag{1.39}$$

## 1.6 Terminology and symbols used in thesis

When dealing with the academic literature concerning the material behaviour of concrete and shotcrete and its modelling for tunnelling one comes across many distinct approaches that differ not only in their basic assumptions and ideas but as well in terms of terminology, used symbols and graphical representations. Hence, when writing this thesis, from a scientific point of view, it was relatively difficult to find a consistent and clear formulation of all the concepts, models and principles that are presented within this work.

In this section the aim is to introduce the adopted terminology used throughout this thesis and provide some further information if a different notation or important symbols are encountered, a fact which is almost unavoidable. It should enable the reader to understand all the text, figures and tables that are presented in the following chapters.

| | |
|---|---|
| $\tilde{A}$ | Chemical affinity |
| $A_e$ | Area of finite element |
| $c$ | Cohesion |
| $D$ | Damage parameter |
| $[D]$ | Constitutive matrix |
| $d$ | Displacement (Chapter 3) |
| $d_{max}$ | Maximum aggregate size |
| $e_{ij}$ | Deviatoric strain tensor |
| $\Delta E$ | Incremental total potential energy |
| $E$ | Young's modulus of elasticity |
| $E_{28}$ | Young's modulus of elasticity for hardened shotcrete at 28 days |
| $E_c$ | Young's modulus of elasticity (Chapter 4) |
| $E_{ci}$ | Young's modulus of elasticity ($= E$) |
| $E_{cc}$ | Young's modulus of elasticity ($= E$) |
| $E_{cm}$ | Secant Young's modulus of elasticity (at $0.4\, f_{cm}$) (CEB-FIP Model Code, 1990) |
| $E_{c1}$ | Secant Young's modulus of elasticity from origin to the peak compressive strength (CEB-FIP Model Code, 1990) |
| $E_d$ | Deviatoric strain |
| $E_k$ | Stiffness of Kelvin spring |
| $E_m$ | Stiffness of Maxwell spring |
| $f_c$ | Uniaxial compressive stress |
| $f$ | Uniaxial compressive stress ($=f_c$) |
| $f_{cp}$ | Uniaxial compressive strength |
| $f_o$ | Uniaxial compressive strength ($=f_{cp}$) |
| $f_{cp,28}$ | Uniaxial compressive strength of hardened shotcrete at 28 days |
| $f_{cp,1}$ | Uniaxial compressive strength of shotcrete at 1 day |

| | |
|---|---|
| $f'_c$ | Uniaxial compressive strength ($= f_{cp}$) |
| $f_{cc}$ | Uniaxial compressive strength ($= f_{cp}$) |
| $f_{cube}$ | Uniaxial compressive cube strength ($= f_{cp}$) |
| $f_{ck}$ | Characteristic uniaxial compressive strength, i.e. strength below which 5 % of all possible strength measurements for a specified concrete may be expected to fall (CEB-FIP Model Code, 1990) |
| $f_{ck,c}$ | Characteristic confined compressive strength (EC 2, 2004) |
| $f_{cd}$ | Uniaxial compressive design strength (EC 2, 2004) |
| $f_{cm}$ | Mean value of the uniaxial compressive strength, $f_{cm} = f_{ck}+8$ MPa (CEB-FIP Model Code, 1990) |
| $f_{cy}$ | Uniaxial compressive yield stress |
| $f_{cy}^{28}$ | Uniaxial compressive yield stress for hardened shotcrete at 28 days |
| $f_{bc}$ | Biaxial compressive strength |
| $f_{bcy}$ | Biaxial compressive yield strength |
| $f_t$ | Unixial tensile stress |
| $f_{tp}$ | Uniaxial tensile strength |
| $f_{ct}$ | Uniaxial tensile strength ($= f_{tp}$) |
| $f_{ctm}$ | Mean value of the uniaxial tensile strength ($= f_{tp}$) (CEB-FIP Model Code, 1990) |
| $f_{ct,sp}$ | Mean value of the splitting tensile strength (CEB-FIP Model Code, 1990) |
| $f_{ct,fl}$ | Mean value of the flexural tensile strength (CEB-FIP Model Code, 1990) |
| $G_f$ | Fracture energy |
| $G_{f1}$ | Fracture energy of plain concrete |
| $G_{f2}$ | Fracture energy related to the contribution of steel fibres |
| $G_c$ | Fracture energy in compression |
| $G_{fo}$ | Base value of fracture energy |
| $G_f^{rc}$ | Fracture energy of reinforced concrete |
| $G_f^{fr}$ | Fracture energy of fibre reinforced concrete |
| $G_{SFRS}$ | Fracture energy of fibre reinforced shotcrete |
| $G$ | Shear modulus |
| $HME$ | Hypothetical Modulus of Elasticity |
| $I_1$, $I_2$, $I_3$ | Stress invariants in structural engineering |
| $J$ | Deviatoric stress invariant |
| $J_1$, $J_2$, $J_3$ | Invariants of deviatoric stress tensor in structural engineering |
| $[J]$ | Jacobian matrix |
| $[K_E]$ | Element stiffness matrix |
| $[K_G]$ | Global stiffness matrix |
| $K$ | Bulk modulus |
| $K_f$ | Bulk modulus of the pore fluid |
| $K_o$ | Coefficient of earth pressure at rest |

| | |
|---|---|
| $K_r$ | Spring stiffness |
| $K_{skel}$ | Bulk modulus of the soil skeleton |
| $\Delta L$ | Incremental work done by applied loads (Chapter 3) |
| $l_{eq}$ | Equivalent length of finite element |
| $l_{eq}^{rc}$ | Equivalent length of finite element for reinforced concrete |
| $l_s$ | Average crack spacing |
| $M$ | Bending moment |
| $N$ | Hoop force |
| $[N]$ | Matrix of shape functions |
| $n_{int}$ | Number of integration points per element ($= n_{IP}$) |
| $p$ | Mean stress |
| $p$ | Internal wall pressure (Chapter 2) |
| $p_o$ | In-situ isotropic stress in the ground before tunnel excavation |
| $p_{eq}$ | Equilibrium pressure acting on tunnel lining |
| $r$ | Degree of hydration ($= \xi$) |
| $\{\Delta R\}$ | Right hand side load vector |
| $RH$ | Relative humidity |
| $R_{dfc}$ | Reduction of compressive strength to be gained between $t_1$ and $t_2$ due to preloading |
| $s_{ij}$ | Deviatoric stress tensor |
| $S$, $T$ | Natural coordinates (Chapter 3) |
| $T$ | Temperature |
| $u$ | Radial displacement (Chapter 2) |
| $u$, $v$ | Horizontal and vertical displacements (Chapter 3) |
| $u_{in}$ | Initial radial wall displacement |
| $V(\sigma, t)$ | Non-linear deformation modulus |
| $V_e$ | Volume of finite element (Chapter 5) |
| $V_e$ | Excavated tunnel volume (Chapter 2) |
| $V_L$ | Volume loss |
| $V_S$ | Volume of the surface settlement trough |
| $W_f$ | Fibre content |
| $\Delta W$ | Incremental strain energy |
| $w$ | Crack opening |
| $w_u$ | Complete crack opening |
| $w_c$ | Complete crack opening ($= w_u$) |
| $x$, $y$ | Coordinates |
| $\alpha_t$ | Coefficient of thermal expansion |
| $\beta$ | Stiffness reduction factor |
| $\beta_p$ | Uniaxial compressive strength ($= f_{cp}$) |
| $\delta_{ij}$ | Kronecker delta |

| | |
|---|---|
| $\varepsilon_c$ | Uniaxial compressive strain |
| $\varepsilon_{cp}$ | Uniaxial compressive peak strain |
| $\varepsilon_{cr}$ | Creep strain |
| $\varepsilon_o$ | Uniaxial compressive peak strain (=$\varepsilon_{cp}$) |
| $\varepsilon_{c1}$ | Uniaxial compressive peak strain (=$\varepsilon_{cp}$) (EC 2, 2004) |
| $\varepsilon_{c2}$ | Uniaxial compressive peak strain (=$\varepsilon_{cp}$) (EC 2, 2004) |
| $\varepsilon_{c2,c}$ | Compressive peak strain for confined stress conditions (EC 2, 2004) |
| $\varepsilon_u$ | Ultimate uniaxial compressive strain |
| $\varepsilon_{cu1}$ | Ultimate uniaxial compressive strain (EC 2, 2004) |
| $\varepsilon_{cu2}$ | Ultimate uniaxial compressive strain (EC 2, 2004) |
| $\varepsilon_{cu2,c}$ | Ultimate compressive strain for confined stress conditions (EC 2, 2004) |
| $\varepsilon_{cco}$ | Uniaxial compressive peak strain (=$\varepsilon_{cp}$) |
| $\varepsilon_{ij}$ | Strain tensor |
| $\varepsilon_{tp}$ | Uniaxial tensile peak strain |
| $\varepsilon_{cto}$ | Uniaxial tensile peak strain (=$\varepsilon_{tp}$) |
| $\varepsilon^p$ | Plastic strain |
| $\varepsilon_v$ | Effective strain |
| $\varepsilon_{vol}$ | Volumetric strain |
| $\eta$ | Safety factors |
| $\eta_k$ | Viscosity of Kelvin dashpot |
| $\eta_m$ | Viscosity of Maxwell dashpot |
| $\kappa$ | Internal damage parameter (Chapter 5) |
| $\lambda$ | Stress relief factor |
| $\mu$ | Poisson's ratio |
| $\mu_{cr}$ | Creep Poisson's ratio |
| $\nu$ | Poisson's ratio (= $\mu$) |
| $\nu_{cc}$ | Poisson's ratio (= $\mu$) |
| $\phi$ | Friction angle |
| $\phi$ | Surface orientation (Chapter 4) |
| $\phi(t, t_o)$ | Creep coefficient |
| $\rho_c$ | Compressive utilization factor |
| $\rho_t$ | Tensile utilization factor |
| $\sigma_f$ | Vector of pore water pressure |
| $\sigma_{ij}$ | Stress tensor |
| $\sigma_c$ | Uniaxial compressive stress (= $f_c$) |
| $\sigma_c$ | Uniaxial compressive strength (Chapter 4) (= $f_{cp}$) |
| $\sigma_{ct}$ | Uniaxial tensile stress (= $f_t$) |
| $\sigma_{oct}$ | Octahedral stress |
| $\sigma_r$ | Radial stress on lining |

| | |
|---|---|
| $\sigma_t$ | Uniaxial tensile stress ($= f_t$) |
| $\bar{\sigma}_{Re}$ | Uniaxial tensile stress ($= f_t$) |
| $\sigma_v$ | Effective stress |
| $\tau_{oct}$ | Octahedral stress |
| $\theta$ | Lode's angle |
| $\theta_{st}$ | Lode's angle in structural engineering |
| $\{\psi\}$ | Residual load vector (Chapter 3) |
| $\xi$ | Degree of hydration |

# Chapter 2

# Tunnelling in urban areas

## 2.1 Introduction

This chapter aims to introduce the reader to various aspects related to the challenging field of tunnelling in soft ground conditions which can be regularly encountered in urban areas. Since shotcrete is one of the main support elements of the New Austrian Tunnelling Method (NATM), the historical background and the main concepts behind this special tunnelling technique will be briefly highlighted. Although NATM should not be regarded as a particular construction method for tunnels, the main steps of the construction procedure for tunnels in urban areas applying shotcrete for temporary support are presented. Furthermore, geotechnical observation and monitoring are of great importance for a safe assessment of the system behaviour during tunnel advance. Several techniques for measuring displacements of and stresses in a shotcrete tunnel lining and the difficulties associated with the correct interpretation of the obtained results are discussed. A review of tunnel lining design approaches that are common in engineering practice, including empirical, analytical and numerical procedures, are given. The single-shell method as a new economic tunnelling technology is introduced, describing briefly some innovative trends for sprayed concrete lined tunnels that have been developed recently. Finally, the presentation of some modelling techniques to account for 3D effects in a 2D plane strain analysis concludes this chapter.

## 2.2 The New Austrian Tunnelling Method

The New Austrian Tunnelling Method (NATM) is a worldwide recognized tunnelling technique developed during 1957 - 1965, where Austrian engineers (Rabcewicz, Pacher, Müller) have taken a decisive part in its development. It has its origin in rock tunnelling, where tunnel construction under heavy rock pressure could successfully be handled by employing the surrounding rock as a part of the support system, which is believed to be one of the main concepts of the NATM. However, in the tunnelling industry confusion still exists regarding a successful and safe application of NATM for tunnnelling in soft ground conditions since there

is a lack of understanding of the essential features and concepts behind NATM. In their paper Karakus & Fowell (2004), try to give an insight into the New Austrian Tunnelling Method by investigating its historical background, main concepts and design philosophy. Furthermore, they raise important questions such as "What is NATM?" and "Is NATM a tunnelling technique or a design philosophy?". Some definitions and ideas found in the literature describing the NATM are presented below.

The original explanation of the method, given by one of the principal inventors of NATM, is stated in Rabcewicz (1964) as:

*... a new method consisting of a thin sprayed concrete lining, closed at the earliest possible moment by an invert to a complete ring - called an "auxiliary arch" - the deformation of which is measured as a function of time until equilibrium is obtained.*

In this publication the use of shotcrete as a ground support element is emphasised with its feature against loosening and stress-rearrangement pressures through an immediate application after opening and the interaction with the neighbouring rock highlighted (see Fig. 2.1).

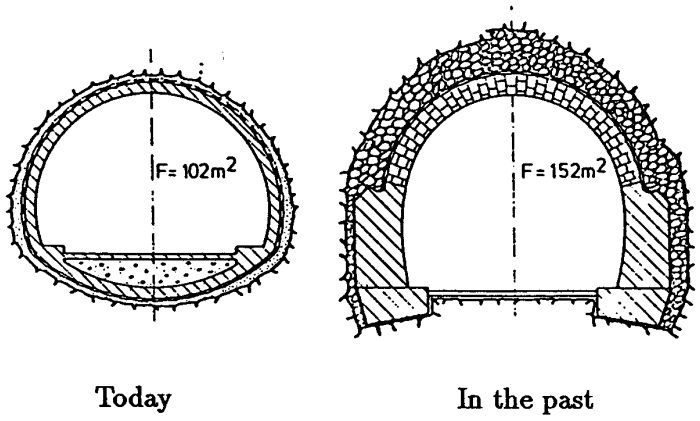



Figure 2.1: New design philosophy for tunnels according to NATM (from Müller & Fecker, 1978)

As the popularity of the technique grew and it began to be practised more widely, some confusion developed as to what was meant by NATM. Therefore the ÖIAV (1980) published a definition in cooperation with the International Tunnelling Association (ITA) in 10 languages, saying:

*The New Austrian Tunnelling Method constitutes a method where the surrounding rock or soil formations of a tunnel are integrated into an overall ring-like support structure. Thus the formations will themselves be part of this supporting structure.*

One of the other Austrian advocates, Prof. Müller, contributed to the international discussion trying to overcome misunderstandings of the NATM by publishing the following definition in Müller (1990):

*The NATM is rather a tunnelling concept with a set of scientifically established principles and ideas which the tunneller tries to follow and should not even be called a construction method, since this implies a method of driving a tunnel.*

Furthermore, he summarized the most characteristic features of the NATM in a list of 22 principles. The most important of these are as follows:

1. The main load bearing component of a tunnel is the surrounding rock mass. Preliminary support and final lining have the function of establishing a load-bearing ring or a three-dimensional spherical bearing shell in the rock mass.

2. Additional support elements should be used to preserve the support resistance of the rock mass and therefore prevent loosening and extensive rock deformations.

3. The thickness of the shotcrete layer should be as thin and flexible as possible and additional strengthening should be obtained by using mesh reinforcement, tunnel ribs and anchors, rather than thickening the lining.

4. The ring closure time is of crucial importance from a mechanical point of view and should be done as soon as possible.

5. In order to optimize the formation of the ground ring, preliminary laboratory tests and deformation measurements in the tunnel should be carried out.

However, his conclusion about the rapid ring closure time in deep tunnels to minimise displacements was not agreed by other engineers (Rabcewicz, Golser). A graphical simplified representation of the principles and effects of NATM can be seen in Fig. 2.2.

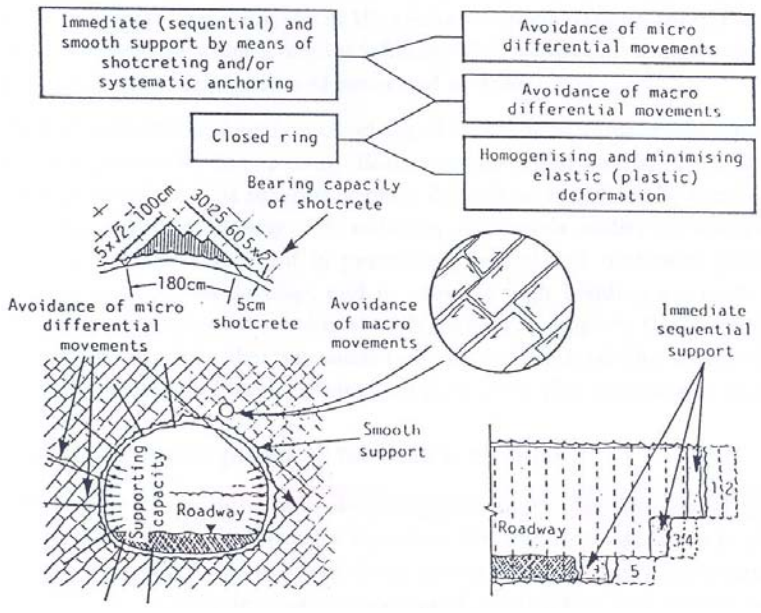



Figure 2.2: Simplified definition of principles and effects of NATM (from Sauer, 1988)

Summarising, the following major principles of NATM can be derived from ICE (1996) and HSE (1996):

1. The inherent strength of the soil or rock around the tunnel domain should be preserved and deliberately mobilised to the maximum extent possible.

2. This mobilisation can be achieved by controlled deformation of the ground although excessive deformations which will result in loss of strength or high surface settlements must be avoided.

3. Initial and primary support elements consisting of systematic rock bolting or anchoring and thin flexible shotcrete linings are used to achieve the particular purposes given in (2). Permanent support works are usually carried out at a later stage.

4. Laboratory tests and monitoring of the deformations of supports and ground should be carried out before and during construction.

5. The responsable engineers involved in the execution, design and supervision of NATM construction must understand and accept the NATM approach and react co-operatively on resolving problems.

6. The length of the unsupported span should be left as short as possible.

Having these main principles of NATM in mind and involving the boundary conditions of each tunnel project (ground conditions, geometrical conditions, settlement restrictions, etc.), one can perform the design of the structural elements and a specific construction process. Nevertheless, it is always very important to distinguish between NATM tunnelling in rock and in soft ground formations, as some points of the above mentioned concept may not be applicable for one or the other ground condition. For this reason, tunnels in soft ground conditions constructed with shotcrete as a main support element are often referred to as "sprayed concrete lined tunnels", or shortly SCL tunnels (Thomas, 2009).

For tunnelling in urban areas limiting surface settlements is one of the main concerns in order to avoid damage to overlying structures. For achieving this, according to ICE (1996) the following principal measures must be undertaken:

- Excavation stages must be sufficiently short, both in terms of dimensions and duration.
- The closure of the sprayed concrete ring must not be delayed.

The flexibility of NATM in soft ground conditions is limited to a certain extent, since design details about the primary support are determined by the designer and then not usually varied. The only aim of tunnel instrumentation and monitoring is therefore to validate the anticipated design without changing it during tunnel advance. It can be concluded that tunnelling in urban areas often follows the construction techniques usually associated with NATM, but does not necessarily employ the entire concept and principles of the New Austrian Tunnelling Method.

## 2.3 Typical tunnel construction process in urban areas

For NATM tunnels in urban areas, construction usually starts from a previously built vertical shaft, which serves as access for personnel and machines and for the removal of excavated material. If ground conditions permit, the full tunnel face is excavated, which is suitable for tunnels up to 30 $m^2$ of face area (ICE, 1996). For tunnelling in overconsolidated fissured clays, such as London Clay, vertical face excavation is usually limited to tunnel diameters of 4 m. If necessary, a full face advance with an inclined face of 60° to 70° is applied. A similar stabilising effect can be achieved by dividing the cross section into a number of small faces - typically crown, bench and invert. Different partial face excavation techniques can be seen in Fig. 2.3.

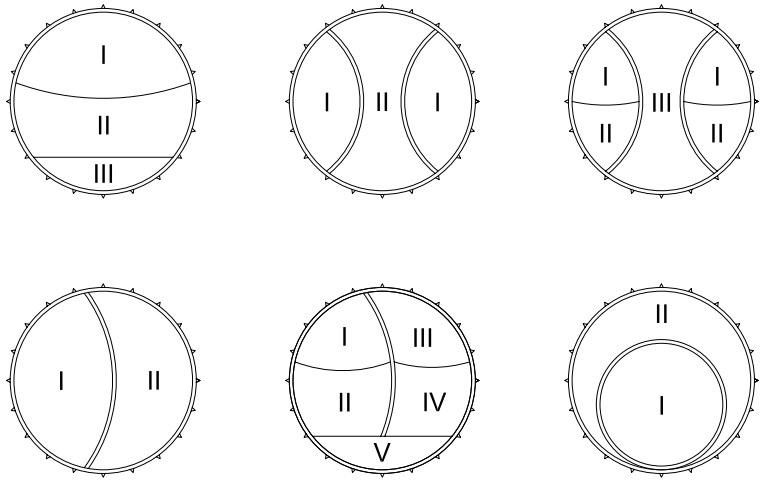



Figure 2.3: Different excavation sequences for NATM tunnel construction

Excavation of the tunnel is incrementally advanced in rounds with a variable length of about 0.5 to 1.5 m, 1 m being a common target (see longitudinal tunnel section in Fig. 2.4). It has been shown that the advance length has a significant influence on stability and settlement behaviour and keeping the support close to the face results in an improvement of settlement control. Directly after excavation shotcrete is sprayed at a high pressure on to the tunnel walls. Generally a 50 mm sealing layer is first applied followed by two layers, each reinforced by steel mesh and forming a typical NATM lining thickness of 20 to 40 cm. As an additional support element, steel lattice girders can be incorporated into the lining to provide some extra stiffness to the support system. They are also used for the correct profiling of the cross section and to achieve the correct shotcrete thickness. Another important factor for soft ground tunnelling at shallow depths is the advance rate and the ring closure times, which appear to vary between 8 and 24 hours from completion of an excavation advance (ICE, 1996). The secondary or final tunnel lining formed of conventional cast concrete is usually installed at a later stage of construction.

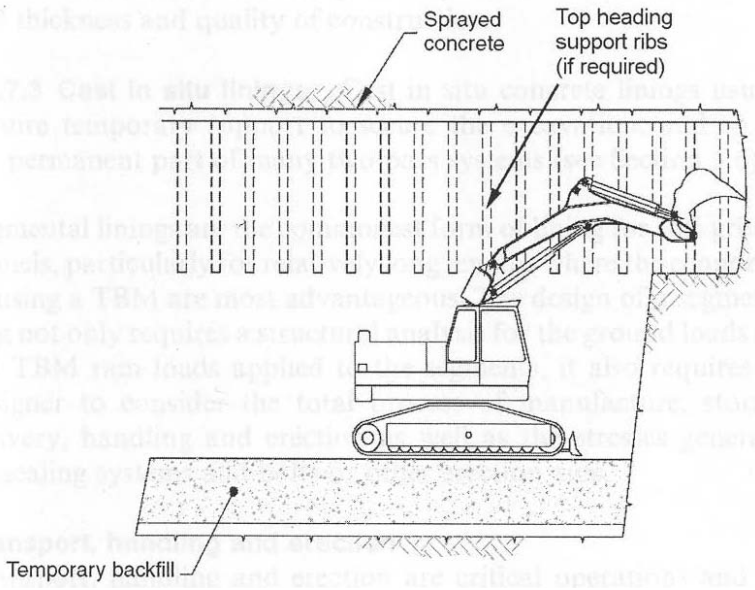



Figure 2.4: Longitudinal tunnel section showing excavation rounds for a bench-invert construction scheme (from ICE, 2004)

## 2.4 The importance of monitoring in tunnelling

As mentioned earlier, observation of the tunnel behaviour during construction using geotechnical measurements is a key element of the NATM and serves as an assessment of the stability of the whole structure. Therefore, extensive instrumentation is nowadays common practice for underground projects, but difficulties remain with the right interpretation of all the measured field data (Rokahr et al., 2005).

Clayton et al. (2000) highlight four principal purposes of field instrumentation and monitoring for shallow shotcrete tunnels in soft ground conditions, which are:

1. Examination of the actual performance and safety of the soil-primary lining system and to assess whether the design is valid.

2. Detection of anomalous behaviour and to provide information upon which remediation in response to unforeseen conditions or behvaiour can be reliably and safely based.

3. To determine whether design modifications, particularly strengthening works or construction details such as advance length, are necessary.

4. To control the day-to-day application of compensation grouting which is commonly used to reduce surface settlements.

The type of instrumentation used during the construction of a tunnel depends highly on the objectives of the monitoring programme, which can be different for each individual project.

Therefore, a detailed monitoring scheme should be set up that meets the prescribed requirements. For the correct choice of an instrument it is important to have in mind its performance under site conditions and the demanded accuracy of certain parameters to be measured. An example of such a detailed monitoring programme at Heathrow Express Terminal 4 can be found in Clayton et al. (2006). The following two sections of this chapter focus mainly on the monitoring of the shotcrete tunnel lining and the right interpretation of the measured data.

### 2.4.1 Measuring and interpretation of displacements

Tunnel wall convergence between reference points bolted on the tunnel lining is usually measured with standard metal tape extensometers having an accuracy of $\pm 0.2$ mm for distances of up to 10 to 15 m (Kavvadas, 2003). However, in most tunnelling projects deformations of the lining are measured in three dimensions by the use of geodetic surveying with total stations and integrated distance measurement. For such applications, optical targets are installed, as illustrated in Fig. 2.5, at regular distances along the tunnel axis, i.e. at sections every 5 to 15 m, showing an accuracy of $\pm 2 - 3$ mm (Jones et al., 2008). One big advantage of this method is that readings of absolute, three dimensional movements can be made from an observation station located outside the area of intensive construction activity (Clayton et al., 2000).

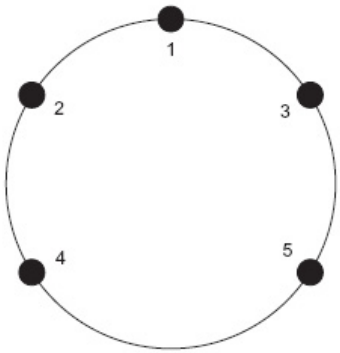



Figure 2.5: Typical arrangement of convergence targets for tunnel lining (from Jones et al., 2008)

One big problem in measuring lining displacements is the start of monitoring, which usually happens a certain amount of time after installation of the shotcrete. However, most of the stress rearrangement and tunnel lining displacements occur before ring closure, since the incomplete ring made of young shotcrete represents a much weaker bearing system than the closed ring, which acts from the structural point of view as a tube. Therefore, some practical diffulties still exist in gaining satisfactory access to the congested working area at the face in order to obtain early displacement measurements that would give a considerable insight into the behaviour of the tunnel.

Once the displacements of the lining are monitored, engineers on site are left with a large

amount of information that has to be carefully interpreted. Usually displacement histories, deflection curves or cross-sectional displacement vectors should enable the responsible engineers to understand the system behaviour during tunnel advance, and react accordingly if critical target values are reached (Schubert & Grossauer, 2004). The assessment of the stability of a tunnel with the help of displacement monitoring is a difficult task, as highlighted by Rokahr et al. (2005). Fig. 2.6 illustrates the need for a proper understanding of the complete system behaviour by showing various possible displacement patterns of a roof lining. In case $A$, the tunnel crown and the left and right footings indicate the same amount of displacement and therefore a translation of the lining takes place which leaves the shotcrete unstressed. In case $B$, the sprayed concrete lining is only subjected to pure hoop forces. In case $C$, only the tunnel crown settles a certain amount with the footings being unchanged and this movement introduces a combination of hoop forces and bending in the lining. Finally, case $D$ is dominated mainly by bending stress. It can be concluded that the same degree of crown settlement can be associated with at least four different stress states within the lining (Rokahr et al., 2005). The displacement pattern of one single point on the tunnel lining is not decisive and it is crucial to consider the displacement combinations of various target points along the tunnel cross section.

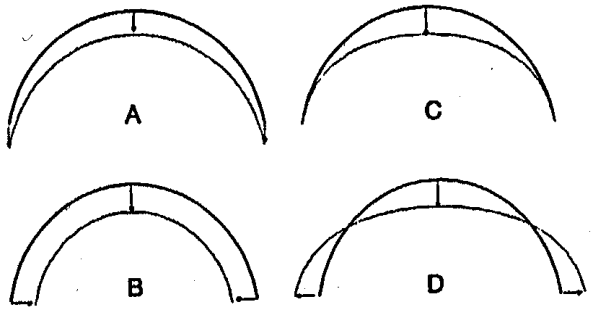



Figure 2.6: Deformation examples of a roof lining (from Rokahr et al., 2005)

### 2.4.2 Measuring and interpretation of stresses in tunnel linings

With the increasing use of numerical methods for the design of tunnel linings relatively good agreement can be achieved between predicted and measured displacements. However, this fact often leads to the misleading assumption that stresses within the shotcrete lining have also been well predicted. In reality, due to the complexity of the loading conditions and the material behaviour of shotcrete at early ages, very little reliable information is available regarding the stress state during tunnel advance. The correct determination of stresses in a tunnel lining is of great importance for estimating the factor of safety and in order to verify that design predictions are reasonable (Thomas et al., 2004).

In the past, several intrusive techniques, such a slot cutting and over- or undercoring, have been successfully used to evaluate stress conditions in shotcrete linings (Clayton et al., 2000). However, these methods provide just one-off measurements and are disruptive to tunnelling

operations and damaging to the lining. A continuous temporal stress variation in the lining, especially in the first 2 to 3 days, is of much greater value for engineers in order to investigate the safety of the tunnel. Two common approaches for achieving this are:

- Pressure cells
- Stress back-calculation from deformation measurements

Usually back-calculation of the stress history in a shotcrete shell is based on the use of strain gauges and rheological models for the mathematical description of the material response. A large number of assumptions has to be introduced in order to capture the complete behaviour of shotcrete at early ages. One widely used technique is the rate of flow method proposed by England & Illston (1965), which will be described later in Chapter 6. However, in the literature it is often stated that an accurate estimation of the stresses within the tunnel lining by back-calculation is not possible due to the large number of errors introduced in the course of deformation measurements and the calculation procedure.

The performance of pressure cells for sprayed concrete linings was assessed in detail in Clayton et al. (2002). Basically, they can be embedded within the shotcrete layer in two different orientations: Radial pressure cells record the stress between the sprayed concrete and the surrounding ground of the tunnel and tangential pressure cells measure the hoop stress within the tunnel lining itself. Examples of such pressure cells can be seen in Fig. 2.7.

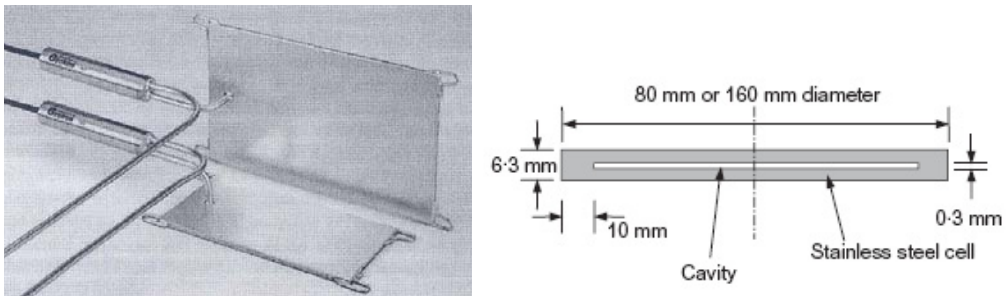



Figure 2.7: Radial and tangential pressure cells (from Clayton et al., 2002 and Jones et al., 2005)

However, a correct recording of the stress history in any medium, such as shotcrete in tunnelling, is difficult due to various factors that influence the performance of a pressure cell. They can be summarized as:

- Installation effects (i.e. cavities around the cell during shotcreting, unwanted rotations, etc.)
- Temperature sensitivity during hydration of the cement paste
- Offsets due to crimping
- Cell properties (cell fluids such as mercury or oil)

The so called Cell Action Factor (CAF) representing the ratio between the recorded pressure and the actual stress in the shotcrete can be used to evaluate how the cell properties affect the interaction of the pressure cell with the surrounding medium. Usually the CAF takes a value close to unity, with an average value of 0.95 (Jones et al., 2005). Some researchers claim that embedded pressure cells are not very reliable for monitoring the actual stress in a tunnel lining. However, they still represent a valuable source of information that can be used to assess whether the anticipated tunnel design assumptions are reasonably justified.

## 2.5 A review of tunnel lining design

The design of a tunnel is a complex process that involves an assessment of the mechanisms of behaviour of the whole structure during tunnel advance, the principal risks and serves as a basis for interpreting results from monitoring (ICE, 2004). However, geological uncertainties in the material properties of the surrounding ground make this process a difficult task to perform. One of the main difficulties is to estimate the loads that act on a tunnel lining in terms of earth pressures and ground water. Given these uncertainties, a design analysis should never be accepted as a definite solution and the sensitivity of the ground-support interaction should be investigated in detail. Furthermore, it should be noted that any design analysis is just an approximation of reality, including several assumptions and probably errors too. Woods & Clayton (1993) mention six sources of errors in modelling of a complex structure such as a tunnel, which are:

- Modelling the geometry of the problem
- Modelling the construction method
- Constitutive modelling of the involved materials and parameter selection
- Theoretical basis of the solution method
- Interpretation of results
- Human errors

Up to now various design methods for tunnels exist in engineering practice, each of them having its advantages and disadvantages. Two main groups of approaches can be distuingished - design methods for "continua" such as encountered in soft ground and/or massive rock, and design methods for "discontinua" when dealing with a jointed rock mass. The most important tunnel design methods will be introduced briefly in the following sections. For further detailed information on tunnel design see ICE (2004).

### 2.5.1 Empirical methods

Empirical methods of tunnel design have been successfully applied mainly in rock tunnelling and to a minor extent in soft ground conditions. They are usually based on assessments of

precedent practice and their support recommendations have been calibrated for a wide range of tunnelling conditions. The two most frequently used empirical design methods that can be found in the literature are:

- Rock Mass Rating (RMR) by Bieniawski (1994)
- Q - Systems by Barton et al. (1974)

Both systems have in common that with the help of certain rock mass parameters, such as strength of the rock, rock quality (weathering), joints, number of sets, frequency, spacing and ground water conditions, a rock mass classification can be established. A combination of these parameters then leads to the support measures being determined from design charts or tables. Obviously, such methods depend highly on the experience of the tunnel engineer or engineering geologist responsible for the rock mass classification and should be used with caution. Some other disadvantages of these empirical methods have been highlighted in the literature (no guidance on the timing of support installation, no consideration of the effects to adjacent structures, factor of safety unknown, etc.). However, the main advantage lies in their simplicity and such empirical methods are therefore suitable for feasibility studies at the concept design stage.

### 2.5.2 Closed-form analytical methods

Analytical or structural design models based on closed-form solutions were widely in use in the past for the planning of tunnels in soft ground conditions and allowed the dimensioning of tunnel linings in a simple and robust way. A comprehensive review of analytical design models for tunnels can be found in Duddeck & Erdmann (1982) and Duddeck & Erdmann (1985). However, most of these models are not capable of modelling the full complexity of a tunnel during construction such as soil deformations ahead of the face, stress relief prior to the installation of support elements or the soil-sructure interaction. The most common assumptions that are made in such an analytical analysis are:

- Circular geometry of tunnel
- 2D plane strain conditions
- Stresses acting on tunnel lining are equal to primary stresses in the undisturbed ground
- Bond between lining and ground for radial and tangential deformations
- Tunnel lining and ground (as a homogeneous material) behave linear elastically

In some cases the principle of superposition is applied when investigating adjacent structures or tunnels, but obviously these analytical models fail to realistically capture the interaction problem of twin-tunnel construction. However, despite these shortcomings, structural models for tunnel lining design can still be a useful tool for a rough design of the involved structural elements at the concept design stage.

#### 2.5.2.1 Continuum analytical methods

Continuum analytical models are commonly based on excavation and lining of a hole in a stressed continuum (ICE, 2004). Fig. 2.8 shows such a continuum model found in Duddeck & Erdmann (1982) for which Engelbreth (1961) derived a closed form solution for the internal forces and deformations of the lining. Further examples can be found in Muir Wood (1975), Einstein & Schwartz (1979) and Duddeck & Erdmann (1985).

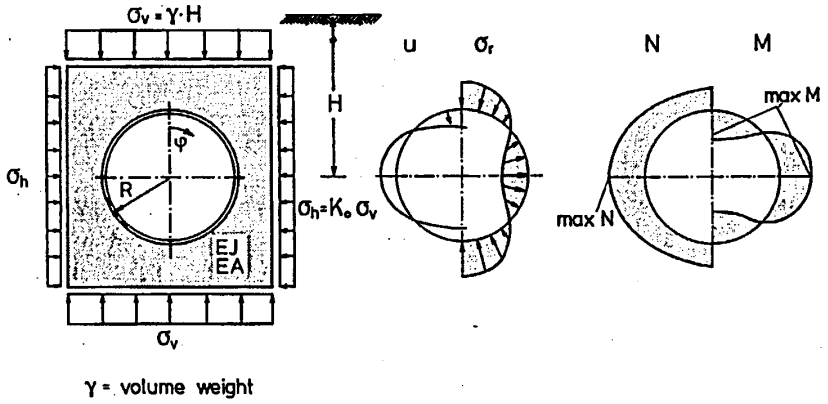



Figure 2.8: Plane strain continuum model and charactersitic distribution of radial displacements $u$, radial stresses on the lining $\sigma_r$, hoop forces $N$ and bending moments $M$ (from Duddeck & Erdmann, 1982)

Since the lining is assumed to be installed immediately before excavation, this fact tends to overestimate the loads acting onto the lining. Some modifications of these models sometimes include a stress relief factor in order to account for a certain stress relaxation before lining installation. Another important fact is that continuum analytical models treat the surrounding ground as a semi-infinite medium and therefore they should only be used for tunnels where the axis is deeper than two tunnel diameters below the surface (ICE, 2004). This restriction implies some limitations for the use of such models for the design of very shallow tunnels in urban areas. Their benefit is obviously their simplicity and they provide the designer quickly with information on the maximum deformations, normal forces and bending moments in the tunnel lining.

#### 2.5.2.2 Convergence-confinement method

The convergence-confinement method for a circular tunnel in an isotropic axisymmetric stress field is graphically illustrated in Fig. 2.9, which contains a graph of the internal wall pressure $p$ versus the radial displacement $u$. From this figure, the displacement and the load acting on the tunnel support are obtained in principle through the intersection of the ground reaction curve of the tunnel and the support reaction line (Oreste, 2003).

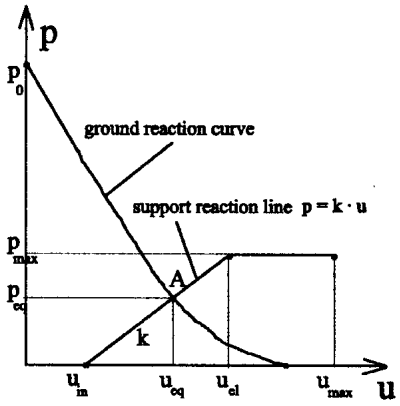



Figure 2.9: The convergence-confinement method (after Oreste, 2003)

$p_o$ is the in-situ isotropic stress in the ground before tunnel excavation. The reaction line of the support element (i.e. shotcrete) is defined by its stiffness $k$ and the initial wall displacement on installation of the support $u_{in}$, which can be seen as a measure of the distance from the tunnel face where the support is installed. In the case of a linear elastic perfectly plastic support material a maximum stress $p_{max}$ and displacement $u_{max}$ can be introduced. At the above mentioned intersection point of the ground reaction curve and the support reaction line (i.e. point $A$ in the above figure), the system is assumed to be in equilibrium and the pressure acting onto the lining $p_{eq}$ and the displacement $u_{eq}$ can be obtained. Due to the assumed axisymmetry for ground behaviour and tunnel geometry, this method is valid only for ground conditions where the coefficient of earth pressure at rest $K_o$ is close to 1.0 and for deep tunnels. Another drawback is that no information is given on the distribution of bending moments in the lining.

#### 2.5.2.3 Bedded-beam-spring models

When designing a tunnel with a bedded-beam-spring model the tunnel lining is simulated as a structural beam element. Furthermore, this beam is attached to the ground which is represented by radial and/or tangential springs, as can be seen in Fig. 2.10. These springs are usually limited to acting only in compression, allowing separation of the lining from the soil formation in the expected area of tensile stresses (tunnel crown). Some uncertainties exist regarding an appropriate estimation of the spring stiffness $K_r$, which in theory can be derived from standard ground investigation tests (ICE, 2004). A critical point in the use of a bedded-beam-spring model is the correct application of the loads at each spring position which may be estimated as a percentage of the vertical and horizontal overburden pressure. Complete closed-form solutions for this model can be found in Schulze & Duddeck (1964).

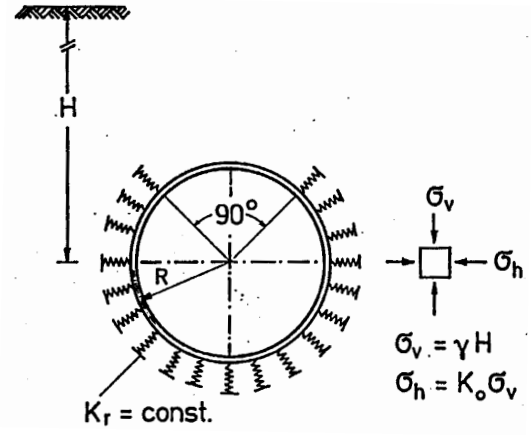



Figure 2.10: Bedded ring model without bedding near the tunnel crown (from Duddeck & Erdmann, 1982)

Recently, bedded-beam-spring models have been widely superseded by more complex numerical methods for tunnel lining design and are rarely in use for the analysis of temporary lining support made of shotcrete. However, they can be useful in the design of final linings where long-term full overburden loading conditions are appropriate (ICE, 1996).

### 2.5.3 Numerical methods

Over the last few decades significant progress has been made in the development of numerical methods for the design of underground structures such as tunnels, replacing almost entirely the previously described simple design methods. The finite element method as one particular type of numerical analysis is capable of simulating complex tunnel construction by taking into account the following aspects:

- Complex tunnel geometry
- Different geological strata
- Advanced constitutive behaviour of ground and supporting materials
- Construction sequences
- Complex boundary conditions
- Ground-support interaction
- Incorporation of adjacent structures (tunnels, buildings, etc.)

Sophisticated 2D and 3D analyses of tunnel construction can be performed capturing the stress-rearrangement in the ground due to tunnel excavation in a realistic way. However, despite all these advantages, results from a numerical analysis should be assessed in the context of the quality of the site investigation, the estimated range of geomechanical properties

and the solution algorithms in the adopted code (ICE, 2004). Numerical methods can be seen as a very powerful tool in the design process providing a detailed understanding of the mechanical behaviour of the tunnel during construction.

#### 2.5.3.1 Bearing-capacity-diagram

Once a numerical analysis has been carried out (i.e. finite element analysis), tunnel design engineers are left with a large number of stresses or structural forces and displacements of the structural elements. In the next step these results can be used to dimension the applied support elements, i.e. shotcrete lining, anchors and steel arches. However, this process is not straightforward, since the consideration of safety factors is not very clear in the case of underground construction and standard codes for surface structures are often not applicable. Therefore, a consistent design code for shotcrete tunnel linings is still lacking in the tunnelling industry.

Sauer et al. (1994) and Wu & Roony (2001) proposed a method to dimension the primary shotcrete lining with the help of the so called "bearing-capacity-diagram". It is based on the following equilibrium condition between the external forces (action) and internal forces (resistance) for bending moment and thrust:

$$\eta_n \, N_e = \eta_s \, N_{is} + \eta_c \, N_{ic} \tag{2.1}$$

and

$$\eta_m \, M_e = \eta_s \, M_{is} + \eta_c \, M_{ic} \tag{2.2}$$

where $N_e$ and $M_e$ are the (external) thrust and bending moment obtained from the finite element analysis and $N_{is}$, $M_{is}$, $N_{ic}$ and $M_{ic}$ are the (internal) thrust and moment in the ultimate limit state for the steel and concrete. The subscripts $s$ and $c$ refer to steel and concrete respectively. The possible safety factors for the loads ($\eta_n$ and $\eta_m$) and material side ($\eta_s$ and $\eta_c$) depend on the applied code and can be taken as an example according to EC 2 or the German standard DIN 1045.

From the above equations the allowable axial thrust $N_a$ and bending moment $M_a$ can be obtained as:

$$N_a = \frac{1}{\eta_n}(\eta_s \, N_{is} + \eta_c \, N_{ic}) \tag{2.3}$$

and

$$M_a = \frac{1}{\eta_m}(\eta_s \, M_{is} + \eta_c \, M_{ic}) \tag{2.4}$$

The safety of a shotcrete lining can therefore be judged by a comparison of the external with the allowable forces. A graphical representation of all possible combinations of the allowable forces $N_a$ and $M_a$ leads to the bearing-capacity-diagram, as illustrated in Fig. 2.11. The main assumption behind this diagram is a linear strain distribution across the thickness of

the shotcrete layer. By applying appropriate constitutive laws for the shotcrete and steel reinforcement, the internal allowable forces of resistance ($N_{is}$, $N_{ic}$, $M_{is}$ and $M_{ic}$) can be computed taking into account the following cross section properties:

- Lining thickness
- Concrete cover
- Reinforcement area

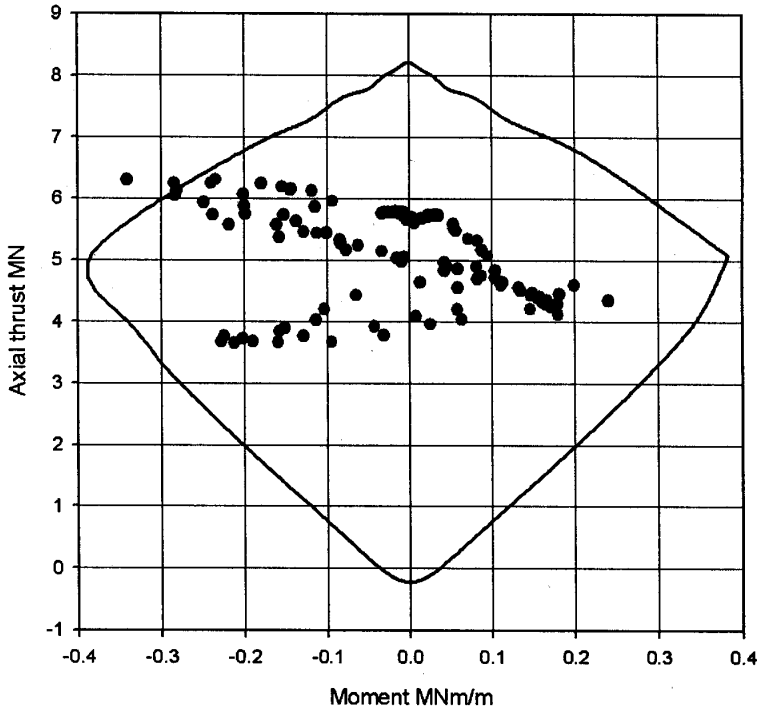



Figure 2.11: Bearing-capacity-diagram for tunnel lining (from Hoek, 2007)

The example presented in Fig. 2.11 has been calculated in Hoek (2007) for a final unreinforced concrete lining with a thickness of 50 cm and a uniaxial compressive strength of 35 MPa. The plotted points refer to axial thrust and bending moment combinations obtained from a finite element analysis. It can be seen that almost all the points fall within the capacity envelope and for these cross sections the design can be regarded as safe. One big drawback of such an approach is the underlying simplicity of the adopted constitutive laws in particular for young shotcrete, which does not include the gradual increase in stiffness and strength with time.

## 2.6 Single-shell method

Conventional tunnel construction according to the principles of the NATM consists of two tunnel shells, each of them having an individual purpose. Directly after excavation, a temporary shotcrete lining is installed to stabilise the opening and to contain short to medium-term

loads. When this lining has fully stabilised and the system has reached equilibrium, which can be months after the completion of the outer shotcrete layer, a relatively thick permanent cast in-situ concrete lining is installed with the aim of bearing long-term loads. In practice this permanent concrete shell is often overdesigned and capable of bearing much higher loads than needed. Furthermore, this second concrete shell provides durability and watertightness either by the use of a waterproof membrane between the temporary and the permanent lining or by the use of appropriate steel reinforcement to reduce crack widths to an acceptable value. In the literature this method of tunnel construction is commonly referred to as the "double shell method".

However, over the last twenty years significant progress has been made in the tunnelling industry and in particular in shotcrete technology. Constituent materials and equipment have improved dramatically and it is nowadays possible to produce a high quality shotcrete that meets the requirements of national standards in terms of durability and watertightness. Therefore, the idea of using a single permanent shotcrete shell as tunnel support has been introduced, replacing the traditional double shell method and reducing construction costs significantly. In ASCCT (2004) a definition for the so called "single-shell construction method" can be found, which states:

*The single-shell construction method is characterised by the fact that all static and structural requirements are fulfilled by a single shell structure. This shell can be produced in one or several operations. The shell structure has to be designed not only to meet the need for support during tunnel driving, but also to fulfil requirements of the finished structure.*

Basically, two forms of execution of such a single shell using shotcrete exist, which are:

- A single-layer sprayed concrete shell, installed directly in the course of tunnel driving having the final thickness of the tunnel lining.
- A composite multi-layer sprayed concrete shell, installed during tunnel driving and subsequent operations to achieve the final thickness of the tunnel lining.

If the shotcrete shell is applied in several steps, it has to be ensured that the shear bonding between the sprayed concrete layers is activated by adequate measures. This can be achieved by cleaning of the surfaces with a mixture of compressed air and water, or preferably by means of a high-pressure water jet (ASCCT, 2004). Fig. 2.12 illustrates a typical tunnel profile for the single-shell method consisting of several individual shotcrete layers.

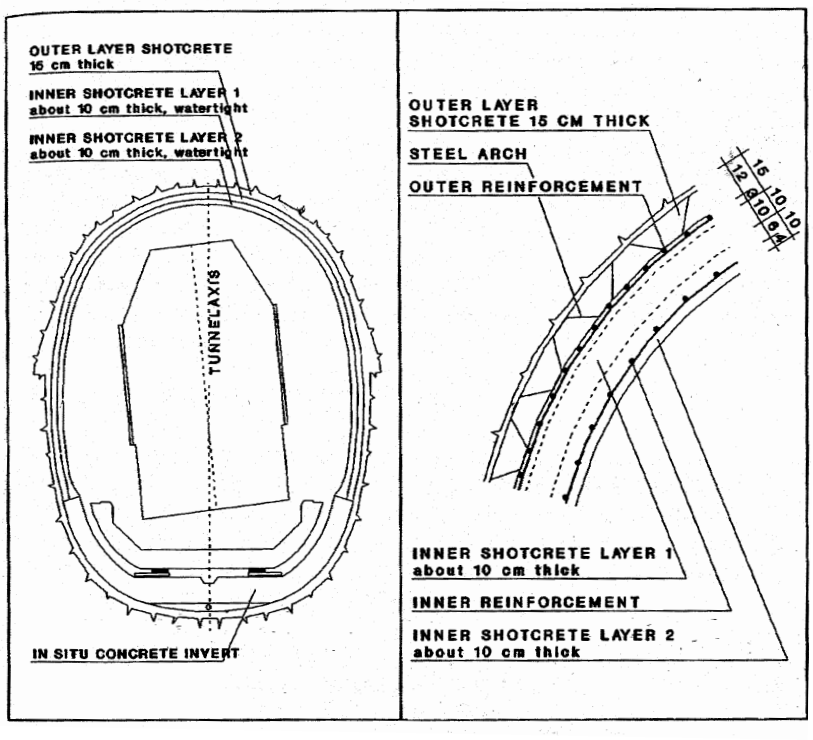



Figure 2.12: Composition of tunnel lining with the single-shell method (from Kusterle & Lukas, 1993)

Despite the economic and time-saving advantages of the single-shell method, according to Pöttler & Klapperich (1999) certain limitations exist, when tunnels are driven under the following conditions:

- Great ingress of water
- Tunnel is located far below ground water level
- Conditions with water corrosive to concrete
- Geological conditions causing large bending moments of the lining leading to cracking and the need for heavy reinforcement

A quantification of the single-shell method from the structural point of view with respect to safety of the overall load-bearing system can be found in Pöttler & Schweiger (1999).

### 2.6.1 Innovative shotcrete tunnelling

One of the biggest infrastructure projects in the UK over the last five years was the new Terminal 5 at Heathrow Airport in London, consisting of large underground structures including 14 km of tunnels for rail and road. The majority of these tunnels were constructed with tunnel boring machines (TBMs), but for more complex elements, such as shafts and tunnel connections, a new innovative single-shell shotcrete-lined method called "LaserShell™" has

been adopted. This particular tunnelling method uses fibre reinforced sprayed concrete and was developed by a collaboration between the two companies, Morgan Est (UK) and Beton- und Monierbau (Austria), with the initial aim of improving the safety of workers at the tunnel face. Its principles are illustrated in Fig. 2.13 and described in detail in Williams (2008) and Eddie & Neumann (2003).

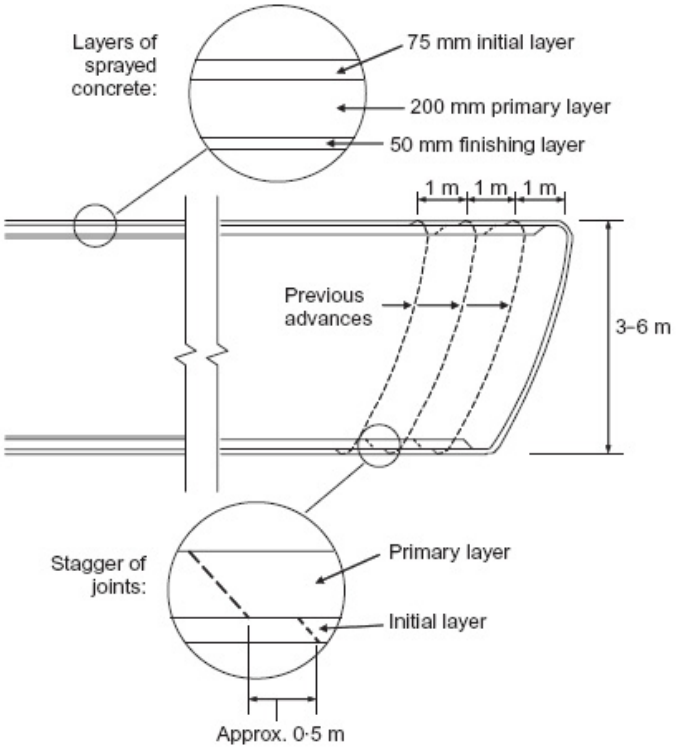



Figure 2.13: The LaserShell™ method (from Jones et al., 2008)

The key features of the LaserShell™ method can be summarized according to Hilar et al. (2005) as follows:

1. The tunnel is constructed full face (up to 5 m diameter in London Clay) in order to minimise the number of construction joints and to increase productivity. Furthermore, an inclined and domed face improves the stability in comparison to a conventional vertical face and tends to reduce surface settlements.

2. Steel-fibre reinforced shotcrete is used exclusively without any conventional wire mesh or lattice girders. This fact improves safety significantly since access to the unsupported face is not necessary anymore. Consequently, the quality of the lining is remarkably better as problems of shadowing behind the lattice girders and the wire mesh can be avoided completely.

3. For the control of the excavation and lining geometry the "TunnelBeamer™" laser

distometer is used, which takes spot readings of the distance to the excavated face or to the lining (see Fig. 2.14).

4. The tunnel lining is constructed as a single-shell, where almost all the sprayed concrete forms part of the watertight permanent lining.

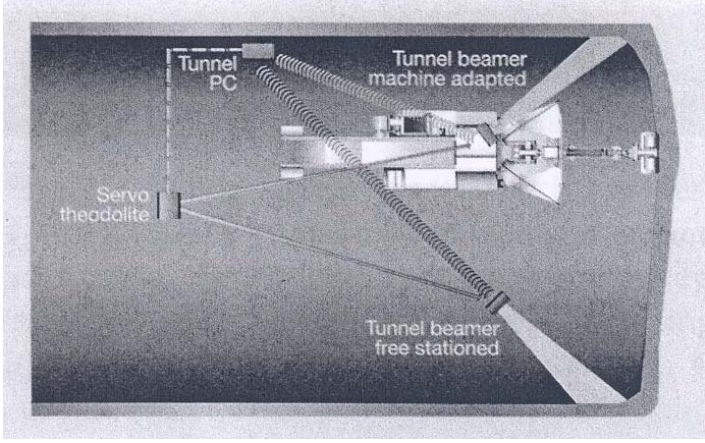



Figure 2.14: TunnelBeamer™ system integration (from Eddie & Neumann, 2003)

As can be seen in Fig. 2.13, the complete shotcrete lining is built up in three individual layers. The initial steel-fibre reinforced layer with a thickness of 75 mm provides instant structural support directly after excavation of the ground and enhances the watertightness of the lining. However, this layer is considered to be sacrificial for design purposes as its resistance might deteriorate with time due to sulphate attack. The primary steel-fibre reinforced shotcrete layer has a thickness of 200 mm and is considered as the permanent load bearing structure. A finishing layer of 50 mm thickness is sprayed onto the existing layers after completion of construction works to provide a smooth lining profile. This material is unreinforced and with low accelerator dosage. Another major improvement of the LaserShell™ method is that robotic spraying techniques are used for the shotcrete application, which guarantees a better material quality during construction.

Despite all these advantages of the LaserShell™ method, some problems regarding the increased amount of reinforcement for zones where high bending can be expected remain unsolved. However, further developments leading to the so called "UltraShell™" method are in progress under the supervision of Morgan Est and Beton- und Monierbau (Eddie et al., 2009).

## 2.7 Modelling 2D tunnel excavation in a numerical analysis

From an extensive literature review it can be concluded that tunnelling is commonly regarded as a highly complex three-dimensional process where stress redistributions take place near the tunnel face. Ground movements not only occur in the radial direction, but also occur in the

longitudinal direction, parallel to the tunnel axis. Furthermore, a significant component of these deformations in the soil mass occur well ahead of the tunnel face before the installation of the tunnel lining, leading to a certain stress relief. A full 3D numerical analysis requires enormous computational resources and is still not frequently performed in engineering practice. Hence, when tunnel construction is simulated in 2D, certain assumptions have to be introduced in order to account for these 3D effects. The available approaches in the literature that are regularly used for 2D analyses are discussed in detail in Potts & Zdravković (2001) and Karakus (2007) and will be described briefly in the following sections.

### 2.7.1 Stress relief method

The stress relief method, or often termed the "convergence-confinement method", was introduced by Panet & Guenot (1982) and is based on the principle of unloading at the tunnel boundaries before construction of the tunnel lining. In Fig. 2.15 the concept of the stress relief method is shown, where a factor $\lambda$ governs the proportion of unloading, which is progressively increasing from 0 to 1 during the analysis. At a prescribed value $\lambda_d$ the lining is installed. The load acting onto the system (ground + lining) after completion of the numerical excavation is then given as:

$$\{\sigma_d\} = (1 - \lambda_d)\,\{\sigma_o\} \tag{2.5}$$

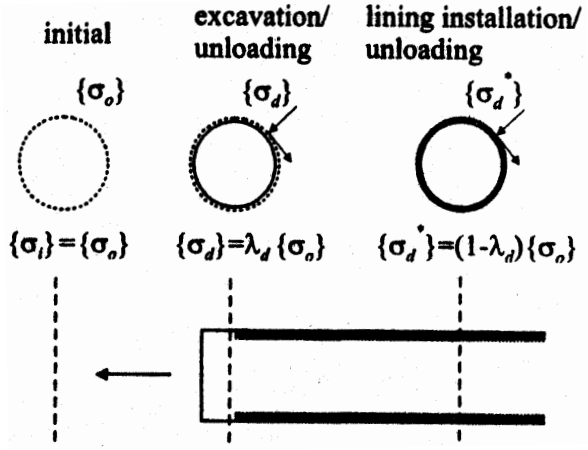



Figure 2.15: Principle of the stress relief method (from Potts & Zdravković, 2001)

### 2.7.2 Stiffness reduction method

The stiffness reduction method was developed by Swoboda (1979) for the modelling of NATM tunnels and uses a support core with a reduced modulus of elasticity. The soil formation at the tunnel face is softened in a controlled way by a reduction factor $\beta$ so that the stiffness of the support core is given as:

$$E'_e = \beta\, E_o \tag{2.6}$$

Fig. 2.16 illustrates the steps of the stiffness reduction method. The tunnel lining is installed before the numerical excavation of the soil is completed. If a staged tunnel construction is applied, i.e. a bench-invert excavation, the procedure can be carried out for each of the excavation areas individually.

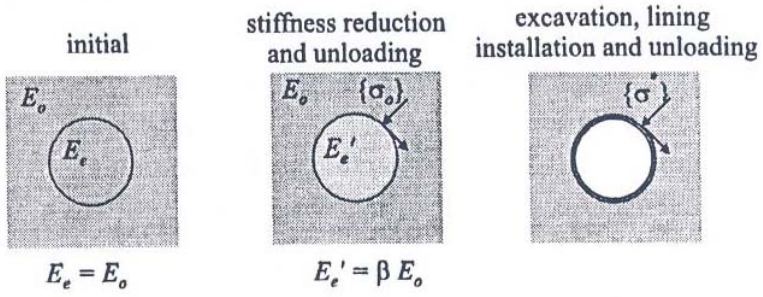



Figure 2.16: Principle of the stiffness reduction method (from Potts & Zdravković, 2001)

### 2.7.3 Gap method

Another method for taking into account 3D effects in a 2D tunnel analysis was presented by Rowe et al. (1983) and is suitable for various tunnelling techniques (NATM, TBM, etc.). The expected ground loss due to tunnel excavation is introduced in the finite element mesh as a predefined void, which is placed around the final tunnel position as indicated in Fig. 2.17. The invert of the tunnel is rested on the underlying soil boundary and a gap parameter is introduced at the crown, representing the vertical distance between the tunnel crown and the initial position before tunnel excavation. As the soil within the tunnel is excavated, the nodal displacements at the tunnel opening are monitored until the void has been closed and the soil is in contact with the predefined position of the tunnel lining. At this stage the soil-lining interaction is activated at this node.

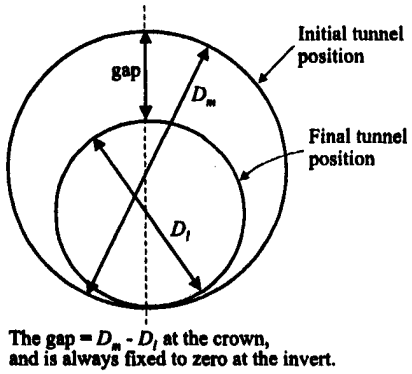



Figure 2.17: Principle of the gap method (from Potts & Zdravković, 2001)

### 2.7.4 Volume loss control method

The principal idea behind the volume loss control method is very similar to that for the stress relief method, with the difference of prescribing a volume loss that will result on completion of

excavation instead of a load reduction factor. Therefore this method is suitable for tunnelling in ground conditions where the volume loss can be estimated before tunnel construction with a high level of confidence, as is the case for London Clay. In the London area the volume loss usually varies between 1 % and 2 % based on field measurements (Potts & Zdravković, 2001). Fig. 2.18 depicts the basic concept of the volume loss control method in a numerical analysis.

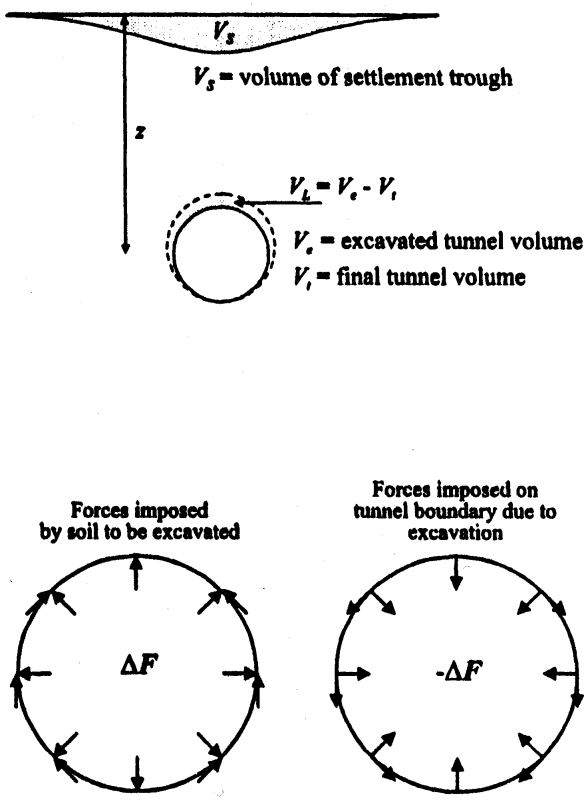



Figure 2.18: Principle of the volume loss control method (from Potts & Zdravković, 2001)

When tunnel excavation is started, the initial equivalent nodal forces $\{F_o\}$ at the tunnel boundary are calculated and reduced in a step-wise manner over a certain number of increments $n$. This incremental reduction equals:

$$\{\Delta F\} = \frac{\{F_o\}}{n} \tag{2.7}$$

The equal and opposite nodal force vector $-\{\Delta F\}$ is applied at the excavation boundary for each of the $n$ increments. The volume loss is monitored continuously throughout this procedure and the tunnel lining is installed on the increment, at which the desired volume loss is achieved. When simulating tunnel excavation in undrained conditions, the volume loss $V_L$ can be calculated from:

$$V_L = \frac{V_S}{V_e} \tag{2.8}$$

where $V_S$ is the volume of the surface settlement trough and $V_e$ the excavated tunnel volume.

The remaining nodal forces act onto the tunnel lining and introduce stresses and displacements. If the tunnel lining has a relatively low stiffness, which can be the case for a shotcrete shell at early ages, some further increase in the volume loss has to be expected and should be taken into account. Finally, it should be noted that the volume loss control method is adopted in this thesis for the analysis of tunnel construction in London Clay, as will be explained later in Chapter 8.

## 2.8 Summary

This chapter dealt with several aspects related to tunnel construction and its design in urban areas. The following key facts can be summarized:

- Shotcrete is one of the main support elements of the New Austrian Tunnelling Method (NATM) and provides temporary stability to the tunnel opening. The main idea behind NATM is to achieve equilibrium of the system after excavation by actively integrating the surrounding ground formation into an overall ring-like support structure. However, the entire range of principles of the NATM is not applicable for tunnelling in soft ground conditions, where a rapid ring closure and surface settlement control are the main concerns during construction.

- Geotechnical observation and monitoring are key elements in any underground structure. Particularly for tunnelling, the shotcrete lining behaviour during tunnel advance is of crucial importance for engineers. Measurements of displacements and stresses serve as a source of information to assess the safety of the structure and to validate the anticipated lining design. However, difficulties exist regarding the applicability of the possible measuring techniques (i.e. optical surveying, strain gauges, pressure cells) and the correct interpretation of the obtained results.

- A literature review has shown that several lining design techniques exist that are widely used in engineering. Starting from simple methods based on empirical observations, some closed-form analytical methods have been developed that are useful at the preliminary design stage (continuum method, convergence-confinement method, bedded-beam-spring models). Common assumptions for these methods are a circular geometry of the tunnel and linear elastic behaviour of the involved materials. Numerical methods are a powerful tool for analysing more complex tunnel geometries, realistic soil-structure interaction and advanced constitutive behaviour.

- The single-shell method as a relatively new technology assumes that all the static and structural requirements are fulfiled by a single shotcrete shell applied in several layers. It replaces the costly double-shell method where a permanent cast in-situ final lining is usually installed months after the completion of tunnel construction. However, certain concerns exist for the application of the single-shell method regarding its durability

and watertightness. New innovations combining safe excavation schemes and the use of fibre-reinforced sprayed concrete layers that act statically as a single shell are in progress.

- When performing a 2D numerical analysis of tunnel construction, certain 3D effects such as stress relief and pre-deformation ahead of the tunnel face should be taken into account. Several techniques for achieving this have been presented, among them the volume loss control method, which will be applied in Chapter 8.

# Chapter 3

# The Finite Element Method

## 3.1 Introduction

The finite element method is a sophisticated form of numerical analysis that is capable of dealing with complex structures in engineering practice. It has been used in many engineering fields over the last thirty years and has more recently been introduced for analysing geotechnical problems. In contrast to simple solution methods, such as limit equilibrium, stress field and limit analysis, the finite element method is capable of satisfying all the four fundamental requirements for a complete theoretical solution: equilibrium of forces, compatibility of displacements, material constitutive behaviour and boundary conditions. It can therefore provide advanced information for a safe design of subsurface structures.

The numerical research group at Imperial College London, led by Prof. D. Potts and Dr. L. Zdravković, has been working at the leading edge of the development and application of the finite element method for practical geotechnical problems. As a result of their research, the Imperial College Finite Element Program (ICFEP) has been developed over the last three decades. This sophisticated code makes use of the displacement based finite element method and is capable of performing both 2D and 3D analysis. All the analyses presented in this thesis have been carried out using ICFEP and 2D plane strain conditions have been applied exclusively.

This chapter aims to give an introduction into the main concept of the finite element method following in principle a procedure presented in Potts & Zdravković (1999). First, the focus is on the basic theory for linear materials and highlighting all the involved steps of a finite element analysis. Furthermore, some modifications that are necessary to enable this theory to be used in geotechnical engineering are presented. However, concrete and shotcrete show a highly non-linear material behaviour under all kinds of loading conditions and therefore the finite element theory for linear materials is extended in such a way, that advanced non-linear elasto-plastic constitutive models can be successfully applied. The solution strategies and algorithms implemented into ICFEP will be discussed in detail.

## 3.2 Finite element theory for linear materials

The following sections describe briefly each of the steps involved in the finite element method, which are:

1. Element discretisation
2. Primary variable approximation
3. Formulation of element equations
4. Boundary conditions
5. Solution of global equations

### 3.2.1 Element discretisation

As a first step in analysing an engineering problem with the finite element method, the geometrical domain to be investigated must be defined and then divided into small regions, the so called finite elements. For a 2D analysis, the shape of these elements is often triangular or quadrilateral and they are connected together at their nodes, forming a mesh over the whole area under consideration. The nodes are usually situated at the corners of the mesh, although additional nodes can be encountered at the midpoints of the straight or curved element sides. This results in 6-noded triangular or 8-noded quadrilateral finite elements. An appropriate mesh design is of crucial importance for a realistic modelling of a structure and the size and number of elements strongly influences the accuracy of the obtained solution. For zones where rapid changes in the unknown variables can be expected it is necessary to refine the mesh by the use of smaller elements. However, an increasing refinement of the mesh leads to high computational costs, consequently an optimum mesh design is recommended.

### 3.2.2 Approximation of primary variable

In the finite element method a primary variable has to be selected. Furthermore, some rules have to be established to define how this primary quantity varies over the finite element. Other quantities are then treated as secondary variables and can be determined once the primary variable has been calculated. In geotechnical engineering it is common to adopt displacements as the primary unknown quantity and other quantities, such as stresses and strains, are treated as secondary variables, resulting from displacements

In the displacement based finite element method the displacement field varies over the problem domain. This method assumes further that the displacements within a finite element can be estimated from the nodal displacements by mathematical functions. These functions are commonly termed “shape functions”. When considering a 2D analysis, the displacement

field is characterised by the two displacements $u$ and $v$, in the horizontal $x$- and vertical $y$-direction respectively. In this case, the displacement field within an element can be described by:

$$\left\{ \begin{array}{c} u \\ v \end{array} \right\} = [N] \left\{ \begin{array}{c} u \\ v \end{array} \right\}_{nodes} \tag{3.1}$$

In this equation $[N]$ is the matrix of the shape functions, which are of a quadratic nature for the higher order 8-noded elements. It is now possible to describe the displacements $u$ and $v$ in terms of their values at the element nodes. These nodal displacements are often referred to as the unknown degrees of freedom. Equation 3.1 reduces the problem of determining the displacement field over the entire geometrical domain to the determination of the displacement components at a finite number of nodes of the finite element mesh.

The type and shape of finite elements to be adopted depends largely on the geometry being modelled and the type of analysis required. Best results are obtained if the elements have reasonable shapes and do not get too distorted during the analysis. In ICFEP, 8-noded, quadrilateral, isoparametric elements are used, as illustrated in Fig. 3.1. It can be seen, that the global element, as it appears in the finite element mesh, is derived from a parent element, which is defined with respect to a natural coordinate system. These natural coordinates $S$ and $T$ vary from -1 to +1. This element is called "isoparametric", since the same shape functions $[N]$, that are used to describe the displacement field within the element, are also adopted to map the geometry of the element from the global to the natural coordinate system.

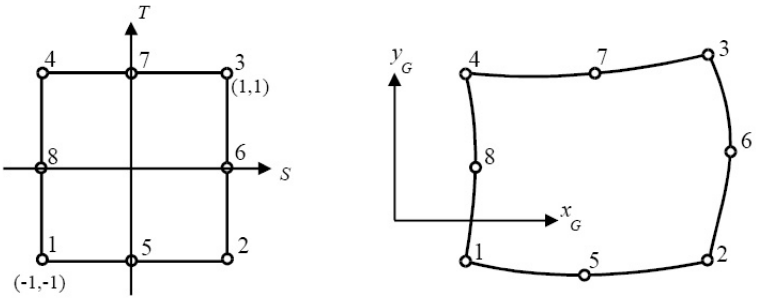



Figure 3.1: 8-noded isoparametric element used in ICFEP (from Potts & Zdravković, 1999)

The global coordinates of a point within the element can be expressed as:

$$x = \sum_{i=1}^{8} N_i \, x_i \qquad \text{and} \qquad y = \sum_{i=1}^{8} N_i \, y_i \tag{3.2}$$

$x_i$ and $y_i$ are the global coordinates of the 8 nodes in the element and $N_i$ are the so called "interpolation functions", which are expressed in terms of the natural coordinates $S$ and $T$ varying from -1 to +1. For each node in the element such an interpolation function exists and takes a value of +1 at the correspondent node. Examples for the quadratic interpolation

functions are given in Potts & Zdravković (1999).

### 3.2.3 Formulation of element equations

For the description of the deformational behaviour of each finite element a set of global equations is needed, combining compatibility, equilibrium and constitutive conditions. Their derivation will be explained here briefly, assuming 2D plane strain conditions.

As introduced earlier, the incremental displacements within a finite element are given through the incremental nodal displacements as:

$$\{\Delta d\} = [N]\ \{\Delta d\}_n \tag{3.3}$$

where

$$\{\Delta d\} = \left\{ \begin{array}{c} \Delta u \\ \Delta v \end{array} \right\} \qquad \text{and} \qquad \{\Delta d\}_n = \left\{ \begin{array}{c} \Delta u \\ \Delta v \end{array} \right\}_{nodes} \tag{3.4}$$

Assuming a compression positive sign convention, the definition of strains as an expression for the mathematical compatibility can be written according to Timoshenko & Goodier (1951) as:

$$\Delta\varepsilon_x = -\frac{\partial \Delta u}{\partial x} \qquad \Delta\varepsilon_y = -\frac{\partial \Delta v}{\partial y} \qquad \Delta\gamma_{xy} = -\frac{\partial \Delta u}{\partial y} - \frac{\partial \Delta v}{\partial x} \qquad \Delta\varepsilon_z = \Delta\gamma_{xz} = \Delta\gamma_{zy} = 0 \tag{3.5}$$

By replacing the displacements in the above equations with the approximations given in equation 3.3, one obtains the following definition of strains with respect to nodal displacements:

$$\{\Delta\varepsilon\} = [B] \left\{ \begin{array}{c} \Delta u \\ \Delta v \end{array} \right\}_n = [B]\ \{\Delta d\}_n \tag{3.6}$$

The matrix $[B]$ only contains derivatives of the shape functions $N_i$ and $\{\Delta d\}_n$ represents the list of nodal displacements for a single element. As mentioned earlier, for isoparametric elements the shape functions are identical to the interpolation functions and depend only on the natural coordinates $S$ and $T$. As a consequence, the derivatives of the shape functions with respect to the global coordinates $x$ and $y$ in the matrix $[B]$ cannot be determined directly. By applying the chain rule of differentiation it can be written that:

$$\left\{ \frac{\partial N_i}{\partial S} \quad \frac{\partial N_i}{\partial T} \right\}^T = [J] \left\{ \frac{\partial N_i}{\partial x} \quad \frac{\partial N_i}{\partial y} \right\}^T \tag{3.7}$$

where $[J]$ is the Jacobian matrix given as follows:

$$[J] = \left[ \begin{array}{cc} \dfrac{\partial x}{\partial S} & \dfrac{\partial y}{\partial S} \\ \dfrac{\partial x}{\partial T} & \dfrac{\partial x}{\partial T} \end{array} \right] \tag{3.8}$$

Hence, by making use of the Jacobian matrix the global derivatives of the shape functions can be obtained as:

$$\begin{bmatrix} \dfrac{\partial N_i}{\partial x} \\ \dfrac{\partial N_i}{\partial y} \end{bmatrix} = \frac{1}{\mid J \mid} \begin{bmatrix} \dfrac{\partial y}{\partial T} & -\dfrac{\partial y}{\partial S} \\ -\dfrac{\partial x}{\partial T} & \dfrac{\partial x}{\partial S} \end{bmatrix} \begin{Bmatrix} \dfrac{\partial N_i}{\partial S} \\ \dfrac{\partial N_i}{\partial T} \end{Bmatrix} \tag{3.9}$$

where $\mid J \mid$ is the Jacobian determinant calculated as:

$$\mid J \mid = \frac{\partial x}{\partial S}\frac{\partial y}{\partial T} - \frac{\partial y}{\partial S}\frac{\partial x}{\partial T} \tag{3.10}$$

In the general case, the constitutive behaviour of a material can be written as:

$$\{\Delta\sigma\} = [D]\{\Delta\varepsilon\} \tag{3.11}$$

where $[D]$ is the constitutive matrix. This equation provides a relationship between the stresses and strains and therefore links equilibrium and compatibility.

The element equations can now be obtained by applying the principle of minimum potential energy, which states that the static equilibrium position of a loaded linear elastic body is the one which minimises the total potential energy. The incremental total potential energy of a body $\Delta E$ is defined as:

$$\Delta E = \Delta W - \Delta L \tag{3.12}$$

where $\Delta W$ is the incremental strain energy and $\Delta L$ the incremental work done by the applied loads. These two quantities are given as:

$$\Delta W = \frac{1}{2}\int_{Vol} \{\Delta\varepsilon\}^T \{\Delta\sigma\}\, dVol \tag{3.13}$$

and

$$\Delta L = \int_{Vol} \{\Delta d\}^T \{\Delta F\}\, dVol + \int_{Srf} \{\Delta d\}^T \{\Delta T\}\, dSrf \tag{3.14}$$

In these two equations $\{\Delta d\}^T = \{\Delta u, \Delta v\}$ is the displacement vector, $\{\Delta F\}^T = \{\Delta F_x, \Delta F_y\}$ the body force vector and $\{\Delta T\}^T = \{\Delta T_x, \Delta T_y\}$ the surface tractions vector (i.e. for line loads or surcharge pressures).

The principle of minimum potential energy can now be expressed mathematically as:

$$\delta\Delta E = \delta\Delta W - \delta\Delta L = 0 \tag{3.15}$$

Substitution of equations 3.13 and 3.14 into equation 3.15 and making use of equations 3.3, 3.6 and 3.11 allows the establishment of the equilibrium equations for a single finite element

which take the following form:

$$[K_E]\ \{\Delta d\}_n = \{\Delta R_E\} \tag{3.16}$$

$[K_E]$ is the element stiffness matrix and is given as:

$$[K_E] = \int_{Vol} [B]^T [D][B] d\,Vol \tag{3.17}$$

$\{\Delta R_E\}$ represents the right hand side load vector and is obtained from:

$$\{\Delta R_E\} = \int_{Vol} [N]^T \{\Delta F\}\, d\,Vol + \int_{Srf} [N]^T \{\Delta T\}\, d\,Srf \tag{3.18}$$

The volume and surface integrals in equations 3.17 and 3.18 are evaluated for isoparametric elements using the natural coordinate system of the parent element $S$ and $T$. As an example, the coordinate transformation for the volume integral can be written as:

$$d\,Vol = t\,dx\,dy = t\ \mid J \mid\ dS\,dT \tag{3.19}$$

In the case of plane strain conditions the thickness $t$ is taken equal to unity. From the procedure presented above it can be observed that the main advantage of the isoparametric element formulation is that the element equations need only be evaluated in the parent coordinate system. The integrals can be carried out over a square, with $S$ and $T$ varying between -1 and +1 and the stiffness matrix for each element in the mesh can be established using a standard procedure.

#### 3.2.3.1 Numerical integration

For the establishment of the stiffness matrix and the right hand side load vector, integrations must be performed (see equations 3.17 and 3.18). Usually an explicit calculation of these integrals is not possible and therefore numerical integration schemes have to be adopted. In ICFEP a Gaussian integration scheme is used, which replaces the integral of a function by a weighted sum of the function evaluated at a number of integration points. When considering a 1D integral of a function $f(x)$ over the domain $-1 < x < +1$ it can be written:

$$\int_{-1}^{+1} f(x)\,dx \approx \sum_{i=1}^{n} W_i\, f(x_i) \tag{3.20}$$

where $f(x_i)$ are the values of the function at the $n$ integration points and $W_i$ are the corresponding values of the weighting coefficients. The number of integration points determines the integration order. The accuracy of the integration obviously increases with a higher inte-

gration order, but at the same time this leads to longer computational time since the number of function evaluations also increases.

When adopting the Gaussian integration scheme, the integration points are often referred to as "Gauss points". In most of the cases a 2 x 2 or a 3 x 3 integration order is used for an 8-noded isoparametric element, which are termed reduced or full integration respectively. The location of the Gauss points for such an 8-noded isoparamtric element in the global and the parent coordinate system is shown in Fig. 3.2.

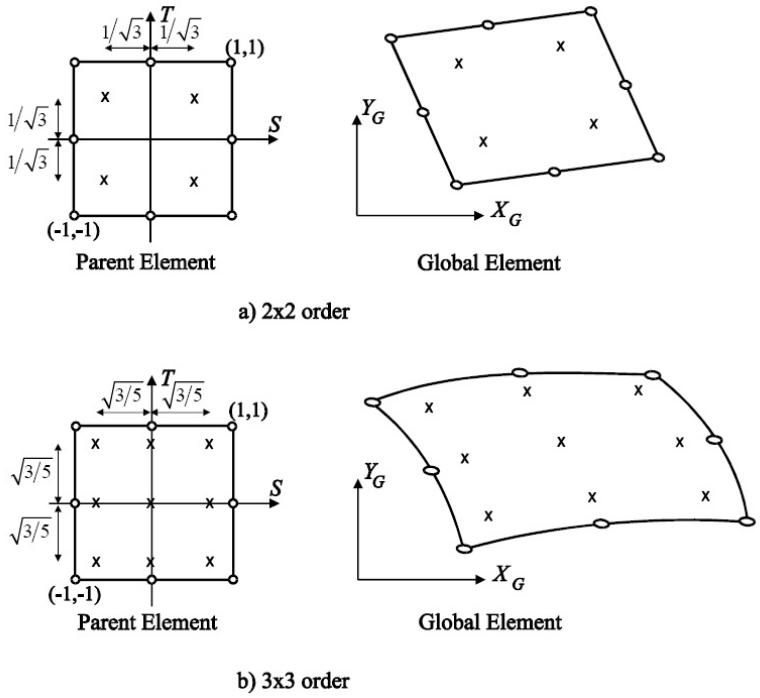



Figure 3.2: Location of Gauss points for 2 x 2 and 3 x 3 integration order (from Potts & Zdravković, 1999)

### 3.2.4 Formulation of global equations

Once the element equations have been formulated it is necessary to assembly these separate element equations into a set of global equations, which are of a similar form and can be written as:

$$[K_G]\{\Delta d\}_{n,G} = \{\Delta R_G\} \tag{3.21}$$

where $[K_G]$ is the global stiffness matrix, $\{\Delta d\}_{n,G}$ the displacement vector of all the nodes for the entire mesh and $\{\Delta R_G\}$ the global right hand side load vector.

The assembly process of transforming the element stiffness matrix into a global stiffness matrix is called "direct stiffness method". The basic principle of this method is that each term of the global stiffness matrix is obtained by summing the individual element contributions whilst taking into account the degrees of freedom which are common between the elements.

A similar technique is applied to the global right hand side load vector, which contains the sum of the individual loads acting on each node. A more detailed description can be found in Potts & Zdravković (1999).

### 3.2.5 Boundary conditions

Appropriate boundary conditions are of great importance in the finite element formulation. These are usually displacement and load conditions that fully define the boundary value problem to be analysed.

Loading conditions include the application of line loads or surcharge pressures and they affect the right hand side vector $\{\Delta R_G\}$ of the global system of equations. Other examples for loading conditions are body forces from excavated or constructed elements. Displacement boundary conditions influence the global nodal displacement vector $\{\Delta d\}_{n,G}$. Sufficient displacement conditions have to be specified at the mesh boundaries in order to avoid any rigid body motion of the whole mesh. If this requirement is not satisfied, the global stiffness matrix becomes singular and the equations can not be solved.

### 3.2.6 Solution of global equations

The last step in the finite element formulation is the solution of the global set of equations in order to obtain the unknown values of the nodal displacements $\{\Delta d\}_{n,G}$. In principle, this global set of equations forms a large system of simultaneous equations which can be solved by several mathematical techniques. One of the most commonly applied solution strategy in finite element analysis is the Gaussian elimination method. For a more detailed description of this method see Potts & Zdravković (1999). Once the nodal displacements of the entire mesh are calculated, secondary quantities such as stresses and strains can be evaluated from equations 3.6 and 3.11.

## 3.3 Geotechnical considerations

The finite element theory presented in the previous sections is applicable to the analysis of any linear elastic continuum. However, several limitations exist regarding a successful application of the theory for the realistic analysis of boundary value problems in geotechnical engineering. Hence, certain modifications have to be made which will be introduced here briefly.

In general, the constitutive behaviour of a material is formulated in terms of total stresses and strains. It is well known that soil exhibits a highly non-linear stress-strain behaviour and can be considered as a two phase material. It consists of a soil skeleton and water that fills the voids of the soil skeleton. In some particular cases, the soil is only partially saturated and air is included in the system. This type of soil is usually treated as a three

phase material, but is not considered within this thesis. In Chapter 1 it was highlighted that in geotechnical engineering the total stress tensor is usually split into effective stresses and pore water pressures due to the two phase nature of soil. This principle of effective stress was formulated mathematically in equation 1.13. For any geotechnical analysis the flow of water through the soil skeleton has to be taken into account and is further coupled with the deformational behaviour of the soil. Therefore, the pore water pressure is introduced as an extra degree of freedom.

In reality two extreme cases can be encountered: When loading is applied on a soil with a relatively high permeability at a low rate, no excess pore water pressures develop. A steady state drainage pattern exists in the soil and fully drained conditions can be assumed. On the contrary, if a soil with a relatively low permeability is loaded rapidly, no flow occurs within the soil and pore water pressures build up, which are linked in a unique way to the deformation of the soil. This condition is termed to be undrained. As will be explained in Chapter 8, undrained conditions are assumed for all the tunnel analyses carried out in this thesis. Therefore, some theoretical background of how to consider pore water pressures in the finite element method will be presented in the following section.

#### 3.3.0.1 Undrained analysis

When performing an undrained analysis in terms of total stresses, no information can be obtained regarding the changes in pore water pressures due to excavation or construction of the soil mass, which sometimes is an important requirement for the design of a geotechnical structure. To overcome this lack of information it is more convenient to describe the constitutive soil behaviour with effective stress parameters. Hence, the principle of effective stresses can be applied and as in equation 1.13 it can be written:

$$\{\Delta\sigma\} = \{\Delta\sigma'\} + \{\Delta\sigma_f\} \tag{3.22}$$

where the vector of pore pressures is given as:

$$\{\Delta\sigma_f\} = \{\Delta u \quad \Delta u \quad \Delta u \quad 0 \quad 0 \quad 0\}^T \tag{3.23}$$

For undrained conditions no flow of water occurs in the soil and the two phases are deforming together. Hence, the strains are the same in each phase and the constitutive behaviour can be written as:

$$\{\Delta\sigma'\} = [D']\,\{\Delta\varepsilon\} \tag{3.24}$$

and

$$\{\Delta\sigma_f\} = [D_f]\,\{\Delta\varepsilon\} \tag{3.25}$$

Making use of these two equations and equation 3.11 gives:

$$[D] = [D'] + [D_f] \tag{3.26}$$

where $[D]$ and $[D']$ are the stiffness matrices in terms of total and effective stresses respectively. $[D_f]$ is the pore fluid stiffness and can be related to the bulk modulus of the pore fluid $K_f$ for the general three dimensional case in the following way:

$$[D_f] = K_f \{b\} \{b\}^T \tag{3.27}$$

with

$$\{b\}^T = \{1 \quad 1 \quad 1 \quad 0 \quad 0 \quad 0 \quad \} \tag{3.28}$$

and the equivalent bulk modulus of the pore fluid $K_e$ as:

$$K_e = \frac{\Delta u}{\Delta \varepsilon_{vol}} \tag{3.29}$$

Usually it is convenient to set $K_e = K_f$ (see Potts & Zdravković, 1999) and therefore the total constitutive matrix can be expressed as:

$$[D] = [D'] + K_f \{b\} \{b\}^T \tag{3.30}$$

It is now straightforward to incorporate the principle of effective stresses into a finite element analysis by replacing the total stress constitutive matrix $[D]$ by equation 3.30. This requires the specification of the effective stress constitutive matrix $[D']$ and the bulk modulus of the pore fluid $K_f$. The determination of unknown nodal displacements follows the standard procedure described in the previous sections. However, when calculating stresses the bulk modulus of the pore fluid is used to determine the changes in pore water pressures. In a similar way, the changes in effective soil stresses are obtained by applying the effective constitutive matrix $[D']$. The changes in total stresses can be calculated according to equation 3.22.

If the bulk modulus of water $K_f$ is set to zero, the analysis reduces to drained conditions and pore fluid pressures do not change during loading. In order to achieve undrained conditions, a relatively high value for $K_f$ has to be specified. In ICFEP it is common practice to simulate undrained conditions by establishing the bulk modulus of the pore fluid from the bulk modulus of the soil skeleton $K_{skel}$ via the following equation:

$$K_f = \beta \, K_{skel} \tag{3.31}$$

where $\beta$ has a value between 100 and 1000. $K_{skel}$ can be evaluated from the effective stress parameters forming the $[D']$ matrix (see Potts & Zdravković, 1999).

## 3.4 Finite element theory for non-linear materials

When dealing with materials that exhibit non-linear constitutive behaviour, the finite element theory presented in the previous sections has to be adapted. In the literature, several mathematical strategies are available for dealing with non-linearity, having in common that the boundary conditions are applied in a series of increments. In the case of non-linear elasto-plastic models that are often used for simulating the material response of concrete and soil, the constitutive matrix $[D]$ is replaced by the elasto-plastic constitutive matrix $[D^{ep}]$ and varies with stress and/or strain. Therefore, the global stiffness matrix $[K_G]$ is not constant any more but changes during the finite element analysis, a fact which makes the solution of the problem more difficult. The set of global equations earlier introduced in equation 3.21 can now be rewritten in an iterative form as:

$$[K_G]^i \{\Delta d\}^i_{n,G} = \{\Delta R_G\}^i \tag{3.32}$$

where $[K_G]^i$ is the incremental global stiffness matrix, $\{\Delta d\}^i_{n,G}$ the vector of incremental nodal displacements, $\{\Delta R_G\}^i$ is the vector of incremental nodal forces and $i$ the increment number. This global set of equations must be solved for each increment during the change in boundary conditions. The final solution is then obtained by summing up the results from each increment. Some popular solution strategies that are commonly in use are the tangent stiffness method, the visco-plastic method and the modified Newton-Raphson scheme. The latter is known as a robust and economic solution technique and was therefore applied for all the analyses performed throughout this thesis. Its basic principle is explained briefly in the next section.

### 3.4.1 The modified Newton-Raphson method

When applying the modifed Newton-Raphson method each increment of equation 3.32 is solved in a number of iterations. Fig. 3.3 illustrates graphically the basic principle of the method for a simple uniaxial loading condition. At the beginning of the first iteration a global stiffness matrix $[K_G]^o$ is calculated from the current stresses at the beginning of the increment. However, during the first iteration the technique recognizes that the solution according to equation 3.32 is likely to be in error due to the non-linear variation of the stiffness matrix over the increment. The predicted displacements $\Delta d^1$ are used to calculate a residual load vector $\psi^1$, which is a measure of the error in the analysis. Equation 3.32 is then solved again in a second iteration, using the residual load vector $\psi^1$ as the right hand side vector. The residual load vector $\psi^2$ at the end of the second iteration is evaluated from the predicted displacements $(\Delta d^1 + \Delta d^2)$.

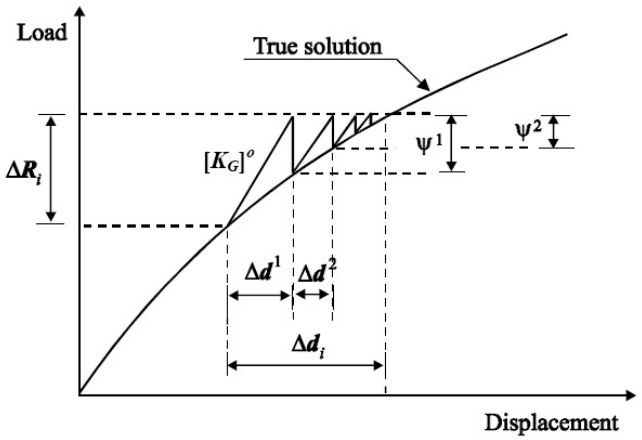



Figure 3.3: Basic principle of the modified Newton-Raphson scheme (after Potts & Zdravković, 1999)

The complete iterative process can be written in a compact mathematical form as:

$$[K_G]^i \left(\{\Delta d\}^i_{n,G}\right)^j = \{\psi\}^{j-1} \tag{3.33}$$

The newly introduced superscript $j$ refers to the iteration number and for the first iteration $\{\psi\}^o = \{\Delta R_G\}^i$. This procedure continues until the prescribed convergence criteria are satisfied. The incremental solution of the unknown displacement quantities is then evaluated by summing up the displacements of each iteration. In ICFEP these convergence limits are set on the size of both the iterative displacements $\left(\{\Delta d\}^i_{n,G}\right)^j$ and the residual loads $\{\psi\}^j$. They are given as:

$$\left\|\left(\{\Delta d\}^i_{n,G}\right)^j\right\| = \sqrt{\left(\left(\{\Delta d\}^i_{n,G}\right)^j\right)^T \left(\{\Delta d\}^i_{n,G}\right)^j} \tag{3.34}$$

and

$$\left\|\{\psi\}^j\right\| = \sqrt{(\{\psi\}^j)^T \{\psi\}^j} \tag{3.35}$$

The iterative displacement norm of equation 3.34 is usually checked against the norms of the incremental and accumulated displacements. Likewise, the norm of the residual loads of equation 3.35 is compared to the norms of the incremental and accumulated global right hand side load vector. For the convergence criteria in ICFEP, 2 % is set as a default value and has been used for the analyses performed within this thesis.

When adopting the modified Newton-Raphson method the incremental global stiffness matrix $[K_G]^i$ is usually calculated and inverted at the beginning of an increment and used for all the further iterations within this increment. This helps to reduce the amount of computation compared to the original Newton-Raphson scheme, where the incremental global stiffness matrix is updated for each iteration. ICFEP enables the user to specify the stiffness matrix to be recalculated every certain number of iterations. Furthermore, sometimes the

global stiffness matrix is determined using the elastic constitutive matrix $[D]$ rather than the elasto-plastic constitutive matrix $[D^{ep}]$, since the predicted solution by equation 3.32 is expected to be in error anyway.

One key step in the modified Newton-Raphson solution technique is the evaluation of the residual load vector $\{\psi\}^j$ for each iteration. It can be determined from the following procedure: First, the current incremental strains at each integration point are calculated from the incremental displacements obtained at the end of the previous iteration. The constitutive model is then integrated along these strain paths in order to estimate the change in stresses, which is added to the stresses at the beginning of the increment. From this current accumulated stress state the equivalent nodal forces can be evaluated. The residual load vector is the difference between these nodal forces and the externally applied loads. For the integration of the constitutive equations along the incremental strain path a method termed "stress point algorithm" is necessary. Several of these algorithms are available in the literature and the one used in ICFEP will be presented in the next section of this chapter.

### 3.4.2 Stress point algorithm

The adopted stress point algorithm for the analyses presented in this thesis is a so called semi-explicit "substepping algorithm" combined with a modified Euler integration scheme, which integrates the constitutive equations over each substep. As mentioned earlier, the objective of such a stress point algorithm is to estimate the incremental stresses $\{\Delta\sigma\}$ from the previously calculated incremental strains $\{\Delta\varepsilon\}$ in order to obtain the accumulated stresses at the end of the increment as:

$$\{\sigma\} = \{\sigma_o\} + \{\Delta\sigma\} \tag{3.36}$$

where $\{\sigma_o\}$ are the stresses at the beginning of the increment. The size of each substep is usually determined by the error in the numerical integration compared to a user defined tolerance. The complete stress change at the end of an iteration is then obtained by summing the stress changes from each substep. A simple graphical representation of the substepping approach for an elasto-plastic material in the $J$-$p$ space can be seen in Fig. 3.4

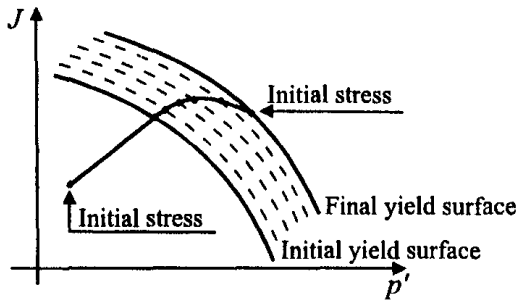



Figure 3.4: Basic principle of the substepping approach (from Potts & Zdravković, 1999)

The following general procedure based on a scheme presented by Sloan (1987) is carried

out: At the beginning, the elastic proportion $\alpha$ of an increment has to be determined by checking the value of the yield function $F$ and adopting some simple interpolation functions (see Potts & Zdravković, 1999). The remaining strain increment associated with elasto-plastic behaviour is therefore equal to $(1-\alpha)\{\Delta\varepsilon\}$. The initial stress and strain components of the remaining elasto-plastic increment are given as:

$$\{\sigma\} = \{\sigma_o\} + \{\Delta\sigma^e\} \tag{3.37}$$

and

$$\{\Delta\varepsilon_s\} = (1-\alpha)\{\Delta\varepsilon\} \tag{3.38}$$

where $\{\sigma_o\}$ are the stresses at the beginning of the increment and $\{\Delta\sigma^e\}$ the elastic proportion of the stress increment. $\{\Delta\varepsilon_s\}$ represents the elasto-plastic part of the total strain increment $\{\Delta\varepsilon\}$ and will be split into a number of substeps in the course of the algorithm. It is assumed that such a substep strain $\{\Delta\varepsilon_{ss}\}$ writes as:

$$\{\Delta\varepsilon_{ss}\} = \Delta T\{\Delta\varepsilon_s\} \tag{3.39}$$

with the proportion $\Delta T$ varying between 0 and 1. Initially it is assumed that just one substep is necessary and hence $\Delta T$ is set to unity. A first estimate of the associated changes in stresses, plastic strains and hardening parameters is obtained by using a first order Euler integration approximation, namely:

$$\{\Delta\sigma_1\} = [D^{ep}(\{\sigma\},\{k\})]\{\Delta\varepsilon_{ss}\} \tag{3.40}$$

$$\{\Delta\varepsilon_1^p\} = \Lambda(\{\sigma\},\{k\},\{\Delta\varepsilon_{ss}\})\frac{\partial P(\{\sigma\},\{m_1\})}{\partial\sigma} \tag{3.41}$$

$$\{\Delta k_1\} = \{\Delta k(\{\Delta\varepsilon_1^p\})\} \tag{3.42}$$

The above quantities are used to calculate the stresses and hardening parameters at the end of the substep according to $\{\sigma\}+\{\Delta\sigma_1\}$ and $\{k\}+\{\Delta k_1\}$ respectively. Consequently, a second estimate for the changes in stresses, plastic strains and hardening parameters over the substep is carried out and is obtained as:

$$\{\Delta\sigma_2\} = [D^{ep}(\{\sigma+\Delta\sigma_1\},\{k+\Delta k_1\})]\{\Delta\varepsilon_{ss}\} \tag{3.43}$$

$$\{\Delta\varepsilon_2^p\} = \Lambda(\{\sigma+\Delta\sigma_1\},\{k+\Delta k_1\},\{\Delta\varepsilon_{ss}\})\frac{\partial P(\{\sigma+\Delta\sigma_1\},\{m_2\})}{\partial\sigma} \tag{3.44}$$

$$\{\Delta k_2\} = \{\Delta k(\{\Delta\varepsilon_2^p\})\} \tag{3.45}$$

Now a more accurate modified Euler estimate of the changes in stresses, plastic strains and hardening parameters can be established as:

$$\{\Delta\sigma\} = \frac{1}{2}(\{\Delta\sigma_1\}+\{\Delta\sigma_2\}) \tag{3.46}$$

$$\{\Delta\varepsilon^p\} = \frac{1}{2}\left(\{\Delta\varepsilon_1^p\} + \{\Delta\varepsilon_2^p\}\right) \tag{3.47}$$

$$\{\Delta k\} = \frac{1}{2}\left(\{\Delta k_1\} + \{\Delta k_2\}\right) \tag{3.48}$$

By subtracting equation 3.40 from 3.46 one obtains an estimate of the local error in the predicted stresses as:

$$E \approx \frac{1}{2}\left(\{\Delta\sigma_2\} - \{\Delta\sigma_1\}\right) \tag{3.49}$$

The relative error in stress for the substep can be expressed as:

$$R = \frac{\|E\|}{\|\{\sigma + \Delta\sigma\}\|} \tag{3.50}$$

This error is checked against a user defined tolerance $SSTOL$ and if the error is unacceptable, i.e. $R > SSTOL$, the initial substep size is reduced further. The above presented procedure is then repeated with a new value of $\Delta T$ in equation 3.39 until the calculated error $E$ is smaller than the defined tolerance and the substep size is accepted. This is followed by an update in the accumulated stresses, plastic strains and hardening parameters and the next substep can be carried out. For further detailed information about the error control and the estimation of the size of the substep see Potts & Zdravković (1999).

## 3.5 Summary

This chapter intended to provide an introduction into the theory of the finite element method. First, the theoretical background for modelling linear elastic materials was discussed in detail, highlighting the principal steps that are involved in such a complex numerical analysis. Second, in order to apply the finite element method to geotechnical engineering problems some modifications for a realistic modelling of soil as a two phase material have been presented, including the principle of effective stresses. However, concrete and shotcrete show highly non-linear stress-strain behaviour in various loading conditions. Therefore the basic finite element theory has to be extended to account for non-linear material behaviour and the necessary numerical algorithms for such a non-linear finite element analysis have been presented. The following aspects can be summarized:

- The finite element method is a powerful tool for analysing complex engineering problems and follows in general the following procedure: element discretisation, approximation of the primary variable, formulation of element equations, boundary conditions and solution of global equations.

- The displacement based finite element method is the most common approach for geotechnical engineering purposes. The variation of the displacement field over the element is the key aspect of this method and can be described by shape functions.

- The formulation of the element equations couples compatibility, equilibrium and con-

stitutive conditions leading to a set of equations that describe the relationship between loads and displacements via the element stiffness. These element equations are then assembled into a global set of equations.

- Boundary conditions with respect to loads and displacements are of crucial importance for a finite element analysis for a full definition of the boundary value problem to be analysed.

- For geotechnical applications soil as a two phase medium has to be considered in a finite element analysis. The incorporation of the principle of effective stresses into the basic theory of the finite element method allows the calculation of pore water pressures and effective soil stresses in an undrained analysis, as presented later in Chapter 8.

- When performing a non-linear finite element analysis some iterative techniques have to be used in order to solve the set of global equations. The modified Newton-Raphson method combined with a semi-explicit substepping algorithm have been adopted as a solution strategy.

# Chapter 4

# Shotcrete Technology

## 4.1 Introduction

Although the history of shotcrete goes back to the beginning of the 20$^{th}$ century, shotcrete technology is a relatively young field of research, where many new innovations regarding material composition and installation equipment have been achieved over the past decades. However, in reality engineers have to face many problems when confronted with the design or construction of sprayed concrete structures due to their limited knowledge about the fundamental principles with respect to material technology and mechanical behaviour. Therefore, the aim of this chapter is to introduce the basic background information about shotcrete technology with a particular focus on material ingredients and installation techniques. It should enable the reader to understand in a better way the complex mechanical behaviour of young shotcrete, that will be discussed in detail in Chapter 5. In the first part of this chapter, the main material components of sprayed concrete will be presented, followed by a short introduction into the chemical reaction of cement hydration. Furthermore, the two different ways of spraying shotcrete in place, dry- and wet-mix, will be explained in detail. Finally, a quick review about different testing techniques of shotcrete at early ages will complete this chapter.

## 4.2 Shotcrete as an engineering material

Shotcrete is a special type of concrete, which was invented at the beginning of the 20$^{th}$ century by Carl Akeley (1864 - 1926), a famous American taxidermist (see Fig. 4.1). He experimented with the pneumatic application of first plasters and then cement mortars to make models of animals for the Field Museum of Natural History in Chicago (Austin & Robins, 1995). Akeley used the simple method of blowing a dry mixture of sand and cement out of a hose with compressed air and wetting it as it was released. In 1911 he obtained patents for both the equipment and method and the material was called "Gunite". One year later, the Cement Gun Company of Allentown, Pennsylvania, took over the patents and

expanded to Europe, bringing this new technology to Germany in 1921 and the UK in 1924. Fig. 4.1 shows the original cement gun designed for the dry-mix process.

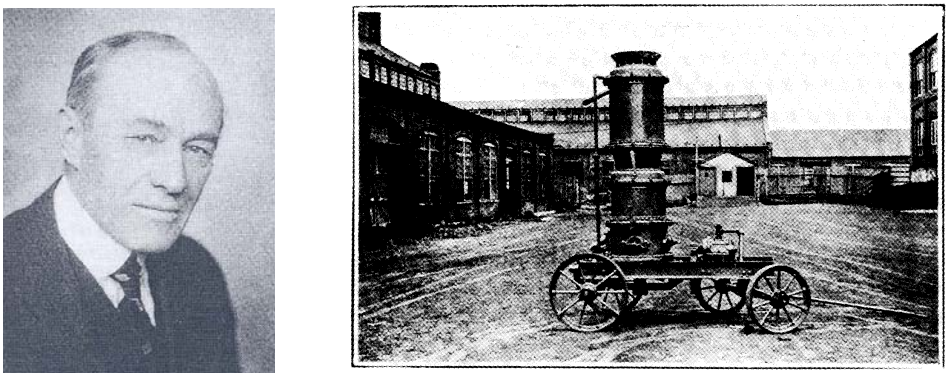


Figure 4.1: Carl Akeley and his first cement-gun

Nowadays several names for the sprayed mixture of aggregates and cement are in use worldwide, among them "Sprayed Concrete" or "Shot Concrete". They all have in common to define this material as mortar or concrete which is pneumatically projected into place at high pressures. The term "Shotcrete" is mainly used in the US when describing a mix whose maximum aggregate size is no more than 10 mm, whereas "Sprayed Concrete" is the more widely used terminology in Europe (SCA, 1999).

Shotcrete has a wide range of applications in all kinds of engineering fields, and each makes use of the uniquely flexible nature of the application technique, which requires minimum formwork and access space to produce flat or curved surfaces (Austin & Robins, 1995). They include:

- New construction and repair of reinforced concrete structures
- Thin arches, domes and shells
- Rock stabilization
- Underground rock support and tunnelling
- Fire protection of steel framed buildings

In 1914, shotcrete was proposed for the first time in underground structures to protect mine drifts against the atmosphere and to make them fireproof (Moussa, 1993). The first application of shotcrete for tunnel construction in the USA is recorded in the early 1920s. In Europe, shotcrete was introduced successfully in 1951 for the Ladano-Mosagno tunnel of the Maggia Hydro-Electric scheme in Switzerland. With the rapid development of tunnelling, shotcrete became more and more popular in underground structures and is nowadays an important support element of the New Austrian Tunnelling Method (NATM). The early sprayed concrete did not show high material quality and large quantities of aggressive additives were

needed to make the material adhere to the ground in order to spray reasonably thick layers (Thomas, 2009). It has largely been associated with rock tunnelling and with the treatment of closely jointed or shattered rocks, such as those found in Alpine regions. Nevertheless, in the 1970s shallow tunnels in soft ground conditions, as part of metro projects in Frankfurt and Munich, were successfully constructed using shotcrete for ground stabilization. In the UK shotcrete technology is relatively new in tunnelling industry and has only become widely used within the last 15 years. Over the last 10 years significant progress has been made regarding the constituent materials, mix formulations and equipment design for shotcrete, but there is still a need for more research and development of design methods, standard test methods and specifications (Austin & Robins, 1995).

Up to now, no internationally accepted framework exists for practical applications, covering the above mentioned aspects for all the different structures involving shotcrete. In the literature the following guidelines and recommendations for shotcrete technology have been found:

1. Austrian Society for Concrete- and Construction Technology, ASCCT (2004): *Sprayed concrete guideline*
2. German Standard DIN 18551 (2005): *Shotcrete - specification, production, design and conformity*
3. AFTES work group Nr. 20 (2000): *Recommendations for the design of sprayed concrete for underground support*
4. American Concrete Institute ACI 506R-05 (2005): *Guide to shotcrete*
5. EFNARC (1996): *European specification for sprayed concrete*
6. European Standard EN 14487-1 (2005): *Sprayed concrete*
7. Sprayed Concrete Association UK (1999): *Introduction to sprayed concrete*

In ASCCT (2004) three different classes of shotcrete are defined according to its structural use in engineering construction:

**SpC I:** Shotcrete without structural use for the sealing of surfaces and short temporary support during construction stages.

**SpC II:** Shotcrete as a structural element for the support of underground excavations, shaft constructions and retaining walls.

**SpC III:** Shotcrete with very special structural use for the construction of single-shell tunnel linings.

For each individual sprayed concrete class certain requirements have to be fulfilled in terms of material properties such as early strength, density of the material, uniformity, permeability and leaching behaviour, frost resistance and chemical exposure. The test requirements to be met differ accordingly and can be found in ASCCT (2004).

## 4.3 Mix design

Like any other ordinary cast structural concrete, shotcrete consists of aggregates, cement and water. A variety of additives and admixtures is often added to the sprayed concrete mix in order to improve or change certain material properties. In the following sections of this chapter each shotcrete component should be discussed briefly.

### 4.3.1 Aggregates

The selection of the maximum aggregate size for shotcrete depends heavily on its structural use, but is normally between 4 and 16 mm (ASCCT, 2004). For sprayed concrete of class SpC II and SpC III the maximum diameter of aggregate should be limited to 11 mm because of its rebound behaviour: the larger the pieces of aggregate, the more of them are lost in rebound, specially when wire mesh is used as reinforcement. This also means, that the in situ material is more finely graded than before spraying, a fact that has to be taken into account in mix design to ensure a balanced in situ material. Both crushed and round aggregates can be used and the grading curve should be smooth, slightly oversanded and be based usually towards the finer end for reasons of pumpability. The moisture content of aggregates is an important factor in the dry mix process. For a moisture content of less than 3 % the dust production will be very high and therefore the optimum value is between 3 and 6 %. Fig. 4.2 shows a typical recommended grading zone for sprayed concrete taken from EFNARC (1996).

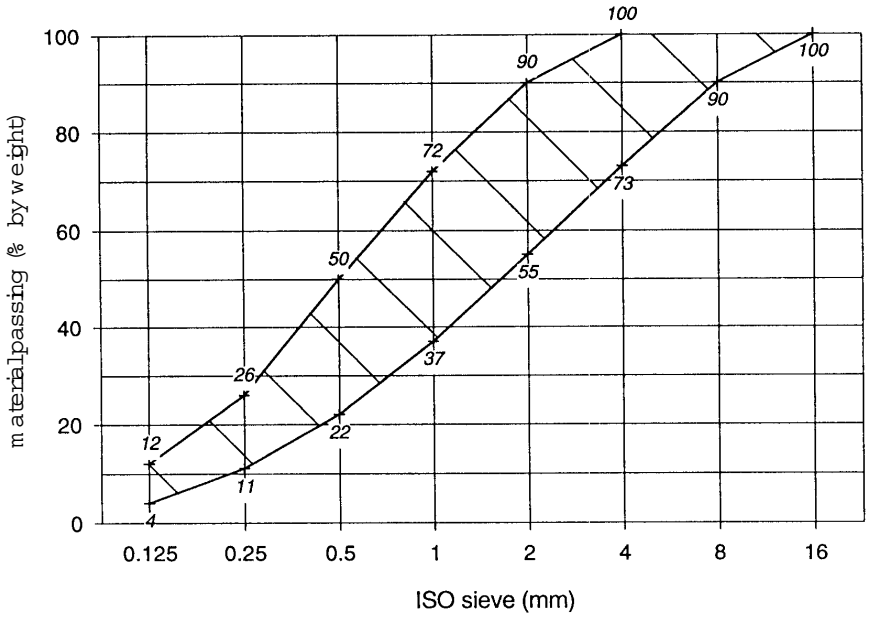



Figure 4.2: Recommended aggregate gradation zone from EFNARC (1996)

### 4.3.2 Cement

As a binder for shotcrete ordinary Portland cements can be used with a dosage between 325 and 450 kg/m$^3$ before casting (Girmscheid, 2000). The amount of cement included in the shotcrete mix depends also on the adopted maximum aggregate size, as can be seen in Fig. 4.3. Due to the rebound of aggregates during spraying, the in situ material is slightly richer in cement than the starting mix. The commencement of cement setting for Portland cement is usually in the range of 1 to 3 hours. Special rapid hardening tunnel cements are used, when high early strengths are required during construction. Such cements are an alternative to an ordinary sprayed concrete with the use of an accelerator, in order to achieve similar effects on the setting time. Concerning the compressive strength of cement the following requirements are reported in Hafez (1995):

| | |
|---|---|
| after 1 day | $\geq 7\,\mathrm{N/mm^2}$ |
| after 28 days | $\geq 39\,\mathrm{N/mm^2}$ |
| after 90 days | $\geq 50\,\mathrm{N/mm^2}$ |

Nowadays Portland cement is increasingly being used with supplementary cementing materials, such as fly ash and silica fume, in both the dry and wet mix processes.

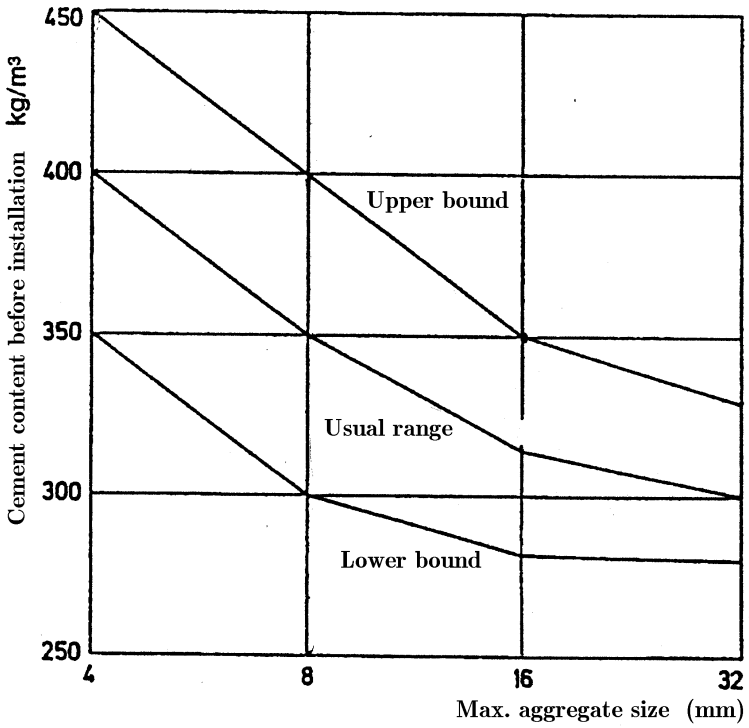



Figure 4.3: Recommended cement content of shotcrete mix before installation depending on maximum aggregate size (from Aldrian, 1991)

### 4.3.3 Water

The water content of a certain mix design plays an important role in the mechanical behaviour of shotcrete. The higher the water-cement ratio, the lower the 28-days compressive strength of concrete, as indicated in Fig. 4.4. This effect is due to the higher porosity which is obtained after hydration when too much water is used for the mixing. However, pumpability requirements dictate that the water-cement ratio for shotcrete is slightly higher than the one for conventional cast concrete (0.3 - 0.4).

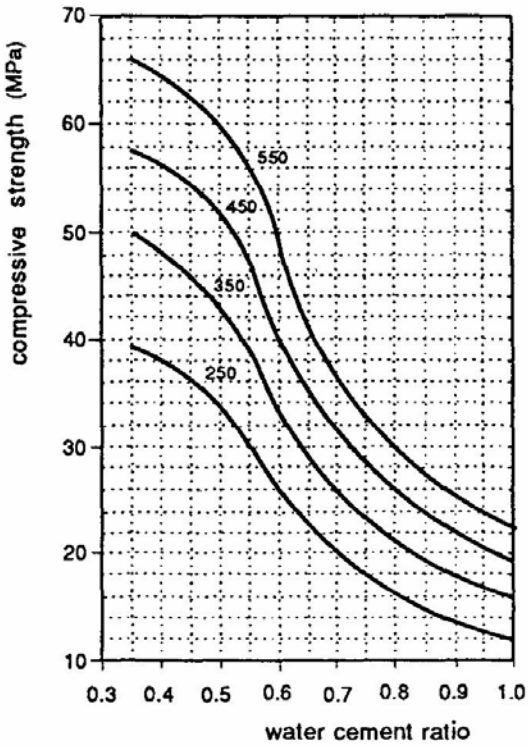



Figure 4.4: Relationship between compressive strength and water-cement ratio for concrete (from Karrer, 1986)

### 4.3.4 Additives

As mentioned before, a variety of additives and admixtures can be added to sprayed concrete to improve certain properties, such as strength, adhesiveness, durability, permeability and rebound behaviour. Higher material costs are often balanced by savings in the volume of shotcrete used and labour.

#### 4.3.4.1 Silica fume

Silica Fume is a highly puzzolanic mineral admixture that has been used mainly to improve concrete durability and as a Portland cement replacement (Wolsiefer & Morgan, 2003). It is a waste product from the metal industry and has been primarily used in the United States, Canada and the Scandinavian countries, but is now finding increasing use elsewhere in the world. In the 1970s it was first used in shotcrete for a tunnel lining construction in Norway. Due to its extreme fineness, the particles fill the microscopic voids between the cement particles, which leads to an increased density and very low permeability of shotcrete. Further, through the use of silica fume high compressive and flexural strengths are achieved with the elimination of the need for accelerators for early strengths. Material cost effectiveness is improved by the reduction of rebound in the dry mix process by up to 50 %. For vertical and overhead spraying, increased one-pass layer thicknesses are possible without using accelerators, thus improving productivity. As a rule of thumb, the dosage of silica fume is given

in various international guidelines for shotcrete as ranging from 5 to 15 % of mass of cement (Austin & Robins, 1995).

#### 4.3.4.2 Accelerators

The setting process of cement can be speeded up by the use of accelerators, which leads to high early strengths of shotcrete in the first 12 hours after spraying. They are chemical products usually available in powdery and liquid form and can be used for both the dry- and the wet-mix processes. In the early days, various water soluble salts of the alkali metals were used to accelerate the setting of cement, most of them based on alkali aluminates in combination with carbonates and hydroxides. However, these chemicals were very caustic and exposed the workmen to a significant danger. The dosage of such an accelerator and its fast reaction with cement has to be proven before spraying and is normally in the range of 2 to 7 % of weight of cement (Girmscheid, 2000). Another advantage of using accelerators is the improved adhesiveness especially for wet-mix shotcrete, which leads to larger application thicknesses. Despite these facts, there were two main drawbacks concerning the use of accelerators for shotcrete. As can be seen in Fig. 4.5, the addition of such an accelerator in the concrete mix can decrease the target 28-day compressive strength of 40 MPa significantly. Secondly, if the accelerator dosage is too high, an existing shotcrete layer will stiffen and harden too fast and therefore aggregates of later applied shotcrete cannot penetrate properly into the existing layer and bounce off. This fact leads to an increased rebound behaviour and loss of material.

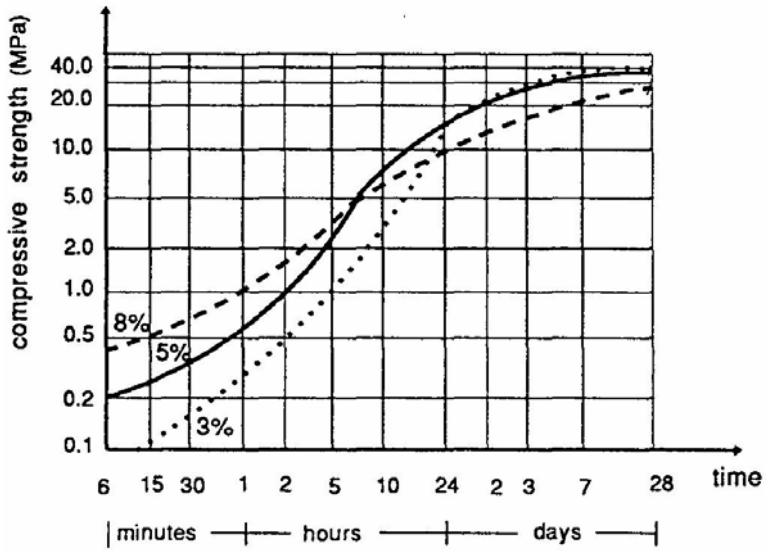



Figure 4.5: Time dependent influence of accelerator dosage on compressive strength (from Kusterle, 1985)

However, in Thomas (2009) it is stated that accelerators of the new generation do not show a reduction of the 28-day strength of shotcrete. They are safer to use and almost alkali-free, which reduces the risk of an alkali reaction in the shotcrete significantly. Jodl

& Kusterle (1998) report new developments for completely alkali-free accelerators of an aluminium hydroxide base, which develop sufficient early strength for even low dosages (4 %) and no difference in the final compressive strength compared to ordinary shotcrete.

#### 4.3.4.3 Plasticisers

Especially for the wet mix process plasticisers are used for a better workability and transport of the fresh shotcrete into the tunnel (Austin & Robins, 1995). Therefore, a lower water-cement ratio can be applied and higher strengths achieved. These types of additives should not be used for the dry-mix process, as the wetting time at the nozzle is too short and the reaction of the plasticisers would only start when the shotcrete is already sprayed on the wall. This results in a running off of shotcrete from the tunnel wall (Girmscheid, 2000).

### 4.3.5 Fibres

The use of fibre reinforced concrete and shotcrete has advanced substantially in the last few years and significant progress has been made regarding the quality of involved materials and application techniques. Due to its advantage of improving certain material properties, fibre reinforced shotcrete has been widely accepted for the support of underground openings, rock slope stabilization or thin shell dome constructions. Three different types of fibres are commonly in use for reinforcing concrete and shotcrete and they will be discussed briefly in the following sections.

#### 4.3.5.1 Steel fibres

The conventional construction of reinforced shotcrete in underground structures involves the application of ordinary wire mesh, which is a very time-consuming and heavy manual process. In the early 1970s, steel fibres were proposed as a new technology for reinforcing shotcrete tunnel linings, where pioneering developments have been achieved by the Scandinavian countries and at the Ruhr University at Bochum in Germany (Franzen, 1992). By replacing welded wire mesh with steel fibres some major economical benefits regarding material and labour costs can be achieved. However, one of the main reasons for using steel fibres for shotcrete is the increase in material ductility and flexural strength, which depends heavily on the amount and type of fibres adopted. Fig. 4.6 contains a compilation of commonly used types of steel fibres available on the market, showing typical fibre cross-sections on the right with dimensions in [mm].

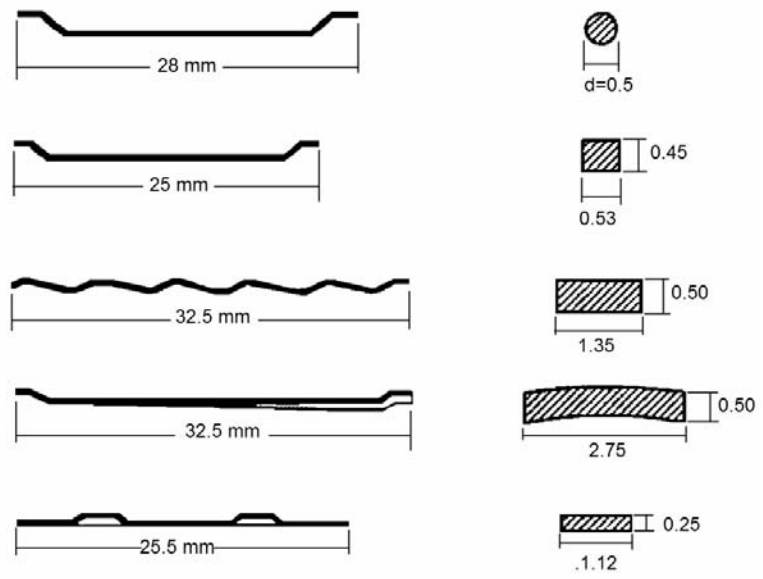



Figure 4.6: Different types of steel fibres used in sprayed concretes (from Banthia et al., 1992)

Long fibres with a length greater than 25 mm and a rather high dosage between 40 and 75 kg/m$^3$ are preferable, with 60 kg/m$^3$ being commonly used in tunnelling and mining applications. Some of the critical and important parameters of steel fibres are:

- Geometry
- Length
- Aspect ratio ($L/D$)
- Steel quality

For a proper mix design the rebound of the steel fibres during the spraying process should be taken into account and therefore a minimum dosage of 30 kg/m$^3$ is proposed in ASCCT (2004). Both installation techniques, dry- and wet-mix, are suitable for the application of steel fibre reinforced concrete. For anchoring reasons, the fibres should be at least twice as long as the largest aggregate. ASCCT (2004) recommends therefore to limit the maximum aggregate size for steel fibre reinforced sprayed concrete to 8 mm. Some negative effects of the steel fibres have to be expected on the pumping and spraying of the mix. Therefore, steel fibre reinforced shotcrete requires the use of microsilica and admixtures that enhance pumpability. The fibre length should not exceed 50 to 60 % of the pumping hose diameter. This results in a maximum fibre length of about 25 mm for manual spraying and 40 mm for robotic application of the shotcrete.

As mentioned earlier, the aspect ratio, defined as the ratio between the length and the equivalent fibre diameter ($L/D$), is of crucial importance for the performance of steel fibres in sprayed concrete, usually ranging from 40 to 60 (Austin & Robins, 1995). From the

mechanical point of view, a higher aspect ratio and volume concentration would be preferable, but unfortunately this leads to difficulties for the mixing, conveying and shooting of the shotcrete mixture. It can be observed that there are some practical and economical limitations for the type and amount of fibres used for reinforcement. In the early days of steel fibre technology most of the fibres were straight and did not show a good testing response regarding pull-out resistance. Consequently, manufacturers focused on improving the aspect ratio of steel fibres by methods such as crimping, introducing bent or enlarged ends or making special deformations on the fibres.

Finally, it can be concluded that steel fibre reinforced shotcrete is a relatively new but powerful technology in the field of tunnelling, where major developments have been achieved over the last 20 years. The continuously increasing use of fibre reinforcement implies enhanced saftey of underground structures and substantial cost savings during construction (Franzen, 1992).

#### 4.3.5.2 Polypropylene fibres

In the late 1980s polypropylene fibres started to find use in concrete engineering, initially at very low addition rates of about $1\,kg/m^3$ (Austin & Robins, 1995). Their mechanical properties were similar to those of plain concrete and therefore they could not enhance the mechanical behaviour significantly. The benefits were limited mainly to providing some resistance against plastic shrinkage cracking and improved strength of the freshly applied shotcrete. Another advantage was the reduced amount of rebound when adopting the wet-mix installation technique. However, recent developments led to new types of plastic fibres made of high quality materials. If moderately dosed, at about 10 to $13\,kg/m^3$, it has been shown that these higher fibre additions in the wet-mix process result in a more ductile material behaviour, similar to the one obtained with steel fibre reinforced concrete or shotcrete. In Fig. 4.7 typical fibrillated polypropylene fibres with a length of 20 to 40 mm are illustrated.

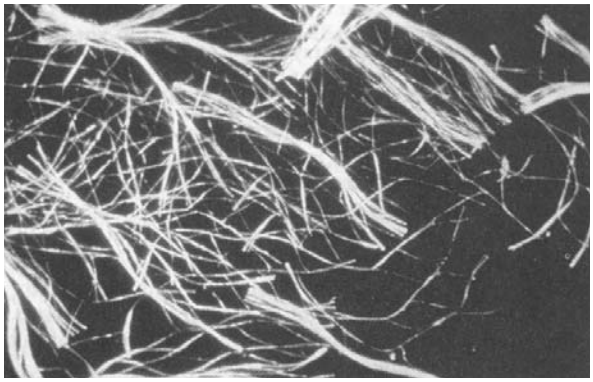


Figure 4.7: Polypropylene fibres used in wet-mix sprayed concrete (from Austin & Robins, 1995)

For dry-mix concrete, the incorporation of higher addition rates is still difficult to achieve,

since the wetting of the shotcrete mixture at the nozzle is simply not capable of adequately coating and embedding the plastic fibres in the cementitious mix before the impact at the surface. As a result the actual in-place fibre content remains relatively low (Austin & Robins, 1995).

#### 4.3.5.3 Glass fibres

A certain concern exists for the use of glass fibres over their long-term durability due to the alkali attack of the glass within the concrete matrix. Therefore, glass fibres are less common for permanent shotcrete structures. However, Austin & Robins (1995) mention one application of the repair to a navigation lock in Washington State.

## 4.4 Cement hydration

When cement is dispersed in water a chemical reaction is started between the clinker components of the cement and the water, which causes hardening of the cement paste. This reaction progresses at different rates for each of the involved components and the reaction products also vary accordingly. In Neville (1981) the main clinker compounds of ordinary Portland cement are given as:

- Tricalcium silicate ($C_3S$)
- Dicalcium silicate ($C_2S$)
- Tricalcium aluminate ($C_3A$)
- Tetracalcium aluminate ferrite ($C_4AF$)

The following part of this chapter describes briefly the main stages of cement hydration and their hydration products.

### 4.4.1 Reaction process

According to Fig. 4.8 three stages of cement hydration can be identified.

**Stage I** Within the first minutes after mixing of cement and water, first needle-shaped crystals of a calcium sulfoaluminate hydrate called ettringite appear on the surface of the cement particles. This phase is still dominated by low strengths of the formed solids and the structure is termed unstable.

**Stage II** A few hours after starting hydration, large prismatic crystals of calcium hydroxide and very small fibrous crystals of calcium silicate hydrates begin to fill the empty space that was formerly occupied by water and the dissolving cement particles. The cement paste is setting and a basic structure is built up.

**Stage III** After some days, the ettringite may become unstable and decompose to form monosulfate hydrate, which has a morphology of hexagonal plates. The strength development of the material is advanced and a stable structure has been established.

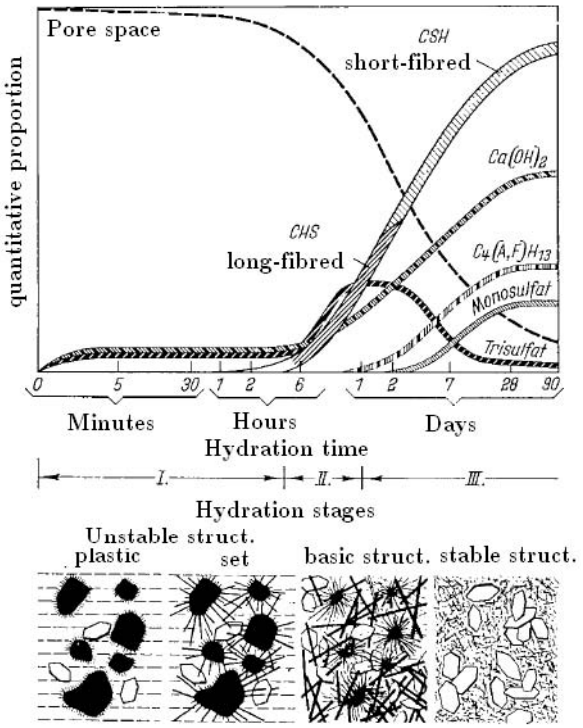



Figure 4.8: Schematic representation of the cement hydration (after Labahn, 1982)

Further information about the complex process of cement hydration can be found in Neville (1981), Byfors (1980) and Mehta & Monteiro (1985).

### 4.4.2 Degree of hydration

In the literature, the degree of hydration is a term often used to quantify how far the reactions between cement and water have developed, varying between 0 (no reactions have occurred) and 1 (cement hydration complete). It is also a useful parameter to describe the development of certain material parameters of the young concrete. However, cement hydration is a very complex process where various chemical reactions are taking place simultaneously and one single parameter might sometimes not be enough to describe the complete hydration process in detail. In Byfors (1980) an overview of different definitions for the degree of hydration $\xi$ available in the literature is given. Among them are:

$$\xi = \frac{\text{Quantity of cement gel formed}}{\text{Quantity of cement gel formed at complete hydration}} \tag{4.1}$$

$$\xi = \frac{\text{Quantity of hydrated cement}}{\text{Original quantity of cement}} \tag{4.2}$$

$$\xi = \frac{\text{Quantity of heat developed}}{\text{Quantity of heat developed at complete hydration}} \tag{4.3}$$

$$\xi = \frac{w_n}{0.25\,c} \tag{4.4}$$

where $w_n$ is the quantity of bound water and $c$ the cement content. As one can imagine, the values of these definitions can differ significantly from each other, particularly at an early age and should therefore be used with caution. The adequate choice of the definition depends to a considerable extent on the method used for determining the degree of hydration. For further information on this topic see Byfors (1980).

## 4.5 Shotcrete installation

Shotcrete can be seen as a special type of concrete, not necessarily because of the mix design but because of the nature of its installation - casting and compacting are done in one single step. In this part of the thesis the reader will be introduced to the different installation techniques of shotcrete, including material preparation, choice of the proper site equipment and the spraying itself. As mentioned before, sprayed concrete finds many applications in engineering but the focus here will be on the use of shotcrete in tunnelling, which involves high volume output. Various production processes have been developed in recent years and the distinguishing features are the preparation of the starting materials and the method of transporting and casting the sprayed concrete in the tunnel. The two main dominating techniques are:

- Dry-mix process

- Wet-mix process

There are essential differences between these two methods and the choice of one or the other depends on many factors of each tunnelling project. The production of shotcrete is mainly equipment orientated, whereas installation depends heavily on the technique and skills of the operatives. The dry-mix process represents the original application method, but recently significant developments and advances have been made to wet-mix technology.

### 4.5.1 Dry-mix process

In the dry spraying method, a dry mixture of aggregates, cement and occasionally powdery additives is transported from the spraying machine into the tunnel by compressed air. At the spraying nozzle, water is added and the mixture can be applied at velocities of about 20 to 30 m/s in order to compact it (Girmscheid, 2000). Modern systems also use liquid accelerators which are added to the shotcrete upstream of the spraying nozzle. The basic concept of the dry mix technology in tunnelling is illustrated in Fig. 4.9.

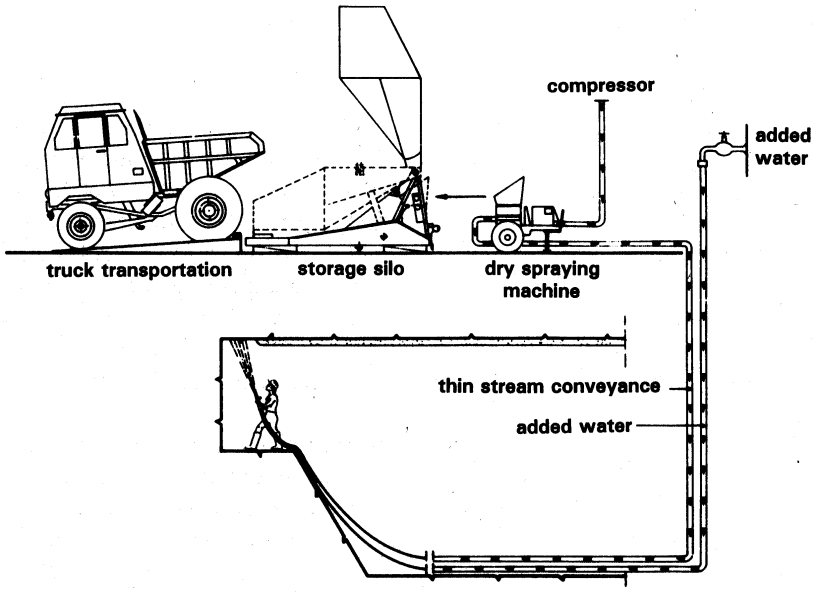



Figure 4.9: Process of dry-mix technology for sprayed concrete (from Austin & Robins, 1995)

In this process, the nozzle operator, or the so called "nozzleman", has a great influence on the quality of the shotcrete since the water content is controlled by him manually. Therefore the water-cement ratio for the dry-mix shotcrete is not a well defined value and normally lies in the range of 0.35 - 0.5 (Austin & Robins, 1995). If the water content is too low, then rebound and dust production increases. On the contrary, if the water-cement ratio is too high, the shotcrete will not stick on the tunnel wall but will run off. A severe problem with dry-mix shotcrete is the high dust production during spraying which leads to very dirty working conditions. This high dust level is due to the compressed air and the relatively high percentage of rebound. A big advantage of the dry-mix technology is its great flexibility. For example,

small quantities of sprayed concrete can be produced easily and necessary breaks in spraying can be bridged without cleaning the equipment. Furthermore, this method ensures transport over long distances (up to 350 m) without problems, thus eliminating the need for frequent movement of the equipment which would be very time consuming. Because of producing shotcrete with higher early strengths due to the lower water-cement ratio compared to the wet-mix process, the dry-mix technology has been preferred in the past and some countries, notably Austria, retain this preference (Thomas, 2009).

### 4.5.2 Wet-mix process

In the wet spraying method, as illustrated in Fig. 4.10, the ready mixed fresh concrete (containing aggregates, cement, water and additives) is transported to the spraying nozzle by compressed air or pumps. This results in a homogeneous concrete mass and causes less dust, because the water is already mixed to the concrete at the very beginning. For this reason, the big advantage of a well defined water-cement ratio can be obtained. The accelerator for increasing the early strength of the shotcrete can be added at the nozzle, as its setting time is just a couple of minutes.

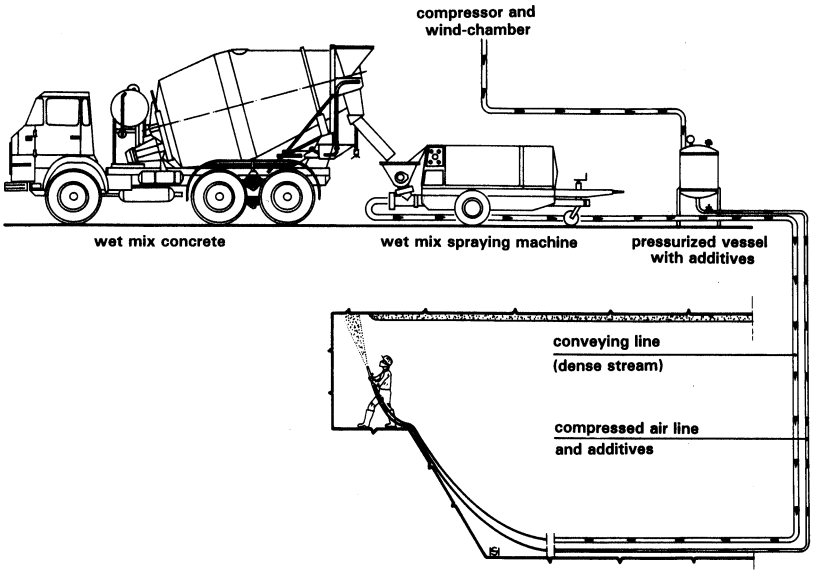



Figure 4.10: Process of wet-mix technology for sprayed concrete (from Austin & Robins, 1995)

An important distinction is made in the literature between three methods of transporting the shotcrete into the tunnel, as shown in Fig. 4.11:

- Thin stream conveying method
- Plug-flow conveying method
- Thick stream conveying method

In the thin stream method, similar to the dry-mix, compressed air is admitted to the fresh concrete in the wet mix machine in order to transport it pneumatically and to spray the shotcrete with a certain velocity. The difference between this method and the plug-flow process is that for the second, only the compressed air necessary for transporting the concrete into the tunnel is admitted to the concrete at the wet machine whereas the air for placement is supplied at the nozzle. During thick stream transport a compact material stream is pumped hydraulically from the wet-mix machine to the nozzle, where compressed air is used again to spray the concrete.

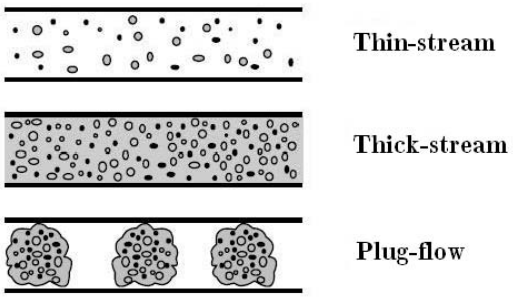



Figure 4.11: Different types of conveying systems for shotcrete (from Girmscheid, 2000)

Some disadvantages of the wet-mix technology are its lack of flexibility, the shorter possible transport distances and the difficulties in handling the filled spraying hose and nozzle. Furthermore, the method is not suitable for processing smaller quantities of shotcrete with numerous breaks in placement, as such stops require the removal of the hardening concrete and a proper cleaning of the complete spraying unit.

### 4.5.3 Spraying technique

It is well accepted practice, that shotcrete should be sprayed at right angles to the target surface at a distance of about 0.5 - 2 m in order to get good compaction and minimum overspray (Austin & Robins, 1995). For overhead spraying the nozzle is kept normally slightly closer to the surface at about 1 m of distance, because gravity reduces the velocity of the particle stream and leads to increased rebound. Girmscheid (2000) highlighted in his publication some key aspects regarding the optimum spraying technique, as illustrated in Fig. 4.12. In this figure $d$ denotes the shotcrete layer thickness, $g_{SB}$ the weight of the installed shotcrete layer, $h$ the adhesion between shotcrete and target surface and $\tau$ the induced shear force acting at the interface. As a general rule material should be built up from the bottom, in order to activate the supporting behaviour of the already applied shotcrete below.

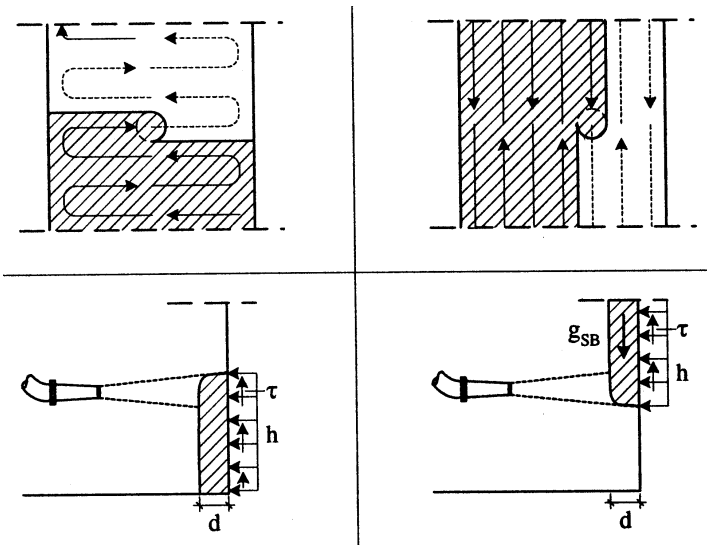



Figure 4.12: Preferred application procedure for sprayed concrete (from Girmscheid, 2000)

Furthermore, the movement of the nozzle has a great influence on the quality of shotcrete. Therefore the nozzle tip should be rotated in such a way that the stream moves in loops across the surface. Special care should be taken to fully encase reinforcement in order to ensure full bond between concrete and steel and guarantee long term durability of the shotcrete structure.

### 4.5.4 Rebound behaviour

When shotcrete is applied to a tunnel wall some of the material is lost in a number of ways and is not part of the finished in situ material any more. Austin & Robins (1995) distinguish three different types of losses that are:

- Overspray = Material missing the target surface
- Rebound = Material which touches the surface but does not adhere
- Cutback = Material that adheres but is subsequently removed whilst plastic to keep the correct profile

The biggest concern is the loss due to rebound, which is in the order of 20 - 30 % for the dry-mix process, but only 10 - 20 % for the wet-mix process. The bouncing off of material is not just an economic loss, but it changes also the in situ proportions of the mix design, because the individual constituents of shotcrete rebound by different amounts. Obviously this has an important effect on the mechanical behaviour of shotcrete. The following factors summarized in Tab. 4.1 play a keyrole in the rebound behaviour of shotcrete:

| Concrete mix design | Installation technology | Boundary conditions |
|---|---|---|
| Water-cement ratio | Spraying angle | Consistency of surface |
| Cement content | Nozzle distance | Reinforcement |
| Grading curve of aggregates | Dry- or wet-mix | Layer thickness |
| Dosage of additives | Transport system | Orientation of surface |

Table 4.1: Influencing factors on rebound behaviour

Parker et al. (1977) carried out some experiments on the rebound behaviour of a dry-mix sprayed concrete with a maximum aggregate size of 13 mm. From their results they concluded that it is much more economical to spray a single thick layer than two separate thinner layers, as shown in Fig. 4.13.

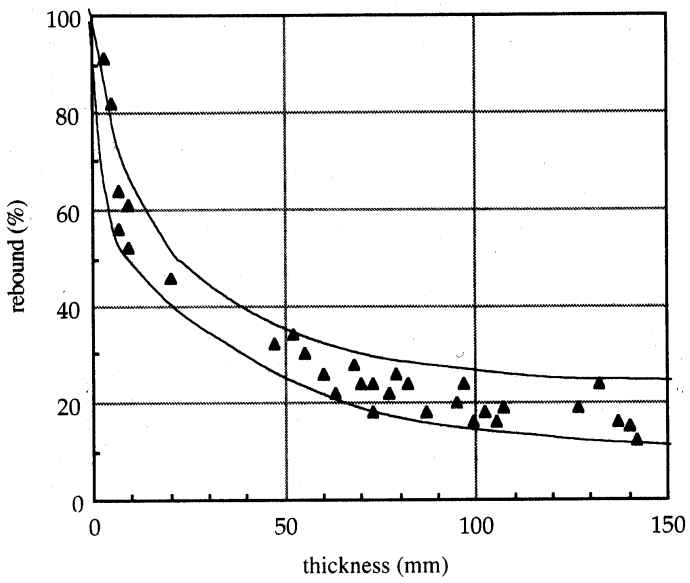



Figure 4.13: Effect of layer thickness on material rebound (from Parker et al., 1977)

The influence of the orientation of the target surface on the rebound behaviour was studied by many researchers, among them Ryan (1975), Gullan (1975) and Kobler (1966). It is generally accepted that the rebound of shotcrete material increases with increasing orientation of the target surface compared to the horizontal direction, as illustrated in Fig. 4.14.

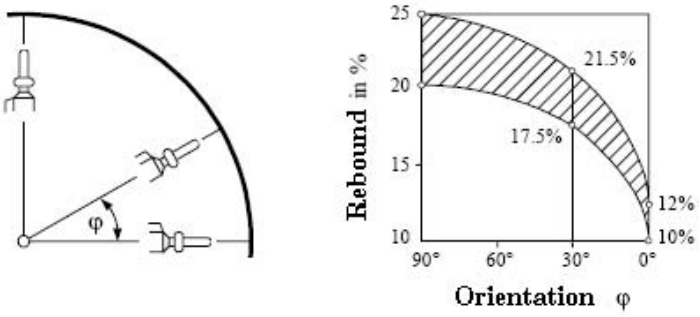



Figure 4.14: Effect of surface orientation on material rebound (from Girmscheid, 2000)

No clear trend has been observed in the literature whether the inclusion of fibres in the shotcrete mix can reduce material rebound during spraying or not. Some researchers report a reduction in rebound of up to 45 % with steel fibre reinforced sprayed concrete (Ryan, 1975). However, it is stated that these enormous reductions might be due to other factors in the spraying process.

Finally, Armelin & Banthia (1998) present in their work a mechanical approach for the simulation of an aggregate particle rebounding from a fresh concrete surface. This mechanical model is based on the theory of rebound and aims to provide some fundamental knowledge on the mechanics of the rebound process. By analysing in detail the particle penetration, the reaction phase and contact time, they intend to predict the amount and composition of the aggregate rebound for an actual dry-mix shotcrete.

## 4.6 Shotcrete testing

The quality control of sprayed concrete during construction is of crucial importance for a safe tunnel lining design, since the shotcrete quality is highly operative dependent. However, it is reported in the literature that testing of young shotcrete is a difficult task to perform, as it is impossible to drill cores until the strength of the material has reached a certain level - for example a uniaxial compressive strength of 10 MPa according to Chang (1994). Sometimes shotcrete samples are sprayed into test panels under field conditions, which also has its shortcomings. In EFNARC (1996) the required tested material properties of sprayed concrete are listed as follows:

- Uniaxial compressive strength and density
- Flexural and residual strength
- Energy absorption class
- Modulus of elasticity
- Bond strength

- Permeability and frost resistance
- Determination of fibre content of shotcrete

Among these material properties, the uniaxial strength in compression is one of the most important ones for describing material quality of shotcrete and is frequently tested during the progress of tunnel construction. ASCCT (2004) provides a range of different test methods for the compressive strength at very early ages, as can be seen in Fig. 4.15. In the first couple of hours after spraying up to a compressive strength of about 1 MPa, penetration needles with a diameter of 3 and 9 mm are used. The measured penetration resistance or depth for a constant applied force allows the estimation of the compressive strength at this early stage of cement hydration. For shotcrete ages up to 2 days the pull-out test finds its use as a testing technique for the uniaxial compressive strength. However, it is stated that the measured strength is somehow a combination of the uniaxial compressive and shear strength with a precision of $\pm 25\,\%$ (Kusterle, 1985). For more or less hardened shotcrete cylindrical core samples taken from the sprayed concrete structue are tested in order to quantifiy material quality. According to EFNARC (1996) the minimum diameter should be 50 mm and the height/diameter ratio should be in the range of 1.0 to 2.0. Alternatively, the uniaxial compressive strength can be determined from cubes cut from sprayed test panels and their strength values converted to the cylindrical strength.

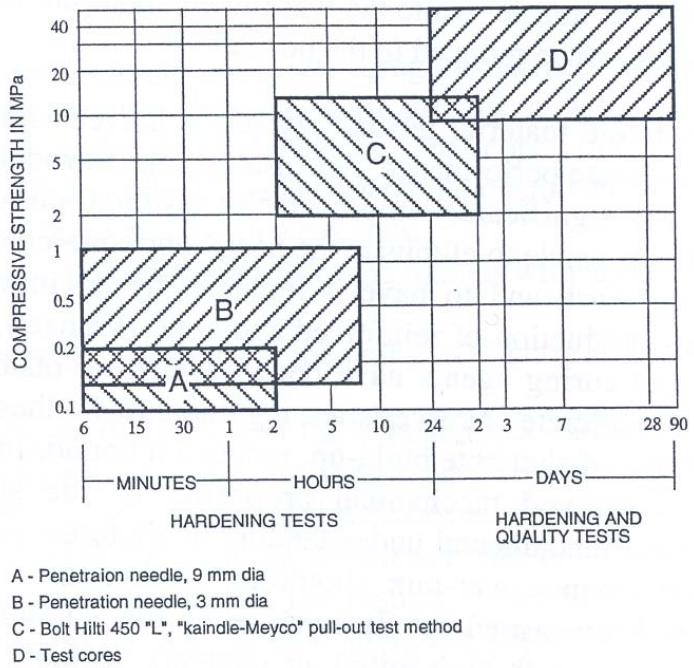



Figure 4.15: Test methods for compressive strength of young shotcrete according to ASCCT (2004)

Chang (1994) proposed a new field testing method that allows the measurement of the uniaxial compressive strength and the Young's modulus at a certain time after casting. A

steel bar with square cross section is inserted into a shotcrete layer immediately after installation. Fig. 4.16 illustrates the basic principle of the method, where the two quantities under investigation can be estimated from the applied torque and the registered angular displacement. The uniaxial compressive strength $\sigma_c$ and the Young's modulus $E_c$ are then calculated from the maximum torque $M_{max}$, the stiffness $k_t$ and the two laboratory calibrated parameters $\alpha$ and $\beta$.

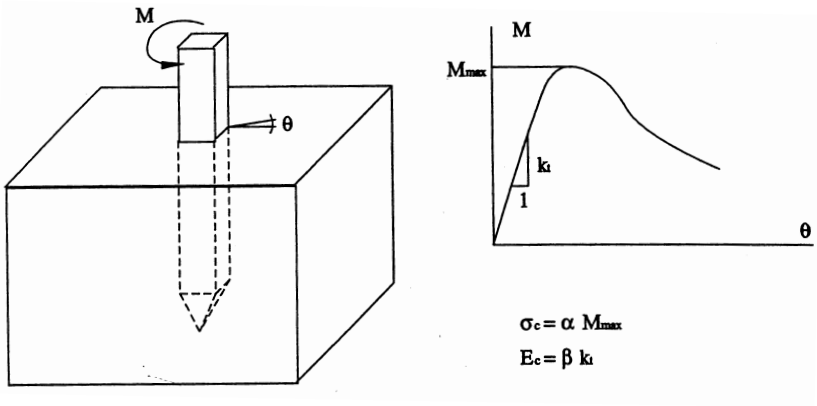



Figure 4.16: Proposed test method for uniaxial compressive strength and Young's modulus by Chang (1994)

## 4.7 Summary

This chapter started with an introduction into the development of sprayed concrete from a historical point of view. An overview of different applications of shotcrete in civil engineering was then given, focusing on the use of shotcrete in subsurface construction such as mining and tunnelling. Regarding the material technology the following key aspects can be summarised:

- As any conventional cast concrete, shotcrete consists of cement, aggregates and water. Each of these components has an important impact on the mechanical behaviour of the shotcrete and has to be addressed in a proper mix design. Additives such as accelerators, plasticisers and silica fume are commonly used to change certain material properties, but they have to be treated with care. Advanced developments have been recently achieved for using steel and polypropylene fibres as a reinforcement replacement for ordinary steel wire meshes.

- Cement hydration is a complex chemical reaction between the clinker components of the cement and water and leads to setting and hardening of the cement paste. Occasionally the so called "degree of hydration" is used in the literature to describe the development of certain material parameters such as stiffness and strength.

- For the installation of shotcrete two different techniques exist - the dry-mix and the wet-mix process. Both technologies differ significantly in material preparation, but have

in common that placing and compacting of the shotcrete is done in one single step by spraying the material at high pressures onto the target surface. Certain advantages and disadvantages exist for each technique, but the tendency in tunnelling is clearly towards the wet-mix process due to its better control of the shotcrete quality (in particular of the water-cement ratio).

- The spraying technique is of great importance for achieving good material quality and this requires excellent skills and training of the nozzle-operator. Rebound of shotcrete is not only an economical loss but influences as well the mechanical behaviour of the material. It leads to a slightly richer cement mix of the in-situ material and this has to be taken into account in the mix design.

- Testing of young sprayed concrete at early ages is a difficult task to perform and no commonly agreed techniques exist in the literature. Usually, shotcrete samples are taken from the tunnel lining or are sprayed into boxes under field conditions, where the compressive strength of the material is the main parameter of interest in the design. For fresh concrete penetration needles and pull-out tests are often used to estimate the compressive strength of the material at early ages of cement hydration.

# Chapter 5

# Mechanical and time-dependent behaviour of concrete and shotcrete

## 5.1 Introduction

In the previous chapter shotcrete as an engineering material has been introduced, highlighting the influence of material technology, such as mix design, installation technique and rebound behaviour, on the mechanical behaviour of sprayed concrete. Therefore, the current chapter deals at first with the fundamental description of the mechanical behaviour of hardened concrete, starting with simple uniaxial conditions in compression and tension. For completeness, it is further explained how concrete behaves mechanically under multiaxial stress states that are nearly always encountered in engineering practice. After a brief introduction into the behaviour of steel fibre reinforced concrete, the mechanical description of concrete is extended to the time-dependent behaviour of shotcrete, emphasising the increase in stiffness and strength with time, the deformability at early ages and wether or not early-age loading has any damage effects on the young shotcrete. Other important time aspects such, as creep and relaxation, shrinkage and temperature induced strains due to cement hydration, are explained in detail and their influence on the mechanical behaviour of a tunnel lining shell discussed.

## 5.2 Uniaxial stress conditions

### 5.2.1 Mechanical behaviour in compression

In a typical uniaxial compression test on cylindrical or cubical concrete samples the following stress-strain relationship, illustrated in Fig. 5.1 as normalised stress versus axial strain, is usually observed: up to about 30 % of its maximum compressive strength, $f_{cp}$, the behaviour of concrete can be assumed nearly linear elastic and the microcracks already existing in the concrete before loading remain unchanged (Chen, 1982). This indicates that the available internal energy is less than the energy required to create new microcrack surfaces. For stresses above this proportionality limit, the shape of the stress-strain curve is closely related

to the mechanism of internal progressive microcracking. With further loading bond cracks start to extend due to stress concentrations at the crack tips and the stress-strain curve becomes more and more non-linear. Between 30 to 50 % of $f_{cp}$ the available internal energy is approximately balanced by the required crack-release energy and crack propagation is stable. For compressive stresses above 70 % of $f_{cp}$ the system is unstable and crack propagation will increase. In Mehta & Monteiro (1985) the special stress level of about 75 % of $f_{cp}$ is termed "critical stress" since it corresponds to the minimum value of volumetric strain, as seen in Fig. 5.1 (assuming a compression positive sign convention).

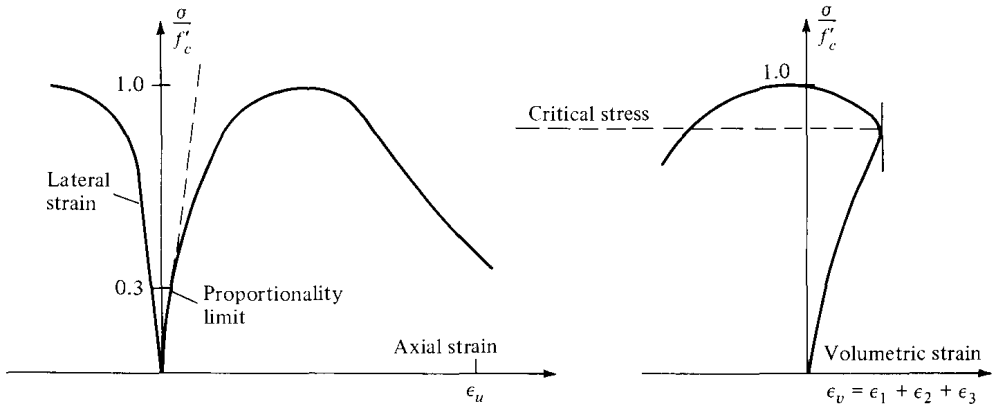



Figure 5.1: Typical plots of stress-strain curves for uniaxial compression (from Chen, 1982) ($f'_c = f_{cp}$)

If loading is continued, the stress-strain curve will bend more sharply and will approach the peak point at $f_{cp}$. Axial compressive peak strains are usually close to a value of 0.2 %. Furthermore, the sign of the volume change is reversed, resulting in a volumetric expansion (dilatancy) near the compressive strength $f_{cp}$ (Chen, 1982). After reaching the peak stress, the stress-strain curve shows a descending part, which is very much dependent on the test conditions and the equipment used. The influence of the length of the tested concrete sample is shown in Fig. 5.2, where an increasing specimen length leads to a more brittle material behaviour after peak. Crushing failure of concrete occurs finally at some ultimate axial compressive strain $\varepsilon_u$, where the stresses abruptly reduce to zero. Swoboda & Moussa (1992) suggested a value for the compressive failure strength of shotcrete, just prior to crushing, between 0.5 and 1.0 times the uniaxial compressive strength $f_{cp}$.

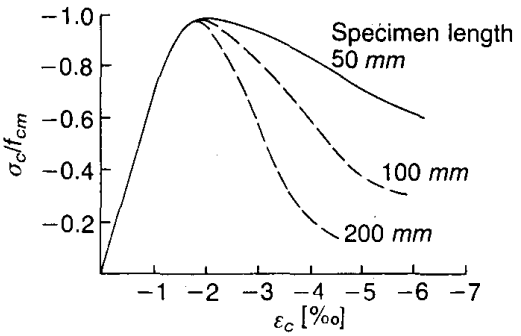



Figure 5.2: Influence of specimen length on post peak behaviour in uniaxial compression (from CEB-FIP Model Code, 1990)

*i) Modulus of elasticity*

The initial Young's modulus of elasticity, $E$, in compression is highly dependent on the uniaxial compressive strength $f_{cp}$ and can be estimated for normal weight concrete by some empirical equations published in the literature (Chen, 1982). The CEB-FIP Model Code (1990) provides the following expression:

$$E_{ci} = E_{co} \left[ \frac{f_{ck} + \Delta f}{f_{cmo}} \right]^{\frac{1}{3}} \tag{5.1}$$

where $E_{ci}$ is the modulus of elasticity (MPa) at a concrete age of 28 days, $\Delta f = 8\,\text{MPa}$, $f_{cmo} = 10\,\text{MPa}$ and $E_{co} = 2.15 \times 10^4\,\text{MPa}$. The characteristic uniaxial compressive strength $f_{ck}$ is defined as that strength below which 5 % of all possible strength measurements for the specified concrete may be expected to fall. Generally, the Young's modulus $E$ and the uniaxial compressive strength $f_{cp}$ are well defined parameters in various national standards and can be taken according to a certain strength class, see EC 2 (2004).

*ii) Poisson's ratio*

According to Neville (1981), for concrete under uniaxial compressive loading the Poisson's ratio $\mu$ takes a value between 0.11 and 0.21. As illustrated in Fig. 5.3, during uniaxial compression loading $\mu$ remains constant until approximately 75 to 80 % of the compressive strength $f_{cp}$. At this stress level $\mu$ starts to increase and in the unstable crushing phase can even become larger than 0.5 (Chen, 1982).

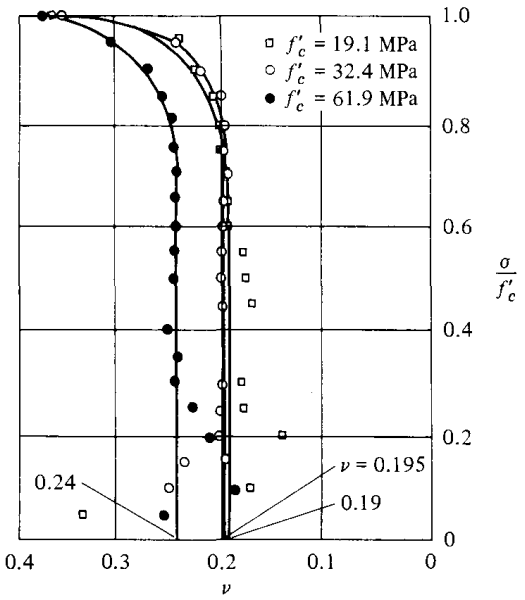



Figure 5.3: Relation between stress level and Poisson's ratio $\mu$ (from Chen, 1982) ($f'_c = f_{cp}$)

### 5.2.2 Mechanical behaviour in tension

Typical stress-strain curves for concrete in uniaxial tension are given in Fig. 5.4.

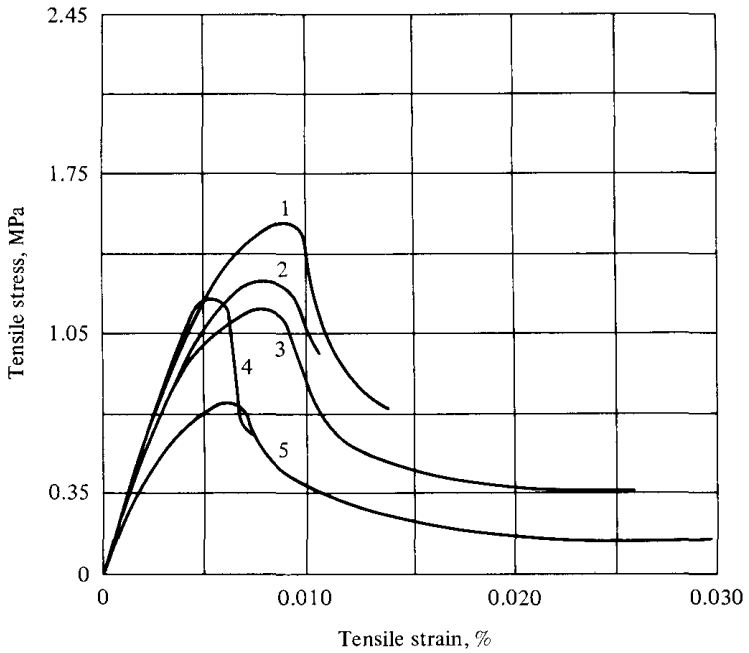



Figure 5.4: Stress-strain curves in tension for different concrete types (from Chen, 1982)

Most of the curves (which represent different concrete types) show an almost linear elastic behaviour up to 70 % of the uniaxial tensile strength $f_{tp}$. In this stress region the creation of new microcracks within the concrete sample is negligible. With further tensile loading

bond microcracks start to occur and the tensile behaviour becomes non-linear. At about 75 % of the tensile strength, $f_{tp}$, the crack propagation becomes unstable and the initiation and growth of new microcracks is very fast (Chen, 1982). On reaching the uniaxial tensile strength $f_{tp}$, much larger and visible cracks at the surface start to appear and the concrete sample is termed to be "cracked". Peak strains for uniaxial tension are considerably smaller than those under uniaxial compression and lie in the range of 0.005 to 0.02 %. Due to the very brittle behaviour of concrete under tensile stresses, it is difficult to follow the descending part of the stress-strain curve in an experiment after reaching the peak stress $f_{tp}$. It is somehow obvious that cracking in concrete is a very discrete problem and deformations localise in a small fracture zone. Outside this fracture zone the material exhibits elastic unloading upon further crack opening. Another interesting phenomenon during crack formation is the fact that, due to the rough crack surfaces, opposite faces will be able to interlock and to transfer a certain amount of shear force, an effect which is often termed "aggregate interlocking".

*i) Tensile strength*

Usually the ratio between uniaxial tensile and compressive strengths is in the range of 0.07 to 0.11 (Mehta & Monteiro, 1985), as can be seen in Fig. 5.5, which contains a compilation of various uniaxial experimental test data.

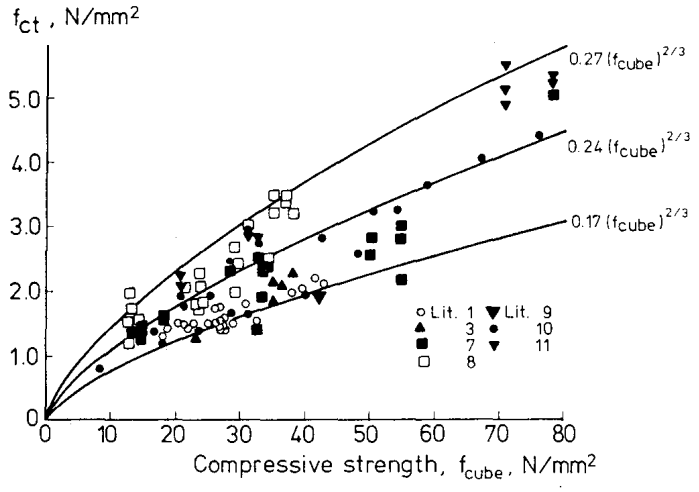



Figure 5.5: Relation between uniaxial tensile and compressive strength (from Byfors, 1980) ($f_{ct} = f_{tp}$, $f_{cube} = f_{cp}$)

Some of the equations found in the literature relating the uniaxial tensile strength, $f_{tp}$, to the uniaxial compressive strength, $f_{cp}$, are given as follows:

The CEB-FIP Model Code (1990) provides the following expression for the mean tensile strength, $f_{ctm}$, associated with the characteristic uniaxial compressive strength, $f_{ck}$:

$$f_{ctm} = f_{ctko,m} \left( \frac{f_{ck}}{f_{cko}} \right)^{\frac{2}{3}} \tag{5.2}$$

with $f_{ctko,m} = 1.40\,\text{MPa}$ and $f_{cko} = 10\,\text{MPa}$. The idea of defining a "mean" value of the tensile strength is to provide an estimate for the uniaxial tensile strength of concrete, which usually shows a great variability due to various influencing factors.

Swoboda & Moussa (1992) used in their work the following equation for calculating the uniaxial tensile strength of shotcrete:

$$f_{tp} = 0.21\, f_{cp}^{\frac{2}{3}} \tag{5.3}$$

Finally, Meschke (1996) adopted in his material model for shotcrete an empirical equation published by Oluokun et al. (1991*b*), which is of the form:

$$f_{tp} = 0.876\, f_{cp}^{0.79} \tag{5.4}$$

The dimension of the strength parameters in this equation is $\text{kN/m}^2$. As an example, for a given uniaxial compressive strength of 30 MPa, the results for the uniaxial tensile strength obtained from the above introduced equations 5.2 to 5.4 range from 2.03 MPa to 3.01 MPa. However, the uniaxial tensile strength of concrete is a parameter which is difficult to measure from the experimental point of view. The three methods that are commonly in use for determining the tensile strength are:

- Splitting test
- Ring test
- Flexural beam test

CEB-FIP Model Code (1990) allows the tensile strength obtained from a splitting test to be converted into the uniaxial tensile strength in the following way:

$$f_{ctm} = 0.9\, f_{ct,sp} \tag{5.5}$$

where $f_{ctm}$ is the mean axial tensile strength and $f_{ct,sp}$ is the mean splitting tensile strength. Likewise, if the tensile strength is obtained from a flexural beam test, the equation below can be used:

$$f_{ctm} = f_{ct,fl}\, \frac{1.5\,(h_b/h_o)^{0.7}}{1 + 1.5\,(h_b/h_o)^{0.7}} \tag{5.6}$$

where $f_{ct,fl}$ is the mean flexural tensile strength, $h_b$ is the depth of the beam and $h_o = 100\,\text{mm}$.

According to Chen (1982), the modulus of elasticity $E$ in uniaxial tension is slightly higher and the Poisson's ratio $\mu$ somewhat lower than in uniaxial compression.

## 5.3 Biaxial stress conditions

In a real structure a purely uniaxial stress state is very rare and most commonly multiaxial stress states are encountered. In the 1970s many investigations were performed on the me-

chanical properties of concrete under biaxial loading conditions, in order to obtain a better understanding of strength, deformational characteristics and cracking behaviour of concrete under such a biaxial stress state. A typical experimental stress-strain curve for concrete under various biaxial stress states is shown in Fig. 5.6 (strains are given in absolute values).

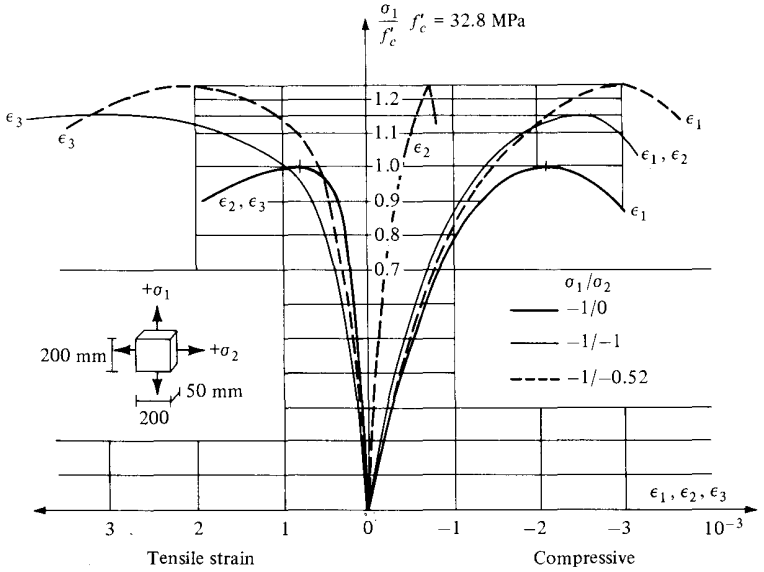



Figure 5.6: Stress-strain relationships for concrete under biaxial compression (from Chen, 1982) ($f'_c = f_{cp}$)

It can be seen clearly that, if some lateral pressure is applied, the maximum compressive strength increases. For the special stress ratio of $\sigma_1/\sigma_2 \cong 0.5$ a maximum increase in strength of about 25 % is achieved (Huber, 2006). This value is reduced to about 16 % at an equal biaxial compression state with $\sigma_1/\sigma_2 = 1.0$. Under the combination of compression and tension the compressive strength decreases almost linearily as the tensile stress is increased. For a biaxial tensile stress state the tensile strength remains almost unchanged and is independent of the applied stress ratio. A range of biaxial tests performed by Kupfer & Gerstle (1973) at different stress ratios ($\sigma_1/\sigma_2$) lead to a biaxial failure envelope, as can be seen in Fig. 5.7.

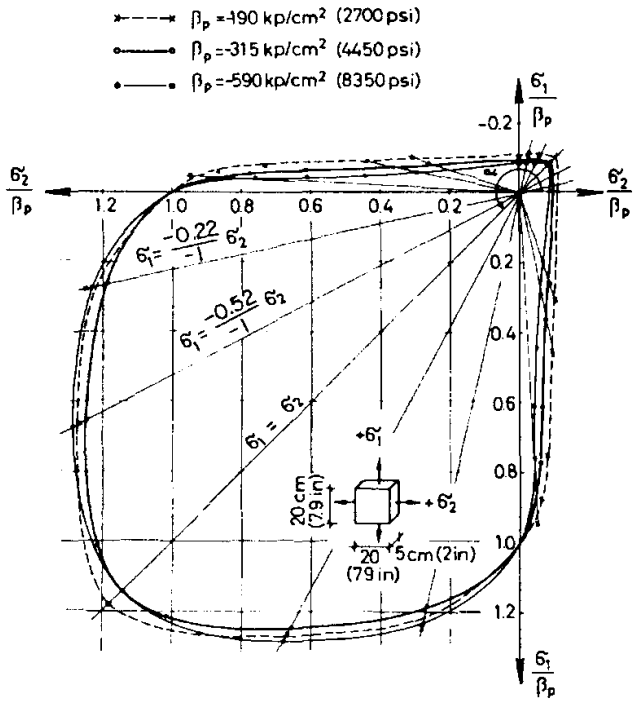



Figure 5.7: Biaxial failure envelope (from Kupfer & Gerstle, 1973) ($\beta_p = f_{cp}$)

Some information about different fracture modes of concrete in biaxial stress conditions can be found in Nelissen (1972). Furthermore, Chen (1982) points out that the stress-strain curves under biaxial loading conditions are different depending on whether the stress states are compressive or tensile.

According to EC 2 (2004), confinement of concrete results in a modification of the stress-strain relationship, where higher strengths and higher critical strains are achieved, whereas the other material characteristics may be considered unaffected. The characteristic confined compressive strength, $f_{ck,c}$, can be calculated from:

$$f_{ck,c} = f_{ck} \left( 1.125 + 2.50 \frac{\sigma_2}{f_{ck}} \right) \tag{5.7}$$

where $\sigma_2$ ($= \sigma_3$) is the effective lateral compressive stress and $f_{ck}$ the characteristic uniaxial compressive strength. The peak strain for confined stress conditions, $\varepsilon_{c2,c}$, i.e. the strain when the characteristic confined compressive strength is fully mobilised, is given as:

$$\varepsilon_{c2,c} = \varepsilon_{c2} \left( \frac{f_{ck,c}}{f_{ck}} \right)^2 \tag{5.8}$$

with $\varepsilon_{c2}$ being the uniaxial compressive peak strain. In a similar way, the ultimate confined compressive strain $\varepsilon_{cu2,c}$, where the concrete is assumed to be crushed, can be estimated from:

$$\varepsilon_{cu2,c} = \varepsilon_{cu2} + 0.2 \frac{\sigma_2}{f_{ck}} \tag{5.9}$$

## 5.4 Triaxial stress conditions

The behaviour of concrete under triaxial stress conditions was investigated, for instance, by Kotsovos & Newman (1978) and van Mier et al. (1987). Similar to biaxial tests, their results showed an increase in compressive strength with increasing confining pressure. Balmer (1949) conducted some triaxial tests at very high confining stress levels and reported compressive strengths of up to 560 MPa. All these experiments indicate that concrete has a fairly constant shape of the failure surface which is a function of the three principal stresses. With the assumption of isotropic material behaviour, the elastic limit (i.e. yield surface) and the failure criterion can be represented as smooth surfaces in principal stress space as shown in Fig. 5.8. For small hydrostatic pressures, the deviatoric cross sections of the surfaces are convex and have the shape of rounded triangles. With increasing hydrostatic compression the deviatoric cross sections become more and more circular, which means that failure in this region is independent of the Lode angle $\theta$. The intersection curves between the yield and failure surfaces and a plane containing the hydrostatic axes with $\theta = \text{const.}$ are often termed "meridians". The general character of these meridians for the failure of concrete is that they are smooth, curved and convex lines, depending on the hydrostatic stress component $I_1$ or $p$.

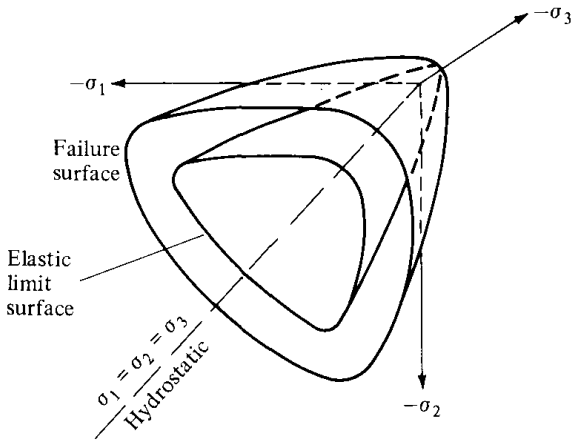



Figure 5.8: Triaxial yield and failure surface for concrete (from Chen, 1982)

## 5.5 Anisotropy of shotcrete

Generally speaking, concrete can be considered as a homogeneous mixture of aggregates, cement and water and is therefore commonly treated as an isotropic material. Anisotropy in shotcrete can be expected due to the spraying process and various uncertainties in material technology and curing conditions (Aldrian, 1991). Furthermore, imperfections of the tunnel shell can introduce a certain anisotropy in the material behaviour that can lead to unexpected loading conditions (Stelzer & Golser, 2002). For experiments regarding the strength development of shotcrete, it is very important to take into account the spraying direction for sample preparation. In standard tests on shotcrete cores the loading direction would

be the same as the spraying direction, which is the opposite in a real tunnel structure, as can be seen in Fig. 5.9. Within the tunnel lining the major compressive stresses would act perpendicular to the spraying direction. According to Thomas (2003), the quantification of this anisotropy for shotcrete in the literature seems to be difficult to establish. Huber (1991) and Fischnaller (1992) tested the early strength of shotcrete with two loading directions and came to the conclusion that the samples that where tested parallel to the spraying direction had a reduced strength of 20 % compared to the samples tested perpendicular to the spraying direction. Steel fibre reinforced concrete exhibits pronounced anisotropy in its behaviour for both compression and tension (Thomas, 2003). However, anisotropy effects of shotcrete are usually ignored in a numerical analysis for the purpose of simplicity.

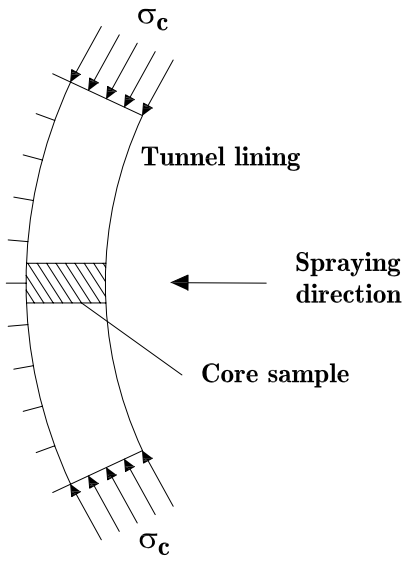



Figure 5.9: Spraying direction and loading conditions in a real tunnel lining

## 5.6 Mechanical behaviour of steel fibre reinforced concrete and shotcrete

As already mentioned in the previous chapter 4, the mechanical properties of concrete can be greatly improved by the addition of steel fibres (Strack, 2007). It is therefore possible to convert concrete from a quasi-brittle material behaviour to a more ductile one. However, it is well known that in an experiment the type, mechanical properties, shape and distribution of the fibres within the concrete matrix play an important role in the obtained material response, as can be seen in Fig. 5.10.

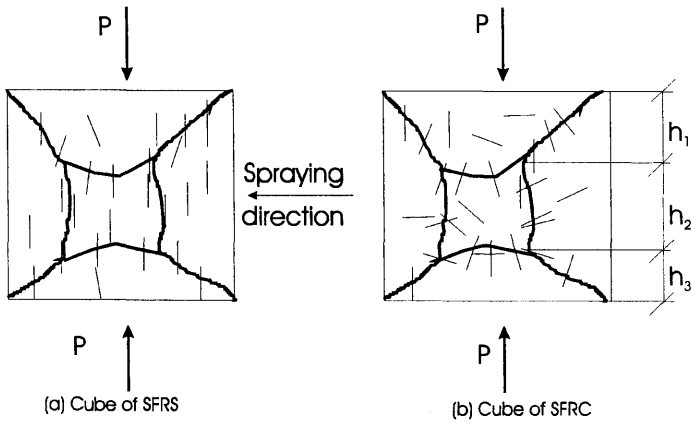



Figure 5.10: Failure mechanism for steel fibre renforced shotcrete and concrete (from Ding & Kusterle, 2000)

For shotcrete, (Fig. 5.10 on the left) the fibre distribution is mainly two-dimensional due to the spraying process and in a tunnel lining the main compressive loads occur parallel to the fibre orientation. For this particular failure mode steel fibres can only improve the cracking behaviour in zones $h_1$ and $h_3$, whereas in zone $h_2$ the fibres do not affect the material behaviour. The situation is different for conventional cast concrete reinforced with steel fibres, where a homogeneous three-dimensional fibre distribution can be expected.

The uniaxial behaviour of hardened fibre reinforced concrete in tension can be best explained by the load-deformation curve in Fig. 5.11.

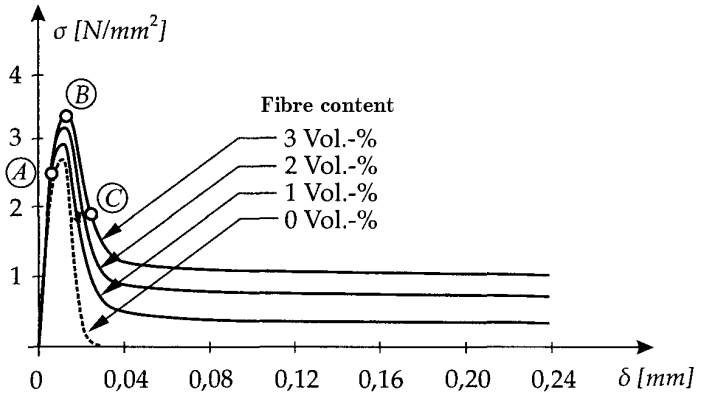



Figure 5.11: Uniaxial stress-deformation characteristics of fibre reinforced concrete (from Thomée, 2005)

For tensile loading up to point $A$ (about 60 to 90 % of the uniaxial peak strength $f_{tp}$) linear elastic material behaviour can be observed, governed by the properties of the plain concrete matrix. With the low fibre content common in engineering practice due to economic reasons, there is no noticeable influence on the Young's modulus. After a non-linear loading phase where micro crackbands start to develop, a small increase in the uniaxial tensile peak strength, $f_{tp}$, might be possible (point $B$). In the post peak regime firstly a steep drop in

stresses occurs with increasing deformation, controlled by the behaviour of the plain concrete matrix. However, when crack opening continues to develop, the steel fibres start to contribute to the load-carrying capacity by transferring tensile stresses across the crack. At point $C$ the reduction in tensile stresses starts to stabilise and a residual tensile strength can be identified. Therefore a more ductile material behaviour in tension is obtained.

The mechanical behaviour of steel fibre reinforced concrete in uniaxial compression shows a similar pattern, as illustrated in Fig. 5.12. The elastic limit appears to be unchanged, located in the range of up to 30 % of the uniaxial compressive peak strength, $f_{cp}$. For hardened concrete the incorporation of steel fibres seems to have almost no influence on the uniaxial compressive peak strength, $f_{cp}$, compared to plain concrete. However, the strain when the peak strength is reached appears to be increased for an increased fibre content. The biggest difference is now noticeable for the post peak behaviour, where a significant increase in the absorbed energy leads to a fairly ductile material behaviour. The reason behind this phenomenon might be that the steel fibres prohibit the lateral elongation which results in a more controlled crack formation in the post peak zone.

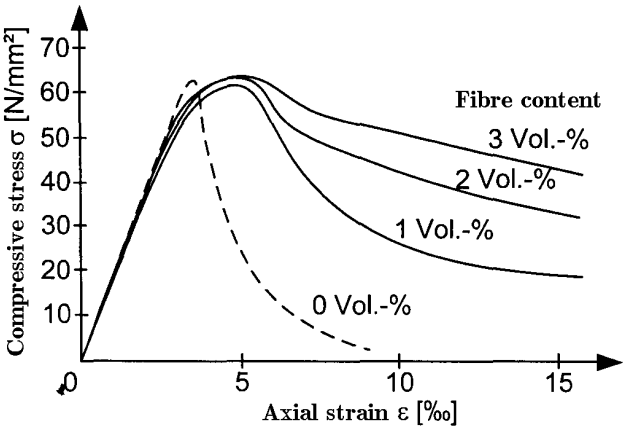



Figure 5.12: Compressive stress-strain curves for fibre reinforced concrete (from Strack, 2007)

Little information is available in the literature about the influence of steel fibres on the behaviour of shotcrete at early ages. Ding & Kusterle (2000) performed uniaxial compression tests on concrete samples with different fibre content (20, 40 and 60 kg/m$^3$) at a starting age ranging from 8 to 72 h. They observed that steel fibres can improve the compressive strength of young concrete, as can be seen in Fig. 5.13, although this improvement in strength does not necessarily increase with a larger dosage of fibres.

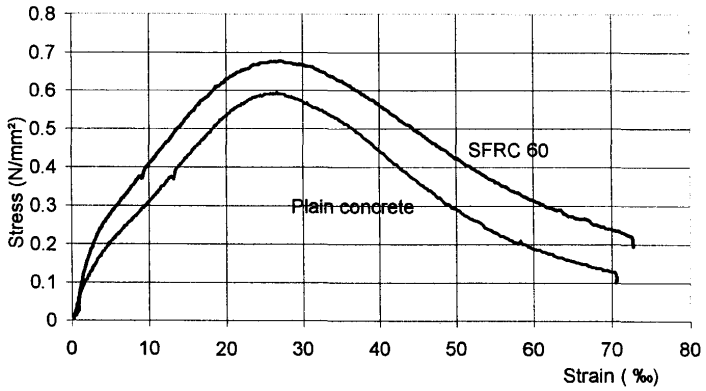



Figure 5.13: Stress-strain curves for plain concrete and steel fibre reinforced concrete with 60 kg/m$^3$ at an age of 9 h (from Ding & Kusterle, 2000)

For concrete older than 30 h this influence on the compressive strength seems to cease. The softening part in the post peak regime descends for both concrete types (plain and steel-fibre reinforced) at the early age in a similar manner. Regarding the energy absorption capacity, it can be mentioned that at early ages steel fibres have a great influence not only on the post peak behaviour but improve as well the ascending part of the stress-strain curve. In Fig. 5.13 an increase of energy absorption until peak of up to 25 % was observed. A similar trend was obtained by Ding & Kusterle (1999) for early age concrete panel tests reinforced with steel fibres and conventional wire mesh.

Camps et al. (2008) investigated the effects of steel fibre reinforcement during cement hydration by uniaxial tension tests at a concrete age of 2, 7 and 28 days. As expected, the plain concrete specimens demonstrated very brittle material behaviour in the tensile post-peak regime for all the different stages of cement hardening. The material response of the concrete samples reinforced with 85 kg/m$^3$ of steel fibres followed the basic behaviour for hardened steel fibre reinforced concrete explained above. Much higher strain levels were achieved than for plain concrete and an increase in ductility was observed. Furthermore, the residual tensile capacity appears to be increasing with hydration development. This post-peak strengthening effect can probably be explained by the improvement of the bond between fibre and concrete matrix during cement hardening.

## 5.7 Time-dependent mechanical behaviour of young shotcrete

For conventional concrete after 28 days, most of the material parameters mentioned in the previous sections for describing the mechanical behaviour are assumed to be constant and well defined values in national standards, which is not the case for shotcrete. It can be expected that as a consequence of the hydration process within the cement paste, the material properties of young shotcrete gradually change and these early age properties control the mechanical interaction between the shotcrete lining of a tunnel and the surrounding soil. In

the hardening cement paste a gradual increase of stiffness and strength is accompanied by a rise in temperature caused by the generated hydration energy. Furthermore, the mechanisms of creep, relaxation and shrinkage can lead to complex stress states within a tunnel lining. Unfortunately, all these time-dependent effects of young shotcrete should not be treated seperately from each other, as they occur as a coupled mechanical process, which is not straightforward to understand and/or quantify.

Complete stress-strain curves for shotcrete under uniaxial compression at different ages were presented by Sezaki et al. (1989). In Fig. 5.14 it can be seen clearly that, in the first 6 hours after installation, shotcrete behaves as a very soft, plastic material with low strength and stiffness. Nevertheless, it is able to resist very high peak and ultimate strains, which are both in the range of per cent. This means that young shotcrete has a high ability to accommodate tunnel deformations that occur after excavation. Shotcrete samples at an age of 12 hours up to 3 days still show a ductile material behaviour, but stiffness and strength have already increased significantly. With further curing time the behaviour becomes more and more brittle because of the cement hardening, till the shotcrete has its highest stiffness and strength after 28 days.

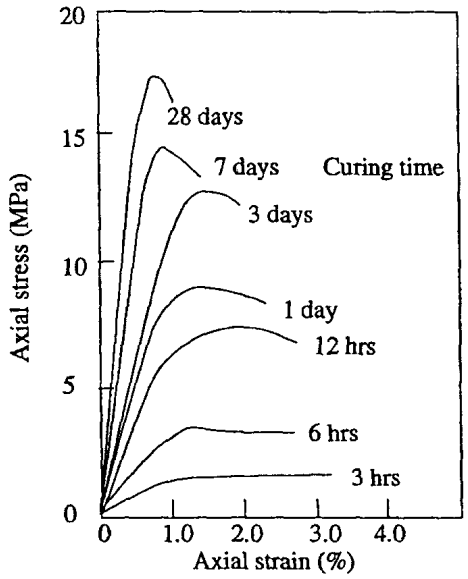



Figure 5.14: Stress-strain curves in compression at different shotcrete ages (from Sezaki et al., 1989)

### 5.7.1 Increase in stiffness and strength

The development of stiffness and strength with time due to hardening of the shotcrete is well reported and investigated in the literature by many researchers. Furthermore, this time-dependency is one of the most influential factors on the axial forces and bending moments in a shotcrete shell and therefore of crucial importance for tunnel lining design (Thomas, 2003). It depends highly on the mix design of the particular shotcrete used for a tunnelling project

and the use of accelerators, speeding up the hardening process, plays an important role.

*i) Young's modulus*

A typical development of the Young's modulus, $E$, with time is shown in Fig. 5.15, including results from Huber (1991) and Fischnaller (1992) who investigated the mechanical properties of shotcrete at very early ages. In such an experimental work, usually the water-cement ratio, temperature and cement type are varied in order to study the growth of the Young's modulus $E$ with time (Byfors, 1980).

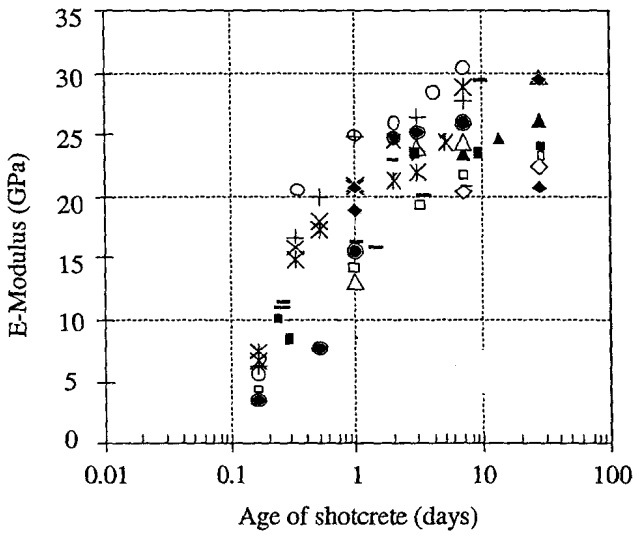



Figure 5.15: Development of Young's modulus $E$ with shotcrete age obtained from various tests (from Chang, 1994)

A quantitative estimation of the increase in stiffness with time is possible with the help of various empirical equations found in the literature. Weber (1979) published an equation of the following form:

$$E(t) = a\, E_{28}\, exp\left(\frac{c}{t^{0.6}}\right) \tag{5.10}$$

with $E_{28}$ being the stiffness for hardened shotcrete at 28 days and $t$ the time in days. The material parameters $a$ and $c$ depend on the type of cement used in the mix design (i.e. cement classes) and can be estimated from Tab. 5.1. Schubert (1988) describes the variation

| Cement class | Z 25<br>Z 35 L<br>Z 45 L | Z 35 F<br>Z 45 F | Z 55 |
|---|---|---|---|
| $a$ | 1.132 | 1.084 | 1.062 |
| $c$ | -0.915 | -0.596 | -0.445 |

Table 5.1: Parameters $a$ and $c$ for increase in Young's modulus $E$ with time (after Weber, 1979)

of stiffness with time, using the stiffness at 28 days $E_{28}$ as a single input parameter, as:

$$E(t) = E_{28}\sqrt{\frac{t}{4.2 + 0.85\,t}} \tag{5.11}$$

Here again $t$ is the age of shotcrete in days. Another empirical formulation based on the test results from Huber (1991) and Fischnaller (1992) and published by Chang (1994) is:

$$E(t) = 1.062\,E_{28}\,exp\left(\frac{-0.446}{t^{0.7}}\right) \tag{5.12}$$

with $E_{28}$ being the Young's modulus of shotrete in GPa at 28 days and $t$ the time in days. In the study of Aydan et al. (1992) the following relationship is adopted:

$$E(t) = 5000\left(1 - \exp^{-0.42\,t}\right) \tag{5.13}$$

The CEB-FIP Model Code (1990) provides the following equation to estimate the increase in stiffness with time:

$$E(t) = E_{28}\,exp\left[s\left(1 - \sqrt{\frac{t_{28}}{t}}\right)\right]^{0.5} \tag{5.14}$$

with $t_{28}$ being the time at 28 days. The cement parameter $s$ governs the increase in stiffness and can be taken according to the type of cement as:

- $s = 0.2$ for rapid hardening high strength cements RS
- $s = 0.25$ for normal and rapid hardening cements N and R
- $s = 0.38$ for slowly hardening cements SL

Byfors (1980) related the increase in stiffness to the development of the uniaxial compressive strength, $f_{cp}$, with time via the mathematical expression given as:

$$E(t) = \frac{E_o\,f_{cp}^{a_1}}{1 + A\,f_{cp}^{(a_1 - a_2)}} \tag{5.15}$$

where $E_o$, $A$, $a_1$ and $a_2$ are material constants fitted to experimental results. Fig. 5.16 shows the experimental relation between Young's modulus $E$ and uniaxial compressive strength $f_{cp}$ on a linear scale. These test data show that the Young's modulus grows more rapidly than the compressive strength. This is an important phenomenon in tunnelling since a higher increase in stiffness may lead to a higher loading rate of the shotcrete shell and higher strengths would be needed to sustain these stresses (Chang, 1994).

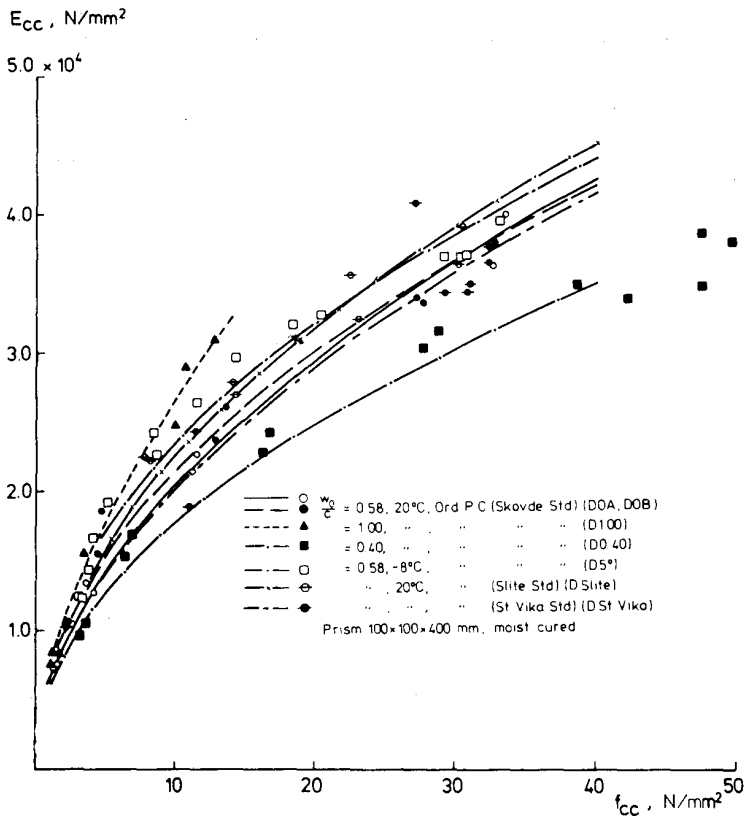



Figure 5.16: Relationship between stiffness and strength (from Byfors, 1980) ($E_{cc} = E$, $f_{cc} = f_{cp}$)

Fig. 5.17 compares graphically some of the earlier presented equations found in the literature for the prediction of the increase of the shotcrete stiffness with time. A value for the Young's modulus at 28 days of 30 GPa has been adopted. Although relatively similar at first sight, some major differences are obtained, particularly at early ages. At a shotcrete age of 12 hours, the Young's modulus according to Weber (1979) and CEB-FIP Model Code (1990) is relatively high, taking a value of 16.2 and 15.7 GPa respectively. This implies that the stiffness of the shotcrete has reached already 50 % of its final stiffness at 28 days. The predictions from Schubert (1988) and Chang (1994) are significantly lower for this stage of cement hydration and values of 9.7 and 9.5 GPa are obtained. However, it should be pointed out that the adopted cement class in equation 5.10 and 5.14 plays an important role in the development of the shotcrete stiffness with time.

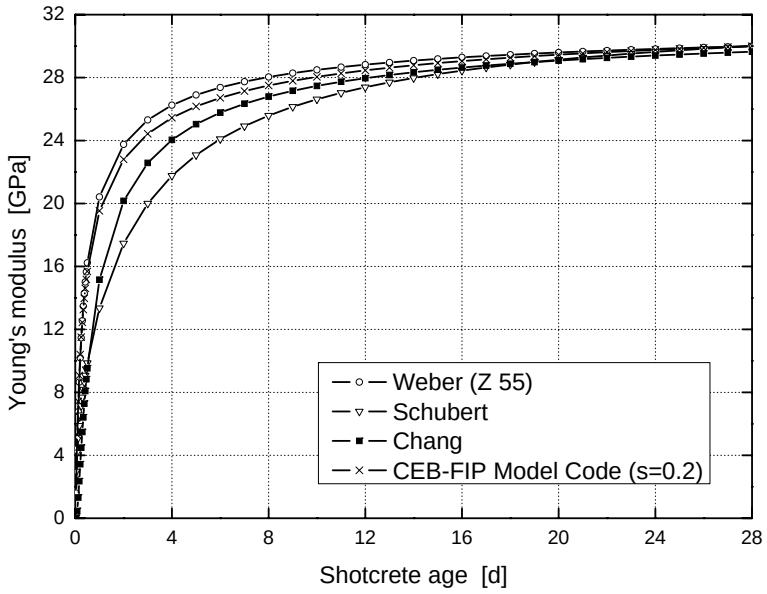



Figure 5.17: Increase in stiffness with time according to various equations from the literature

*ii) Poisson's ratio*

The Poisson's ratio $\mu$ of early age concrete and shotcrete has received very little attention in the literature and test results are therefore rare. Byfors (1980) states that the influencing factors for the development of the Poisson's ratio with time are the type and quantity of aggregates used in the concrete mix. Oluokun et al. (1991*a*) performed an experimental study on the early age behaviour of concrete and for various concrete mixes, with a water-cement ratio ranging from 0.388 to 0.763, they came to the conclusion that the Poisson's ratio appears to be insensitive to steam curing. Furthermore, the obtained values were generally the same for all ages and conditions of curing. However, Aydan et al. (1992) showed some results for the variation of the Poisson's ratio of shotcrete with time, which are of a different nature, as can be seen in Fig. 5.18. At early ages $\mu$ seems to be very high, with values of about 0.45. Within the first 3 days after spraying, this value reduces significantly to an almost constant value of 0.18, which is also predicted by the equation given by Aydan et al. (1992):

$$\mu\,(t) = 0.18 + 0.32\,\exp^{-5.6\,t} \tag{5.16}$$

where the time $t$ is in days.

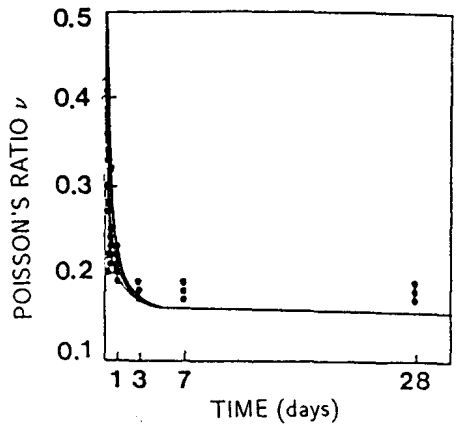



Figure 5.18: Variation of Poisson's ratio with time (from Aydan et al., 1992) ($\nu = \mu$)

Test results from Byfors (1980) indicate that the variation of the Poisson's ratio is linked to the development of the uniaxial compressive strength, $f_{cp}$. Fig. 5.19 shows that $\mu$ decreases very rapidly during the early stage when the strength is still small, starting from a value of 0.48. At a uniaxial compressive strength of around $1\,\mathrm{N/mm^2}$ $\mu$ has its minimum value of about 0.15 and increases afterwards, when hardening of the cement paste continues.

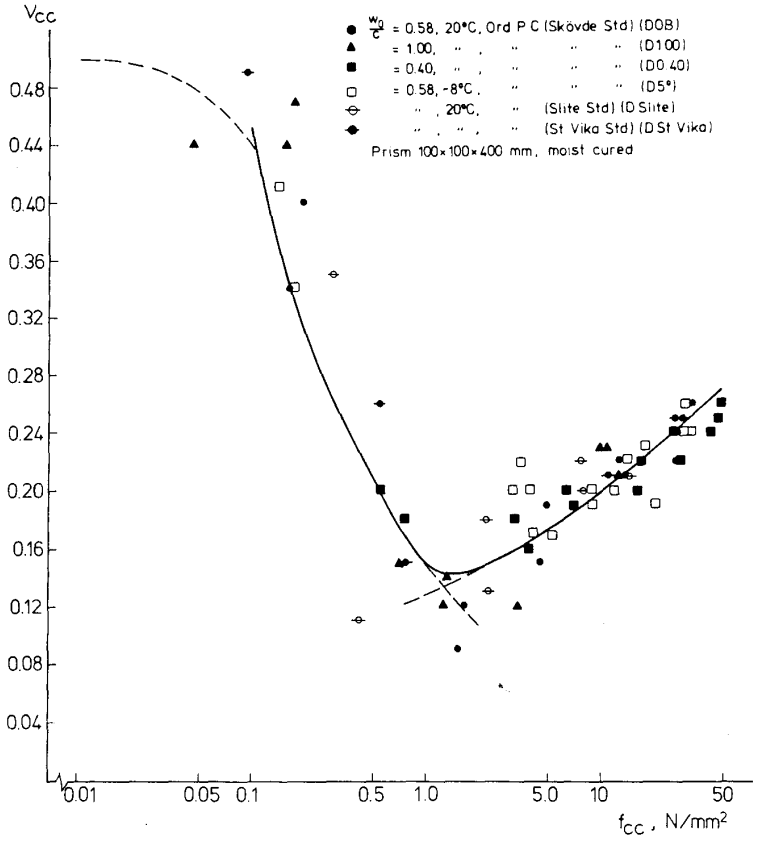



Figure 5.19: Relation between Poisson's ratio and compressive strength (from Byfors, 1980) ($f_{cc} = f_{cp}$, $\nu_{cc} = \mu$)

A mathematical expression of the form given below is proposed, that couples the development of the Poisson's ratio with the increase in uniaxial compressive strength $f_{cp}$.

$$\mu\,(t) = a\, f_{cp}^{b} \tag{5.17}$$

where $a$ and $b$ are material constants. For the range of tests considered by Byfors (1980), the proposed values for these parameters are summarized in Tab. 5.2:

| Parameter | $f_{cp} \leq 1\,\text{MPa}$ | $f_{cp} > 1\,\text{MPa}$ |
|---|---|---|
| $a$ | 0.148 | 0.098 to 0.164 |
| $b$ | -0.486 | 0.102 to 0.281 |

Table 5.2: Parameters $a$ and $b$ for development of Poisson's ratio $\mu$ (after Byfors, 1980

*iii) Compressive strength*

Similar to the Young's modulus, the growth of the uniaxial compressive strength, $f_{cp}$, with time has been widely studied in the literature for early age concrete, including both dry- and wet-mix shotcrete. Fig. 5.20 shows some data from the literature regarding the development of the uniaxial compressive strength with time.

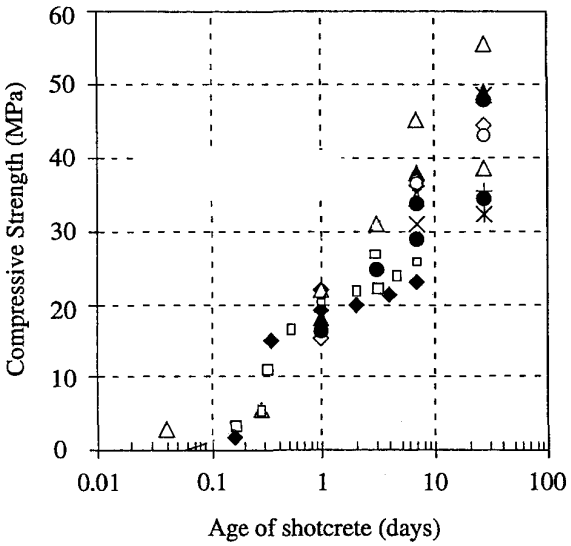



Figure 5.20: Development of uniaxial compressive strength, $f_{cp}$, with shotcrete age obtained from various tests (from Chang, 1994)

Again, the large influence of mix design and installation technique results in a certain scatter of published test data, that makes it difficult to calculate the strength at a certain shotcrete age with accuracy. However, a variety of equations can be found in the literature that describe the increase in strength with time. In general, these expressions should be treated with care, not to be taken as an absolute value, and always validated against actual test data for each tunnelling project.

Weber (1979) proposed the following equation:

$$f_{cp}(t) = a\, f_{cp,28}\, exp\left(\frac{c}{t^{0.55}}\right) \tag{5.18}$$

where $t$ is the shotcrete age in days and $f_{cp,28}$ the uniaxial compressive strength for hardened shotcrete at 28 days. The parameters $a$ and $c$ are material constants depending on the cement type (i.e. cement class) and the water-cement ratio. For different cement types their values are given in Tab. 5.3.

| Cement class | Z 25 | Z 35 F | Z 55 |
|---|---|---|---|
| | Z 35 L | Z 45 F | |
| | Z 45 L | | |
| $a$ | 1.45 | 1.27 | 1.20 |
| $c$ | -2.32 | -1.49 | -1.14 |

Table 5.3: Parameters $a$ and $c$ for increase in uniaxial compressive strength, $f_{cp}$, with time (after Weber, 1979)

In the constitutive model for shotrete developed by Meschke et al. (1996), two different functions for describing the increase in uniaxial compressive strength with time were applied:

$$f_{cp}(t) = f_{cp,1}\left(\frac{t+0.12}{24}\right)^{0.72453} \qquad \text{for} \qquad t < 24\,\text{h} \tag{5.19}$$

where $f_{cp,1}$ is the uniaxial compressive strength after 24 hours and $t$ the time in hours. For $t > 24\,\text{h}$ the following empirical relation is adopted:

$$f_{cp}(t) = a_c\, exp\left(-\frac{b_c}{t}\right) \qquad \text{for} \qquad t > 24\,\text{h} \tag{5.20}$$

The determination of the constants $a_c$ and $b_c$ is based on the values for the uniaxial compressive strength at 24 hours and at 28 days. They can be obtained as:

$$a_c = \frac{f_{cp,28}}{exp\,(\ln(\kappa)/27)} \qquad \text{and} \qquad b_c = -\frac{672}{27}\, ln(\kappa) \tag{5.21}$$

with $\kappa = f_{cp,1}/f_{cp,28}$ and $f_{cp,28}$ is the uniaxial compressive strength at 28 days. Research from Chang (1994) includes a curve to match published data from the literature. The following expression is proposed:

$$f_{cp} = 1.105\, f_{cp,28}\, exp\left(\frac{-0.743}{t^{0.7}}\right) \tag{5.22}$$

Golser et al. (1990) adopted an equation that uses just one single input parameter, the

uniaxial compressive strength at 28 days. It can be written as:

$$f_{cp}(t) = f_{cp,28}\sqrt{\frac{t}{101 + 0.85\,t}} \tag{5.23}$$

The CEB-FIP Model Code (1990) uses the following expression:

$$f_{cp}(t) = f_{cp,28}\,exp\left[s\left(1 - \sqrt{\frac{t_{28}}{t}}\right)\right] \tag{5.24}$$

where $s$ is a cement parameter controlling how fast the strength increases with time. $s$ depends on the cement type and takes the same values as used to determine the Young's modulus (see equation 5.14), namely:

- $s = 0.2$ for rapid hardening high strength cements RS
- $s = 0.25$ for normal and rapid hardening cements N and R
- $s = 0.38$ for slowly hardening cements SL

A graphical representation of various of the above presented equations for predicting the development of the compressive strength with time can be seen in Fig. 5.21. In this example, the compressive strength of hardened shotcrete at 28 days was assumed to be 30 MPa, which is even exceeded by the proposed equation from Chang (1994).

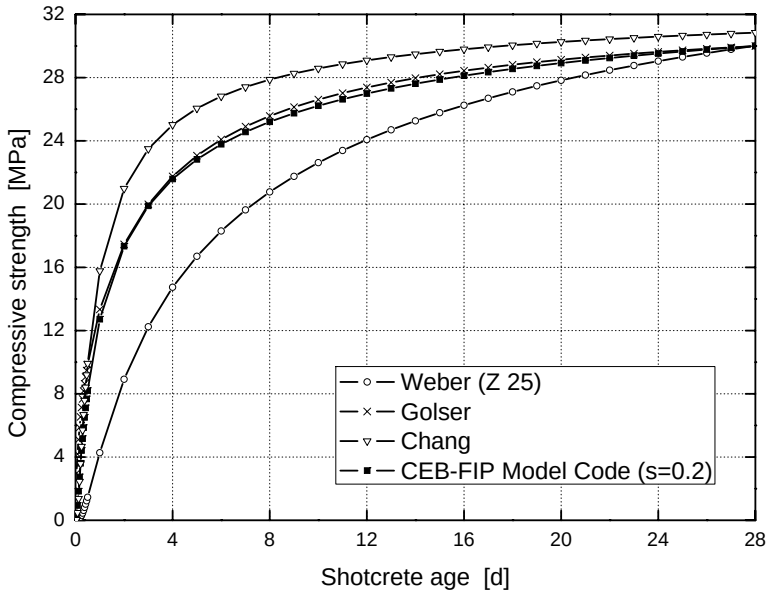



Figure 5.21: Development of uniaxial compressive strength with time according to various equations from the literature

For the stability of a shotcrete tunnel lining during construction, the gain in shotcrete strength with time is of crucial importance. In ASCCT (2004) three early strength classes,

$J_1$, $J_2$ and $J_3$, are defined for young shotcrete, that is concrete at an age less than 24 h. As mentioned in chapter 4, for vertical and overhead application in a tunnel, the increase in strength controls its ability to stick to the surface. For spraying shotcrete to the tunnel crown, a strength of 0.1 to 0.2 MPa after 2 min is required. At the same time, to minimise rebound and dust, the early strength of shotcrete should not be bigger than 0.2 MPa after 2 min. However, in the case of a large amount of groundwater penetrating into the tunnel, an increased early strength is necessary (ASCCT, 2004). For each of these early-age strength classes certain requirements exist and they are defined as follows:

**Class $J_1$:** Shotcrete of this early-strength class is used for the application of thin layers on dry surfaces. It is not meant for structural use and has the advantage of low dust production.

**Class $J_2$:** For the spraying of thick layers on vertical or overhead surfaces with structural use, shotcrete has to fulfill the requirements of this early-strength class.

**Class $J_3$:** Due to the high dust production and rebound, shotcrete of Class $J_3$ should just be used when absolutely necessary (high ground water pressures, very fast tunnel advance, etc.)

In Fig. 5.22 the minimum strengths of each class $J_1$, $J_2$ and $J_3$ (limited by the lines $A$, $B$ and $C$) are defined graphically for young shotcrete up to an age of 24 hours.

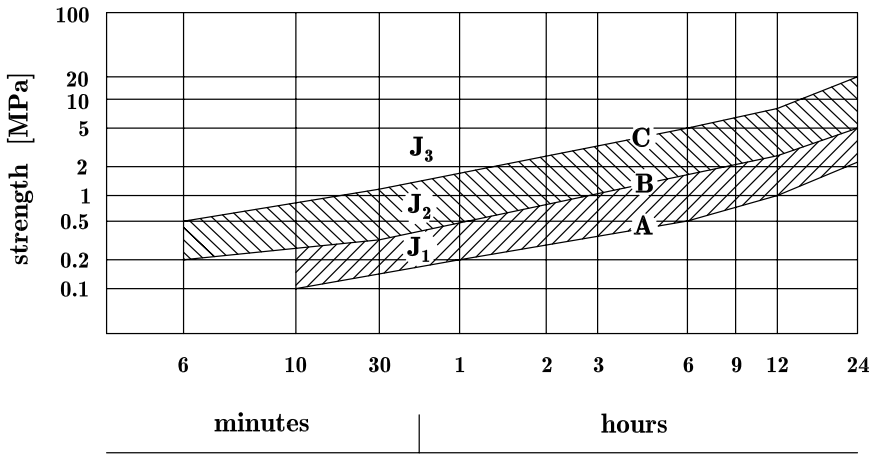



Figure 5.22: Early-age strength classes for young shotcrete (after ASCCT, 2004)

*iv) Tensile strength*

The tensile strength in general is rarely considered in the design of a tunnel lining according to national standards (Thomas, 2009) and therefore test data for young shotcrete is hardly available in the literature. Byfors (1980) states that the growth of the tensile strength with time is influenced basically by the same factors as those which govern the compressive strength.

Kasai et al. (1971) presented results showing how the relationship between compressive and tensile strength changes at an early age, as can be seen in Fig. 5.23.

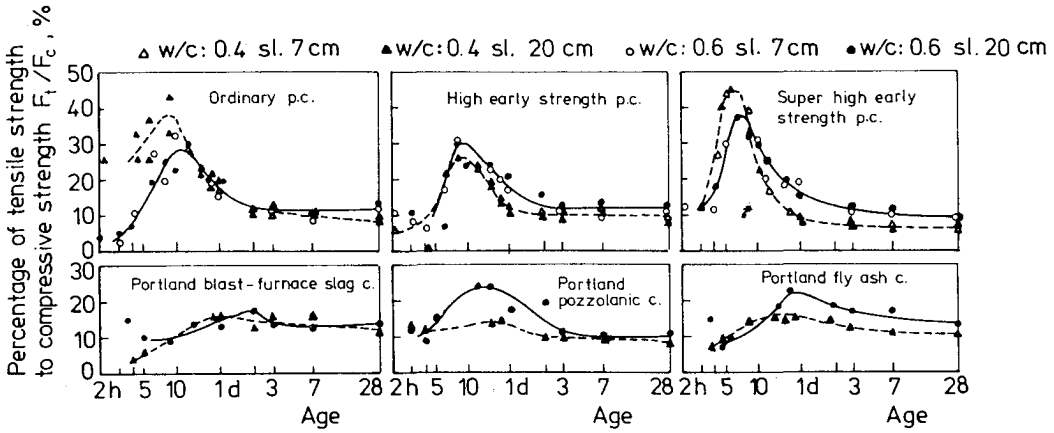



Figure 5.23: Ratio between tensile and compressive strength at early concrete ages (from Kasai et al., 1971) ($F_t = f_{tp}$, $F_c = f_{cp}$)

These observations are in conflict with experiments by Weigler (1974), where the tensile strength grows linearily with the compressive strength at a constant strength ratio of about 0.08.

Byfors (1980) performed some tests on young concrete and described the relationship between the uniaxial tensile strength, $f_{tp}$, and the uniaxial compressive strength, $f_{cp}$, at early ages with the following equation:

$$f_{tp}(t) = 0.082\, f_{cp}(t)^{1.09} \tag{5.25}$$

This expression has an exponent close to 1.0 and consequently an almost linear relation appears to occur for young concrete, resulting in a similar increase in uniaxial tensile strength with time as for the uniaxial compressive strength. Meschke et al. (1996) adopted in their work an empirical relation which can be written as:

$$f_{tp}(t) = 0.876\, f_{cp}(t)^{0.79} \tag{5.26}$$

*v) Yield stress*

The time-dependency of the elastic limit in either compression or tension is difficult to quantify as there is hardly any information available in the literature. Thomas (2003) investigated the ratio of the yield stress to the peak stress in compression by visual estimation from published stress-strain curves. Some data suggested a value of 0.70 to 0.85 of the peak stress, whereas others tended to be in the generally accepted range of 0.25 to 0.4. Due to this considerable scatter it was not possible to detect any particular time-dependency of the yield stress ratio. Meschke et al. (1996) assumed in their constitutive model for shotcrete a time-

dependent yield stress $f_{cy}$ which is linked to the uniaxial compressive strength $f_{cp}$ via a constant ratio, as given in the following equation:

$$f_{cy}(t) = \frac{f_{cy}^{28}}{f_{cp}^{28}} f_c(t) \tag{5.27}$$

where $f_{cy}^{28}$ and $f_{cp}^{28}$ are the uniaxial yield stress and the uniaxial compressive peak strength for hardened shotcrete at 28 days. No information has been found in the literature regarding the elastic limit of young concrete in tensile stress conditions.

### 5.7.2 Deformability at early ages

For the full description of a complete stress-strain curve for concrete under uniaxial stress conditions the strains at peak and failure strength might be the necessary input parameters. For conventional cast concrete these are constant values and do not change with time. However, as mentioned before, shotcrete at early ages shows a very soft and ductile material behaviour and can withstand large strains without being completely damaged (ICE, 2004). This means that a young shotcrete lining has the ability to accommodate tunnel deformations that occur immediately after shotcrete installation close to the tunnel face (Chang, 1994).

*i) Compressive peak strains*

For hardened concrete the uniaxial compressive strains at peak strength are in the range of 0.15 to 0.25 % and up to 0.35 % at failure strength. However, in Golser (1999) it is reported that in tests performed on 2-hour old shotcrete the material failed at strains of about 2 % when loaded in compression. Graziani et al. (2005) mentioned that freshly applied shotcrete typically exhibits plastic behaviour with strains at failure strength even as high as 3 to 4 %. This fact is supported by test data for the uniaxial compressive peak strains from Sezaki et al. (1989) developing with the uniaxial compressive strength for different accelerator dosages, as can be seen on the left in Fig. 5.24. It should be mentioned that Sezaki et al. (1989) termed the peak strains as "failure" strains in this plot. This figure shows on the right a data collection for young shotcrete from the literature performed by Thomas (2003). Although a considerable scatter exists, it appears that there is a decreasing trend for the compressive peak strains with time.

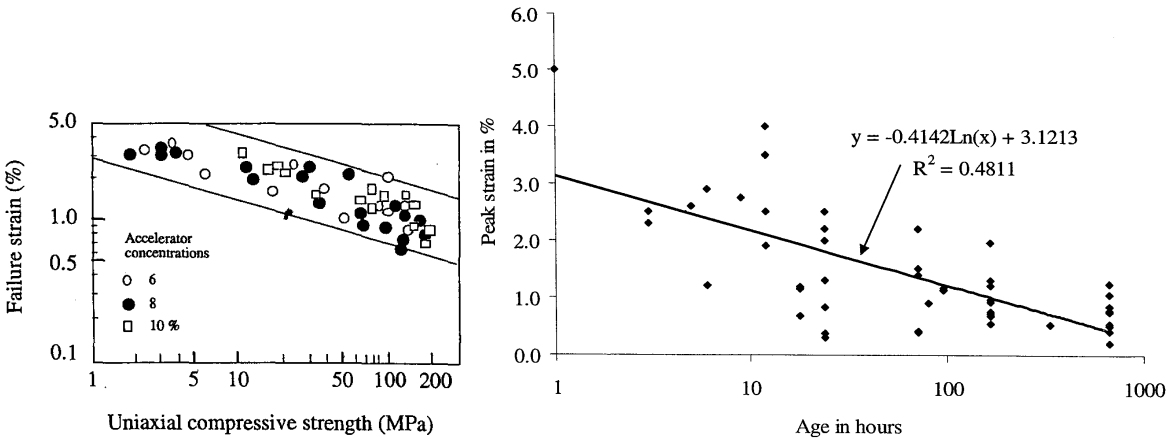



Figure 5.24: Development of compressive strains at peak strength with uniaxial compressive strength and time (from Sezaki et al., 1989 and Thomas, 2003)

Wierig (1971) observed in his experiments that compressive peak strains for young concrete are also much higher than those of hardened concrete, as indicated in Fig. 5.25. During the first hours these strains are reducing rapidly and reach a minimum at about 1 day of concrete age. Afterwards a slight increase in the peak strains with concrete ageing can be identified. Byfors (1980) performed an extensive experimental parametric study investigating the deformational behaviour of young concrete by varying the water-cement ratio, temperature and cement types. His results show a similar trend with high compressive peak strains of up to 1.5 % for samples at an age of 6 h.

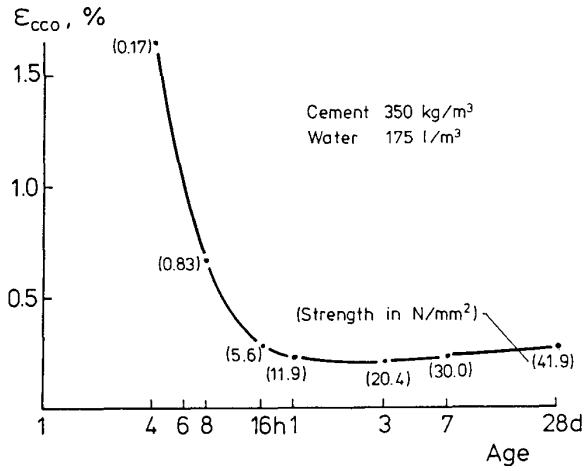



Figure 5.25: Development of compressive peak strains with shotcrete age (from Wierig, 1971)

Regarding the deformability of shotcrete at early ages Rokahr et al. (2005) are of a completely different opinion to the researchers introduced above. They state that a slow build-up load only causes failure at a "measured" strain which far exceeds the straining limit of hardened concrete. According to them, this measured large strain includes a considerable proportion of creep strains which already occur during the loading phase. Consequently, they

conclude that for quick loading conditions the compressive peak strain of young shotcrete is far below that of hardened concrete, a fact which is clearly the opposite to the earlier presented information. However, the work presented within this thesis follows the route of larger deformability of shotcrete at early ages.

For the mathematical description of the compressive peak strains for early age concrete and shotcrete various equations can be found in the literature. Thomas (2003) fitted a regression curve to his data collection in Fig. 5.24, which is given as:

$$\varepsilon_{cp}(t) = -0.4142\, ln(t) + 3.1213 \tag{5.28}$$

where $t$ is the shotcrete age in hours and $\varepsilon_{cp}$ the compressive peak strain in per cent. On the basis of experimental tests conducted by Byfors (1980), a trilinear relation for the compressive peak strain is proposed by Meschke et al. (1996), which can be written as:

$$\varepsilon_{cp}\,(t) = \begin{cases} 0.06 - \dfrac{0.0575}{8}\, t & \text{for} \quad 0 \leq t < 8\,h \\ 0.0025 - \dfrac{0.0008}{8}\,(t-8) & \text{for} \quad 8\,h \leq t < 16\,h \\ 0.0017 + \dfrac{0.0003}{654}\,(t-16) & \text{for} \quad t \geq 16\,h \end{cases} \tag{5.29}$$

where $t$ is the shotcrete age in hours. For their sprayed concrete model Jones et al. (2008) fitted a curve to the compressive strains at peak strength data from tests and the following relationship was found:

$$\varepsilon_{cp} = 0.0136\, f_{cp}^{-0.47} \tag{5.30}$$

where $f_{cp}$ is the time-dependent uniaxial compressive peak strength. De Schutter (1999) presented some data for young concrete, where high peak strains of early age concrete were reducing to a minimum value at a compressive strength of about 10 MPa. Based on this data set, he described mathematically the development of compressive peak strains with the mean compressive peak strength $f_{cm}$ by the expression given below:

$$\varepsilon_{cp} = 0.000948 \left(\frac{f_{cm}\,(t)}{f_{cmo}}\right)^{\frac{1}{3}} + \frac{0.000664}{\sqrt{\frac{f_{cm}(t)}{f_{cmo}}}} \tag{5.31}$$

where $t$ is the time in days and $f_{cmo} = 10$ MPa. Finally, as mentioned earlier, some experimental work on the early age deformability of conventional concrete was conducted by Byfors (1980). The compressive peak strain is presented as a function of the time-dependent uniaxial compressive peak strength in the following way:

$$\varepsilon_{cp} = a\, f_{cp}(t)^b \tag{5.32}$$

where $a$ and $b$ are two correlation coefficients that can be taken from Tab. 5.4.

| Compressive strength | $a$ | $b$ |
|---|---|---|
| $f_{cp} \leq 5\,\text{MPa}$ | 0.244 | -0.652 |
| $f_{cp} > 5\,\text{MPa}$ | 0.0467 | 0.331 |

Table 5.4: Parameters $a$ and $b$ for development of peak strains with uniaxial compressive strength (after Byfors, 1980)

*ii) Tensile peak strain*

Although the early age deformability of shotcrete in tension is of crucial importance regarding the cracking behaviour of tunnel linings due to shrinkage and temperature effects, hardly any information can be found in the literature. From the few test results available, a similar pattern as for the compressive peak strains can be observed, as indicated in Fig. 5.26.

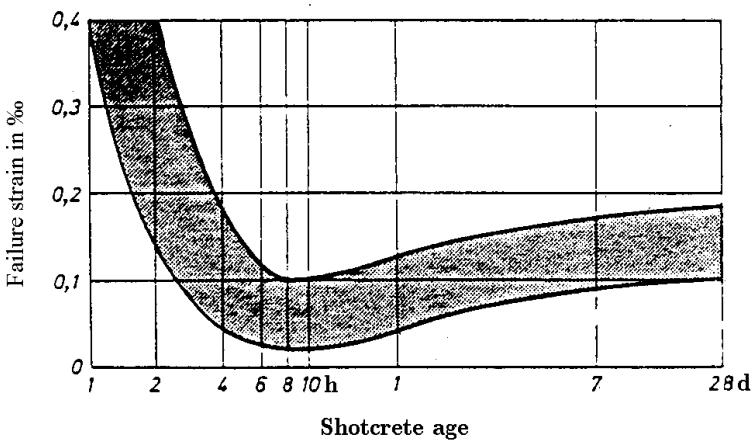



Figure 5.26: Development of tensile peak strains with shotcrete age (from Kusterle & Lukas, 1990)

At early ages the tensile peak strains (or termed "failure" strains in Fig. 5.26) appear to be in the range of 0.02 to 0.05 %, reducing significantly within the first hours after spraying. At a shotcrete age of about 12 hours this drop seems to stop and even a slight increase in the magnitude of the tensile peak strain may be identified. Byfors (1980) conducted some tension tests on young concrete and established a relation between the tensile and compressive peak strain depending on the development of the compressive strength, as can be seen in Fig. 5.27. At low strength levels, i.e. when the concrete is still very young, the tensile peak strain is approximately just about 3 % of the compressive peak strain. Starting from the period when the tensile and the compressive peak strain are at a possible minimum, the tensile peak strain grows far more rapidly than the compressive peak strain. In the case of hardened concrete at 28 days, the tensile peak strain is finally about 8 to 9 % of the compressive peak strain.

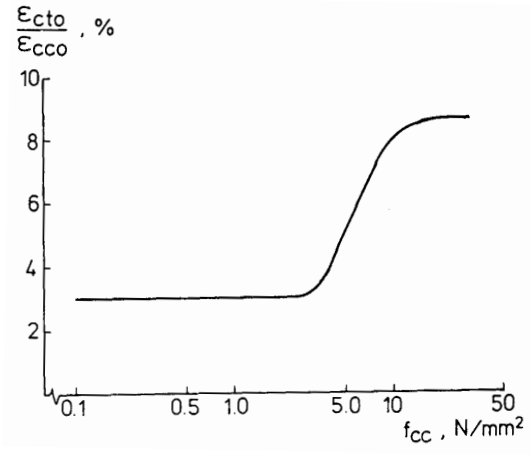



Figure 5.27: Ratio between tensile and compressive peak strain with compressive strength (from Byfors, 1980) ($f_{cc} = f_{cp}$, $\varepsilon_{cto} = \varepsilon_{tp}$, $\varepsilon_{cco} = \varepsilon_{cp}$)

### 5.7.3 Damage effects due to early-age loading

During tunnel construction, the very young shotcrete is loaded immediately after being sprayed onto the free tunnel walls, leading to possible stress levels within the lining that are relatively high or can even be close to failure. The question arises whether this early-age loading causes some damage to the internal structure of the shotcrete and whether it influences the further increase in stiffness and strength and mechanical behaviour at later stages of construction. From the published information in the literature this aspect is not clear and various opinions exist among researchers.

Moussa (1993) performed some experimental work investigating the effect of early age loading on cylindrical shotcrete core samples. He introduced a damage parameter, $R_{dfc}$, which represents the reduction of the compressive strength to be gained in the mean time of two loading cycles ($t_1$ to $t_2$). By fitting a linear function to the obtained test data it can be written that:

$$R_{dfc} = 2.532 \left( \frac{\sigma_o}{f_{cp,t1}} - 0.691 \right) \tag{5.33}$$

where $\sigma_o$ is the applied stress for the first loading at time $t_1$ and $f_{cp,t1}$ is the respective compressive strength. According to this equation, the reduction of the gain of strength due to damage of the material can be neglected for shotcrete preloaded by a stress less than 69.1 % of the uniaxial compressive strength at the loading age $t_1$. If the sample was preloaded up to the peak strength and immediately unloaded ($\sigma_o / f_{cp,t1} = 1.0$), the reduction of the peak strength at a later age would increase up to 78 %. However, it can be seen in Fig. 5.28 that there is a considerable scatter in the obtained results from which this relationship has been obtained.

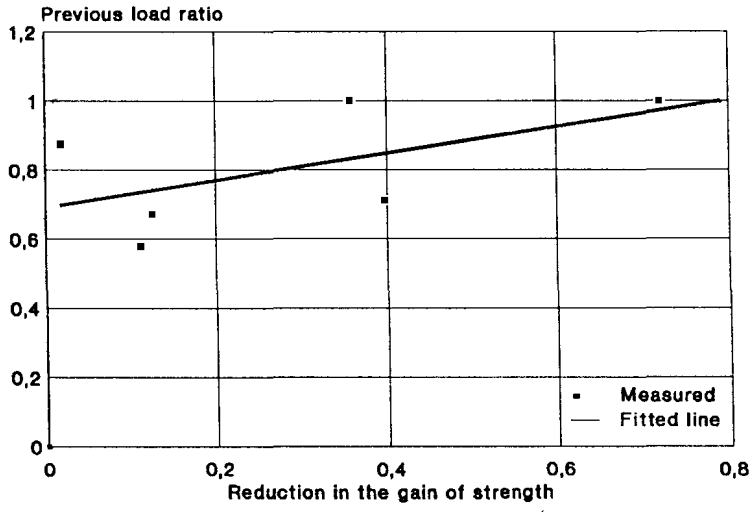



Figure 5.28: Reduction in gain of uniaxial compressive strength due to preloading (from Moussa, 1993)

On the other hand, Aldrian (1991) reported on some experimental tests performed by Golser et al. (1990) that indicated a different behaviour. In some particular creep tests shotcrete samples were loaded at an age ranging from 8 to 672 h for a duration of 3 weeks. By comparing the compressive strength of the samples at the end of the loading period with unloaded samples, they found that the preloaded samples had a compressive strength that was up to 50 % higher than the one of the unloaded samples. Two possible explanations were given by Aldrian (1991). First, the increase in compressive strength might be due to the fact that the chemical process of cement hydration changes under a sustained stress. Second, a compressive stress applied for a long period leads to a certain mechanical compaction within the structure of the shotcrete sample that strengthens the material.

Abdel-Jawad & Haddad (1992) carried out some experimental work in order to study the healing capacity of concrete subjected to overloading within the first three days after casting. Concrete samples were first loaded in compression at an age of 8, 16, 24 and 72 hours and reloaded at 7, 28 and 90 days. It was observed that loading the concrete at an age beyond 8 hours and up to 90 % of its compressive failure load had no effect on the later strength development. Nevertheless, samples loaded firstly in compression at an age of 8 hours showed a loss in strength of about 25 %. They concluded that moist curing is an essential requirement for the healing capacity of young concrete, although complete healing of cracks in damaged samples does not mean complete strength regain. In the retesting of healed specimens the failure mode always initiated from existing cracks.

Finally, Lu et al. (2004) conducted extensive research into the damage of concrete due to triaxial loading history. Their damage parameter $D$, representing the compressive strength reduction after a certain loading history, is linked to the maximum axial strain by the following

expression:

$$D = D_o + A\, e^{-(\varepsilon_1 - \varepsilon_o)/B} \tag{5.34}$$

where $D$ is the damage parameter in both the axial and lateral directions, $\varepsilon_1$ the maximum axial strain due to the applied stress $\sigma$, and $D_o$, $\varepsilon_o$, $A$ and $B$ are parameters correlated to the lateral confining pressure. It was concluded that the lateral pressure is the main factor that affects the damage development in concrete.

## 5.8 Creep and relaxation

Creep is the terminology for defining the gradual increase in strain with time under a sustained stress and can be of considerable importance in structural mechanics. The reverse process of creep is called relaxation and describes the progressive decrease in stress with time for a specimen that is subjected to a constant strain. For concrete structures both phenomena are related to moisture movement, when such a stress or strain is applied. Neville (1970) distuingishes between creep of concrete under conditions of no moisture movement to or from the ambient medium which is often referred to as "basic creep". The additional creep is termed "drying creep", caused by the concurrent drying process of the material. The general form of a strain-time curve for a material subjected to creep can be seen in Fig. 5.29.

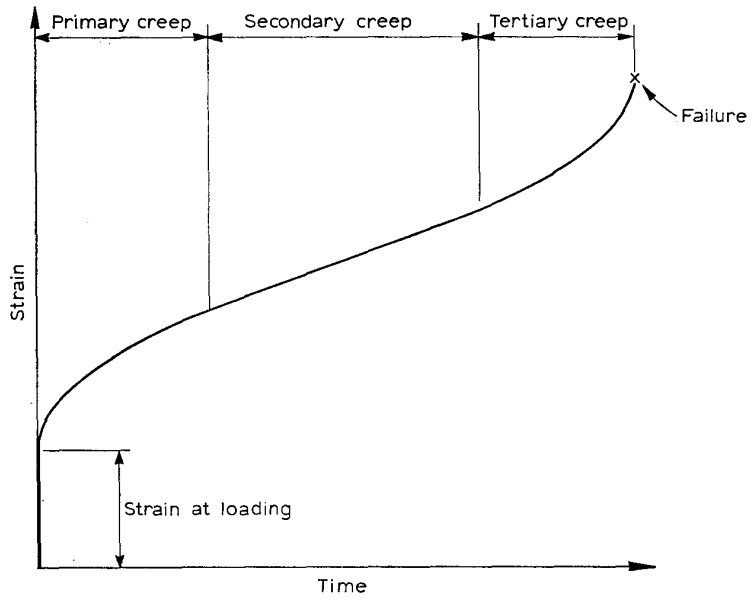



Figure 5.29: General form of strain development with time due to creep (from Neville, 1970)

At the start of loading at time zero an instantaneous deformation occurs, consisting primarily of an elastic component but may include as well an irreversible plastic part. With further development of time, three stages of creep can be identified, these are:

- Primary creep

- Secondary creep
- Tertiary creep

In the primary creep phase, the creep rate decreases with time followed by the range of steady state creep where a minimum constant creep rate can be identified. A straight line for secondary creep may be a convenient approximation. The tertiary creep phase is dominated by an increasing creep rate leading to creep failure due to microcracking within the concrete sample. This phase may or may not exist, depending on the applied stress level. On unloading, together with the instantaneous elastic recovery, there will be a gradual recovery of a portion of creep, meaning that creep components can be divided into a reversible and irreversible part, see Fig. 5.30.

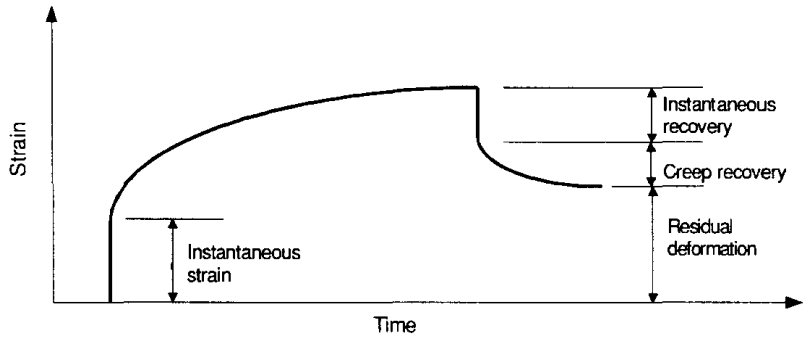



Figure 5.30: Creep recovery at unloading (from Bosnjak, 2000)

Practically, almost all the creep data available in the literature refer to experimental work for concrete in uniaxial compression. This might be due to the fact that concrete structures are designed for utilising the high compressive strength of concrete rather than the low tensile capacity. Furthermore, creep tests in uniaxial compression are much easier to perform than under other complex stress states. However, when the cracking behaviour of early age concrete is the purpose of an analysis, the creep behaviour under tensile stresses might be of considerable importance. Atrushi (2003) studied the creep capacity of young concrete in compression and tension performing some experimental tests. From the obtained results it was observed that the creep rates within the first 24 hours after loading where higher for compression than for tension. Afterwards, both creep rates decreased continually with time, but the decrease in tensile creep was much less pronounced than in compressive creep. Generally, it was concluded that the magnitude of creep in tension for equal stress levels is higher than in compression and this is in accordance with investigations performed by Illston (1965).

In a uniaxial compression test, creep not only occurs in the axial direction but also in the normal directions, which is referred to as lateral creep. Similar to the approach used in elasticity, the ratio of the lateral creep strain to the axial creep strain is often termed the creep Poisson's ratio, $\mu_{cr}$. In the literature there is no clear agreement on the magnitude of

the creep Poisson's ratio (Neville, 1970). Some researchers found it to be zero and others reported the same value as the elastic Poisson's ratio. Fig. 5.31 shows the possible theoretical values of lateral creep predicted by the creep Poisson's ratio.

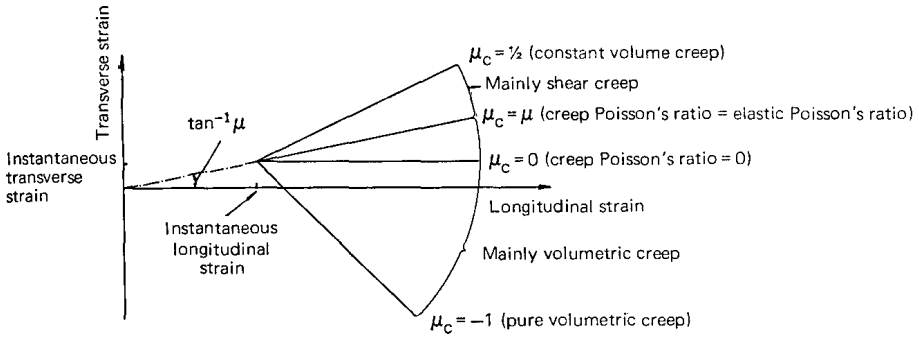



Figure 5.31: Possible values of creep Poisson's ratio $\mu_{cr}$ under uniaxial stress (from Neville, 1970)

For creep in multiaxial stress conditions it follows that there is creep induced by the applied stress in a particular direction and also creep due to the Poisson's ratio effect of creep in the two normal directions. The question arises whether these strains occur independently of each other and the principle of superposition is applicable, or whether the behaviour is more complex. Neville (1970) presented some results from multiaxial compression tests which indicated that creep in a multiaxial loading system is significantly lower than under a uniaxial stress. Furthermore, the value of the creep Poisson's ratio varies in the three principal stress directions and it follows that creep strains under multiaxial compression can not be simply superposed. Experimental work by Gopalakrishnan et al. (1969) showed that even under isotropic compression considerable creep deformation takes place. Hence, the principle of superposition does not hold for creep and creep in multiaxial loading conditions is a complex phenomenon that cannot be simply estimated from uniaxial creep measurements.

### 5.8.1 Mechanisms behind creep

A number of theories exist in the literature which try to reveal the cause of creep, but it has to be mentioned that the mechanisms behind creep are not fully understood (Thomas, 2003). However, it is recognised that, since creep can be related to the removal of absorbed water, its origin lies within the cement paste (Mehta & Monteiro, 1985). In contrary to shrinkage, for creep an applied stress is the driving force leading to a loss of physically absorbed water. A minor cause of the contraction of the cement-aggregate system could be the removal of water held by hydrostatic tension in small capillaries of the hydrated cement paste. Another theory states that creep is the result of a rearrangement of the capillary structure of the cement paste due to the applied load. Flow theories assume that the hydrated cement paste acts as a highly viscous liquid whose viscosity increases with time as a result of chemical changes within the structure. The occurrence of delayed elastic response in the aggregates could be

another cause of creep in concrete. Due to the bond between the cement paste and the aggregates, an applied stress is gradually transformed from the former concrete component to the latter, which consequently starts to deform elastically. Hence, the delayed elastic strain in the aggregates contributes to the total creep. Further information about different mechanisms behind creep is given in Neville (1970).

### 5.8.2 Influencing factors

As already pointed out, creep is a very complex process where various factors influence the mechanism behind it. Through his experimental work Byfors (1980) summarised them as:

- Concrete age at loading (or degree of hydration)
- Loading time
- Concrete composition and mix design
- Temperature
- Moisture conditions (Relative Humidity $RH$)
- Applied stress level

Fig. 5.32 provides a schematic presentation of the influence of these factors.

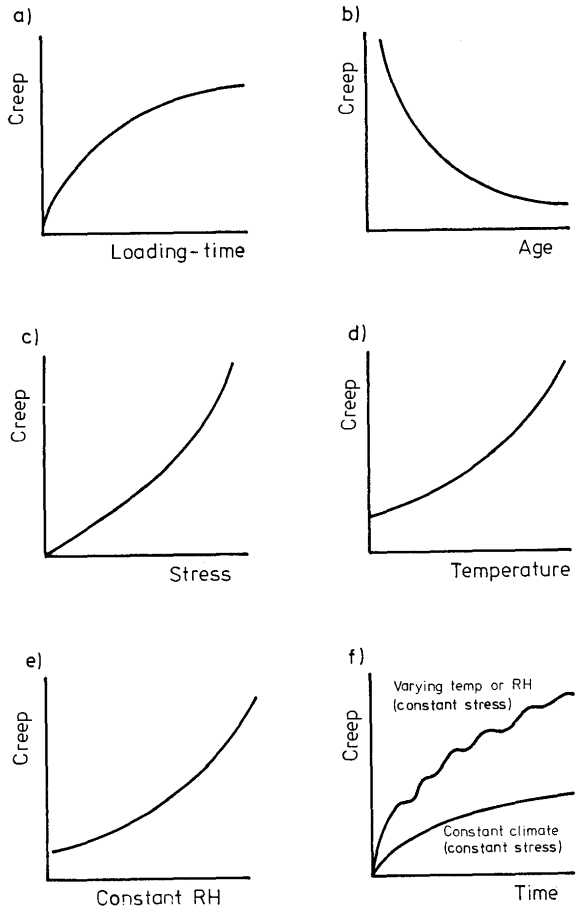



Figure 5.32: Factors influencing creep (from Byfors, 1980)

At very early ages concrete and shotcrete are very creep active media since the developed strength is still at a low level and hence the applied stress levels are high. For instance, Davis et al. (1934) compared the creep of water-stored concrete samples subjected to a constant stress during 80 months. The ratio of the creep deformations of the specimens loaded at 7 days, 28 days and 3 months averaged at $3:2:1$. They noted further that the rate of creep during the first few weeks under load was much higher for concrete loaded at an early age than for older age. However, Kuwajima (1999) reported that for young shotcrete this early age dependency of creep is just relevant for an age of up to 40 hours, since the strength development happens faster compared to conventional cast concrete. Parrott (1978) compiled the test results on early age creep from various researchers as can be seen in Fig. 5.33. The graph illustrates the creep as a relative ratio to the creep deformation at an age of loading of 28 days. The age dependency of creep is clearly visible and can be directly related to the process of cement hydration. After a rapid decrease in creep at early ages, the influence of age seems to stabilise from a concrete age of 100 days onwards. The considerable scatter in the test data around 1 day age may be linked also to the differences in the degree of hydration which is more marked at an early age.

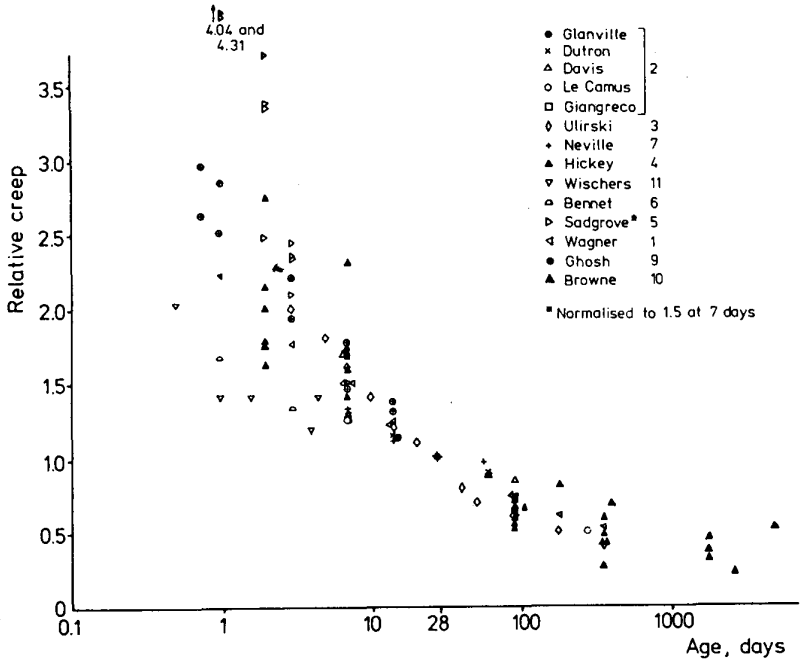



Figure 5.33: Relative creep with age at loading (from Byfors, 1980)

The quantification of creep for young shotcrete is not straightforward, but Thomas (2003) states that, according to the test data by Huber (1991), a sample loaded at an age of 8 days may creep around 25 % more than a similar sample loaded at 28 days.

In the literature it is well accepted knowledge that in uniaxial compression, up to a stress level of 0.4, creep is proportional to the applied stress (Neville, 1970), as can be seen in Fig. 5.34. Above this level the creep behaviour becomes non-linear and is believed to increase at an increasing rate. This fact is strongly linked to the internal microcracking that takes place in a concrete specimen during loading at high stress levels. A sufficiently high sustained stress can produce failure in the sample, which is also referred to as tertiary creep or static fatigue failure. This stress level dependency explains further why young concrete and shotcrete exhibit higher creep rates than at older ages. Due to the low concrete strength at early ages the stress level for a constant applied load is relatively high at the beginning of loading and decreases with time as the strength development continues. Hence, creep is greater for more slowly hydrating concretes (Thomas, 2003).

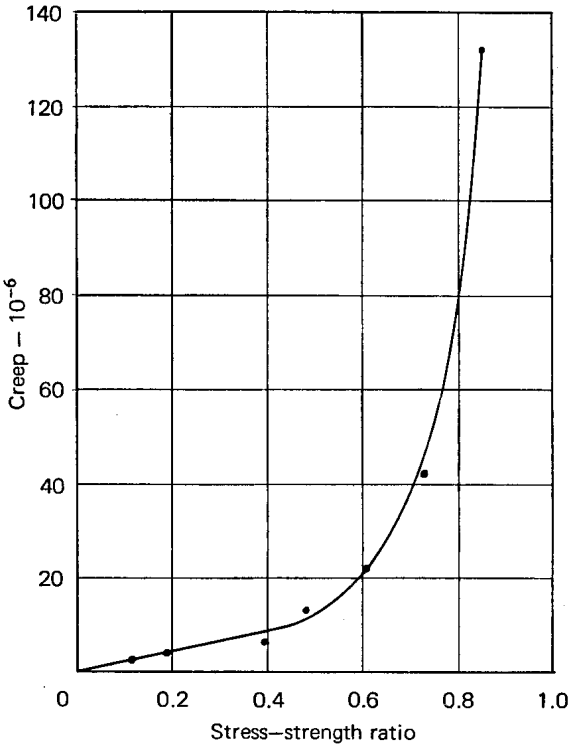



Figure 5.34: Creep for different stress levels (from Neville, 1970)

Since the origin of creep is believed to lie within the cement paste, the type and amount of cement adopted in the mix design is another factor influencing creep (Neville, 1981). It is reported that creep increases with increasing cement content, a fact which is of great importance for shotcrete since its composition is richer in cement than conventional cast concrete due to the rebound behaviour (see Chapter 4). The type of cement influences the creep behaviour in so far as it has an impact on the concrete strength development with time. The same rule applies to the water-cement ratio and to the fineness of the cement. However, studies with different cement types have failed to show a simple direct correlation between creep and the chemical composition of the cement. Cement replacements, such as microsilica, reduce the porosity and therefore may reduce as well the drying creep, since they restrict water movement within the concrete (Thomas, 2003).

Certain physical properties of the aggregate also have an influence on the creep of concrete, where it appears that the modulus of elasticity is the most important factor (Neville, 1981). A higher modulus leads to a decrease in creep since a greater restraint is offered by the aggregate to the potential creep of the cement paste. Furthermore, it may be expected that the porosity of the aggregate plays a direct role in the moisture movement within the concrete and therefore has an influence on the creep behaviour. According to Neville (1970), other parameters, such as grading, maximum size and shape of the aggregate, only have an indirect impact on the creep.

One of the most influencing factors on creep is the relative humidity of the air surrounding the concrete. As a general rule it can be assumed that creep is higher the lower the relative humidity (Neville, 1981), as indicated in Fig. 5.35. This influence, which is strongly linked to the process of drying, is much smaller for samples that are in hygral equilibrium with the surrounding medium prior to the application of the load. Hence, it can be said that concrete which exhibits high shrinkage shows generally also high creep. Therefore, these two phenomena appear to be coupled and linked to the same aspect of the structure of the hydrated cement paste and it is very difficult to separate them completely.

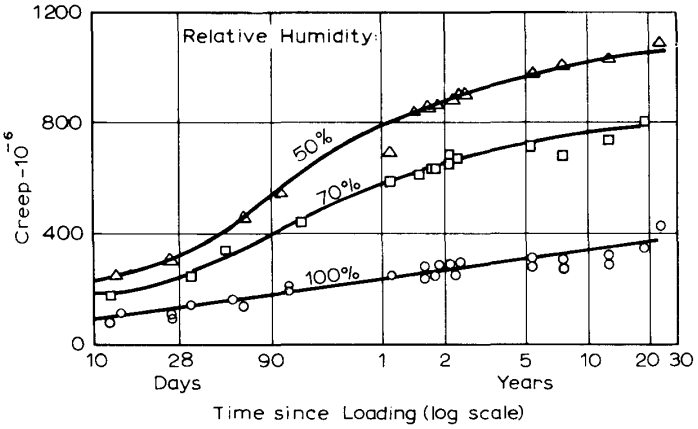



Figure 5.35: Creep for different relative humidity (from Neville, 1981)

Regarding the impact of temperature on the creep behaviour of concrete it is important to mention that the rate of creep increases with an increase in temperature. In Mehta & Monteiro (1985) it is reported that the creep rate at a temperature of about 70 °C is approximately 3.5 times higher than at 21 °C. However, Thomas (2003) states that these temperature effects on creep can be ignored for tunnel linings since the increase in temperature is relatively small and short-lived.

Finally, Ding (1998) investigated the creep behaviour of fibre reinforced concrete and shotcrete at early ages of 11 h. For the first 24 hours after loading the concrete samples with a fibre content of 20 and 40 kg/m$^3$ showed a significant reduction in creep deformation. In contrary, the specimens with 60 kg/m$^3$ fibre content developed almost the same creep deformation as the plain concrete. With increasing age the influence of steel fibres on the creep behaviour becomes more apparent. The biggest reduction in creep of 45 % was obtained for the concrete samples with 40 kg/m$^3$ at 240 h after loading, whereas the reduction for the 60 kg/m$^3$ samples was approximately 12 %. It can be concluded that steel reinforcement (fibres or wire mesh) has the potential for reducing creep deformation at early ages, but there is no direct quantifiable relation between the amount of reinforcement and the creep reduction.

### 5.8.3 Creep in tunnelling

The importance of shotcrete creep in tunnelling has been highlighted by many researchers, among them Rokahr & Lux (1987), Pöttler (1990), Schubert (1988), Golser et al. (1990), Thomas (2003), Aldrian (1991), Hesser (2000), Yin (1996), Huber (2006), Fischnaller (1992) and Walter (1997). As mentioned above, young shotcrete is a very creep active medium and this property is of crucial importance in tunnelling, where a shotcrete shell is immediately loaded to relatively high stress levels directly after installation. In Fig. 5.36 Pöttler (1993) illustrated schematically the development of stresses in a certain cross section of the lining during tunnel advance.

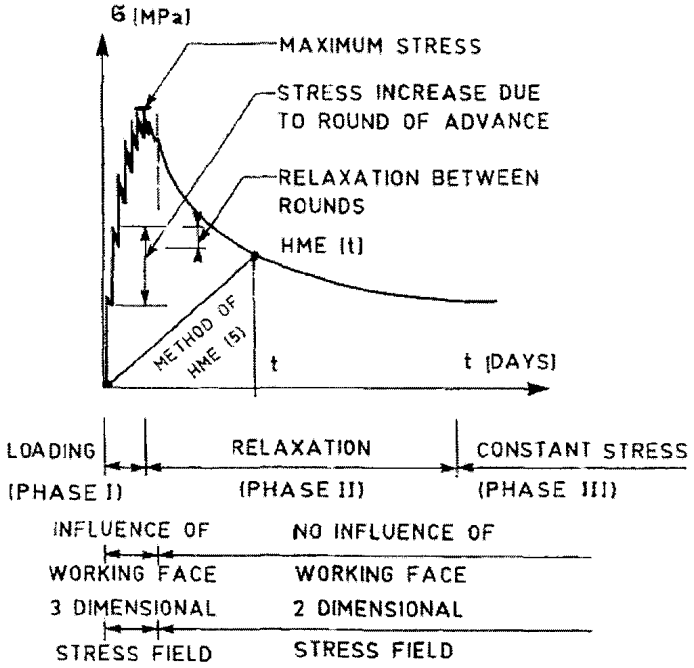



Figure 5.36: Development of lining stresses during tunnel advance (from Pöttler, 1993)

This figure shows that due to every excavation step the stresses in the lining increase, where the amount of loading depends heavily on the advance length and rate. But between every two rounds relaxation takes place in the very young shotcrete and stresses decrease by a certain amount. These relaxation phases are influenced by the stress level within the shotcrete shell, the creep capacity of the young shotcrete and the tunnel advance. Therefore the maximum stresses that occur in a lining are normally smaller than expected. Further, it is clearly visible that this maximum stress does not occur directly at the tunnel face, but a couple of excavation rounds behind, within a distance of 2 to 3 tunnel diameters, because of three dimensional arching of the ground. Once the maximum stress is reached, no further loading and influence of the working face takes place and the stresses reduce to a fairly constant stress level. In a tunnel analysis one should take into account the three dimensional stress field up to the point of maximum stress. For bigger distances behind the tunnel face a

two dimensional analysis would be sufficient.

According to Rokahr & Lux (1987) Fig. 5.37 shows the development of hoop stresses in a certain cross section of the tunnel lining with radial displacements (marked as $w$ in the figure). Similar to the previous figure, due to tunnel advance both the radial displacements and the hoop stresses increase. During two excavation rounds the shotcrete is creep active and deformations continue to increase. As can be inferred, creep and relaxation are processes that are taking place within the material simultaneously, leading normally to the phenomenon of relatively large displacements and lower than expected stresses (Rokahr & Lux, 1987). However, Pöttler (1993) states that stress relaxation is not of importance for shallow tunnels with an overburden of less than 2 to 3 tunnel diameters, but additional deformations due to creep occur.

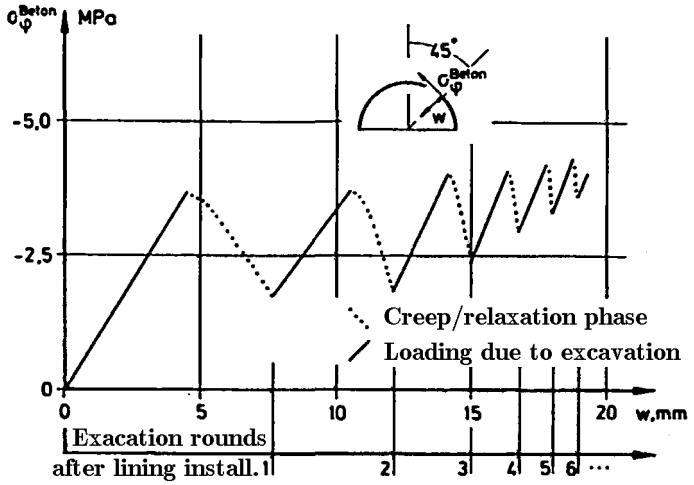



Figure 5.37: Creep and relaxation during tunnel advance (from Rokahr & Lux, 1987)

## 5.9 Shrinkage

During the process of cement hydration at early ages, concrete or shotcrete undergoes a certain change in volume which is mainly due to shrinkage or swelling. These are generally stress-independent deformations caused by drying or wetting and therefore proper curing conditions are of great importance for the hydration of concrete (Neville, 1981). Kuwajima (1999) states that in tunnelling the moisture provided by the soil plays a major role in the shrinkage process, resulting in a swelling at the invert region of the lining and reduced shrinkage in other areas. Furthermore, in the area of the tunnel crown shrinkage strains are highly related to the presence of air ventilation. If part of a concrete structure is restrained, the shrinkage of concrete can introduce stresses in the structure that may lead to cracking, as can be seen in Fig. 5.38.

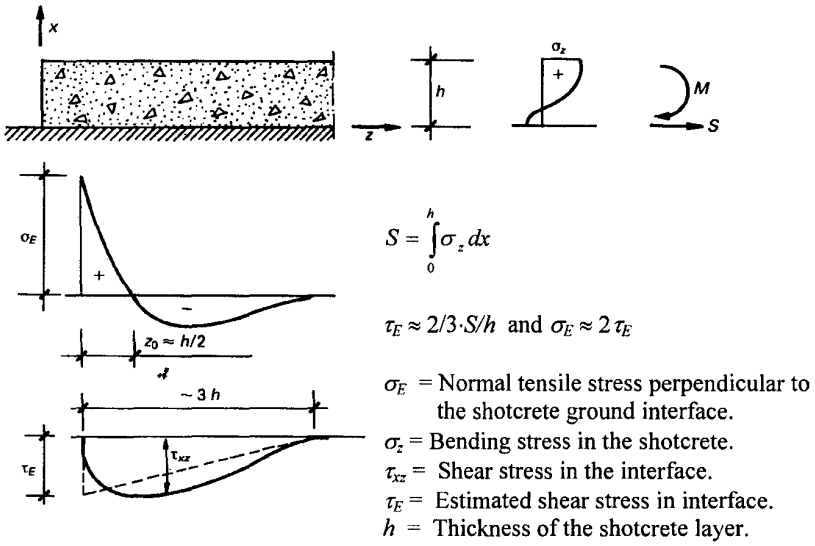



Figure 5.38: Concept of shrinkage induced stresses (from Malmgrem et al., 2005)

When the bending stress $\sigma_z$ reaches the maximum tensile strength, which is very low for young shotcrete, cracks start to occur perpendicular to the interface between the new shotcrete layer and the soil and concerns may arise regarding the watertightness of the lining. In a similar manner failure takes place when the normal tensile stress $\sigma_E$ exceeds the bond strength of the interface. However, when such shrinkage induced stresses are to be expected, it has to be taken into account that these stresses might be reduced significantly by the mechanism of creep (Malmgrem et al., 2005).

### 5.9.1 Mechanisms behind shrinkage

Thomas (2009) distinguishes 4 basic types of shrinkage that have different origins and are described here briefly:

#### 5.9.1.1 Plastic shrinkage

While the concrete is still in a plastic state at a very early age, it can happen that in the case of insufficient protection some volumetric contraction takes place caused by the loss of water from the surface due to evaporation, or by the suction from adjacent dry soil or an existing concrete (Mehta & Monteiro, 1985). This phenomenon is referred to as plastic shrinkage and can lead to surface cracking, where cracks are usually parallel to one another and spaced about 0.3 to 1.0 m apart. In Tab. 5.5 Neville (1981) gives some absolute values for the magnitude of plastic shrinkage at 8 hours after casting, depending on the wind velocity.

#### 5.9.1.2 Drying shrinkage

Contrary to plastic shrinkage, drying shrinkage takes place in the hardened cement paste as water is lost to the air (Thomas, 2009). The removal of free water in larger voids and capillary

| Wind velocity (m/s) | Shrinkage ($10^{-6}$) |
|---|---|
| 0 | 1 700 |
| 0.6 | 6 000 |
| 1.0 | 7 300 |
| 7.0 to 8.0 | 14 000 |

Table 5.5: Absolute values for plastic shrinkage (Relative humidity 50 %, Temperature 20 °C) (from Neville, 1981)

pores causes little or no shrinkage, but as drying continues, absorbed water in the cement paste is removed and leads to irreversible volume changes. In general, sprayed concrete shows higher drying shrinkage than conventional cast concrete due to the slightly different mix design, installation technique and curing conditions in a tunnel (Austin & Robins, 1995). However, Hills (1982) states that shrinkage values for sprayed concrete lie broadly within the expected range for cast concretes.

#### 5.9.1.3 Autogeneous shrinkage

Autogeneous shrinkage of concrete and shotcrete is defined as the macroscopic volume change occurring with no moisture transferred to the exterior surrounding environment (Holt, 2001). It is associated with the chemical hydration process of the cement particles, where water is drawn from the capillary pores and localised drying of these pores takes place. This process is often termed "self-desiccation" and causes the cement matrix to contract (Thomas, 2009). In the literature it is agreed that autogeneous shrinkage cannot be prevented by casting, placing or curing methods, but must be addressed by the correct mix design.

#### 5.9.1.4 Carbonation shrinkage

This type of shrinkage occurs mostly in the surface layers of concrete limited to a depth of 2 cm (Holt, 2001). Carbonation is the chemical process where the hardened cement paste reacts with moisture and carbon dioxide in the air. This leads to a certain volume change and a reduction in the $pH$ of the concrete, which is of big concern regarding the corrosion of reinforcing steel. Therefore carbonation of concrete and shotcrete is a durabilty issue that takes a long time to affect a structure. Houst (1997) reported that carbonation shrinkage is highly dependent on the concrete density and quality, but typical values for the highest carbonation shrinkage at a relative humidity of 70 to 80 % after 100 days would reach 3 to 4 mm/m.

### 5.9.2 Factors influencing shrinkage

Shrinkage of concrete and shotcrete is a complex process where many factors are influencing the early volume changes. Most of them are related to mix design, but also the installation technique in the case of shotcrete, environmental conditions and curing, and storage conditions can have a great impact on shrinkage.

Since the origin of shrinkage lies in general in the cement paste, it is sensitive to the water content of the concrete. Fig. 5.39 shows the general pattern where a higher water content leads to an increased drying shrinkage (Neville, 1981).

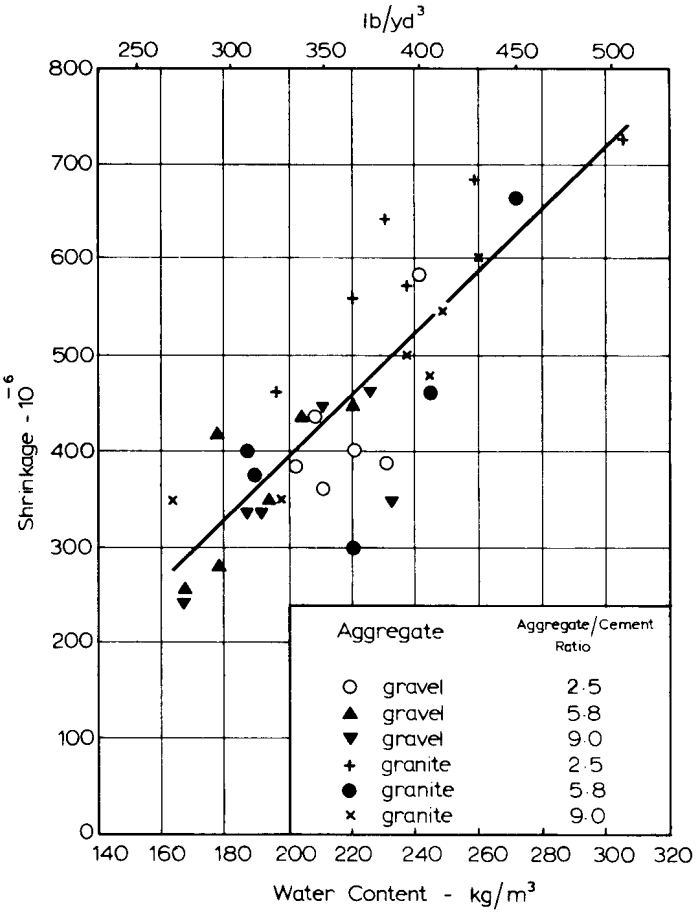



Figure 5.39: Influence of water content on absolute values of shrinkage (from Neville, 1981)

The properties of the adopted cement type have little influence on the shrinkage behaviour, although for a given water-cement ratio shrinkage increases with higher cement content (Malmgrem et al., 2005). Tab 5.6 contains some values for the drying shrinkage of shotcrete after six months, applied either as wet-mix or dry-mix. It can be seen that the wet-mix method with its higher water-cement ratio indicated higher shrinkage deformation than the dry-mix technique.

| | Wet-mix | Dry-mix |
|---|---|---|
| Water-cement ratio | 0.54 - 0.61 | 0.31 - 0.42 |
| Cement content (kg/m$^3$) | 375 - 475 | 550 - 700 |
| Shrinkage after 6 months (%) | 0.08 - 0.1 | 0.045 - 0.07 |

Table 5.6: Drying shrinkage after Hills, 1982

This fact is also reported by Neubert & Manns (1993), who investigated the effect of accelerating admixtures on the mechanical properties of shotcrete. Their test results presented in Fig. 5.40 illustrate that an increased amount of accelerators leads to an increase in shrinkage, in particular for the wet-mix method. This influence seems not to be so large for the dry-mix shotcrete. Further experimental work on shrinkage of wet- and dry-mix shotcrete can be found in Cornejo-Malm (1995).

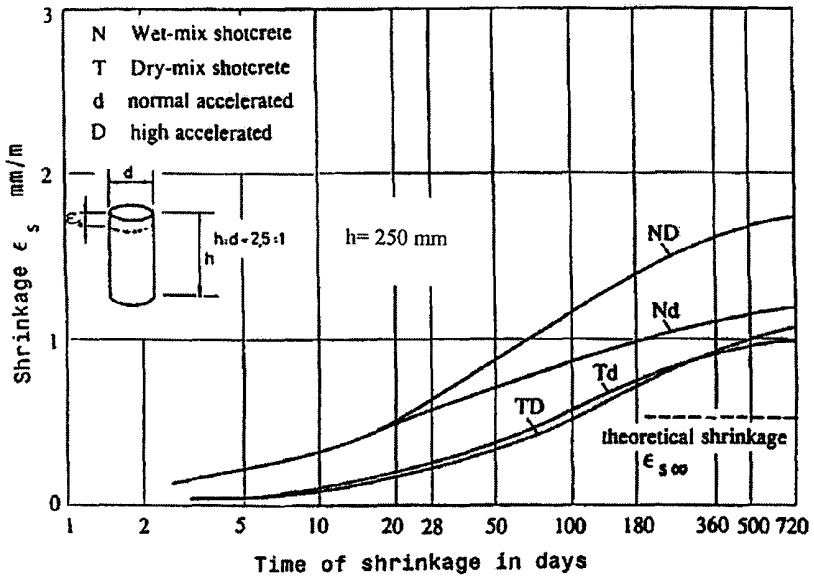



Figure 5.40: Shrinkage of shotcrete (from Neubert & Manns, 1993)

The aggregate used in the concrete mix restrains the amount of shrinkage that can actually be realised and therefore shrinkage can be reduced by an increased aggregate content, as shown in Fig. 5.41.

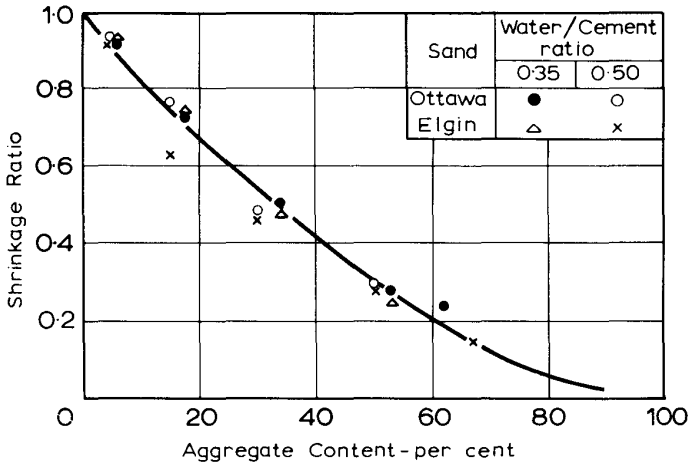



Figure 5.41: Influence of aggregate content in concrete on the ratio of shrinkage of concrete to the shrinkage of neat cement paste (from Neville, 1981)

The same effect is achieved by increasing the maximum aggregate size, that leads to a leaner mix and hence results in a lower shrinkage (Neville, 1981). Furthermore, Wolfsier & Morgan (1993) concluded that the addition of silica fume in the mix design (about 45 - 50 kg/m$^3$) can reduce slightly the shrinkage of shotcrete. In contrast, Thomas (2009) reported that fine materials added to the concrete, such as silica fume and fly ash, are known to increase shrinkage strains.

Ding (1998) worked on the technological properties of young steel fibre reinforced concrete and shotcrete, investigating also their shrinkage behaviour. For conventional cast concrete he observed that the inclusion of 60 kg/m$^3$ steel fibres led to a reduction in shrinkage of about 30 % after 320 h. At early ages within the first 24 h this reduction rises even up to 60 %. A similar trend was obtained for steel fibre reinforced shotcrete, although a higher fibre content (90 kg/m$^3$) was necessary to minimise shrinkage deformation. In addition, Malmberg (1977) stated that steel fibres were effective in distributing the cracking that occurs for restrained shrinkage and in restricting the crack widths.

Another important influencing factor for shrinkage is the relative humidity of the medium surrounding the concrete structure, as can be seen in Fig. 5.42. This figure illustrates that for a relative humidty of 100 % concrete starts to swell rather than to reduce its volume. Thomas (2003) reports that in a tunnel the relative humidity is around 50 %, with a fairly constant temperature within the range from 12 to 24 °C.

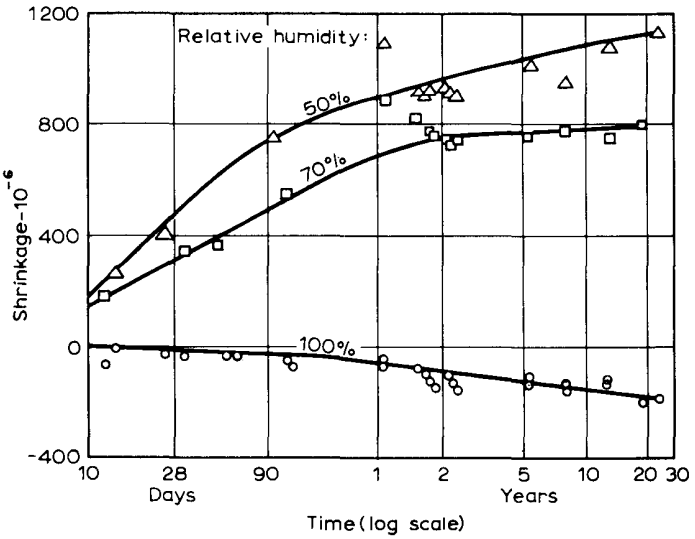



Figure 5.42: Influence of relative humidity on absolute values for shrinkage (from Neville, 1981)

It can be summarised that sprayed concrete exhibits higher drying shrinkage than conventional cast concrete. However, Austin & Robins (1995) relate this effect to the typical lower aggregate-cement ratio and higher cement contents due to rebound for shotcrete, rather than the spraying process itself.

## 5.10 Temperature induced deformation

The chemical reaction of the cement hydration in early-age concrete and shotcrete is an exothermic process, where energy is released in form of heat. Due to this temperature changes the tunnel lining expands and contracts within the first few days after shotcrete installation. Similar to shrinkage, if this thermal deformations are restrained stresses are introduced within the concrete structure, leading to a compressive stress in the case of expansion, and a tensile stress for the cooling phase when the temperature is decreasing again. Obviously, the thermal boundary conditions, such as ventilation, temperature in the tunnel and surface temperature of the excavated ground, highly influence the temperature distribution within the shotcrete layer, but a typical profile of temperature development over time can be seen in Fig. 5.43.

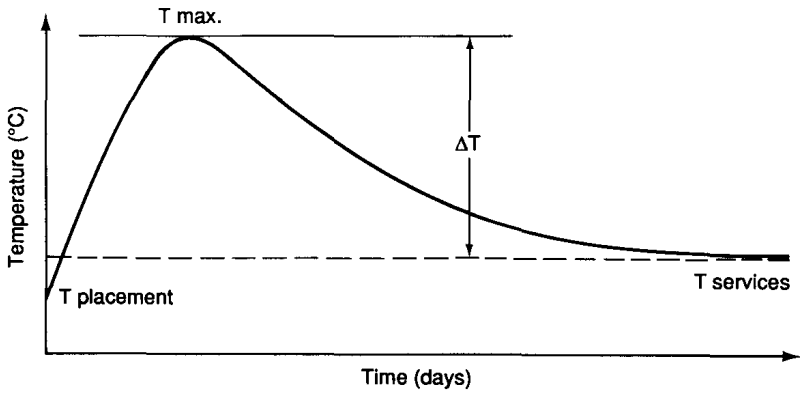



Figure 5.43: Temperature development in hardening concrete (from Mehta & Monteiro, 1985)

According to Thomas (2003) the maximum temperature rise depends on the following factors:

- Thickness of the sprayed concrete layer
- Initial temperature of the concrete mix
- Rate of cement hydration

In Kusterle & Lukas (1993) it is reported that, typically, the maximum temperature rise occurs around the centre of the lining and can reach values of up to 25 °C for a 30 cm thick shotcrete layer. Tab 5.7 gives a guideline to estimate the maximum temperature rise in the shotcrete depending on the layer thickness.

| Shotcrete layer thickness | $\Delta T$ from initial concrete temperature to $T_{max}$ | Temperature drop for 35 h after $T_{max}$ |
|---|---|---|
| 2 - 3 cm | 2 - 4 °C | negligible |
| 5 - 10 cm | 6 - 9 °C | 4 - 7 °C |
| 10 - 15 cm | 10 - 15 °C | 8 - 12 °C |
| 30 cm | 25 °C | 17 °C |

Table 5.7: Maximum temperature rise as a function of layer thickness (after Kusterle & Lukas, 1993)

It can be concluded that in order to keep the hydration temperature to a low level, the application of a shotcrete lining as a layered system is preferable (Kusterle & Lukas, 1993). Cornejo-Malm (1995) measured the development of hydration temperature for both dry- and wet-mix shotcrete samples and observed that for the dry-mix the peak temperature $T_{max}$ occurred between 8 to 10 h after casting, whereas for the wet-mix shotcrete $T_{max}$ was between 10 to 14 h. This is in general in accordance with Huber (1991) who detected the maximum temperature rise in his shotcrete samples between 9 to 12 h after spraying. His

experimental results showed further that, due to the addition of accelerators in the mix design, the development of hydration temperature is speeded up.

As mentioned earlier, the initial tendency of the lining to expand can introduce compressive stresses. However, since the Young's modulus is still very low at this early age, these compressive stresses are expected to be of no major importance for the structural behaviour of the lining. The situation is different for the cooling phase where, due to contraction, significant tensile stresses can develop that may lead to cracking of the shotcrete shell. Another important effect of hydration temperature is reported by Jones et al. (2008). Radial pressure cells installed at the front-shunt tunnel at Heathrow Terminal 5 indicated that, due to the temperature expansion of the lining at early ages, the ground pressure acting on the tunnel can reach up to 100 % of the overburden pressure, exposing the lining to the highest potential stress in the first 24 h after spraying. Nevertheless, in most cases researchers do not take into account the thermal effects of shotcrete at early ages.

For the mathematical description of the early age deformation of shotcrete due to hydration heat, the coefficient of thermal expansion is of great importance and it can be written:

$$\varepsilon_{th} = \alpha_t \, \Delta T \tag{5.35}$$

where $\varepsilon_{th}$ is the thermal strain and $\Delta T$ the increase in temperature. $\alpha_t$ is the coefficient of thermal expansion for shotcrete and is generally assumed to be the same as for conventional cast concrete (Thomas, 2003). Here again, the magnitude of $\alpha_t$ depends on the thermal properties of the cement, aggregates and their proportions in the mix (Neville, 1981). According to CEB-FIP Model Code (1990) for the purpose of structural analysis the coefficient of thermal expansion for hardened concrete at 28 days may be taken as $\alpha_t = 10 \times 10^{-6}\,°\mathrm{C}^{-1}$. In Byfors (1980) a literature review on the thermal properties of young concrete at early ages can be found. From the collected data it appears that $\alpha_t$ is not a constant material parameter, but decreases with increasing concrete age, as can be seen in Fig. 5.44.

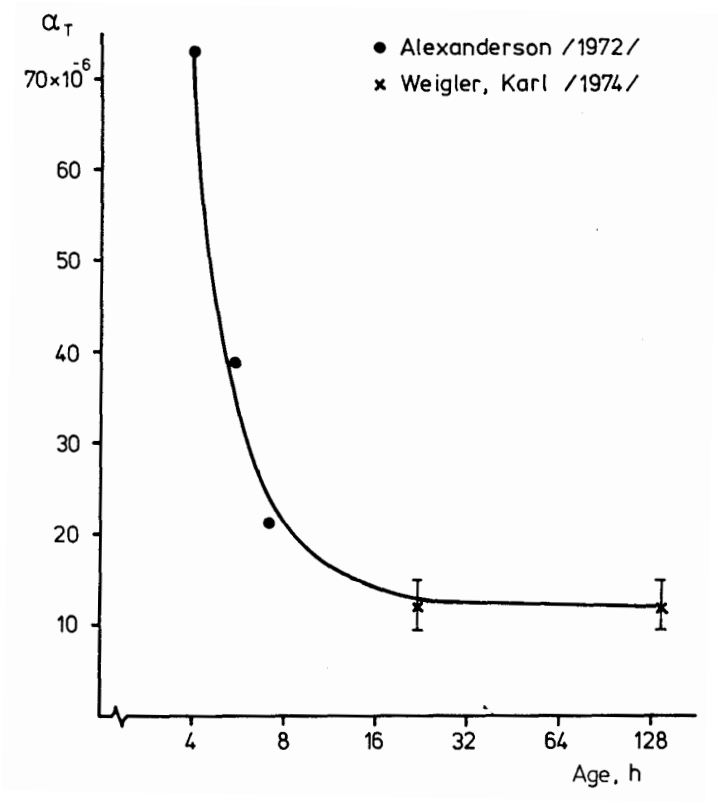



Figure 5.44: Age dependency for the coefficient of thermal expansion $\alpha_t$ (-/°C)(from Byfors, 1980)

## 5.11 Summary

The purpose of this chapter was to provide an introduction into the mechanical and time-dependent behaviour of concrete and shotcrete under various loading conditions. The following topics have been discussed in detail:

- Hardened concrete in uniaxial compression and tension shows a highly non-linear material behaviour, where crushing and cracking of the concrete govern the post-peak behaviour. Increased compressive strengths can be expected for concrete in biaxial and triaxial loading conditions, leading to smooth yield and failure surfaces.

- From the available data in the literature it is difficult to quantify any anisotropy of shotcrete that might be expected due to the spraying process.

- The incorporation of steel fibres in the concrete mix design results in a more ductile material behaviour, particularly for the post peak stress regime in tension.

- Shotcrete at early ages shows a relatively plastic and ductile material response with low stiffness and strength. Furthermore, higher strain limits can be achieved due to the increased deformability of shotcrete at early stages of cement hydration. With

curing time material behaviour becomes more and more brittle, caused by the increase in stiffness and strength with time. However, compressive and tensile strains at peak and failure strengths appear to reduce during cement hydration.

- The effect of compressive preloading of shotcrete samples at early ages on the development of the compressive strength at later stages is not very clear. In the literature both types of results can be found, i.e. an increase and a reduction in the strength values.
- Creep and relaxation are important aspects in shotcrete behaviour related to "time", depending on various factors, such as loading age, stress level, temperature, moisture conditions and concrete composition. It is believed that creep in tunnelling leads to a certain reduction in the expected lining stresses and is therefore of a beneficial nature.
- Deformations of young shotcrete that occur due to shrinkage and increased hydration temperature might be important to consider in a realistic tunnel lining design, since these two phenomena can lead to cracking of the shotcrete shell. Their origin lies within the cement paste of the concrete and can be addressed in the mix design.

# Chapter 6

# Modelling of concrete and shotcrete

## 6.1 Introduction

After having introduced the main characteristics of the time-dependent mechanical behaviour of concrete and shotcrete in Chapter 5, the aim of the current chapter is to give the reader an overview about certain aspects of modelling a quasi-brittle material such as concrete and shotcrete both in compression and tension. It starts with presenting simple approaches based on empirical observations and elasticity, moving then on to more complex constitutive models that can be used in a finite element analysis. A short introduction into the classical theory of elasto-plasticity serves as a background for presenting some basic elasto-plasticity models that are commonly applied for the modelling of hardened concrete. The simulation of the post-peak and cracking behaviour of unreinforced and reinforced concrete and its associated localization problems will be discussed briefly. Furthermore, some attention will be given to the modelling of the time-dependent phenomena of creep, shrinkage and hydration temperature induced strains, with a special focus on shotcrete behaviour. Finally, a review of different constitutive models adopted for tunnel lining design that can be found in the literature will conclude this chapter.

## 6.2 Empirical models for concrete in compression

A starting point for developing an empirical constitutive law is experimental data from various tests focusing mainly on uniaxial stress conditions in either compression or tension. Through results obtained from a series of experiments a curve fitting process is normally performed, that aims to derive the material parameters used in the proposed model functions. Although this approach seems quite simple and straightforward, some difficulties exist associated with the testing techniques of concrete, in particular for the post-peak behaviour. Other aspects that highly influence the result of such a material test can be the precision of the testing machine, the rate of loading, size of the tested specimen and statistical variations of the material properties from sample to sample (Babu et al., 2005). Popovics (1970) provides a

review of different empirical stress-strain relationships for concrete under compression and a few of them are presented below.

The CEB-FIP Model Code (1990) approximates the stress-strain curve for concrete under uniaxial compression shown in Fig. 6.1 with the following equation:

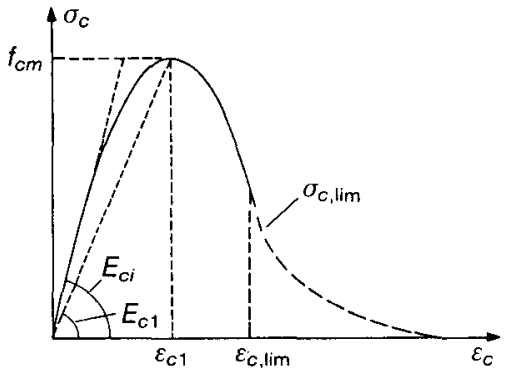



Figure 6.1: Stress-strain diagram for uniaxial compression (from CEB-FIP Model Code, 1990)

$$\sigma_c = -\frac{\dfrac{E_{ci}}{E_{c1}}\dfrac{\varepsilon_c}{\varepsilon_{c1}} - \left(\dfrac{\varepsilon_c}{\varepsilon_{c1}}\right)^2}{1 + \left(\dfrac{E_{ci}}{E_{c1}} - 2\right)\dfrac{\varepsilon_c}{\varepsilon_{c1}}} f_{cm} \qquad \text{for} \qquad |\,\varepsilon_c\,| < |\,\varepsilon_{c,lim}\,| \tag{6.1}$$

where $E_{ci}$ is the initial tangent modulus, $\sigma_c$ the uniaxial compressive stress, $\varepsilon_c$ the uniaxial compressive strain, $\varepsilon_{c1}$ is taken as an absolute value of $-0.0022$ (-) and $E_{c1}$ is the secant modulus from the origin to the peak compressive stress $f_{cm}$. The use of this equation is limited to compressive strains smaller than the limit strain $\varepsilon_{c,lim}$. For further straining, the descending branch of the stress-strain curve may be described by

$$\sigma_c = -\left[\left(\frac{1}{\varepsilon_{c,lim}/\varepsilon_{c1}}\xi - \frac{2}{(\varepsilon_{c,lim}/\varepsilon_{c1})^2}\right)\left(\frac{\varepsilon_c}{\varepsilon_{c1}}\right)^2 + \left(\frac{4}{\varepsilon_{c,lim}/\varepsilon_{c1}} - \xi\right)\frac{\varepsilon_c}{\varepsilon_{c1}}\right]^{-1} f_{cm} \tag{6.2}$$

with

$$\xi = \frac{4\left[\left(\dfrac{\varepsilon_{c,lim}}{\varepsilon_{c1}}\right)^2\left(\dfrac{E_{ci}}{E_{c1}} - 2\right) + 2\dfrac{\varepsilon_{c,lim}}{\varepsilon_{c1}} - \dfrac{E_{ci}}{E_{c1}}\right]}{\left[\dfrac{\varepsilon_{c,lim}}{\varepsilon_{c1}}\left(\dfrac{E_{ci}}{E_{c1}} - 2\right) + 1\right]^2} \tag{6.3}$$

The values for $E_{ci}$, $E_{c1}$ and $\varepsilon_{c,lim}$ can be estimated for various concrete grades from the following Tab. 6.1:

| Concrete grade | C 12 | C 20 | C 30 | C 40 | C 50 | C 60 | C 70 | C 80 |
|---|---|---|---|---|---|---|---|---|
| $E_{ci}$ (GPa) | 27 | 30.5 | 33.5 | 36.5 | 38.5 | 41 | 42.5 | 44.5 |
| $E_{c1}$ (GPa) | 9 | 12.5 | 17.5 | 22 | 26.5 | 31 | 35.5 | 40 |
| $\varepsilon_{c,lim}$ (%) | -0.5 | -0.42 | -0.37 | -0.33 | -0.30 | -0.28 | -0.26 | -0.24 |

Table 6.1: $E_{ci}$, $E_{c1}$ and $\varepsilon_{c,lim}$ for various concrete grades after CEB-FIP Model Code (1990)

For short-term loading tests in uniaxial compression Desayi & Krishnan (1964) proposed a stress-strain relation given by:

$$f = \frac{E\,\varepsilon}{1 + \left(\frac{\varepsilon}{\varepsilon_o}\right)^2} \tag{6.4}$$

where $f$ is the uniaxial compressive stress at any compressive strain $\varepsilon$, $\varepsilon_o$ the strain at maximum compressive stress $f_o$ and $E$ the tangent modulus that can be calculated from:

$$E = \frac{2f_o}{\varepsilon_o} \tag{6.5}$$

The descending part of the above equation is valid up to a failure stress $k\,f_o$ at a maximum strain $\varepsilon_c$. Fig. 6.2 shows a comparison of stress-strain curves of tested cylindrical concrete samples with those plotted from equation 6.4.

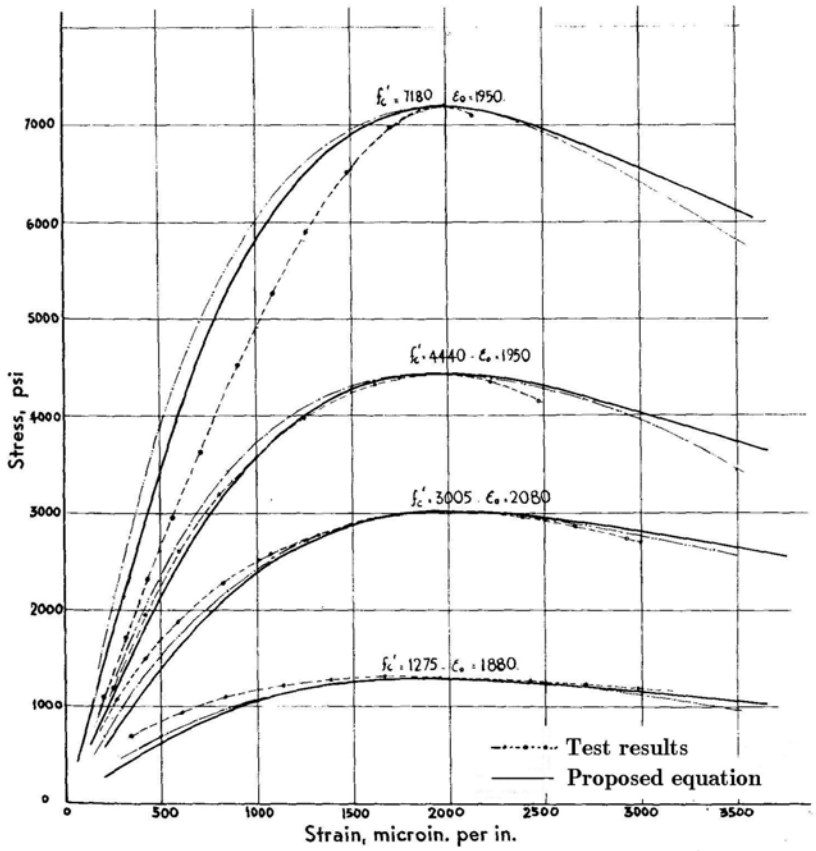



Figure 6.2: Uniaxial compressive stress strain curves for concrete (from Desayi & Krishnan, 1964)

Another expression for the uniaxial compressive stress-strain behaviour which shows good fit to experimental data is the one developed by Sargin (1968). It is of a non-dimensional mathematical form and applicable for both the confined (= lateral applied stress) and uniaxial case:

$$Y = \frac{AX + BX^2}{1 + CX + DX^2} \tag{6.6}$$

where

$$Y = \frac{f}{f_o} \qquad \text{and} \qquad X = \frac{\varepsilon}{\varepsilon_o} \tag{6.7}$$

$f$ represents the compressive stress at strain $\varepsilon$, while $f_o$ is the peak stress at strain $\varepsilon_o$. Two sets of constants $A$, $B$, $C$ and $D$ are required, one set for the ascending portion and a second set for the descending portion of the curve depending on the applied boundary conditions during the test. Fig. 6.3 compares model predictions with experimental data for different lateral confining pressures $fr$.

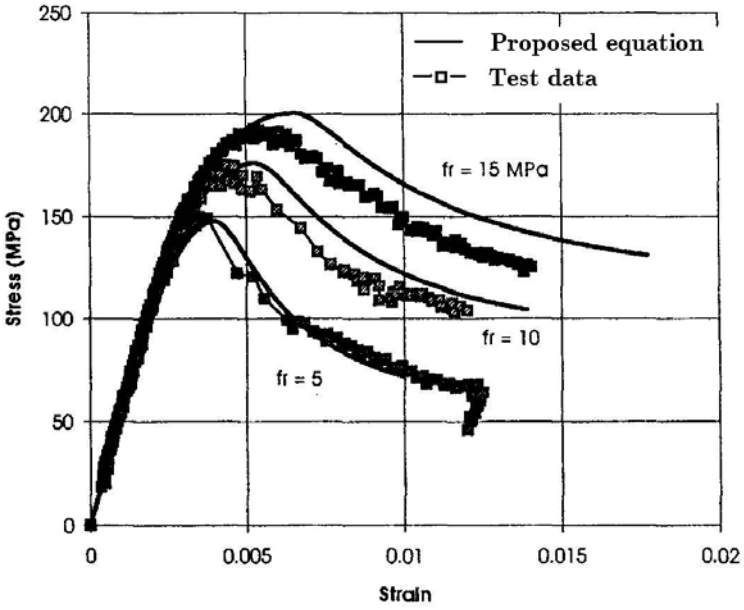



Figure 6.3: Compressive stress-strain curves for different lateral confining pressures (from Attard & Setunge, 1996)

EC 2 (2004) provides two different uniaxial compressive stress-strain curves, both shown in Fig. 6.4.

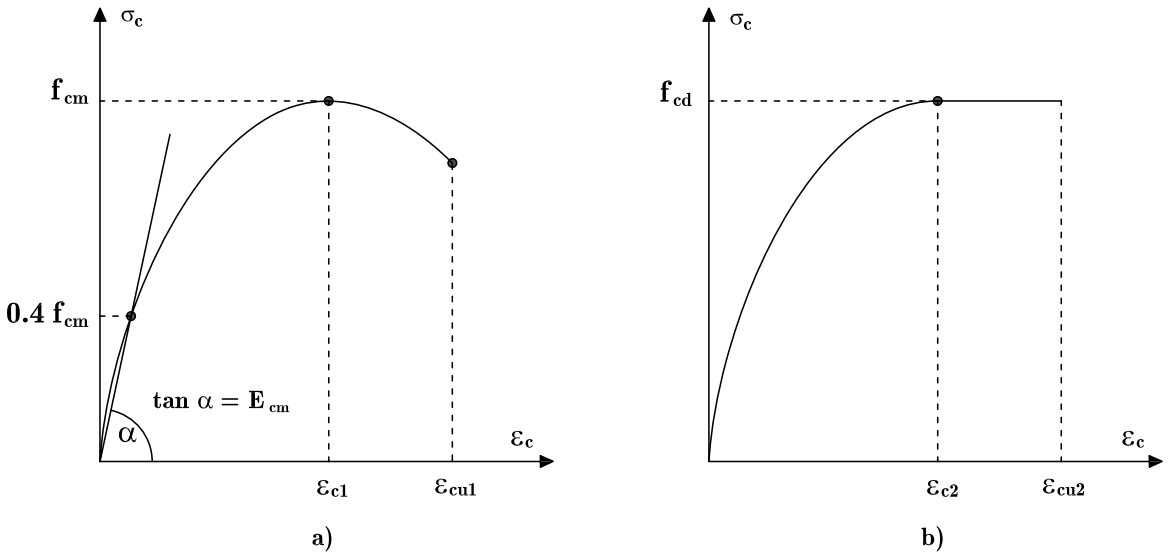



Figure 6.4: Uniaxial compressive stress-strain curves for a) non-linear structural analysis and b) for the design of cross-sections (after EC 2, 2004)

The first one is intended to be used for a non-linear structural analysis and the relation between the uniaxial compressive stress $\sigma_c$ and the uniaxial compressive strain $\varepsilon_c$ is given as:

$$\frac{\sigma_c}{f_{cm}} = \frac{k\,\eta - \eta^2}{1 + (k-2)\,\eta} \tag{6.8}$$

where $\eta$ and $k$ can be estimated through the strain at peak stress $\varepsilon_{c1}$ and the secant modulus of elasticity $E_{cm}$ (at $0.4\, f_{cm}$)as:

$$\eta = \frac{\varepsilon_c}{\varepsilon_{c1}} \qquad \text{and} \qquad k = \frac{1.05\, E_{cm}\, \varepsilon_{c1}}{f_{cm}} \tag{6.9}$$

In the case of the non-linear design of a concrete cross-section, the following stress-strain curve may be adopted:

$$\sigma_c = \begin{cases} f_{cd}\left[1 - \left(1 - \dfrac{\varepsilon_c}{\varepsilon_{c2}}\right)^n\right] & \text{for} \quad 0 \le \varepsilon_c \le \varepsilon_{c2} \\ f_{cd} & \text{for} \quad \varepsilon_{c2} \le \varepsilon_c \le \varepsilon_{cu2} \end{cases} \tag{6.10}$$

where $f_{cd}$ is the uniaxial compressive design strength, $n$ an exponential parameter ranging from 1.4 to 2.0, $\varepsilon_{c2}$ the compressive strain at reaching the maximum strength and $\varepsilon_{cu2}$ the ultimate compressive strain. For the most common strength classes C 12 to C 50 typical values for the above concrete parameters according to EC 2 (2004) would be:

| $E_{cm}$ | $\varepsilon_{c1}$ | $\varepsilon_{cu1}$ | $\varepsilon_{c2}$ | $\varepsilon_{cu2}$ |
|---|---|---|---|---|
| (GPa) | (%) | (%) | (%) | (%) |
| 27 to 37 | 0.18 to 0.245 | 0.35 | 0.20 | 0.35 |

Table 6.2: Material parameters for concrete taken from EC 2 (2004)

## 6.3 Constitutive models based on elasticity

### 6.3.1 Linear elastic models

If a material behaves linear elastically the incremental stresses can be associated with the strains via the following constitutive equation:

$$\{\Delta\sigma\} = [D]\,\{\Delta\varepsilon\} \tag{6.11}$$

where $\{\Delta\sigma\}$ is the incremental stress vector, $\{\Delta\varepsilon\}$ the incremental strain vector and $[D]$ is the elastic stiffness matrix. Furthermore, in the case of an isotropic material, it can be shown that only two independent elastic constants are necessary to describe the material behaviour, i.e. the Young's Modulus $E$ and the Poisson's ratio $\mu$. Therefore the elastic stiffness matrix

takes the symmetric form shown in the following equation:

$$[D] = \frac{E}{(1+\mu)(1-2\mu)} \begin{bmatrix} 1-\mu & \mu & \mu & 0 & 0 & 0 \\ \mu & 1-\mu & \mu & 0 & 0 & 0 \\ \mu & \mu & 1-\mu & 0 & 0 & 0 \\ 0 & 0 & 0 & \frac{1-2\mu}{2} & 0 & 0 \\ 0 & 0 & 0 & 0 & \frac{1-2\mu}{2} & 0 \\ 0 & 0 & 0 & 0 & 0 & \frac{1-2\mu}{2} \end{bmatrix} \tag{6.12}$$

For geotechnical analysis, the elastic soil behaviour is often more convenient to describe in terms of the elastic shear modulus $G$ and the bulk modulus $K$. They can be related to the Young's modulus $E$ and the Poisson's ratio $\mu$ via the following expressions:

$$G = \frac{E}{2(1+\mu)} \qquad \text{and} \qquad K = \frac{E}{3(1-2\mu)} \tag{6.13}$$

In spite of its obvious shortcomings, apparently the linear elastic theory is still the most commonly applied stress-strain relation in industry for modelling the complex non-linear material behaviour of concrete and in particular of shotcrete.

### 6.3.2 Non-linear elastic models

A logical first step to improve the model predictions for concrete within the concept of elasticity is to incorporate material parameters that depend on stress and/or strain level. In this way some of the main characteristics of concrete behaviour presented in Chapter 5 can be captured. In the case of an isotropic material there are only two parameters required, $E$ and $\mu$ or $K$ and $G$, and therefore the inclusion of non-linearity in the model formulation is relatively straightforward. In the following a non-linear elastic model developed by Kotsovos & Newman (1978), based on experimental results obtained at Imperial College London as part of an international cooperative programme, is presented. The model aims to describe mathematically the ascending branch of the stress-strain relationship of concrete under any stress state. Therefore, in the analysis of the experimental data, each stress and strain state is decomposed into a hydrostatic and a deviatoric component. For the description of the non-linear compressive stress-strain curve the following expressions of the secant bulk and shear moduli, varying with the octahedral stresses $\sigma_{oct}$ and $\tau_{oct}$, are given:

$$\frac{K_s}{K_o} = \frac{1}{1 + 0.52\left(\frac{\sigma_{oct}}{f_c}\right)^{1.09}} \tag{6.14}$$

and

$$\frac{G_s}{G_o} = \frac{1}{1 + 3.57 \left( \frac{\tau_{oct}}{f_c} \right)^{1.7}} \tag{6.15}$$

The tangent expressions are written in a similar form as:

$$\frac{K_t}{K_o} = \frac{1}{1 + 1.08 \left( \frac{\sigma_{oct}}{f_c} \right)^{1.09}} \tag{6.16}$$

and

$$\frac{G_t}{G_o} = \frac{1}{1 + 9.63 \left( \frac{\tau_{oct}}{f_c} \right)^{1.7}} \tag{6.17}$$

where $K_o$ and $G_o$ are the initial values at the start of loading. However, it should be pointed out that a simple derivation of the tangent expressions from the secant formulation is not straightforward, as $\sigma_{oct}$ and $\tau_{oct}$ are unknown functions of the volumetric and deviatoric strain components. A graphical representation of the above equations is shown in Fig. 6.5 together with experimental test data.

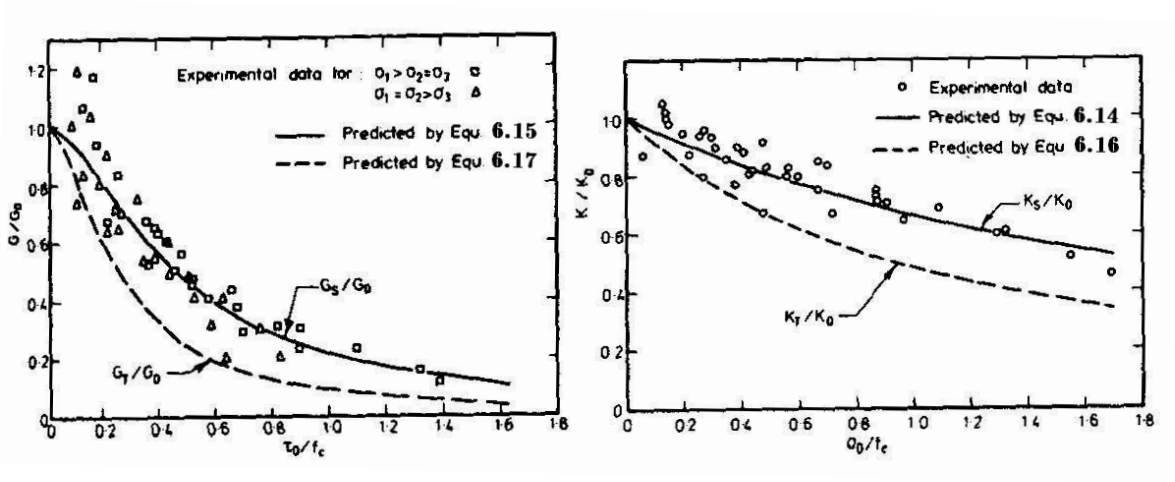



Figure 6.5: Variation of bulk and shear moduli with $\sigma_{oct}$ and $\tau_{oct}$ (from Kotsovos & Newman, 1978)

## 6.4 Classical theory of elasto-plasticity

Over the last three decades considerable improvements have been achieved in simulating the complex non-linear behaviour of concrete under multi-axial stress states. Nowadays, in the literature a large variety of constitutive models based on elasto-plasticity can be found that make it possible to analyse concrete structures by means of the finite element method. In the next sections the four essential ingredients required to formulate such an elasto-plastic constitutive model will be presented briefly. A more detailed description can be found in

Potts & Zdravković (1999). It should be noted that the procedure presented here focuses only on the time-independent behaviour of a material such as hardened concrete at 28 days. An extension to the basic theory of elasto-plasticity for the time-dependent behaviour of shotcrete can be found in chapter 7.

### 6.4.1 Basic concepts

*i) Coincidence of axes*
Contrary to the elastic material behaviour, it is assumed that for an elasto-plastic material law the principal directions of accumulated stress and incremental plastic strain coincide.

*ii) Yield surface*
In order to separate purely elastic behaviour from elasto-plastic behaviour a scalar function of the stress state $\{\sigma\}$ and the state parameters $\{k\}$, which can be related to hardening/softening parameters, is needed. This yield function can be written as:

$$F\left(\{\sigma\},\{k\}\right) = 0 \tag{6.18}$$

The value of the yield function $F$ is used to identify the type of material behaviour, as can be seen in Fig. 6.6 for the biaxial stress space.

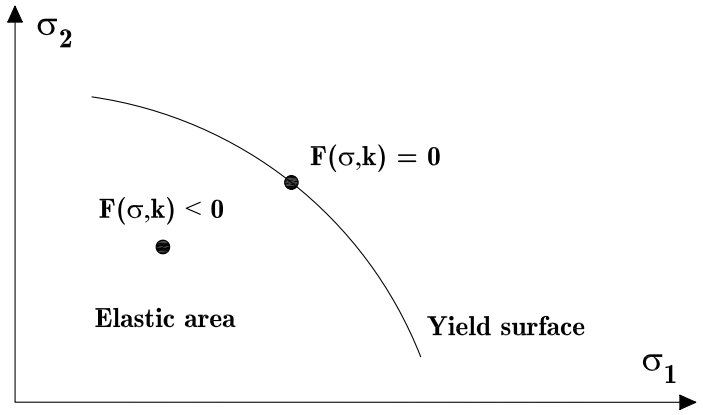



Figure 6.6: Yield surface and stress states for elastic and elasto-plastic material behaviour

Two different scenarios can be encountered.

1. Stress state within the yield surface ($F < 0$) $\longrightarrow$ Purely elastic material behaviour
2. Stress state on the yield surface ($F = 0$) $\longrightarrow$ Elasto-plastic material behaviour

*iii) Flow rule and plastic potential function*
A flow rule is required to determine the direction of plastic straining at every stress state. This is usually achieved by assuming a plastic potential surface $P$, which is of the form:

$$P\left(\{\sigma\},\{m\}\right) = 0 \tag{6.19}$$

The outward vector normal to the plastic potential surface has components which provide an indication of the relative magnitudes of the plastic strain increment components. Therefore the flow rule can be expressed as:

$$\{d\varepsilon^p\} = \Lambda \frac{\partial P\left(\{\sigma\},\{m\}\right)}{\partial \sigma} \tag{6.20}$$

where $\{\varepsilon^p\}$ is the plastic strain increment vector. The scalar parameter $\Lambda$ controls the magnitude of the plastic strain components and depends on the hardening/softening rules which will be discussed later.

In the case of the plastic potential function being identical with the yield function ($F\left(\{\sigma\},\{k\}\right) = P\left(\{\sigma\},\{m\}\right)$), the flow rule is said to be "associated" and a normality condition applies. The flow rule is defined as "non-associated" in the general case, where the plastic potential function differs from the yield function ($F\left(\{\sigma\},\{k\}\right) \neq P\left(\{\sigma\},\{m\}\right)$).

The assumption of an associated flow rule is a common simplification for the modelling of concrete. However, experimental data indicate that associated flow rules might not be the most appropriate assumption for predicting the material response of concrete (Babu et al., 2005). Some researchers, among them Smith et al. (1989), Grassl et al. (2002), Vermeer & de Borst (1984) and Frantziskonis et al. (1986), observed some dilatancy during shearing of concrete, characterized by volume changes associated with shear distortion of the material. Typical yield functions for concrete fail to predict this behaviour. In addition, data from uniaxial stress-strain curves for concrete in compression show that concrete exhibits non-linear volume change, displaying contraction at low load levels and dilation when the peak strength is approached (Babu et al., 2005; Chen, 1982). Therefore in the literature various forms of the plastic potential functions can be found with the aim of predicting the volumetric behaviour of concrete in a more realistic way. Further information about appropriate plastic potential functions for concrete is available in Han & Chen (1986), Dvorkin et al. (1989) and Onate et al. (1988).

*iv) Hardening and softening rule*

A hardening/softening rule is required for specifying the evolution of the yield surface in the course of plastic deformation. It defines how the state parameters $\{k\}$ vary with plastic straining and enables the calculation of the scalar parameter $\Lambda$ given in equation 6.20. If a material is perfectly plastic no hardening/softening occurs and the state parameters $\{k\}$ are constant and as a consequence no hardening/softening rule is required. Otherwise, the hardening parameters control the change in size of the yield surface and it is common to relate them to the components of the accumulated plastic strain. The material is assumed to be "strain hardening/softening". Alternatively, the motion of the yield surface in the stress space can be related to the increase in plastic work $\left(W^p = \int \{\sigma\}^T \{\Delta\varepsilon^p\}\right)$, and the material is said to follow a "work hardening/softening" concept.

With the help of a hardening/softening rule the scalar multiplier $\Lambda$ can be determined through the following procedure: when the material is at yield the stress state must satisfy the yield function so that $F(\{\sigma\},\{k\}) = 0$; as a consequence, the total differential of the yield function can be expressed as $dF = 0$, which is known as the "consistency condition"; applying the chain rule of differentiation gives:

$$dF = \left\{\frac{\partial F(\{\sigma\},\{k\})}{\partial \sigma}\right\}^T \{d\sigma\} + \left\{\frac{\partial F(\{\sigma\},\{k\})}{\partial k}\right\}^T \left[\frac{\partial k}{\partial \varepsilon^p}\right] \{d\varepsilon^p\} = 0 \tag{6.21}$$

By substituting the flow rule (equation 6.20) into the above equation it becomes:

$$dF = \left\{\frac{\partial F(\{\sigma\},\{k\})}{\partial \sigma}\right\}^T \{d\sigma\} + \left\{\frac{\partial F(\{\sigma\},\{k\})}{\partial k}\right\}^T \left[\frac{\partial k}{\partial \varepsilon^p}\right] \Lambda \frac{\partial P(\{\sigma\},\{m\})}{\partial \sigma} = 0 \tag{6.22}$$

Rearrangement of this equation leads to:

$$\Lambda = \frac{1}{A} \left\{\frac{\partial F(\{\sigma\},\{k\})}{\partial \sigma}\right\}^T \{\Delta\sigma\} \tag{6.23}$$

where $A$ is a hardening modulus and can be expressed as:

$$A = -\left\{\frac{\partial F(\{\sigma\},\{k\})}{\partial k}\right\}^T \left[\frac{\partial k}{\partial \varepsilon^p}\right] \left\{\frac{\partial P(\{\sigma\},\{m\})}{\partial \sigma}\right\} \tag{6.24}$$

Finally, for simple elasto-plastic models, the elastic part of a constitutive model describes the purely elastic material behaviour when the current stress state remains within the yield surface. Furthermore, it defines as well the elastic deformations that occur as part of the elasto-plastic behaviour, if the stress state is on the yield surface. However, advanced constitutive models show non-linear elasto-plastic behaviour even before the conventional yield surface is touched.

### 6.4.2 Formulation of the elasto-plastic constitutive matrix

In the following, the derivation of the elasto-plastic constitutive matrix needed for the description of the relationship between incremental stresses and incremental strains is presented. This relationship can be written as:

$$\{\Delta\sigma\} = [D^{ep}]\ \{\Delta\varepsilon\} \tag{6.25}$$

where $[D^{ep}]$ is used to distinguish that the constitutive behaviour is elasto-plastic. The incremental total strains can be split into elastic and plastic components:

$$\{\Delta\varepsilon\} = \{\Delta\varepsilon^e\} + \{\Delta\varepsilon^p\} \tag{6.26}$$

The changes in stresses are related to the changes in elastic strains by the elastic constitutive matrix $[D]$ in the form:

$$\{\Delta\sigma\} = [D]\ \{\Delta\varepsilon^e\} \tag{6.27}$$

Making use of equations 6.26 and 6.27 gives:

$$\{\Delta\sigma\} = [D]\ (\{\Delta\varepsilon\} - \{\Delta\varepsilon^p\}) \tag{6.28}$$

By substituting the flow rule (equation 6.20) into the above equation one obtains:

$$\{\Delta\sigma\} = [D]\ \{\Delta\varepsilon\} - \Lambda\ [D] \left\{\frac{\partial P\left(\{\sigma\},\{m\}\right)}{\partial\sigma}\right\} \tag{6.29}$$

Combining equation 6.23 and 6.29 results in the following expression for the scalar multiplier:

$$\Lambda = \frac{\left\{\dfrac{\partial F\left(\{\sigma\},\{k\}\right)}{\partial\sigma}\right\}^T [D]\ \{\Delta\varepsilon\}}{\left\{\dfrac{\partial F\left(\{\sigma\},\{k\}\right)}{\partial\sigma}\right\}^T [D] \left\{\dfrac{\partial P\left(\{\sigma\},\{m\}\right)}{\partial\sigma}\right\} + A} \tag{6.30}$$

Substitution of this equation into equation 6.29 gives a relation between the incremental stresses and the incremental strains:

$$\{\Delta\sigma\} = [D]\,\{\Delta\varepsilon\} - \frac{[D] \left\{\dfrac{\partial P\left(\{\sigma\},\{m\}\right)}{\partial\sigma}\right\} \left\{\dfrac{\partial F\left(\{\sigma\},\{k\}\right)}{\partial\sigma}\right\}^T [D]\,\{\Delta\varepsilon\}}{\left\{\dfrac{\partial F\left(\{\sigma\},\{k\}\right)}{\partial\sigma}\right\}^T [D] \left\{\dfrac{\partial P\left(\{\sigma\},\{m\}\right)}{\partial\sigma}\right\} + A} \tag{6.31}$$

Therefore, the elasto-plastic constitutive matrix is:

$$[D^{ep}] = [D] - \frac{[D] \left\{\dfrac{\partial P\left(\{\sigma\},\{m\}\right)}{\partial\sigma}\right\} \left\{\dfrac{\partial F\left(\{\sigma\},\{k\}\right)}{\partial\sigma}\right\}^T [D]}{\left\{\dfrac{\partial F\left(\{\sigma\},\{k\}\right)}{\partial\sigma}\right\}^T [D] \left\{\dfrac{\partial P\left(\{\sigma\},\{m\}\right)}{\partial\sigma}\right\} + A} \tag{6.32}$$

### 6.4.3 Multi-surface plasticity

Sometimes the behaviour of concrete is described by two yield surfaces, controlling either the compressive or the tensile behaviour in multiaxial loading conditions. In this section, the theory for the elasto-plastic constitutive matrix of one single yield surface introduced in the previous section is extended for the case when two yield surfaces $F_1$ and $F_2$ act simultaneously, following a procedure from Potts & Zdravković (1999). As before, the incremental total strains can be divided into elastic and plastic components. In addition, the plastic components can be further split into plastic strains associated with each of the two yield surfaces. This gives:

$$\{\Delta\varepsilon\} = \{\Delta\varepsilon^e\} + \left\{\Delta\varepsilon^{p1}\right\} + \left\{\Delta\varepsilon^{p2}\right\} \tag{6.33}$$

In a similar form as equation 6.28 it can be written that:

$$\{\Delta\sigma\} = [D]\left(\{\Delta\varepsilon\} - \left\{\Delta\varepsilon^{p1}\right\} - \left\{\Delta\varepsilon^{p2}\right\}\right) \tag{6.34}$$

Two flow rules relate the incremental plastic strains $\left\{\Delta\varepsilon^{p1}\right\}$ and $\left\{\Delta\varepsilon^{p2}\right\}$ to the plastic potential functions $P_1$ and $P_2$. They can be expressed as:

$$\{d\varepsilon^{p1}\} = \Lambda_1 \frac{\partial P_1\left(\{\sigma\},\{m\}\right)}{\partial\sigma} \qquad \text{and} \qquad \{d\varepsilon^{p2}\} = \Lambda_2 \frac{\partial P_2\left(\{\sigma\},\{m\}\right)}{\partial\sigma} \tag{6.35}$$

where $\Lambda_1$ and $\Lambda_2$ are the two scalar multipliers. Substituting the two flow rules given in equation 6.35 into equation 6.34 results in:

$$\{\Delta\sigma\} = [D]\{\Delta\varepsilon\} - \Lambda_1[D]\left\{\frac{\partial P_1}{\partial\sigma}\right\} - \Lambda_2[D]\left\{\frac{\partial P_2}{\partial\sigma}\right\} \tag{6.36}$$

When the material is plastic and both yield surfaces are active, the stress state must satisfy both yield functions, so that $F_1 = 0$ and $F_2 = 0$. Using the chain rule of differentiation, the consistency condition is obtained as:

$$dF_1 = \left\{\frac{\partial F_1}{\partial\sigma}\right\}^T \{d\sigma\} + \left\{\frac{\partial F_1}{\partial k_1}\right\}^T \left[\frac{\partial k_1}{\partial\varepsilon^{p1}}\right]\left\{d\varepsilon^{p1}\right\} = 0 \tag{6.37}$$

and

$$dF_2 = \left\{\frac{\partial F_2}{\partial\sigma}\right\}^T \{d\sigma\} + \left\{\frac{\partial F_2}{\partial k_2}\right\}^T \left[\frac{\partial k_2}{\partial\varepsilon^{p2}}\right]\left\{d\varepsilon^{p2}\right\} = 0 \tag{6.38}$$

Substituting equation 6.36 into equations 6.37 and 6.38 leads to:

$$dF_1 = \left\{\frac{\partial F_1}{\partial\sigma}\right\}^T [D]\{d\varepsilon\} - \Lambda_1\left\{\frac{\partial F_1}{\partial\sigma}\right\}^T [D]\left\{\frac{\partial P_1}{\partial\sigma}\right\} - \Lambda_2\left\{\frac{\partial F_1}{\partial\sigma}\right\}^T [D]\left\{\frac{\partial P_2}{\partial\sigma}\right\} - \Lambda_1 A_1 = 0 \tag{6.39}$$

and

$$dF_2 = \left\{\frac{\partial F_2}{\partial\sigma}\right\}^T [D]\{d\varepsilon\} - \Lambda_1\left\{\frac{\partial F_2}{\partial\sigma}\right\}^T [D]\left\{\frac{\partial P_1}{\partial\sigma}\right\} - \Lambda_2\left\{\frac{\partial F_2}{\partial\sigma}\right\}^T [D]\left\{\frac{\partial P_2}{\partial\sigma}\right\} - \Lambda_2 A_2 = 0 \tag{6.40}$$

where the hardening moduli $A_1$ and $A_2$ are:

$$A_1 = -\frac{1}{\Lambda_1}\left\{\frac{\partial F_1}{\partial k_1}\right\}\left[\frac{\partial k_1}{\partial\varepsilon^{p1}}\right]\left\{d\varepsilon^{p1}\right\} \tag{6.41}$$

and

$$A_2 = -\frac{1}{\Lambda_2}\left\{\frac{\partial F_2}{\partial k_2}\right\}\left[\frac{\partial k_2}{\partial\varepsilon^{p2}}\right]\left\{d\varepsilon^{p2}\right\} \tag{6.42}$$

Equations 6.39 and 6.40 can be rewritten in a simpler form as:

$$\Lambda_1 L_{11} + \Lambda_2 L_{12} = T_1 \qquad \text{and} \qquad \Lambda_1 L_{21} + \Lambda_2 L_{22} = T_2 \tag{6.43}$$

with:

$$
\begin{aligned}
L_{11} &= \left\{\frac{\partial F_1}{\partial \sigma}\right\}^T [D] \left\{\frac{\partial P_1}{\partial \sigma}\right\} + A_1 \\
L_{22} &= \left\{\frac{\partial F_2}{\partial \sigma}\right\}^T [D] \left\{\frac{\partial P_2}{\partial \sigma}\right\} + A_2 \\
L_{12} &= \left\{\frac{\partial F_1}{\partial \sigma}\right\}^T [D] \left\{\frac{\partial P_2}{\partial \sigma}\right\} \\
L_{21} &= \left\{\frac{\partial F_2}{\partial \sigma}\right\}^T [D] \left\{\frac{\partial P_1}{\partial \sigma}\right\} \\
T_1 &= \left\{\frac{\partial F_1}{\partial \sigma}\right\}^T [D] \{d\varepsilon\} \\
T_2 &= \left\{\frac{\partial F_2}{\partial \sigma}\right\}^T [D] \{d\varepsilon\}
\end{aligned}
\tag{6.44}
$$

The solution for $\Lambda_1$ and $\Lambda_2$ can be obtained from equation 6.43 as:

$$
\Lambda_1 = \frac{L_{22}T_1 - L_{12}T_2}{L_{11}L_{22} - L_{12}L_{21}} \qquad \text{and} \qquad \Lambda_2 = \frac{L_{11}T_2 - L_{21}T_1}{L_{11}L_{22} - L_{12}L_{21}} \tag{6.45}
$$

Finally, combining these two equations with equation 6.36 gives the elasto-plastic constitutive matrix in the case when the two yield surfaces are active simultaneously:

$$
[D^{ep}] = [D] - \frac{[D]}{\Omega}\left[\left\{\frac{\partial P_1}{\partial \sigma}\right\}\{b_1\}^T + \left\{\frac{\partial P_2}{\partial \sigma}\right\}\{b_2\}^T\right][D] \tag{6.46}
$$

where

$$
\Omega = L_{11}L_{22} - L_{12}L_{21} \tag{6.47}
$$

and

$$
\{b_1\} = L_{22}\left\{\frac{\partial F_1}{\partial \sigma}\right\} - L_{12}\left\{\frac{\partial F_2}{\partial \sigma}\right\} \qquad \text{and} \qquad \{b_2\} = L_{11}\left\{\frac{\partial F_2}{\partial \sigma}\right\} - L_{21}\left\{\frac{\partial F_1}{\partial \sigma}\right\} \tag{6.48}
$$

## 6.5 Basic plasticity models for concrete

### 6.5.1 Rankine criterion

To describe the brittle failure of concrete in tension a maximum tensile stress criterion, often called the Rankine criterion or tension-cut-off (Chen, 1982), is generally used. It is a one parameter model that assumes that failure takes place when the maximum principal stress at any point inside the material reaches the tensile strength $f_{tp}$, regardless of any other normal or shear stresses that occur on other planes through this stress point. In terms of the maximum principal stress this failure criterion can be expressed by the following equation (assuming a tension positive sign convention):

$$
\sigma_1 = f_{tp} \tag{6.49}
$$

Making use of the geotechnical stress invariants (see chapter 1) this equation can be written within the range of $-30° \leq \theta \leq +30°$:

$$F\,(p,\,J,\,\theta) = p + \frac{2J}{\sqrt{3}}\,\sin\left(\theta + \frac{2\pi}{3}\right) - f_t = 0 \tag{6.50}$$

Fig. 6.7 illustrates the cross sectional shape in the deviatoric plane and in the $J - p$ space.

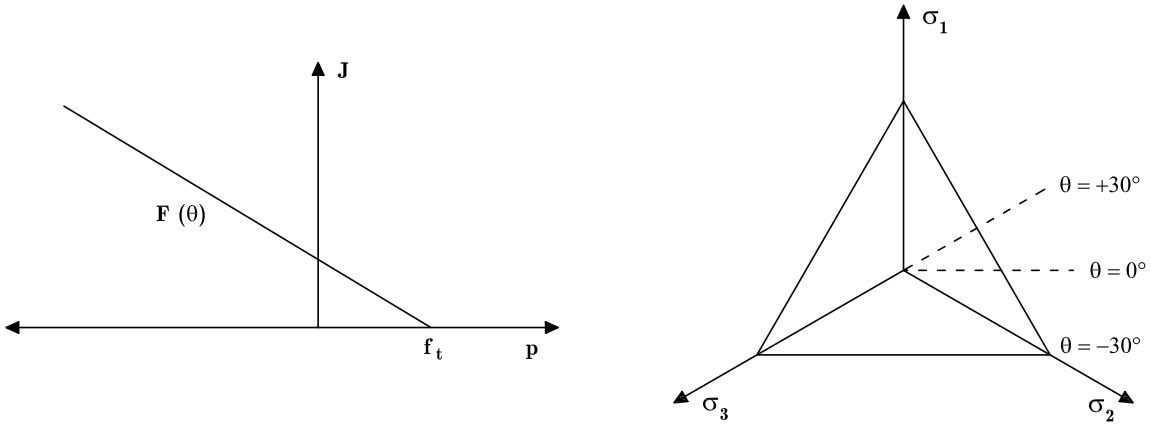



Figure 6.7: Rankine criterion in $J$-$p$ (left) and principal stress space (right)

### 6.5.2 Mohr-Coulomb criterion

The well known Mohr-Coulomb criterion dates back to 1773 and can be expressed as a two parameter model, where the limiting shear stress $\tau$ in a plane is only dependent on the normal stress $\sigma$ which is acting in the same plane. The failure envelope for the corresponding Mohr circles is shown in Fig. 6.8 and given by the equation:

$$|\tau| = c + \sigma \tan\phi \tag{6.51}$$

where $c$ is the cohesion and $\phi$ represents the internal friction angle of the material.

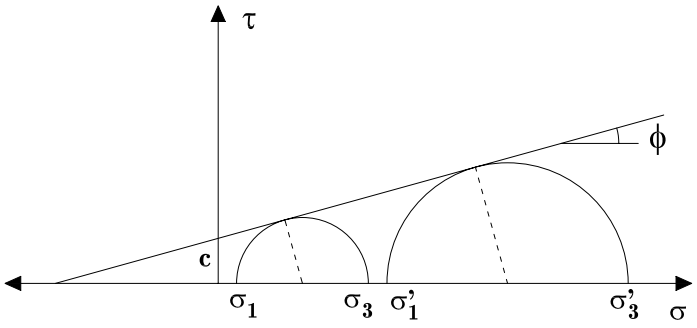



Figure 6.8: Mohr-Coulomb failure criterion

Failure of material will occur for all states of stress for which the largest Mohr circle touches

the failure envelope. This means that the intermediate principal stress has no influence on the failure. The two material parameters $c$ and $\phi$ are related to the uniaxial compressive and tensile strength in the following way:

$$\mid f_{cp} \mid = \frac{2c\cos\phi}{1-\sin\phi} \tag{6.52}$$

and

$$\mid f_{tp} \mid = \frac{2c\cos\phi}{1+\sin\phi} \tag{6.53}$$

The friction angle $\phi$ is obtained from:

$$\frac{f_c}{f_t} = \frac{1+\sin\phi}{1-\sin\phi} \tag{6.54}$$

Using the geotechnical stress invariants the Mohr-Coulomb criterion can be written as:

$$F\left(p,\, J,\, \theta\right) = J - \left(\frac{c}{\tan\phi} + p\right) g\left(\theta\right) = 0 \tag{6.55}$$

where

$$g\left(\theta\right) = \frac{\sin\phi}{\cos\theta + \frac{\sin\theta\,\sin\phi}{\sqrt{3}}} \tag{6.56}$$

In the principal stress space the deviatoric cross section plots as an irregular hexagon, which can be seen on the right in Fig. 6.9. For moderate values of mean stress this model describes reasonably well the failure of a brittle-ductile material like concrete, but is most of the time combined with a Rankine tension cut-off when tensile stresses occur (Chen, 1982). As mentioned before, one big disadvantage is that the intermediate stress $\sigma_2$ is not taken into account. This fact implies that the biaxial compressive strength $f_{bc}$ for concrete (when $\sigma_1 = \sigma_2$) is the same as the uniaxial compressive strength $f_{cp}$, which is contrary to experimental results. When hydrostatic pressure is increased, the failure surfaces in the $J$-$p$ space should be curved lines, which is not the case for the Mohr-Coulomb criterion as indicated in Fig. 6.9. Furthermore, when used in numerical analysis, the corners of the failure surface represent singularities, which can be difficult do handle.

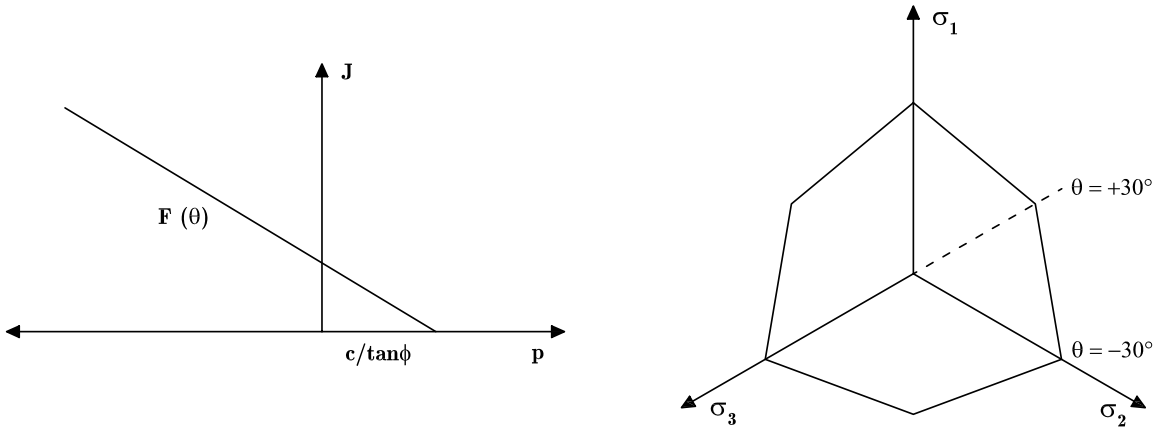



Figure 6.9: Mohr-Coulomb criterion in $J$-$p$ (left) and principal stress space (right)

### 6.5.3 Drucker-Prager criterion

To overcome the problem of the corners and associated singularities of the Mohr-Coulomb criterion, the Drucker-Prager criterion was developed. The failure surface is given as:

$$F\,(p,\,J) = \alpha\,p + J - k = 0 \tag{6.57}$$

where $\alpha$ and $k$ are material parameters that can be related to the uniaxial compressive and tensile strength in several ways. This failure surface in principal stress space is clearly a circular cone whose meridians in the $p$-$J$ space and the deviatoric cross sections can be seen in Fig. 6.10.

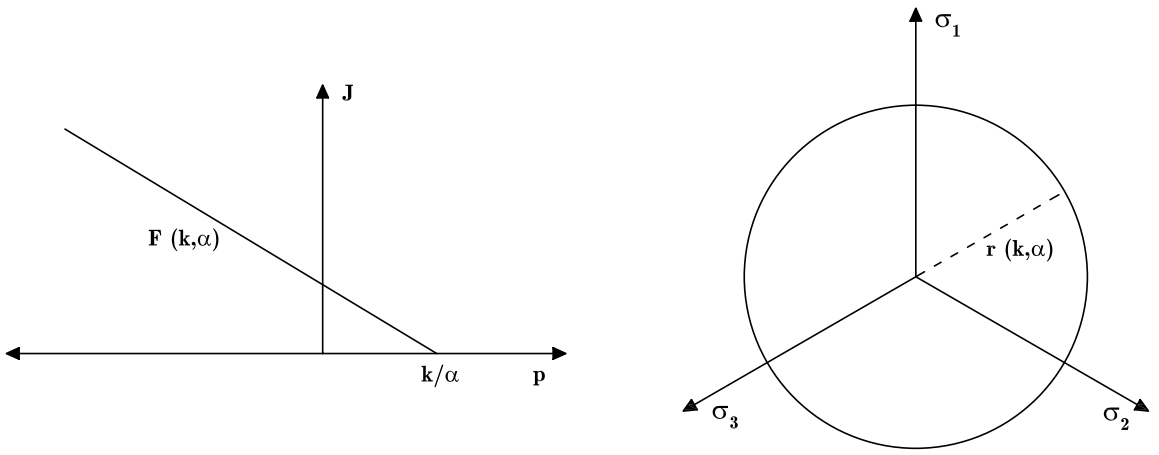



Figure 6.10: Drucker-Prager criterion in $J$-$p$ (left) and principal stress space (right)

One of the shortcomings of this material model is the independence of the failure surface on the Lode angle $\theta$, which has been proved to be the contrary for concrete. Through the parameters $\alpha$ and $k$ it is possible to adjust the failure surface to the Mohr-Coulomb hexagon resulting in either an inscribing, circumscribing or best fit circle (see Potts & Zdravković

(1999)).

### 6.5.4 Chen & Chen criterion

For the modelling of concrete, Chen & Chen (1975) proposed a constitutive model that describes concrete as an elasto-plastic, isotropic material. Three material parameters are used to define either the failure or the yield surface both in compression and tension in the principal stress space. Furthermore, it is a plasticity model based on flow theory and includes isotropic hardening of concrete for multiaxial loading conditions. Assuming that the failure of concrete depends on the deviatoric stresses and the hydrostatic pressure, the following surfaces can be established by using the structural stress invariants $I_1$ and $J_2$, which were earlier introduced in Chapter 1 (see Fig. 6.11).

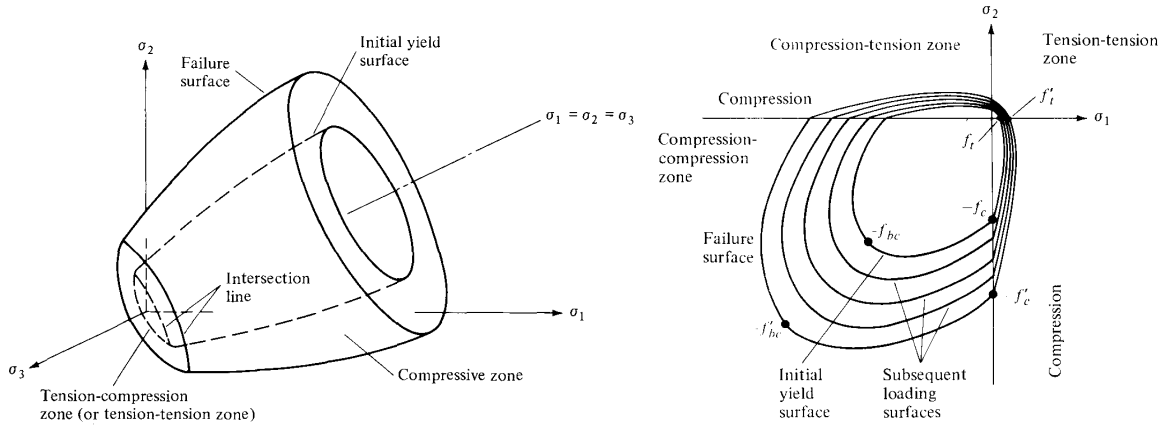



Figure 6.11: Yield and failure surfaces of Chen & Chen criterion in the principal (left) and biaxial stress space (right) (from Chen, 1982)

*i) Failure surfaces*

On the basis of experimental test data the failure surface for the compression-compression region representing the peak stress state can be written as:

$$F_{uc} = J_2 + \frac{1}{3} A_{uc} I_1 - \tau_{uc}^2 = 0 \tag{6.58}$$

In the tension-tension or tension-compression zone the failure surface is given as:

$$F_{ut} = J_2 - \frac{1}{6} {I_1}^2 + \frac{1}{3} A_{ut} I_1 - \tau_{ut}^2 = 0 \tag{6.59}$$

*ii) Yield surfaces*

For the description of the onset of plastic deformation two first yield surfaces are introduced. They enclose the elastic area and have a similar form as the failure surfaces. In the

compression-compression region the yield surface becomes:

$$F_{oc} = J_2 + \frac{1}{3} A_{oc} I_1 - \tau_{oc}^2 = 0 \tag{6.60}$$

The equation of the yield surface for the tension-tension and tension-compression zone has the following form:

$$F_{ot} = J_2 - \frac{1}{6} {I_1}^2 + \frac{1}{3} A_{ot} I_1 - \tau_{ot}^2 = 0 \tag{6.61}$$

In the above equations the variables $A_{uc}$ and $A_{ut}$ are material constants describing the ultimate stress state at peak stress and can be determined as functions of the uniaxial compressive strength $f_{cp}$, the uniaxial tensile strength $f_{tp}$ and the biaxial compressive strength $f_{bc}$ (i.e. when $\sigma_1 = \sigma_2 > \sigma_3$). In a similar way, the parameters $A_{oc}$ and $A_{ot}$ represent a yield stress state and are obtained from the uniaxial compressive yield stress $f_{cy}$, the uniaxial tensile yield stress $f_{ty}$ and the biaxial compressive yield stress $f_{bcy}$. For a stress state on the yield surface the parameter $\tau$ takes the yield value of $\tau_{oc}$ for the compression-compression region and $\tau_{ot}$ for the tension-tension and tension-compression region. In the same way, the ultimate values of $\tau$ at peak stress are $\tau_{uc}$ and $\tau_{ut}$.

The involved material parameters for the compression-compression surfaces can be summarised as:

$$\alpha_c = \frac{A_{uc} - A_{oc}}{\tau_{uc}^2 - \tau_{oc}^2} \qquad \beta_c = \frac{A_{oc} \cdot \tau_{uc}^2 - A_{uc} \cdot \tau_{oc}^2}{\tau_{uc}^2 - \tau_{oc}^2} \tag{6.62}$$

$$A_{uc} = \frac{f_{bc}^{*\,2} - 1}{2 f_{bc}^* - 1} \cdot f_{cp} \qquad A_{oc} = \frac{f_{bc}''^2 - f_c''^2}{2 f_{bc}'' - f_c''} \cdot f_{cp} \tag{6.63}$$

$$\tau_{uc}^2 = \frac{2 f_{bc}^* - f_{bc}^{*\,2}}{3\left(2 f_{bc}^* - 1\right)} \cdot f_{cp}^2 \qquad \tau_{oc}^2 = \frac{f_c'' f_{bc}'' \left(2 f_c'' - f_{bc}''\right)}{3\left(2 f_{bc}'' - f_c''\right)} \cdot f_{cp}^2 \tag{6.64}$$

$$f_c'' = \frac{f_{cy}}{f_{cp}} \qquad f_{bc}'' = \frac{f_{bcy}}{f_{cp}} \qquad f_{bc}^* = \frac{f_{bc}}{f_{cp}} \tag{6.65}$$

The material parameters for the tension-tension and tension-compression region may be calculated from:

$$\alpha_t = \frac{A_{ut} - A_{ot}}{\tau_{ut}^2 - \tau_{ot}^2} \qquad \beta_t = \frac{A_{ot} \cdot \tau_{ut}^2 - A_{ut} \cdot \tau_{ot}^2}{\tau_{ut}^2 - \tau_{ot}^2} \tag{6.66}$$

$$A_{ut} = \frac{1 - f_t^*}{2} \cdot f_{cp} \qquad A_{ot} = \frac{f_c'' - f_t''}{2} \cdot f_{cp} \tag{6.67}$$

$$\tau_{ut}^2 = \frac{f_t^*}{6} \cdot f_{cp}^2 \qquad \tau_{ot}^2 = \frac{f_c'' f_t''}{6} \cdot f_{cp}^2 \tag{6.68}$$

$$f_t^* = \frac{f_{tp}}{f_{cp}} \qquad f_t'' = \frac{f_{ty}}{f_{cp}} \tag{6.69}$$

These parameters give fixed values for the initial yield surfaces at the onset of plastic deformations and for the surfaces at peak stress. However, for the general description of the yield surfaces (termed "loading functions" later in this section), the parameters $\alpha_c$, $\alpha_t$, $\beta_c$ and $\beta_t$ will be needed in equations 6.75 and 6.76.

*iii) Zoning of the stress state*

As the failure and yield surfaces are different for the purely compression region and the other 3 tension regions, it is important to determine the correct stress zones in an analysis. In the biaxial stress plane this zoning is quite obvious as can be seen easily in Fig. 6.11. But for the generalization to the triaxial stress space some linear functions have to be introduced for seperating the stress states, which pass through the uniaxial compression and the uniaxial tensile state. The following conditions have to be satisfied:

Compression-compression region:

$$I_1 < 0 \qquad \text{and} \qquad \sqrt{J_2} + \frac{I_1}{\sqrt{3}} < 0 \tag{6.70}$$

Compression-tension region:

$$I_1 < 0 \qquad \text{and} \qquad \sqrt{J_2} + \frac{I_1}{\sqrt{3}} > 0 \tag{6.71}$$

Tension-compression region:

$$I_1 > 0 \qquad \text{and} \qquad \sqrt{J_2} - \frac{I_1}{\sqrt{3}} > 0 \tag{6.72}$$

Tension-tension region:

$$I_1 > 0 \qquad \text{and} \qquad \sqrt{J_2} - \frac{I_1}{\sqrt{3}} < 0 \tag{6.73}$$

Fig. 6.12 illustrates the four different stress zones in the $I_1$-$\sqrt{J_2}$ space together with the yield, failure and subsequent loading functions.

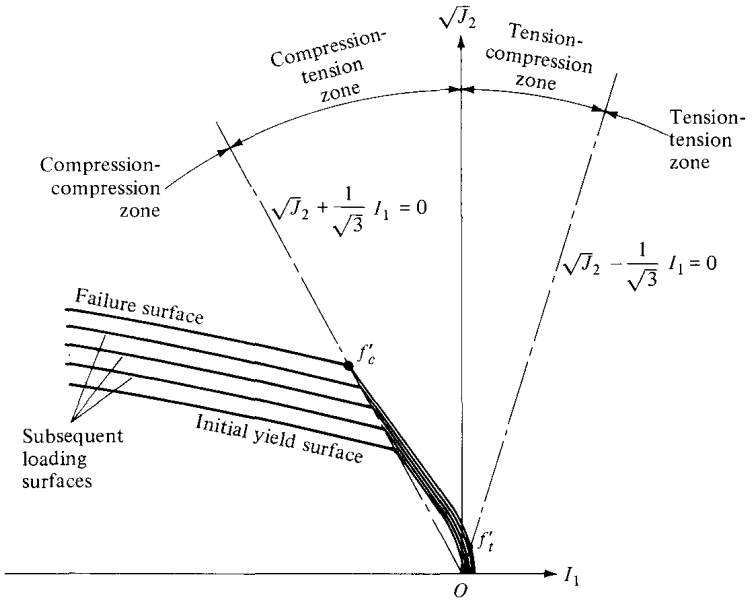



Figure 6.12: Zoning of the stress state (from Chen, 1982) ($f'_c = f_{cp}$, $f'_t = f_{tp}$)

*iv) Loading functions*

Concrete is assumed to be a strain hardening material and therefore the variable $\tau$ is used as a hardening parameter governed by the plastic strains $\varepsilon^p$. For isotropic strain hardening a general loading function can be written as:

$$F(\sigma) - \tau^2(\varepsilon^p) = 0 \tag{6.74}$$

where $\tau$ is the hardening parameter, representing the so called "equivalent (effective) stress". When a stress state is on the yield surface, the function $F(\sigma)$ is such that it equals the initial yield stress $\tau_{oc}$ or $\tau_{ot}$ and $F$ reduces to the yield function $F_{oc}$ or $F_{ot}$. For further loading the yield surfaces expand and plastic deformations occur until they reach the failure surface at peak strength $F_{uc}$ or $F_{ut}$. The development of the subsequent yield surfaces is governed by the "equivalent (effective) plastic strains" $\varepsilon^p$. The equivalent stress-strain relation can be directly obtained from a uniaxial compressive test and therefore it is possible to compare a multiaxial stress state with a simple uniaxial stress state. For the compression-compression region the following loading function is derived from equations 6.58 and 6.60:

$$F(\sigma) = \frac{J_2 + \frac{\beta_c}{3} I_1}{1 - \frac{\alpha_c}{3} I_1} = \tau^2 \tag{6.75}$$

Similiarly, the loading function for the tension-tension and the tension-compression region has the following form (obtained from equations 6.59 and 6.61):

$$F(\sigma) = \frac{J_2 - \frac{1}{6}I_1^2 + \frac{\beta_t}{3}I_1}{1 - \frac{\alpha_t}{3}I_1} = \tau^2 \tag{6.76}$$

The two compressive and tensile material parameters $\alpha$ and $\beta$ can be determined from equations 6.62 and 6.66.

*v) Hardening rule*

For the description of the isotropic expansion of the loading functions a hardening rule is needed. As mentioned before, the hardening parameter $\tau$ depends on the equivalent plastic strains $\varepsilon^p$ and varies between $\tau_o < \tau < \tau_u$. The components of plastic strains which are obtained from an associated flow rule ($F(\sigma) = P(\sigma)$) are assumed to accumulate into an equivalent plastic strain as:

$$\varepsilon^p = \int d\varepsilon^p = \int \sqrt{d\varepsilon_{ij}^p d\varepsilon_{ij}^p} \tag{6.77}$$

The following uniaxial stress-strain relation in Fig. 6.13 may be adopted.

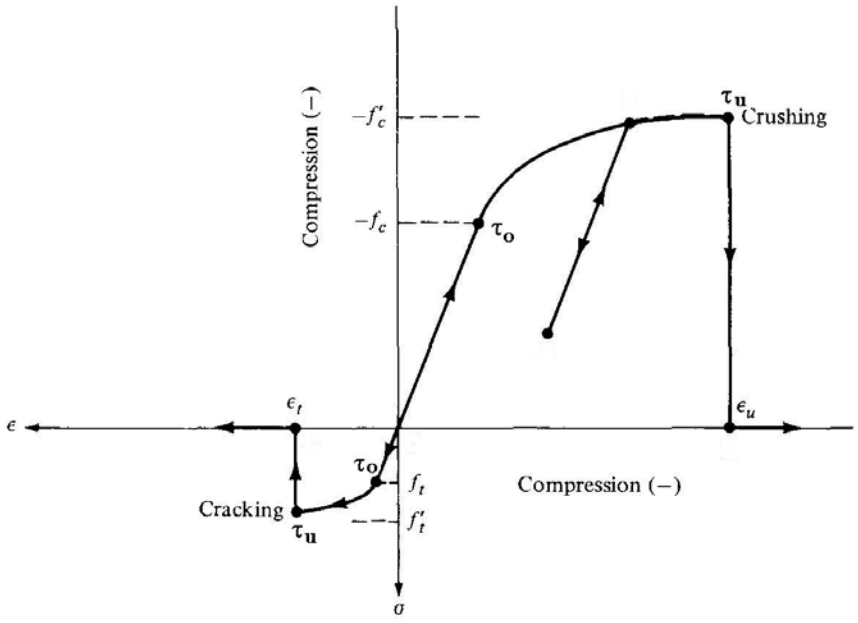



Figure 6.13: Idealised uniaxial stress-strain curve for concrete (from Chen, 1982) ($f_c = f_{cy}$, $f_c' = f_{cp}$, $f_t = f_{ty}$, $f_t' = f_{tp}$)

When a stress point touches the yield surface plastic deformations start to occur and the hardening parameter takes the value of $\tau_o$ (associated with the yield stress). For further loading, both surfaces for compression and tension expand simultaneously and plastic deformations start to develop. The relation between $\tau$ and $\varepsilon^p$ is assumed to be non-linear until it

reaches the peak point $\tau_u$ at peak strength for both compression and tension. In the post-peak regime either perfectly plastic behaviour or linear softening of concrete takes place, which would result in isotropic contraction of the surfaces. In Fig. 6.13 such a post-peak zone is neglected. At an ultimate plastic strain $\varepsilon_u^p$ the material is assumed to be completely crushed or cracked and the equivalent stress $\tau$ reduces to zero.

### 6.5.5 Further sophisticated constitutive models for concrete

An overview of other plasticity models for concrete of higher order can be found in Babu et al. (2005). Some of these models are extensions or modifications of existing constitutive models and by incorporating more model parameters it is possible to capture the main characteristics of the failure surface of concrete more realistically. Therefore, sophisticated yield surfaces have a smooth and convex shape and plot as non-circular cross-sections in the deviatoric plane. The following models can be encountered in the literature:

- Three parameter models: Bresler-Pister criterion (1958), William-Warnke criterion (1975)
- Four parameter models: Ottosen criterion (1977), Reimann criterion (1965), Hsieh-Ting-Chen criterion (1979)

For limiting the failure of concrete under purely hydrostatic pressure in compression Hofstetter et al. (1993) proposed a so called cap-model. Huber (2006) took up this idea and introduced a cap of spherical shape, coupled with a conventional Drucker-Prager criterion for the behaviour in compression. More recently constitutive models based on fracture and continuum damage have been developed, where the microstructural degradation process, i.e. the degradation of the Young's modulus upon unloading in the post-peak regime, is modelled at a phenomenological level (Meschke et al., 1998). Finally, micromechanical models attempt to develop the macroscopic stress-strain relationship from the mechanics of the microstructure (Babu et al., 2005). However, it has to be questioned if such models are from a practical point of view more suitable for the modelling of shotcrete in a boundary value problem.

## 6.6 Modelling post-peak behaviour of concrete

### 6.6.1 Post-peak behaviour in tension

As already highlighted in Chapter 5, crack formation of concrete and its propagation is a highly discrete problem and difficult to handle in a numerical analysis. According to Chen (1982) two different types of approaches for the numerical simulation of concrete fracture can be identified:

1. Discrete crack model
2. Smeared crack model

The selection of an adequate cracking model depends strongly on the purpose of the analysis to be performed. If the aim is the general overall behaviour of a concrete structure, without any particular need for realistic crack patterns and local stress concentrations, the smeared crack approach is probably the best choice. On the contrary, if the area of interest to be analysed is a very local one, a discrete crack model might be more useful to adopt. The basic principles and the associated problems of each approach are discussed briefly below.

#### 6.6.1.1 Discrete crack model

In the discrete crack approach, which started to be developed in the late 1960s, a crack is introduced as a geometric entity. This is normally achieved by disconnecting the displacement at nodal points of adjoining elements, when the nodal force ahead of the crack tip exceeds a tensile strength criterion, as can be seen in Fig. 6.14. As a consequence cracks are forced to propagate along element boundaries, introducing a certain mesh bias (De Borst et al., 2004). Complex and time-consuming techniques, such as automatic remeshing, are needed in order to overcome such problems. These limitations and difficulties involved with proper robust three-dimensional implementations result in a very limited acceptance of the use of discrete crack models (Chen, 1982).

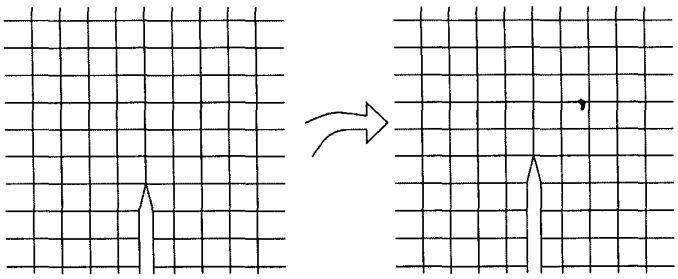


Figure 6.14: Early discrete crack modelling (from De Borst et al., 2004)

#### 6.6.1.2 Smeared crack model

In the smeared crack approach the cracked concrete is assumed to remain as a continuum (Chen, 1982). A single crack is not discrete but implies an infinite number of parallel fissures across the part of the finite element where the crack occurs. Generally, when the principal stress at a certain integration point reaches the tensile strength, a crack is initiated leading to orthotropic material behaviour and a deterioration of the current stiffness and strength at that particular integration point. Experimental results lead to the conclusion that plain concrete is not a perfectly brittle material, but that it has some residual load-carrying capacity after reaching its tensile strength (De Borst, 2002). Therefore, the material exhibits tensile strain-softening and a descending branch has to be introduced into a model to capture the gradually diminishing tensile strength of concrete upon further crack opening. If the direction of the crack remains orthogonal to the direction of the major principal stress, a rotating smeared

crack model is obtained, whereas a fixed direction of the crack at crack initiation leads to a fixed smeared crack model.

However, it is well reported in the literature that the inclusion of strain-softening material behaviour in a numerical analysis leads to certain difficulties (Cendón et al., 2000; Meschke, 1996; Pamin, 1994; Vermeer & Brinkgreve, 1994; Arsland & Sture, 2008; Zervos et al., 2007; Mosler & Meschke, 2004; De Borst et al., 2004; Möller et al., 2004; Bićanić & Pearce, 1996; De Borst, 1987). Initiation of strain localisation results in material instability, the loss of ellipticity of the governing equations and spurious mesh sensitivity may appear (Mosler & Meschke, 2004). According to Pamin (1994) these problems can be handled by either modelling cracking in a discrete way (see above) or applying an enhanced continuum approach, where three concepts have been proved to be successful so far:

1. Cosserat (micropolar) continuum
2. Non-local (integral) model
3. Higher-order gradient continuum

All these regularisation techniques have in common that they make use of an internal length parameter related to the specific material. Due to their complexity and the requirement for a sufficiently fine resolution of the localisation zone to guarantee mesh objectivity resulting in high computational effort, these approaches are of limited value for analysing a real boundary value problem in engineering practice.

An elegant way to eliminate mesh dependency of a strain-softening material in a numerical analysis was presented by Hillerborg et al. (1976). In their work a method is proposed in which fracture mechanics is incorporated into a cracking model based on an energy balance approach, often termed "fictitious crack model". Since cracking of concrete is a discrete process, a stress-crack-opening relationship is adopted to describe the post-peak behaviour in tension, as can be seen in Fig. 6.15.

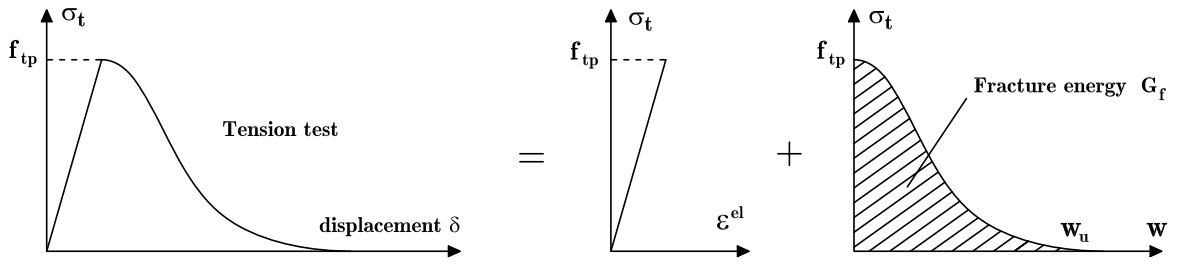



Figure 6.15: Deformation characteristics of tensile post-peak behaviour

The governing parameter for this curve is the so called fracture energy $G_f$, which represents the energy required to propagate a tensile crack of unit area until complete crack

opening. The graphical interpretation of the fracture energy is the area below the stress-crack-opening curve and it can be written as:

$$G_f = \int_{w=0}^{w_u} \sigma \, dw \tag{6.78}$$

Therefore, the fracture energy is independent of the test method or size of the sample and can be interpreted as a real material parameter. In the absence of experimental data, the CEB-FIP Model Code (1990) allows to estimate the value for $G_f$ for hardened concrete at 28 days from the following equation:

$$G_f = G_{fo} \left( \frac{f_{cm}}{f_{cmo}} \right)^{0.7} \tag{6.79}$$

where $f_{cm}$ is the mean compressive strength and $f_{cmo} = 10\,\text{MPa}$. $G_{fo}$ is the base value of fracture energy and depends on the maximum aggregate size $d_{max}$. Table 6.3 provides the following values:

| $d_{max}$ (mm) | $G_{fo}$ (Nmm/mm$^2$) |
|---|---|
| 8 | 0.025 |
| 16 | 0.030 |
| 32 | 0.058 |

Table 6.3: Base values of fracture energy $G_{fo}$ from CEB-FIP Model Code (1990)

Although very few results are available in the literature concerning the fracture energy of early age concrete and shotcrete, experiments show that the fracture energy is not constant, but of an increasing nature with time or degree of hydration (Gutsch & Rostásy, 1994). De Schutter & Taerwe (1997) proposed an equation based on the degree of hydration which is of the following form:

$$\frac{G_f(r)}{G_f(r=1)} = \left( \frac{r - r_o}{1 - r_o} \right)^d \tag{6.80}$$

where $r$ is the degree of hydration, $G_f(r=1)$ is the specific fracture energy at a degree of hydration $r = 1$ and $r_o$ and $d$ are parameters. Brameshuber & Hilsdorf (1989) derived an equation for the fracture energy from their test results with different Portland cements, where $G_f$ increases with time. Lackner & Mang (2004) use the experimental work of Brameshuber & Hilsdorf (1989) to establish a function for the linear increase in fracture energy with degree of hydration:

$$G_f = 0.488 + 77.8\,\xi \tag{6.81}$$

with $\xi$ being the degree of hydration ranging from 0 to 1 and $G_f$ the fracture energy in $10^{-3}\,\text{Nmm/mm}^2$. The data set for one particular cement together with the above expression

is shown in Fig. 6.16.

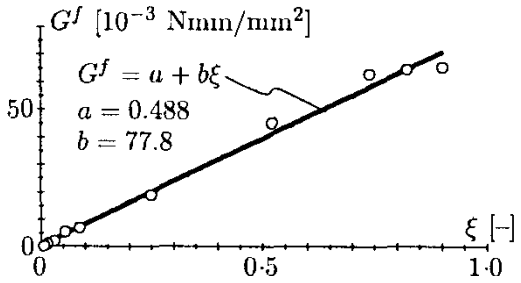



Figure 6.16: Intrinsic material function for fracture energy (from Lackner & Mang, 2004)

De Borst & van den Boogaard (1994) investigated the modelling of deformation and cracking in early age concrete by applying a smeared crack model. Although they concentrate on the issue that the fracture energy appears to be an increasing parameter with time, they neglected this and adopted a much simpler approach with a constant strain input parameter. Finally, De Schutter & Taerwe (1997) make the criticism that even at some major international conferences regarding the behaviour of early-age concrete, no or very little attention is paid to the experimental study of the evolution of the softening behaviour of concrete during hardening.

For the modelling of crack formation in a finite element analysis within the smeared crack concept, the crack-opening has to be transformed into a crack-strain via a length parameter:

$$\varepsilon = \frac{w}{l_{eq}} \tag{6.82}$$

In this equation, $l_{eq}$ is the equivalent length of a finite element (or sometimes termed characteristic length) and should correspond to a representative dimension of the mesh size. Therefore it depends in general on the chosen element type, size, shape and integration order (Feenstra, 1993; Thomée, 2005). In the literature a couple of approaches for estimating $l_{eq}$ can be found and most of them ignore the orientation of the crack within the element and simply relate the equivalent length to the area of the element. Rots (1988) suggested the following equation for a 2D element:

$$l_{eq} = \alpha \sqrt{A_e} \tag{6.83}$$

where $A_e$ is the area of the element and $\alpha$ a scalar factor, being 1.0 for quadratic elements and $\sqrt{2}$ for linear elements. Feenstra (1993) mentions that this approximation is relatively accurate if the mesh is not distorted too much and when the cracks are aligned with the element boundaries. He states further, that the choice of the equivalent length depends also on the problem to be analysed. Thomée (2005) and Haufe (2001) showed in their work that this approach is suitable for most practical applications in engineering practice. Strack (2007) applied in his research on the numerical modelling of steel fibre reinforced concrete an

equation suggested by Pölling (2000), taking into account the number of integration points per element $n_{int}$:

$$l_{eq} = \sqrt{\frac{A_e}{n_{int}}} \tag{6.84}$$

Huber (2006) used in his analyses a similar equation for volumetric elements proposed by Bićanić et al. (1994):

$$l_{eq} = \sqrt[3]{\frac{V_e}{n_{IP}}} \tag{6.85}$$

where $V_e$ is the volume of the finite element and $n_{IP}$ the number of integration points.

With the introduction of the characteristic length and the fracture energy as additional parameters, it is guaranteed that during material softening the same amount of energy is released within the element until complete crack opening and hence the results obtained are objective with regard to mesh refinement. A more sophisticated and consistent estimation and discussion of the equivalent length can be found in Oliver (1989).

For an unreinforced cracked concrete section, the CEB-FIP Model Code (1990) provides a bilinear stress-crack-opening relation as can be seen in Fig. 6.17.

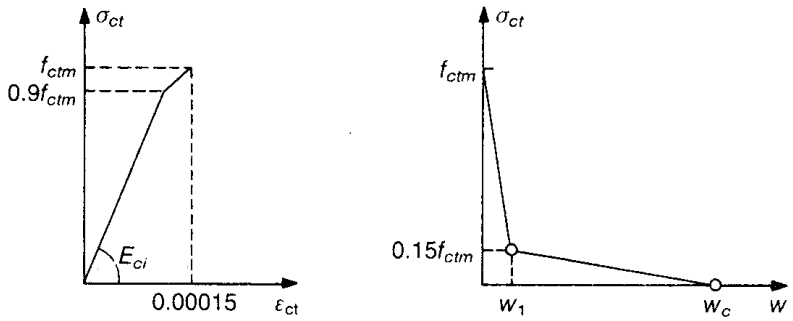



Figure 6.17: Stress-strain and stress-crack-opening diagram for uniaxial tension (from CEB-FIP Model Code, 1990)

The mathematical description is as follows:

$$\sigma_{ct} = f_{ctm}\left(1 - 0.85\,\frac{w}{w_1}\right) \qquad \text{for} \qquad 0.15 f_{ctm} \leq \sigma_{ct} \leq f_{ctm} \tag{6.86}$$

and

$$\sigma_{ct} = \frac{0.15 f_{ctm}}{w_c - w_1}\,(w_c - w) \qquad \text{for} \qquad 0 \leq \sigma_{ct} < 0.15 f_{ctm} \tag{6.87}$$

where $\sigma_{ct}$ is the uniaxial tensile stress, $w$ the crack opening (mm), $w_1$ the crack opening (mm) at a tensile stress of $0.15 f_{ctm}$ and $w_c$ the complete crack opening (mm) at zero stress. $w_c$ may be estimated from:

$$w_c = \alpha_f\,\frac{G_f}{f_{ctm}} \tag{6.88}$$

with $G_f$ being the fracture energy in Nmm/mm$^2$ and $f_{ctm}$ the mean uniaxial tensile strength in MPa. The coefficient $\alpha_f$ depends on the maximum aggregate size $d_{max}$ and is given in Tab. 6.4.

| $d_{max}$ (mm) | 8 | 16 | 32 |
|---|---|---|---|
| $\alpha_f$ (-) | 8 | 7 | 5 |

Table 6.4: Coefficient $\alpha_f$ to estimate $w_c$ (from CEB-FIP Model Code, 1990)

Haufe (2001), Meschke (1996), Feenstra (1993) and Huber (2006) describe the post-peak behaviour of concrete in tension with an exponential function where an internal damage parameter $\kappa$ controls the decay in the uniaxial tensile stress $\sigma_t$ with crack growth:

$$\sigma_t = f_{ctm}\, exp\left(\frac{\kappa}{\kappa_u}\right) \tag{6.89}$$

where the ultimate damage parameter is calculated as:

$$\kappa_u = \frac{G_f}{l_{eq} f_{ctm}} \tag{6.90}$$

König & Duda (1991) compared different stress-crack-opening relations suggested by various researchers in the literature, as can be seen in Fig. 6.18, and they concluded that apart from the linear softening, which is often chosen because of simplicity, all the curves have in common that the initial branch is very steep, transforming into a flat part on approaching or reaching zero. Furthermore, the most practical applications seem to be insensitive to the exact shape of the softening curve adopted.

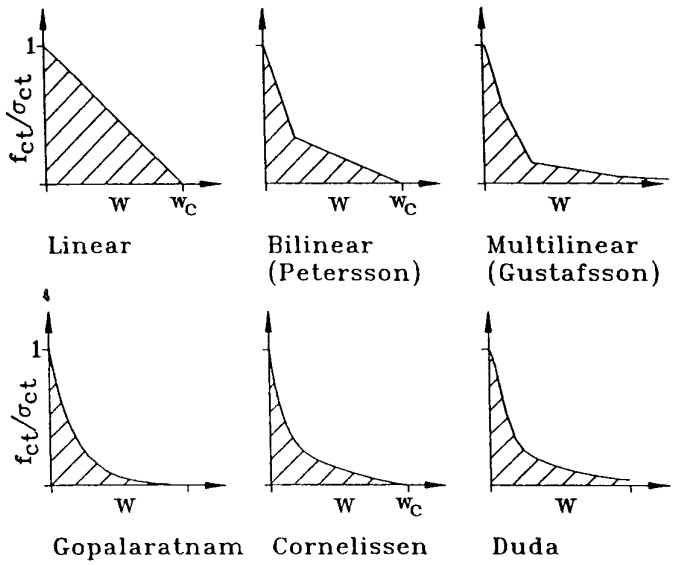



Figure 6.18: Some proposed stress-crack-opening relations (from Moussa, 1993)

#### 6.6.1.3 Effect of reinforcement

Huber (2006) distinguishes three different types of modelling of steel reinforcement for analyzing reinforced concrete structures (see Fig. 6.19), which are:

1. Discrete modelling
2. Smeared modelling
3. Embedded modelling

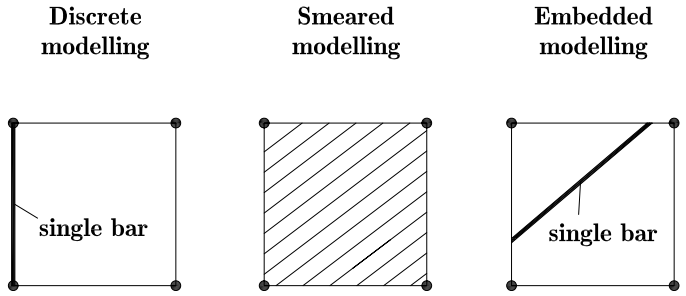



Figure 6.19: Models for reinforcement

In the discrete modelling concept, reinforcement is simulated as individual elements, usually aligned along the boundaries of the concrete elements. Therefore, a proper constitutive model for steel has to be involved describing the uniaxial behaviour of the reinforcement bars. However, one drawback of this approach is that a high level of mesh refinement is required in the area near the reinforcement bars, which results in high computational effort. Furthermore, complex interface elements have to be used in order to capture the real bond-slip behaviour between concrete and steel (Huber, 2006). Examples for this type of modelling reinforcement are given in Eierle & Schikora (1999).

Probably the most frequent method for analysing reinforced concrete structures is to smear or evenly distribute the reinforcement over the concrete element (Feenstra, 1993). This is achieved by modifying the constitutive equations taking into account the additional internal forces and stiffness due to the reinforcement bars, leading to a certain anisotropic behaviour of the concrete element. This methodology was used by Haufe (2001) for performing some numerical studies on reinforced plates, shells and folded plates.

Finally, the embedded formulation of reinforced concrete considers steel bars as discrete elements but with the difference that the elements are of the same type as the concrete elements (number of nodes, degrees of freedom, shape functions). Therefore, a uniaxial steel bar is transformed into a two- or three-dimensional element and then embedded into the concrete element. A big advantage of this method is that any orientation of the reinforcement bar within the element can be chosen and results of the overall structure are independent of

the alignement of reinforcement. For further information about the embedded reinforcement concept seek Huber (2006).

Due to the complexity of the three approaches presented above regarding discretization and real bond-slip behaviour, reinforcement is rarely considered in a finite element analysis of tunnel construction (Thomas, 2003).

However, in the case of a smeared crack model it is possible to take into account the effect of reinforcement by modifying the post-peak behaviour of concrete in tension and the so called "tension-stiffening effect" is introduced. This term is used to describe the interaction between steel reinforcement and concrete after crack formation (Moussa, 1993). The existence of reinforcement improves the softening response of concrete by contributing to the overall stiffness of the system. This is achieved by a gradual redistribution of internal forces from concrete to reinforcement during crack propagation due to their bond behaviour until a stabilised crack pattern has developed. The average stresses in the concrete would not decrease with further crack opening as quickly as in the case of plain concrete but would gradually reduce to zero, as indicated in Fig. 6.20.

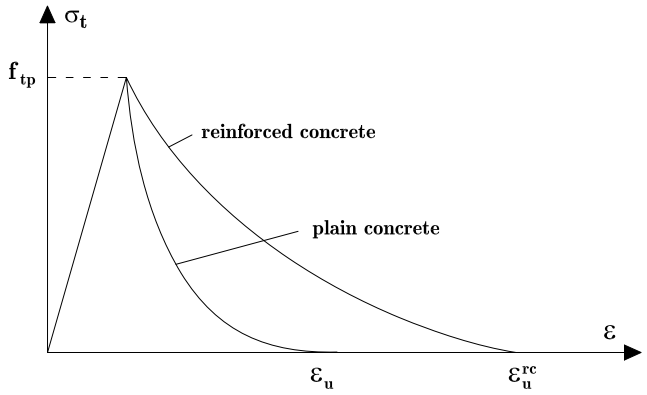



Figure 6.20: Principal effect of tension-stiffening on post-peak behaviour of concrete

In the literature many attempts can be found to model the tension-stiffening effect for reinforced concrete, among them Nayal & Rasheed (2006), Ebead & Marzouk (2005), Bischoff & Paixao (2004) and Fields & Bischoff (2004). Fig. 6.21 shows a collection of some stress-strain diagrams for concrete in tension by Gilbert & Warner (1978), including the tension-stiffening effect.

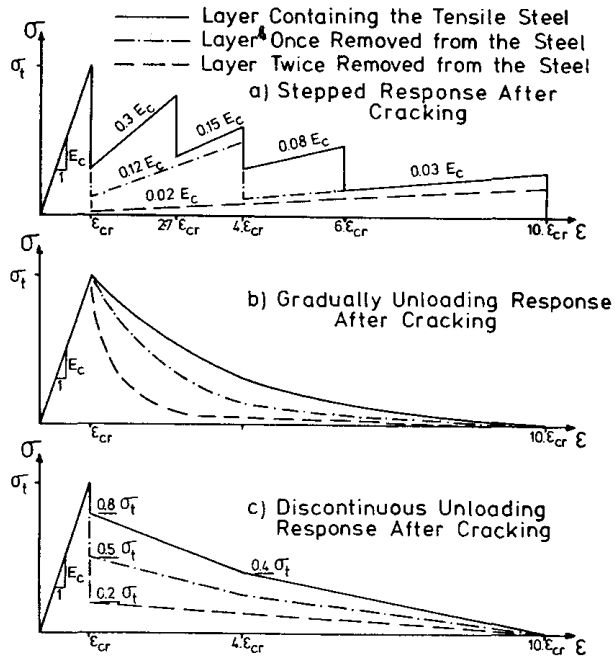



Figure 6.21: Stress-strain diagram for reinforced concrete in tension (from Gilbert & Warner, 1978)

Feenstra (1993) critisises the fact that in most of the different formulations for tension-stiffening that can be encountered in the literature no reference is made to the fracture energy, which is actually released in the material. For a numerical analysis he suggested to estimate the fracture energy for reinforced concrete $G_f^{rc}$ in the following way:

$$G_f^{rc} = G_f \left(1 + \frac{l_{eq}}{l_s}\right) \tag{6.91}$$

where $G_f$ is the fracture energy of a single crack and $l_{eq}$ the equivalent length of the finite element. $l_s$ is the average crack spacing which is in general a function of the bar diameter, the concrete cover and the reinforcement ratio and can be calculated according to the CEB-FIP Model Code (1990). Haufe (2001) states that in a finite element analysis of reinforced concrete it is possible that several cracks occur within one element and therefore he proposed to establish the length parameter used for regularisation as:

$$l_{eq}^{rc} = min\,(l_s,\, l_{eq}) \tag{6.92}$$

In a similar way Bockhold (2005) evaluates the fracture energy for reinforced concrete through:

$$G_f^{rc} = max\left(G_f,\, \frac{l_{eq}}{l_s}\, G_f\right) \tag{6.93}$$

Lackner & Mang (2003) investigated the cracking of reinforced shotcrete tunnel shells by adopting a smeared cracking concept. They take into account the tension-stiffening effect by

multiplying the fracture energy by a factor $\gamma > 1$:

$$G_f^{rc} = \gamma\, G_f \tag{6.94}$$

This factor $\gamma$ is computed by means of a 1D composite model presented in Lackner & Mang (2000) consisting of one steel bar embedded in shotcrete including a non-linear bond slip-bond stress relation extended for ageing materials. From their calculations they derived a linear function for $\gamma$ (see Fig. 6.22), depending on the cement hydration degree $\xi$ which can be expressed as:

$$\gamma\,(\xi) = 22.8 - 15.0\,\xi \tag{6.95}$$

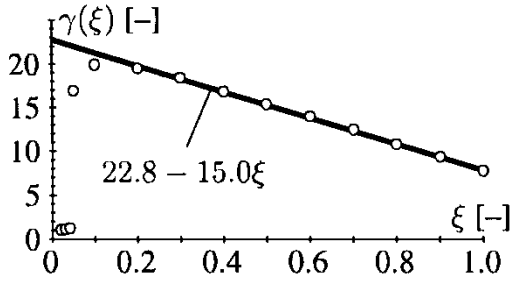



Figure 6.22: Material function for $\gamma$ depending on degree of hydration $\xi$ (from Lackner & Mang, 2003)

However, it is to be questioned if such approaches are suitable for the description of reinforced shotcrete, since the assessment of crack spacing, bond-slip behaviour and other mechanical aspects for shotcrete at early ages are still not clear from a scientific point of view.

#### 6.6.1.4 Modelling steel fibre reinforced concrete (SFRC)

As already mentioned in Chapter 5, the inclusion of steel fibres in concrete or shotcrete results in a more ductile material behaviour after peak for both compression and tension. Thomée (2005) gives an overview about different qualitative stress-crack-opening relations for tension from various researchers (Hillerborg, 1985; Kooiman, 2000; Matsuo et al., 1995; Kützing, 2000), which can be seen in Fig. 6.23.

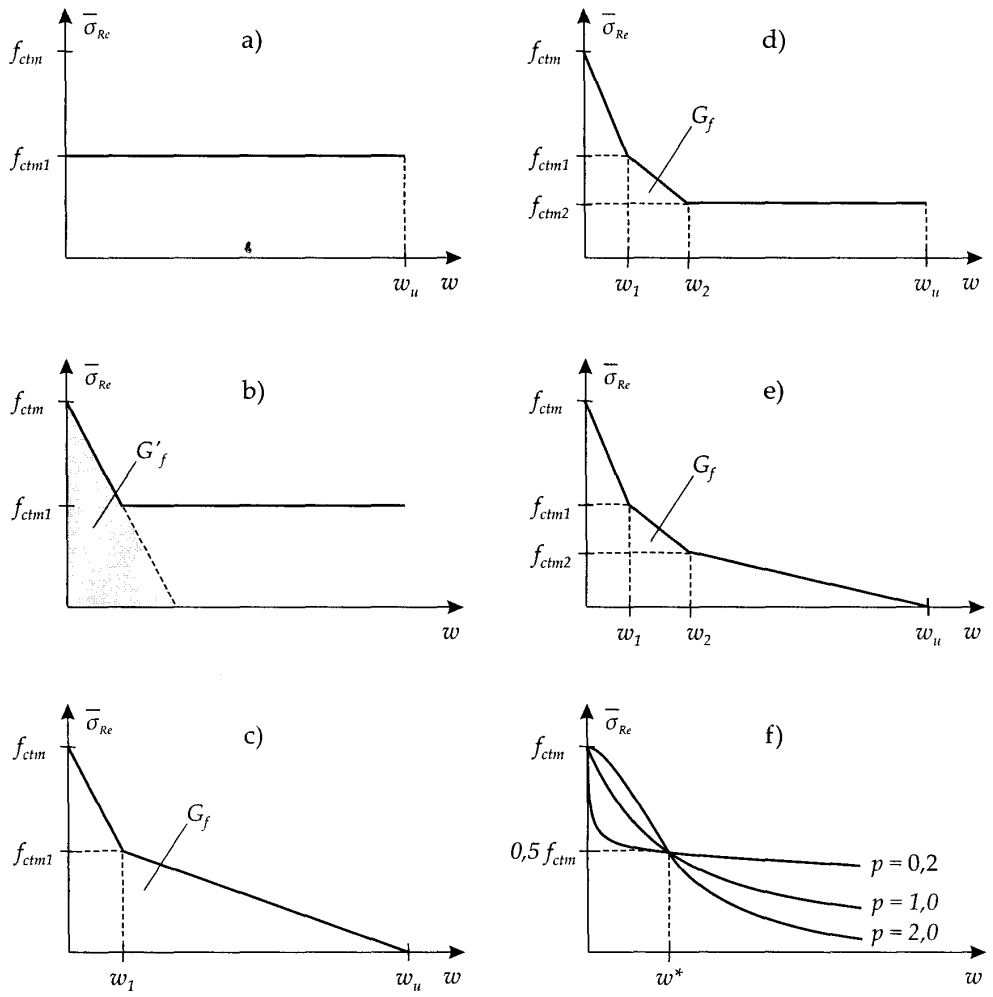



Figure 6.23: Different stress-crack-opening relations for steel fibre reinforced concrete (from Thomée, 2005)

From these curves it can be observed that for the uniaxial behaviour, the softening branch can be separated basically into two parts. Directly after reaching the maximum tensile stress there is a steep drop in stresses, since the mechanical contribution of the steel fibres is still low and the governing parameter is the fracture energy of plain concrete. In the second part the stresses appear to stabilise with an almost constant or a slightly decreasing value. Stang & Aarre (1992) describe the post peak behaviour with the following expression (curve f) in Fig. 6.23):

$$\sigma_t = \frac{f_{ctm}}{1 + \left(\frac{w}{w^*}\right)^p} \tag{6.96}$$

Through an empirical variation of the involved parameters $p$ and $w^*$ the curve can be fitted to the post-peak behaviour of concrete with various steel fibre contents. Kazemi et al. (2007) concluded that in principle the stress-crack-opening curve depends heavily on the type and the amount of fibres adopted. Thomée (2005) developed in his research a stress-crack-opening relation consisting of an exponential and a linear softening branch that can be seen in Fig. 6.24.

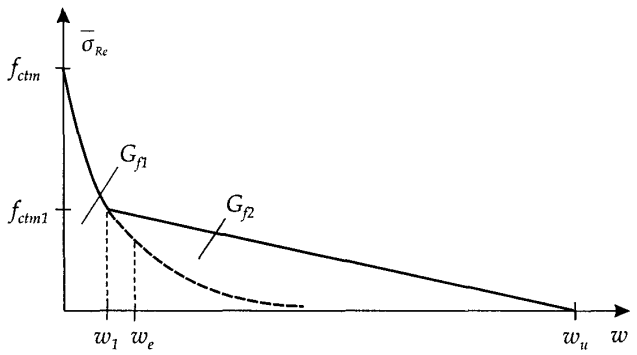



Figure 6.24: Uniaxial tensile stress-crack-opening relation (from Thomée, 2005)

In order to use this model in a finite element analysis he converted the crack opening $w$ into a strain $\varepsilon$ via the equivalent length $l_{eq}$ (see previous sections). At crack opening the exponential softening curve for plain concrete proposed by Feenstra (1993) controls the decay in tensile stress and is given as:

$$\sigma_t = f_{ctm}\, exp\left(-\frac{\varepsilon}{\varepsilon_e}\right) \qquad \text{for} \qquad \varepsilon < \varepsilon_1 \tag{6.97}$$

with

$$\varepsilon_e = \frac{G_{f1}}{f_{ctm}\, l_{eq}} \qquad \text{and} \qquad \varepsilon_1 = -ln\left(\frac{f_{ctm1}}{f_{ctm}}\right)\varepsilon_e \tag{6.98}$$

where $f_{ctm}$ is the tensile strength, $f_{ctm1}$ a residual tensile strength and $G_{f1}$ the fracture energy of plain concrete. The linear softening branch representing the impact of steel fibres can be expressed as:

$$\sigma_t = f_{ctm1} - \left(f_{ctm1}\,\frac{\varepsilon - \varepsilon_1}{\varepsilon_u - \varepsilon_1}\right) \qquad \text{for} \qquad \varepsilon_1 < \varepsilon < \varepsilon_u \tag{6.99}$$

where

$$\varepsilon_u = \varepsilon_1 + \frac{2\left(G_{f2} + G'_{f1}\right)}{f_{ctm1}\, l_{eq}} \qquad \text{and} \qquad G'_{f1} = G_{f1}\, exp\left(-\frac{\varepsilon_1 f_{ctm} l_{eq}}{G_{f1}}\right) \tag{6.100}$$

$G_{f2}$ is the part of the total fracture energy that can be related to the contribution of the steel fibres and may be estimated from experimental tests. In his numerical examples Thomée (2005) used values for $G_{f2}$ ranging from $2.10^{-3}$ to $9.10^{-3}\,\mathrm{MNm/m^2}$. Barros & Figuieiras (1999) provide some empirical equations that allow the calculation of the increased total fracture energy from the amount of fibres used in the concrete mix. Their equations are of the type:

$$\frac{G_f^{fr}}{G_{fo}} = a + b\, W_f \tag{6.101}$$

where $G_f^{fr}$ is the total fracture energy including fibres, $G_{fo}$ the fracture energy of plain

concrete, $W_f$ the fibre content in per cent of concrete weight and $a$ and $b$ two constants depending on the type of fibre. Fig. 6.25 shows some test results for the total fracture energy increasing with volumetric content of steel fibres. For further information about modelling the effect of steel fibres on the behaviour of concrete and shotcrete see Strack (2007).

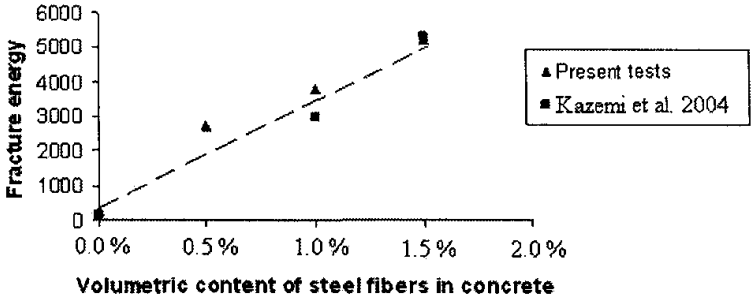



Figure 6.25: Increase in fracture energy with fibre content (from Kazemi et al., 2007)

### 6.6.2 Post-peak behaviour in compression

For a consistent formulation of the complete post-peak behaviour, the softening behaviour of concrete in compression can be treated in a similar context as the tensile regime. According to Feenstra (1993) a compressive fracture energy $G_c$ as a real material parameter describes the softening behaviour of concrete in compression. Such an assumption can be considered reasonable since the underlying failure mechanisms for compression and tension in the post-peak regime are identical, i.e. continuous crack growth at micro level. According to experiments performed by Vonk (1992), the compressive fracture energy $G_c$ ranges from 10 to 25 $\mathrm{Nmm/mm^2}$ and is therefore roughly 50-100 times the tensile fracture energy $G_f$. With the help of the equivalent length $l_{eq}$ regularisation of the softening behaviour is achieved and the post peak behaviour can be described as mesh independent.

## 6.7 Modelling of creep

Since it was observed from experimental data that the progress of creep follows a definite pattern, many attempts have been made to express creep in a mathematical way. It is well known that initially, after the application of loading, a considerable amount of creep takes place, resulting in a steep deformation curve at the beginning, followed by a flattening curve controlled by reducing creep rates. However, Neville (1970) states that it is not clear whether there is a finite limit to creep after infinite time or not. Therefore, two broad types of creep laws exist: those which tend to a limiting value and those which increase indefinitely. In the following sections a selection of different creep models available in the literature is presented, with a particular focus on the attempts to model the complex creep behaviour of shotcrete.

### 6.7.1 Basic expressions for creep

According to Neville (1970) the existing basic creep expressions date back to the 1930s and can be divided into the following groups:

- Power expressions (Shank, 1935)
- Exponential expressions (Thomas, 1933)
- Hyperbolic expressions (Ross, 1937)
- Logarithmic expressions (U.S. Bureau of Reclamation, 1955)

All the parameters involved in such creep models are of empirical or quasi-rational nature and therefore their application for general cases has to be treated with caution. This fact makes the application of a basic creep model for shotcrete relatively difficult, since the creep behaviour of sprayed concrete appears to be highly non-linear, depending on age of loading, stress level, temperature and other aspects related to material technology. One of the simplest expressions for predicting uniaxial concrete creep was suggested by Straub (1930) and is of the form:

$$\varepsilon_{cr} = Q\,\sigma^A\,t^B \tag{6.102}$$

where $t$ is the time, $\varepsilon_{cr}$ are the creep strains, $\sigma$ is the applied stress and $A$, $B$ and $Q$ are parameters depending on the properties of concrete, the time of application of the load and the units used in the analysis. Alkhiami (1995) and Probst (1999) suggested some values for these parameters based on experimental results. Kuttner (1989) introduced this model in a slightly modified form for the simulation of creep in shotcrete. It can be written as:

$$\varepsilon_{cr} = \frac{A}{m+1}\,\sigma^n\,t^{m+1} \tag{6.103}$$

where $A$ is the temperature-dependent material parameter and $m$ and $n$ are material constants. As this expression is one of the standard creep models in the finite element code ABAQUS, a couple of researchers adopted this model in their work for the analysis of shotcrete as tunnel support, among them Kienberger (1999), Galler (1997) and Golser (1999).

### 6.7.2 Rheological units

The use of rheological models for describing the viscoelastic behaviour of concrete and shotcrete is quite common in engineering practice due to their simplicity. Mostly an arrangement of several rheological units (Hook spring, Newton dashpot and St. Venant plastic element) serves for the prediction of uniaxial creep behaviour of concrete by fitting rheological properties to the observed behaviour from experimental tests. Therefore, the fitted constants represent the material behaviour of a particular concrete or shotcrete under given conditions and are not generally applicable. This fact is a severe drawback since it is the actual data that predict the model and not vice versa. Furthermore, a detailed understanding

of the fundamental creep behaviour is lost as these models imply nothing about the molecular mechanisms responsible for creep. However, they can be useful for visualizing the basic creep effects and especially the superposition of deformations. A detailed overview of different rheological models can be found in Neville (1970) and Flügge (1967) and the basic ones are presented in the following sections.

#### 6.7.2.1 Kelvin model

Fig. 6.26 shows the Kelvin model, where a spring and a dashpot are in parallel so that they undergo the same displacement. The spring is characterised with a spring stiffness $E_k$, while the dashpot is described by the viscosity coefficient $\eta_k$.

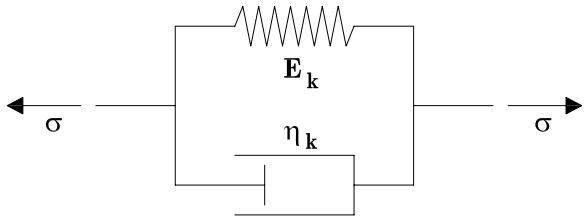



Figure 6.26: Kelvin body

The total applied stress is the sum of the forces on the individual elements and it can be written as:

$$\begin{aligned} \sigma &= \sigma_{spring} + \sigma_{dashpot} \\ \varepsilon &= \varepsilon_{spring} = \varepsilon_{dashpot} \end{aligned} \tag{6.104}$$

with

$$\begin{aligned} \sigma_{spring} &= E_k\,\varepsilon \\ \sigma_{dashpot} &= \eta_k\,\dot{\varepsilon} \end{aligned} \tag{6.105}$$

Substitution leads to a differential equation:

$$\sigma(t) = E_k\,\varepsilon + \eta_k\,\dot{\varepsilon} \tag{6.106}$$

with the solution taking the form:

$$\varepsilon = \frac{\sigma}{E_k}\left(1 - \exp^{-\frac{t}{\tau_k}}\right) \tag{6.107}$$

where $\tau_k = \eta_k/E_k$ is the "retardation time", representing the time required for the deformation to attain a value equal to $1/\exp$ of its ultimate magnitude. Fig. 6.27 shows the deformation under a sustained load and after its removal, approaching full recovery asymptotically. Therefore, the Kelvin model is suitable for predicting the phenomenon of delayed elasticity.

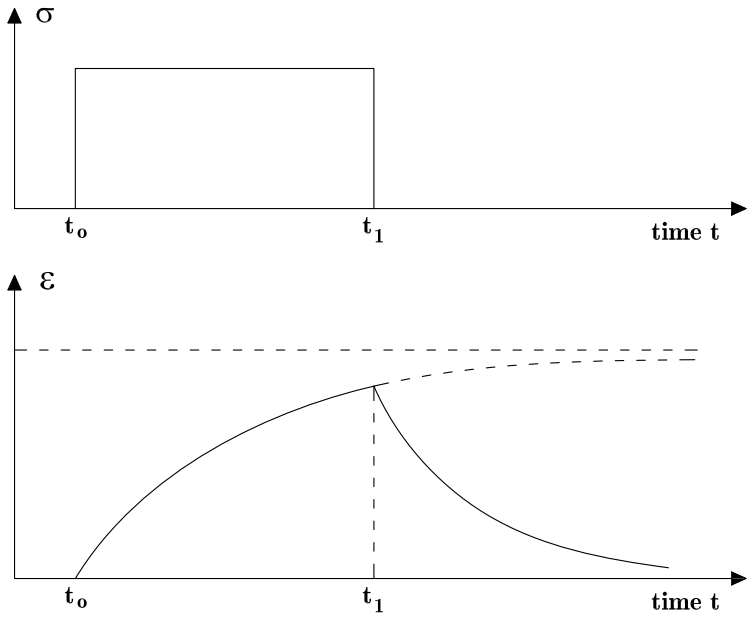



Figure 6.27: Deformation response of Kelvin model

#### 6.7.2.2 Maxwell model

The Maxwell model consists of a spring and a dashpot in series (see Fig. 6.28), where the load carried by both elements is the same:

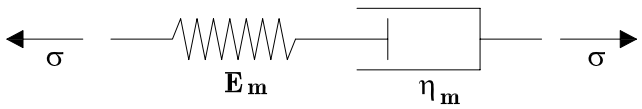



Figure 6.28: Maxwell body

The mathematical formulation is given as:

$$\begin{aligned} \sigma &= \sigma_{spring} = \sigma_{dashpot} \\ \varepsilon &= \varepsilon_{spring} + \varepsilon_{dashpot} \end{aligned} \tag{6.108}$$

Making use of equation 6.105 results in a differential equation which can be expressed as:

$$\dot{\varepsilon} = \frac{\dot{\sigma}}{E_m} + \frac{\sigma}{\eta_m} \tag{6.109}$$

Hence, the increase in deformation is given as:

$$\varepsilon = \frac{\sigma}{E_m} + \frac{\sigma}{\eta_m}\, t \tag{6.110}$$

Under a sustained load the development of the deformation is unlimited and consequently the model represents a liquid. Furthermore, with a constant viscosity parameter $\eta_m$ the deforma-

tion curve is a straight line, whereas a non-linear expression for $\eta_m$ leads to a curved shape (Vaishnav & Kesler, 1961). After removal of the load, a permanent or plastic deformation remains, as can be seen in Fig. 6.29.

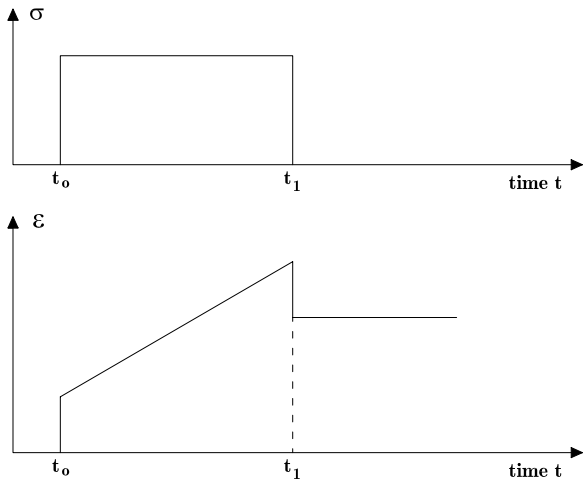



Figure 6.29: Deformation response of Maxwell model

If the Maxwell model is subjected to a constant deformation it exhibits the property of relaxation and the reduction in stress can be written as:

$$\sigma = \sigma_o \exp^{-\frac{t}{\tau_m}} \tag{6.111}$$

where $\sigma_o$ is the initial stress and $\tau_m = \eta_m / E_m$ the so called "relaxation time" representing the time in which the stress relaxes to $1/\exp$ of its original value.

#### 6.7.2.3 Burger model

A more complex rheological body is the Burger model, which is a series combination of a Kelvin model and a Maxwell model, as shown in Fig. 6.30.

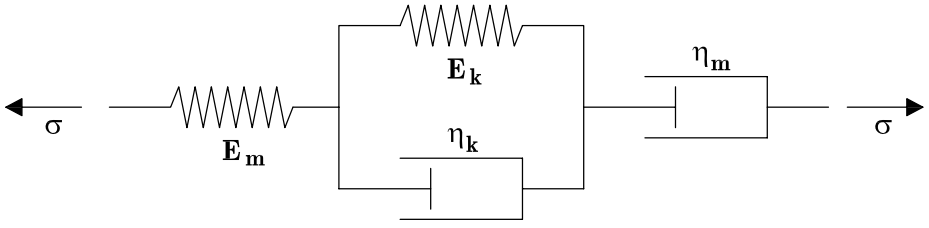



Figure 6.30: Burger body

Consequently, the deformation response of a Burger model is the sum of its Kelvin and Maxwell components and it can be written as:

$$\varepsilon = \frac{\sigma}{E_m} + \frac{\sigma}{\eta_m}\, t + \frac{\sigma}{E_k} \left(1 - \exp^{-\frac{E_k}{\eta_k}\, t}\right) \tag{6.112}$$

where the subscripts $k$ and $m$ refer to the Kelvin and Maxwell components respectively. Fig. 6.31 indicates schematically the deformation response of a Burger model. Directly after the load is applied an instantaneous elastic deformation takes place followed by a time-dependent increase in deformation at a decreasing rate, tending asymptotically to a straight inclined line. On removal of the load, firstly the elastic recovery takes place followed by a time-dependent recovery approaching a horizontal line. Hence, part of the time-dependent deformation is irreversible and it is believed that the Burger model represents qualitatively the creep behaviour of concrete reasonably well.

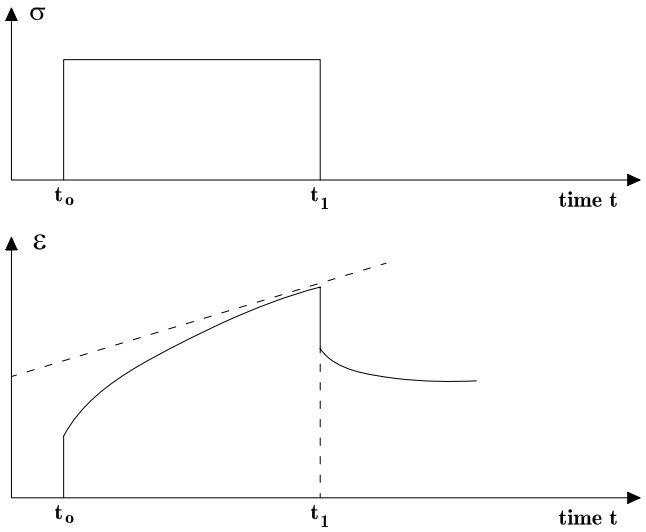



Figure 6.31: Deformation response of Burger model

#### 6.7.2.4 Rheological models used for modelling shotcrete behaviour

In the literature a couple of models based on the combination of various rheological bodies can be found for simulating creep deformation of young shotcrete. Most of them have in common that they include sophisticated functions for their rheological parameters depending on shotcrete age and stress level, in order to capture in a better way the complex behaviour observed in experimental tests. The basic principles of these models are presented here with the aim of highlighting the problems involved in their development.

On the basis of eight conventional short term creep tests, with loading ages varying between 4 h to 168 h, Kuwajima (1999) proposed a linear Kelvin model for describing the viscoelastic deformation of young shotcrete. It is of the form:

$$\frac{\varepsilon_c(t)}{\sigma_o} = \frac{1}{E_t}\left(1 - \exp^{-\frac{E_t}{\eta}t}\right) \tag{6.113}$$

with $1/E_t$ being the final specific creep and $E_t/\eta$ indicates how fast the creep deformation would develop. It was concluded that, although creep presents a strong age dependency for the early ages, after an age of 10 hours a time-independent creep model can be applied. The

suggested values of the creep parameters are the following:

$$\frac{1}{E_t} = 0.03\,\mathrm{GPa}^{-1} \qquad \text{and} \qquad \frac{E_t}{\eta} = 0.003\,\mathrm{min}^{-1} \tag{6.114}$$

Rokahr & Lux (1987) take into account that the creep rate of young shotcrete is decreasing with time and depends highly on the applied stress level (see Fig. 6.32).

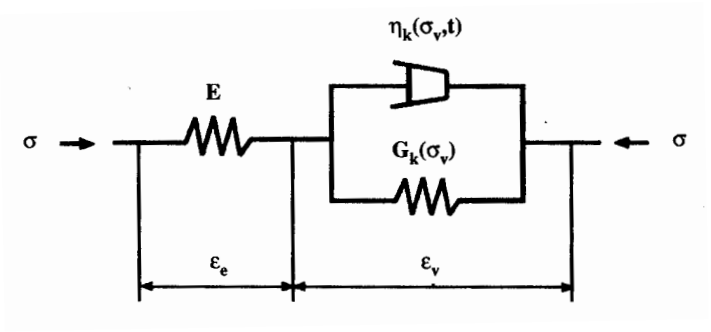



Figure 6.32: Non-linear Kelvin model after Rokahr & Lux (1987) (from Hesser, 2000)

Their proposed creep law is a modified Kelvin model based on strain-hardening theory and the viscous strain rate can be written as:

$$\{\dot{\varepsilon}_v\} = \left[\frac{1}{2\eta_k\left(\sigma_v, t\right)}\left(1 - 3\,\frac{\varepsilon_v}{\sigma_v}\,G_k\left(\sigma_v\right)\right)\right]\,[M_2]\,\{\sigma\} \tag{6.115}$$

where $\{\dot{\varepsilon}_v\}$ is the creep rate vector, $\{\sigma\}$ the stress vector, $\sigma_v$ the effective stress, $\varepsilon_v$ the effective strain and $[M_2]$ a filter matrix. The effective strain and stress respectively are given in Hesser (2000) as:

$$\varepsilon_v = \frac{\sqrt{2}}{3}\sqrt{\left(\varepsilon_1 - \varepsilon_2\right)^2 + \left(\varepsilon_2 - \varepsilon_3\right)^2 + \left(\varepsilon_3 - \varepsilon_1\right)^2} \tag{6.116}$$

and

$$\sigma_v = \sqrt{\frac{1}{2}}\sqrt{\left(\sigma_1 - \sigma_2\right)^2 + \left(\sigma_2 - \sigma_3\right)^2 + \left(\sigma_3 - \sigma_1\right)^2} \tag{6.117}$$

No information could be found about the formulation of the filter matrix $[M_2]$. The usual viscosity parameters are replaced by viscosity functions, which are expressed as:

$$\bar{G}_k = 3\,G_k = G_k^*\,\exp^{k_1\sigma_v} \qquad \text{and} \qquad \bar{\eta}_k = 3\,\eta_k = \eta_k^*\,t^n\,\exp^{k_2\sigma_v} \tag{6.118}$$

Values for the above material parameters $G_k^*$, $\eta_k^*$, $n$, $k_1$ and $k_2$, used in the time- and stress-dependent viscosity functions, based on tests performed by Wierig & Gollasch (1967) can be found in Hesser (2000) and Yin (1996).

Peterson (1989) performed long term creep tests over 10 days on shotcrete samples starting at an age of 30 h. Based on his experimental results he published the following non-linear

creep model based on time-hardening theory:

$$\{\dot{\varepsilon}_v\} = \frac{1}{3\,\bar{\eta}_k\,(\sigma_v, t)}\,\exp^{-t\,\frac{\bar{G}_k(\sigma_v)}{\bar{\eta}_k(\sigma_v,t)}}\,\frac{3}{2}\,[M_2]\,\{\sigma\} \tag{6.119}$$

As in the previous model, the creep rate is dependent on time and stress-level. However, one drawback of this formulation is that it is limited to the lower stress regime (smaller than $\sim$10 MPa), otherwise the creep rate would decrease with increasing stress, which does not represent real creep behaviour (Yin, 1996). Pöttler (1990) tried to overcome this problem by proposing a creep model of a polynomial form, given as:

$$\{\dot{\varepsilon}^v\} = \left[\alpha\,(t)\;\sigma_v^2 + \beta\,(t)\;\sigma_v^3\right]\frac{3}{2}\,[M_2]\,\{\sigma\} \tag{6.120}$$

with

$$\begin{aligned}\alpha\,(t) &= \left(0.02302 - 0.01803\,t + 0.00501\,t^2\right)\;10^{-3}\\ \beta\,(t) &= \left(0.03729 - 0.06656\,t + 0.02396\,t^2\right)\;10^{-4}\end{aligned} \tag{6.121}$$

With the help of the above modification the applicable stress range for the correct modelling of creep is extended. However, over the first 1.5 days the model predicts a creep rate that is reducing as one would expect to observe in an experimental test. For creep tests longer than that, the model simulates a creep rate that would suddenly increase again, which is not realistic (Hesser, 2000). Zheng (1989) developed a non-linear creep model based on the combination of various rheological bodies, as can be seen in Fig. 6.33.

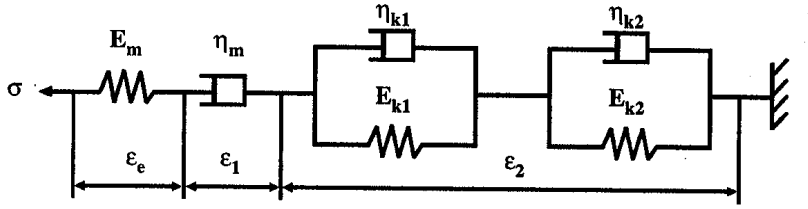



Figure 6.33: Constitutive behaviour of shotcrete after Zheng (1989) (from Hesser, 2000)

The time-dependent Newton dashpot is intended to describe the creep deformation of young concrete $\varepsilon_1$, whereas the behaviour of older concrete is simulated by two Kelvin units which are placed in series ($\varepsilon_2$). The creep rate for young concrete is estimated according to Peterson (1989) and the creep rate for older concrete can be calculated from:

$$\{\dot{\varepsilon}_2\} = \frac{3}{2}\sum_{r=1}^{2}\frac{1}{\eta_{k,r}}\,\exp^{-t\,\frac{E_{k,r}}{\eta_{k,r}}}\,[M_2]\,\{\sigma\} \tag{6.122}$$

Yin (1996) provides some values for the material parameters but states also that some inconsistency exists for this model regarding the parameter derivation and that the applicable stress range is limited. Zachow (1995) modifies the model presented by Peterson (1989) by

proposing new viscosity functions in order to obtain better agreement with lab test data for shotcrete. In his work the creep rate is given as:

$$\{\dot{\varepsilon}_v\} = \frac{\sigma_v + n_1\, exp\left(-\dfrac{t^{n_2}}{\sigma_v}\right)\left(n_2\, t^{n_2}\, ln\,(t) - \sigma_v\right)}{\bar{\eta}_k}\, \exp^{-\frac{\bar{G}_k}{\bar{\eta}_k}\, t} \tag{6.123}$$

where the viscosity function equals:

$$\bar{\eta}_k = \bar{\eta}_k^*\, \exp^{k_2 \sigma_v}\; t^{n_1\, exp\left(-\frac{t^{n_2}}{\sigma_v}\right)} \tag{6.124}$$

where $k_2$, $n_1$ and $n_2$ are material parameters that can be derived from shotcrete creep tests.

Hesser (2000) agrees on the fact that with this model a better reproduction of creep behaviour is possible, but shows as well that certain limitations exist regarding the applicable shotcrete age (max. 14 days) and stress range (less than 35 MPa). Another empirical creep model is published by Yin (1996) using an exponential function for the creep rate.

$$\{\dot{\varepsilon}\} = \frac{3}{2}\, a\,(t)\; \sigma_v^{b(t)-1}\, M_2\; \{\sigma\} \tag{6.125}$$

with

$$a\,(t) = A_1\, exp\left(\frac{A_2}{A_3 + t}\right) \qquad \text{and} \qquad b\,(t) = B_1\, exp\left(\frac{B_2}{B_3 + t}\right) \tag{6.126}$$

$A_1$, $A_2$, $A_3$, $B_1$, $B_2$ and $B_3$ are material parameters for a particular shotcrete type. On the basis of published information in the open literature Thomas (2003) defined an age-dependent Kelvin body for uniaxial short-term creep of shotcrete. He extended the model further for the 3D case and it can be written as:

$$\dot{e}_{ij} = \frac{\dot{S}_{ij}}{2G} + \frac{S_{ij}}{2}\, \frac{1}{\eta_k}\, \left(1 - \exp^{-\frac{G_k}{\eta_k}\, t}\right) \tag{6.127}$$

where $G$ is the elastic shear modulus, $S_{ij}$ is the deviatoric stress, $\dot{S}_{ij}$ the deviatoric stress rate and $\dot{e}_{ij}$ the deviatoric strain rate. The viscosity functions are given as:

$$\eta_k = \frac{1.5\, 10^{11}\; \exp^{\frac{-1.5}{t^{0.6}}}}{2\,(1+\mu)} \qquad \text{and} \qquad G_k = \frac{8.0\, 10^{6}\; \exp^{\frac{-1.0}{t^{0.4}}}}{2\,(1+\mu)} \tag{6.128}$$

with $\mu$ being the Poisson's ratio. Finally, the rheological model from Hauggaard et al. (1997) used for modelling creep of early age concrete is a non-linear Burger model as shown in Fig. 6.34.

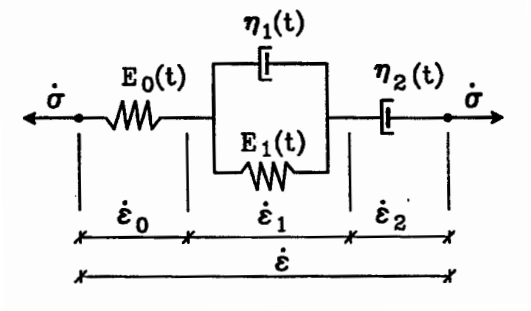



Figure 6.34: Non-linear Burger model (from Hauggaard et al., 1997)

The development of this model contains also a complex generalisation to 3D and the viscosity functions are given as:

$$
\begin{aligned}
E(t) &= a\, exp\left(-\left(\frac{b}{t}\right)^{c}\right) \\
\eta(t) &= a\,(1 - exp(-b\,t))\,(1 - c\,exp(-d\mid t - f\mid^{e}))
\end{aligned}
\tag{6.129}
$$

where $a$, $b$, $c$, $d$, $e$ and $f$ are concrete dependent parameters. These equations take into account that the viscosity increases only slightly initially and after about 200 hours the major increase takes place, as can be seen in Fig. 6.35.

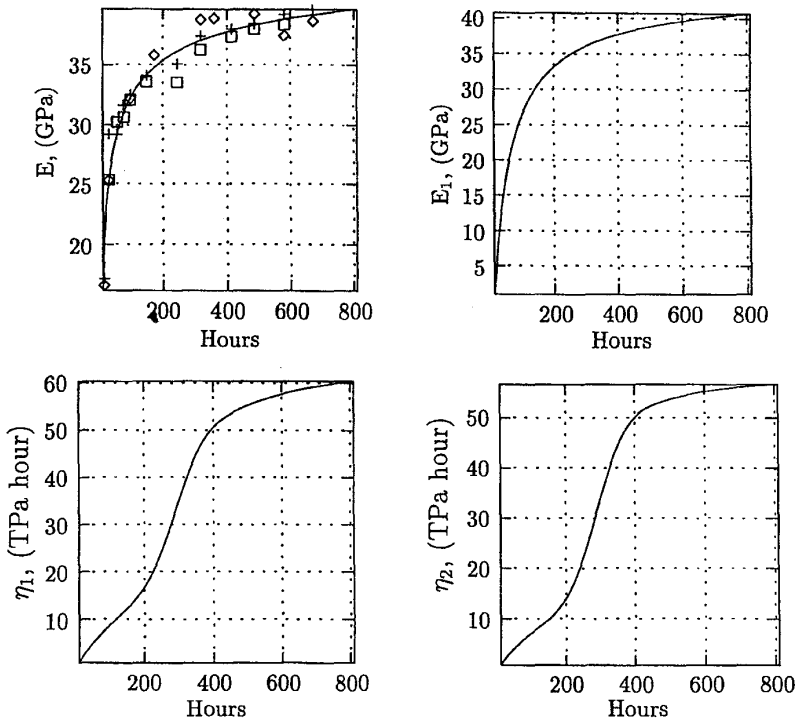



Figure 6.35: Functions for viscosity and stiffness in non-linear Burger model (from Hauggaard et al., 1997)

Further expressions of the viscosity functions for a non-linear Burger model can be found

in Bosnjak (2000), Hagihara et al. (2002) and Atrushi (2003).

### 6.7.3 Creep according to EC 2 (2004)

EC 2 (2004) provides a procedure for the calculation of creep deformation for normal cast concrete structures. Jones (2007) aimed to verify that these creep predictions are also applicable for sprayed concrete and can be used in a numerical analysis of tunnel construction. His investigations are based on comparisons with some numerical results from Thomas (2003), who defined an age-dependent generalised Kelvin model for uniaxial creep and fitted the involved parameters to creep tests on shotcrete samples in the literature (see section above).

According to EC 2 (2004) uniaxial compressive creep of concrete is considered via a creep coefficient $\phi$ which relates the time-dependent behaviour to the elastic deformation:

$$\varepsilon_c\,(t, t_o) = \phi\,(t, t_o)\;\frac{\sigma_c}{E} \tag{6.130}$$

where $\sigma_c$ is the applied compressive stress and $E$ the Young's modulus. The creep coefficient is a function of various influencing factors, such as:

- Relative humidity $RH$
- Mean compressive concrete strength $f_{cm}$
- Concrete age at loading $t_o$
- Cross sectional area $A$ and perimeter of member $u$ in contact with the atmosphere
- Cement type $\alpha$
- Temperature $T$

If the compressive stress of concrete at the age of loading $t_o$ exceeds 45 % of the compressive strength, then creep non-linearity should be considered and the creep coefficient $\phi(t, t_o)$ in equation 6.130 is replaced by:

$$\phi_k\,(t, t_o) = \phi\,(t, t_o)\;exp\,(1.5\,(k_\sigma - 0.45)) \tag{6.131}$$

with $k_\sigma = \sigma_c / f_{cm}$ being the stress level. Considering a shotcrete tunnel lining of 30 cm thickness, cement class N, a compressive cylinder strength of 30 MPa and a relative humidity of 80 %, Jones (2007) showed that reasonable agreement can be achieved by comparing the procedure from EC 2 (2004) with experimental data for shotcrete. It is further stated to divide the elastic modulus by 1.5 to allow for creep in a numerical model, taking into account that much of the loading in tunnel construction would occur at early ages.

### 6.7.4 Rate of flow method

The rate of flow method was suggested by England & Illston (1965) and is based on the division of creep into reversible and irreversible components. The principle is shown in Fig. 6.36, where the total strains consist of instantaneous elastic strains, delayed elastic strains and irreversible "flow" strains. Several modifications of the method exist for the description of creep of shotcrete developed by various researchers at the University for Mining and Metallurgy in Leoben, Austria. They are presented here briefly.

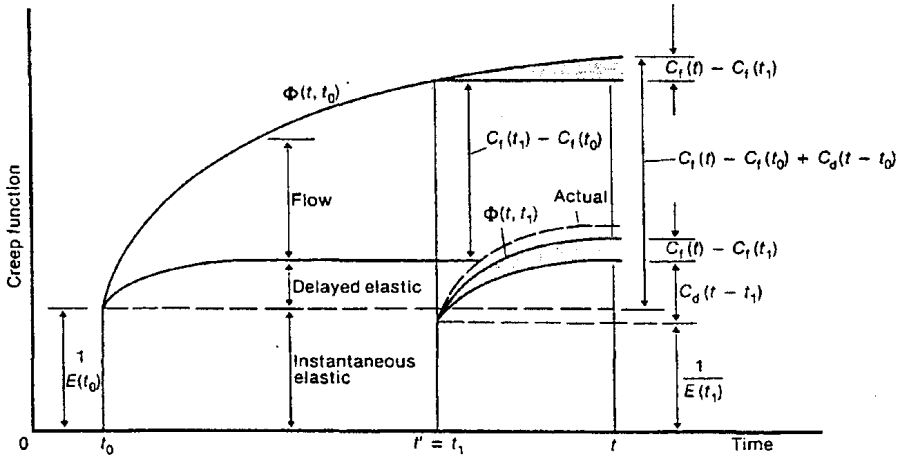



Figure 6.36: Deformation history with time(from England & Illston, 1965)

#### 6.7.4.1 Rate of flow method after Schubert (1988)

The deformation of shotcrete in uniaxial compression can be decomposed into 4 different components, as illustrated in Fig. 6.37 and explained in the list below. Upon loading some instantaneous elastic deformation occurs followed by a time-dependent creep deformation. This creep deformation is made up of a reversible "delayed" elastic component and the irreversible viscous deformation. Furthermore, the total deformation includes some deformation developing with time due to hydration temperature and shrinkage of the shotcrete.

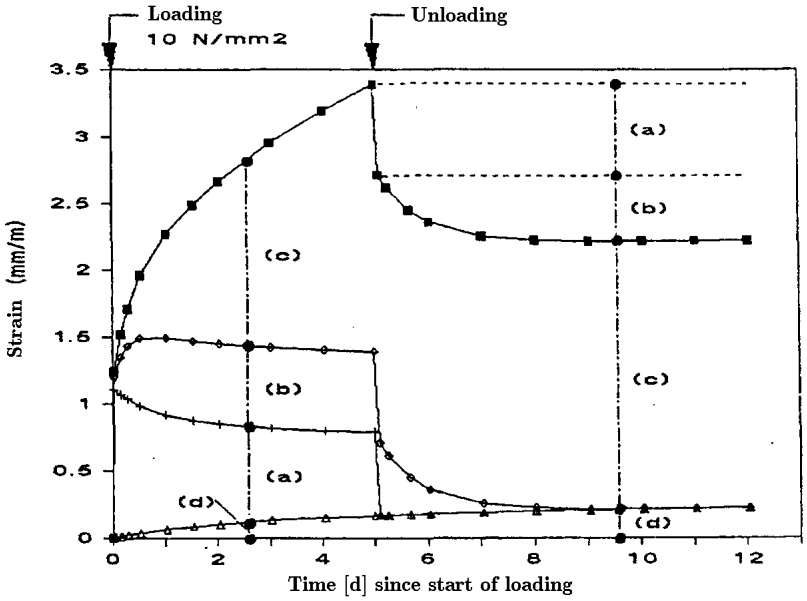



Figure 6.37: Deformation components for young shotcrete (from Schubert, 1988)

a) Instantaneous elastic deformation, governed by the time-dependent Young's modulus $E(t)$

b) Delayed elastic creep deformation, approaching a limit strain

c) Irreversible viscous deformation (or so called "flow")

d) Deformation due to shrinkage and hydration temperature

For the calculation of each component, the stress-strain history is divided into time steps $\Delta t$ and the total strain is written as:

$$\varepsilon_2 = \varepsilon_1 + \frac{\sigma_1 - \sigma_2}{E\,(t)} + \Delta\varepsilon_v + \Delta\varepsilon_d + \Delta\varepsilon_{sh} + \Delta\varepsilon_t \tag{6.132}$$

where $\varepsilon_1$ and $\sigma_1$ are the strains and stresses at the beginning of the increment at time $t_1$, $\varepsilon_2$ and $\sigma_2$ the strains and stresses at the end of the increment at time $t_2$, $E\,(t)$ the time-dependent Young's modulus, $\Delta\varepsilon_{sh}$ the change in shrinkage deformation and $\Delta\varepsilon_t$ the change in thermal deformation. The irreversible viscous strains are given as:

$$\Delta\varepsilon_v = \sigma_2\,\Delta C(t) \tag{6.133}$$

The function $\Delta C\,(t)$ controls the change of the specific irreversible creep deformation and is given by:

$$C\,(t) = A\,t^{\frac{1}{3}} \tag{6.134}$$

with $A$ being a material constant and $t$ the time in days. The change in delayed elastic strains can be estimated from:

$$\Delta\varepsilon_d = (\sigma_2\, C_{d,\infty} - \varepsilon_{d1}) \left(1 - \exp^{\frac{-\Delta\, C(t)}{Q}}\right) \tag{6.135}$$

where $\varepsilon_{d1}$ is the delayed elastic creep strain at the beginning of the time increment, $Q$ a material constant and $C_{d,\infty}$ the limit deformation at infinity per unit stress. If the deformation history of a tunnel shell is known, the stresses in the lining can be estimated by rearrangement of equation 6.132:

$$\sigma_2 = \frac{\varepsilon_2 - \varepsilon_1 + \dfrac{\sigma_1}{E\,(t)} + \varepsilon_{d1} \left(1 - \exp^{-\frac{\Delta C(t)}{Q}}\right) - \Delta\varepsilon_{sh} - \Delta\varepsilon_t}{\dfrac{1}{E\,(t)} + \Delta C\,(t) + C_{d,\infty} \left(1 - \exp^{-\frac{\Delta C(t)}{Q}}\right)} \tag{6.136}$$

For the calculation of shrinkage and temperature strains see sections 6.8 and 6.9.

#### 6.7.4.2 Rate of flow method after Golser et al. (1990)

A further modification to the above method was proposed by Golser et al. (1990). Instead of using the time-dependent Young's modulus $E\,(t)$ they suggested to apply a so called deformation modulus $V\,(t)$, which also includes the non-linear stress-dependency of the stiffness. It can be expressed (in GPa) as:

$$V\,(\sigma, t) = E_{28} \left(b_o\,(t) + b_1\,(t)\, \frac{\sigma}{\beta_D\,(t)} + b_2\,(t) \left(\frac{\sigma}{\beta_D\,(t)}\right)^2\right) \tag{6.137}$$

with

$$\begin{aligned} b_o(t) &= 1.36 \sqrt{\frac{t}{22 + 1.78\, t}} \\ b_1(t) &= 2.23 \cdot 10^{-3} \sqrt{\frac{t}{0.1 + 0.075\, t}} \\ b_2(t) &= 2.23 \cdot 10^{-6} \sqrt{\frac{t}{1810 + 0.1\, t}} \end{aligned} \tag{6.138}$$

The parameter $t$ is the time in hours. The increase in the uniaxial compressive strength with time is considered in the function $\beta_D(t)$.

#### 6.7.4.3 Rate of flow method after Aldrian (1991)

In his work, Aldrian (1991) tried to improve the rate of flow method after Golser et al. (1990) in order to facilitate the calibration of the involved model parameters and to obtain a better prediction for the creep behaviour of young shotcrete during the first couple of days after casting. Similar to Golser et al. (1990), a deformation modulus is used for calculating the

instantaneous strain, depending on time $t$ and stress level $\alpha$ ($= \sigma/\beta_D$):

$$V(t,\alpha) = E_{28}\,\frac{1}{22.5}\,\left[(1-\alpha)\;25\sqrt{\frac{t}{25+1.2\,t}} + 3\,\alpha\,\sqrt{\frac{t}{100+0.9\,t}}\right] \tag{6.139}$$

with $\alpha$ varying from 0 to 1. For describing the creep behaviour Aldrian (1991) introduced the irreversible viscous deformation of the following form:

$$\Delta\varepsilon_v = \sigma_2\,\Delta C\,\left(\exp^{8\alpha-6}+1\right) \tag{6.140}$$

taking into account the non-linear relation between irreversible creep and applied stress via the stress level $\alpha$. The increase in irreversible creep strains with time is defined through a new function $C(t)$ as:

$$C(t) = A\,(t-t_1)^{0.25\,\alpha^{0.2}} \tag{6.141}$$

where $t_1$ (in days) is the age of shotcrete at first loading.

Summarising, the rate of flow method is a special approach for back-calculating stresses from strain histories and was adopted in several two dimensional analyses of tunnel construction (i.e. Kienberger (1999)). However, Thomas (2003) states that, according to Rathmair (1997), it has not been possible to implement this method in a three dimensional finite element analysis. Furthermore, a certain criticism exists that the method relies on the principle of superposition and that there is no allowance for plastic strains (Thomas, 2003).

## 6.8 Modelling of shrinkage

For the simulation of shrinkage strains Huo & Wong (2006) give an overview of five different shrinkage models available in the literature based on empirical observations. Their published research focuses on the early-age behaviour of high performance concrete (HPC) deck slabs under different curing methods, comparing experimental test results with different model predictions. The three most basic of the adopted models are presented in the following sections with the aim of highlighting the main parameters involved in shrinkage behaviour.

### 6.8.1 Shrinkage after American Concrete Institute (ACI)

The following equation is suggested by ACI (1992) for the estimation of shrinkage strains at any time:

$$\varepsilon_{sh}\,(t) = \varepsilon_{sh,\infty}\,\frac{t}{B+t} \tag{6.142}$$

where $\varepsilon_{sh,\infty}$ is the ultimate shrinkage strain and $B$ a parameter governing the increase in shrinkage strains with age of drying $t$ (see Fig. 6.38). The above equation was found to be the most common one adopted by several authors for the prediction of shrinkage in shotcrete (Kienberger, 1999; Schubert, 1988; Walter, 2003; Aldrian, 1991; Golser, 1999; Galler, 1997).

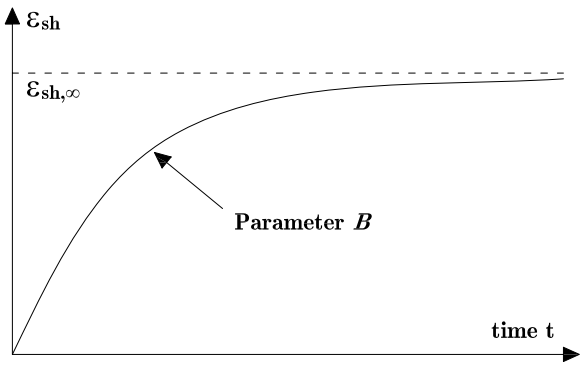



Figure 6.38: Development of shrinkage strains with time (after ACI, 1992)

### 6.8.2 Shrinkage after Bazant Model B3

Bažant & Baweja (1995) proposed to calculate the so called "mean shrinkage strain" in a cross section according to:

$$\varepsilon_{sh}\left(t, t_o\right) = -\varepsilon_{sh\infty}\, k_h\, S\left(t\right) \tag{6.143}$$

with the time dependency given as:

$$S(t) = \tanh\sqrt{\frac{t - t_o}{\tau_{sh}}} \tag{6.144}$$

$\varepsilon_{sh\infty}$ is the time-dependent ultimate shrinkage and $t_o$ is the age when drying begins. This model takes further into account the humidity dependence (see Fig. 6.39, the coefficient $k_h$ can be estimated from the relative humidity $h$), size and shape of the concrete member (via $\tau_{sh}$), the concrete compressive strength at 28 days, the used cement type, curing conditions and the water content of the concrete. Meschke (1996) included this shrinkage law in his viscoplastic material model for a complete description of the time-dependent shotcrete behaviour.

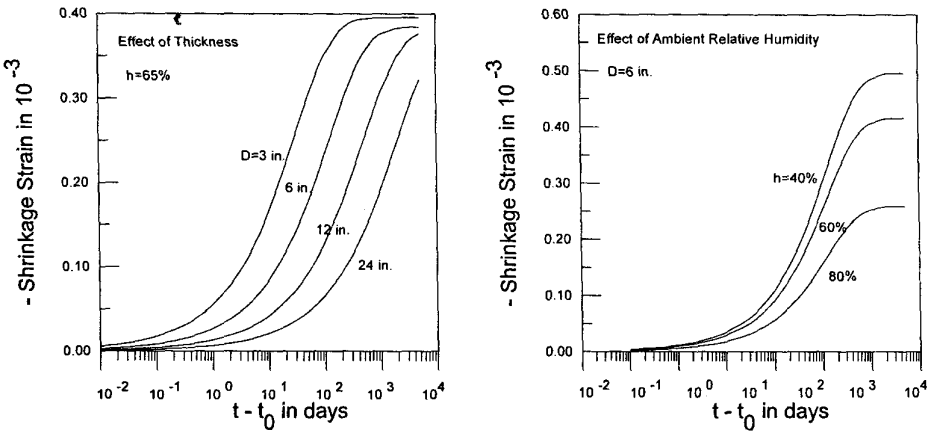



Figure 6.39: Typical shrinkage curves given by Model B3 (from Bažant & Baweja, 1995)

### 6.8.3 Shrinkage after Gardner & Lockman (2001)

In their publication, a design-office procedure for calculating shrinkage is presented in the following way:

$$\varepsilon_{sh} = \varepsilon_{shu}\,\beta\,(h)\;\beta\,(t) \tag{6.145}$$

with

$$\beta(h) = \left(1 - 1.18\,h^4\right) \qquad \text{and} \qquad \beta(t) = \left(\frac{t - t_c}{t - t_c + 0.15\,(V/S)^2}\right)^{0.5} \tag{6.146}$$

where $h$ is the relative humidity expressed as a decimal (not in %), $t$ the age of concrete, $t_c$ the age when drying commenced (end of moist curing) and $V/S$ the volume-surface ratio. Furthermore, the ultimate shrinkage $\varepsilon_{shu}$ depends on the cement type ($K$) and the mean compressive strength of the concrete at 28 days, $f_{cm28}$, and can be estimated from:

$$\varepsilon_{shu} = 1000\,K\,\left(\frac{30}{f_{cm28}}\right)^{0.5}\,10^{-6} \tag{6.147}$$

The model predictions are compared with experimental results for 115 data sets for shrinkage and it was observed that agreement was within $\pm\,30\,\%$.

## 6.9 Modelling hydration temperature in concrete structures

The estimation of the increase in temperature with time in a concrete structure due to cement hydration is a complex process controlled by material technology and external boundary conditions (i.e. adiabatic or semi-adiabatic curing). According to RILEM (1998) the numerical models for the prediction of the temperature development in cement-based systems like concrete and shotcrete can be subdivided into two different families of models, which are:

1. Models on a micro level, allowing for physico-chemical processes and mechanisms occurring on the micro- or even nano-level material scale (Garboczi & Bentz, 1992)

2. Models on a macro level, developed for the prediction of temperature fields in real concrete structures and used in engineering practise (Bosnjak, 2000)

Several analytical methods for the determination of a temperature field were proposed in the late thirties (i.e. Carlson (1937)) and most of them are based on the Fourier differential equation for heat conduction, which is given as:

$$\rho\,c\,\frac{\partial T}{\partial t} = k\,\left[\frac{\partial^2 T}{\partial x^2} + \frac{\partial^2 T}{\partial y^2} + \frac{\partial^2 T}{\partial z^2}\right] + Q\,(t, x, y, z) \tag{6.148}$$

where $k$ is the thermal conductivity, $T$ the temperature, $\rho$ the mass density, $c$ the specific heat and $Q$ is the rate of internal heat generation per unit volume depending on the coordinates $x, y, z$ and time $t$. The correct estimation of the function $Q$ is a central part in temperature

calculation of early age-concrete and several definitions can be found in the literature, among them Reinhardt et al. (1982) and Freiesleben Hansen & Pederson (1977).

Such an approach is mostly suitable for concrete structures of a certain thickness and mass and usually not performed in engineering practice for the temperature calculation in a tunnel shotcrete shell, where heat boundary conditions and input parameters are difficult to establish.

Schubert (1988) includes temperature induced deformations in his constitutive model for early-age shotcrete and suggests the following mathematical function based on experimental laboratory tests performed by Rabensteiner (1988):

$$\varepsilon_{th} = 30 \left[ -\cos\left(250\, t^{0.25}\right) + 1 \right] \tag{6.149}$$

Nevertheless, Schubert (1988) states that the magnitude of these temperature strains $\varepsilon_{th}$ might differ considerably from those in a real shotcrete tunnel shell due to different mass and boundary conditions, but that the basic shape of the development might be realistic. Meschke (1996) considers temperature induced strains that are uniform throughout the shotcrete body and independent of the acting stress through the following vector formulation:

$$\varepsilon_{ij} = \alpha \, (T - T_o) \, \delta_{ij} \tag{6.150}$$

where $T$ is the hydration temperature, $T_o$ a reference temperature, $\alpha$ the coefficient of thermal expansion and $\delta_{ij}$ the Kronecker-delta. However, no further information about the temperature development with time is given.

## 6.10 A review of different constitutive models applied for tunnel lining design

### 6.10.1 Hypothetical Modulus of Elasticity (HME)

The first attempt to realistically model the behaviour of shotcrete for tunnel lining design was introduced by Pöttler (1985). In his work a Hypothetical Modulus of Elasticity (HME) was derived treating shotcrete as a pseudo-elastic material. Essentially, the HME represents a simple reduction of the Young's modulus $E$ at 28 days by various factors accounting for the following aspects:

- 3D effects
- Creep and shrinkage
- Ageing of shotcrete (i.e. increase of stiffness and strength with time)
- Time-dependent history of loading

Through an extensive parametric study published in Pöttler (1990), changing various parameters involved in tunnel construction, it was concluded that a value of HME=7 GPa gives the highest stresses in the shotcrete lining. These stresses are referred to as short-term values and occur at a distance of one tunnel diameter behind the tunnel face. Although this method appears to be straightforward, Thomas (2003) states that there exists no established means of determining the reduction factors for calculating the HME from the Young's modulus $E$. Powell et al. (1997) adopted the HME-approach in their analyses of the platform tunnels for the Heathrow Express at Terminal 4, estimating a value of the reduced lining stiffness by back analysis for the required volume loss at ground surface. Their values ranged from 0.75 GPa to 2 GPa for young shotcrete immediately after excavation and reached the full stiffness of 25 GPa at later stages of construction.

Karakus & Fowell (2003) investigated different excavation types by using a reduced stiffness depending on the distance to the tunnel face as shown in Fig. 6.40.

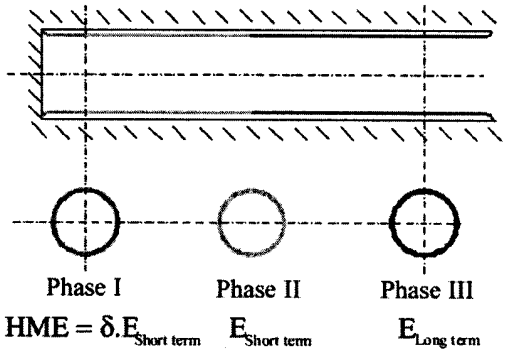



Figure 6.40: Principle of the HME-approach (from Karakus & Fowell, 2003)

Other influencing parameters were the ground strength, shape and size of the area to be excavated and the number of excavation stages until ring closure. The values for the HME ranged from 0.15 GPa to 5 GPa. As a result they suggested a correlation between the HME and the maximum surface settlement $s_{max}$ of the form:

$$HME = a\, s_{max}^{b} \tag{6.151}$$

where $a$ and $b$ are two constants depending on the face advance sequence.

Finally, in the analyses of the CTRL North Downs Tunnel performed by Watson et al. (1999) a reduced stiffness of 7.5 GPa was adopted for young shotcrete not older than 10 days and 15 GPa for old shotcrete. The maximum tunnel lining stress was further limited to a compressive shotcrete strength of 5 MPa and 16.75 MPa as can be seen in Fig. 6.41.

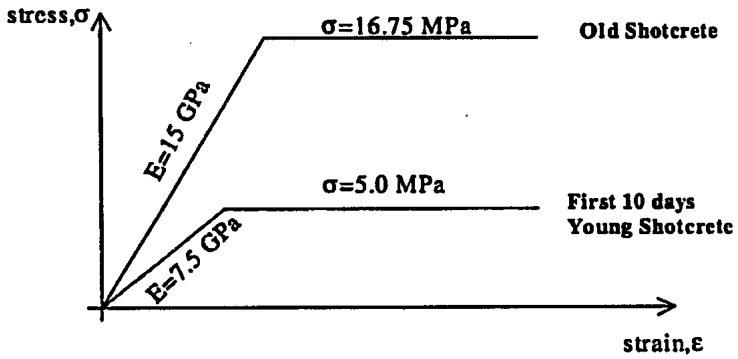



Figure 6.41: Stress-strain behaviour of young and old shotcrete (from Watson et al., 1999)

From these observations in the literature it can be concluded that no common agreement exists on suitable values for the HME that can be used for a realistic and safe design of shotcrete tunnel linings.

### 6.10.2 Non-linear beam model by Moussa (1993)

Moussa (1993) developed a constitutive model for simulating the response of shotcrete under incremental loading with time. The material behaviour includes non-linear hardening and softening in compression and cracking of shotcrete in tension. In the case of reinforced concrete, the tension-stiffening effect has been taken into account. Furthermore, shotcrete was treated as a time-dependent material considering the increase in strength with time. One important part in this research was the attempt to capture plastic deformations in shotcrete due to early loading by applying an incremental stress-strain history based model as depicted in Fig. 6.42.

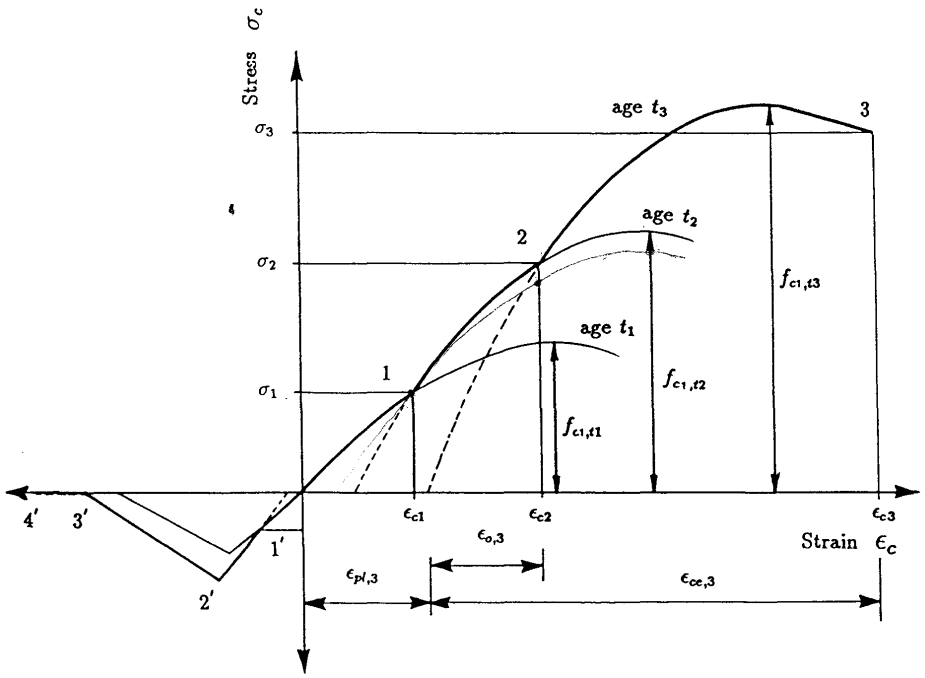



Figure 6.42: Proposed model for stress-strain history of shotcrete (from Moussa, 1993)

The effect of initial damage due to previous loading on the gain in compressive strength with time has been considered. Moussa (1993) applied this model for analyzing a 2D tunnel construction with a single permanent shotcrete shell. Excavation was performed in two stages (top-heading and invert) with a temporary invert for the intermediate construction stage. The lining was modelled by a layered beam element consisting of 3 layers, each of them having different age and straining history. Results showed that after ring closure the axial forces in the lining where reduced by about 25 % in the crown and 60 % for the invert. The assumed shotcrete non-linearity and strain history seemed to have an important influence also on the bending moments in the lining, which were reduced by about 70 % for corners and 50 % for other parts of the lining. A general increase of deformation in the lining combined with a change in the deformation mode has been observed. The impact of initial damage during the increase of shotcrete strength on the structural lining behaviour is not very clear from the results presented, but generally a lower load capacity could be expected. Finally, it was concluded that the applied constitutive model had little influence on the behaviour of the ground adjacent to the tunnel, where surface settlements depend mainly on the tunnel depth. A slight increase in ground deformations and plastic soil regions has been obtained.

### 6.10.3 Post-failure modelling of shotcrete by Hafez (1995)

Hafez (1995) implemented in his work the three parameter model developed by Chen & Chen (1975) into the finite element code FINAL, assuming constant material parameters and therefore ignoring the time-dependent behaviour of shotcrete. In a 3D analysis of the Lambach Tunnel in Austria he studied the behaviour of the tunnel shotcrete shell by adopting an elastic

and a non-linear elasto-plastic material model. In a comparison of those two approaches it was noticed that the increase of surface settlements due to the elasto-plastic material response is about 52 %, whereas the crown displacement showed an increased vertical displacement of 26 % compared to the simple linear elastic constitutive law. Furthermore, Hafez (1995) concluded that the elasto-plastic material behaviour has a significant influence on the tunnel face, as the movement of the unsupported face in the elasto-plastic analysis was about twice the movement in the elastic approach. Cross sectional forces within the tunnel shell were generally significantly smaller in the elasto-plastic analysis.

### 6.10.4 Viscoplastic material model for shotcrete by Meschke (1996)

Meschke (1996) presented a sophisticated model for shotcrete which is formulated on the basis of multi-surface viscoplasticity with time-adjusted material parameters. The ductile behaviour of concrete in compression is accounted for by a Drucker-Prager yield surface, including non-linear hardening and perfectly plastic material behaviour after peak. The brittle behaviour of plain concrete in tension is modelled by a Rankine failure criterion considering isotropic softening after peak in the context of the smeared crack concept (see Fig. 6.43).

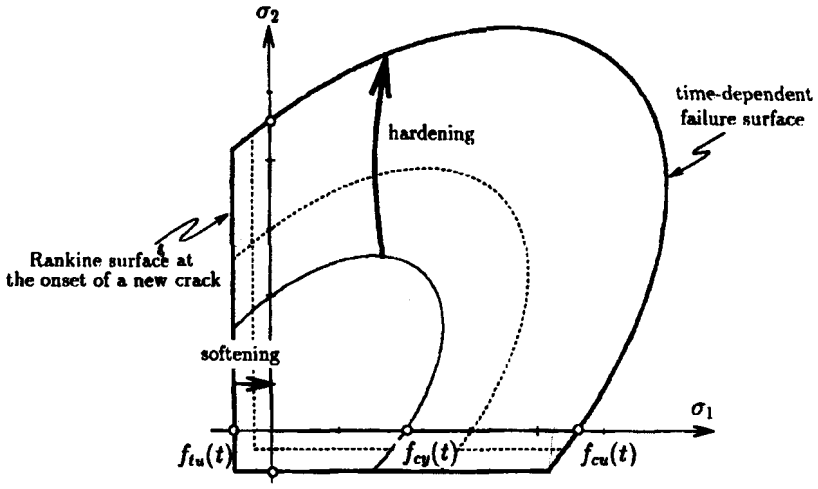



Figure 6.43: Loading surfaces of the viscoplastic material model for shotcrete (from Meschke et al., 1996)

For exponential softening, the involved softening parameters are related to the element size via the fracture energy (see Section 6.6.1.2) in order to avoid strong mesh-dependency. In the case of linear softening the softening modulus is related in a simple way to the Young's modulus. Furthermore, time-dependent functions for the increase in shotcrete stiffness and strength and the development of peak strains with time are presented based on experimental results. The essential phenomena of creep and relaxation of shotcrete have been taken into account by adopting a viscoplastic rheological model based on the material law by Duvaut & Lions (1972). A shortcoming of this creep model is the description of creep with only one single creep parameter and the restriction of viscoplastic strains to an elasto-plastic stress

state. Therefore, viscous deformations in the elastic area are not accounted for by the model. To complete the model the effects of shrinkage and hydration temperature are included in the model formulation. In Meschke et al. (1996) this proposed constitutive law was used for a 3D numerical simulation of the excavation of a single-track tunnel in a creep-active soil, modelling the tunnel lining with solid elements. Construction was performed according to the principles of NATM in three stages, i.e. top-heading, bench and invert. From the results it was observed that the stress state within the shotcrete shell is almost biaxial. The load-carrying behaviour of the shotcrete linings is dominated by the formation of a stress ring in the circumferential direction of the shotcrete lining. Stress redistribution takes place from the freshly sprayed concrete parts to the neighbouring parts, which have gained already a sufficient larger strength and stiffness. Walter (1997) refined this material law for shotcrete by including additional creep terms based on the rate of flow method (see Section 6.7.4) for covering as well the elastic area. Further information about the presented constitutive model can be found as well in Kropik & Mang (1995).

### 6.10.5 Shotcrete model based on chemoplasticity by Hellmich et al. (1999*a*)

Lackner et al. (2006) published some research about hybrid analysis for the quantification of stress states in tunnel shells applying a highly complex material model for shotcrete developed by Hellmich et al. (1999*a*) and Sercombe et al. (2000). The thermo-chemo-mechanical material model is formulated within the framework of thermodynamics of chemically reactive porous media. Phenomena on the micro-level of the material are interpreted macroscopically by means of state variables and energetically conjugated thermodynamic forces (Lackner et al., 2002). The chemical reaction of hydration between cement and water is described by a scalar variable, referred to as the degree of hydration $\xi$. It is obtained by relating the mass of reaction product per unit volume $m$, to the mass of reaction products at the end of cement hydration. Therefore it can be written as:

$$\xi = \frac{m}{m_\infty} \tag{6.152}$$

The evolution of $\xi$ is an underlying intrinsic material function being independent of field variables and boundary effects. It is of an Arrhenius type law and given as:

$$\dot{\xi} = \tilde{A}\, exp\left(-\frac{E_a}{RT}\right) \tag{6.153}$$

where $T$ is the absolute temperature, $E_a$ is the activation energy and $R$ is the universal constant for ideal gases with $R$=8315 J/(mol K). The chemical affinity $\tilde{A}$ is the driving force of the cement hydration and for shotcrete it depends mainly on $\xi$. Lackner et al. (2002) established the following analytical expression:

$$\tilde{A}\,(\xi) = a\,\frac{1 - exp\,(-b\xi)}{1 + c\xi^d} \tag{6.154}$$

with $a, b, c$ and $d$ being material constants. Therefore, the mechanical properties of shotcrete are controlled by the degree of hydration $\xi$ and six material functions are required within the model formulation (see Fig. 6.44):

a) Normalised chemical affinity $\tilde{A}$

b) Compressive strength $f_c$

c) Young's modulus $E$

d) Chemical shrinkage strain $\varepsilon^s$

e) Charactersitic time for short term creep $\tau_w$

f) Final viscous compliance $J^v_\infty$

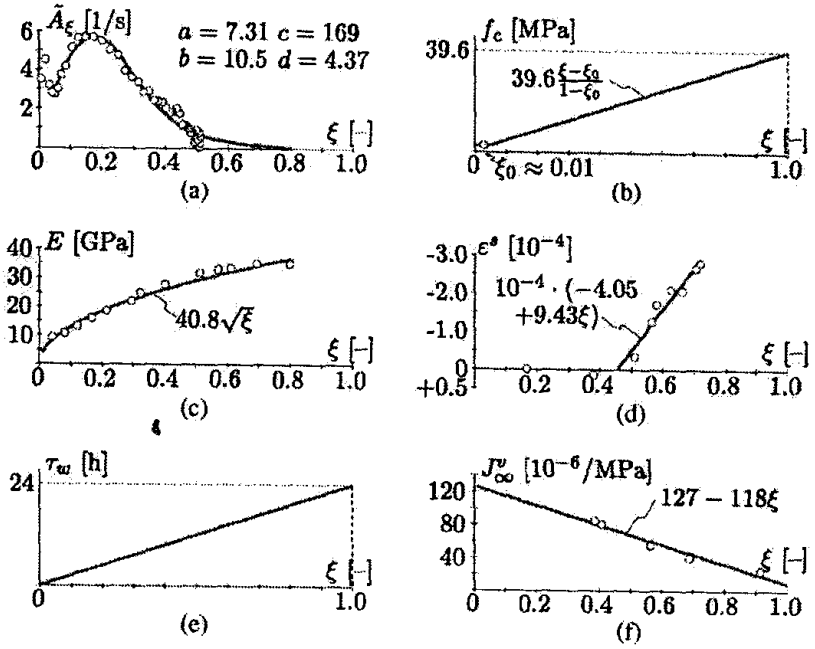



Figure 6.44: Intrinsic material functions of shotcrete (from Lackner et al., 2002)

The mechanical behaviour of shotcrete is controlled further by two yield surfaces of a Drucker-Prager type for compression and a Rankine criterion for the tensile behaviour including isotropic hardening and softening, as shown in Fig. 6.45.

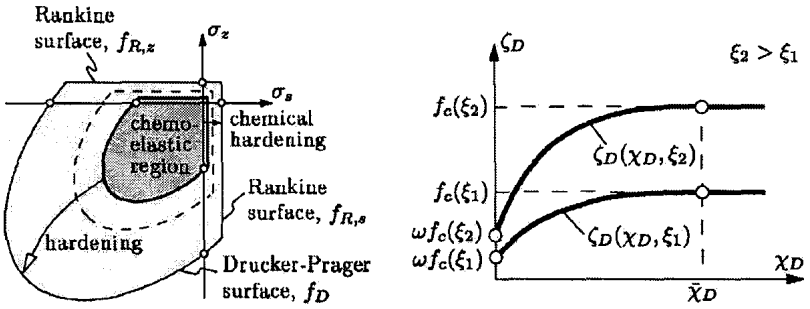



Figure 6.45: Yield surfaces and hardening law for chemoplasticity model for shotcrete (from Lackner et al., 2006)

Applying this constitutive model in a 2D analysis of a circular NATM tunnel in a creep active soil, Hellmich et al. (1999*b*) and Hellmich et al. (2000) observed that the bending moments in a tunnel shell are strongly influenced by the stiffness of the shell, which depends both on the chemical hardening characteristics of the shotcrete mixture and on the degree of plasticising within the shell. Furthermore, they concluded that chemical shrinkage always leads to a reduction of bending moments by the formation of cracking. The high creep capacity of young shotcrete tends to increase the horizontal inward movements of the tunnel section as a consequence of the redistribution of the stresses in the soil after excavation. Generally, creep is the dominant factor in areas where high stresses are generated and can lead to some changes in the overall structural behaviour of the tunnel lining (change of signs of bending moments). According to their results, temperature also appears to be an important factor for the behaviour of the shell. A higher temperature leads to higher bending moments due to the faster hardening and stiffening of the shotcrete. Finally, tangential forces within the tunnel lining seem to be practically independent of the material law used for shotcrete and depend exclusively on the stress distribution that has taken place in the soil before the hardening process of the shotcrete starts.

### 6.10.6 Assessment of constitutive models for shotcrete by Thomas (2003)

In his research, Thomas (2003) investigated the behaviour of shotcrete for tunnelling by adopting a large variety of different constitutive laws found in the literature. The key aspects of his analyses were the ageing of the material properties, the non-linear stress-strain behaviour, creep and shrinkage. At first instance, a large-scale laboratory load test on a ring of sprayed concrete was simulated numerically, moving then on to the numerical modelling of 3D tunnel construction. The set of analyses involved the following material behaviour for shotcrete, implemented into the finite difference program FLAC:

- Linear elastic with constant and age-dependent stiffness
- Non-linear elastic model after Kotsovos & Newman (1978) including time-dependent material parameters

- Hypothetical Modulus of Elasticity (HME)
- Simple plasticity models (Drucker-Prager, Mohr-Coulomb) adopting perfectly plastic post-peak behaviour, strain-hardening and time-dependency
- Various creep models based on Kelvin model assuming different viscosity functions
- Shrinkage model

From the obtained results it was concluded that the choice of the constitutive model for shotcrete affects the stress distribution within the tunnel lining. Lower lining stiffness results in higher deformation coupled with lower stresses. Ageing of the elastic modulus, non-linearity of the stress strain curve and creep all lead to higher strain and deformation levels. The relative stiffness of the ground and the lining appears to be a governing factor for the loads in the lining and its movements. Hence, the importance of the soil-structure interaction was highlighted. Creep models are often said to represent "softer" shotcrete models, although the input data for the involved creep functions are usually quite scattered. Essentially, creep leads to a reduction in lining stresses and this effect is generally accepted as being beneficial for lining design. However, this depends heavily on the ability of the ground to sustain the remainder of the load. Bending moments were more strongly influenced than hoop forces by the constitutive model adopted, depending also on the geometrical shape of the tunnel cross section. Some details of the constitutive model may also be significant, for example the assumed shape of the failure surface in the deviatoric plane (Drucker-Prager or Mohr-Coulomb). Finally, it was stated that in a full 3D analysis the effect of an advanced constitutive model for sprayed concrete was noticed mainly within the first few metres of the lining behind the tunnel face.

## 6.11 Summary

The topic of the current chapter was to give an introduction into the modelling of a quasi-brittle material such as concrete or shotcrete, covering the mechanical behaviour both in compression and tension. Furthermore, an overview of different approaches available in the literature to simulate the time-dependent phenomena of creep, shrinkage and hydration temperature that occur in concrete structures were presented. The following conclusions can be drawn:

- A large number of empirical models based on experimental data exist for modelling concrete, taking into account the non-linear material behaviour before peak. However, one big drawback is that these models focus mainly on uniaxial stress conditions in compression and tension and can hardly be used in a numerical analysis. Nonetheless, simple concrete models have been developed within the framework of elasto-plasticity, that are capable of reproducing the main characteristics of the material behaviour in multiaxial loading conditions.

- The Chen & Chen (1975) concrete model represents a more advanced constitutive model for hardened concrete based on elasto-plasticity, where the material behaviour in compression and tension is governed by two yield surfaces. On the onset of plastic deformation these two surfaces move together simultaneously in the principal stress space and isotropic strain-hardening controls the material behaviour before reaching peak.

- Cracking of concrete in tension is a relatively difficult phenomenon to model, since in reality it is a highly discrete and localised problem that occurs in a concrete structure. For simulating cracking in a numerical analysis two different approaches exist, i e. the discrete and the smeared crack model. However, when treating cracking of concrete within the framework of continuum mechanics, one has to face severe problems that are usually associated with strain-softening materials. A simple approach based on fracture energy was presented to avoid spurious mesh dependency on the obtained results.

- For considering steel reinforcement of concrete or shotcrete three different approaches exist in the literature (i.e. discrete, smeared and embedded reinforcement models). It was highlighted that due to their complexity, reinforcement is hardly considered in the analysis of tunnel construction. However, sometimes it is convenient to adopt the stress-strain behaviour of concrete in tension by introducing the so called "tension-stiffening effect". This interaction of concrete and steel leads to a slightly softer material response of concrete in the tensile post peak regime. When analysing steel-fibre reinforced concrete structures a fracture energy based approach might be a possible solution for simulating the increase in ductility of concrete behaviour in tension.

- No well accepted framework exists in the literature for the modelling of concrete creep and in particular for young shotcrete at early ages, which is a very creep active medium. Apart from some basic mathematical functions, in most of the cases a combination of rheological units serves for the calculation of creep deformation in concrete structures (Kelvin-, Maxwell- and Burger-model). By establishing complex viscosity and stiffness functions it is possible to fit model predictions to uniaxial compressive test data. However, very limited information is available for the extension of creep to 3D or how to deal with creep of concrete in tensile stress conditions.

- Three simple models for predicting shrinkage deformation of concrete have been presented. They all have in common that they are based mainly on experimental data and take into account factors such as relative humidity, concrete strength in compression, geometry of the structure to be investigated and concrete composition.

- The modelling of the increase in temperature due to cement hydration in hardening concrete or shotcrete is a complex process, mostly performed for the analysis of relatively thick concrete structures. Little information is available in the literature on

how to incorporate these temperature effects in a constitutive model for the practical analysis of shotcrete tunnel shells.

# Chapter 7

# A constitutive Model for Shotcrete

## 7.1 Introduction

In this chapter a non-linear constitutive model for the time-dependent behaviour of shotcrete based on elasto-plasticity is presented, which was developed during this research project. The well known Chen & Chen (1975) concrete model, described in Chapter 6, was selected as a starting point because of its relative simplicity and capability to simulate the main characteristics of the mechanical behaviour of hardened concrete. However, it was decided to modify this constitutive model in such a way that a better reproduction of the complex mechanical behaviour of sprayed concrete was possible. Therefore it was necessary to implement two yield surfaces that move independently from each other in stress space, being governed by two different hardening parameters - one for compression and one for tension. Cracking of shotcrete is considered within the smeared-crack concept. Furthermore, the main material parameters of the model are changing with time according to test data for shotcrete that can be found in the literature. As a result it will be shown that the developed constitutive model is capable of simulating the transition from a ductile and plastic material behaviour at early ages to a quasi-brittle material response after curing at 28 days. Other mechanical aspects related to time, such as creep, shrinkage or effects due to cement hydration temperature, are also considered within the current model formulation. Anisotropy effects that might be observed due to the spraying process are not taken into account and therefore material behaviour is assumed to be isotropic. After a robust numerical implementation into the Imperial College Finite Element Program (ICFEP, Potts & Zdravković (1999)) the outcome was a sophisticated constitutive model for sprayed concrete that can be applied for the analysis of complex boundary value problems in tunnelling. Finally, some model predictions for single element runs presented at the end of this chapter show the model capabilities but also its limitations.

## 7.2 Formulation of the constitutive model

As mentioned in the introduction of this chapter, the original Chen & Chen (1975) concrete model contains some shortcomings for the correct reproduction of shotcrete behaviour that are discussed here briefly.

Firstly, uniaxial tests of hardened concrete indicate that the stress-strain curves for compression and tension are different in shape, in particular for the post-peak behaviour. The original Chen & Chen (1975) concrete model does not account for this fact and the non-linear hardening curves are assumed to be identical. Consequently, the two yield surfaces move together simultaneously in stress space, being governed by only one single hardening parameter (see equation 6.77). In a first step it was tried to improve this drawback by implementing two different hardening and softening rules for compression and tension controlled by two different hardening parameters. Unfortunately, the problem that arose during some test analyses was the following: the two yield surfaces given in equations 6.75 and 6.76 are supposed to be connected to each other at their intersection point in the $J$-$p$ or $I_1$-$\sqrt{J_2}$ space at any time. However, their mathematical nature is such that some restrictions exist regarding the minimum and maximum size of both yield surfaces, which is controlled by the strength values used for the description of the hardening and softening rules, otherwise convexity of the yield surfaces is lost. Therefore it would not be possible to entirely fit these hardening and softening curves to experimental data.

Secondly, during the hardening process of the cement paste the material parameters of shotcrete are a function of time and hence are not constant. Furthermore, shotcrete behaviour includes also creep, shrinkage and thermal deformation due to the cement hydration. The original Chen & Chen (1975) concrete model was formulated for hardened concrete at 28 days and does not contain any time-dependency.

Due to these major shortcomings it was decided to incorporate some important modifications to the original model formulation. In the following sections of this chapter the new structure of the modified Chen & Chen (1975) model for the behaviour of shotcrete is presented and discussed in detail. Throughout the complete model description a tension positive sign convention is adopted in the model development and the yield functions for both compression and tension are formulated in terms of the geotechnical stress invariants $p$, $J$ and $\theta$, previously introduced in Chapter 1.

### 7.2.1 Structure of the model

In the present constitutive model for shotcrete, the classical theory of elasto-plasticity for hardening and softening materials along with its algorithmic formulations is extended to account for the effects of ageing, creep, shrinkage and thermal deformation. The increase in the strength properties of shotcrete implies that the adopted yield surfaces are considered to

be time-dependent and the yield condition for a single surface can be expressed as:

$$F\left(\{\sigma\},\{k\},t\right)=0 \tag{7.1}$$

where $\{\sigma\}$ is the current stress state, $\{k\}$ the vector of state (or hardening) parameters and $t$ represents the time. Applying the principle of superposition the total strains are made up of elastic strains $\varepsilon^{el}$, conventional plastic strains $\varepsilon^{p}$ arising from the yield and plastic potential surfaces, creep strains $\varepsilon^{cr}$, shrinkage strains $\varepsilon^{sh}$ and thermal strains $\varepsilon^{th}$ due to the generated heat during cement hydration. It can be written that:

$$\varepsilon=\varepsilon^{el}+\varepsilon^{p}+\varepsilon^{c} \tag{7.2}$$

with the irrecoverable strains $\varepsilon^{c}$ given as:

$$\varepsilon^{c}=\varepsilon^{cr}+\varepsilon^{sh}+\varepsilon^{th} \tag{7.3}$$

Each of those components will be described in detail in the following sections.

### 7.2.2 Yield Function and Plastic Potential in compression

The yield surface used to enclose the elastic region and to describe the onset of plastic deformation of the shotcrete in multi-axial compression is based on the results of biaxial tests performed by Kupfer & Gerstle (1973) and was originally formulated by Chen & Chen (1975). In the current development, this yield surface is applied to describe shotcrete behaviour in compression and is given by the following equation:

$$F_c=J^2+A_c\,p-\tau_c^2=0 \tag{7.4}$$

where

$$A_c=\frac{e^2-1}{2e-1}\,f_c \tag{7.5}$$

and

$$\tau_c^2=\frac{2e-e^2}{3\,(2e-1)}\,f_c^2 \tag{7.6}$$

The parameter $e$ is a dimensionless biaxial strength parameter and accounts for the fact that the strength of concrete under biaxial compression ($\sigma_1=\sigma_2$) is up to 25 % higher than under uniaxial conditions. Meschke (1996) proposed a value of $e=1.16$. For geometric reasons regarding the elliptical shape of the adopted yield surface in the biaxial stress space, this parameter $e$ is limited to the following range:

$$1<e<e_{max}=\frac{1+\sqrt{3}}{2} \tag{7.7}$$

Fig. 7.1 shows the two yield surfaces for both compression and tension, where the compression surface takes an elliptical shape in the biaxial stress space (on the left) and a parabolic one in the $J$-$p$ space (on the right). Experimental data justify that these shapes are appropriate to describe the behaviour of concrete reasonably well (Chen & Chen, 1975).

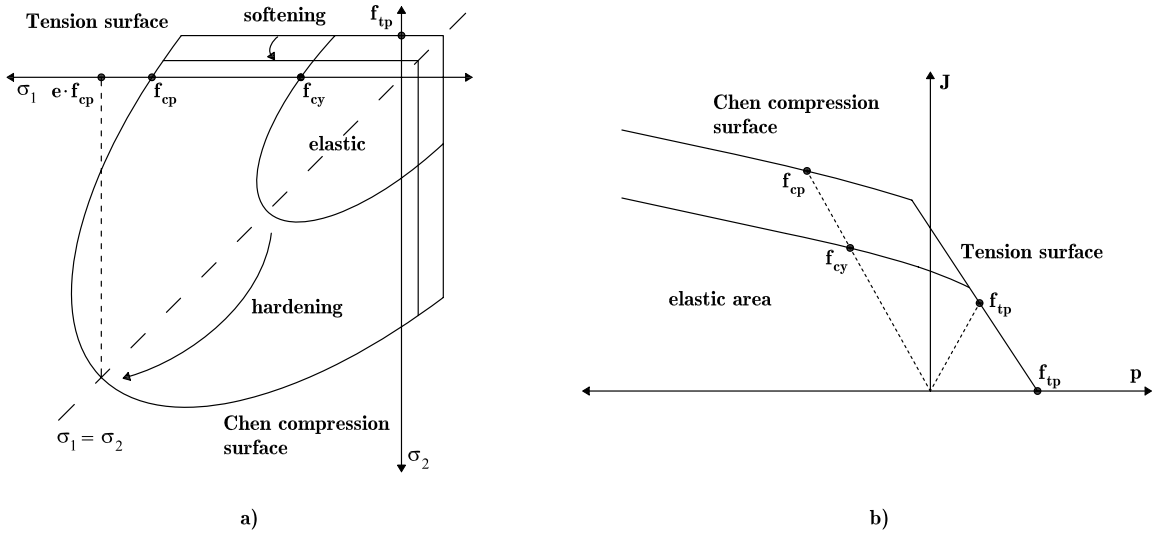



Figure 7.1: Compression and tension yield surfaces in a) the biaxial stress space and b) the $J$-$p$ space

Since equation 7.4 is independent of the Lode angle $\theta$, the compression surface plots as a circle in the deviatoric plane. Furthermore, the size of the yield surface is governed by the parameter $f_c$, which represents an "equivalent uniaxial compressive strength" and is a function of the plastic strains and time. Hence, the surface expands and contracts isotropically according to plastic strain hardening and softening rules that will be described in detail in Section 7.3.1. Furthermore, the surface also moves due to the increase in strength with time, as will be presented later in Section 7.4.1. In the absence of detailed experimental data for a realistic characterisation of the volumetric behaviour of shotcrete, an associated flow rule is adopted and therefore the yield surface $F_c$ equals the plastic potential $P_c$, so it can be written:

$$F_c\left(p, J\right) = P_c\left(p, J\right) \tag{7.8}$$

### 7.2.3 Yield Function and Plastic Potential in tension

For the numerical description of the quasi-brittle material behaviour of shotcrete in tension, a modified Rankine criterion after Thomée (2005) is used, see Fig. 7.1. Contrary to the original Rankine failure criterion, the adopted yield surface includes hyperbolic rounding near the apex in order to avoid numerical problems associated with the singularity present in the

original criterion. The tension yield surface can be written as:

$$F_t = p + \left[ \left( \frac{2J}{\sqrt{3}} sin\left(\theta + \frac{2\pi}{3}\right)\right)^n + (af_t)^n \right]^{\frac{1}{n}} - f_t = 0 \tag{7.9}$$

Fig. 7.2 represents a close up view of the apex zone of the yield function in the biaxial stress space (on the left) and the $J$-$p$ space (on the right), indicating the difference between the original Rankine criterion and the modified tension yield surface adopted in the current model formulation.

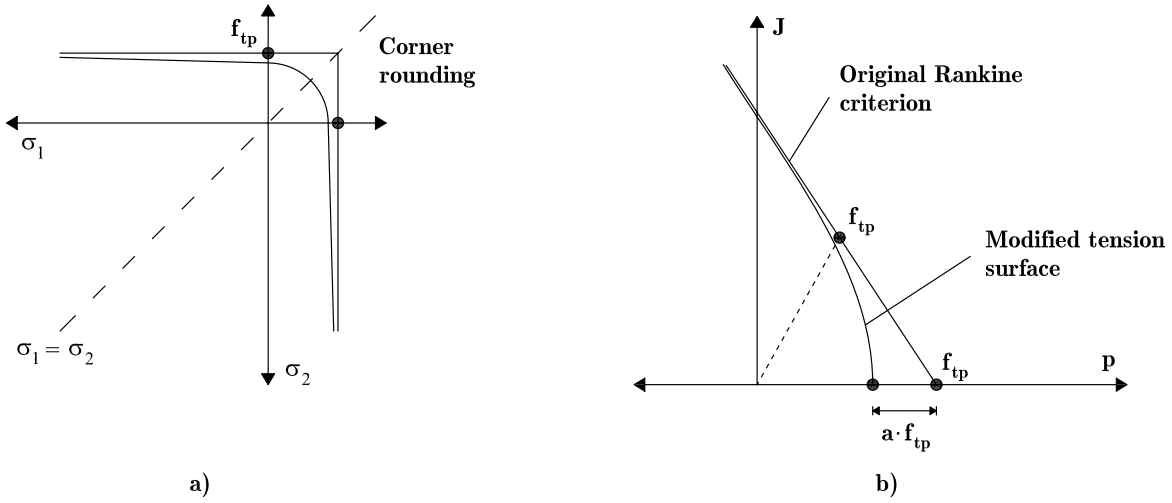



Figure 7.2: Apex rounding for tension surface in a) the biaxial stress space and b) the $J$-$p$ space

The parameter $a$ is the apex tolerance and describes the distance between the two intersection points of the original and the modified Rankine yield surface with the hydrostatic axes, whereas the rounding of the surface is controlled by the parameter $n$. Furthermore, the above presented yield function depends on the Lode angle $\theta$ and plots as a triangle in the deviatoric plane. The corners of this triangle are treated in a similar manner to the other yield surfaces implemented in ICFEP with corners in the deviatoric plane. A rounding parameter $CORTOL$ is introduced, which represents a corner tolerance for $\theta = +30°$ (i.e. triaxial extension). Within this corner tolerance, the partial derivatives of the yield function and the plastic potential are rounded in a linear way. Similar to the compression surface, the parameter $f_t$ represents an "equivalent uniaxial tensile strength" and varies with plastic strains and time, resulting in isotropic expansion and contraction of the surface in the general stress space. The mathematical description of these hardening and softening rules is presented in Section 7.3.2.

In order to avoid a stress path going beyond the yield surface during an analysis, which would result in a forbidden stress state, another tolerance parameter had to be introduced for the apex region. The parameter $TIPTOL$ denotes a vertical limit, which is linked to the

current intersection point of the modified tension surface with the hydrostatic axes, as can be seen in Fig. 7.3.

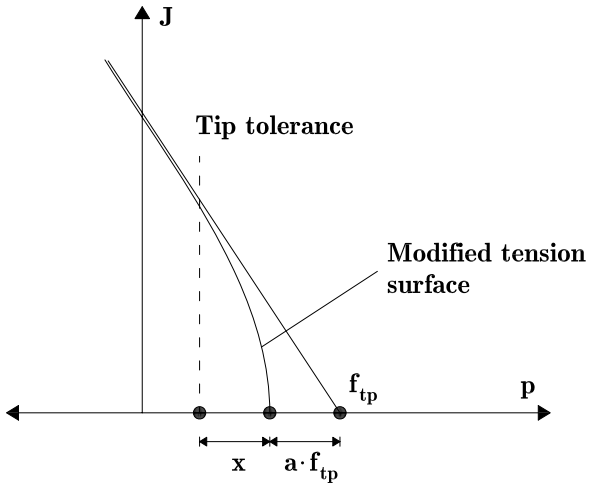



Figure 7.3: Tip tolerance for apex region of tension surface

For the tensile peak strength it can be written:

$$x = f_{tp}\,(1-a)\,TIPTOL \tag{7.10}$$

Therefore, this tip limit is moving during plastic strain hardening/softening and the increase in tensile strength. If during the sub-stepping algorithm of an analysis the mean stress $p$ appears to go past this limit, the stress point is forced to stick to the tip limit by setting any further changes in mean stress $\Delta p$ to zero.

As in the case of the compression surface, associated conditions are assumed and it can be written:

$$F_t\,(p, J, \theta) = P_t\,(p, J, \theta) \tag{7.11}$$

## 7.3 Hardening and softening rules

The basis for the non-linear and independent evolution of the two implemented yield surfaces in the general stress space in the course of plastic deformation are uniaxial stress-strain curves for concrete in compression and tension. Since the strain-hardening concept is applied, the chosen hardening parameters are a function of the plastic strain history. If the compression surface is the active yield surface, hardening and softening is controlled by the minor principal plastic strain $\varepsilon_3^p$. In the case of the tension surface being the active surface, the motion of the yield surface is governed by the major principal plastic strain $\varepsilon_1^p$. However, as the current model also includes the time-dependent behaviour of shotcrete, the choice of a proper hardening parameters used in the model formulation is not straightforward. Fig. 7.4 illustrates the problem:

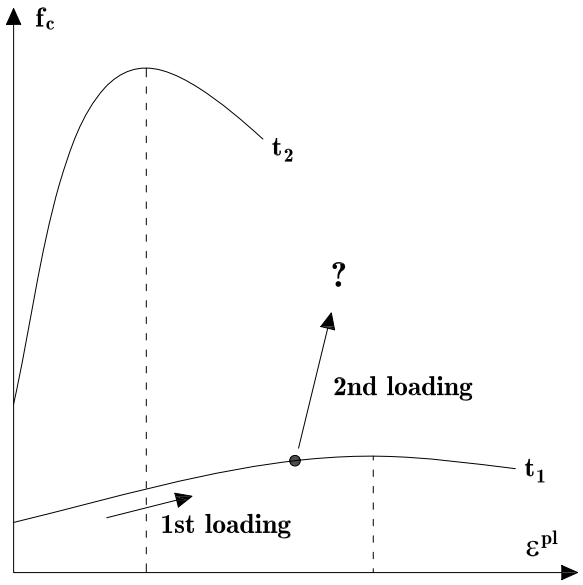



Figure 7.4: Strain hardening concept for time-dependent matrials

From published data in the literature it appears that the material behaviour of sprayed concrete becomes more and more brittle with curing time, resulting in a decrease in the strain at peak strength. Assume a shotcrete sample is loaded up to a certain compressive plastic strain (less than that required to reach peak strength, see Fig. 7.4) at an early age $t_1$ . After loading, a certain amount of time $\Delta t$ elapses (without any further straining) and the loading is then continued at time $t_2$. During the elapsed time $\Delta t$ the compressive peak strength increases but the compressive strain associated with this new peak strength would have reduced such that, for the further stress path, it is not clear where the stress point would touch the yield surface again beyond peak. To overcome this dilemma it was decided to adopt normalised stress-strain curves for both compression and tension, where the normalisation is performed in terms of the peak strengths and the plastic peak strains at time $t$. The following two sections describe the mathematical functions of the hardening and softening rules adopted in the current model.

### 7.3.1 Compression

As mentioned above, the hardening and softening rule in compression follows a uniaxial stress-strain curve where the normalised equivalent uniaxial compressive strength is given as:

$$f_{c,n} = \frac{f_c}{f_{cp}\left(t\right)} \tag{7.12}$$

Similarly, the minor principal plastic strain $\varepsilon_3^p$ is normalised by the peak compressive plastic strain at time $t$, $\varepsilon_{cp}^p\left(t\right)$, such that the compressive hardening parameter $H_c$ can be written as:

$$H_c = \frac{\varepsilon_3^p}{\varepsilon_{cp}^p\left(t\right)} \tag{7.13}$$

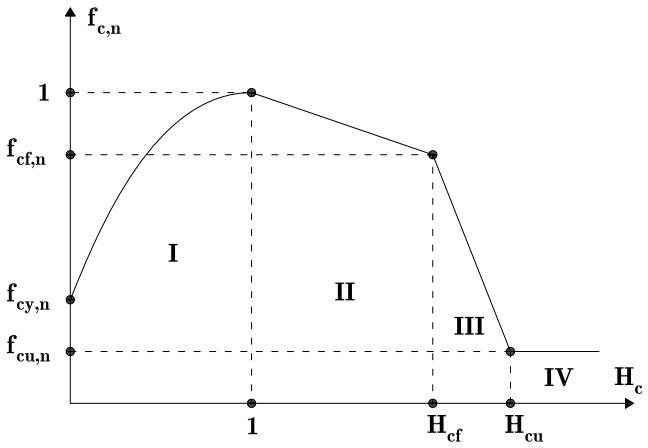



Figure 7.5: Normalised stress-strain curve for shotcrete in compression

Fig. 7.5 shows the normalised stress-strain curve that is applied in the current model formulation, consisting of 4 different zones for hardening and softening:

*Zone I:* $0 \leq H_c \leq 1$

As soon as the current stress state touches the yield surface the behaviour becomes elasto-plastic and the normalised stress-strain curve follows a parabolic hardening, starting from the normalised compressive yield stress $f_{cy,n}$ up to peak at unity. The following equation is adopted:

$$f_{c,n} = f_{cy,n} + (1 - f_{cy,n}) \left(2H_c - H_c^2\right) \tag{7.14}$$

*Zone II:* $1 < H_c \leq H_{cf}$

If any further straining occurs after peak, a linear softening branch is applied until failure of the shotcrete is reached at the normalised compressive failure strength $f_{cf,n}$. At this point, in a real compression test the shotcrete is assumed to be completely crushed and stresses would reduce to zero. The equation for the adopted softening part is given as:

$$f_{c,n} = 1 + \frac{f_{cf,n} - 1}{H_{cf} - 1} (H_c - 1) \tag{7.15}$$

*Zone III:* $H_{cf} < H_c \leq H_{cu}$

For numerical purposes a normalised ultimate compressive strength $f_{cu,n}$ is introduced to describe the linear reduction in stresses after failure given by:

$$f_{c,n} = f_{cf,n} + \frac{f_{cu,n} - f_{cf,n}}{H_{cu} - H_{cf}} (H_c - H_{cf}) \tag{7.16}$$

*Zone IV:* $H_c > H_{cu}$

In this zone no further changes in stress occur with further straining and therefore the normalised compressive stress remains constant.

$$f_{c,n} = f_{cu,n} \tag{7.17}$$

In the equations 7.14 to 7.17 five dimensionless material parameters are needed for the mechanical description of the hardening and softening behaviour in compression, which are based on the values of hardened shotcrete at the age of 28 days and are assumed to be constant with time. They are the following:

Normalised compressive yield stress:

$$f_{cy,n} = \frac{f_{cy,28}}{f_{cp,28}} \tag{7.18}$$

Normalised compressive failure strength:

$$f_{cf,n} = \frac{f_{cf,28}}{f_{cp,28}} \tag{7.19}$$

Normalised compressive ultimate strength:

$$f_{cu,n} = \frac{f_{cu,28}}{f_{cp,28}} \tag{7.20}$$

Normalised compressive failure strain:

$$H_{cf} = \frac{\varepsilon^p_{cf,28}}{\varepsilon^p_{cp,28}} \tag{7.21}$$

Normalised compressive ultimate strain:

$$H_{cu} = \frac{\varepsilon^p_{cu,28}}{\varepsilon^p_{cp,28}} \tag{7.22}$$

The material parameters for the implemented stress-strain curve depend on the type of shotcrete used and can be estimated from experimental uniaxial tests or published data. It should be emphasized that a plastic strain hardening concept is applied and the adopted stress-strain curve is formulated for plastic strains. Therefore, the total peak strain at 28 days, $\varepsilon_{cp,28}$, needs to be reduced by the elastic component in order to obtain the plastic peak strain $\varepsilon^p_{cp,28}$, as written below:

$$\varepsilon^p_{cp,28} = \varepsilon_{cp,28} - \frac{f_{cp,28}}{E_{28}} \tag{7.23}$$

where $E_{28}$ is the Young's modulus for hardened shotcrete at 28 days.

For a correct description of the softening part regarding mesh dependency it is recommended to estimate the normalised compressive failure strain $H_{cf}$ from the compressive fracture energy $G_c$, as highlighted in the previous Chapter 6. Fig. 7.6 illustrates the basic principle adopted for the current model:

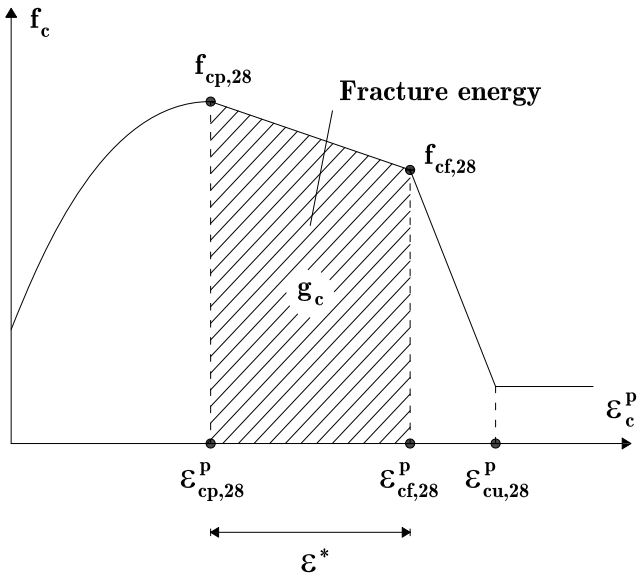



Figure 7.6: Fracture energy concept for shotcrete in compression

In a uniaxial compression test for hardened shotcrete at 28 days, it is assumed that the complete compressive fracture energy $G_c$ is the area below the stress-displacement curve from peak until failure, where the shotcrete is believed to be completely crushed. With the help of the equivalent length $l_{eq}$ of the finite element it is possible to transform this stress-displacement relation into a typical plastic stress-strain curve and it can be written as:

$$g_c = \frac{G_c}{l_{eq}} = \frac{f_{cp,28} + f_{cf,28}}{2}\,\varepsilon^* \tag{7.24}$$

Rearrangement of this equation leads to:

$$\varepsilon^* = \frac{2\,G_c}{l_{eq}\,(f_{cp,28} + f_{cf,28})} \tag{7.25}$$

The plastic failure strain at 28 days as a softening parameter is therefore dependent on the element size and can be obtained as:

$$\varepsilon^p_{cf,28} = \varepsilon^p_{cp,28} + \varepsilon^* \tag{7.26}$$

Finally, the normalised plastic failure strain $H_{cf}$ is then calculated according to equation 7.21. Since the ultimate plastic compressive strain $\varepsilon^p_{cu,28}$ is of purely numerical purpose, it is convenient to choose the magnitude of this limit strain to be close to the plastic failure strain $\varepsilon^p_{cf,28}$. However, in order to avoid the so called "snap-back behaviour" (Thomée, 2005) in the total stress-strain curve which is caused by an excessive softening rate (see Fig. 7.7), it is necessary that the following condition is fulfilled:

$$\varepsilon^p_{cu,28} \geq \varepsilon^p_{cf,28} + \bar{\varepsilon} \tag{7.27}$$

with

$$\bar{\varepsilon} = \frac{f_{cf,28} - f_{cu,28}}{E_{28}} \tag{7.28}$$

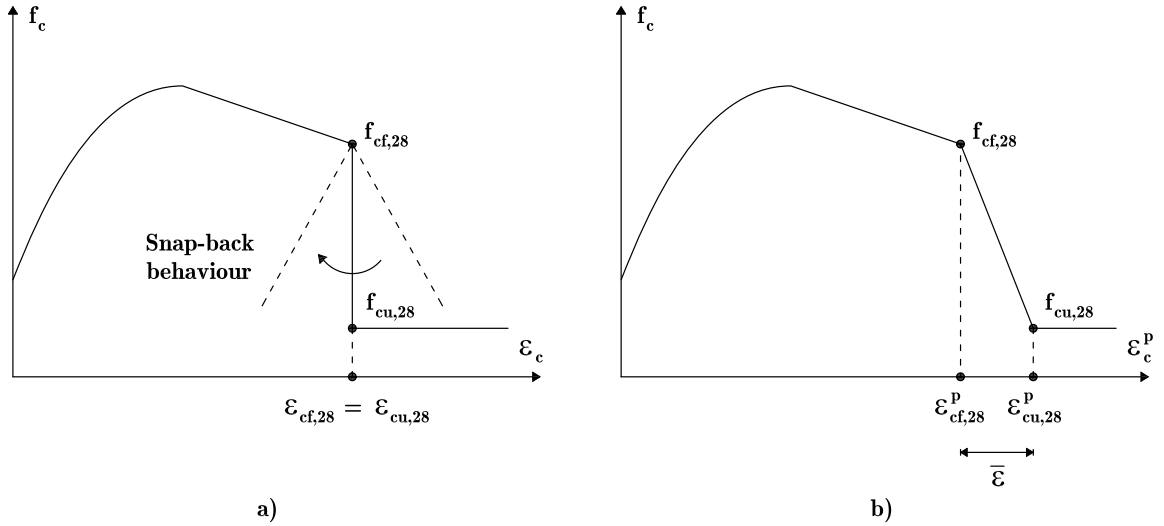



Figure 7.7: a) Snap back behaviour for total stress-strain curve, b) Limited ultimate plastic compressive strain

A certain limitation exists for the choice of the ultimate compressive strength $f_{cu,28}$ due to numerical reasons, as illustrated for the biaxial stress space in Fig. 7.8.

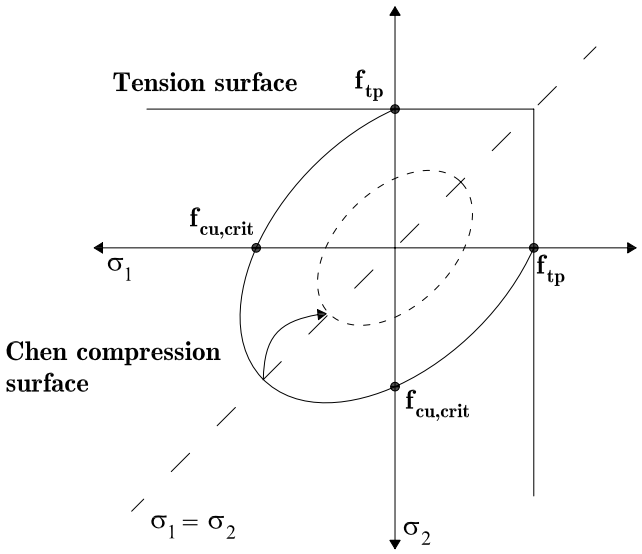



Figure 7.8: Critical value of the ultimate compressive strength for hardened concrete at 28 days

Although the basic idea for introducing this ultimate strength parameter is to reduce concrete stresses to a value close to zero after crushing failure, a critical value $f_{cu,crit}$ is established in oder to avoid the contraction of the compressive yield surface below the tension

yield surface. Otherwise this would mean that even the purely tensile material behaviour would be governed by the compression yield surface, which is an unacceptable scenario (see dashed ellipse in Fig. 7.8). Therefore, the following condition derived from the compressive yield surface given in equation 7.4 for $J = 0$ and depending on the maximum tensile stress, which is the tensile peak strength at 28 days, $f_{tp,28}$, and the biaxial strength parameter $e$ has to be fulfilled:

$$f_{cu,28} \geq f_{cu,crit} = 3\, f_{tp,28}\, \frac{e^2 - 1}{2e - e^2} \tag{7.29}$$

The same condition applies also to the compressive yield stress and it can be written in a similar manner:

$$f_{cy,28} \geq f_{cy,crit} = 3\, f_{tp,28}\, \frac{e^2 - 1}{2e - e^2} \tag{7.30}$$

### 7.3.2 Tension

For the tension surface, a similar approach as for the compression surface is adopted and the normalised equivalent uniaxial tensile stress results in:

$$f_{t,n} = \frac{f_t}{f_{tp}\,(t)} \tag{7.31}$$

After normalizing the major principal plastic strain $\varepsilon_1^p$ the tensile hardening parameter is given as:

$$H_t = \frac{\varepsilon_1^p}{\varepsilon_{tp}^p\,(t)} \tag{7.32}$$

The uniaxial tensile plastic peak (or cracking) strain $\varepsilon_{tp}^p\,(t)$ is assumed to develop with time in the same way as the compressive plastic peak strain and is given as:

$$\varepsilon_{tp}^p\,(t) = \delta\, \varepsilon_{cp}^p\,(t) \tag{7.33}$$

where $\delta$ represents a constant proportion between the plastic tensile and compressive peak strains for hardened shotcrete at 28 days:

$$\delta = \frac{\varepsilon_{tp,28}^p}{\varepsilon_{cp,28}^p} \tag{7.34}$$

Similar to the compression hardening and softening, the complete normalised stress-strain curve in tension is divided into 3 different zones.

*Zone I* $\quad 0 \leq H_t \leq 1$

Although concrete tests under tension show almost linear elastic behaviour before peak, a yield stress of about 90% of the tensile peak strength can be identified (Feenstra, 1993). Therefore a small parabolic hardening zone is introduced given by the following equation:

$$f_{t,n} = f_{ty,n} + (1 - f_{ty,n})\left(2H_t - H_t^2\right) \tag{7.35}$$

One normalised material parameter is used to describe mathematically the onset of yielding, based on the ratio between the yield stress and the tensile peak strength for hardened shotcrete at 28 days. The normalised tensile yield stress can be written as:

$$f_{ty,n} = \frac{f_{ty,28}}{f_{tp,28}} \tag{7.36}$$

For the post-peak behaviour of shotcrete two different options exist within the smeared crack concept of the current constitutive model, which will be described in detail in the following sections.

#### 7.3.2.1 Option A - Linear softening

Zone II and III of option A are characterised by linear softening after peak and followed by a constant stress in the ultimate stress range, as can be seen in Fig. 7.9.

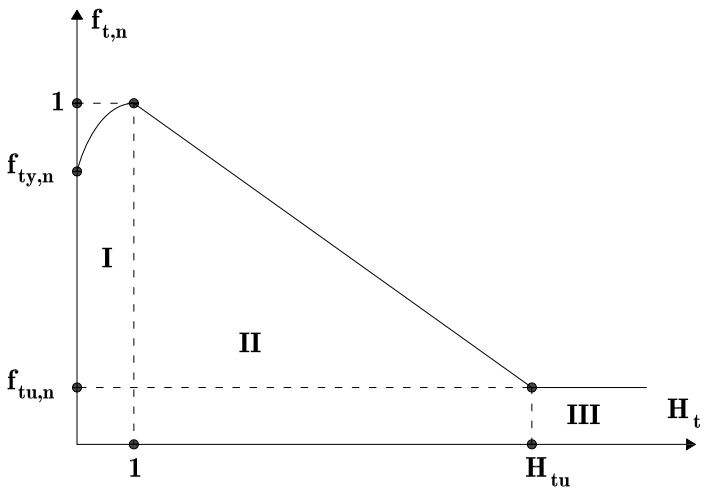



Figure 7.9: Normalised hardening and softening curve in tension for option A

*Zone II:* $1 < H_t \leq H_{tu}$
After initiation of cracking at the peak strength, tensile strength reduce with further straining in a linear way until an ultimate tensile strength is reached. The equation for the linear softening branch in tension can be written as:

$$f_{t,n} = 1 + \frac{f_{tu,n} - 1}{H_{tu} - 1} \, (H_t - 1) \tag{7.37}$$

*Zone III:* $H_t > H_{tu}$
Once the ultimate tensile stress is reached in Zone III, there is no further change in stresses with continuing straining and therefore the normalised tensile strength remains constant.

$$f_{t,n} = f_{tu,n} \tag{7.38}$$

Two normalised material parameters control this linear post peak behaviour, which are:

Normalised ultimate tensile strength:

$$f_{tu,n} = \frac{f_{tu,28}}{f_{tp,28}} \tag{7.39}$$

Normalised tensile ultimate strain:

$$H_{tu} = \frac{\varepsilon^p_{tu,28}}{\varepsilon^p_{tp,28}} \tag{7.40}$$

In order to avoid the spurious mesh dependency that is well known to occur for materials that undergo tensile strain softening, similar to the compression behaviour, a fracture energy based approach is proposed to estimate the softening parameter involved in this model. Fig. 7.10 shows the basic principle for a uniaxial tension test for hardened shotcrete at 28 days.

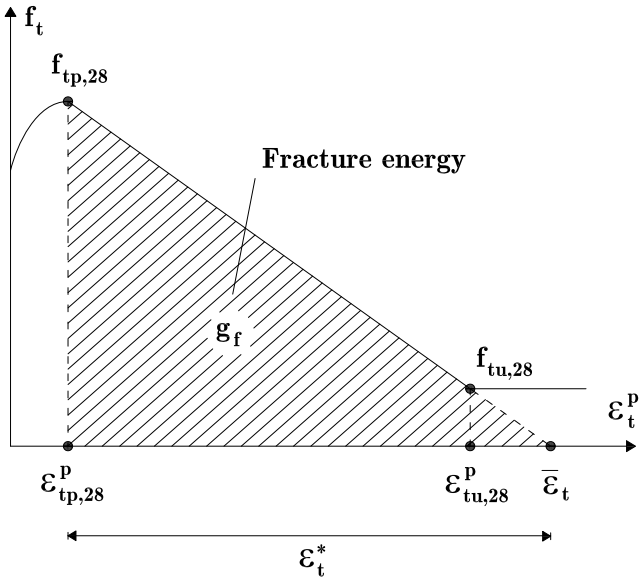



Figure 7.10: Fracture energy concept for shotcrete in tension with linear softening

The total fracture energy in tension $G_f$ needed for complete crack opening is represented as the area below the curve from peak until zero stress. Mesh dependency is now overcome by regularising the tensile stress-crack-opening relation with the equivalent length of the finite element $l_{eq}$. This procedure results in the following expression:

$$g_f = \frac{G_f}{l_{eq}} = \frac{f_{tp,28}\left(\bar{\varepsilon}_t - \varepsilon^p_{tp,28}\right)}{2} \tag{7.41}$$

where $\bar{\varepsilon}_t$ is the plastic tensile strain at zero stress and can be obtained by rearrangement as:

$$\bar{\varepsilon}_t = \varepsilon^p_{tp,28} + \varepsilon^*_t \tag{7.42}$$

The distance between the peak strain $\varepsilon^p_{tp,28}$ and $\bar{\varepsilon}_t$ is given as:

$$\varepsilon^*_t = \frac{2G_f}{l_{eq}\, f_{tp,28}} \tag{7.43}$$

Consequently, the plastic ultimate strain for hardened shotcrete in tension can be estimated as:

$$\varepsilon^p_{tu,28} = \varepsilon^p_{tp,28} + \frac{2G_f\,(f_{tp,28} - f_{tu,28})}{l_{eq} f^2_{tp,28}} \tag{7.44}$$

Similar to the condition in compression, the plastic stress-strain curve must not be too steep otherwise the total stress-strain relation would result in unstable material behaviour. For the tensile linear softening rate the following condition has to be fulfilled:

$$\varepsilon^p_{tu,28} \geq \varepsilon^p_{tp,28} + \hat{\varepsilon}_t \tag{7.45}$$

with

$$\hat{\varepsilon}_t = \frac{f_{tp,28} - f_{tu,28}}{E_{28}} \tag{7.46}$$

#### 7.3.2.2 Option B - Exponential softening

In contrast to the softening behaviour in the previous option, in option B the gradual decrease in strength with crack propagation in Zone II is described by an exponential softening law that is followed again by a constant strength regime in Zone III, as indicated in Fig. 7.11.

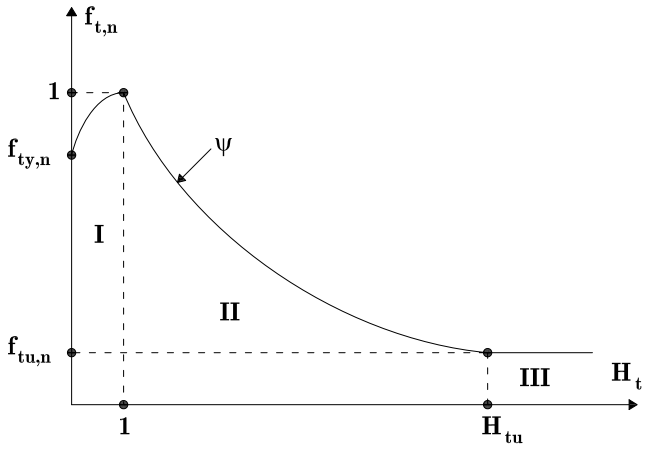



Figure 7.11: Normalised hardening and softening curve in tension for option B

*Zone II:* $1 < H_t \leq H_{tu}$

The mathematical expression for the reduction in tensile strength with plastic straining in this zone is given by the following equation:

$$f_{t,n} = exp\,[-\psi\,(H_t - 1)] \tag{7.47}$$

where $\psi$ is the normalised softening parameter that governs the decay in tensile strength. This exponential reduction in tensile strength continues until an ultimate tensile strength is reached and hence the normalised tensile ultimate strain can be calculated from:

$$H_{tu} = 1 - \frac{\ln\left(\frac{f_{tu,28}}{f_{tp,28}}\right)}{\psi} \tag{7.48}$$

*Zone III:* $H_t > H_{tu}$

As in option A, Zone III of option B shows a material behaviour with constant strength controlled by the ultimate tensile strength that can be chosen to be close to zero.

$$f_{t,n} = f_{tu,n} \tag{7.49}$$

The normalised ultimate tensile strength $f_{tu,n}$ as a material parameter can be obtained from equation 7.39.

Regarding the choice of the proper softening parameter $\psi$ it is recommended to estimate this parameter again from the fracture energy of hardened shotcrete at 28 days, $G_f$. By integrating the plastic stress-strain curve from peak strain to infinity the area below the curve, which represents the fracture energy, is obtained, as can be seen in Fig. 7.12.

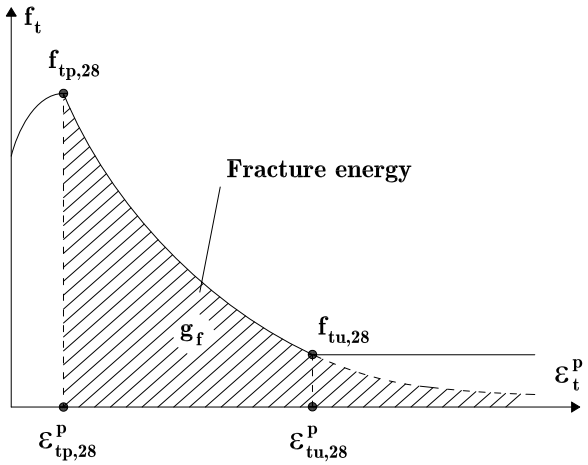



Figure 7.12: Fracture energy concept for shotcrete in tension with exponential softening

It can be written:

$$g_f = \frac{G_f}{l_{eq}} = \int_{\varepsilon^p_{tp,28}}^{+\infty} f_{tp,28}\, exp\left[-\frac{1}{\kappa}\left(\varepsilon^p_t - \varepsilon^p_{tp,28}\right)\right] \mathrm{d}\varepsilon^p_t \tag{7.50}$$

where $\kappa$ is a softening parameter depending on the fracture energy $G_f$ and the equivalent length of the finite element $l_{eq}$. Solving the integral and rearranging results in:

$$\kappa = \frac{G_f}{l_{eq}\, f_{tp,28}} \tag{7.51}$$

In the present constitutive model a normalised hardening and softening rule is adopted and therefore the normalised softening parameter from equation 7.47 can be written as:

$$\psi = \frac{1}{\kappa}\, \varepsilon^p_{tp,28} = \frac{l_{eq}\, f_{tp,28}\, \varepsilon^p_{tp,28}}{G_f} \tag{7.52}$$

Snap back behaviour of the total stress strain curve can be avoided by the following condition derived from the derivative of the softening curve in Zone II taking into account the elastic deformation:

$$\psi \leq \frac{\varepsilon^p_{tp,28}\, E_{28}}{f_{tp,28}} \tag{7.53}$$

## 7.4 Time-dependent material behaviour

As mentioned in the introduction to this chapter, the current constitutive model for shotcrete accounts for time-dependent material behaviour. This means that the main material parameters used in the formulation of the elasto-plastic model are developing gradually with time during cement hydration. Due to the increase in the strength parameters both in compression and tension the adopted yield surfaces are not only moving in stress space with plastic strain hardening or softening, but also expand simultaneously with time. Although cement hydration is a relatively long process, it is assumed that in an analysis, for hardened shotcrete after 28 days no further change in material properties takes place. Therefore:

- Shotcrete age $\leq$ 28 days $\rightarrow$ Changing material properties
- Shotcrete age $>$ 28 days $\rightarrow$ Constant material properties

The inclusion of time-dependent material behaviour in a numerical analysis requires the specification of the initial age of the shotcrete at installation $t_o$. This input parameter may be chosen by the user but a minimum age of $t_o = 1$ h has been adopted in this thesis. Finally, constitutive laws that describe the evolution of creep, shrinkage and temperature deformation were developed and will be discussed in detail in the following sections.

### 7.4.1 Increase in stiffness and strength with time

*i) Young's modulus*

For the development of the stiffness with time a well established equation from CEB-FIP

Model Code (1990) has been adopted within the current model formulation. It is given by:

$$E(t) = E_{28} \left[ exp\left( s \left( 1 - \sqrt{\frac{t_{28}}{t}} \right) \right) \right]^{0.5} \tag{7.54}$$

where $E_{28}$ is the Young's modulus for hardened shotcrete at 28 days and $t_{28}$ is the time at 28 days in the corresponding time units used in the analysis. The cement parameter $s$ usually takes a value smaller than 1 and controls how fast the stiffness increases with time, as indicated in Fig. 7.13.

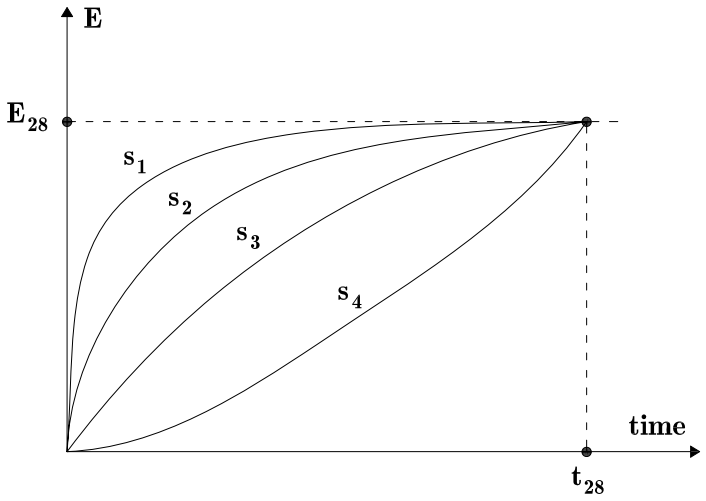



Figure 7.13: Increase in stiffness with time for various values of cement parameter $s$

Furthermore, a smaller value of $s$ results in a faster increase in stiffness with time ($s_1 < s_2 < s_3 < s_4 < 1$). This curve predicts generally a high initial increase in stiffness for the first hours after shotcrete installation, which becomes less pronounced with increasing time until it reaches the full stiffness of hardened shotcrete $E_{28}$ at $t_{28}$. In the case of absence of any experimental data for shotcrete the following values for $s$ are provided by the CEB-FIP Model Code (1990):

- $s = 0.2$ for rapid hardening high strength cements RS
- $s = 0.25$ for normal and rapid hardening cements N and R
- $s = 0.38$ for slowly hardening cements SL

The incremental stiffness formulation needed for the numerical implementation is given as:

$$\dot{E}(t) = \frac{d\,E(t)}{d\,t} = \frac{E_{28}\,t_{28}\,s\,exp\left( s \left( 1 - \sqrt{\frac{t_{28}}{t}} \right) \right)^{0.5}}{\sqrt{t_{28}}\,t^{\frac{3}{2}}} \tag{7.55}$$

The Poisson's ratio $\mu$ is taken as a constant value and any possible time-dependency is therefore ignored.

*ii) Compressive strength*

The hardening and softening curve for compression presented in Section 7.3.1 requires for its normalisation knowledge of the development of the compressive peak strength with time. Similar to the increase in stiffness, an expression from the CEB-FIP Model Code (1990) was chosen, which yields:

$$f_{cp}(t) = f_{cp,28}\, exp\left[s\left(1 - \sqrt{\frac{t_{28}}{t}}\right)\right] \tag{7.56}$$

where $f_{cp,28}$ is the compressive peak strength at 28 days and $s$ a cement parameter, which is of the same nature as the one introduced for the increase in stiffness with time. The development of the compressive yield, failure and ultimate strength is linked to the compressive peak strength via the constant ratios given in equations 7.18 to 7.20. Therefore, these strength values develop in the same manner as the compressive peak strength, as can be seen in Fig. 7.14.

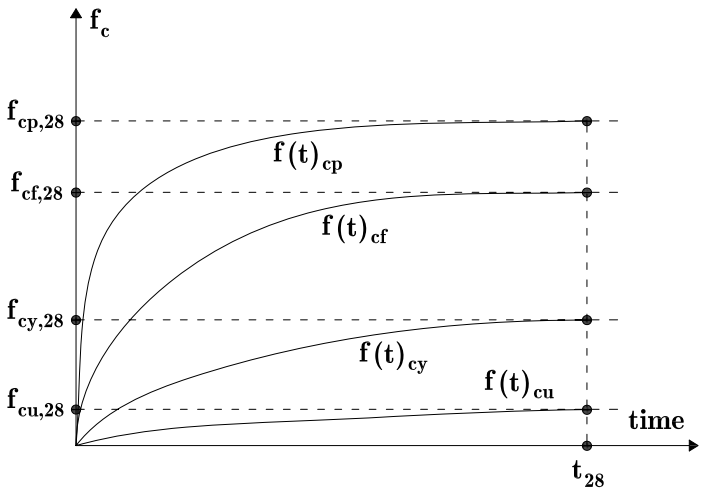



Figure 7.14: Qualitative increase in compressive yield, peak, failure and ultimate strength with time

*iii) Tensile strength*

A similar equation as presented above for the development of the compressive peak strength with time applies also to the increase in the tensile peak strength with time. It can be written as:

$$f_{tp}(t) = f_{tp,28}\, exp\left[s\left(1 - \sqrt{\frac{t_{28}}{t}}\right)\right] \tag{7.57}$$

where $s$ is the same cement parameter already adopted for the compressive strength parameters.

### 7.4.2 Shotcrete deformability at early ages

As explained in Chapter 5, young shotcrete appears to have the ability to withstand higher deformations at early age loading than hardened shotcrete. This fact is taken into account in the current constitutive model by making the plastic compressive peak strains vary with time according to the following equation:

$$\varepsilon_{cp}^{p}(t) = A \left[\ln\left(\frac{t}{t_1}\right)\right]^{B} + C \tag{7.58}$$

where $t_1$ is the time of 1 hour in the corresponding time unit. The constants $A$, $B$ and $C$ should be chosen to fit the experimental test data. For the analysis presented in this thesis this was achieved by using the plastic uniaxial compressive peak strain $\varepsilon_{cp,t_1}^{p}$ at time $t_1 = 1\,\text{h}$, the plastic uniaxial compressive peak strain $\varepsilon_{cp,t_2}^{p}$ at an intermediate time $t_2$ and the plastic uniaxial compressive peak strain for hardened shotcrete at 28 days, $\varepsilon_{cp,28}^{p}$. $A$, $B$ and $C$ are then obtained as:

$$A = \frac{\varepsilon_{cp,28}^{p} - \varepsilon_{cp,t_1}^{p}}{\left[\ln\left(\frac{t_{28}}{t_1}\right)\right]^{B}} \quad \text{and} \quad B = \frac{\ln\left(\frac{\varepsilon_{cp,t_2}^{p} - \varepsilon_{cp,t_1}^{p}}{\varepsilon_{cp,28}^{p} - \varepsilon_{cp,t_1}^{p}}\right)}{\ln\left(\frac{\ln\left(\frac{t_2}{t_1}\right)}{\ln\left(\frac{t_{28}}{t_1}\right)}\right)} \quad \text{and} \quad C = \varepsilon_{cp,t_1}^{p} \tag{7.59}$$

Fig. 7.15 illustrates equation 7.58 and the involved material parameters. The reason for using the intermediate plastic uniaxial compressive peak strain at time $t_2$ is that it allows the control of the rate of decay in plastic uniaxial compressive peak strains with time. A convenient choice for the intermediate time $t_2$ could be for instance 24 h after shotcrete installation.

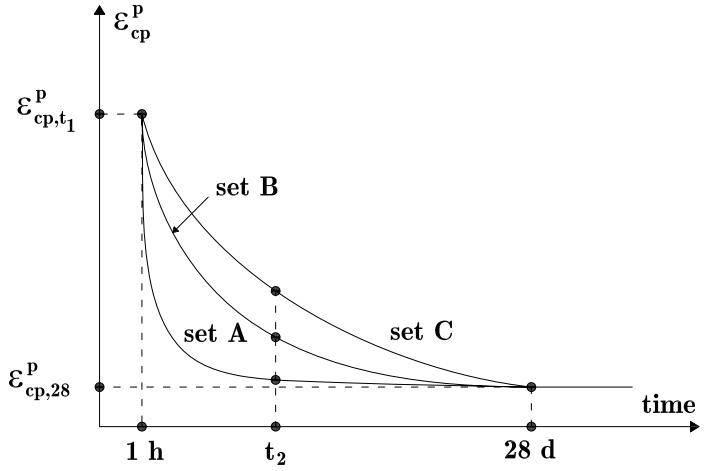



Figure 7.15: Development of plastic uniaxial compressive peak strains with time

Set A would represent a shotcrete having a very brittle type of material behaviour, where

the compressive peak strains reduce quickly within the first hours after casting to an almost constant level, whereas, set C indicates a softer material response. It should be noted that the above curve (equation 7.58) describes the development of the plastic uniaxial compressive peak strains and for model calibration the time-dependent elastic strain component has to be taken into account. In this respect it is noted that that:

$$\varepsilon_{cp}^{p}(t) = \varepsilon_{cp}(t) - \frac{f_{cp}(t)}{E(t)} \tag{7.60}$$

As mentioned in Section 7.3.2, the plastic uniaxial tensile peak strains $\varepsilon_{tp}^{p}(t)$ are assumed to develop with time in the same manner as the plastic uniaxial compressive peak strains, being related to each other via the constant ratio $\delta$ (see equation 7.33).

### 7.4.3 Creep and relaxation

Chapter 5 highlighted the importance of the phenomena of creep and relaxation for young shotcrete and its influence in tunnelling. In the current constitutive model a creep law is proposed that is based on the rheological body illustrated in Fig. 7.16.

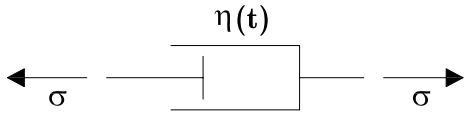



Figure 7.16: Time-dependent rheological body for creep

In the uniaxial case the deformation due to creep is described by a single dashpot, which is characterised by a time-dependent viscosity $\eta(t)$. The mathematical expression for the irrecoverable creep strains (either compressive or tensile) based on Neville (1970) is:

$$\varepsilon^{cr} = \sigma \frac{t - t_o}{\eta(t)} \tag{7.61}$$

where $t_o$ denotes the starting age of the shotcrete and $\sigma$ is the applied compressive or tensile stress. Fig. 7.17 shows the development of creep strains due to loading at time $t_o$. The instantaneous deformation at loading consists of elastic and plastic strain components, followed by the increasing creep strains with time. Equation 7.61 implies further that the loading of shotcrete begins immediately after its installation at time $t_o$ and creep strains start to occur, which can be considered as realistic in the application for tunnel construction.

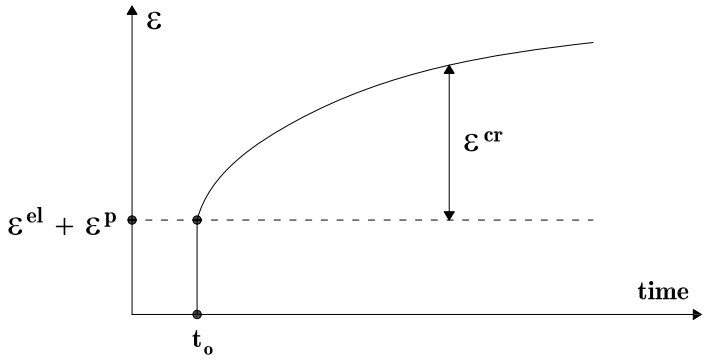



Figure 7.17: Development of creep strains with time upon loading at time $t_o$

The time-dependent viscosity function proposed in the current model can be written as:

$$\eta(t) = \eta_o \left(\frac{t}{t_1}\right)^n \tag{7.62}$$

The parameter $\eta_o$ is the starting viscosity at an age of $t = 1\,\text{h}$ and $n$ is a viscosity exponent that governs the increase in viscosity with time. As in equation 7.58, $t_1$ refers to a time value of 1 h in the corresponding time units used in the analysis. Fig. 7.18 illustrates the development of the shotcrete viscosity with time for various values of $n$.

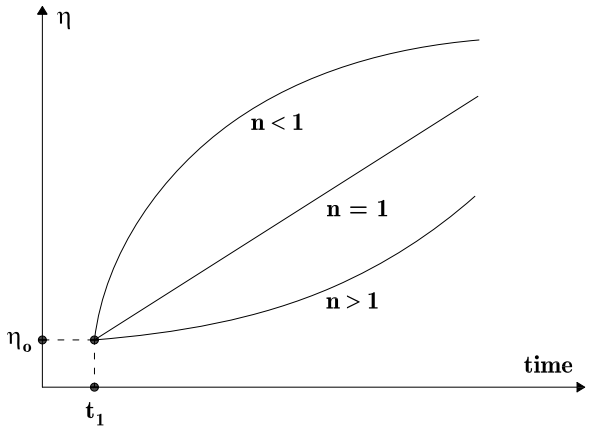



Figure 7.18: Increase in shotcrete viscosity with time

As can be seen, a value of $n = 1$ results in a linear increase in viscosity with time. However, assuming a value of $n > 1$ has to be treated with care since this can lead to a negative creep rate for shotcrete at very early ages. Sometimes it is convenient to give the magnitude of creep, not for the actual applied stress, but per unit stress. This creep strain is referred to as specific creep and can be written for the uniaxial case as:

$$\varepsilon_{sp}^{cr} = \frac{\varepsilon^{cr}}{\sigma} = \frac{t - t_o}{\eta(t)} \tag{7.63}$$

Since in multiaxial loading conditions creep occurs in more than one direction, the above

introduced uniaxial creep law has to be extended for the general stress space. This is achieved by assuming a so called creep potential $P^{cr}$ for both compression and tension. Similar to the case of simple elasto-plasticity, a creep flow rule can be established which enables the calculation of the incremental creep strain vector in a numerical analysis. This creep flow rule can be written as:

$$\{d\varepsilon^{cr}\} = \lambda^{cr} \frac{\partial P^{cr}(\{\sigma\})}{\partial \sigma} \Delta t \tag{7.64}$$

where $\lambda^{cr}$ is the creep multiplier controlling the magnitude of the developing creep strains. It is associated with the specific creep rate, which can be expressed as:

$$\dot{\varepsilon}_{sp}^{cr} = \frac{d\,\varepsilon_{sp}^{cr}}{d\,t} = \frac{t\ (1-n) + n\,t_o}{t_1\,\eta_o\left(\frac{t}{t_1}\right)^{n+1}} \tag{7.65}$$

For simplicity reasons and in the absence of experimental data, the creep potential functions $P^{cr}$ for compression and tension have been chosen to be the same as the plastic potential for the establishment of the conventional plastic strains. Therefore, the creep potential for compressive behaviour is:

$$P_c^{cr} = J^2 + A_c\,p - \tau_c^2 \tag{7.66}$$

and the tensile creep potential can be written as:

$$P_t^{cr} = p + \left[\left(\frac{2J}{\sqrt{3}} sin\left(\theta + \frac{2\pi}{3}\right)\right)^n + (a f_t)^n\right]^{\frac{1}{n}} - f_t \tag{7.67}$$

Fig. 7.19 shows the plastic potential surfaces for both compression and tension in the biaxial stress space and $J$-$p$ space. Furthermore, the directions of the incremental creep strain vectors, according to the creep flow rule given in equation 7.64, passing through the current stress state are indicated.

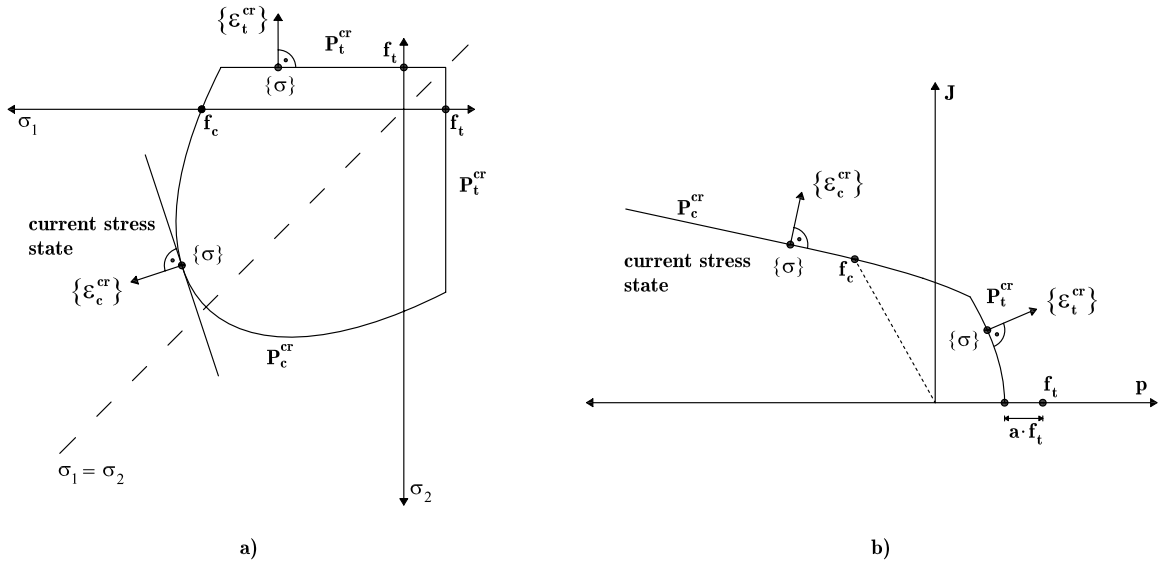



Figure 7.19: Creep potential surfaces and incremental creep strain vectors following a creep flow rule

In the case of a compressive stress state the minor principal stress $\sigma_3$ is the governing factor and the creep multiplier can be written as:

$$\lambda_c^{cr} = \frac{\dot{\varepsilon}_{sp}^{cr}\,\Delta\sigma_3}{\dfrac{\partial P_c^{cr}}{\partial \sigma_3}} \tag{7.68}$$

Similarly, if the current stress state is of a tensile nature, the creep multiplier is expressed as a function of the major principal stress $\sigma_1$:

$$\lambda_t^{cr} = \frac{\dot{\varepsilon}_{sp}^{cr}\,\Delta\sigma_1}{\dfrac{\partial P_t^{cr}}{\partial \sigma_1}} \tag{7.69}$$

A crucial step in a numerical analysis of creep is now the selection of the active creep potential surface in the case of the current stress state being elastic. It was decided to base this decision on the magnitude of the principal stresses $\sigma_1$ and $\sigma_3$ according to the following criteria:

$$\begin{aligned} \text{If} \quad & \sigma_1 < DUM \text{ and } \sigma_3 < DUM \quad \longrightarrow \quad \text{Compressive creep potential active} \\ & \text{Else} \qquad\qquad\qquad\quad \longrightarrow \quad \text{Tensile creep potential active} \end{aligned}$$

with

$$DUM = Min[\mid \sigma_1 \mid, \mid \sigma_3 \mid] * 0.001 + SMLTOL \tag{7.70}$$

where $SMLTOL$ is a user defined tolerance.

### 7.4.4 Shrinkage

Deformation of the shotcrete due to shrinkage caused by the hardening phase of the cement paste and drying is accounted for in the present constitutive model by the following shrinkage model according to ACI (1992) (see also Section 6.8.1).

$$\varepsilon^{sh} = -\varepsilon_{\infty}^{sh} \frac{t}{B+t} \tag{7.71}$$

where $\varepsilon_{\infty}^{sh}$ is the ultimate shrinkage strain reached at time infinity. Since shotcrete tends to reduce its volume during shrinkage, these strains are introduced as negative (compressive) strain components in equal parts to the $x$-, $y$- and $z$-direction. The constant B is a parameter (in time units) that controls how fast this ultimate shrinkage strain is approached, as can be seen in Fig. 7.20. As illustrated, for a lower $B$ value ($B_1 < B_2 < B_3$), in the corresponding time units used in the analysis, the increase in shrinkage deformation is faster. The incremental formulation of the above shrinkage law is obtained as:

$$\dot{\varepsilon}^{sh} = \frac{d\varepsilon^{sh}}{dt} = -\varepsilon_{\infty}^{sh} \frac{B}{(B+t)^2} \tag{7.72}$$

Finally, these induced shrinkage strains contribute to the plastic strain components and hence are assumed to be irrecoverable.

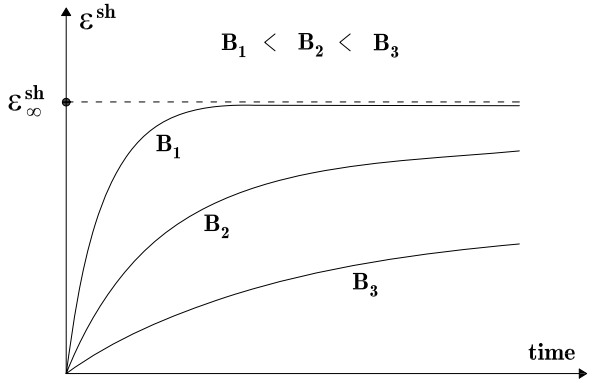



Figure 7.20: Adopted shrinkage model and the influence of parameter $B$

### 7.4.5 Temperature induced strains

For the modelling of the expansion and contraction of the shotcrete at very early ages due to the cement hydration, an approach based on the proposed equation by Schubert (1988) (see Section 6.9) is adopted. The temperature distribution within a shotcrete layer is assumed to be constant across the thickness of the shotcrete body and hence internal variations due to thermal boundary conditions are ignored. The thermal deformations that develop during the

hardening of the cement paste can be estimated from:

$$\varepsilon^{th} = \alpha_{th}\,\Delta T\,(t) \tag{7.73}$$

where $\alpha_{th}$ is the coefficient of thermal expansion and is assumed to be constant with time. $\Delta T\,(t)$ represents the increase in hydration temperature over time and is given by the following equation:

$$\Delta T\,(t) = \frac{\Delta T_{max}}{2}\,\left[1 - \cos\left(A_t\,t^{C_t}\right)\right] \tag{7.74}$$

where $\Delta T_{max}$ is the maximum increase in temperature above the ambient environmental temperature in the tunnel that occurs after shotcrete installation at the time $t_{max}$, see Fig. 7.21.

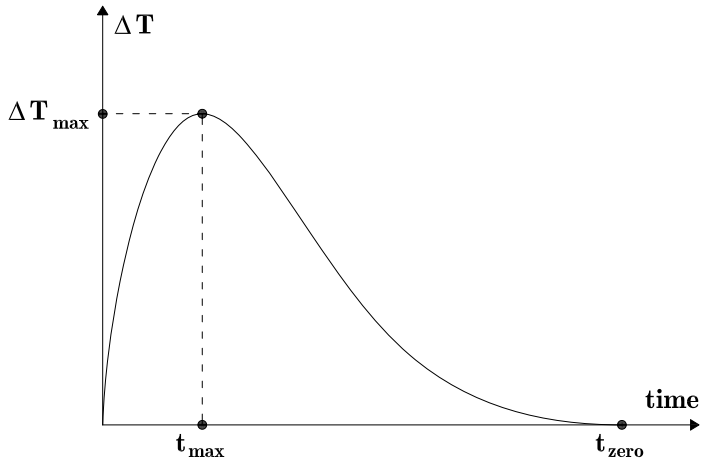



Figure 7.21: Development of $\Delta T$ with time

With increasing time, $\Delta T$ starts to reduce again and the shotcrete tends to contract until there is no further influence of the hydration temperature at the time $t_{zero}$. For a time $t$ larger than $t_{zero}$ no thermal strains occur. The two constants $A_t$ and $C_t$ in equation 7.74 can be established from the above introduced parameters through the expressions given below:

$$A_t = \frac{\pi}{t_{max}^{C_t}} \qquad \text{and} \qquad C_t = \frac{\ln 2}{\ln\left(\dfrac{t_{zero}}{t_{max}}\right)} \tag{7.75}$$

For the numerical implementation of the current constitutive model the thermal strain rate $\dot{\varepsilon}^{th}$ is needed and can be calculated as:

$$\dot{\varepsilon}^{th} = \frac{d\varepsilon^{th}}{dt} = \alpha_{th}\frac{\Delta T_{max}}{2}\,A_t\,C_t\,t^{C_t-1}\,\sin\left(A_t\,t^{C_t}\right) \tag{7.76}$$

Furthermore, these thermal strains are treated as irrecoverable (or plastic) volumetric strains and are added to the strain tensor in equal parts to the $x$-, $y$- and $z$-direction.

## 7.5 Summary of parameters

A constitutive model for the time-dependent behaviour of shotcrete has been presented and discussed in detail in the previous sections. The following tables, Tab. 7.1 to 7.3, summarise the model parameters that are required for its use in ICFEP. It should be noted that the time-dependent plasticity model incorporating creep, shrinkage and thermal effects is implemented as NON-LINEAR MODEL 55 in the series of constitutive models available in ICFEP. However, the time-dependency of the stiffness has been treated as a separate model (MODEL 53), which belongs to the family of the SMALL-STRAIN-STIFFNESS models. Consequently both SMALL-STRAIN-STIFFNESS MODEL 53 and NON-LINEAR MODEL 55 must be used together in order to model both stiffness and strength varying with time.

| Time-dependent plasticity model | | |
|---|---|---|
| $f_{cp,28}$ | $> 0$ | Compressive peak strength at 28 days |
| $f_{cy,28}$ | $f_{cy,crit} < f_{cy,28} \leq f_{cp,28}$ | Compressive yield stress at 28 days |
| $f_{cf,28}$ | $f_{cf,crit} < f_{cf,28} \leq f_{cp,28}$ | Compressive failure strength at 28 days |
| $f_{cu,28}$ | $0 < f_{cu,28} \leq f_{cf,28}$ | Compressive ultimate strength at 28 days |
| $e$ | $1 < e < e_{max}$ | Biaxial strength parameter |
| $f_{tp,28}$ | $0 < f_{tp,28} \leq f_{cp,28}$ | Tensile peak strength at 28 days |
| $f_{ty,28}$ | $0 < f_{ty,28} \leq f_{tp,28}$ | Tensile yield stress at 28 days |
| $f_{tu,28}$ | $0 < f_{tu,28} \leq f_{tp,28}$ | Tensile ultimate strength at 28 days |
| $s$ | $> 0$ | Cement parameter for increase in strength |
| $\varepsilon^p_{cp,28}$ | $> 0$ | Plastic compressive peak strain at 28 days |
| $\varepsilon^p_{cf,28}$ | $> \varepsilon_{cp,28}$ | Plastic compressive failure strain at 28 days |
| $\varepsilon^p_{cu,28}$ | $> \varepsilon_{cf,28}$ | Plastic compressive ultimate strain at 28 days |
| $\varepsilon^p_{cp,t_2}$ | $> \varepsilon_{cp,28}$ | Plastic compressive peak strain at time $t_2$ |
| $\varepsilon^p_{cp,t_1}$ | $> \varepsilon_{cp,t_2}$ | Plastic compressive peak strain at time $t_1$ |
| $\varepsilon^p_{tp,28}$ | $> 0$ | Plastic tensile peak strain at 28 days |
| $\varepsilon^p_{tu,28}$ | $> \varepsilon_{tp,28}$ | Plastic tensile ultimate strain at 28 days |
| or | | |
| $\psi$ | $< 0$ | Exponential softening exponent |
| $t_1$ | $> 0$ | Time corresponding to 1 hour |
| $t_{28}$ | $> 0$ | Time corresponding to 28 days |
| $t_2$ | $t_1 < t_2 < t_{28}$ | Time corresponding to $\varepsilon^p_{cp,t_2}$ |
| $t_o$ | $\geq t_1$ | Initial shotcrete age |
| $CORTOL$ | $0^\circ < CORTOL < 15^\circ$ | Tensile deviatoric corner tolerance |
| $a$ | $0 < a \leq 1$ | Tensile apex tolerance tolerance |
| $n$ | $n \geq 1$ | Tensile rounding parameter |
| $TIPTOL$ | $\geq 0$ | Tip tolerance |

Table 7.1: Summary of parameters for time-dependent plasticity model (all the strength and strain parameters are uniaxial parameters)

| Creep, shrinkage and temperature model | | |
|---|---|---|
| $\eta_o$ | $> 0$ | Initial creep viscosity |
| $n$ | $> 0$ | Creep viscosity exponent |
| $\varepsilon_\infty^{sh}$ | $\geq 0$ | Ultimate shrinkage strain |
| $B$ | $> 0$ | Shrinkage parameter |
| $\alpha_{th}$ | $\geq 0$ | Coefficient of thermal expansion |
| $\Delta T_{max}$ | $\geq 0$ | Maximum increase in hydration temperature |
| $t_{max}$ | $> 0$ | Time $t$ when $\Delta T_{max}$ occurs |
| $t_{zero}$ | $> t_{max}$ | Time $t$ when increase in hydration temperature $\Delta T$ is zero |

Table 7.2: Summary of model parameters for creep, shrinkage and thermal strains

| Time-dependent elasticity model | | |
|---|---|---|
| $E_{28}$ | $> 0$ | Young's modulus of hardened shotcrete at 28 days |
| $s$ | $> 0$ | Cement parameter for increase in stiffness |
| $\mu$ | $-1.0 < \mu < 0.5$ | Poisson's ratio (constant) |
| $t_{28}$ | $> 0$ | Time corresponding to 28 days |
| $t_o$ | $\geq t_1$ | Initial shotcrete age |

Table 7.3: Summary of parameters for time-dependent elasticity model

## 7.6 Formulation of the elasto-plastic constitutive matrix for time-dependent materials

In this section the formulation of the elasto-plastic constitutive matrix, $[D^{ep}]$, for a time-dependent material such as shotcrete is presented in detail. This is an extension of the theory for conventional elasto-plastic materials introduced in Section 6.4.2, including the additional factor "time" in the adopted yield surfaces and deformations due to creep, shrinkage and hydration temperature.

In this time-dependent elasto-plastic constitutive model for shotcrete the change in stresses is related to the change in total strains via the elasto-plastic constitutive matrix $[D^{ep}]$. This relationship can be expressed as:

$$\{\Delta\sigma\} = [D^{ep}]\ \{\Delta\varepsilon\} \tag{7.77}$$

The changes in total strains can be divided into three components, the elastic strains, the

plastic strains and the irreversible strains due to creep, shrinkage and thermal effects. It can be written:

$$\{\Delta\varepsilon\} = \{\Delta\varepsilon^{el}\} + \{\Delta\varepsilon^{p}\} + \{\Delta\varepsilon^{c}\} \tag{7.78}$$

with

$$\{\Delta\varepsilon^{c}\} = \{\Delta\varepsilon^{cr}\} + \{\Delta\varepsilon^{sh}\} + \{\Delta\varepsilon^{th}\} \tag{7.79}$$

The changes in stresses are related to the elastic strains through the elastic constitutive matrix $[D]$ as following:

$$\{\Delta\sigma\} = [D]\,[\{\Delta\varepsilon\} - \{\Delta\varepsilon^{p}\} - \{\Delta\varepsilon^{c}\}] \tag{7.80}$$

The change in irreversible strains $\{\Delta\varepsilon^{c}\}$ yields:

$$\{\Delta\varepsilon^{c}\} = \underbrace{\lambda^{cr}\left\{\frac{\partial P^{cr}}{\partial\sigma}\right\}\Delta t}_{creep} + \underbrace{\delta_{ij}\,\dot{\varepsilon}^{sh}\,\Delta t}_{shrinkage} + \underbrace{\delta_{ij}\,\dot{\varepsilon}^{th}\,\Delta t}_{temperature} \tag{7.81}$$

where $\delta_{ij} = \delta_{ji}$ is the Kronecker delta, which is defined as being equal to $+1$ if $i$ and $j$ are the same numbers and 0 otherwise. By applying the flow rule for the conventional plastic strains given in equation 6.20, equation 7.80 can be written as:

$$\{\Delta\sigma\} = [D]\left[\{\Delta\varepsilon\} - \{\Delta\varepsilon^{c}\} - \lambda\left\{\frac{\partial P}{\partial\sigma}\right\}\right] \tag{7.82}$$

As mentioned previously, the yield function depends on the stress state $\{\sigma\}$, the hardening (or state) parameters $\{k\}$ and the time $t$. In the case of the material being plastic the yield condition results in:

$$F(\{\sigma\},\,\{k\},\,t) = 0 \tag{7.83}$$

When the material is yielding, the consistency condition requires that the stress state remains always on the yield surface, so that $dF = 0$. By applying the chain rule of differentiation for a plastic strain hardening/softening material one obtains:

$$dF = \left\{\frac{\partial F}{\partial\sigma}\right\}^{T}\{\Delta\sigma\} + \left\{\frac{\partial F}{\partial k}\right\}^{T}\left[\frac{\partial k}{\partial\varepsilon^{p}}\right]\{\Delta\varepsilon^{p}\} + \frac{\partial F}{\partial t}\Delta t = 0 \tag{7.84}$$

Rearrangement of this equation leads to:

$$\{\Delta\sigma\} = \frac{-\left\{\dfrac{\partial F}{\partial k}\right\}^{T}\left[\dfrac{\partial k}{\partial\varepsilon^{p}}\right]\{\Delta\varepsilon^{p}\} - \dfrac{\partial F}{\partial t}\Delta t}{\left\{\dfrac{\partial F}{\partial\sigma}\right\}^{T}} \tag{7.85}$$

Combining equations 7.82 and 7.85 results in:

$$[D]\left[\{\Delta\varepsilon\}-\{\Delta\varepsilon^c\}\right]-\lambda\,[D]\left\{\frac{\partial P}{\partial\sigma}\right\}=-\frac{\left\{\frac{\partial F}{\partial k}\right\}^T\left[\frac{\partial k}{\partial\varepsilon^p}\right]\{\Delta\varepsilon^p\}+\frac{\partial F}{\partial t}\Delta t}{\left\{\frac{\partial F}{\partial\sigma}\right\}^T} \tag{7.86}$$

and further

$$\begin{aligned}\left\{\frac{\partial F}{\partial\sigma}\right\}^T[D]\left[\{\Delta\varepsilon\}-\{\Delta\varepsilon^c\}\right] \;-\; \lambda\,[D]\left\{\frac{\partial P}{\partial\sigma}\right\}\left\{\frac{\partial F}{\partial\sigma}\right\}^T = \\ -\left[\left\{\frac{\partial F}{\partial k}\right\}^T\left[\frac{\partial k}{\partial\varepsilon^p}\right]\{\Delta\varepsilon^p\}+\frac{\partial F}{\partial t}\Delta t\right]\end{aligned} \tag{7.87}$$

From this equation the plastic multiplier $\lambda$ can be obtained as:

$$\lambda=\frac{\left\{\frac{\partial F}{\partial\sigma}\right\}^T[D]\left[\{\Delta\varepsilon\}-\{\Delta\varepsilon^c\}\right]+\frac{\partial F}{\partial t}\Delta t}{[D]\left\{\frac{\partial P}{\partial\sigma}\right\}\left\{\frac{\partial F}{\partial\sigma}\right\}^T+A} \tag{7.88}$$

where $A$ denotes the hardening modulus, which is given as:

$$A=-\frac{1}{\lambda}\left\{\frac{\partial F}{\partial k}\right\}^T\left[\frac{\partial k}{\partial\varepsilon^p}\right]\{\Delta\varepsilon^p\} \tag{7.89}$$

Making use of equations 7.82 and 7.88 leads to:

$$\{\Delta\sigma\}=[D]\left[\{\Delta\varepsilon\}-\{\Delta\varepsilon^c\}\right]-\frac{\left\{\frac{\partial F}{\partial\sigma}\right\}^T[D]\left[\{\Delta\varepsilon\}-\{\Delta\varepsilon^c\}\right]+\frac{\partial F}{\partial t}\Delta t}{[D]\left\{\frac{\partial P}{\partial\sigma}\right\}\left\{\frac{\partial F}{\partial\sigma}\right\}^T+A}[D]\left\{\frac{\partial P}{\partial\sigma}\right\} \tag{7.90}$$

Further rearrangement of the above equation results in:

$$\begin{aligned}\{\Delta\sigma\}=[D]\left[\{\Delta\varepsilon\}-\{\Delta\varepsilon^c\}\right] \;-\; \frac{[D]\left\{\frac{\partial P}{\partial\sigma}\right\}\left\{\frac{\partial F}{\partial\sigma}\right\}^T[D]\left[\{\Delta\varepsilon\}-\{\Delta\varepsilon^c\}\right]}{[D]\left\{\frac{\partial P}{\partial\sigma}\right\}\left\{\frac{\partial F}{\partial\sigma}\right\}^T+A}- \\ -\frac{[D]\left\{\frac{\partial P}{\partial\sigma}\right\}\frac{\partial F}{\partial t}\Delta t}{[D]\left\{\frac{\partial P}{\partial\sigma}\right\}\left\{\frac{\partial F}{\partial\sigma}\right\}^T+A}\end{aligned} \tag{7.91}$$

Finally, a relationship between the changes in stresses and strains for the time-dependent

material shotcrete can be obtained as:

$$\{\Delta\sigma\} = [D^{ep}]\,[\{\Delta\varepsilon\} - \{\Delta\varepsilon^c\}] - \{\Delta\sigma^c\} \tag{7.92}$$

where $[D^{ep}]$ is the conventional elasto-plastic constitutive matrix given as:

$$[D^{ep}] = [D] - \frac{[D]\left\{\frac{\partial P}{\partial \sigma}\right\}\left\{\frac{\partial F}{\partial \sigma}\right\}^T [D]}{[D]\left\{\frac{\partial P}{\partial \sigma}\right\}\left\{\frac{\partial F}{\partial \sigma}\right\}^T + A} \tag{7.93}$$

and $\{\Delta\sigma^c\}$ is an additional generated stress vector that accounts for the time-dependent behaviour of the yield surfaces. It can be written:

$$\{\Delta\sigma^c\} = \frac{[D]\left\{\frac{\partial P}{\partial \sigma}\right\}\frac{\partial F}{\partial t}\Delta t}{[D]\left\{\frac{\partial P}{\partial \sigma}\right\}\left\{\frac{\partial F}{\partial \sigma}\right\}^T + A} \tag{7.94}$$

In the case of purely elastic material behaviour this stress vector reduces to zero.

## 7.7 Correction of the right hand side load vector

Chapter 3 introduced the basic theory behind the establishment of the governing equations that are necessary to describe the deformational behaviour of each element during a finite element analysis. However, this procedure did not include the aspects affecting these governing element equations that arise due to the time-dependent nature of the material behaviour of sprayed concrete. Therefore, this section is a continuation from Section 3.2.3 and the previous Section 7.6 and explains in detail how the right hand side load vector is determined in the case of a time-dependent material behaviour.

The principle of minimum potential energy requires the determination of the strain energy, which can be written as:

$$\Delta W = \frac{1}{2}\int_{Vol} \{\Delta\varepsilon\}^T \{\Delta\sigma\} \mathrm{d}Vol \tag{7.95}$$

by integrating over the volume of the body. This equation can be rearranged as:

$$\Delta W = \frac{1}{2}\int_{Vol} \{\Delta\varepsilon\}^T [[D^{ep}]\,[\{\Delta\varepsilon\} - \{\Delta\varepsilon^c\}] - \{\Delta\sigma^c\}]\,\mathrm{d}Vol \tag{7.96}$$

and further

$$\Delta W = \frac{1}{2}\int_{Vol} \left(\{\Delta\varepsilon\}^T [D^{ep}]\,[\{\Delta\varepsilon\} - \{\Delta\varepsilon^c\}] - \{\Delta\varepsilon\}^T \{\Delta\sigma^c\}\right)\,\mathrm{d}Vol \tag{7.97}$$

The incremental total potential energy $\Delta E$ of a body is now defined as:

$$\Delta E = \Delta W - \Delta L \tag{7.98}$$

with $\Delta L$ being the work done by the applied loads, which is given in equation 3.14 of Chapter 3. It can be written as:

$$\begin{aligned}\Delta E &= \frac{1}{2}\int_{Vol}\{\Delta\varepsilon\}^T[D^{ep}]\left[\{\Delta\varepsilon\}-\{\Delta\varepsilon^c\}\right]\mathrm{d}Vol - \frac{1}{2}\int_{Vol}\{\Delta\varepsilon\}^T\{\Delta\sigma^c\}\mathrm{d}Vol \\ &\quad - \int_{Vol}\{\Delta d\}^T\{\Delta F\}\mathrm{d}Vol - \int_{Srf}\{\Delta d\}^T\{\Delta T\}\mathrm{d}Srf \end{aligned} \tag{7.99}$$

This equation can be further expressed as:

$$\begin{aligned}\Delta E &= \sum_{i=1}^{N}\Bigg(\frac{1}{2}\int_{Vol}\{\Delta d\}_n^T[B]^T[D^{ep}][B]\{\Delta d\}_n\mathrm{d}Vol - \frac{1}{2}\int_{Vol}\{\Delta d\}_n^T[B]^T[D^{ep}]\{\Delta\varepsilon^c\}\mathrm{d}Vol \\ &\quad - \frac{1}{2}\int_{Vol}\{\Delta d\}_n^T[B]^T\{\Delta\sigma^c\}\mathrm{d}Vol - \int_{Vol}\{\Delta d\}^T\{\Delta F\}\mathrm{d}Vol \\ &\quad - \int_{Srf}\{\Delta d\}^T\{\Delta T\}\mathrm{d}Srf\Bigg)\end{aligned} \tag{7.100}$$

After minimising the potential energy with respect to the incremental nodal displacements, the right hand side load vector $\{\Delta R_E\}$ gets an extra term $\phi$ due to the time-dependency of the adopted yield functions and the strain components accounting for creep, shrinkage and hydration temperature, which can be written as:

$$\phi = +\frac{1}{2}\int_{Vol}[B]^T\{\Delta\sigma^c\}\mathrm{d}Vol + \frac{1}{2}\int_{Vol}[B]^T[D^{ep}]\{\Delta\varepsilon^c\}\mathrm{d}Vol \tag{7.101}$$

## 7.8 Multi-surface plasticity for time-dependent materials

Section 6.4.3 of the previous chapter dealt with the theoretical background of elasto-plasticity in the case when several yield surfaces are active at the same time. Within the current section, this theory is extended for the developed time-dependent constitutive model for shotcrete, where during an analysis both the compression and the tension yield surface can be controlling the mechanical behaviour simultaneously. The numerical formulation includes also the time-dependent nature of the adopted yield surfaces which leads to the mathematical procedure presented below:

If the stress state during an analysis is such that both the compression and the tension yield surfaces are moving simultaneously in the stress space, the change in total strains can be divided into the components given below:

$$\{\Delta\varepsilon\} = \{\Delta\varepsilon^e\} + \left\{\Delta\varepsilon^{p1}\right\} + \left\{\Delta\varepsilon^{p2}\right\} + \{\Delta\varepsilon^c\} \tag{7.102}$$

where $\left\{\Delta\varepsilon^{p1}\right\}$ denotes the change in plastic strains due to the compression yield surface being active and $\left\{\Delta\varepsilon^{p2}\right\}$ the change in plastic strains given by the tension yield surface. The strain component $\{\Delta\varepsilon^{c}\}$ describes the additional irreversible strains according to the adopted constitutive behaviour for creep, shrinkage and thermal deformation and can be written in the case of multiplasticity as:

$$\{\Delta\varepsilon^{c}\} = \frac{1}{2}\lambda_c^{cr}\left\{\frac{\partial P_c^{cr}}{\partial\sigma}\right\}\Delta t + \frac{1}{2}\lambda_t^{cr}\left\{\frac{\partial P_t^{cr}}{\partial\sigma}\right\}\Delta t + \delta_{ij}\,\dot{\varepsilon}^{sh}\Delta t + \delta_{ij}\,\dot{\varepsilon}^{th}\Delta t \tag{7.103}$$

In this equation $\lambda_c^{cr}$ and $\lambda_t^{cr}$ are the creep multipliers for the compressive and the tensile creep behaviour and were previously introduced in equations 7.68 and 7.69 respectively. It should be noted that the equal contribution of both creep potentials expressed by the factor $1/2$ is an arbitrary assumption. The changes in stresses are related to the changes in elastic strains through the elastic constitutive matrix $[D]$ as:

$$\{\Delta\sigma\} = [D]\,\{\Delta\varepsilon^{e}\} \tag{7.104}$$

It follows that:

$$\{\Delta\sigma\} = [D]\,[\{\Delta\varepsilon\} - \{\Delta\varepsilon^{c}\} - \left\{\Delta\varepsilon^{p1}\right\} - \left\{\Delta\varepsilon^{p2}\right\}] \tag{7.105}$$

The plastic strain components for both yield surfaces can be obtained from the flow rules, that read as:

$$\left\{\Delta\varepsilon^{p1}\right\} = \lambda_1\left\{\frac{\partial P_1}{\partial\sigma}\right\} \qquad \text{and} \qquad \left\{\Delta\varepsilon^{p2}\right\} = \lambda_2\left\{\frac{\partial P_2}{\partial\sigma}\right\} \tag{7.106}$$

Substitution into equation 7.105 results in:

$$\{\Delta\sigma\} = [D]\,[\{\Delta\varepsilon\} - \{\Delta\varepsilon^{c}\} - \lambda_1\left\{\frac{\partial P_1}{\partial\sigma}\right\} - \lambda_2\left\{\frac{\partial P_2}{\partial\sigma}\right\}] \tag{7.107}$$

As mentioned earlier, both yield functions depend on the stress state $\{\sigma\}$, the state (or hardening) parameters $\{k\}$ and time $t$. They can be expressed as:

$$F_1(\{\sigma\},\,\{k\},\,t) = 0 \qquad \text{and} \qquad F_2(\{\sigma\},\,\{k\},\,t) = 0 \tag{7.108}$$

Applying the consistency condition to both yield functions results in the following total differentials for both the compressive and the tensile behaviour:

$$dF_1 = \left\{\frac{\partial F_1}{\partial\sigma}\right\}^T\{\Delta\sigma\} + \left\{\frac{\partial F_1}{\partial k}\right\}^T\left[\frac{\partial k}{\partial\varepsilon_3^p}\right]\{\Delta\varepsilon^{p}\} + \frac{\partial F_1}{\partial t}\Delta t = 0 \tag{7.109}$$

and

$$dF_2 = \left\{\frac{\partial F_2}{\partial\sigma}\right\}^T\{\Delta\sigma\} + \left\{\frac{\partial F_2}{\partial k}\right\}^T\left[\frac{\partial k}{\partial\varepsilon_1^p}\right]\{\Delta\varepsilon^{p}\} + \frac{\partial F_2}{\partial t}\Delta t = 0 \tag{7.110}$$

By substituting equation 7.107 into the above equations one obtains:

$$\begin{aligned} dF_1 &= \left\{\frac{\partial F_1}{\partial \sigma}\right\}^T [D](\{\Delta\varepsilon\} - \{\Delta\varepsilon^c\}) - \lambda_1 \left\{\frac{\partial F_1}{\partial \sigma}\right\}^T [D] \left\{\frac{\partial P_1}{\partial \sigma}\right\} - \\ &\quad -\lambda_2 \left\{\frac{\partial F_1}{\partial \sigma}\right\}^T [D] \left\{\frac{\partial P_2}{\partial \sigma}\right\} + \left\{\frac{\partial F_1}{\partial k}\right\}^T \left[\frac{\partial k}{\partial \varepsilon_3^p}\right] \{\Delta\varepsilon^p\} + \\ &\quad + \frac{\partial F_1}{\partial t}\Delta t = 0 \end{aligned} \tag{7.111}$$

and

$$\begin{aligned} dF_2 &= \left\{\frac{\partial F_2}{\partial \sigma}\right\}^T [D](\{\Delta\varepsilon\} - \{\Delta\varepsilon^c\}) - \lambda_1 \left\{\frac{\partial F_2}{\partial \sigma}\right\}^T [D] \left\{\frac{\partial P_1}{\partial \sigma}\right\} - \\ &\quad -\lambda_2 \left\{\frac{\partial F_2}{\partial \sigma}\right\}^T [D] \left\{\frac{\partial P_2}{\partial \sigma}\right\} + \left\{\frac{\partial F_2}{\partial k}\right\}^T \left[\frac{\partial k}{\partial \varepsilon_1^p}\right] \{\Delta\varepsilon^p\} + \\ &\quad + \frac{\partial F_2}{\partial t}\Delta t = 0 \end{aligned} \tag{7.112}$$

Furthermore, $A_1$ and $A_2$ are defined as:

$$A_1 = -\frac{1}{\lambda_1} \left\{\frac{\partial F_1}{\partial k}\right\}^T \left[\frac{\partial k}{\partial \varepsilon_3^p}\right] \{\Delta\varepsilon^p\} \tag{7.113}$$

and

$$A_2 = -\frac{1}{\lambda_2} \left\{\frac{\partial F_2}{\partial k}\right\}^T \left[\frac{\partial k}{\partial \varepsilon_1^p}\right] \{\Delta\varepsilon^p\} \tag{7.114}$$

Combining these two equations with equations 7.111 and 7.112 leads to:

$$\begin{aligned} dF_1 &= \left\{\frac{\partial F_1}{\partial \sigma}\right\}^T [D](\{\Delta\varepsilon\} - \{\Delta\varepsilon^c\}) - \lambda_1 \left\{\frac{\partial F_1}{\partial \sigma}\right\}^T [D] \left\{\frac{\partial P_1}{\partial \sigma}\right\} - \\ &\quad -\lambda_2 \left\{\frac{\partial F_1}{\partial \sigma}\right\}^T [D] \left\{\frac{\partial P_2}{\partial \sigma}\right\} - \lambda_1 A_1 + \frac{\partial F_1}{\partial t}\Delta t = 0 \end{aligned} \tag{7.115}$$

and

$$\begin{aligned} dF_2 &= \left\{\frac{\partial F_2}{\partial \sigma}\right\}^T [D](\{\Delta\varepsilon\} - \{\Delta\varepsilon^c\}) - \lambda_1 \left\{\frac{\partial F_2}{\partial \sigma}\right\}^T [D] \left\{\frac{\partial P_1}{\partial \sigma}\right\} - \\ &\quad -\lambda_2 \left\{\frac{\partial F_2}{\partial \sigma}\right\}^T [D] \left\{\frac{\partial P_2}{\partial \sigma}\right\} - \lambda_2 A_2 + \frac{\partial F_2}{\partial t}\Delta t = 0 \end{aligned} \tag{7.116}$$

For simplification it can be rewritten:

$$\lambda_1 L_{11} + \lambda_2 L_{12} = T_1 \qquad \text{and} \qquad \lambda_1 L_{21} + \lambda_2 L_{22} = T_2 \tag{7.117}$$

The coefficients $L_{11}$, $L_{12}$, $L_{21}$ and $L_{22}$ are now the same as for a material without the time-dependent response and can therefore be written as:

$$\begin{aligned} L_{11} &= \left\{\frac{\partial F_1}{\partial \sigma}\right\}^T [D] \left\{\frac{\partial P_1}{\partial \sigma}\right\} + A_1 \\ L_{22} &= \left\{\frac{\partial F_2}{\partial \sigma}\right\}^T [D] \left\{\frac{\partial P_2}{\partial \sigma}\right\} + A_2 \\ L_{12} &= \left\{\frac{\partial F_1}{\partial \sigma}\right\}^T [D] \left\{\frac{\partial P_2}{\partial \sigma}\right\} \\ L_{21} &= \left\{\frac{\partial F_2}{\partial \sigma}\right\}^T [D] \left\{\frac{\partial P_1}{\partial \sigma}\right\} \end{aligned} \tag{7.118}$$

It can be seen that the parameters $T_1$ and $T_2$ contain an additional term accounting for the time-dependent nature of the yield functions and are obtained as:

$$T_1 = \left\{\frac{\partial F_1}{\partial \sigma}\right\}^T [D] \left(\{\Delta\varepsilon\} - \{\Delta\varepsilon^c\}\right) + \frac{\partial F_1}{\partial t}\,\Delta t \tag{7.119}$$

and

$$T_2 = \left\{\frac{\partial F_2}{\partial \sigma}\right\}^T [D] \left(\{\Delta\varepsilon\} - \{\Delta\varepsilon^c\}\right) + \frac{\partial F_2}{\partial t}\,\Delta t \tag{7.120}$$

As a solution for the plastic strain multipliers $\lambda_1$ and $\lambda_2$ it can be written:

$$\lambda_1 = \frac{L_{22}T_1 - L_{12}T_2}{L_{11}L_{22} - L_{12}L_{21}} \qquad \text{and} \qquad \lambda_2 = \frac{L_{11}T_2 - L_{21}T_1}{L_{11}L_{22} - L_{12}L_{21}} \tag{7.121}$$

By setting $\Omega = L_{11}\,L_{22} - L_{12}\,L_{21}$ these equations are expressed as:

$$\lambda_1 = \frac{L_{22}T_1 - L_{12}T_2}{\Omega} \qquad \text{and} \qquad \lambda_2 = \frac{L_{11}T_2 - L_{21}T_1}{\Omega} \tag{7.122}$$

Substituting these expressions for $\lambda_1$ and $\lambda_2$ into equation 7.105 leads to:

$$\begin{aligned} \{\Delta\sigma\} \;=\; & [D]\left(\{\Delta\varepsilon\} - \{\Delta\varepsilon^c\}\right) - \frac{[D]}{\Omega}\left\{\frac{\partial P_1}{\partial \sigma}\right\}\left[L_{22}\left(\left\{\frac{\partial F_1}{\partial \sigma}\right\}^T [D]\left(\{\Delta\varepsilon\} - \{\Delta\varepsilon^c\}\right) + \right.\right. \\ & \left. + \frac{\partial F_1}{\partial t}\,\Delta t\right) - L_{12}\left(\left\{\frac{\partial F_2}{\partial \sigma}\right\}^T [D]\left(\{\Delta\varepsilon\} - \{\Delta\varepsilon^c\}\right) + \frac{\partial F_2}{\partial t}\,\Delta t\right)\Bigg] - \\ & \frac{[D]}{\Omega}\left\{\frac{\partial P_2}{\partial \sigma}\right\}\left[L_{11}\left(\left\{\frac{\partial F_2}{\partial \sigma}\right\}^T [D]\left(\{\Delta\varepsilon\} - \{\Delta\varepsilon^c\}\right) + \frac{\partial F_2}{\partial t}\,\Delta t\right) - \right. \\ & \left. L_{21}\left(\left\{\frac{\partial F_1}{\partial \sigma}\right\}^T [D]\left(\{\Delta\varepsilon\} - \{\Delta\varepsilon^c\}\right) + \frac{\partial F_1}{\partial t}\,\Delta t\right)\right] \end{aligned} \tag{7.123}$$

Rearrangement of the above equation yields in:

$$\{\Delta\sigma\} + \frac{[D]}{\Omega}\left\{\frac{\partial P_1}{\partial\sigma}\right\}\left[L_{22}\frac{\partial F_1}{\partial t}\Delta t - L_{12}\frac{\partial F_2}{\partial t}\Delta t\right] + \frac{[D]}{\Omega}\left\{\frac{\partial P_2}{\partial\sigma}\right\}\left[L_{11}\frac{\partial F_2}{\partial t}\Delta t - \right.$$
$$\left. - L_{21}\frac{\partial F_1}{\partial t}\Delta t\right] = \left[[D] - \frac{[D]}{\Omega}\left\{\frac{\partial P_1}{\partial\sigma}\right\}\left[L_{22}\left\{\frac{\partial F_1}{\partial\sigma}\right\}^T[D] - L_{12}\left\{\frac{\partial F_2}{\partial\sigma}\right\}^T[D]\right] - \right.$$
$$\left. - \frac{[D]}{\Omega}\left\{\frac{\partial P_2}{\partial\sigma}\right\}\left[L_{11}\left\{\frac{\partial F_2}{\partial\sigma}\right\}^T[D] - L_{21}\left\{\frac{\partial F_1}{\partial\sigma}\right\}^T[D]\right]\right](\{\Delta\varepsilon\} - \{\Delta\varepsilon^c\}) \qquad (7.124)$$

Finally, the change in stresses is given as:

$$\{\Delta\sigma\} + \frac{[D]}{\Omega}\left\{\frac{\partial P_1}{\partial\sigma}\right\}\left[L_{22}\frac{\partial F_1}{\partial t}\Delta t - L_{12}\frac{\partial F_2}{\partial t}\Delta t\right] + \frac{[D]}{\Omega}\left\{\frac{\partial P_2}{\partial\sigma}\right\}\left[L_{11}\frac{\partial F_2}{\partial t}\Delta t - \right.$$
$$\left. - L_{21}\frac{\partial F_1}{\partial t}\Delta t\right] + [D^{ep}]\{\Delta\varepsilon^c\} = [D^{ep}]\{\Delta\varepsilon\} \qquad (7.125)$$

where the elasto-plastic constitutive matrix can be expressed as:

$$\begin{aligned}[D^{ep}] &= [D] - \frac{[D]}{\Omega}\left\{\frac{\partial P_1}{\partial\sigma}\right\}\left[L_{22}\left\{\frac{\partial F_1}{\partial\sigma}\right\}^T[D] - L_{12}\left\{\frac{\partial F_2}{\partial\sigma}\right\}^T[D]\right] - \\ &\quad - \frac{[D]}{\Omega}\left\{\frac{\partial P_2}{\partial\sigma}\right\}\left[L_{11}\left\{\frac{\partial F_2}{\partial\sigma}\right\}^T[D] - L_{21}\left\{\frac{\partial F_1}{\partial\sigma}\right\}^T[D]\right] \end{aligned} \qquad (7.126)$$

The additional generated stress vector accounting for the time-dependent nature of the adopted yield surfaces can be obtained as:

$$\begin{aligned}\{\Delta\sigma^c\} &= \frac{[D]}{\Omega}\left\{\frac{\partial P_1}{\partial\sigma}\right\}\left[L_{22}\frac{\partial F_1}{\partial t}\Delta t - L_{12}\frac{\partial F_2}{\partial t}\Delta t\right] + \\ &\quad + \frac{[D]}{\Omega}\left\{\frac{\partial P_2}{\partial\sigma}\right\}\left[L_{11}\frac{\partial F_2}{\partial t}\Delta t - L_{21}\frac{\partial F_1}{\partial t}\Delta t\right] \end{aligned} \qquad (7.127)$$

## 7.9 Model implementation

The numerical implementation of the presented constitutive model for shotcrete into the finite element program ICFEP involved the following steps:

1. Calculation of the elasto-plastic constitutive matrix $[D^{ep}]$ according to Section 7.6 or 7.8, which allows the establishment of the element stiffness matrix $[K_E]$. This includes the incorporation of the time-dependent behaviour of the adopted yield surfaces by calculating the additional stress contribution $\{\Delta\sigma^c\}$. The element stiffness matrix is then assembled into the global stiffness matrix $[K_G]$ in order to form the global set of equations, where the right hand side load vector is corrected by the factor $\phi$ given in Section 7.7.

2. Calculation of the residual load vector $\{\psi\}^j$ at the end of each iteration during the modified Newton-Raphson scheme which is used as the non-linear solver. This is achieved

by integrating the constitutive equations along the incremental strain path by a substepping algorithm to estimate the stress changes (see Chapter 3). This procedure requires the calculation of the changes in stresses, plastic strains and hardening parameters during each substep.

By inspecting equations 6.20, 7.93 and 7.94 it can be observed that the following terms are required:

- Partial derivatives of the yield functions with respect to stress $\{\partial F/\partial\sigma\}$
- Partial derivatives of the plastic potential functions with respect to stress $\{\partial P/\partial\sigma\}$
- Partial derivatives of the yield functions with respect to time $\partial F/\partial t$
- The elastic constitutive matrix $[D]$
- The hardening modulus $A$

The following sections present the necessary calculations neeeded for the robust numerical implementation of the current constitutive model for shotcrete into ICFEP for each of the two yield surfaces that are adopted.

### 7.9.1 Selection of the active yield surface

The selection of the active yield surface during an analysis is based on the values of the compressive yield function $F_c$ and the tensile yield function $F_t$ calculated from the current stress state. Three different scenarios are possible, which are the following:

1. $F_t \geq -YTOL$ and $F_t > F_c$ $\rightarrow$ Tension surface active
2. $F_c \geq -YTOL$ and $F_c > F_t$ $\rightarrow$ Compression surface active
3. $F_c \geq -YTOL$ and $F_t \geq -YTOL$ $\rightarrow$ Both surfaces active

where $YTOL$ is a user defined tolerance, specifying the numerical tolerance on the yield function.

### 7.9.2 Derivatives of the stress invariants

The general derivatives of the stress invariants $p$, $J$ and $\theta$ will be used in the following sections:

$$\left\{\frac{\partial p}{\partial \sigma}\right\} = \frac{1}{3}\left\{1 \quad 1 \quad 1 \quad 0 \quad 0 \quad 0\right\}^T \tag{7.128}$$

$$\left\{\frac{\partial J}{\partial \sigma}\right\} = \frac{1}{2J}\left\{\sigma_x - p \quad \sigma_y - p \quad \sigma_z - p \quad 2\,\tau_{xy} \quad 2\,\tau_{xz} \quad 2\,\tau_{yz}\right\}^T \tag{7.129}$$

$$\left\{\frac{\partial\theta}{\partial\sigma}\right\} = \frac{\sqrt{3}}{2\cos(3\theta)\,J^3}\left[\frac{3\,det\,s}{J}\left\{\frac{\partial J}{\partial\sigma}\right\} - \left\{\frac{\partial(det\,s)}{\partial\sigma}\right\}\right] \tag{7.130}$$

with

$$\begin{aligned} det\,s &= (\sigma_x - p)(\sigma_y - p)(\sigma_z - p) - (\sigma_x - p)\,\tau_{yz}^2 - (\sigma_y - p)\,\tau_{zx}^2 - \\ &\quad -(\sigma_z - p)\,\tau_{xy}^2 + 2\,\tau_{xy}\,\tau_{yz}\,\tau_{zx} \end{aligned} \tag{7.131}$$

### 7.9.3 Partial derivatives for the compression yield surface

In this case, when only the compressive yield surface is active, the mechanical behaviour of shotcrete is goverened by the yield function given in equation 7.4. The calculation of the partial derivative of the yield function with respect to stress, $\{\partial F_c/\partial\sigma\}$, will be given first, followed by the partial derivative of the yield function with respect to time, $\partial F_c/\partial t$.

*i) Calculation of* $\{\partial F_c/\partial\sigma\}$

As $F_c$ is independent of $\theta$, it can be written:

$$\left\{\frac{\partial F_c}{\partial\sigma}\right\} = \frac{\partial F_c}{\partial p}\left\{\frac{\partial p}{\partial\sigma}\right\} + \frac{\partial F_c}{\partial J}\left\{\frac{\partial J}{\partial\sigma}\right\} \tag{7.132}$$

with

$$\frac{\partial F_c}{\partial p} = A_c \qquad \text{and} \qquad \frac{\partial F_c}{\partial J} = 2J \tag{7.133}$$

Since associated conditions are adopted for the current constitutive model, the derivative of the compressive plastic potential with respect to stress, $\{\partial P_c/\partial\sigma\}$, equals the derivative of the compressive yield function and this can be expressed as:

$$\left\{\frac{\partial F_c}{\partial\sigma}\right\} = \left\{\frac{\partial P_c}{\partial\sigma}\right\} \tag{7.134}$$

*ii) Calculation of* $\partial F_c/\partial t$

The calculation of the derivative of the compressive yield function with respect to time involves the following calculations:

$$\frac{\partial F_c}{\partial t} = \left[\frac{\partial F_c}{\partial A_c}\frac{\partial A_c}{\partial f_c} + \frac{\partial F_c}{\partial\tau_c}\frac{\partial\tau_c}{\partial f_c}\right]\frac{\partial f_c}{\partial t} \tag{7.135}$$

with

$$\frac{\partial F_c}{\partial A_c} = p \qquad \text{and} \qquad \frac{\partial A_c}{\partial f_c} = \alpha_c \tag{7.136}$$

In addition it can be written:

$$\frac{\partial F_c}{\partial\tau_c} = -2\tau_c \qquad \text{and} \qquad \frac{\partial\tau_c}{\partial f_c} = \sqrt{\beta_c} \tag{7.137}$$

Therefore equation 7.135 can be rewritten as:

$$\frac{\partial F_c}{\partial t} = \left[\alpha_c\, p - 2\,\tau_c\,\sqrt{\beta_c}\right]\,\frac{\partial f_c}{\partial t} \tag{7.138}$$

The derivative of the equivalent uniaxial compressive strength with respect to time, $\partial f_c/\partial t$, is now required for all four zones of the normalised hardening and softening curve, earlier described in Section 7.3.1. This term can be expressed as:

Zone I:

$$\begin{aligned}\frac{\partial f_c}{\partial t} &= \left[f_{cy,n} + (1 - f_{cy,n})\left(2H_c - H_c^2\right)\right]\, f_{cp}(t)\,\frac{s}{2}\,\frac{\sqrt{t_{28}}}{t^{\frac{3}{2}}} - \\ &\quad -2\, f_{cp}(t)\,(1 - f_{cy,n})\,(1 - H_c)\,\frac{H_c}{\varepsilon^p_{cp}(t)}\,\frac{A\,B}{t}\,\left(\ln\left(\frac{t}{t_1}\right)\right)^{B-1}\end{aligned} \tag{7.139}$$

Zone II:

$$\begin{aligned}\frac{\partial f_c}{\partial t} &= \left[1 + \frac{f_{cf,n} - 1}{H_{cf} - 1}\,(H_c - 1)\right]\, f_{cp}(t)\,\frac{s}{2}\,\frac{\sqrt{t_{28}}}{t^{\frac{3}{2}}} - \\ &\quad f_{cp}(t)\,\frac{f_{cf,n} - 1}{H_{cf} - 1}\,\frac{H_c}{\varepsilon^p_{cp}(t)}\,\frac{A\,B}{t}\,\left(\ln\left(\frac{t}{t_1}\right)\right)^{B-1}\end{aligned} \tag{7.140}$$

Zone III:

$$\begin{aligned}\frac{\partial f_c}{\partial t} &= \left[f_{cf,n} + \frac{f_{cu,n} - f_{cf,n}}{H_{cu} - H_{cf}}\,(H_c - H_{cf})\right]\, f_{cp}(t)\,\frac{s}{2}\,\frac{\sqrt{t_{28}}}{t^{\frac{3}{2}}} - \\ &\quad -f_{cp}(t)\,\frac{f_{cu,n} - f_{cf,n}}{H_{cu} - H_{cf}}\,\frac{H_c}{\varepsilon^p_{cp}(t)}\,\frac{A\,B}{t}\,\left(\ln\left(\frac{t}{t_1}\right)\right)^{B-1}\end{aligned} \tag{7.141}$$

Zone IV:

$$\frac{\partial f_c}{\partial t} = f_{cu,n}\, f_{cp}(t)\,\frac{s}{2}\,\frac{\sqrt{t_{28}}}{t^{\frac{3}{2}}} \tag{7.142}$$

As discussed previously, the material parameters for shotcrete are changing for a shotcrete age less than 28 days but are constant afterwards. This implies that for the time $t > t_{28}$ during an analysis the derivative $\partial f_c/\partial t$ becomes zero.

### 7.9.4 Partial derivatives for the tension yield surface

The yield function given in equation 7.9 controls the material response of shotcrete in tension. Similar to the compression surface, the derivative of the yield function with respect to stress, $\{\partial F_t/\partial\sigma\}$, is established first, followed by the derivative of the yield function with respect to time, $\partial F_t/\partial t$.

*i) Calculation of* $\{\partial F_t/\partial\sigma\}$

It is given that:

$$\left\{\frac{\partial F_t}{\partial \sigma}\right\} = \frac{\partial F_t}{\partial p}\left\{\frac{\partial p}{\partial \sigma}\right\} + \frac{\partial F_t}{\partial J}\left\{\frac{\partial J}{\partial \sigma}\right\} + \frac{\partial F_t}{\partial \theta}\left\{\frac{\partial \theta}{\partial \sigma}\right\} \tag{7.143}$$

with

$$\frac{\partial F_t}{\partial p} = 1 \tag{7.144}$$

$$\frac{\partial F_t}{\partial J} = \left[\left(\frac{2J}{\sqrt{3}}\sin\left(\theta+\frac{2\pi}{3}\right)\right)^n + (a\,f_t)^n\right]^{\frac{1-n}{n}} J^{n-1}\left(\frac{2}{\sqrt{3}}\sin\left(\theta+\frac{2\pi}{3}\right)\right)^n \tag{7.145}$$

and

$$\begin{aligned}\frac{\partial F_t}{\partial \theta} &= \left[\left(\frac{2J}{\sqrt{3}}\sin\left(\theta+\frac{2\pi}{3}\right)\right)^n + (a\,f_t)^n\right]^{\frac{1-n}{n}}\left(\frac{2J}{\sqrt{3}}\right)^n\cdot \\ &\quad\cdot\left(\sin\left(\theta+\frac{2\pi}{3}\right)\right)^{n-1}\cos\left(\theta+\frac{2\pi}{3}\right)\end{aligned} \tag{7.146}$$

As in the case of the compression surface, associated conditions are applied for determining the tensile plastic potential and therefore the following expression for the derivative of the tensile plastic potential with respect to stress, $\{\partial P_t/\partial\sigma\}$, can be established:

$$\left\{\frac{\partial F_t}{\partial \sigma}\right\} = \left\{\frac{\partial P_t}{\partial \sigma}\right\} \tag{7.147}$$

*ii) Calculation of $\partial F_t/\partial t$*

The following procedure applies to the determination of the derivative of the tensile yield function with respect to time, $\partial F_t/\partial t$:

$$\frac{\partial F_t}{\partial t} = \frac{\partial F_t}{\partial f_t}\frac{\partial f_t}{\partial t} \tag{7.148}$$

with

$$\frac{\partial F_t}{\partial f_t} = \left[\left(\frac{2J}{\sqrt{3}}\sin\left(\theta+\frac{2\pi}{3}\right)\right)^n + (a\,f_t)^n\right]^{\frac{1-n}{n}} a^n\,f_t^{n-1} - 1 \tag{7.149}$$

The derivative of the equivalent uniaxial tensile strength with respect to time, $\partial f_t/\partial t$, has to be calculated for each of the 3 zones of the normalised hardening/softening curve for tension presented in section 7.3.2.

Zone I:

$$\begin{aligned}\frac{\partial f_t}{\partial t} &= \left[f_{ty,n} + (1-f_{ty,n})\left(2H_t - H_t^2\right)\right] f_{tp}(t)\,\frac{s}{2}\,\frac{\sqrt{t_{28}}}{t^{\frac{3}{2}}} - \\ &\quad -2\,f_{tp}(t)\,(1-f_{ty,n})\,(1-H_t)\,\frac{H_t}{\varepsilon^p_{cp}(t)}\,\frac{A\,B}{t}\left(\ln\left(\frac{t}{t_1}\right)\right)^{B-1}\end{aligned} \tag{7.150}$$

Zone II:
In the case of the linear softening in option A it can be written as:

$$\begin{aligned}\frac{\partial f_t}{\partial t} &= \left[1+\frac{f_{tu,n}-1}{H_{tu}-1}\left(H_t-1\right)\right] f_{tp}(t)\,\frac{s}{2}\,\frac{\sqrt{t_{28}}}{t^{\frac{3}{2}}} - \\ &\quad -f_{tp}(t)\,\frac{f_{tu,n}-1}{H_{tu}-1}\,\frac{H_t}{\varepsilon^p_{cp}(t)}\,\frac{A\,B}{t}\,\left(\ln\left(\frac{t}{t_1}\right)\right)^{B-1}\end{aligned} \tag{7.151}$$

If the softening is described by the exponential function given in option B, it can be expressed as:

$$\begin{aligned}\frac{\partial f_t}{\partial t} &= \exp\left(-\psi\left(H_t-1\right)\right)\, f_{tp}(t)\,\frac{s}{2}\,\frac{\sqrt{t_{28}}}{t^{\frac{3}{2}}} + \\ &\quad +\psi\, f_{tp}(t)\,\exp\left(-\psi\left(H_t-1\right)\right)\,\frac{H_t}{\varepsilon^p_{cp}(t)}\,\frac{A\,B}{t}\,\left(\ln\left(\frac{t}{t_1}\right)\right)^{B-1}\end{aligned} \tag{7.152}$$

Zone III:

$$\frac{\partial f_t}{\partial t} = f_{tu,n}\, f_{tp}(t)\,\frac{s}{2}\,\frac{\sqrt{t_{28}}}{t^{\frac{3}{2}}} \tag{7.153}$$

Regarding the time-dependency of the yield function, the same rule applies for the tension surface as for the compression surface: material parameters are considered to be constant for a shotcrete age larger than 28 days and therefore $\partial f_t/\partial t$ reduces to zero if $t > t_{28}$ during the analysis.

### 7.9.5 Calculation of the hardening modulus for the compression surface

In Section 7.3.1 it was mentioned that the minor principal plastic strain $\varepsilon_3^p$ is controlling the motion of the compression yield surface in the general stress space. Following equation 7.89, the hardening modulus $A$ for the compression surface being the active yield surface can be written as:

$$A = -\frac{1}{\lambda}\,\frac{\partial F_c}{\partial \varepsilon_3^p}\,\Delta\varepsilon_3^p \tag{7.154}$$

The general flow rule given in equation 6.20 for an elasto-plastic material can now be specified for the compression surface of the current constitutive model as:

$$\Delta\varepsilon_3^p = -\lambda\,\frac{\partial F_c}{\partial \sigma_3} \tag{7.155}$$

Combining these two equations one obtains the hardening modulus as:

$$A = \frac{\partial F_c}{\partial \varepsilon_3^p}\,\frac{\partial F_c}{\partial \sigma_3} \tag{7.156}$$

The derivative of the compression surface with respect to the minor principal plastic strain, $\partial F_c/\partial\varepsilon_3^p$, is given as:

$$\frac{\partial F_c}{\partial \varepsilon_3^p} = \left[\frac{\partial F_c}{\partial A_c}\,\frac{\partial A_c}{\partial f_c} + \frac{\partial F_c}{\partial \tau_c}\,\frac{\partial \tau_c}{\partial f_c}\right]\,\frac{\partial f_c}{\partial \varepsilon_3^p} \tag{7.157}$$

The terms $\partial F_c/\partial A_c$, $\partial A_c/\partial f_c$, $\partial F_c/\partial \tau_c$ and $\partial \tau_c/\partial f_c$ have been presented in equations 7.136 and 7.137. Furthermore, the derivative of the equivalent uniaxial compressive stress with respect to the minor principal plastic strain, $\partial f_c/\partial \varepsilon_3^p$ is required for all the four zones of the normalised hardening/softening curve for compression introduced in Section 7.3.1.

Zone I:

$$\frac{\partial f_c}{\partial \varepsilon_3^p} = \frac{2\, f_{cp}(t)\,(1 - f_{cy,n})\,(1 - H_c)}{\varepsilon_{cp}^p(t)} \tag{7.158}$$

Zone II:

$$\frac{\partial f_c}{\partial \varepsilon_3^p} = f_{cp}(t)\,\frac{f_{cf,n} - 1}{(H_{cf} - 1)\,\varepsilon_{cp}^p(t)} \tag{7.159}$$

Zone III:

$$\frac{\partial f_c}{\partial \varepsilon_3^p} = f_{cp}(t)\,\frac{f_{cu,n} - f_{cf,n}}{(H_{cu} - H_{cf})\,\varepsilon_{cp}^p(t)} \tag{7.160}$$

Zone IV:

$$\frac{\partial f_c}{\partial \varepsilon_3^p} = 0 \tag{7.161}$$

In addition, the derivative of the compression surface with respect to the minor principal stress, $\partial F_c/\partial \sigma_3$, is required for the calculation of the hardening modulus $A$. It can be written:

$$\frac{\partial F_c}{\partial \sigma_3} = \frac{\partial F_c}{\partial p}\,\frac{\partial p}{\partial \sigma_3} + \frac{\partial F_c}{\partial J}\,\frac{\partial J}{\partial \sigma_3} \tag{7.162}$$

The derivatives $\partial F_c/\partial p$ and $\partial F_c/\partial J$ have already been established in equation 7.133. The missing terms can be expressed as:

$$\frac{\partial p}{\partial \sigma_3} = \frac{1}{3} \qquad \text{and} \qquad \frac{\partial J}{\partial \sigma_3} = \frac{1}{2\,J}\,(\sigma_3 - p) \tag{7.163}$$

Finally, the hardening modulus $A$ for the compression surface can be determined as:

$$A = \left(\alpha_c\, p - 2\,\tau_c\,\sqrt{\beta_c}\right)\left(\frac{A_c}{3} + \sigma_3 - p\right)\,\frac{\partial f_c}{\partial \varepsilon_3^p} \tag{7.164}$$

### 7.9.6 Calculation of the hardening modulus for the tension surface

In contrast to the compression surface, the governing parameter for the tensile plastic strain hardening/softening is the major principal plastic strain $\varepsilon_1^p$, as highlighted in Section 7.3.2. Therefore, the hardening modulus for the tensile material behaviour can be expressed as:

$$A = -\frac{1}{\lambda}\,\frac{\partial F_t}{\partial \varepsilon_1^p}\,\Delta\varepsilon_1^p \tag{7.165}$$

The general flow rule from equation 6.20 yields for the tension surface:

$$\Delta\varepsilon_1^p = \lambda\,\frac{\partial F_t}{\partial \sigma_1} \tag{7.166}$$

Rearrangement leads to:

$$A = -\frac{\partial F_t}{\partial \varepsilon_1^p} \frac{\partial F_t}{\partial \sigma_1} \tag{7.167}$$

The derivative of the tension surface with respect to the major principal plastic strain, $\partial F_t / \partial \varepsilon_1^p$, can be written as:

$$\frac{\partial F_t}{\partial \varepsilon_1^p} = \frac{\partial F_t}{\partial f_t} \frac{\partial f_t}{\partial \varepsilon_1^p} \tag{7.168}$$

The term $\partial F_t / \partial f_t$ was introduced in equation 7.149. Similar to the compression surface, the derivative of the equivalent uniaxial tensile stress with respect to the major principal plastic strain, $\partial f_t / \partial \varepsilon_1^p$, has to be calculated for each zone of the normalised hardening/softening curve presented in Section 7.3.2.

Zone I:

$$\frac{\partial f_t}{\partial \varepsilon_1^p} = \frac{2\, f_{tp}(t)\, (1 - f_{ty,n})\, (1 - H_t)}{\varepsilon_{tp}^p(t)} \tag{7.169}$$

Zone II:
In the case of linear softening in option A it can be written:

$$\frac{\partial f_t}{\partial \varepsilon_1^p} = f_{tp}(t)\, \frac{f_{tu,n} - 1}{(H_{tu} - 1)\, \varepsilon_{tp}^p(t)} \tag{7.170}$$

For the exponential softening in option B it can be expressed:

$$\frac{\partial f_t}{\partial \varepsilon_1^p} = -\psi\, f_{tp}(t)\, \frac{\exp\left(-\psi\, (H_t - 1)\right)}{\varepsilon_{tp}^p(t)} \tag{7.171}$$

Zone III:

$$\frac{\partial f_t}{\partial \varepsilon_1^p} = 0 \tag{7.172}$$

Furthermore, the derivative of the tensile yield function with respect to the major principal stress, $\partial F_t / \partial \sigma_1$ is needed, which is given as:

$$\frac{\partial F_t}{\partial \sigma_1} = \frac{\partial F_t}{\partial p} \frac{\partial p}{\partial \sigma_1} + \frac{\partial F_t}{\partial J} \frac{\partial J}{\partial \sigma_1} + \frac{\partial F_t}{\partial \theta} \frac{\partial \theta}{\partial \sigma_1} \tag{7.173}$$

The derivatives $\partial F_t / \partial p$, $\partial F_t / \partial J$ and $\partial F_t / \partial \theta$ were calculated in equations 7.144, 7.145 and 7.146 respectively. The missing terms can be established as:

$$\frac{\partial p}{\partial \sigma_1} = \frac{1}{3} \qquad \text{and} \qquad \frac{\partial J}{\partial \sigma_1} = \frac{1}{2\, J}\, (\sigma_1 - p) \tag{7.174}$$

furthermore

$$\frac{\partial \theta}{\partial \sigma_1} = \frac{\sqrt{3}}{2 \cos(3\theta)\, J^3} \left[ \frac{3\, det\, s}{J} \frac{1}{2\, J}\, (\sigma_1 - p) - \frac{1}{3}\, (2\, \sigma_2\, \sigma_3 - \sigma_1\, \sigma_3 - \sigma_1\, \sigma_2) \right] \tag{7.175}$$

Combining the above equations, the hardening modulus for the tension surface can finally be determined as:

$$A = -\left(Q\,a^n\,f_t^{n-1} - 1\right)\,\left(\frac{1}{3} + (\sigma_1 - p)\,R + \frac{1}{3}\,(2\,\sigma_2\,\sigma_3 - \sigma_1\,\sigma_3 - \sigma_1\,\sigma_2)\,S\right)\,\frac{\partial f_t}{\partial \varepsilon_1^p} \tag{7.176}$$

with

$$P = \frac{2}{\sqrt{3}}\,\sin\left(\theta + \frac{2\pi}{3}\right) \tag{7.177}$$

$$Q = \left[(P\,J)^n + (a\,f_t)^n\right]^{\frac{1-n}{n}} \tag{7.178}$$

and

$$R = P^n\,J^{n-2}\,\frac{Q}{2} + \frac{Q\;(P\,J)^n\;\cos\left(\theta + \frac{2\pi}{3}\right)\;3\,det\,s}{2\,P\;\cos\left(3\theta\right)\;J^5} \tag{7.179}$$

$$S = -\frac{Q\;(P\,J)^n\;\cos\left(\theta + \frac{2\pi}{3}\right)}{P\;\cos\left(3\theta\right)\;J^3} \tag{7.180}$$

### 7.9.7 Calculation of the elastic constitutive matrix

The elastic constitutive matrix has been introduced in Section 6.3.1 of the previous chapter. It can be expressed in terms of the time-dependent Young's modulus $E(t)$ and the constant Poisson's ratio $\mu$ as:

$$[D] = \frac{E(t)}{(1+\mu)\,(1-2\mu)}\begin{bmatrix} 1-\mu & \mu & \mu & 0 & 0 & 0 \\ \mu & 1-\mu & \mu & 0 & 0 & 0 \\ \mu & \mu & 1-\mu & 0 & 0 & 0 \\ 0 & 0 & 0 & \frac{1-2\mu}{2} & 0 & 0 \\ 0 & 0 & 0 & 0 & \frac{1-2\mu}{2} & 0 \\ 0 & 0 & 0 & 0 & 0 & \frac{1-2\mu}{2} \end{bmatrix} \tag{7.181}$$

with the development of the time-dependent Young's modulus $E(t)$ given in equation 7.54.

### 7.9.8 Calculation of the changes in the compressive hardening parameter

The normalised hardening parameter which controls the motion of the compression yield surface in general stress space has been introduced in equation 7.13. The change of this hardening parameter during an analysis can be expressed as:

$$\Delta H_c = \frac{\partial H_c}{\partial \varepsilon_3^p}\,\Delta\varepsilon_3^p + \frac{\partial H_c}{\partial \varepsilon_{cp}^p(t)}\,\frac{\partial \varepsilon_{cp}^p(t)}{\partial t}\,\Delta t \tag{7.182}$$

The involved derivatives in the above equation can be calculated as:

$$\frac{\partial H_c}{\partial \varepsilon_3^p} = \frac{1}{\varepsilon_{cp}^p(t)} \tag{7.183}$$

$$\frac{\partial H_c}{\partial \varepsilon_{cp}^p(t)} = -\frac{H_c}{\varepsilon_{cp}^p(t)} \tag{7.184}$$

$$\frac{\partial \varepsilon_{cp}^p(t)}{\partial t} = \frac{A\,B}{t}\,\left[\ln\left(\frac{t}{t_1}\right)\right]^{B-1} \tag{7.185}$$

Therefore, for a shotcrete age less than 28 days the change in the compressive hardening parameter can be written as:

$$\Delta H_c = \frac{1}{\varepsilon_{cp}^p(t)}\,\Delta\varepsilon_3^p - \frac{H_c}{\varepsilon_{cp}^p(t)}\,\frac{A\,B}{t}\,\left[\ln\left(\frac{t}{t_1}\right)\right]^{B-1}\,\Delta t \tag{7.186}$$

In the case of $t > t_{28}$ this equation reduces to:

$$\Delta H_c = \frac{1}{\varepsilon_{cp}^p(t)}\,\Delta\varepsilon_3^p \tag{7.187}$$

### 7.9.9 Calculation of the changes in the tensile hardening parameter

Equation 7.32 presented the normalised hardening parameter for the tension yield surface where the major principal plastic strain, $\varepsilon_1^p$ controls the hardening and softening of the shotcrete. The change in the tensile hardening parameter during an analysis can be expressed as:

$$\Delta H_t = \frac{\partial H_t}{\partial \varepsilon_1^p}\,\Delta\varepsilon_1^p + \frac{\partial H_t}{\partial \varepsilon_{tp}^p(t)}\,\frac{\partial \varepsilon_{tp}^p(t)}{\partial t}\,\Delta t \tag{7.188}$$

The following derivatives can be calculated:

$$\frac{\partial H_t}{\partial \varepsilon_1^p} = \frac{1}{\varepsilon_{tp}^p(t)} \tag{7.189}$$

$$\frac{\partial H_t}{\partial \varepsilon_{tp}^p(t)} = -\frac{H_t}{\varepsilon_{tp}^p(t)} \tag{7.190}$$

$$\frac{\partial \varepsilon_{tp}^p(t)}{\partial t} = \frac{\delta\,A\,B}{t}\,\left[\ln\left(\frac{t}{t_1}\right)\right]^{B-1} \tag{7.191}$$

Combining these equations, the change in the normalised tensile hardening parameter becomes:

$$\Delta H_t = \frac{1}{\varepsilon_{tp}^p(t)}\,\Delta\varepsilon_1^p - \frac{H_t}{\varepsilon_{cp}^p(t)}\,\frac{A\,B}{t}\,\left[\ln\left(\frac{t}{t_1}\right)\right]^{B-1}\,\Delta t \tag{7.192}$$

For $t > t_{28}$ the above equation becomes:

$$\Delta H_t = \frac{1}{\varepsilon_{tp}^p(t)}\,\Delta\varepsilon_1^p \tag{7.193}$$

## 7.10 Model calibration

The aim of the following sections is to derive the necessary material parameters needed for the above presented constitutive model for shotcrete, so that the model can be validated and used in a boundary value problem. Since any experimental work on shotcrete behaviour was not part of this research, this model calibration is performed mainly with the help of published data. It should be mentioned that a complete set of test data for one particular shotcrete type at various ages is rare, if not impossible to find. Furthermore, tests on shotcrete focus mainly on the uniaxial compression behaviour and no information could be found on the early age material behaviour in tension. Test results for multiaxial loading conditions are hardly considered in any experimental research programme. Unfortunately, since there is a large amount of influencing factors on the material behaviour (mix design, spraying technique, rebound behaviour, etc.) almost all of the experimental results available in the literature show a considerable scatter, which makes a precise derivation of model parameters difficult. Sample preparation seems to be another key factor, where the factor "time" plays an important role. However, it will be shown that the developed constitutive model is capable of predicting the main characteristics of shotcrete behaviour, including the transition from a very ductile to a more brittle material response with curing time. Finally, some curve fitting for published data on creep, shrinkage and hydration temperature is also presented.

### 7.10.1 Increase in stiffness and compressive strength

Huber (1991) performed a series of 5 tests on shotcrete samples, taken from the Inntal Tunnel in Austria, with different accelerator contents. The specimens where sprayed in the dry-mix method directly at the tunnel construction site into a sample-preparation box, avoiding the inclusion of rebound material, and had a size of $10 \times 10 \times 40\,\text{cm}$. The shotcrete mix proportions were the following (Tab. 7.4):

| Aggregates (0/12 mm) | Cement PZ 275 | Water | Accelerator |
|---|---|---|---|
| $1800\,\text{kg/m}^3$ | $350\,\text{kg/m}^3$ | 160 l | 5 and 7 % |

Table 7.4: Mix design for tested shotcrete (from Huber, 1991)

During the load controlled compression tests the increase in stiffness and strength was measured for different shotcrete ages of up to 168 h. Fig. 7.22 and Fig. 7.23 illustrate the obtained results for all the 5 tests.

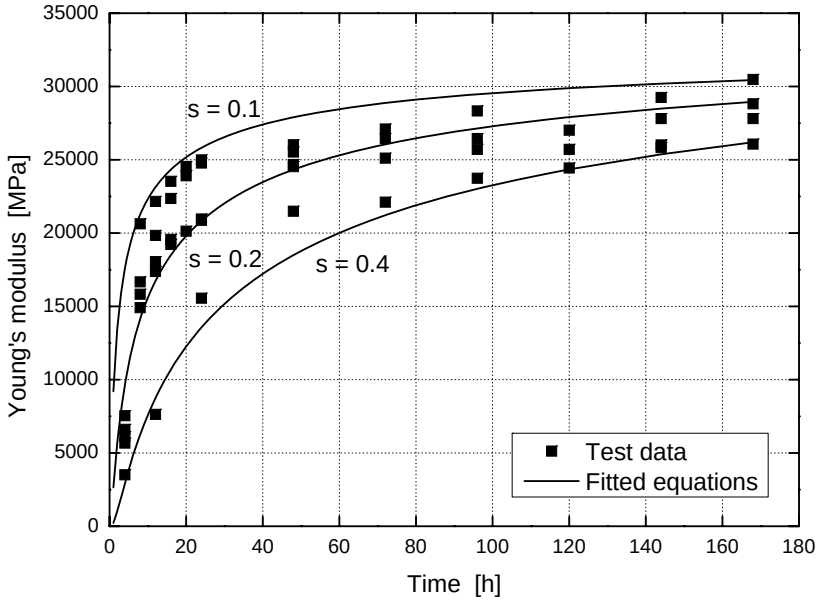



Figure 7.22: Parameter fitting for increase in stiffness with time (after Huber, 1991)

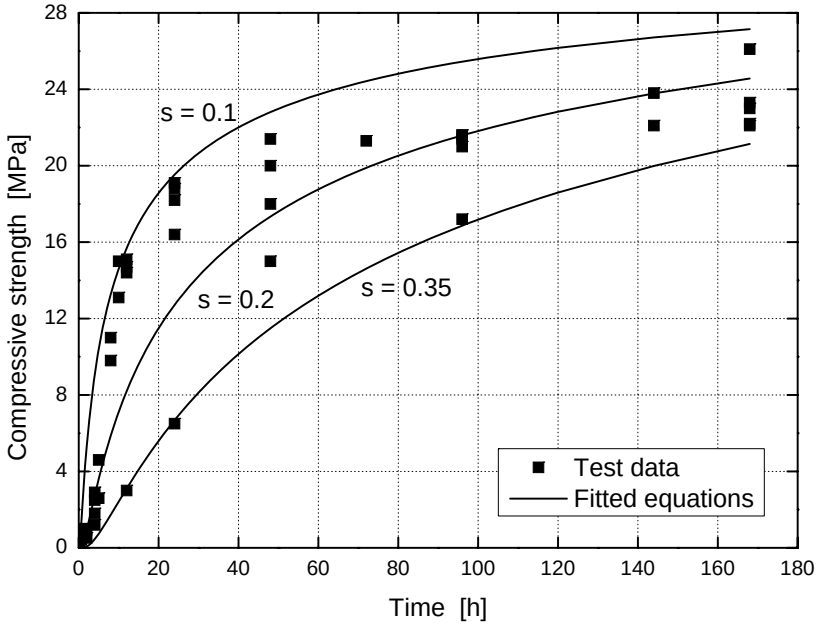



Figure 7.23: Parameter fitting for increase in compressive strength with time (after Huber, 1991)

From the experimental data it can be seen that the development of stiffness with time appears to grow somewhat faster than the increase in compressive strength with time, which is consistent with the adopted model equations. Furthermore, by fitting the involved parameters for equation 7.54 and 7.56, a possible scatter in the test data can be covered by establishing a lower bound, upper bound and intermediate curve, which would represent an optimum fit. As a reference model parameter for the Young's modulus at 28 days a value of $E_{28} = 32\,\mathrm{GPa}$

has been chosen to be a reasonable value. The compressive strength for hardened shotcrete at 28 days was estimated as $f_{cp,28} = 30\,\text{MPa}$. Tab. 7.5 contains the possible values of the cement parameter $s$ for both the increase in stiffness and strength according to the model equations used for the graphical illustration in Fig. 7.22 and Fig. 7.23.

| | $s$ for stiffness (-) | $s$ for strength (-) |
|---|---|---|
| Upper bound | 0.1 | 0.1 |
| Lower bound | 0.4 | 0.35 |
| Intermediate value | 0.2 | 0.2 |

Table 7.5: Cement parameter for increase in stiffness and strength fitted to test data from Huber (1991)

### 7.10.2 Complete uniaxial compression tests at different shotcrete ages

As mentioned in Section 5.7 of Chapter 5, Sezaki et al. (1989) performed an advanced experimental study on the mechanical properties of early age shotcrete in compression. Their tests involved the analysis of the development of the compressive strength, the Young's modulus and the failure strain with curing time for the following specified wet-mix, summarised in Tab. 7.6:

| Max. size of aggregate (mm) | W/C (%) | Water ($kg/m^3$) | Cement ($kg/m^3$) | Sand ($kg/m^3$) | Gravel ($kg/m^3$) | Accelerator concentration (%) |
|---|---|---|---|---|---|---|
| 10 | 57 | 217 | 380 | 1115 | 633 | 6, 8, 10 |

Table 7.6: Mix design for tested shotcrete (from Sezaki et al., 1989)

The first step for calibrating the corresponding equations of the presented constitutive model was to fit the increase in stiffness and compressive strength according to the adopted model equations 7.54 and 7.56 to the obtained test data, as can be seen in Fig. 7.24 and Fig. 7.25.

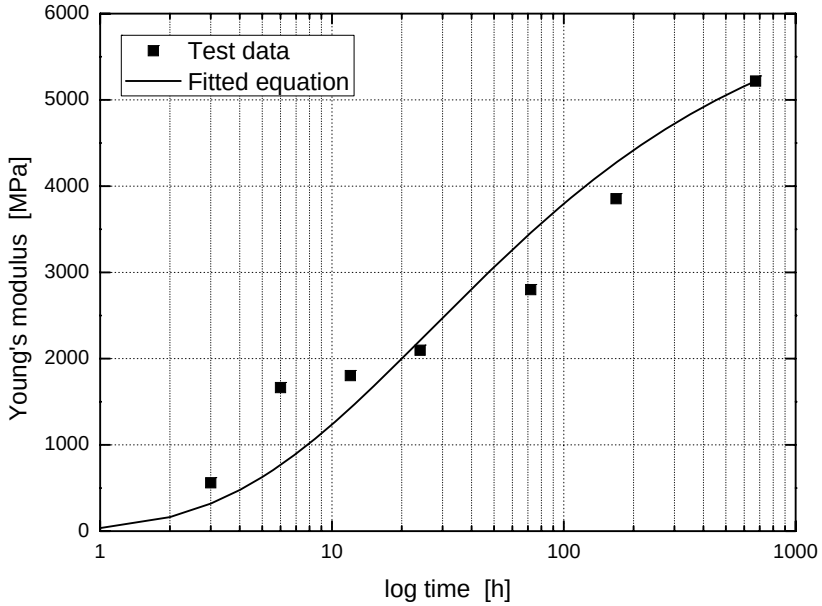



Figure 7.24: Parameter fitting for increase in stiffness with time (after Sezaki et al., 1989)

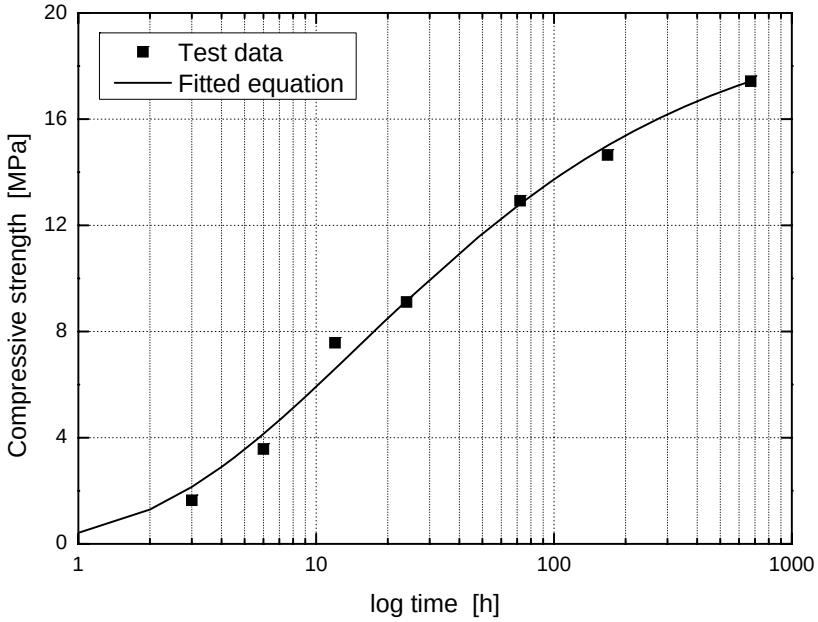



Figure 7.25: Parameter fitting for increase in compressive strength with time (after Sezaki et al., 1989)

The next step in the calibration procedure involved the parameter fitting of the total peak and failure strains at various shotcrete ages according to the adopted model equation. It was highlighted earlier that the presented constitutive model is formulated within the concept of plastic strain hardening/softening. Furthermore, equation 7.58 is established for the development of the plastic peak strains and therefore it is of crucial importance for a correct model calibration to incorporate the elastic strain components via the stiffness and

strength (see Section 7.4.2). Fig. 7.26 illustrates the fitted model equations to the obtained test data measured from the published uniaxial compressive stress strain curves by Sezaki et al. (1989).

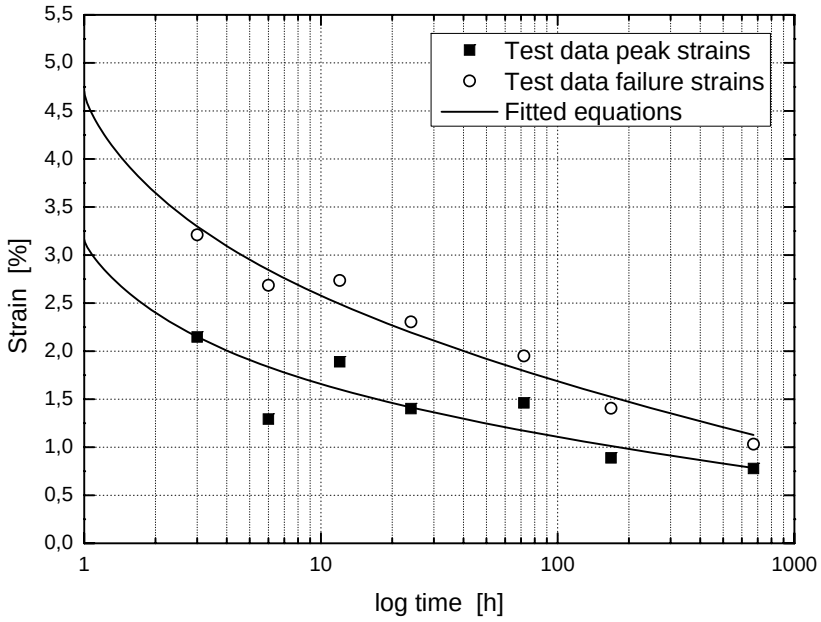



Figure 7.26: Parameter fitting for development of total peak and failure strains (after Sezaki et al., 1989)

Finally, with the estimated model parameters the complete uniaxial stress strain curves in compression at different shotcrete ages can be established up to failure, where the concrete is assumed to be crushed. In Fig. 7.27 it can be seen that with such a calibration procedure very good agreement can be achieved with the test data and the complex behaviour of shotcrete at early ages can be captured in a realistic way.

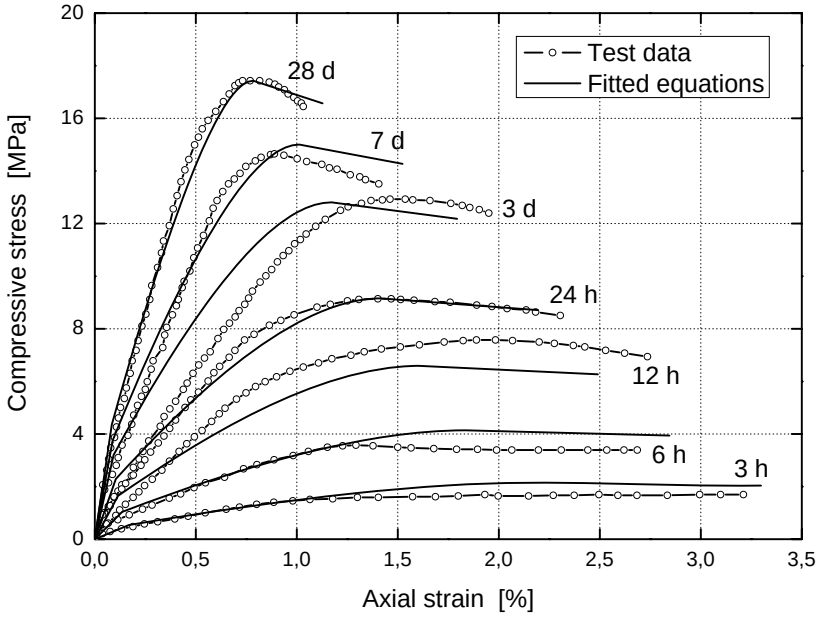



Figure 7.27: Parameter fitting for complete stress strain curves in compression for shotcrete at various ages (after Sezaki et al., 1989)

The material parameters used to obtain the fitted equations in the above plots are summarized in Tab. 7.7.

| $E_{28}$ | $s$ | $f_{cp,28}$ | $f_{cy,28}$ | $f_{cf,28}$ | $s$ | $\varepsilon^p_{cp,28}$ | $\varepsilon^p_{cf,28}$ | $\varepsilon^p_{cp,t_1}$ | $\varepsilon^p_{cp,t_2}$ | $t_2$ |
|---|---|---|---|---|---|---|---|---|---|---|
| (MPa) | (-) | (MPa) | (MPa) | (MPa) | (-) | (%) | (%) | (%) | (%) | (h) |
| 5220 | 0.4 | 17.4 | 4.4 | 16.6 | 0.15 | 0.45 | 0.81 | 2.00 | 1.00 | 24 |

Table 7.7: Fitted stiffness and strength parameters

It should be noted that the obtained stiffness for hardened shotcrete at 28 days, $E_{28}$, appears to be very low compared to the usual stiffness quoted in the literature for concrete. However, it was not possible to find any reason for this apparent anomaly in the paper by Sezaki et al. (1989).

### 7.10.3 Creep deformation in uniaxial compression

High quality data for creep of shotcrete at various stages of hydration is difficult to find in the literature. Although shotcrete is a very creep active medium in the first hours after casting, it seems that systematic testing to understand the principal behaviour behind creep is still lacking. Furthermore, from the available test results it is sometimes not possible to derive appropiate model parameters since necessary additional information regarding stiffness and strength parameters are often missing. However, Outterside (2003) worked on the behaviour of young shotcrete by interpreting test data from an unpublished report by Kusterle (1999)

commissioned by Morgan Tunnelling. In this research project, creep tests started at shotcrete ages of around 11 hours after spraying, which was the earliest possible time, given the fact that the shotcrete had to harden to allow measurements to be taken. Three compressive tests were performed on wet mix specimens of $15 \times 15 \times 30\,\text{cm}$ with a constant applied stress of 3.2 MPa (Test 1), 5.2 MPa (Test 2) and 7.2 MPa (Test 3). The duration of all three tests was roughly 250 hours, after which the load was removed. Tab. 7.8 summarizes the creep tests.

| | Shotcrete age at start of loading | Applied stress |
|---|---|---|
| Test 1 | 11 h | 3.2 MPa |
| Test 2 | 24 h | 5.2 MPa |
| Test 3 | 34 h | 7.2 MPa |

Table 7.8: Test series performed by Kusterle (1999)

As the compressive strength increases rapidly within the first 100 hours after casting, the stress level within the shotcrete samples would reduce significantly. Fig. 7.28 shows the obtained test results for creep including the instantaneous deformation at the onset of loading.

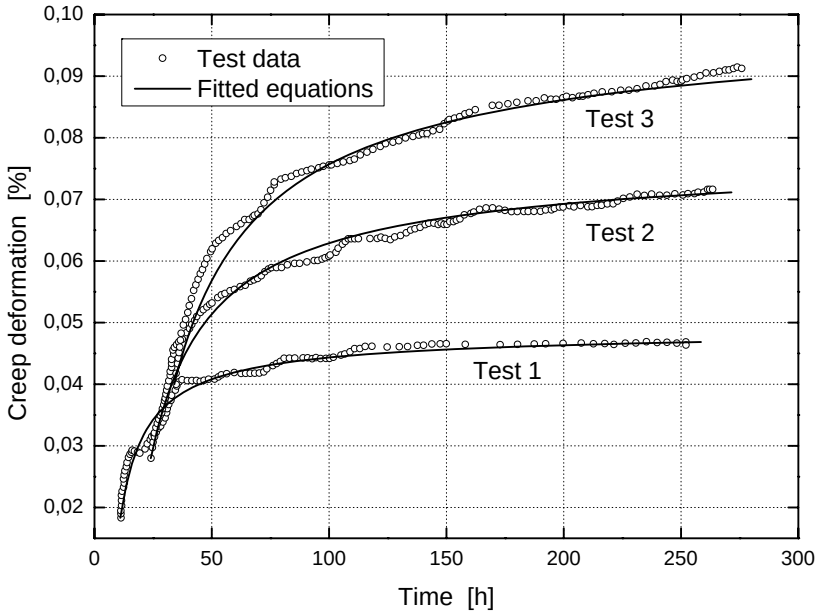



Figure 7.28: Parameter fitting for development of creep deformation at various stages of hydration (after Kusterle, 1999)

The calibrated model parameters for the time-dependent viscosity function given in equation 7.62 are summarized in the following Tab. 7.9

| | $\eta_o$ | n |
|---|---|---|
| | (kPa × h) | (-) |
| Test 1 | $12 \times 10^6$ | 0.98 |
| Test 2 | $13 \times 10^6$ | 0.97 |
| Test 3 | $16 \times 10^6$ | 0.96 |

Table 7.9: Fitted model parameters for predicting creep deformation

By comparing these experimental data with the fitted model equations it can be seen that by assuming a time-dependent viscosity function the model is capable of predicting the main characteristics of shotcrete creep highlighted in Chapter 5.

### 7.10.4 Shrinkage

Thomas (2003) presented in his work a data collection for shrinkage from several researchers, among them Cornejo-Malm (1995), Ding (1998) and Golser et al. (1989). The available data consist of experimental results from various types of shotcrete, including for example wet- and dry-mix, steelfibre reinforced shotcrete of different mix proportions. Additional test data from other researchers that could be found in the literature were incorporated resulting in an extensive shrinkage data collection, as illustrated in Fig. 7.29. It can be seen that a considerable scatter can be identified. Therefore, it was decided to calibrate the model parameters given in equation 7.71 for an upper bound, lower bound and an intermediate curve that represents approximately an average or optimum fit. Tab. 7.10 gives the estimated

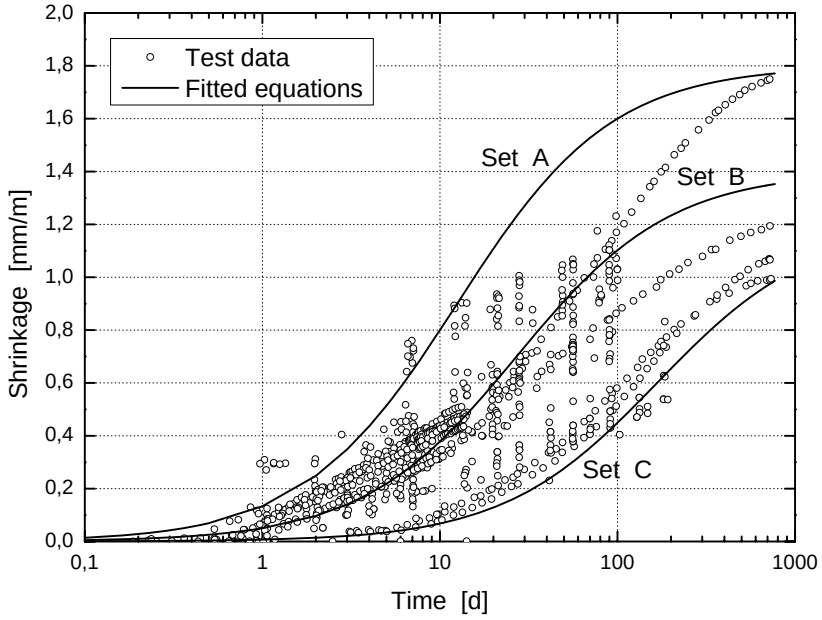



Figure 7.29: Parameter fitting for development of shrinkage deformation

model parameters for the three different sets.

| | $\varepsilon_\infty^{sh}$ | $B$ |
|---|---|---|
| Upper bound - Set A | 1.8 ‰ | 12.5 d |
| Lower bound - Set C | 1.2 ‰ | 167 d |
| Intermediate curve - Set B | 1.4 ‰ | 27 d |

Table 7.10: Fitted model parameters for shrinkage deformation

### 7.10.5 Temperature development during cement hydration

For the same test series on shotcrete samples, introduced in Section 7.10.1, Huber (1991) also measured the temperature development within the specimens during the cement hydration for the first 24 hours. Fig. 7.30 summarizes the obtained results and shows a possible parameter fitting according to equation 7.74.

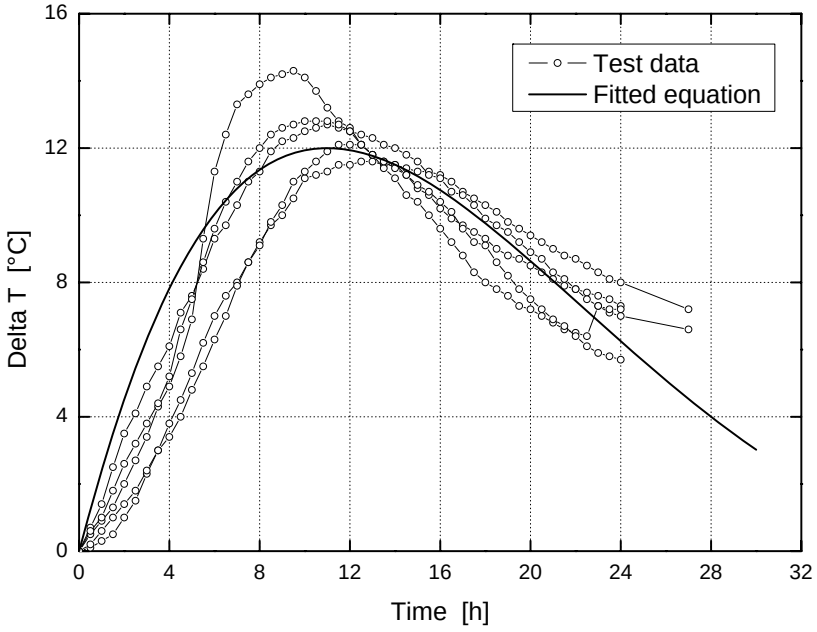



Figure 7.30: Parameter fitting for development of hydration temperature with time (from Huber, 1991)

As expected, for all the test samples the maximum increase in hydration temperature $\Delta T_{max}$ occurs between 9 and 12 hours after spraying. The maximum temperature rise measured was about 14.5 °C. This value might not be appropriate for a real tunnel shell, where due to different thermal boundary and mass conditions this value could be higher than for a single shotcrete sample. However, the general trend of the temperature and thermal deformation development can be assumed to be of the same nature. The adopted model equation

7.74, involving the fitted model parameters given in Tab. 7.11, represents a good simulation for the obtained test data and relatively good agreement is achieved.

| $\Delta T_{max}$ | $t_{max}$ | $t_{zero}$ |
|---|---|---|
| 12 °C | 11 h | 43 h |

Table 7.11: Fitted model parameters for temperature history

## 7.11 Model validation

In the previous section it was shown that it is possible to calibrate the adopted equations of the presented constitutive model against experimental test data for various types of shotcrete found in the literature. These calibrations covered mainly uniaxial stress-strain curves in compression including the increase in stiffness and strength, creep deformation at early ages, volume changes due to shrinkage and the temperature history during cement hydration. In the current section, the aim is to prove that the robust numerical implementation of the constitutive model as presented in Section 7.9 was performed correctly and that model predictions from ICFEP coincide with analytical solutions. This procedure is carried out by taking up some of the obtained model parameters from the previous section and applying them to single element runs in ICFEP.

### 7.11.1 Increase in stiffness with time

The development of the Young's modulus E with time was numerically tested for ten different values of the cement parameter $s$, which governs the increase in stiffness with time. The chosen values for $s$ ranged from 0.1 to 1.0 and the shotcrete had an initial age of $t_o = 1\,\text{h}$. Fig. 7.31 illustrates the curves from the analytical solution (i.e. equation 7.54) compared to model predictions from ICFEP. The values of the stiffness at various shotcrete ages are normalised by the stiffness of hardened shotcrete at 28 days, $E_{28}$, resulting in unity at $t_{28}$ for all the curves. The influence of the cement parameter $s$ can be clearly seen. Values for $s$ close to 1.0 result in a very slow increase of the Young's modulus during the first hours after spraying. In contrast, a value for $s$ of 0.1 already predicts a stiffness of a bit less than 30 % of the full stiffness $E_{28}$ at the beginning of the test for $t_o = 1\,\text{h}$.

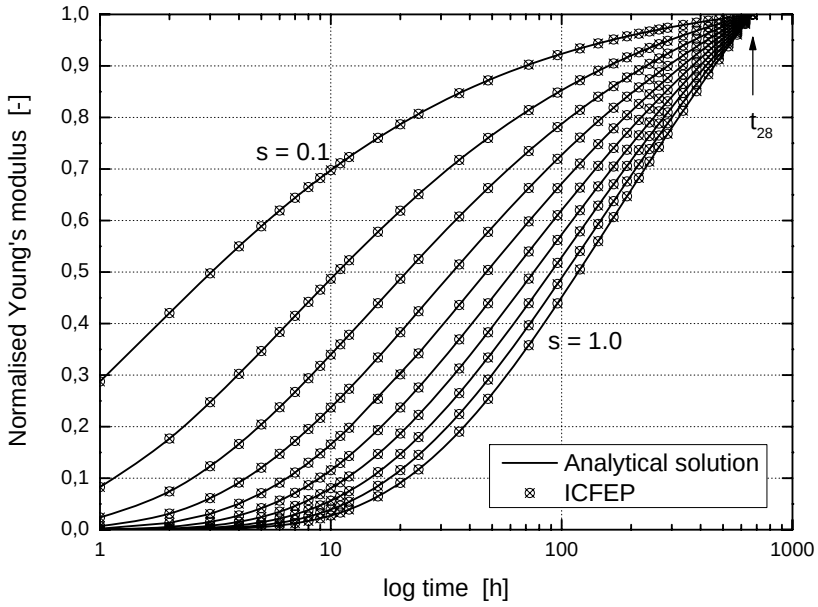



Figure 7.31: Comparison of model predictions with analytical solutions for increase in stiffness with time

### 7.11.2 Uniaxial loading in compression and tension

In Section 7.10.2 some experimental data for uniaxial compression tests at various shotcrete ages carried out by Sezaki et al. (1989) were presented and appropriate model parameters derived. During the testing of the numerical implementation these model parameters were applied to single element runs for both compression and tension. Since for the tensile behaviour of young shotcrete no particular set of data could be found in the literature, the necessary model parameters were estimated in such a way that they would represent realistic material behaviour as could be expected for shotcrete. The simulations focused mainly on uniaxial loading conditions performed in a deformation controlled way in order to capture also the post peak behaviour of shotcrete.

Fig. 7.32 shows the uniaxial stress-strain curves for shotcrete in compression at different stages of cement hydration. It is shown that the implemented equations for the increase in the compressive strength parameters (yield, peak and failure) and for the development of the plastic strain limits (peak and failure) are correct (i.e. they agree with the test data, see also Fig. 7.27) and model predictions agree well with analytical solutions.

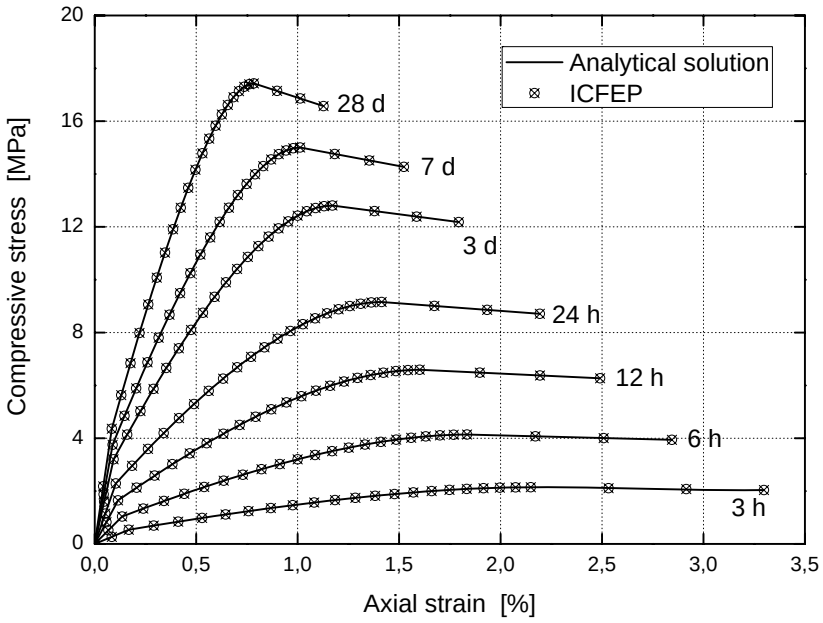



Figure 7.32: Comparison of model predictions with analytical solutions for stress-strain curves at different shotcrete ages

For clarity, the drop in strength from the failure strength down to the residual strength at ultimate level was omitted in the above figure. However, in Fig. 7.33 the complete stress strain curve for a shotcrete at an age of 6 h and 28 d is illustrated, including the ultimate stress regime of zone 4 of the normalised hardening/softening curve. It is shown that the increase in ultimate strength and the reduction in the ultimate plastic strain with time follow the same equation as for the other involved strength and strain limit values.

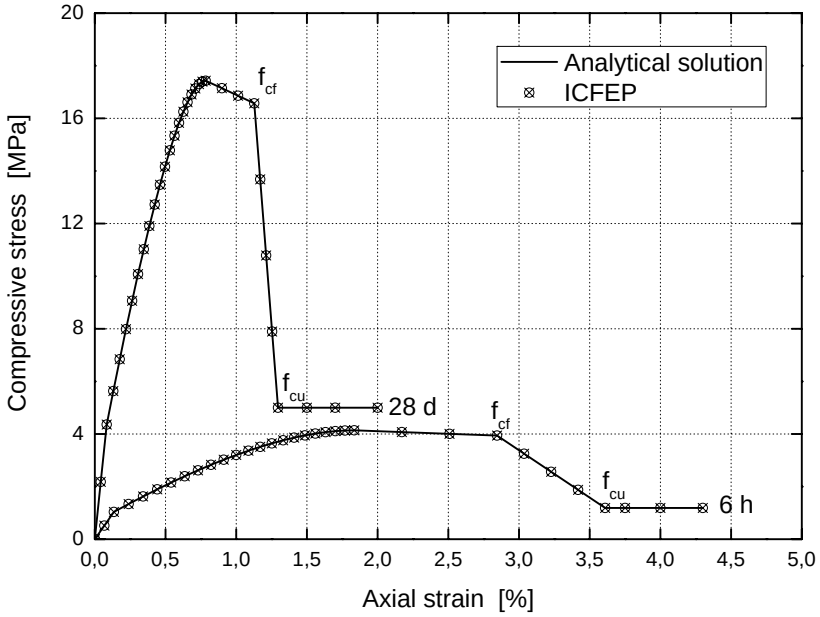



Figure 7.33: Comparison of model predictions with analytical solutions for complete stress-strain curves at two different shotcrete ages

As mentioned earlier, test data for shotcrete at early ages under tensile stresses are hard to find in the literature. Therefore, some assumptions had to be made during the numerical testing procedure of the implemented tensile behaviour. It is well reported that the tensile strength of concrete is about 10 % of the compressive strength showing little hardening behaviour before reaching peak (see Chapter 5). The post peak response during a tensile test is a highly discrete problem mainly goverened by concrete composition and the testing equipment. However, the following tensile model parameters summarised in Tab. 7.12 have been adopted in the series of numerically performed tests.

| $f_{ty}$ | $f_{tp}$ | $f_{tu}$ | $\varepsilon^p_{tp}$ | $\varepsilon^p_{tu}$ | $\psi$ |
|---|---|---|---|---|---|
| (MPa) | (MPa) | (MPa) | (%) | (%) | (-) |
| 1.57 | 1.74 | 0.1 | 0.01 | 0.15 | -0.2 |

Table 7.12: Adopted model parameters for tensile behaviour

The cement parameter $s$, which controls the development of the strength parameters, was chosen to be the same as obtained previously in Section 7.10.2 ($s = 0.15$). For the post peak regime, softening branches following either a linear or exponential function were tested. Fig. 7.34 shows the tensile uniaxial stress-strain curves for shotcrete at various ages, starting at an early age of 3 h adopting the linear reduction in tensile stresses after peak according to option A.

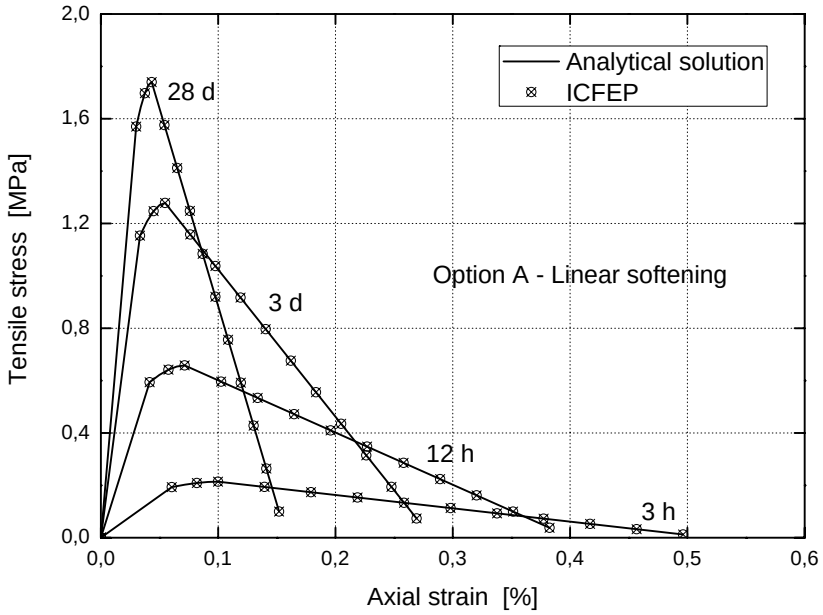



Figure 7.34: Comparison of model predictions with analytical solutions for stress-strain curves in tension for various shotcrete ages (Option A)

If an exponential softening branch is chosen according to option B, the softening parameter $\psi$ controls the decay in tensile stresses with further straining, as can be seen in Fig. 7.35.

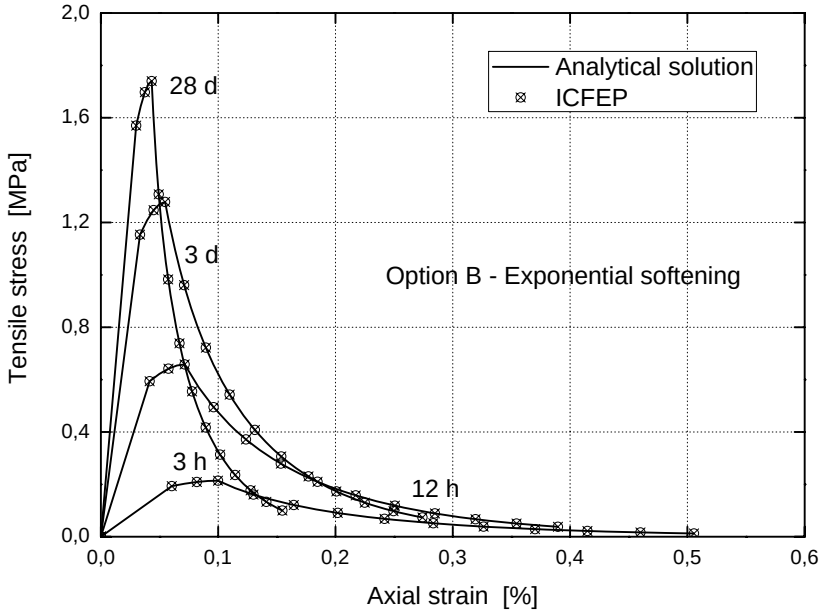



Figure 7.35: Comparison of model predictions with analytical solutions for stress-strain curves in tension for various shotcrete ages (Option B)

From both figures it can be seen that, similar to the mechanical behaviour in compression, shotcrete shows a transition from a relatively ductile to a stiff and quasi-brittle material response at 28 days. During the increasing curing time, the fracture energy, interpreted as

the area below the stress-strain curve, starts to grow in a similar manner as the strength parameters.

### 7.11.3 Biaxial loading in compression

One important characteristic of the current constitutive model is the fact that under biaxial stress confinement shotcrete can exhibit higher compressive strength values than under uniaxial conditions. This increase in compressive strength is governed by the biaxial strength parameter $e$ and is usually in the range of up to 25 % for stress conditions of $\sigma_1 = \sigma_2$. In the course of the numerical testing of the implemented constitutive model a value of $e = 1.15$ was adopted, which results in biaxial strength values that are 15 % higher than the uniaxial strengths. It is assumed that this biaxial strength ratio remains constant during the cement hydration and therefore the biaxial strength increases in the same manner as in the uniaxial case. Fig. 7.36 illustrates this mechanical behaviour for two numerical tests for shotcrete at an age of 6 h and 28 d. Both tests were performed with axisymmetric boundary conditions and were deformation controlled, in order to investigate the post peak behaviour until the ultimate stress regime is reached.

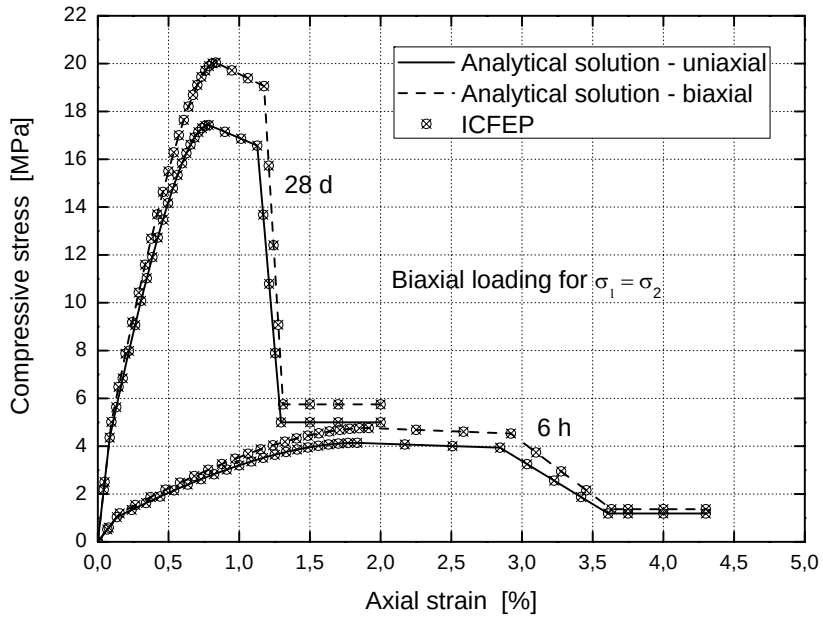



Figure 7.36: Comparison of model predictions with analytical solutions for uniaxial and biaxial compressive loading at a shotcrete age of 6 h and 28 d

By comparing the obtained results with uniaxial test runs it can be clearly seen that all the strength values (yield, peak, failure and ultimate) are increased. Furthermore, strain limits appear to be slightly larger than for the uniaxial stress strain curves, although the same plastic strain parameters from the previous sections were adopted. This results from the fact that the elastic proportion of the total strains is increased at all stages of cement hydration. Again, the numerical results from ICFEP coincide with the analytical solutions

and it is shown that the numerical implementation was carried out correctly.

### 7.11.4 Creep

In Section 7.10.3 three uniaxial creep tests in compression, performed by Kusterle (1999), were introduced and appropriate model parameters derived. For the numerical testing of the implemented creep subroutine, the parameter set of Test 1 was taken and applied to further creep simulations with ICFEP. Six numerical creep tests in compression were carried out with a different shotcrete age at the beginning of loading, $t_o$. The following Tab. 7.13 summarizes the test series:

| | Test 1 | Test 2 | Test 3 | Test 4 | Test 5 | Test 6 |
|---|---|---|---|---|---|---|
| Initial shotcrete age $t_o$ | 6 h | 24 h | 48 h | 96 h | 168 h | 336 h |

Table 7.13: Initial shotcrete ages for performed creep tests

The duration of each creep test was 200 hours. Fig. 7.37 shows the specific creep per unit stress (see equation 7.63), comparing the analytical solutions with the obtained numerical results from ICFEP. The applied stress is not of importance for the specific creep and is therefore not mentioned here. It can be observed that the young shotcrete in test T 1 is very creep active, predicting relatively high creep rates. These creep rates reduce significantly with increasing shotcrete age, resulting in a lower creep magnitude for test T 6. It should be pointed out that with increasing shotcrete age, the creep curves become more and more straight, which is probably not what would be expected in a real creep test for almost hardened shotcrete. The limited number of creep parameters within the viscosity function given in equation 7.62 ($\eta_o$ and $n$) seems not to be appropriate to cover the complete mechanical creep phenomenon for the whole time range of the cement hydration process. However, the presented constitutive model appears to be able to predict well the creep behaviour of relatively young shotcrete within the first couple of days after spraying. For hardened shotcrete at 28 days, with a different set of model parameters a better simulation of creep deformation is possible.

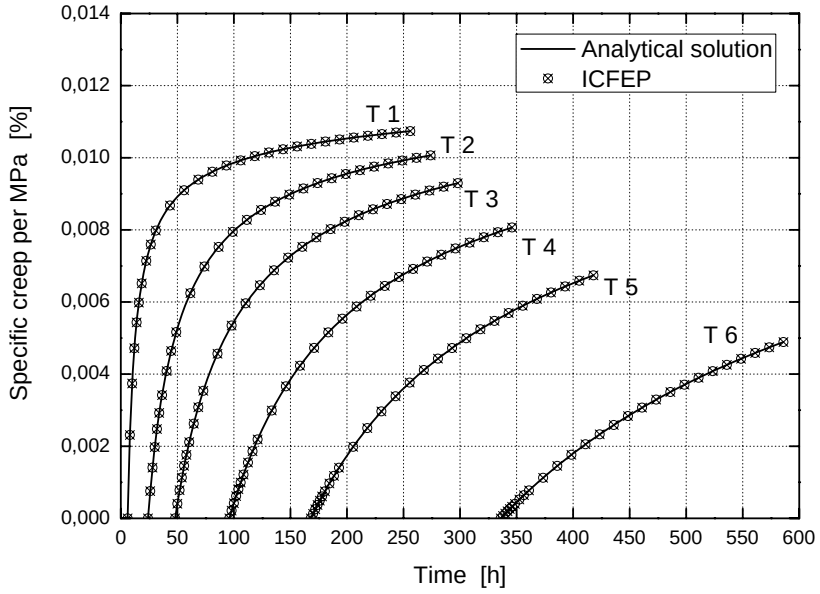



Figure 7.37: Comparison of model predictions with analytical solutions for creep deformation ($n = 0.98$)

In a second series of numerical creep simulations, a different set of model parameters was adopted. The initial shotcrete ages were the same as in the first test series, but the value of the viscosity exponent was now changed to $n = 1.3$. The initial viscosity $\eta_o$ was kept the same as in the previous test series. Fig. 7.38 shows the analytical solutions compared with model predictions obtained from ICFEP.

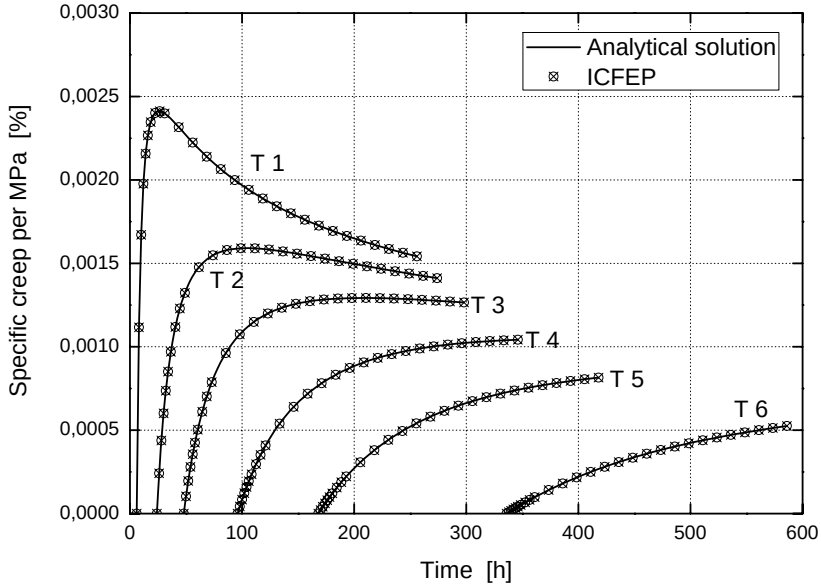



Figure 7.38: Comparison of model predictions with analytical solutions for creep deformation with $n > 1$

It can be clearly seen that the viscosity exponent $n$ is of crucial importance for creep

analysis. Tests T 1 to T 3 predict relatively high creep strains at the beginning of the tests directly after loading, as one would expect. However, after this initial steep increase in creep, deformations reach a maximum value and reduce with continuation of the test. This means that negative creep would be induced which is not realistic at all. Creep curves for test T 4 and T 5 do not show this phenomenon and indicate a reasonable behaviour and development of deformations. From these observations it can be concluded that during model calibration the creep viscosity parameter $n$ has to be treated with caution. A value of $n > 1$ might be appropriate for analysing old shotcrete resulting in better agreement with test data, but should not be adopted in an analysis where the shotcrete is given a very small initial age $t_o$.

### 7.11.5 Shrinkage

The numerical testing of the adopted shrinkage model involved a small parametric study for the shrinkage parameter $B$. This parameter was varied between 10 and 200 d and an ultimate shrinkage value of $\varepsilon_\infty^{sh} = 0.1\,\%$ was chosen. Furthermore, the shotcrete was given an initial age of $t_o = 1$ h and shrinkage was predicted for a time of up to 200 days. Fig. 7.39 illustrates the different shrinkage curves obtained by ICFEP compared with analytical solutions.

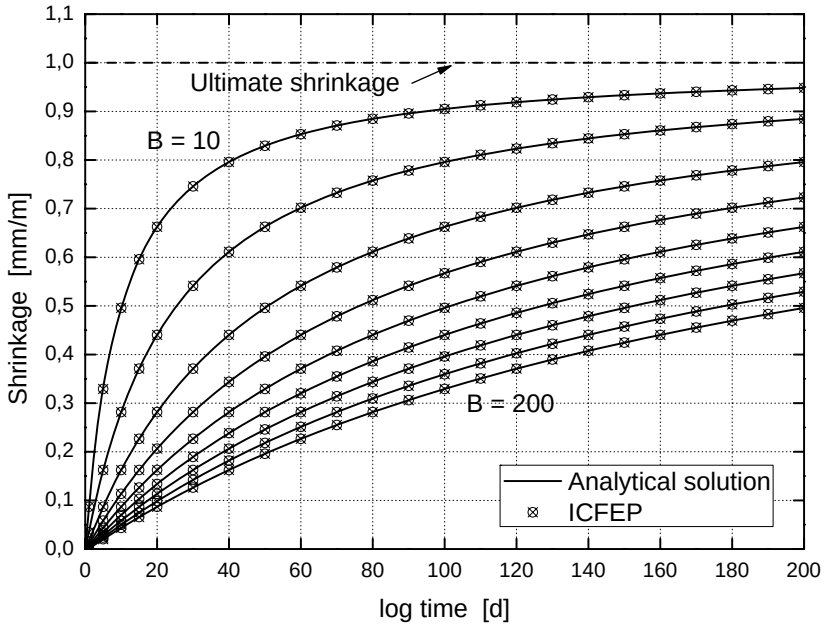



Figure 7.39: Comparison of model predictions with analytical solutions for shrinkage deformation

It should be noted that in this figure, the shrinkage strain is plotted as positive, although implementation into ICFEP was performed as a negative (i.e. compressive) strain resulting in contraction. The lowest value of $B = 10$ d gives a relatively steep increase in shrinkage deformation directly after spraying. This behaviour is not so pronounced for increasing values of $B$ (25, 50, 75, 100, 125, 150 and 175 d). As expected, the highest value of $B = 200$ d predicts a slow, almost linear, development of shrinkage and volume reduction. One particular point

to mention is that, although a value of 0.1 % was adopted for the ultimate shrinkage value, all the curves are approaching a slightly different value since shrinkage deformation starts to develop at an initial age of $t_o = 1\,\text{h}$. Therefore, the ultimate shrinkage for all the model predictions is reduced by the corresponding shrinkage strain at the initial age, $\varepsilon^{sh}(t = 1\,\text{h})$.

### 7.11.6 Thermal strains

Two different hydration temperature histories were tested in the course of the numerical implementation of the present constitutive model into ICFEP. The first temperature development follows the experimental data on shotcrete samples published by Huber (1991) and the fitted model parameters were discussed in Section 7.10.5. For the second numerical test run the following parameters in Tab. 7.14 were chosen:

| $\Delta T_{max}$ | $t_{max}$ | $t_{zero}$ |
|---|---|---|
| 25 °C | 11 h | 96 h |

Table 7.14: Model parameters for second test series of temperature history

By specifying a value for the coefficient of thermal expansion of $\alpha_{th} = 10 \times 10^6\,/°\text{C}$, the temperature induced strain histories illustrated in Fig. 7.40 are obtained.

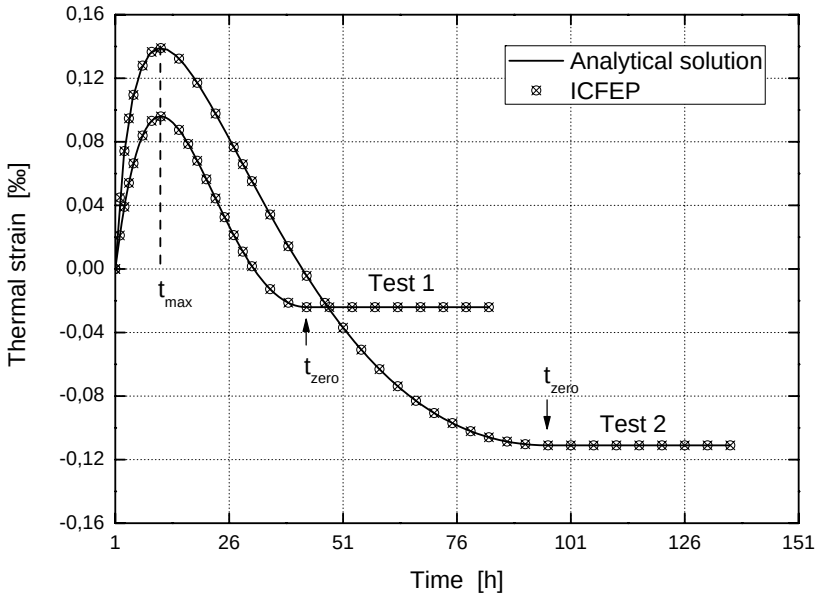



Figure 7.40: Comparison of model predictions with analytical solutions for hydration temperature induced strains

As in the case of shrinkage, temperature deformations start to build up at an initial age for shotcrete of $t_o = 1\,\text{h}$ increasing rapidly up to peak at a time of $t = 11\,\text{h}$. After reaching the maximum rise in temperature, the shotcrete starts to contract again, resulting

in negative (tensile) strains due to the fact that the strain at the initial age of 1 h, $\varepsilon^{th}(t = 1\,\text{h})$ has to be subtracted. The developed strains during this cooling phase of the shotcrete are of crucial importance regarding the possible cracking behaviour of the material in the case of restrained conditions. After reaching the time $t_{zero}$ there is no further influence of the hydration temperature for both test runs and deformations remain constant.

## 7.12 Summary

In this chapter a sophisticated constitutive model for the behaviour of shotcrete has been presented, which is a modification of the well known Chen & Chen (1975) concrete model. After a robust numerical implementation into ICFEP, the model was calibrated and validated against experimental data for young shotcrete available in the literature. The following key features of the model can be summarised:

- The mechanical behaviour of shotcrete in compression and tension is controlled by two yield surfaces that move independently from each other in stress space. This expansion and contraction is controlled by plastic strain hardening/softening and the increase in strength with time during cement hydration. Cracking of the shotcrete is considered within the smeared crack concept.

- The hardening and softening of the material during an analysis follows uniaxial stress-strain curves that are based on typical experimental tests. Due to the time-dependent material behaviour, normalised hardening parameters for both compression and tension have been adopted in order to model more realistically complex loading scenarios with respect to time.

- The main material parameters of the model are time-dependent and account for the increase in stiffness and strength with time. Furthermore, the increased deformability of young shotcrete at early ages was taken into account by assuming a time-dependent function for the plastic peak strains in compression and tension.

- Creep of shotcrete at various stages of cement hydration is simulated by a Newton dashpot which is characterised by a non-linear function for the shotcrete viscosity. This uniaxial creep law is extended into 3D with the help of creep potential functions for both compression and tension.

- Shrinkage and temperature induced deformations during cement hydration are considered as irreversible volumetric components of the total strains. Their development with time is based on standard functions that can be found in the literature.

# Chapter 8

# Analysis of tunnel excavation in London Clay

## 8.1 Introduction

The following chapter investigates the influence of the constitutive model developed for shotcrete on tunnel lining design in a boundary value problem. Although a realistic assessment of tunnel construction would require a full 3D simulation, the analyses presented in this study were performed in 2D due to computational limitations. In order to obtain a detailed understanding of the behaviour of a shotcrete shell during tunnel construction it was decided not to model a real case study, but to analyse a tunnel excavation that would be typical for the London area. Furthermore, three different types of excavation sequences have been investigated, which are the following:

- Type 1 - Full face excavation
- Type 2 - Bench and invert excavation
- Type 3 - Sidewall drift

The sophisticated elasto-plasticity model presented in Chapter 7 was applied for modelling the tunnel lining and results are compared with much simpler approaches that still represent the current state-of-the-art for the simulation of shotcrete tunnel linings, i.e. linear elastic and the Hypothetical Modulus of Elasticity (HME). Through an extensive parametric study, varying the main parameters related to construction sequence, material behaviour and initial stress conditions, it was possible to detect critical stages during tunnel construction and to understand the fundamental behaviour of a shotcrete shell in a better and more detailed way. It should be noted that some of the parameters adopted in the analyses might appear unrealistic at first sight, but given the fact that most tunnel failures occur because of unexpected heavy loading conditions caused by the variability in material parameters (ground and shotcrete), these assumptions are justifiable.

## 8.2 Geometry of the problem

Fig. 8.1 illustrates the adopted geometry and ground conditions for the chosen boundary value problem, that will be discussed in detail in the following sections.

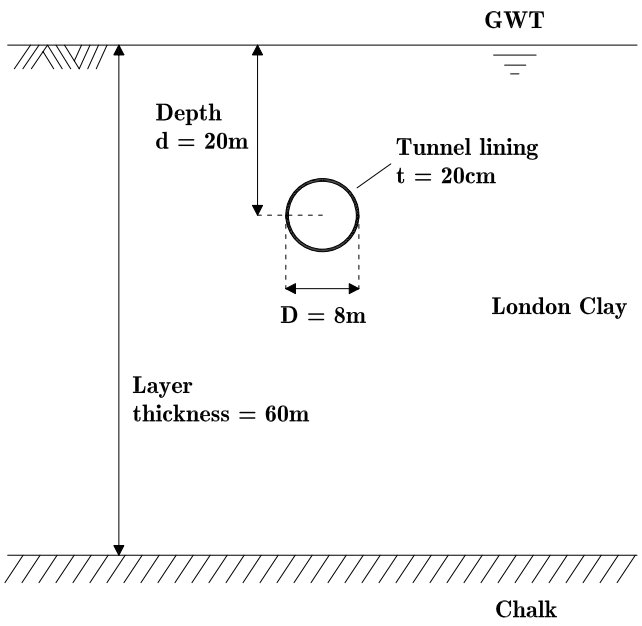



Figure 8.1: Layout of tunnel geometry and ground conditions

The circular tunnel to be analysed within this research has an outer diameter of 8 m and its centre is located at a depth of 20 m below the ground surface, which leads to a tunnel overburden of 16 m. As a temporary support element, a shotcrete layer of 20 cm thickness will be installed immediately after excavation of the ground resulting in a inner clear profile of the tunnel of 7.60 m. Since tunnel excavation in reality is performed relatively quickly, undrained conditions are assumed and any consolidation effects that might occur are ignored throughout the whole analysis. Furthermore, the whole tunnel is being excavated in a 60 m thick layer of London Clay overlying a layer of chalk, which represents a typical ground profile in the western London area. For the bulk unit weight of London Clay a value of $\gamma = 20\,\mathrm{kN/m^3}$ has been chosen. Although in many cases under-drained pore pressure profiles can be encountered in London (Potts & Zdravković, 2001), the groundwater conditions are assumed to be hydrostatic with the ground water table (GWT) situated at the ground surface level. Any further subsurface structures in the vicinity of the tunnel are not taken into account in order to avoid interaction effects, which are not the purpose of this study.

As mentioned above in the introduction, three different excavation sequences are adopted within this investigation. These are shown in Fig. 8.2.

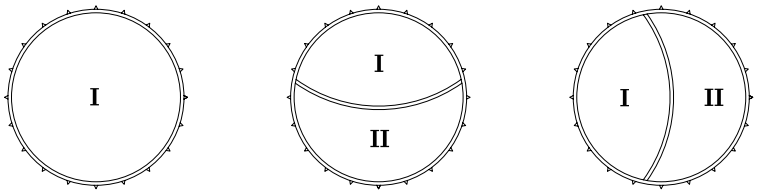



Figure 8.2: Three different excavation sequences for tunnel analyses

For Type 1, the tunnel is to be constructed full face and the complete circular lining ring is installed directly after excavation of the complete tunnel cross section. Type 2 represents a bench-invert excavation, where the upper half of the tunnel cross section is excavated first, followed by the invert region. For stability reasons and in order to minimize surface settlements, a temporary invert made of sprayed concrete with a thickness of 15 cm is considered in the intermediate construction stage. Furthermore, the geometry of this temporary invert shows a curvature with a radius of 10 m. Finally, excavation of the tunnel according to Type 3 starts with the construction of the left side-gallery including a temporary sidewall consisting of a 15 cm thick shotcrete layer. Similar to Type 2, this sidewall is curved with a radius of 10 m. After excavation of the right gallery in the second step, the tunnel profile is completed and the lining installation can be finished.

## 8.3 Ground conditions in London area and initial stresses

London Clay is the predominant soil formation that can be encountered in the London area in the course of subsurface construction and usually has a thickness in the range of 50 to 150 m (Gasparre, 2005). This clay is well known to be highly overconsolidated and it is a typical example of a stiff plastic clay showing brittle behaviour and localization of strains. Furthermore, London Clay is characterised by natural discontinuities, such as laminations, backs and fissures, whose engineering importance are emphasized in the open literature. Its mechanical properties are influenced by many geological aspects, such as weathering or erosion. Eddie et al. (2009) state that for tunnelling according to the principles of NATM, London Clay represents an ideal medium, which is relatively easy to handle. For further information regarding an advanced laboratory characterisation of London Clay see Gasparre (2005).

The heavy overconsolidation of the adopted soil formation gives rise to high horizontal effective stresses, resulting in $K_o$ values that are usually greater than 1. It is reported that in the upper 10 m of the London Clay $K_o$ varies between 2 and 2.5 and this value tends to decrease with increasing depth, falling to 1.5 at about 30 m depth. Within this research, two different $K_o$-profiles were established, which are both constant with depth as can be seen in Fig. 8.3.

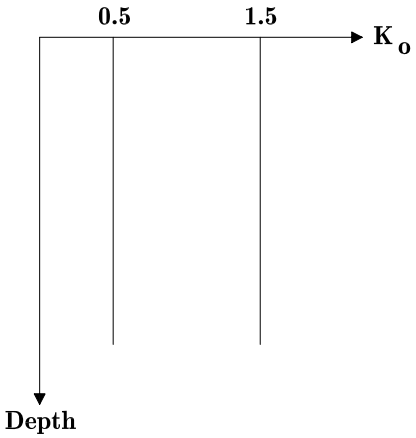



Figure 8.3: Adopted $K_o$-profiles for performed analyses

For all the performed analyses adopting excavation Type 1, the influence of both $K_o$-profiles on the behaviour of the tunnel shell was investigated. However, for the tunnel excavation following the construction scheme of Type 2 and Type 3, one single $K_o$-profile with a value of 1.5 was adopted for simplicity reasons. The initial stresses at the beginning of each analysis were therefore calculated in terms of effective stresses as:

$$\sigma'_v = (\gamma - \gamma_w)\, z \qquad \text{and} \qquad \sigma'_h = K_o\, \sigma'_v \tag{8.1}$$

where $\sigma'_v$ and $\sigma'_h$ are the vertical and horizontal effective stresses respectively. $z$ is the depth below ground surface in metres and $\gamma_w$ the bulk unit weight of water, which is taken as $9.81\,\mathrm{kN/m^3}$.

## 8.4 Finite element model

All the analyses of this study were performed using ICFEP (Imperial College Finite Element Program), the in house finite element code of the Geotechnics Section at Imperial College in London, written and developed by Prof. Potts and recently by Dr. Zdravković. It is a sophisticated and powerful finite element program for the analysis of geotechnical problems and operates on Sun UNIX workstations and servers. As mentioned earlier, tunnel construction was investigated by a 2D plane strain model. The undrained conditions of the London Clay were simulated by prescribing high bulk compressibility of the pore fluid.

### 8.4.1 Mesh and boundary conditions

Fig. 8.4 shows the general layout of the finite element mesh used for the numerical calculations with its boundary conditions concerning displacements.

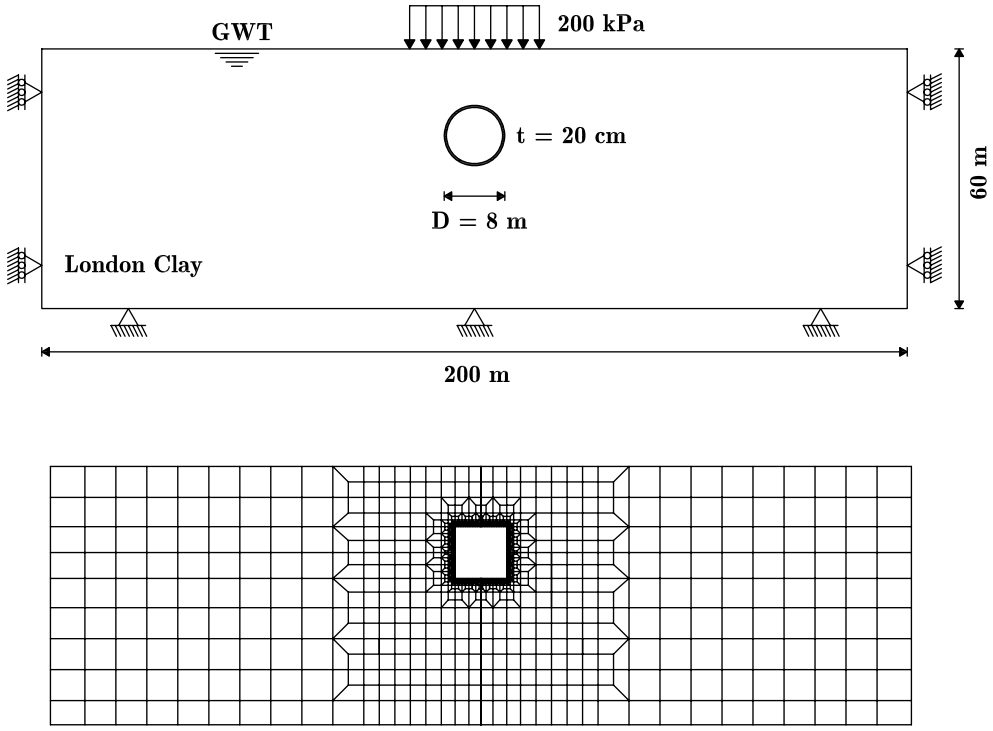



Figure 8.4: General layout of the 2D finite element mesh (without inner core)

The mesh has a total size of 200 m × 60 m and the bottom boundary is placed at the top of the chalk layer. Along this mesh boundary, both displacements in the vertical and horizontal directions are restricted to zero. On the right and left hand sides of the mesh vertical displacements are permitted, but horizontal movements are not allowed to take place. The ground surface is a stress free boundary. In general, the applied mesh consists of eight-noded quadrilateral isoparametric elements, which are constructed in blocks. Two types of blocks can be distuingished in ICFEP, as indicated in Fig. 8.5. As one can imagine, transitional blocks are used for the transition of smaller to bigger elements. The Gauss Integration points, for which the main equations are solved, are located inside the element. Reduced $(2 \times 2)$ integration is applied in all analyses presented here.

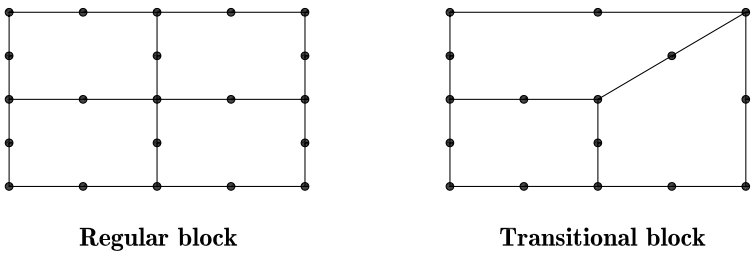



Figure 8.5: Two types of blocks forming the finite element mesh

From Fig. 8.4 it can be seen that the model includes a surface surcharge of 200 kPa placed over a distance of 2.5 tunnel diameters. This additional load was applied in order to inves-

tigate the effect of the construction of a possible surface structure on the tunnel shell and therefore to study in detail the behaviour of the young shotcrete lining under heavy loading conditions. It is appreciated that this is a rather hypothetical situation compared with what might happen in reality.

Obviously, for all the three excavation Types 1 to 3, individual meshes had to be designed to account for differences in the geometry and construction sequence. For simplicity reasons it was decided to adapt just the area in the vicinity of the tunnel lining and keep the rest of the finite element mesh the same for all the three excavation types. Fig. 8.6 to 8.8 illustrate a zoom into the core of the applied meshes 1 to 3 respectively.

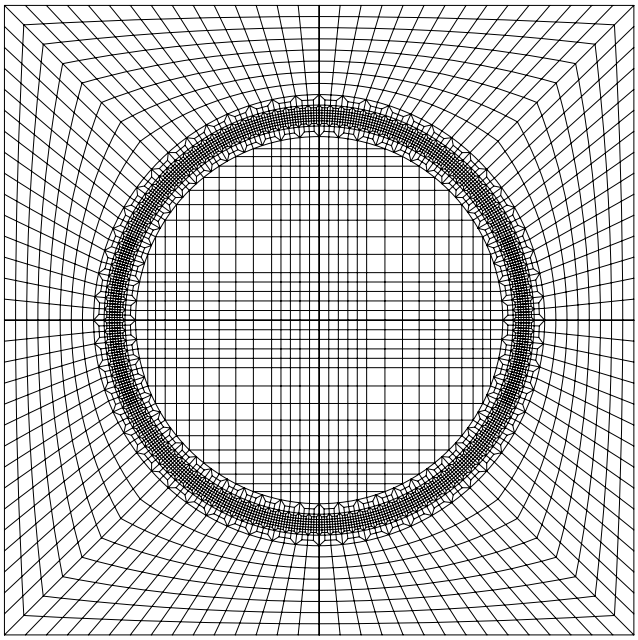


Figure 8.6: Zoom of mesh 1 for excavation Type 1: full face excavation

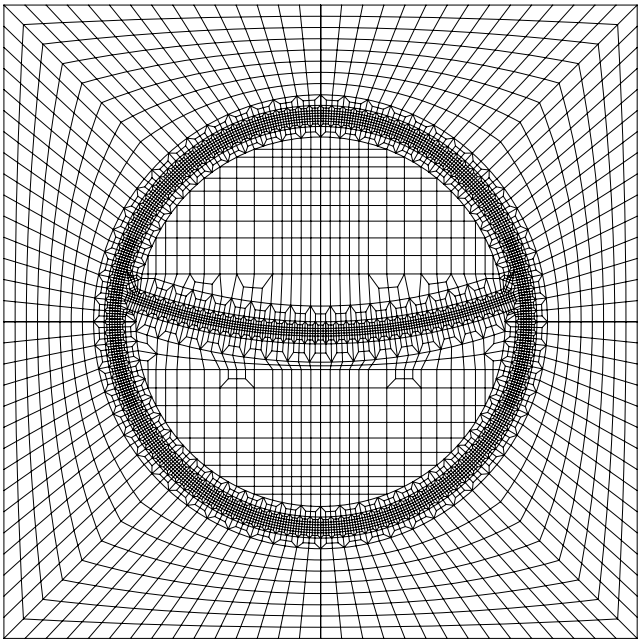


Figure 8.7: Zoom of mesh 2 for excavation Type 2: bench-invert excavation

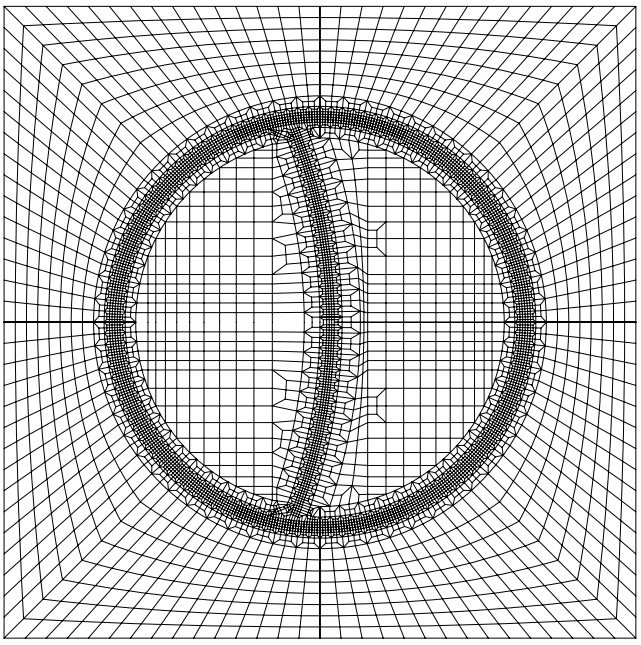


Figure 8.8: Zoom of mesh 3 for excavation Type 3: sidewall drift

Both the lining and soil were modelled by solid elements and refinement of the mesh was performed in the zones of high and low changes in stresses and strains. Since the mechanical behaviour of the shotcrete shell was of special interest during this research, the tunnel lining was simulated by four elements across its thickness resulting in a quadratic element shape with a size of roughly $5\,\mathrm{cm} \times 5\,\mathrm{cm}$. Therefore, a more accurate stress distribution over the lining thickness was achieved with the help of 8 Gauss Intergration points. For the temporary

invert and sidewall of excavation Types 2 and 3, three elements were used to represent the shotcrete thickness of 15 cm. It should be noted that the need for a relatively fine mesh when simulating the tunnel lining with solid elements is a major drawback of the developed finite element model, resulting in high computational effort. Finally, the following Tab. 8.1 summarizes the important information for all the three meshes that were used within this study.

| | Number of blocks | Number of elements | Number of nodes |
|---|---|---|---|
| Mesh 1 | 1006 | 6840 | 20611 |
| Mesh 2 + 3 | 1361 | 7804 | 23503 |

Table 8.1: Summary for mesh 1, 2 and 3

### 8.4.2 Modelling of construction sequence

The simulation of a particular construction sequence in a finite element code like ICFEP involves the elimination and/or activation of certain elements within the finite element mesh. In this study, tunnel construction was modelled in two dimensions and the volume loss method, described earlier in Chapter 2, was applied in order to account for some 3D effects, such as pre-deformation ahead of the tunnel face. Typical field measurements of tunnel construction in the London area show that the volume loss $V_L$ usually lies in the range of 1 to 2 % (Potts & Zdravković, 2001). Therefore, a target of 1.5 % was chosen for the current study and the construction sequence of the three different excavation types was adapted for the linear elastic shotcrete model in order to fufill this criterion.

#### 8.4.2.1 Excavation Type 1: Full face excavation

Tab. 8.2 gives an overview of the construction steps adopted for excavation Type 1 (full face). Since the $K_o$-profile, and therefore the initial stress conditions, highly influence the development of the volume loss as the tunnel is excavated, the increment at which the lining is installed is different for both sets of analyses.

| | $K_o = 0.5$ | $K_o = 1.5$ |
|---|---|---|
| 1) Excavation | Increments 1 to 10 | |
| 2) Installation of lining | Increment 3 | Increment 5 |
| 3) Surface loading | Increments 11 to 50 | |

Table 8.2: Construction sequence for excavation Type 1

During excavation, all the elements within the tunnel, within the outer diameter of 8 m,

are removed and equivalent nodal forces, simulating excavation, applied at the tunnel boundary. Furthermore, these forces are stepwise reduced over 10 increments. At the particular increment where the desired volume loss is achieved, the complete lining ring is installed by activating (i.e. constructing) the respective lining elements in one single step. The remaining equivalent nodal forces are released until excavation is completed. Surface loading takes place over 40 increments, resulting in an additional loading of 5 kPa per increment. Fig. 8.9 illustrates the adopted construction sequence.

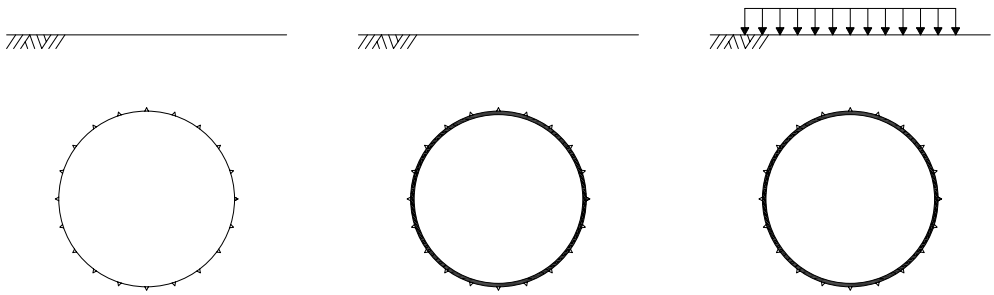



Figure 8.9: Graphical representation of construction sequence for excavation Type 1

#### 8.4.2.2 Excavation Type 2: Bench-invert excavation

Construction of the tunnel according to excavation Type 2 is performed numerically in several steps as can be seen in Tab. 8.3. It should be noted that just one single $K_o$-profile with a value of 1.5 is adopted for analysing this particular tunnel advance.

| | |
|---|---|
| 1) Excavation of bench | Increments 1 to 12 |
| 2) Installation of upper shell | Increment 7 |
| 3) Excavation of invert | Increments 14 to 25 |
| 4) Installation of lower shell | Increment 14 |
| 5) Surface loading | Increments 26 to 65 |

Table 8.3: Construction sequence for excavation Type 2

The soil elements of the tunnel bench are removed over twelve increments and again the equivalent nodal forces on the excavation boundary are reduced in a stepwise manner in order to allow for some pre-relaxation ahead of the tunnel face. The installation of the upper lining shell, including the temporary invert, takes place in one single step by constructing the respective lining elements in increment 7. The temporary invert is then removed and excavation of the invert region continued from increment 14 to 25. The lining is completed by activating the lining elements belonging to the lower shotcrete shell immediately in increment 14 and the surface surcharge is applied incrementally until construction is finished in

increment 65. It should be noted that in increment 13 no particular numerical construction or excavation is performed. This increment is therefore used to simulate the distance between the tunnel face and the completion of the lining ring, that usually happens in reality a couple of metres behind the front of the tunnel. Since it is not possible to capture a longitudinal distance along the tunnel axis in a 2D analysis, this means that a certain amount of time $\Delta t$ will elapse during this increment, leading to a different shotcrete age of the upper and lower shell at later construction stages. The desired volume loss is measured on the whole tunnel face. Finally, Fig. 8.10 shows graphically the above described construction sequence for the bench-invert excavation.

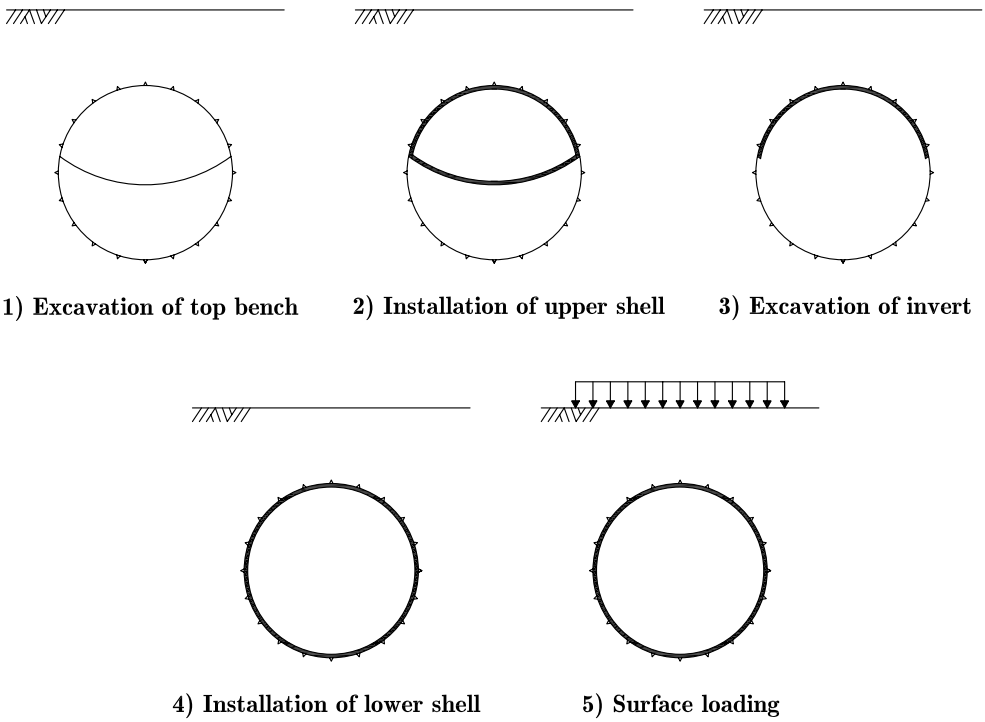



Figure 8.10: Graphical representation of construction sequence for excavation Type 2

#### 8.4.2.3 Excavation Type 3: Sidewall drift

The numerical construction sequence for excavation Type 3 is summarized in Tab. 8.4. As in the previous case in Section 8.4.2.2, one constant $K_o$-profile with a value of 1.5 was adopted for the tunnel runs of this particular excavation type.

| | |
|---|---|
| 1) Excavation of left gallery | Increment 1 to 12 |
| 2) Installation of left shell | Increment 6 |
| 3) Excavation of right gallery | Increment 14 to 25 |
| 4) Installation of right shell | Increment 14 |
| 5) Surface loading | Increment 26 to 65 |

Table 8.4: Construction sequence for excavation Type 3

In the first step of construction the soil elements of the left side gallery are removed and replaced by equivalent nodal forces. The excavation process, simulated by the removal of these nodal forces, takes place over 12 increments, while the left shotcrete shell is placed in increment 6 together with the temporary sidewall. Tunnel construction is then continued in increment 14 by eliminating the temporary sidewall and the remaining soil elements of the right side gallery. Here again, the shotcrete ring is completed in increment 14 by activating the corresponding lining elements. After the complete release of the equivalent nodal forces in increment 25, the surface surcharge of 200 kPa is placed on top of the tunnel over 40 increments. Similar to the approach adopted for excavation Type 2, increment 13 has the purpose of simulating the longitudinal distance between the left and right side gallery and therefore a certain amount of time $\Delta t$ elapses in the adopted 2D model. Fig. 8.11 illustrates the described construction procedure.

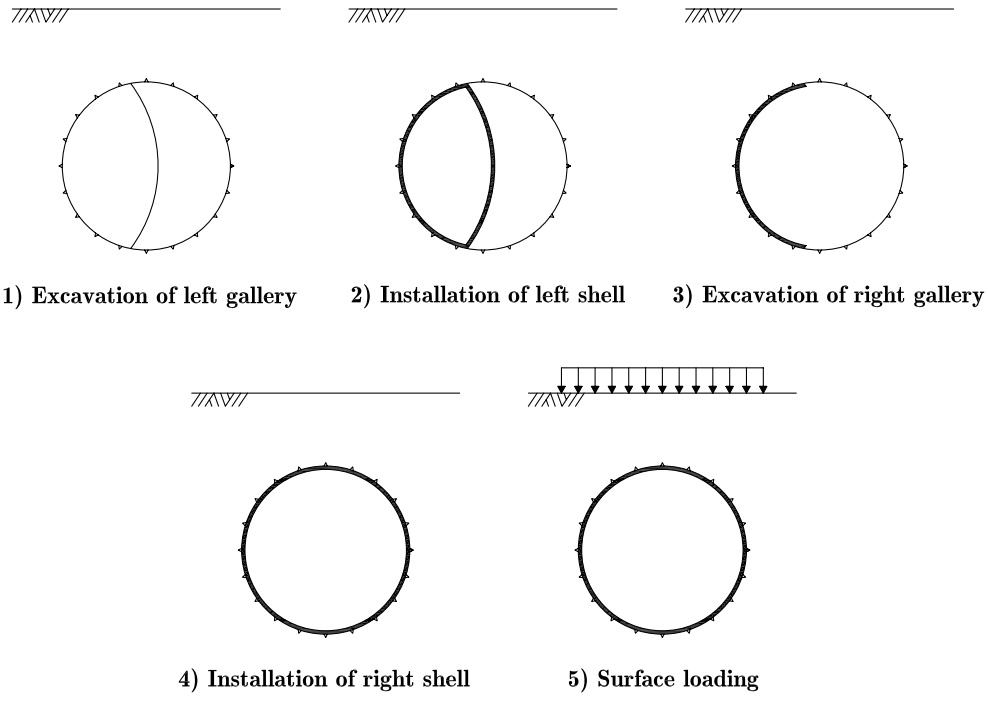



Figure 8.11: Graphical representation of construction sequence for excavation Type 3

## 8.5 Adopted constitutive models and material parameters

### 8.5.1 Tunnel lining - Shotcrete

As already highlighted in the introduction to this chapter, the aim of the performed study is to investigate the behaviour of a shotcrete tunnel lining for various excavation types by applying the sophisticated constitutive model for young shotcrete, that was developed Chapter 7. Furthermore, the obtained results from these analyses are compared with other approaches commonly used in engineering practice due to their simplicity. Hence, the following four constitutive laws for shotcrete are adopted:

- Linear elastic (LE)
- Hypothetical Modulus of Elasticity (HME)
- Non-linear elasto-plasticity model (NL)
- Time-dependent non-linear elasto-plasticity model (TPM)

When modelling the tunnel lining as a linear elastic isotropic material, a value for the Young's modulus of hardened shotcrete at 28 days of $E = 30\,\text{GPa}$ has been chosen. In the case of the Hypothetical Modulus of Elasticity (HME) a reduced stiffness of $E = 7\,\text{GPa}$ is applied, which represents a reasonable value taken from the literature (see Pöttler (1990)). For both types of analysis a constant Poisson's ratio of $\mu = 0.2$ has been used. For the non-linear elasto-plastic model (NL) and the time-dependent non-linear elasto-plastic model (TPM) the constitutive model described in the previous chapter was used.

The establishment of appropiate material parameters for these models is not straightforward and is discussed here in detail. Basically, two different types of shotcrete have been used to model the tunnel lining, which are:

- Excavation Type 1 $\longrightarrow$ Unreinforced shotcrete
- Excavation Type 2 and 3 $\longrightarrow$ Steel-fibre reinforced shotcrete (SFRS)

With the developed constitutive model it is possible to incorporate the effect of steel fibres on the material response by a slight modification of the normalised stress-strain curve in tension, whereas the compressive behaviour remains unaffected.

Firstly, the following strength parameters, summarised in Tab. 8.5, have been chosen to represent shotcrete behaviour (unreinforced and SFRS) both in compression and tension.

| $f_{cp,28}$ (MPa) | $f_{cy,28}$ (MPa) | $f_{cf,28}$ (MPa) | $f_{cu,28}$ (MPa) | $e$ (-) | $f_{tp,28}$ (MPa) | $f_{ty,28}$ (MPa) | $f_{tu,28}$ (MPa) | $s$ (-) | $t_{28}$ (h) |
|---|---|---|---|---|---|---|---|---|---|
| 30.0 | 7.5 | 24.0 | 5.0 | 1.15 | 3.0 | 2.4 | 0.1 | 0.2 | 672.0 |

Table 8.5: Basic strength parameters for shotcrete

Furthermore, Tab. 8.6 contains the applied numerical parameters needed for the description of the tensile yield surface:

| $a$ | $n$ | $TIPTOL$ | $CORTOL$ |
|---|---|---|---|
| (-) | (-) | (-) | (°) |
| 3.0 | 0.01 | 0.01 | 1.0 |

Table 8.6: Numerical parameters for tension yield surface

Secondly, for the complete description of the normalised stress-strain curve both in compression and tension the deformability parameters listed in Tab. 8.7 have been adopted.

| $\varepsilon^p_{cp,28}$ | $\varepsilon^p_{cf,28}$ | $\varepsilon^p_{cu,28}$ | $\varepsilon^p_{cp,t_2}$ | $\varepsilon^p_{cp,t_1}$ | $\varepsilon^p_{tp,28}$ | $\psi$ | $\psi_{SFRS}$ | $t_1$ | $t_2$ |
|---|---|---|---|---|---|---|---|---|---|
| (%) | (%) | (%) | (%) | (%) | (%) | (-) | (-) | (h) | (h) |
| 0.5 | 0.97 | 1.3 | 1.6 | 3.5 | 0.02 | -0.47 | -0.0043 | 1.0 | 24.0 |

Table 8.7: Basic deformability parameters for shotcrete

The choice of the compressive plastic peak strain for hardened shotcrete at 28 days, $\varepsilon^p_{cp,28}$, is in accordance with the suggested values given by Swoboda & Moussa (1992). Taking into account the elastic strain component, the total cracking (or peak) strain of hardened shotcrete in tension has been selected to be 5 % of the total compressive peak strain (see Byfors (1980)) throughout the whole hardening process of the cement paste. Furthermore, it is important to note that all the above mentioned softening parameters are estimated by applying the fracture energy approach earlier presented in Sections 6.6.1.2, 6.6.1.4, 7.3.1 and 7.3.2. The following input parameters were involved in the mathematical calibration procedure:

- Fracture energy in compression: $G_c = 6.4\,\mathrm{Nmm/mm^2}$ (see Vonk (1992))
- Fracture energy of unreinforced shotcrete in tension: $G_{f1} = 0.064\,\mathrm{Nmm/mm^2}$ for $d_{max} = 8\,\mathrm{mm}$ (CEB-FIP Model Code, 1990)
- Fracture energy for SFRS in tension: $G_{SFRS} = G_{f1} + G_{f2}$ with $G_{f2} = 6.9\,\mathrm{Nmm/mm^2}$ (see Thomée (2005))
- Equivalent length of lining elements: $l_{eq} = \sqrt{A_e} = 50\,\mathrm{mm}$ (see equation 6.83 after Rots (1988))

The selection of the appropriate material parameters regarding the development of the plastic peak strains with time is based on published data by Thomas (2003) and Sezaki et al. (1989), as can be seen in Fig. 8.12.

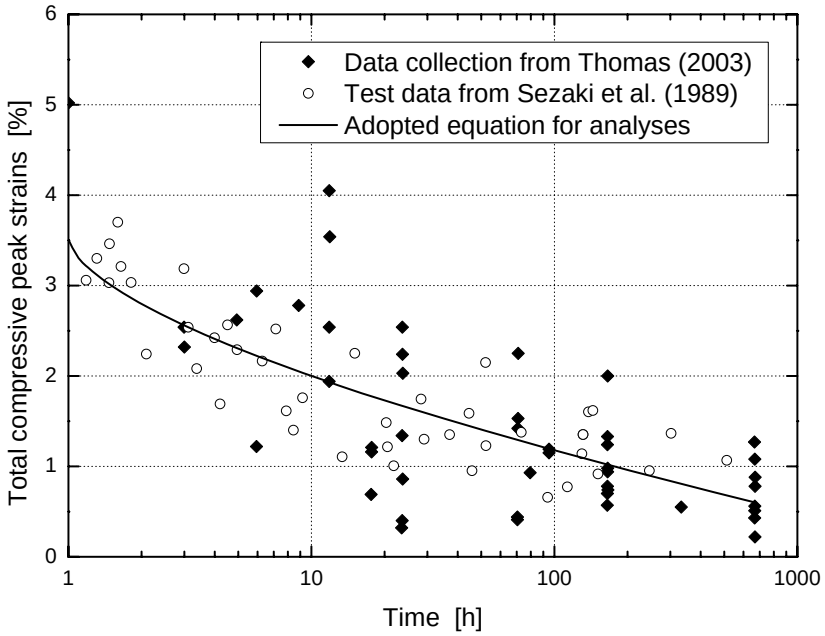



Figure 8.12: Development of total uniaxial compressive peak strains with time

In this figure, the variation of the total compressive peak strains is established by including the elastic strain components for this particular shotcrete with the given strength and stiffness parameters. It can be seen that the obtained curve represents a good fit to the test data from the literature.

The increase in stiffness with time is accounted for by the basic shotcrete parameters summarized in Tab. 8.8

| $E_{28}$ | $s$ | Poisson's ratio $\mu$ |
|---|---|---|
| (MPa) | (-) | (-) |
| 30000 | 0.2 | 0.2 |

Table 8.8: Basic stiffness parameters for shotcrete

The treatment of the time-dependent material behaviour of shotcrete in this numerical analysis requires the specification of the initial age of the young shotcrete $t_o$. In order to capture the mechanical properties at very early ages, this parameter $t_o$ was set to 1 hour. In the case of the non-linear elasto-plasticity model (NL), where no time-dependency is included during the analyses, the initial age is chosen to be $t_o = 28$ days and therefore all the material properties are constant and do not change with time.

For analysing the impact of creep, shrinkage and hydration temperature on the mechanical behaviour of the constructed shotcrete tunnel lining, the parameters given below in Tab. 8.9 were adopted for all the three excavation Types 1 to 3.

| $\eta_o$ | $n$ | $\varepsilon_\infty^{sh}$ | $B$ | $\Delta T_{max}$ | $t_{max}$ | $t_{zero}$ |
|---|---|---|---|---|---|---|
| (kPa h) | (-) | (%) | (h) | (° C) | (h) | (h) |
| $12 \times 10^6$ | 0.97 | 0.14 | 648.0 | 35.0 | 12.0 | 96.0 |

Table 8.9: Basic material parameters for creep, shrinkage and hydration temperature

These parameters were mainly taken and/or estimated from data available in the literature (see Section 7.10 about model calibration) and should represent realistic values that one could expect for shotcrete.

Concluding, all the above introduced material parameters for shotcrete were used as a basic set in the numerical analysis of tunnel construction according to the three different construction sequences. As already highlighted in the introduction to this chapter, a parametric study on the main material parameters involved was performed in order to investigate the impact of each of the components on the mechanical behaviour of the shotcrete lining during tunnel advance. These variations in material parameters will be discussed in detail in Section 8.6 of this chapter.

### 8.5.2 Soil - London Clay

For modelling the mechanical behaviour of London Clay a relatively simple Mohr-Coulomb model was adopted. However, since this constitutive model describes soil as a linear elastic, perfectly plastic material it was decided to couple the Mohr-Coulomb plastic criterion with a small-strain-stiffness model of the Jardine et al. (1986) type. By doing this, it is possible to capture the highly non-linear material response of London Clay before yielding. In the following, a brief introduction into the structure of the model is given.

The adopted small-strain-stiffness model assumes that soil behaviour is isotropic and that the bulk and shear moduli vary with mean effective stress $p'$ and strains. The equations defining the model behaviour can be written as:

$$\frac{G_{tan}}{p'} = \frac{A}{3} + \frac{B}{3}\cos\left(\alpha X^\gamma\right) - \frac{B\,\alpha\,X^{\gamma-1}\sin\left(\alpha X^\gamma\right)}{6.909} \tag{8.2}$$

with

$$X = \log_{10}\left(\frac{E_d}{\sqrt{3}C}\right) \tag{8.3}$$

where $G_{tan}$ is the tangent shear modulus and $E_d$ the deviatoric strain. $A$, $B$, $C$, $\alpha$ and $\gamma$ are model parameters. A similar expression for the variation of the bulk modulus is adopted, namely:

$$\frac{K_{tan}}{p'} = R + S\,\cos\left(\delta Y^\mu\right) - \frac{S\,\delta\,\mu\,Y^{\mu-1}\sin\left(\delta Y^\mu\right)}{2.303} \tag{8.4}$$

with

$$Y = \log_{10}\left(\frac{|\,\varepsilon_{vol}\,|}{T}\right) \tag{8.5}$$

In this equation $K_{tan}$ is the tangent bulk modulus and $\varepsilon_{vol}$ the volumetric strain. $R$, $S$, $T$, $\delta$ and $\mu$ are model parameters. In Fig. 8.13 typical variations of the secant shear and bulk moduli for London Clay are shown, indicating the decay in stiffness with increasing straining.

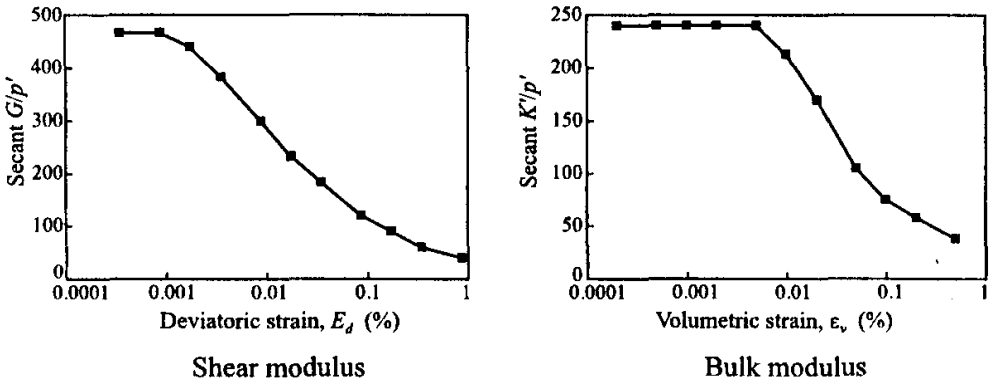



Figure 8.13: Variation of the shear and bulk moduli with strain level (from Potts & Zdravković, 1999)

For the present study, the strength parameters in Tab. 8.10 have been adopted for the Mohr-Coulomb criterion.

| Cohesion | Angle of shearing resistance | Angle of dilatancy |
|---|---|---|
| $c' = 5\,\text{kPa}$ | $\phi' = 25\,^\circ$ | $\nu = 12.5\,^\circ$ |

Table 8.10: Strength parameters for London Clay

The stiffness parameters for describing the non-linear small-strain-stiffness model are summarized in Tab. 8.11. It is common to set minimum ($E_{d,min}$, $\varepsilon_{vol,min}$) and maximum ($E_{d,max}$, $\varepsilon_{vol,max}$) strain limits below which and above which the moduli vary with $p'$ alone, and not with strain. Furthermore, minimum values for $G$ and $K$ can be specified for the soil.

| $A$ | $B$ | $C$ | $\alpha$ | $\gamma$ | $E_{d,min}$ | $E_{d,max}$ | $G_{min}$ |
|---|---|---|---|---|---|---|---|
| 970.0 | 890.0 | 0.001 % | 1.470 | 0.700 | $1.7321 \times 10^{-3}$ % | 0.17321 % | 3333.3 kPa |

| $R$ | $S$ | $T$ | $\delta$ | $\mu$ | $\varepsilon_{vol,min}$ | $\varepsilon_{vol,max}$ | $K_{min}$ |
|---|---|---|---|---|---|---|---|
| 772.5 | 712.5 | 0.001 % | 2.069 | 0.420 | $5.0 \times 10^{-3}$ % | 0.15 % | 4000.0 kPa |

Table 8.11: Stiffness parameters for London Clay

## 8.6 Tunnel analyses

In Chapter 5 it was emphasized, that experimental data on shotcrete behaviour at early ages show a considerable scatter mainly due to the large number of influencing parameters regarding mix design, application technique and testing procedures. Furthermore, it is even more difficult to interpret field data from tunnel monitoring, since the adopted construction process plays an important role. Within this research, the aim was to gain a better insight into the behaviour of shotcrete in tunnelling through an extensive parametric study. The parameter variation for the three excavation types focused on the following aspects:

- Initial stress conditions in the ground (for excavation Type 1)
- Elapsed time during tunnel excavation and surface loading
- Increase in stiffness and strength of shotcrete with time
- Development of shotcrete deformability with time
- Influence of creep, shrinkage and hydration temperature

### 8.6.1 Parametric study for excavation Type 1

Tab. 8.12 summarises the performed tunnel runs for excavation Type 1 for both $K_o$-profiles simulating different shotcrete ages at the end of excavation and loading.

| Run | Shotcrete age at end of excavation (Inc 10) (h) | Shotcrete age at end of loading (Inc 50) (h) |
|---|---|---|
| TPM 1 | 2.0 | 4.0 |
| TPM 2 | 4.0 | 8.0 |
| TPM 3 | 8.0 | 16.0 |
| TPM 4 | 12.0 | 24.0 |
| TPM 5 | 16.0 | 32.0 |
| TPM 6 | 24.0 | 48.0 |
| TPM 7 | 36.0 | 72.0 |
| TPM 8 | 48.0 | 96.0 |
| TPM 9 | 72.0 | 144.0 |
| TPM 10 | 96.0 | 192.0 |
| TPM 11 | 144.0 | 288.0 |
| TPM 12 | 168.0 | 336.0 |
| TPM 13 | 336.0 | 672.0 |
| TPM 14 | 672.0 | 1344.0 |

Table 8.12: Shotcrete ages for different time-runs for excavation Type 1

Regarding the possible effects of the increase in stiffness and strength with time, the analyses listed in Tab. 8.13 were carried out. It should be noted that for these analyses time-run TPM 6 was chosen as a reference run, since it represents a realistic tunnelling scenario. This results in a shotcrete age of 24 h after excavation and 48 h at the end of surface loading.

| Run | Description |
|---|---|
| STRENGTH 1 | Cement parameter $s = 0.1$ |
| STRENGTH 2 | Cement parameter $s = 0.3$ |
| STRENGTH 3 | Cement parameter $s = 0.4$ |
| STRENGTH 4 | Cement parameter $s = 0.5$ |
| STRENGTH 5 | Stiffness and strength reduced by 25 % |
| STRENGTH 6 | Stiffness and strength reduced by 50 % |

Table 8.13: Tunnel runs simulating variation in stiffness and strength

The estimated reductions in stiffness and strength for the runs STRENGTH 5 and 6 represent a realistic scenario, when the design quality of shotcrete is not achieved at the construction site due to rebound behaviour or other uncertainties regarding material installation.

The parametric study investigating the influence of the deformability of the shotcrete at an early age involved the analyses summarized in Tab. 8.14 and illustrated in Fig. 8.14. Here again, run TPM 6 serves as a reference run to compare the obtained results, and therefore the shotcrete has an age of 24 h at the end of excavation and 48 h at the end of the surface loading.

| Run | Description | $\varepsilon^p_{cp,28}$ (%) | $\varepsilon^p_{cp,t_1}$ (%) | $\varepsilon^p_{cp,t_2}$ (%) |
|---|---|---|---|---|
| STRAIN 1 | Upper bound | 1.20 | 4.50 | 2.50 |
| STRAIN 2 | Lower bound | 0.10 | 2.50 | 0.8 |
| STRAIN 3 | Brittle behaviour | 0.50 | 3.50 | 1.00 |
| STRAIN 4 | Constant strain | 0.10 | 0.20 | 0.15 |

Table 8.14: Tunnel runs simulating the variation in the development of shotcrete deformability with time

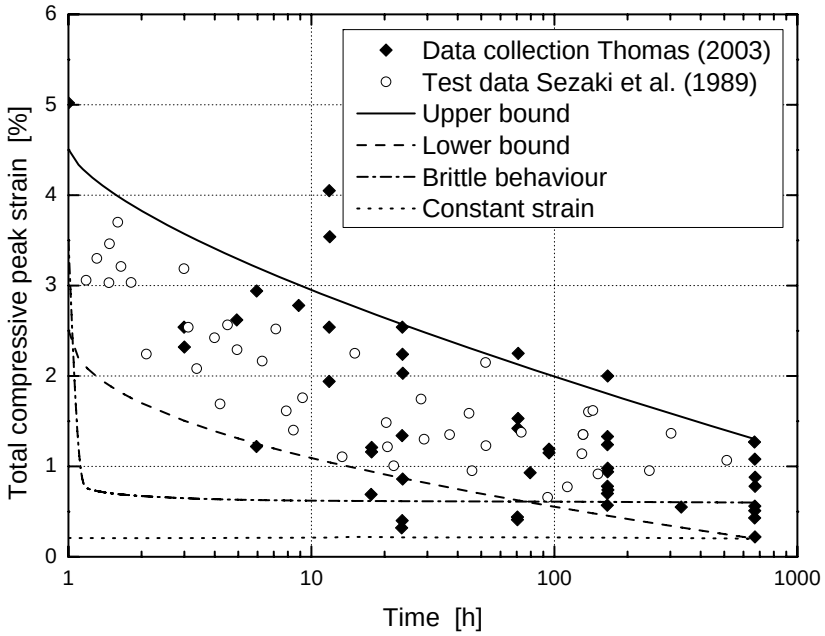



Figure 8.14: Variation of the compressive peak strains with time

Tab. 8.15 contains the main information about the performed calculations with respect to creep, shrinkage and hydration temperature.

| Run | Additional elapsed time after loading (Inc 51 to 100) (h) |
|---|---|
| CREEP (C) | 672.0 |
| SHRINKAGE (SH) | 672.0 |
| TEMPERATURE (T) | 48.0 |
| C + SH + T | 672.0 |

Table 8.15: Tunnel runs simulating creep, shrinkage and hydration temperature

### 8.6.2 Parametric study for excavation Type 2

Tab. 8.16 lists the performed time-runs applying different shotcrete ages for tunnel construction following the Type 2 excavation scheme. Similar to the previous Type 1 excavation scheme, a number of parametric studies were carried out, investigating the influence of the rate of increase of stiffness and strength with time and of the deformability of the shotcrete. A description of these analyses is summarised in Tab. 8.17.

| Run | End of excavation bench (Inc 12) | Increment 13 | End of excavation invert (Inc 25) | | End of surface loading (Inc 65) | |
|---|---|---|---|---|---|---|
| | Shotcrete age of upper shell | $\Delta t$ | Shotcrete age of upper shell | Shotcrete age of lower shell | Shotcrete age of upper shell | Shotcrete age of lower shell |
| | (h) | (h) | (h) | (h) | (h) | (h) |
| TPM 1 | 4.0 | 0.0 | 8.0 | 4.0 | 12.0 | 8.0 |
| TPM 2 | 4.0 | 12.0 | 20.0 | 4.0 | 24.0 | 8.0 |
| TPM 3 | 4.0 | 24.0 | 32.0 | 4.0 | 36.0 | 8.0 |
| TPM 4 | 4.0 | 48.0 | 56.0 | 4.0 | 60.0 | 8.0 |
| TPM 5 | 12.0 | 0.0 | 24.0 | 12.0 | 36.0 | 24.0 |
| TPM 6 | 12.0 | 12.0 | 36.0 | 12.0 | 48.0 | 24.0 |
| TPM 7 | 12.0 | 24.0 | 48.0 | 12.0 | 60.0 | 24.0 |
| TPM 8 | 12.0 | 48.0 | 72.0 | 12.0 | 84.0 | 24.0 |
| TPM 9 | 24.0 | 0.0 | 48.0 | 24.0 | 72.0 | 48.0 |
| TPM 10 | 24.0 | 12.0 | 60.0 | 24.0 | 84.0 | 48.0 |
| TPM 11 | 24.0 | 24.0 | 72.0 | 24.0 | 96.0 | 48.0 |
| TPM 12 | 24.0 | 48.0 | 96.0 | 24.0 | 120.0 | 48.0 |

Table 8.16: Shotcrete ages for different time-runs for excavation Type 2

| Run | Description |
|---|---|
| STRENGTH 1 | Cement parameter $s = 0.1$ |
| STRENGTH 3 | Cement parameter $s = 0.4$ |
| STRENGTH 5 | Stiffness and strength reduced by 25 % |
| STRAIN 3 | Brittle behaviour |
| STRAIN 4 | Constant strain |

Table 8.17: Tunnel runs simulating the variation of increase in stiffness and strength and shotcrete deformability with time

It is important to note that for these parametric studies, TPM 7 of Tab. 8.16 has been chosen as the reference run to compare results and therefore the same amount of time elapses during the process of excavation and surface loading. The respective model parameters for STRAIN 3 and 4 can be found in the previous Section 8.6.1.

For analysing the effect of creep, shrinkage and hydration temperature, the tunnel runs listed in Tab. 8.18 have been performed.

| Run | Correspondent time-run | Additional elapsed time after surface loading |
|---|---|---|
| CREEP (C) | TPM 7 | 672.0 |
| SHRINKAGE (SH) | TPM 7 | 672.0 |
| TEMPERATURE (T) | TPM 7 | 72.0 |
| C + SH + T | TPM 7 | 672.0 |

Table 8.18: Tunnel runs simulating creep, shrinkage and hydration temperature for excavation Type 2

### 8.6.3 Parametric study for excavation Type 3

Since the construction sequence of excavation Type 3 is, from a numerical point of view, very similar to the one of excavation Type 2, most of the parameters in the current investigation are varied in the same way as presented in the previous Section 8.6.2. Tab. 8.19 contains a review of the adopted shotcrete ages for the two staged tunnel construction with sidewall drift.

Regarding the possible effects of the development of stiffness, strength and shotcrete deformability with time, creep, shrinkage and hydration temperature, the same tunnel runs

| Run | End of excavation left gallery (Inc 12) Shotcrete age of left shell (h) | Increment 13 $\Delta t$ (h) | End of excavation right gallery (Inc 25) Shotcrete age of left shell (h) | Shotcrete age of right shell (h) | End of surface loading (Inc 65) Shotcrete age of left shell (h) | Shotcrete age of right shell (h) |
|---|---|---|---|---|---|---|
| TPM 1 | 4.0 | 0.0 | 8.0 | 4.0 | 12.0 | 8.0 |
| TPM 2 | 4.0 | 12.0 | 20.0 | 4.0 | 24.0 | 8.0 |
| TPM 3 | 4.0 | 24.0 | 32.0 | 4.0 | 36.0 | 8.0 |
| TPM 4 | 4.0 | 48.0 | 56.0 | 4.0 | 60.0 | 8.0 |
| TPM 5 | 12.0 | 0.0 | 24.0 | 12.0 | 36.0 | 24.0 |
| TPM 6 | 12.0 | 12.0 | 36.0 | 12.0 | 48.0 | 24.0 |
| TPM 7 | 12.0 | 24.0 | 48.0 | 12.0 | 60.0 | 24.0 |
| TPM 8 | 12.0 | 48.0 | 72.0 | 12.0 | 84.0 | 24.0 |
| TPM 9 | 24.0 | 0.0 | 48.0 | 24.0 | 72.0 | 48.0 |
| TPM 10 | 24.0 | 12.0 | 60.0 | 24.0 | 84.0 | 48.0 |
| TPM 11 | 24.0 | 24.0 | 72.0 | 24.0 | 96.0 | 48.0 |
| TPM 12 | 24.0 | 48.0 | 96.0 | 24.0 | 120.0 | 48.0 |

Table 8.19: Shotcrete ages for different time-runs for excavation Type 3

already introduced in Tab. 8.17 and 8.18 were carried out and compared with the reference run TPM 7.

## 8.7 Discussion of results

The following part of this thesis deals with the presentation and interpretation of the results obtained from the performed analyses that were described in detail in the previous sections. For a detailed understanding of the effects of tunnel construction the focus was therefore on the following aspects for all three excavation sequences:

- Surface settlements and volume loss
- Hoop stress distribution and utilisation factor within shotcrete tunnel lining
- Displacements of tunnel shell
- Effective stresses and pore water pressures in the ground surrounding the tunnel

In order to work out possible critical stages during tunnel construction, it was decided to analyse the results at various stages of construction, i.e. at the end of excavation, end of surface loading or 28 days after completion of the tunnel. The stress distributions for the particular cross sections of the lining indicated in Fig. 8.15 and the utilisation factor for lining extrados or intrados were investigated.

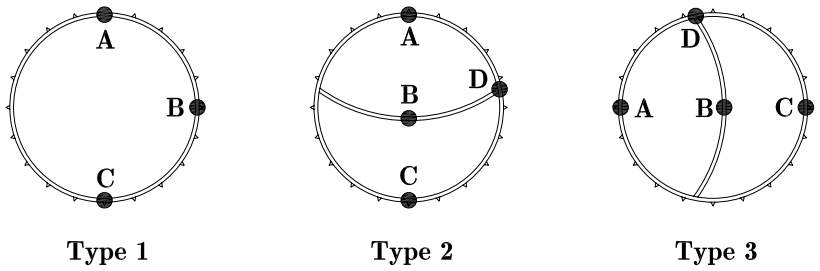



Figure 8.15: Analysed cross sections of tunnel lining for all three excavation sequences

The intersection of the temporary invert or sidewall of excavation Type 2 and 3 with the circular lining is of special interest, since they represent areas where high stresses could be expected. Hence, the maximum and minimum stresses in the following area indicated in Fig. 8.16 were investigated in detail for an intermediate construction stage.

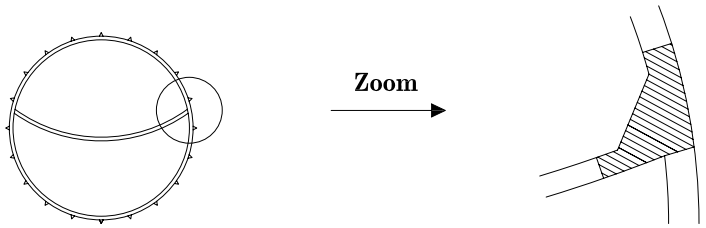



Figure 8.16: Zoom into connection point of temporary invert with tunnel lining for excavation Type 2

Horizontal and vertical displacements of particular points of the tunnel lining intrados, as shown in Fig. 8.17, have been processed over the whole construction and loading sequence so that a detailed study of the deformational behaviour of the lining was possible.

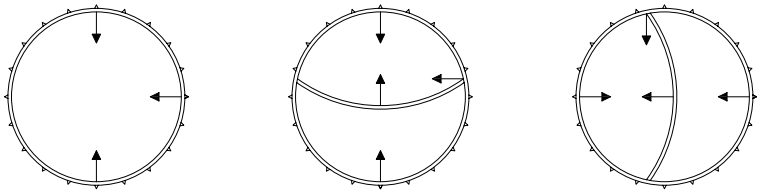



Figure 8.17: Investigated lining displacements for all three excavation sequences

The formulation of the constitutive model for shotcrete presented in Chapter 7 allows the utilisation factor for a particular Gauss point to be established with the help of the normalised hardening parameters $H_c$ for compression and $H_t$ for tension. Based on those two parameters, the utilisation factor $\rho_c$ can be written for a compressive stress state as:

$$\rho_c = \begin{cases} f_{c,n} & \text{for} \quad H_c \leq 1 \\ 1 & \text{for} \quad H_c > 1 \end{cases} \tag{8.6}$$

In a similar way, the utilisation factor $\rho_t$ is given for a tensile stress state as:

$$\rho_t = \begin{cases} f_{t,n} & \text{for} \quad H_t \leq 1 \\ 1 & \text{for} \quad H_t > 1 \end{cases} \tag{8.7}$$

A value of unity indicates that the particular stress state is already beyond peak and that shotcrete behaviour is goverened by strain-softening. If $\rho_t = 1$ the shotcrete is likely to crack in tension.

### 8.7.1 Surface settlements and volume loss

#### 8.7.1.1 Excavation Type 1

Fig. 8.18 contains the obtained results regarding the surface settlement troughs for runs LE, HME and TPM 1 to 6 at the end of tunnel excavation, applying a $K_o$-profile of 0.5. It can be seen that all runs show a similar shape resembling a typical Gaussian distribution curve often referred to in the literature. However, due to the early age behaviour of young shotcrete, the maximum settlements that occur directly above the axis of the tunnel differ significantly in magnitude. As expected, due to the high lining stiffness of the linear elastic approach (LE), settlements are relatively small, with a maximum value of 21 mm. Although the adopted stiffness for the HME model is just 25 % of the LE-stiffness, results are relatively close, showing a maximum settlement of 23 mm. The largest surface settlement was obtained for run TPM 1 with almost 82 mm. This results from the low age of the young shotcrete at the end of excavation (2 h). With increasing shotcrete age (TPM 2 to 6) the behaviour of the lining becomes stiffer and settlements reduce drastically, from 55 to 25 mm. For the runs TPM 7 to 14 no difference compared to the linear elastic approach was noticeable and therefore these runs are not included in Fig. 8.18. The same observation was made for the non-linear analysis (NL) where the material properties of shotcrete at an age of 28 days were applied and no time-dependency exists anymore. Therefore, it can be concluded that for hardened shotcrete the non-linear pre-yield behaviour is not affecting the surface settlement predictions.

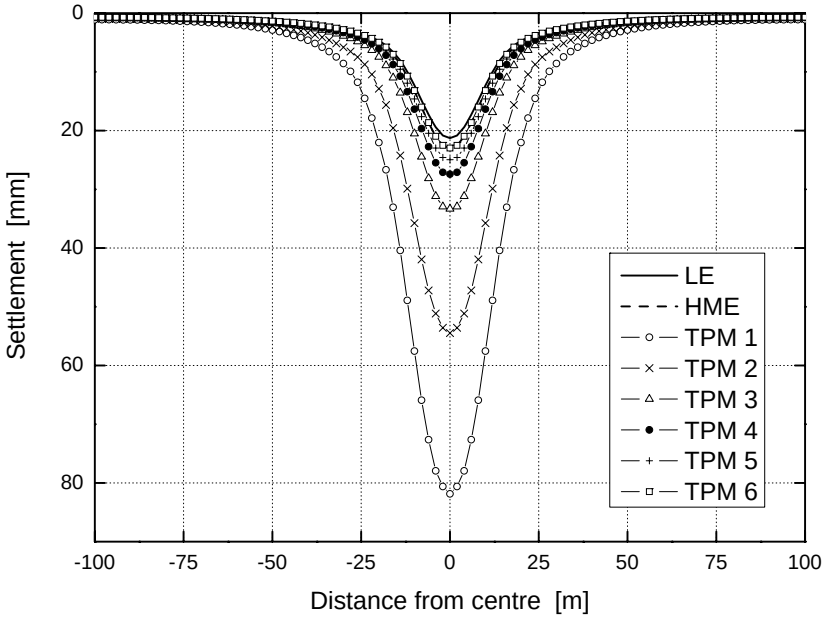



Figure 8.18: Surface settlements at end of tunnel excavation (Excavation Type 1, $K_o = 0.5$)

For a $K_o$-profile of 1.5, settlements are in general smaller in magnitude due to the high horizontal stresses in the ground before tunnel excavation. However, Fig. 8.19 shows a similar

pattern for the surface settlements for the runs LE, HME and TPM 1 to 6. The linear elastic and HME approach represent a very stiff lining behaviour with maximum surface settlements of just 14 and 15 mm respectively. Again, run TPM 1 is governed by the low lining stiffness at the age of 2 h and settlements increase up to 39 mm. These settlements reduce with an increase in shotcrete age from 30 mm down to 14 mm. No noticeable difference in the settlement behaviour has been detected for runs NL and TPM 7 to 14.

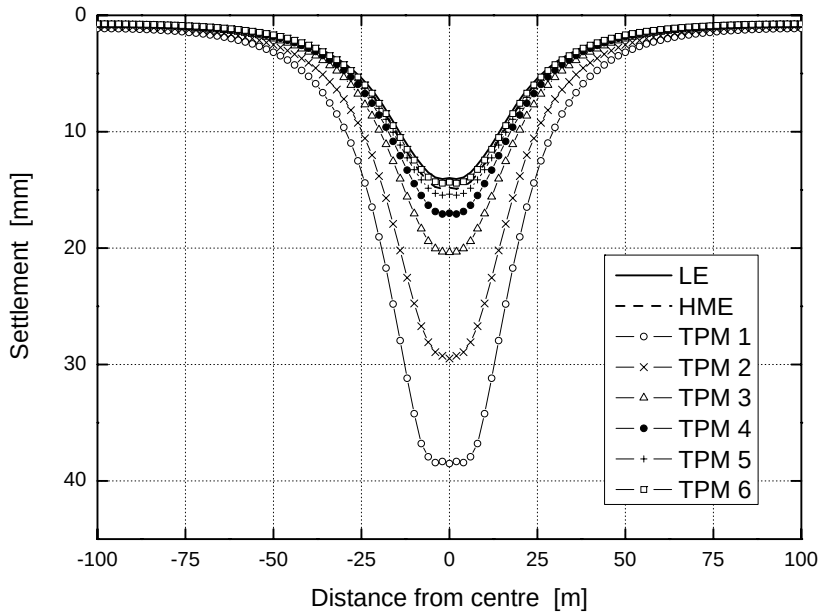



Figure 8.19: Surface settlements at end of tunnel excavation (Excavation Type 1, $K_o = 1.5$)

Fig. 8.20 compares the development of the volume loss $V_L$ calculated from the above presented surface settlement troughs for both $K_o$-profiles. A clear general trend can be identified, which is a reducing volume loss with increasing shotcrete age at the end of tunnel excavation (Inc 10). Run TPM 1 predicts for both $K_o$-profiles extremely high values of volume loss with 5.63 % for $K_o = 0.5$ and 3.84 % for $K_o = 1.5$. These values are clearly above the target value of 1.5 %. If construction is performed slower, i.e. the elapsed time during excavation increases, the volume loss reduces until no further significant difference is obtained for runs TPM 6 and above. For runs TPM 7 to 14 the volume loss appears to be constant, which is the same for the non-linear run NL.

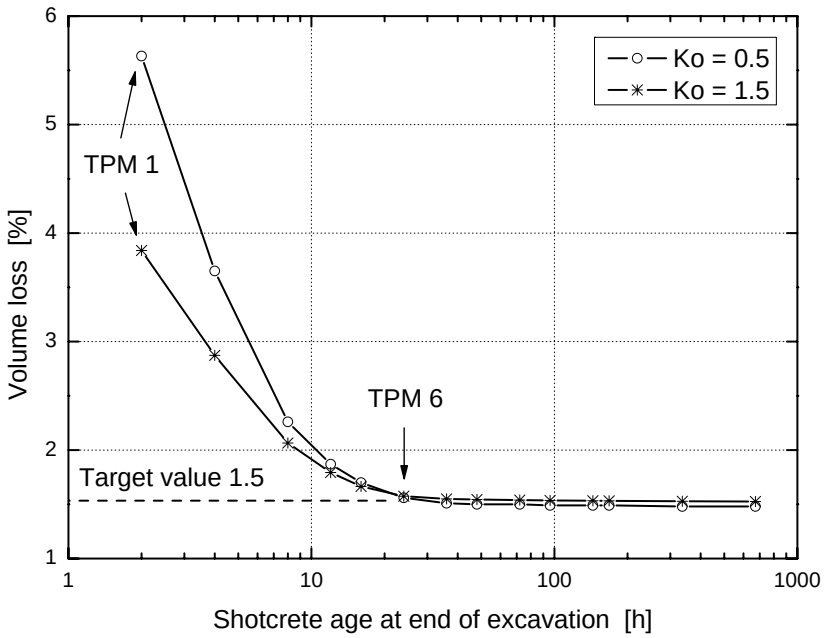



Figure 8.20: Predicted volume loss for both $K_o$-profiles adopting different shotcrete ages at the end of tunnel excavation (Excavation Type 1)

Fig. 8.21 contains a compilation of settlement troughs for analyses where the increase in stiffness and strength with time was the main parameter under investigation. Results are compared with the reference run TPM 6 showing a maximum settlement of 23 mm. STRENGTH 2 to 4 represent tunnel runs with a different cement parameter $s$, which controls the hardening of the cement paste. It can be seen that an increase in $s$ leads to higher settlements, as one would expect, since the development of the stiffness is retarded significantly. STRENGTH 2 to 4 lead to a maximum surface settlement of 27, 35 and 44 mm respectively. As a consequence, the volume loss $V_L$ for those runs is clearly above the target value, reaching 2.95 % for run STRENGTH 4. For runs STRENGTH 5 and 6, the 28 days stiffness and strength was reduced by 25 and 50 % respectively. This scenario results in maximum settlements that are 10 and 32 % higher than in run TPM 6 (25 and 30 mm). Results from run STRENGTH 1 are not included in the figure, as no significant difference in the results compared to TPM 6 was noticed.

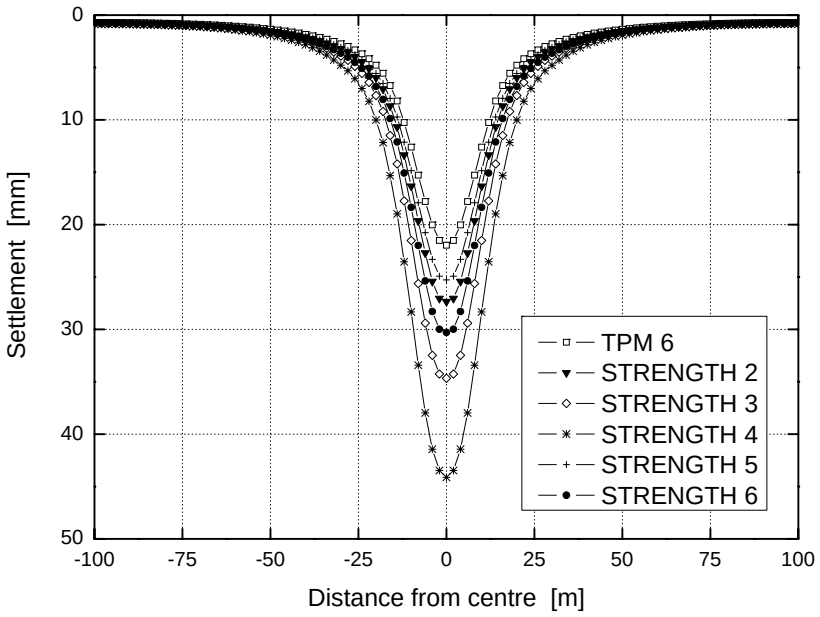



Figure 8.21: Surface settlements for different developments of stiffness and strength of shotcrete with time (Excavation Type 1, $K_o = 0.5$)

A similar picture is obtained for the same type of investigation adopting a $K_o$-profile of 1.5 as can be seen in Fig. 8.22

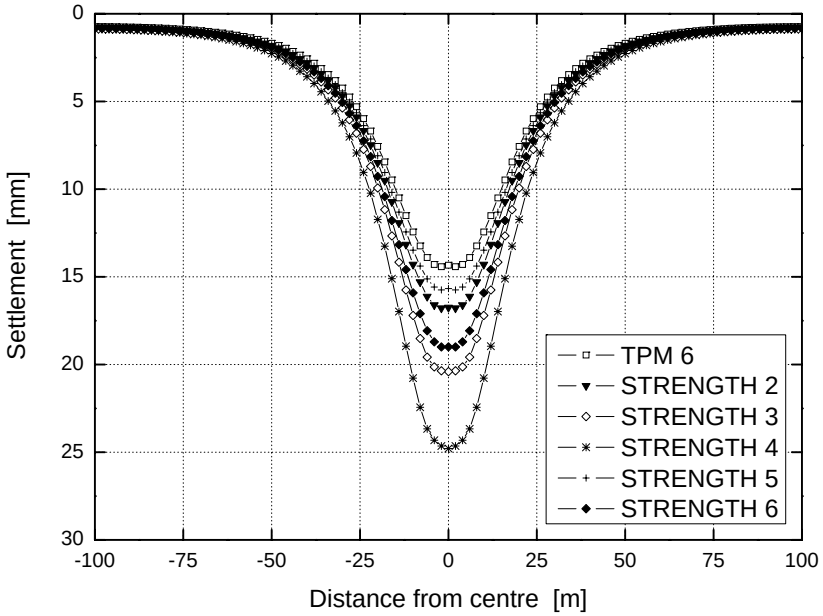



Figure 8.22: Surface settlements for different developments of stiffness and strength of shotcrete with time (Excavation Type 1, $K_o = 1.5$)

The influence of the early age deformability of the shotcrete on the surface settlement behaviour, adopting a $K_o$-profile of 0.5, is illustrated in Fig. 8.23. Maximum settlements above the tunnel axis vary between 22.3 and 23.2 mm. This difference is even less pronounced for

$K_o = 1.5$ and can therefore be neglected.

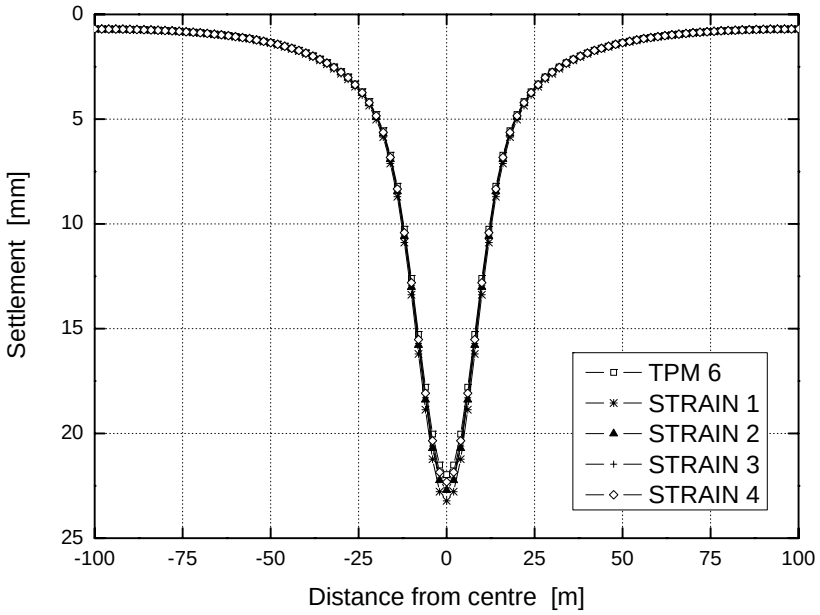



Figure 8.23: Surface settlements for different shotcrete deformabilities (Excavation Type 1, $K_o = 0.5$)

Very little influence has been obtained of the time-dependent aspects of creep, shrinkage and hydration temperature on the surface settlement behaviour during tunnel construction, as can be seen in Fig. 8.24 for a $K_o$-profile of 0.5. The inclusion of the development of shotcrete hydration temperature leads to a small reduction in volume loss and maximum surface settlement (22.6 mm) compared to reference run TPM 6, since the lining tends to expand slightly during the first 12 h after installation. The opposite effect has been noticed for the run SHRINKAGE, where due to the decrease in shotcrete volume with time a surface volume loss of 1.57 % can be expected at the end of excavation in Inc 10. Taking into account the creep of early age shotcrete in run CREEP, does not make any difference at all for the settlement behaviour compared to run TPM 6 and volume loss and maximum surface settlements are identical.

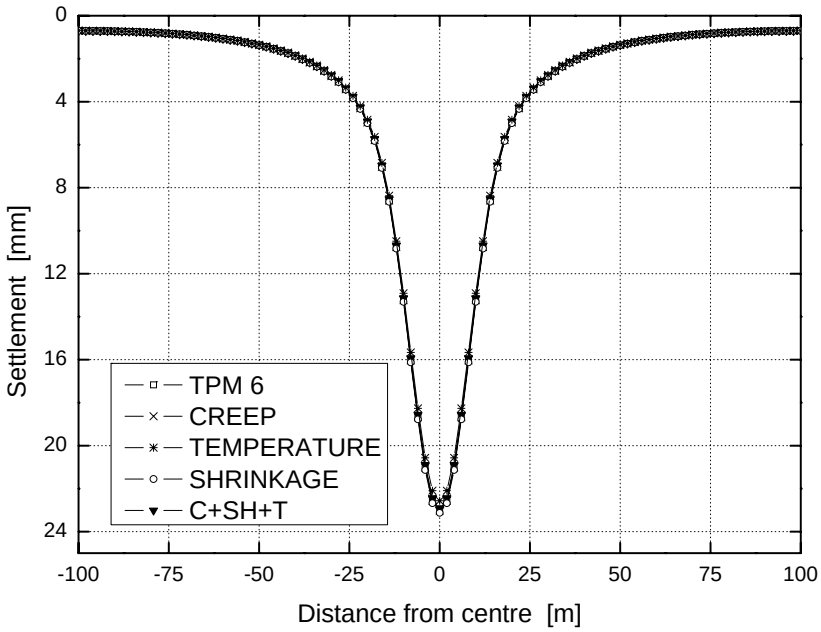



Figure 8.24: Surface settlements for analysis of creep, shrinkage and hydration temperature of shotcrete (Excavation Type 1, $K_o = 0.5$)

Results are similar when adopting a $K_o$-profile of 1.5 with maximum surface settlements ranging from 14.0 to 14.6 mm, as shown in Fig. 8.25.

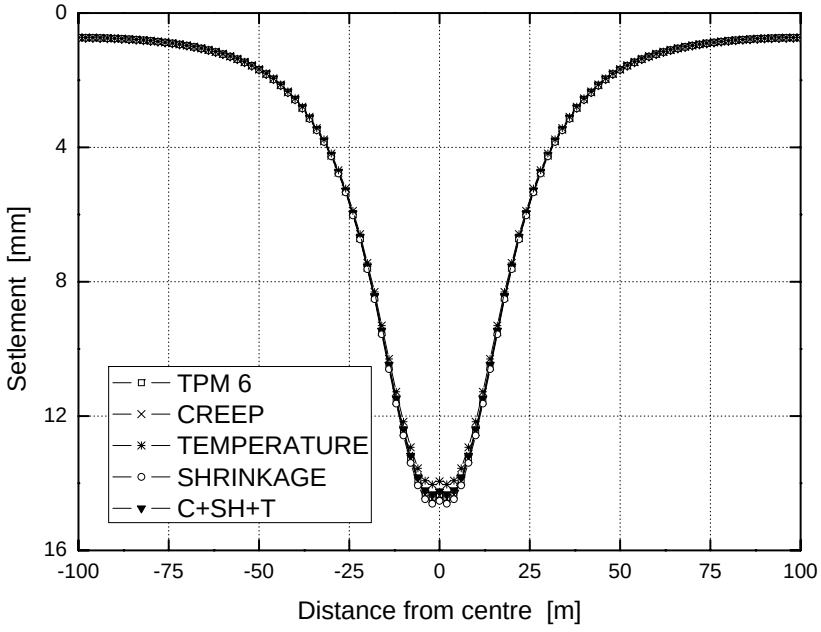



Figure 8.25: Surface settlements for analysis of creep, shrinkage and hydration temperature of shotcrete (Excavation Type 1, $K_o = 1.5$)

A complete set of results for the settlement behaviour of excavation Type 1 for both $K_o$-profiles can be found in the Appendix.

#### 8.7.1.2 Excavation Type 2

The following Fig. 8.26 illustrates the settlement troughs obtained for the tunnel construction according to excavation Type 2. At the end of bench excavation (Inc 12), which represents an intermediate construction stage, the linear elastic model (LE) for shotcrete predicts a maximum settlement of 20.5 mm. Slightly higher values are obtained when adopting non-linearity for hardened shotcrete (NL) and the HME approach. The analysis for TPM 1 shows the highest value of maximum settlements of 26.8 mm due to the early age properties of shotcrete. When construction of the tunnel is continued by excavating the invert region of the tunnel cross section, the settlement troughs for all the performed analyses except TPM 1 seem to move upwards resulting in smaller maximum surface settlements at the end of excavation than at the intermediate stage. In addition, the shape of these settlement troughs tends to change slightly by getting wider in such a way that the aimed volume loss of 1.5 % is achieved for the linear elastic model (LE). For TPM 1, the maximum settlements continue to increase during invert excavation up to a final value of 29.2 mm. TPM 5 and 9, which represent analyses with older and consequently stiffer shotcrete, predict maximum settlements of 16.1 and 18.2 mm respectively.

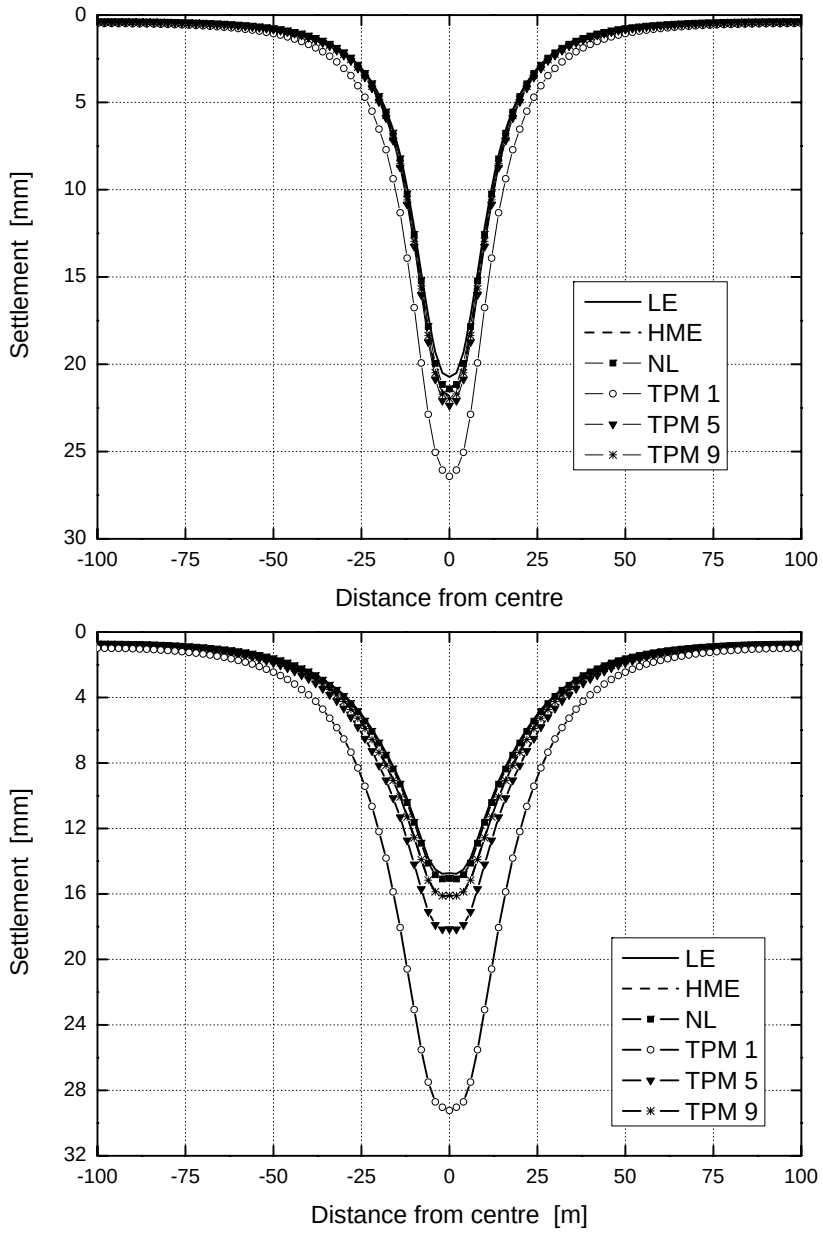



Figure 8.26: Surface settlements for various time-runs at the end of bench excavation (Inc 12, top) and end of invert excavation (Inc 25, bottom)

The reason behind performing the time runs TPM 1 to 4 was to simulate the longitudinal distance between bench and invert excavation by adopting some amount of elapsed time $\Delta t$ (Inc 13) in the present 2D analysis. As a consequence, the upper tunnel shell has a different shotcrete age and material properties than the lower one, which is installed at a later time of construction (Inc 14). However, Fig. 8.27 shows that there is no influence of the intermediate time $\Delta t$ on the predicted settlement behaviour since the settlement troughs for TPM 1 to 4 are almost identical or show negligable differences. It can be concluded that it is not possible to capture the real 3D effect of staged tunnel excavation on the settlement profiles in a 2D analysis.

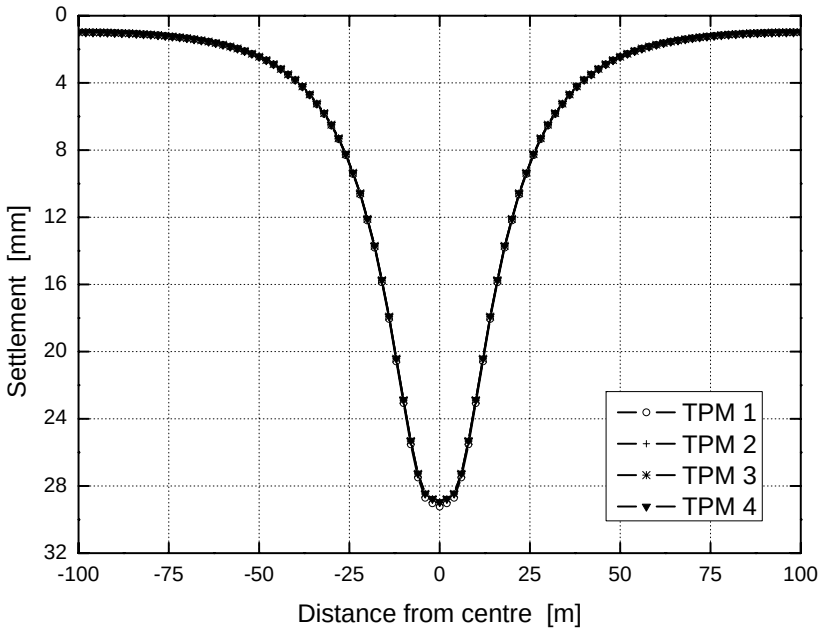



Figure 8.27: Surface settlements after complete excavation for runs TPM 1 to 4

The runs STRENGTH 1, 3 and 5 model different developments of the increase in shotcrete stiffness and strength with time as summarised in Tab. 8.17. The reference run TPM 7 in Fig. 8.28 shows a maximumm surface settlement of 18.2 mm, whereas the maximum value of STRENGTH 1 is reduced to 15.6 mm since the stiffness and strength of the shotcrete increase more quickly with time ($s = 0.1$). Maximum settlements of STRENGTH 3 reach up to 30.1 mm due to the retarded development of the lining stiffness ($s = 0.4$). This results in a relatively high volume loss of 2.78 %, which is far above the target value of 1.5 %. If the stiffness and strength of shotcrete are reduced by 25 % (STRENGTH 5), an increase in maximum settlements of 11 % can be expected.

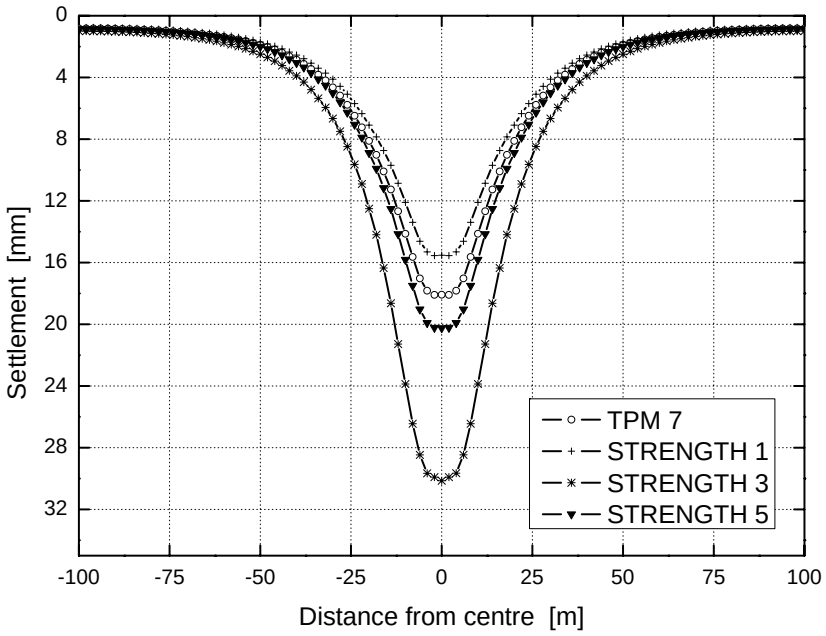



Figure 8.28: Surface settlements after complete excavation for various developments in stiffness and strength

By looking at the settlement troughs shown in Fig. 8.29, it can be concluded that the shotcrete deformability at early ages plays only a minor role in the realistic prediction of the settlement behaviour. Maximum settlements vary from 16.2 mm for run STRAIN 4 (constant peak strains) to 18.2 mm for run TPM 7.

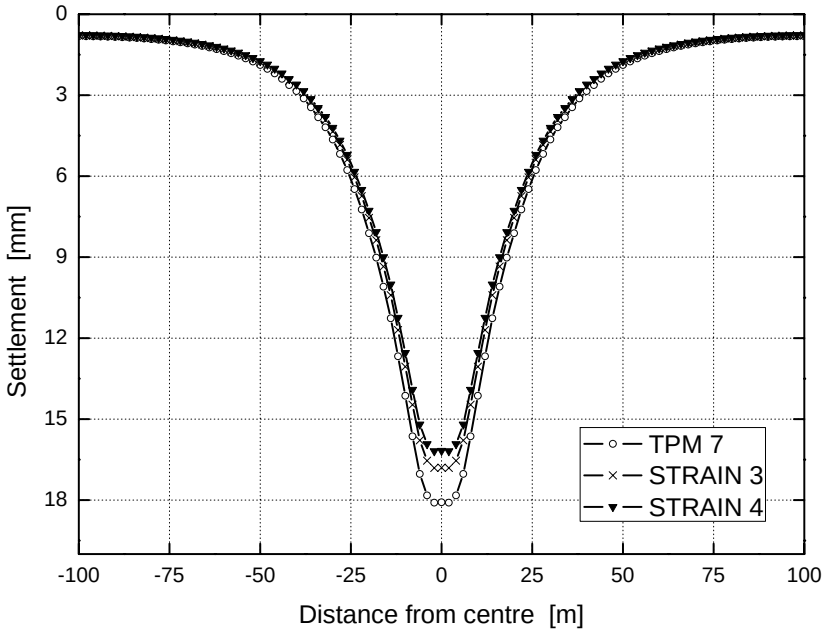



Figure 8.29: Surface settlements after complete excavation for various shotcrete deformabilities

Finally, Tab. 8.20 summarises the obtained results regarding volume loss and maximum surface settlements for all the performed analyses for excavation Type 2. It should be noted that only the linear elastic (LE) and the non-linear (NL) run fulfill the volume loss criterion of 1.5 %. For very young shotcrete the volume loss can increase up to almost 2.8 %, which is likely to be an unacceptable value.

| Run | Volume loss $V_L$ (%) | Maximum settlement $\delta$ (mm) |
|---|---|---|
| Linear elastic (LE) | 1.48 | 14.8 |
| HME | 1.61 | 16.1 |
| Non-linear (NL) | 1.51 | 15.1 |
| TPM 1 | 2.71 | 29.2 |
| TPM 5 | 1.80 | 18.2 |
| TPM 9 | 1.62 | 16.1 |
| STRENGTH 1 | 1.57 | 15.6 |
| STRENGTH 3 | 2.78 | 30.1 |
| STRENGTH 5 | 1.97 | 20.2 |
| STRAIN 3 | 1.67 | 16.8 |
| STRAIN 4 | 1.62 | 16.2 |
| CREEP | 1.80 | 18.1 |
| SHRINKAGE | 1.80 | 18.2 |
| TEMPERATURE | 1.78 | 17.8 |
| C+SH+T | 1.80 | 18.1 |

Table 8.20: Volume loss and maximum surface settlement for various time-runs at completion of tunnel excavation (Inc 25) for excavation Type 2

#### 8.7.1.3 Excavation Type 3

Fig. 8.30 illustrates the development of surface settlements during tunnel construction according to excavation Type 3 for various runs adopting different constitutive behaviour for shotcrete. At the end of excavation of the left side gallery (Inc 12), all the predicted surface settlement troughs have a relatively irregular shape with the maximum settlement occurring to the sides of the tunnel centre line. This effect occurs due to the temporary sidewall that is installed as an intermediate support element. At this stage of tunnel construction the predicted settlements are in the range of 8 to 10 mm for the runs LE, HME, TPM 5 and 9. No difference to LE has been observed when adopting the non-linear model (NL). This irregularity is not so pronounced for run TPM 1, which shows a relatively flat area of the size

of double the tunnel diameter directly above the tunnel axis. The maximum settlements for TPM 1 reach up to almost 16 mm. When construction of the tunnel continues by excavating the right side gallery, surface settlement predictions seem to follow again a distribution similar to a Gaussian distribution curve and the maximum settlements tend to increase, which was not the case for excavation Type 2. Due to the high lining stiffness, the linear elastic model (LE) shows the smallest settlements with 12.6 mm at completion of tunnel excavation (Inc 25). The HME approach with its softer lining stiffness predicts slightly larger settlements with a maximum of 14.6 mm. This result is almost identical with run TPM 9, where the lower tunnel shell has a shotcrete age of 24 h and the upper shell 48 h. As might be expected, TPM 1 simulating a relatively high loading rate on young shotcrete predicts the largest surface settlements of up to 27.4 mm. From these analyses it can be observed again that with increasing shotcrete age settlements tend to reduce because of the further developed lining stiffness.

As for the the case of excavation Type 2, the elapsed time $\Delta t$ in Inc 13, simulating the distance between the face of the left and right side gallery, has no influence on the settlement behaviour (runs TPM 2, 3, 4, 6, 7, 8, 10, 11 and 12). It is therefore not possible to capture the full stress rearrangement by adopting different shotcrete ages for the left and right tunnel shell in a 2D analysis.

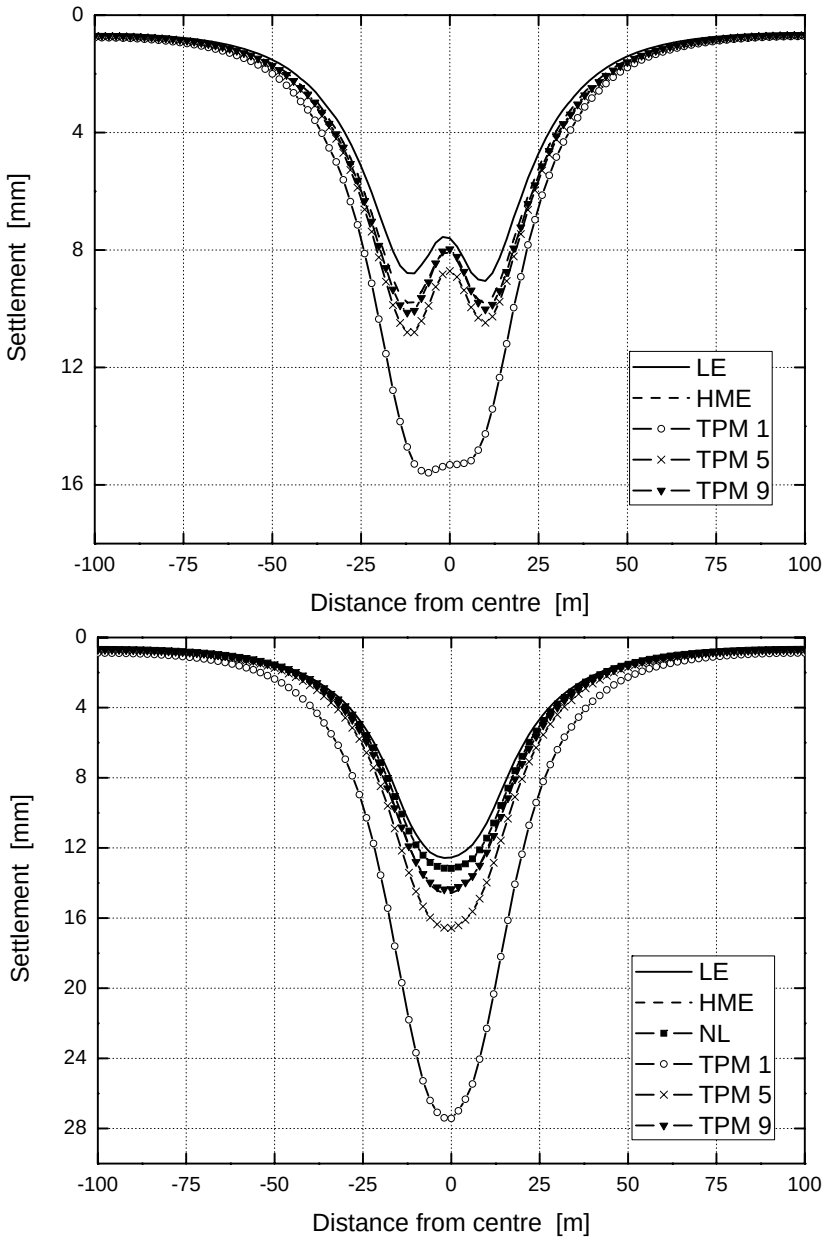



Figure 8.30: Surface settlements for various time-runs at the end of excavation of the left side gallery (Inc 12, top) and end of complete excavation (Inc 25, bottom) for excavation Type 3

Results differ significantly when adopting different developments of stiffness and strength for shotcrete in runs STRENGTH 1, 3, and 5, as can be seen in Fig. 8.31. When simulating a fast increase in lining stiffness for run STRENGTH 1 ($s = 0.1$), the maximum settlements reduce by 2.7 mm compared to run TPM 7 to an absolute value of 13.9 mm. A relatively high cement parameter of $s = 0.4$ for run STRENGTH 3 leads to a slow increase in stiffness and therefore surface settlements increase significantly of up to 28.1 mm. By reducing the stiffness and strength by 25 %, the obtained maximum surface settlements for run STRENGTH 5 are 13 % higher (18.7 mm) compared to run TPM 7.

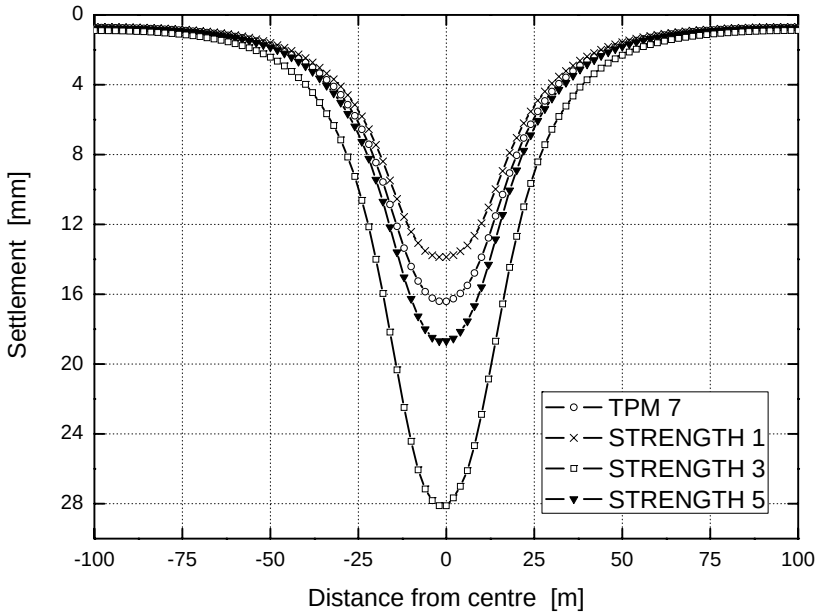



Figure 8.31: Surface settlements after complete excavation for various developments of stiffness and strength for excavation Type 3

Fig. 8.32 investigates the influence of early age shotcrete deformability on the surface settlement behaviour at the end of tunnel excavation (Inc 25). The run STRAIN 3 represents a very brittle material behaviour, where the compressive peak strains reduce quickly with increasing shotcrete age (see Tab. 8.17). As a result, the maximum settlements are slightly reduced compared to reference run TPM 7 and reach a value of 15.2 mm. When adopting a constant compressive and tensile peak strain in run STRAIN 4, the surface settlements tend to be smaller with a maximum value of 14.6 mm.

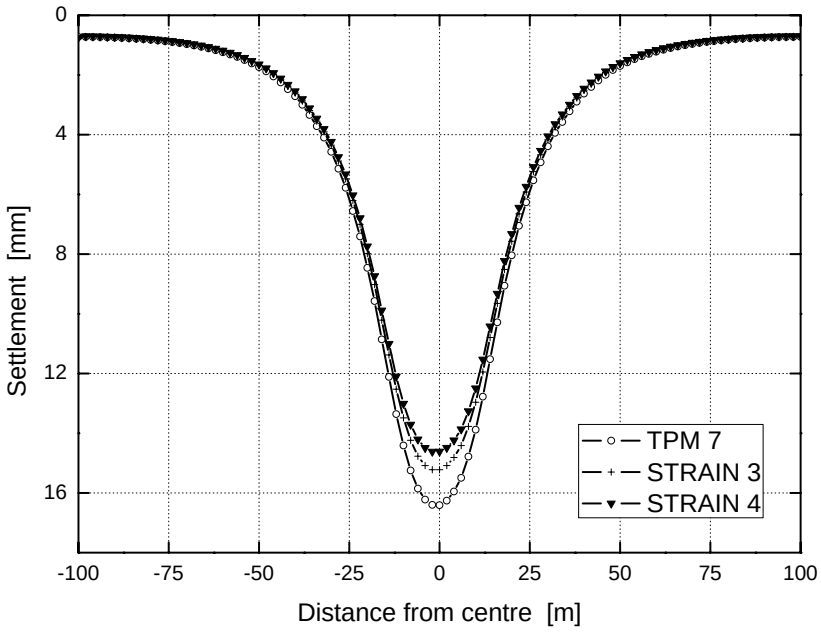



Figure 8.32: Surface settlements after complete excavation for various shotcrete deformabilities for excavation Type 3

Tab. 8.21 contains a summary of the results for all the performed analyses of excavation Type 3 regarding surface settlement behaviour. It can be seen clearly, that most of the runs adopting young shotcrete behaviour show a relatively high volume loss of up to 2.74 %. Runs LE, HME, NL and STRENGTH 1 predict a volume loss close to 1.5 % reaching the target value. Maximum surface settlements vary for all runs from 12.6 mm (LE) to 28.1 mm (STRENGTH 4).

| Run | Volume loss $V_L$ (%) | Maximum settlement $\delta$ (mm) |
|---|---|---|
| Linear elastic (LE) | 1.37 | 12.6 |
| HME | 1.53 | 14.6 |
| Non-linear (NL) | 1.45 | 13.2 |
| TPM 1 | 2.66 | 27.4 |
| TPM 5 | 1.73 | 16.6 |
| TPM 9 | 1.54 | 14.4 |
| STRENGTH 1 | 1.51 | 13.9 |
| STRENGTH 3 | 2.74 | 28.1 |
| STRENGTH 5 | 1.91 | 18.7 |
| STRAIN 3 | 1.62 | 15.2 |
| STRAIN 4 | 1.57 | 14.6 |
| CREEP | 1.72 | 16.4 |
| SHRINKAGE | 1.72 | 16.5 |
| TEMPERATURE | 1.70 | 16.2 |
| C+SH+T | 1.73 | 16.5 |

Table 8.21: Volume loss and maximum surface settlement for various time-runs at completion of tunnel excavation (Inc 25) for excavation Type 3

From these observations it can be concluded that the stiffness of the shotcrete at early ages is of crucial importance for a realistic prediction of surface settlements and volume loss. Relatively fast tunnel excavation can lead to unacceptable surface movements during the first 24 hours, where the stiffness properties of shotcrete have not yet developed enough to form a stiff ring. Modelling the tunnel shell as a linear elastic material (LE) leads to relatively small surface settlements and volume loss due to the very high lining stiffness from the very beginning of tunnel construction. These results can be slightly improved by adopting the HME approach and a reduced stiffness. When simulating shotcrete behaviour with the time-dependent elasto-plasticity model the correct development of the stiffness with time is a key parameter for the realistic prediction of surface settlement troughs. Therefore, the cement parameter $s$ should be treated with caution. The deformability of very young shotcrete at early ages plays a minor role in the surface settlement behaviour, where results vary within a relatively small range for excavation Types 2 and 3. Creep, shrinkage and shotcrete hydration temperature seem to have very little or almost no influence on the predicted settlement behaviour during tunnel excavation. However, due to the expansion of the lining during cement hydration the surface settlements tend to reduce slightly.

### 8.7.2 Hoop stress distribution and utilisation factor

#### 8.7.2.1 Excavation Type 1

As explained in the introduction to this section, the stress distribution within the shotcrete shell was investigated for several cross sections of the tunnel lining. Fig. 8.33 shows how the obtained horizontal stresses vary across the lining thickness at the tunnel crown for various adopted constitutive models at the end of excavation (Inc 10), assuming a $K_o$-profile of 0.5. It should be noted that the lining intrados is located at 0.0 m, whereas the lining extrados is situated at a distance of 0.20 m. It can be seen that the linear elastic model (LE) predicts large bending of the lining with a maximum compressive stresses of -8.3 MPa and a tensile stress of 0.58 MPa. This bending is significantly reduced for the HME approach due to the reduced elastic stiffness with maximum and minimum compressive stresses of -5.1 and -2.7 MPa respectively. However, the time-dependent runs TPM 1 to 6 appear to predict almost no bending at all, and the mechanical behaviour is mainly governed by hoop compression. Since the compressive strength is not fully developed at these early stages of shotcrete hydration, these compressive stresses are at a relatively low level ranging from -1.3 (TPM 1) to about -4.0 MPa (TPM 6). With further increase in shotcrete age (TPM 7 to 14), the material response of the shotcrete becomes stiffer and significant bending of the lining is introduced, approaching the linear elastic model (LE). Non-linearity of hardened shotcrete at 28 days (NL) does not play an important role at the end of excavation and no difference to the linear elastic model has been identified.

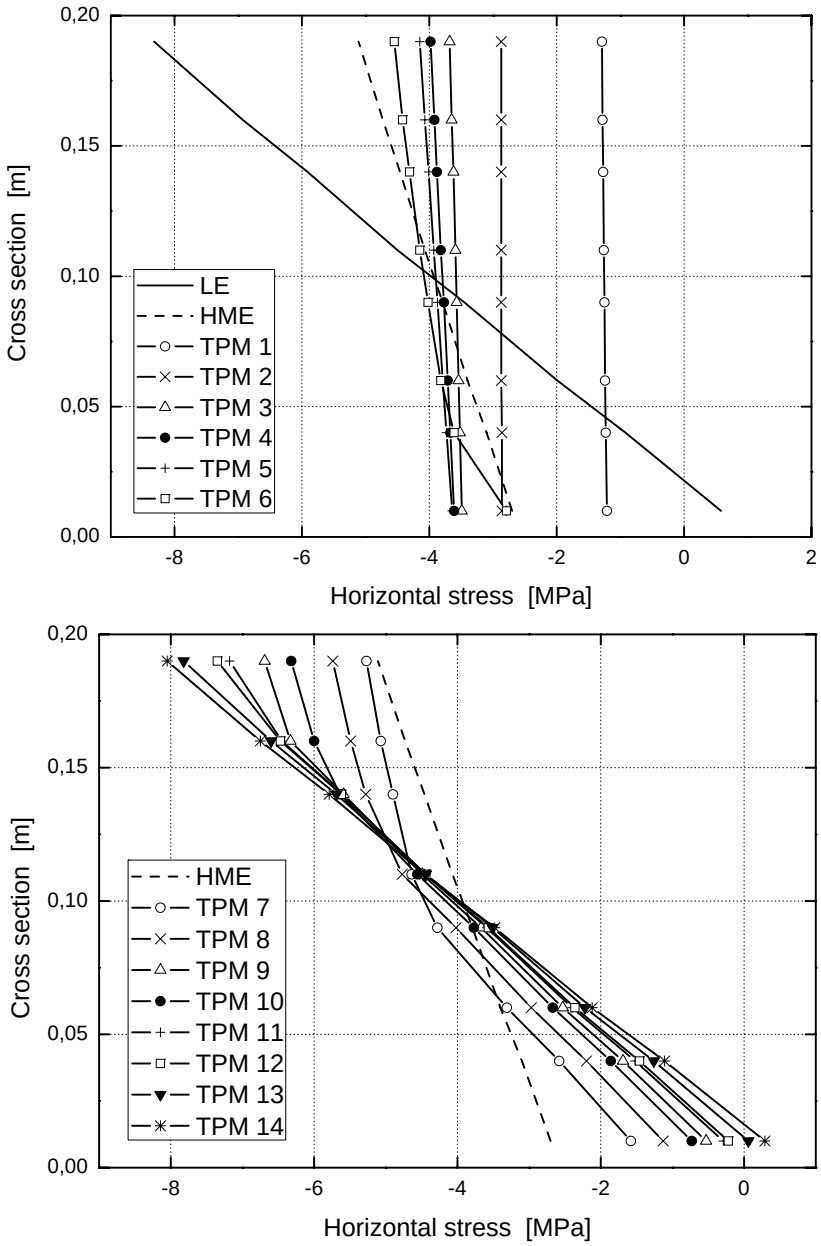



Figure 8.33: Horizontal hoop stress distribution for crown at end of excavation (Inc 10) for $K_o = 0.5$

These differences in lining behaviour for different constitutive models and elapsed time become even more pronounced when loading of the shotcrete shell is continued by placing the surface surcharge on top of the tunnel, see Fig. 8.34. The linear elastic model (LE) predicts compressive stresses of up to -36.5 MPa and tensile stresses of 27.2 MPa, which result in a huge and probably unrealistic bending moment. Furthermore, the shotcrete is obviously not able to sustain such a large tensile stress and therefore cracking of the lining would occur in the region of the crown. This large bending is reduced by applying the HME approach, but still unrealistic tensile stresses would be induced at the lining intrados (5.0 MPa). When adopting the non-linear approach (NL) it can be observed that stresses are changed due to the

non-linear hardening and softening of shotcrete at the onset of plastic deformation. On the lining extrados compressive stresses reach a level of -20.1 MPa and are far below the uniaxial strength. Tensile stresses on the lining intrados are restricted to 3.0 MPa by the adopted tensile yield surface and cracking of the shotcrete takes place for almost half the width of the cross section. The runs TPM 1 to 6, still present relatively low bending compared to the LE and HME approach and maximum compressive stresses vary between -3.6 and -10.2 MPa. All these runs also predict low tensile stresses at the lining intrados which are in the range of 0.2 to 1.7 MPa. Here again, with increasing shotcrete age, the material behaviour becomes more and more brittle and a highly non-linear stress distribution can be observed, where cracking and consequently tensile strain softening play an important role at the lining intrados (TPM 7 to 14).

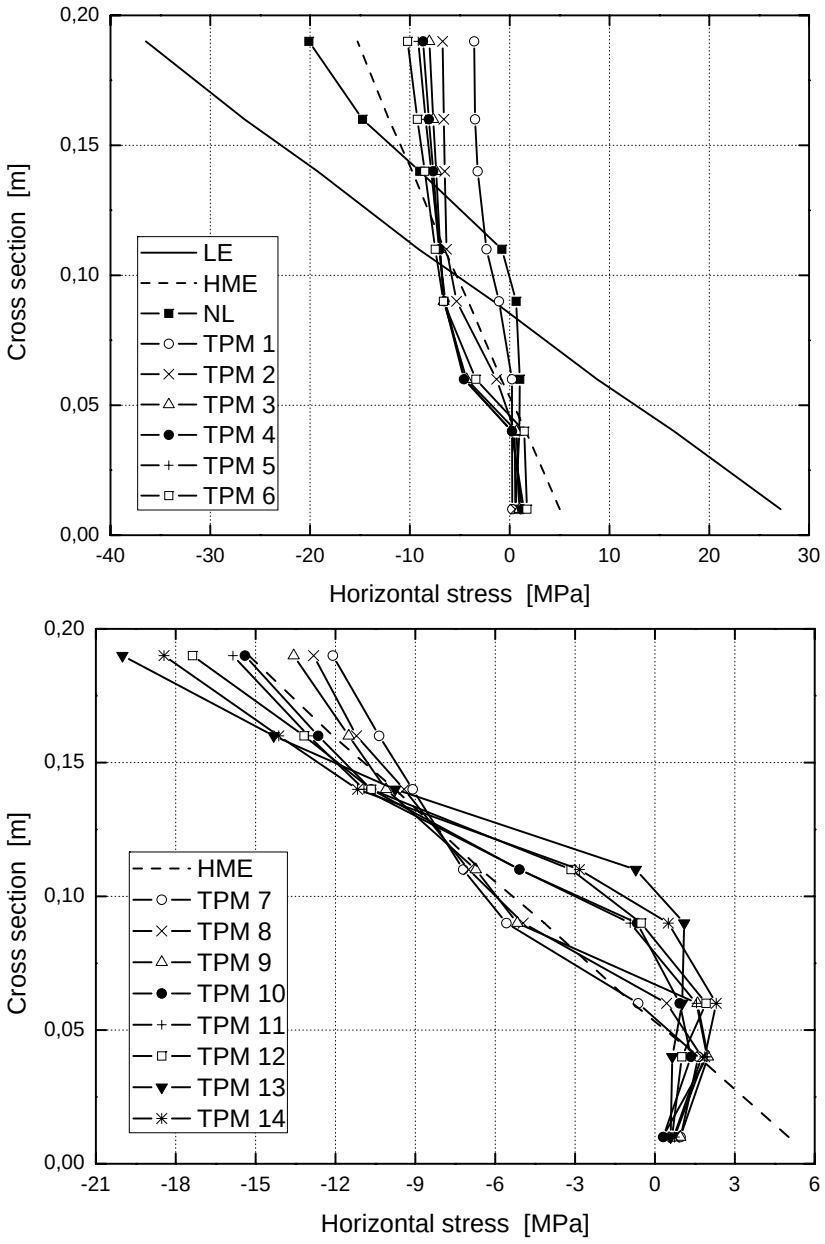



Figure 8.34: Horizontal hoop stress distribution for crown at end of loading (Inc 50) for $K_o = 0.5$

The effect of the development of stiffness and strength on the stress distribution within the tunnel lining can be studied in Fig. 8.35, which illustrates the vertical stresses at the right tunnel sidewall at the end of excavation, adopting a $K_o$-profile of 0.5. In this plot, the lining intrados is again located at 0.0 m, whereas the lining extrados is situated at a distance of 0.20 m. An interesting fact is that almost all of the performed analyses predict mainly hoop compression without any bending at all, apart from run STRENGTH 1. For this particular run an accelerated stiffness and strength increase is assumed ($s = 0.1$) and therefore stresses are at a higher level compared to the reference run TPM 6 (-4.7 MPa). The lowest compressive stress is predicted by run STRENGTH 4 (-3.7 MPa) due to the retarded

stiffness and strength development as a result of adopting the cement parameter $s = 0.5$. A reduction of the stiffness and strength by 25 and 50 % (runs STRENGTH 5 and 6) leads to a slightly smaller compressive stress ranging between -4.0 and -5.0 MPa.

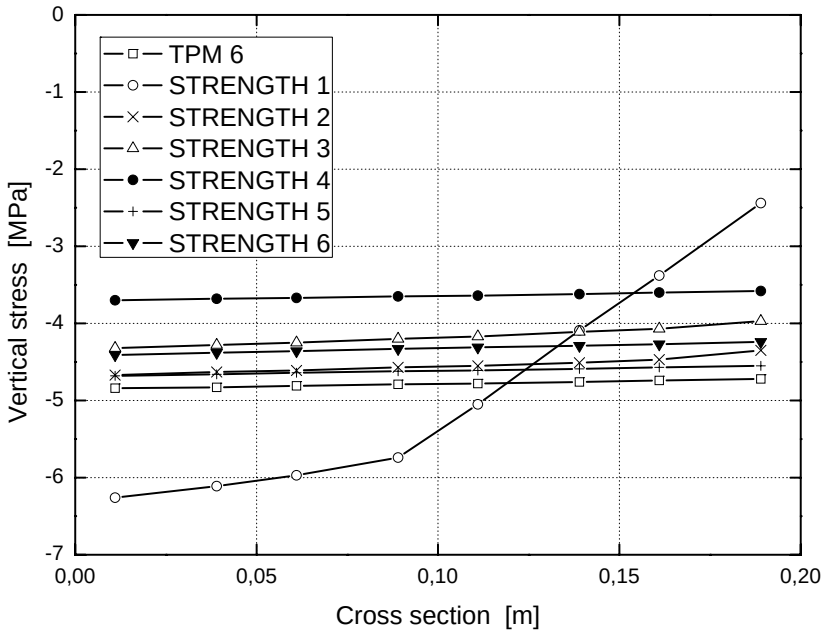



Figure 8.35: Vertical hoop stress distribution in right sidewall at end of excavation (Inc 10) for various developments of stiffness and strength adopting $K_o = 0.5$

A similar observation can be made when looking at the horizontal hoop stresses in the tunnel invert at the end of surface loading (Inc 50), adopting a $K_o$-profile of 0.5, as illustrated in Fig. 8.36. Here, the lining extrados is located at 0.0 m and the lining intrados at a cross-sectional distance of 0.2 m. At the end of the whole construction process (excavation and surface loading) the stiffness of reference run TPM 6 is already developed such that some bending has been introduced, predicting compressive stresses of -7.8 MPa and -1.2 MPa. The higher stiffness characterising run STRENGTH 1 leads to an increased bending of the invert with compressive stresses of -9.3 MPa and tensile stresses of 1.8 MPa, that could result in cracking. It is worth mentioning that even runs STRENGTH 3 and 5, which represent a retarded increase in stiffness and strength, show some tensile stresses of 0.3 and 0.6 MPa respectively at the lining intrados. Bending of the invert is significantly decreased for run STRENGTH 6, where the shotcrete stiffness and strength were reduced by 50 %.

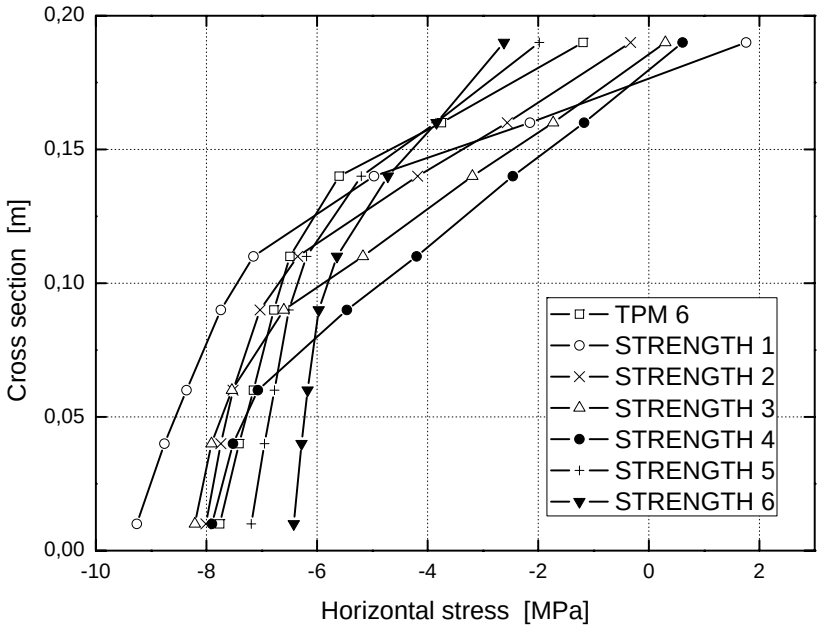



Figure 8.36: Horizontal hoop stress distribution in invert at end of loading (Inc 50) for various developments of stiffness and strength adopting $K_o = 0.5$

The impact of early age shotcrete deformability on the stress formation within a tunnel lining has been investigated in Fig. 8.37, where the horizontal stresses in the tunnel crown at the end of surface loading (Inc 50) are illustrated, adopting a $K_o$-profile of 0.5. The compressive stresses at the lining extrados vary over a wide range from -9.0 MPa for the run STRAIN 1 (upper bound of compressive peak strains) to -18.9 MPa for run STRAIN 4. Even for the tensile stresses on the lining intrados a significant difference can be identified. Due to the constant low strain level of the peak strains for run STRAIN 4, half of the cross section appears to be cracked and stresses drop down to the ultimate tensile strength. Strain softening occurs also for run STRAIN 3, representing very brittle material behaviour of the shotcrete. Due to the early age of the shotcrete in runs STRAIN 1 and 2, the full tensile strength of 3.0 MPa is not reached completely and tensile stresses take a value of 1.60 MPa. It can be concluded that, for a tunnel lining under heavy loading conditions, the admissible strain levels at early ages play an important role particularly for the cracking behaviour and lead to highly non-linear stress distributions over the cross section.

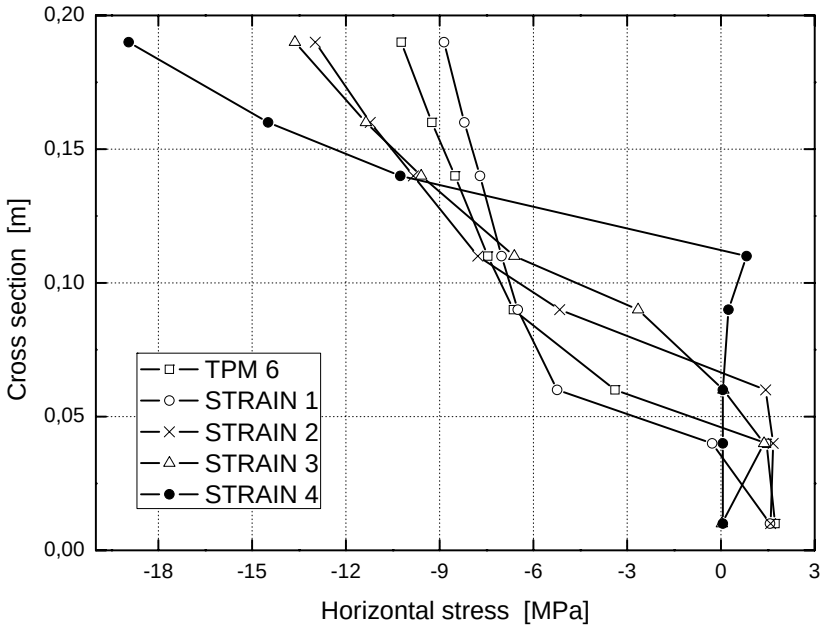



Figure 8.37: Horizontal hoop stress distribution in crown at end of loading (Inc 50) for various developments of shotcrete deformability adopting $K_o = 0.5$

Fig. 8.38 and 8.39 contain the results for the analysis of shotcrete creep, shrinkage and hydration temperature during tunnel construction, adopting a $K_o$-profile of 0.5. Here again, run TPM 6 was taken as a reference run, but an additional amount of elapsed time was added after the end of surface loading from Inc 51 to 100 (see Tab. 8.15). Fig. 8.38 shows the vertical stress distribution in the right tunnel sidewall at the end of Inc 100 and results are compared with those from run TPM 6 after Inc 50. It can be seen that, due to shotcrete creep at relatively early ages, the bending of the cross section is slightly reduced with maximum compressive stresses of -9.9 MPa at the lining intrados (0.0 m) and -5.9 MPa at the lining extrados (0.2 m). This result is surprising, since creep of young shotcrete is usually considered to be of significant influence on the stress distribution within a shotcrete tunnel lining. Due to the development of heat during cement hydration, compressive stresses at the lining extrados reduce to -4.6 MPa and slightly increase up to -10.6 MPa at the lining intrados. The incorporation of shotcrete shrinkage shows almost no effect and a very similar stress distribution compared to run TPM 6 was obtained.

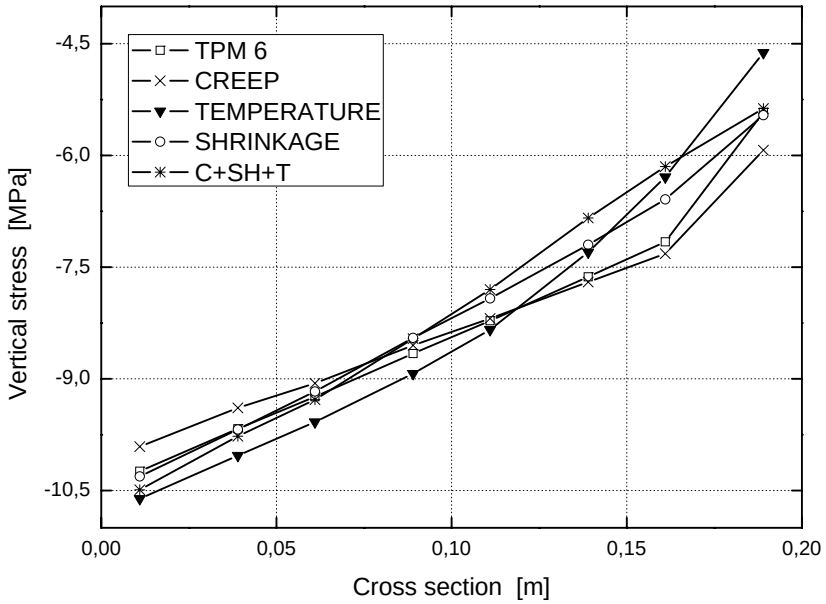



Figure 8.38: Vertical hoop stress distribution in right tunnel sidewall for analysis of creep, shrinkage and hydration temperature adopting $K_o = 0.5$

In Fig. 8.39 the horizontal hoop stresses at the tunnel crown are illustrated for the same type of analyses as before. Once again, shotcrete creep leads to a slight reduction in bending of the cross section with a compressive stress of -9.2 MPa at the lining extrados (0.2 m) and a tensile stress of 0.5 MPa at the lining intrados (0.0 m). One important observation that can be made is that the early age shrinkage of shotcrete results in cracking of the shotcrete shell at the lining intrados and strain softening is introduced.

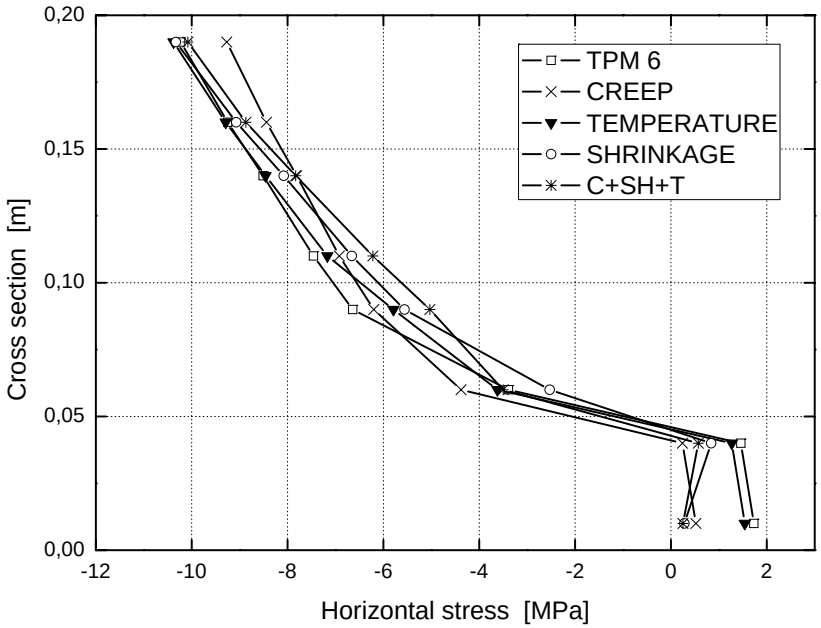



Figure 8.39: Horizontal hoop stress distribution in tunnel crown for analysis of creep, shrinkage and hydration temperature adopting $K_o = 0.5$

In Fig. 8.40 the vertical stresses within the right tunnel sidewall are plotted for various amounts of elapsed time during excavation and loading and compared with the simple analyses LE and HME, adopting a $K_o$-profile of 1.5. Once again, the linear elastic model (LE) predicts large bending of the cross section with compressive stresses of -0.90 MPa at the lining intrados and -6.70 MPa at the lining extrados. This bending mechanism is significantly reduced when simulating shotcrete with the HME approach where the compressive stresses range from -3.2 to -4.4 MPa. It can be seen that in this case the HME approach represents a good approximation for the time-dependent runs TPM 3 to 6. Run TPM 1 is characterised by a very low stiffness and strength and therefore the mechanical behaviour of the tunnel sidewall is goverened mainly by hoop compression without any bending (-1.0 MPa). The same conclusion applies for run TPM 2 although compressive stresses are already slightly larger with a value of -2.3 MPa. Runs TPM 7 to 14 show a relatively stiff behaviour of the shotcrete due to their increased shotcrete age and overestimate the bending of the cross section compared to the HME approach. Compressive stresses appear to vary linearily over the cross section from -1.1 to -6.5 MPa for TPM 14.

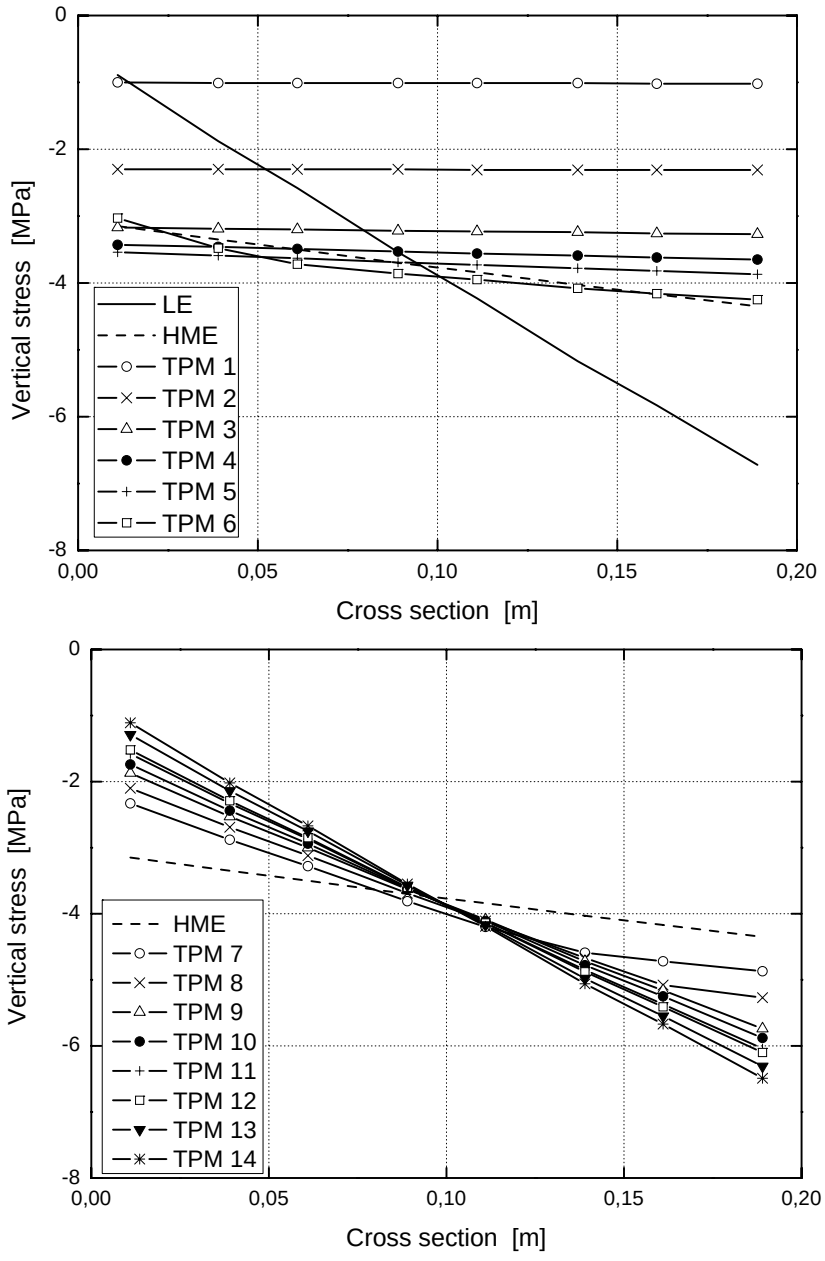



Figure 8.40: Vertical hoop stress distribution for right sidewall at end of excavation (Inc 10) for $K_o = 1.5$

When looking at the vertical hoop stress distribution in the tunnel sidewall at Inc 50, it is very important to highlight that during the surface loading a change in loading direction takes place. This mechanism is illustrated in Fig. 8.41.

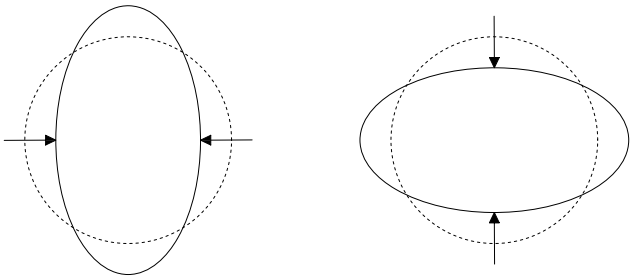



Figure 8.41: Change in bending direction of tunnel lining due to tunnel excavation with initial stresses for $K_o = 1.5$ and surface loading

In Fig. 8.42 the compressive stresses for the linear elastic model (LE) vary from -13.3 MPa on the lining intrados to -0.7 MPa at the lining extrados. Including non-linearity for hardened shotcrete at 28 days (NL) changes this stress distribution slightly and leads to smaller compressive stresses at the lining intrados due to plastic deformation. However, runs TPM 1 to 6 still show hardly any bending of the cross section at all and stresses vary from -3.5 MPa (TPM 1) to -6.4 MPa (TPM 6). The HME approach predicts some reduced stresses compared to the linear elastic model (LE) due to its lower stiffness. The non-linear distribution of the lining stresses becomes much more pronounced for runs TPM 7 to 14, where results differ significantly from each other with compressive stresses ranging from -7.7 to -10.8 MPa at the lining intrados and from -1.1 to -4.5 MPa at the lining extrados. The HME approach can be seen as a good approximation for runs TPM 7 and 8, but TPM 14 clearly overpredicts the bending of the cross section.

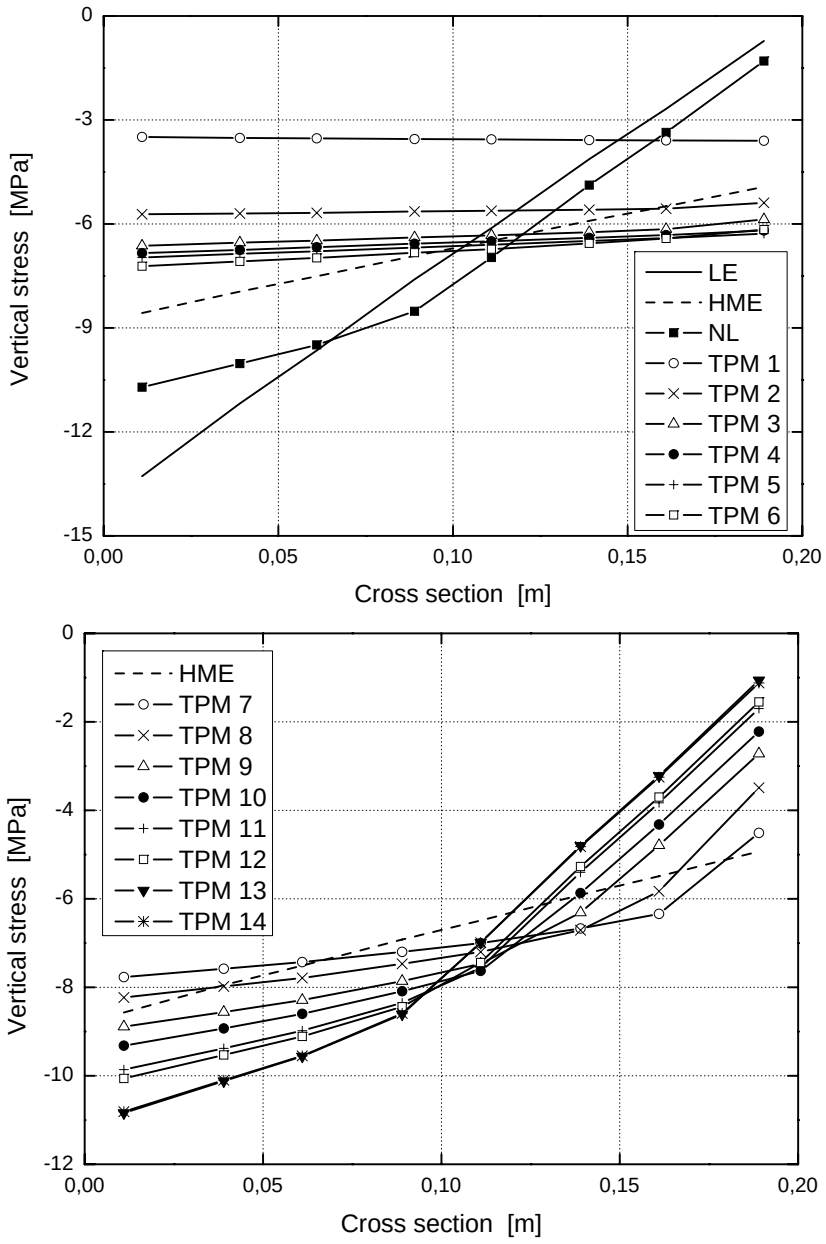



Figure 8.42: Vertical hoop stress distribution for right sidewall at end of loading (Inc 50) for $K_o = 1.5$

Once again, the influence of the development of the shotcrete stiffness and strength with time has been studied in detail for the analyses adopting a $K_o$-profile of 1.5, as shown in Fig. 8.43. Results from various analyses have been compared with reference run TPM 6. Run STRENGTH 1 predicts relatively large bending of the right tunnel sidewall at the end of excavation in Inc 10, due to the accelerated stiffness and strength increase controlled by the cement parameter $s = 0.1$. For this analysis stresses vary from -1.8 MPa at the lining intrados (0.0 m) to -5.8 MPa at the lining extrados. Runs STRENGTH 2 to 6 show almost no bending of the cross section and stresses are generated mainly as hoop compression. Run STRENGTH 4, which has a cement parameter of $s = 0.5$ predicts very small compressive

stresses of -2.8 MPa. These stresses are slightly larger for runs STRENGTH 2 and 3, since their development of shotcrete stiffness and strength is happening faster due to their cement parameters $s = 0.3$ and $s = 0.4$. Reducing both the stiffness and strength of the shotcrete by 25 % in run STRENGTH 5 leads to a reduction in compressive stresses of 10 % at the lining extrados, whereas this result is reversed at the lining intrados. A very similar trend applies also to run STRENGTH 6, where a stiffness and strength reduction of 50 % was adopted.

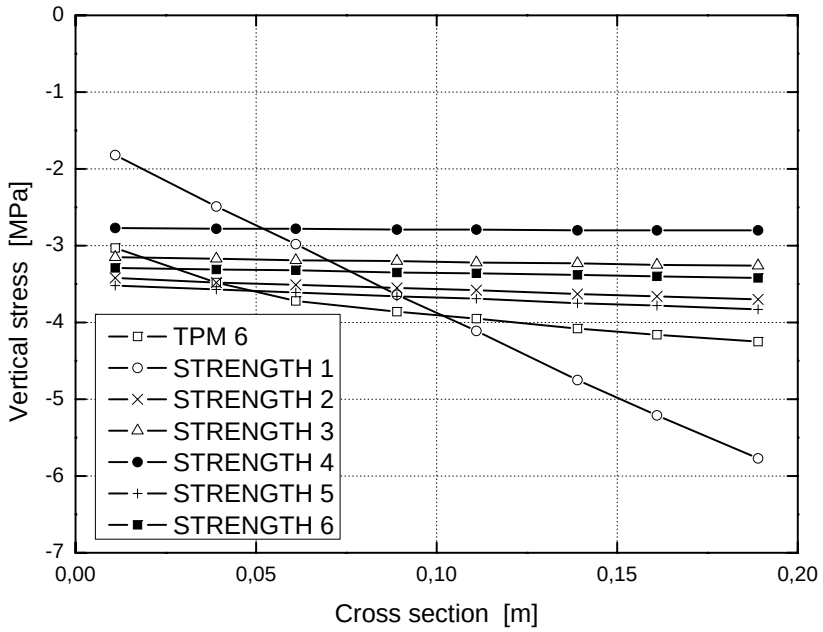



Figure 8.43: Vertical hoop stress distribution in right sidewall at end of excavation (Inc 10) for various developments of stiffness and strength adopting $K_o = 1.5$

Fig. 8.44 focuses on the horizontal stress distribution in the tunnel invert at the end of surface loading (Inc 50), for analysis adopting $K_o = 1.5$. The same conclusions can be drawn as before: a retarded or reduced increase in shotcrete stiffness and strength leads to a softer lining behaviour where bending of the cross section is reduced and smaller compressive stresses are generated. In this figure the lining extrados is located at 0.0 m and the lining intrados is situated at a cross-sectional distance of 0.2 m. Run STRENGTH 4 predicts the lowest compressive stresses that vary almost linearily over the cross section with a value of -1.4 MPa at the lining intrados and -6.4 MPa at the lining extrados. The lowest bending of the cross section is obtained by run STRENGTH 6, which has a reduced stiffness and strength by 50 %. On the lining intrados, results for the runs TPM 6 and STRENGTH 1, 5 and 6 are almost identical reaching about -3.0 MPa.

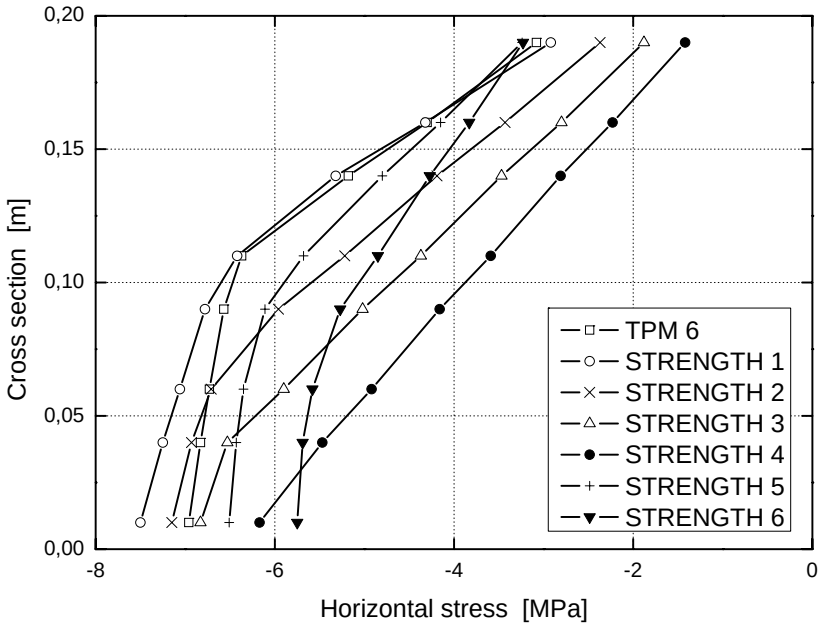



Figure 8.44: Horizontal hoop stress distribution in invert at end of loading (Inc 50) for various developments of stiffness and strength adopting $K_o = 1.5$

For a $K_o$-profile of 1.5, the difference in results regarding stress distributions over the lining thickness due to early age deformability of the shotcrete is not so pronounced as for $K_o = 0.5$ (see Fig. 8.37). Fig. 8.45 contains the cross-sectional stress distributions for the horizontal stresses at the tunnel crown for various analyses at the end of surface loading in Inc 50. Compared to reference run TPM 6, runs STRAIN 2 and 3, which represent a relatively brittle shotcrete behaviour, show slightly incrased bending of the tunnel crown, with tensile stresses at the lining intrados (0.0 m) of 1.1 MPa and compressive stresses at the lining extrados (0.2 m) of -8.0 MPa. The increased straining capacity of run STRAIN 1 (upper bound of peak strains) makes almost no difference and results are close to those of run TPM 6. When adopting a constant low strain limit for the compressive and tensile peak strains in run STRAIN 4, stresses rise up significantly and may lead to cracking on the lining intrados with a maximum tensile stress of 1.7 MPa. On the lining extrados, compressive stresses reach a value of almost -10.0 MPa and are therefore about 40 % larger than for TPM 6.

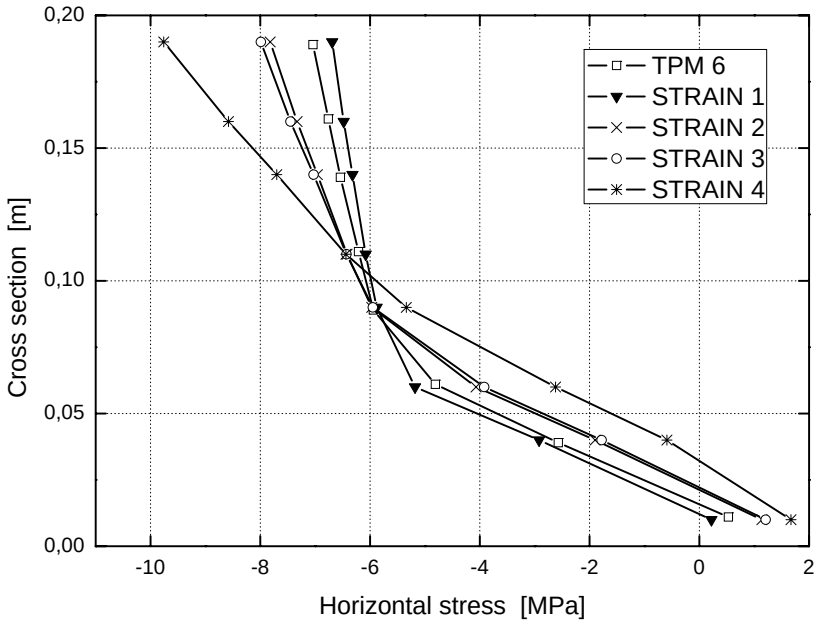



Figure 8.45: Horizontal hoop stress distribution in crown at end of loading (Inc 50) for various developments of shotcrete deformability $K_o = 1.5$

The influence of creep, shrinkage and hydration temperature of early age shotcrete on the mechanical behaviour of the tunnel lining can be studied in Fig. 8.46 and 8.47, for analysis adopting a $K_o$-profile of 1.5. When looking at the vertical stress distribution in the right tunnel sidewall at Inc 100 (28 days after completion of the surface loading) in Fig. 8.46, it can be observed that in this case creep hardly affects the generated stresses compared to reference run TPM 6. However, the generation of hydration temperature leads to a larger bending of the cross section with compressive stresses of -7.7 MPa at the lining intrados (0.0 m) and -5.2 MPa at the lining extrados (0.2 m). When combining all the three components of creep, shrinkage and hydration temperature together (run C+SH+T), an almost linear stress distribution across the lining section with an increased bending compared to run TPM 6 is obtained.

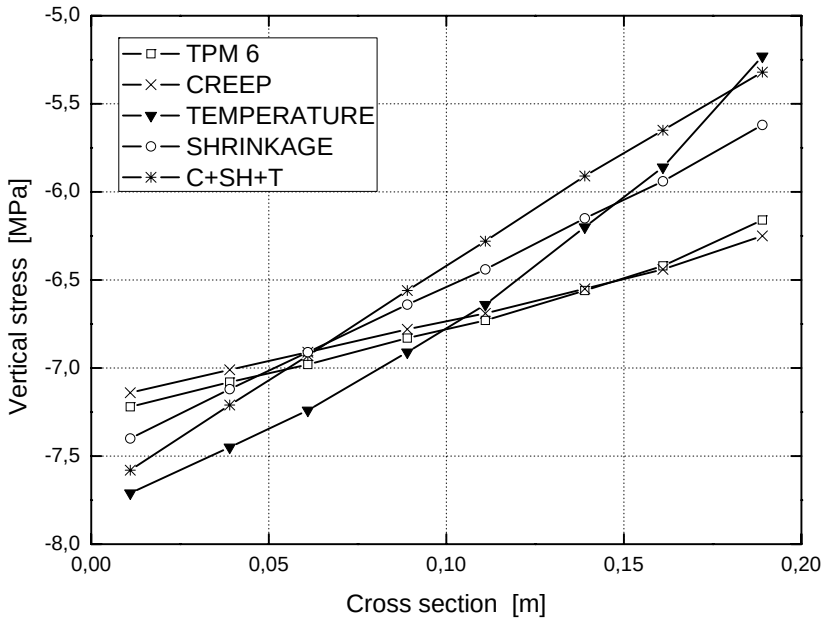



Figure 8.46: Vertical hoop stress distribution in right tunnel sidewall for analysis of creep, shrinkage and hydration temperature adopting $K_o = 1.5$ (Inc 100)

The situation is different at the tunnel crown, as illustrated in Fig. 8.47. The consideration of shotcrete creep slightly reduces the bending of the cross section, with stresses located exclusively in the compressive stress regime. The same mechanism is obtained by including shrinkage in the analyses, where compressive stresses of -6.2 MPa are obtained at the lining extrados (0.2 m) and -0.5 MPa at the lining intrados (0.0 m). Run C+SH+T leads to a significant reduction in bending of the tunnel crown compared to reference run TPM 6, which indicates, that the combination of these time-dependent aspects can have an important impact on the lining behaviour during tunnel construction.

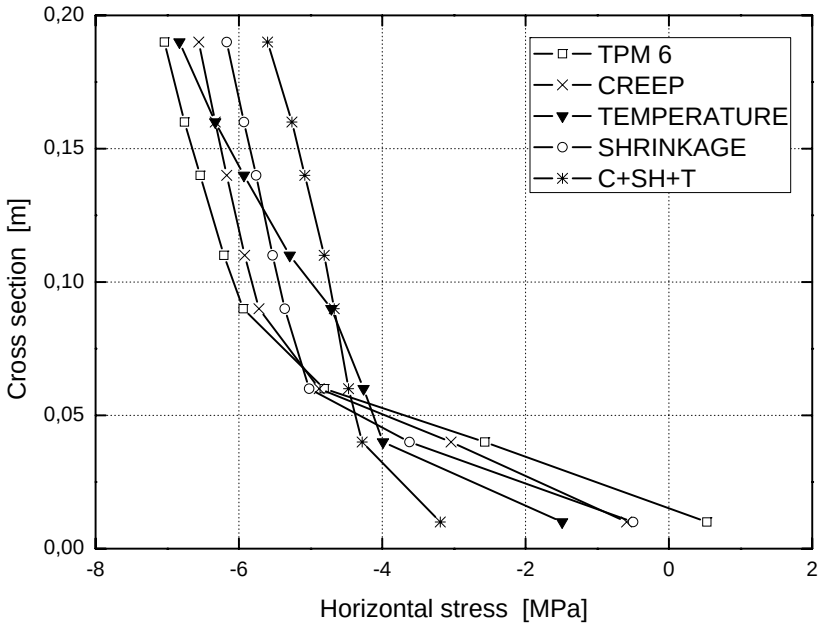



Figure 8.47: Horizontal hoop stress distribution in tunnel crown for analysis of creep, shrinkage and hydration temperature adopting $K_o = 1.5$ (Inc 100)

Fig. 8.48 shows the maximum stress levels (or utilisation factors) that occur in the course of tunnel excavation and surface loading at the intrados of the lining at the tunnel crown for both $K_o$-profiles. First, it can be seen that the run TPM 1 predicts for both types of analyses a very high stress level of almost $\rho_c = 0.8$ for $K_o = 1.5$ and even failure ($\rho_c = 1.0$) for $K_o = 0.5$. The material response is governed exclusively by compression due to the very low stiffness and strength level at a shotcrete age of 2 to 4 h and the compressive yield surface controls the mechanical behaviour. For $K_o = 1.5$ this stress level reduces quickly with increasing shotcrete age until it reaches a minimum of about $\rho_c = 0.25$ for run TPM 6, where the shotcrete has an age of 48 h at the end of surface loading. For older shotcrete, the behaviour of the lining intrados switches to tensile stresses and stress levels immediately rise up to a high value of about $\rho_t = 0.85$. The situation is somewhat similar when adopting a $K_o$-profile of 0.5. For runs TPM 2 to 5 the compressive stress level slightly reduces to $\rho_c = 0.97$ since the compressive strength of the shotcrete becomes a bit more developed with increasing shotcrete age. However, for runs TPM 6 to 14, the mechanical behaviour of the lining intrados is goverened by tensile stresses which go beyond peak and experience strain softening. Consequently, cracking of the shotcrete shell occurs and the stress level $\rho_t$ reaches unity.

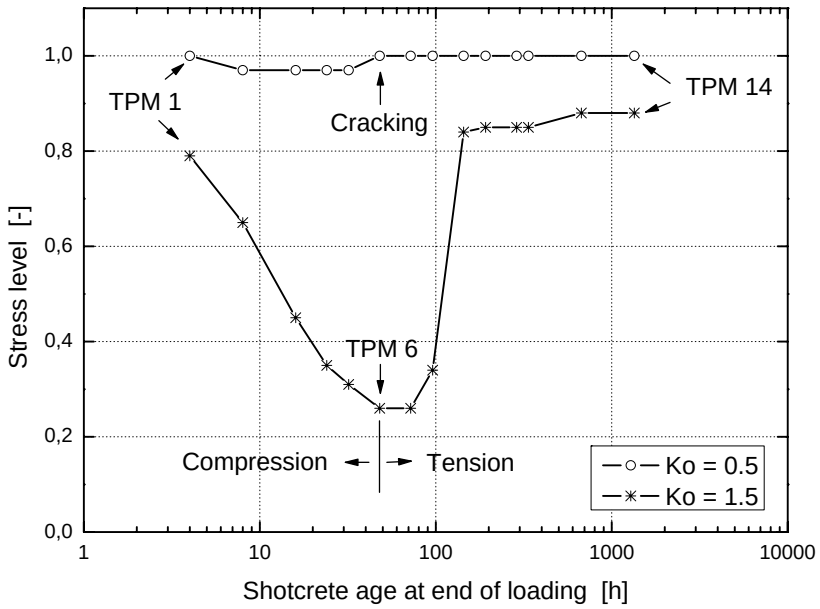



Figure 8.48: Stress level for different shotcrete ages at intrados of tunnel crown for both $K_o$-profiles

In Fig. 8.49 the maximum stress levels of the shotcrete at the intrados of the right tunnel sidewall are investigated for both $K_o$-profiles. Here again, the compressive stress levels for run TPM 1 are very high, taking a value of $\rho_c = 0.98$ for $K_o = 1.5$ and $\rho_c = 1.0$ for $K_o = 0.5$. For older shotcrete of runs TPM 2 to 6, these stress levels reduce relatively quickly and most importantly remain of a compressive nature, where the compressive yield function controls the mechanical behaviour. When adopting $K_o = 1.5$ the compressive stress levels seem to stabilise for runs TPM 6 to 14 on a constant level of $\rho_c = 0.29$. This value is slightly higher ($\rho_c = 0.43$) for $K_o = 0.5$ and even increases a small amount for runs TPM 9 to 14.

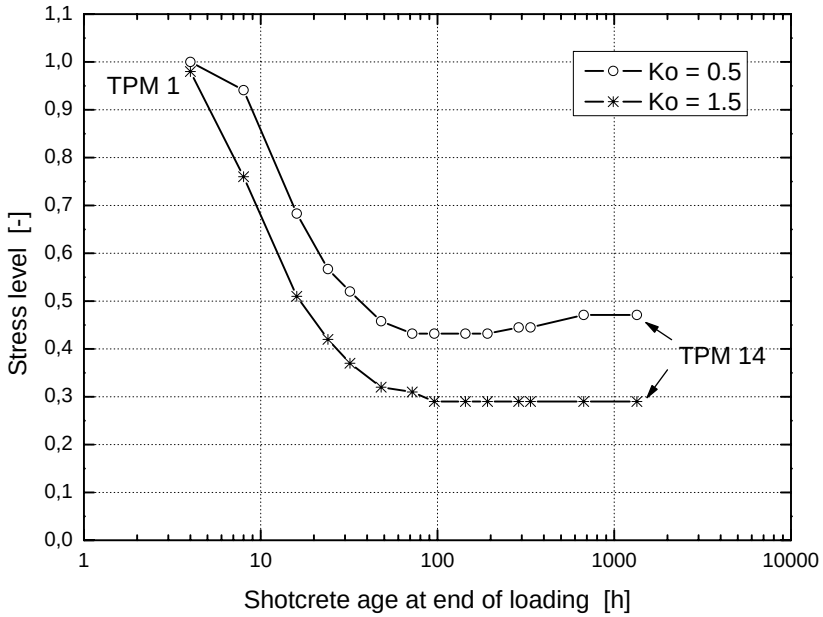



Figure 8.49: Stress level for different shotcrete ages at intrados of tunnel sidewall for both $K_o$-profiles

For completion, the stress levels at the lining intrados of the tunnel invert are presented for both $K_o$-profiles in Fig. 8.50. As in the previous case of the tunnel crown, the mechanical behaviour for runs TPM 1 to 6 is dominated by compressive stresses and stress levels reduce from $\rho_c = 0.75$ down to a constant level of $\rho_c = 0.25$ for $K_o = 1.5$. In the case of $K_o = 0.5$, the mechanism is different. The stress level for TPM 1 is very close to failure but reduces in the same way as for $K_o = 1.5$ down to a relatively low level of $\rho_c = 0.26$. With increasing age, the governing behaviour is of tensile nature and the tensile stress levels rise up for runs TPM 7 to 13, until the shotcrete even cracks during run TPM 14.

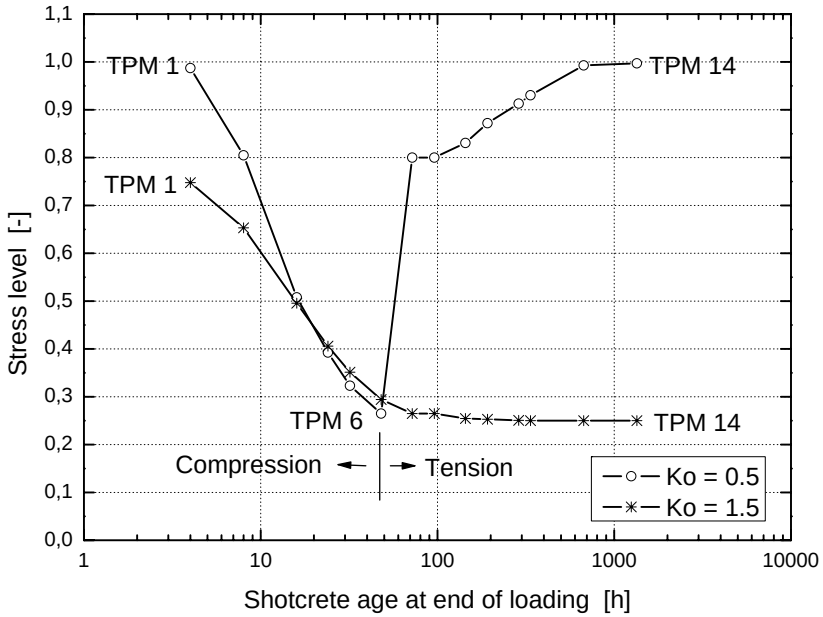



Figure 8.50: Stress level for different shotcrete ages at intrados of tunnel invert for both $K_o$-profiles

Tables 8.22 and 8.23 summarize the results regarding the maximum stress level in the lining intrados at the tunnel crown, right sidewall and invert for various developments of stiffness and strength. For both $K_o$-profiles it can be observed that the faster increase in stiffness and strength for run STRENGTH 1 ($s = 0.1$) leads to a small reduction in the maximum stress level. For $K_o = 1.5$ there is even no plastic deformation noticeable for the intrados at the tunnel crown and invert and the stress state remains below the compression yield surface. On the other hand, when the increase of shotcrete stiffness and strength is retarded as in the case of runs STRENGTH 2 to 4, the stress levels rise up to almost failure ($\rho_c = 0.94$) for $K_o = 0.5$ and $\rho_c = 0.72$ for $K_o = 1.5$ at the intrados of the right tunnel sidewall. The reduction of the stiffness and strength by 25 % leads to a compressive stress level that is about 40 % higher than in the reference run TMP 6. Run STRENGTH 6 represents a reduction of the shotcrete stiffness and strength by 50 % and consequently the compressive stress levels increase of up to 90 % in the case of the tunnel invert. The utilisation factor in the tunnel crown seems to be unchanged by the variation of stiffness and strength for the $K_o$-profile of 0.5. In this case cracking of the shotcrete takes place throughout all analyses indicated by a stress level of unity.

| Run | Intrados sidewall | Intrados crown | Intrados invert |
|---|---|---|---|
| | $\rho_c$ | $\rho_t$ | $\rho_c$ |
| | (-) | (-) | (-) |
| TPM 6 | 0.46 | 1.00 | 0.26 |
| STRENGTH 1 | 0.41 | 1.00 | 0.25 |
| STRENGTH 2 | 0.59 | 1.00 | 0.39 |
| STRENGTH 3 | 0.76 | 1.00 | 0.58 |
| STRENGTH 4 | 0.94 | 1.00 | 0.76 |
| STRENGTH 5 | 0.57 | 1.00 | 0.35 |
| STRENGTH 6 | 0.76 | 1.00 | 0.50 |

Table 8.22: Utilisation factor for variation in development of stiffness and strength for excavation Type 1 at end of surface loading ($K_o = 0.5$)

| Run | Intrados sidewall | Intrados crown | Intrados invert |
|---|---|---|---|
| | $\rho_c$ | $\rho_c$ | $\rho_c$ |
| | (-) | (-) | (-) |
| TPM 6 | 0.32 | 0.26 | 0.29 |
| STRENGTH 1 | 0.28 | elastic | elastic |
| STRENGTH 2 | 0.41 | 0.37 | 0.41 |
| STRENGTH 3 | 0.56 | 0.51 | 0.54 |
| STRENGTH 4 | 0.72 | 0.65 | 0.67 |
| STRENGTH 5 | 0.41 | 0.32 | 0.37 |
| STRENGTH 6 | 0.82 | 0.43 | 0.48 |

Table 8.23: Utilisation factor for variation in development of stiffness and strength for excavation Type 1 at end of surface loading ($K_o = 1.5$)

The effect of shotcrete deformability at early ages on the stress level within the tunnel lining can be analysed with the help of Tab. 8.24 and 8.25. Run STRAIN 1, which represents a softer material behaviour through larger peak strains for both compression and tension, shows a slightly decreased stress level compared to reference run TPM 6 for both adopted $K_o$-profiles. However, when a more brittle material response of shotcrete is assumed, as in the case of runs STRAIN 2 and 3, the stress level at the intrados of the right tunnel sidewall tends to increase significantly for $K_o = 0.5$, reaching values of $\rho_c = 0.58$. When a constant strain level is applied in run STRAIN 4, the stresses in the lining intrados of the tunnel crown suddenly switch from compressive behaviour to a tensile one and consequently

the stress level rises rapidly. A value of unity for both $K_o$-profiles indicates cracking of the shotcrete. A similar mechanism is observed for the tunnel invert when adopting $K_o = 0.5$ although the stress level is slightly below peak. From these results it can be concluded that the deformability of early age shotcrete has an important influence on the utilisation factor of a tunnel lining, leading in some cases to cracking and strain softening behaviour. Furthermore, it appears that cracking of the lining intrados of the tunnel crown is very likely to happen when adopting a $K_o$-profile of 0.5 independently of the applied deformability values of runs STRAIN 1 to 4.

| Run | Intrados sidewall | Intrados crown | Intrados invert |
|---|---|---|---|
| | $\rho_c$ | $\rho_t$ | $\rho_c$ |
| | (-) | (-) | (-) |
| TPM 6 | 0.46 | 1.00 | 0.26 |
| STRAIN 1 | 0.42 | 0.91 | 0.26 |
| STRAIN 2 | 0.56 | 1.00 | 0.28 |
| STRAIN 3 | 0.58 | 1.00 | 0.27 |
| STRAIN 4 | 0.80 | 1.00 | $\rho_t = 0.98$ |

Table 8.24: Utilisation factor for variation in shotcrete deformability for excavation Type 1 at end of surface loading ($K_o = 0.5$)

| Run | Intrados sidewall | Intrados crown | Intrados invert |
|---|---|---|---|
| | $\rho_c$ | $\rho_c$ | $\rho_c$ |
| | (-) | (-) | (-) |
| TPM 6 | 0.32 | 0.26 | 0.29 |
| STRAIN 1 | 0.31 | 0.26 | 0.28 |
| STRAIN 2 | 0.37 | 0.28 | 0.31 |
| STRAIN 3 | 0.37 | 0.29 | 0.31 |
| STRAIN 4 | 0.47 | $\rho_t = 1.00$ | 0.37 |

Table 8.25: Utilisation factor for variation in shotcrete deformability for excavation Type 1 at end of surface loading ($K_o = 1.5$)

#### 8.7.2.2 Excavation Type 2

In this section, the hoop stress generation within the shotcrete shell for various tunnel cross sections due to tunnel construction according to excavation Type 2, following a bench and invert excavation scheme, will be discussed in detail. For all analyses a constant $K_o$-profile

of 1.5 was adopted.

Fig. 8.51 illustrates the horizontal hoop stresses in the tunnel invert for various analyses regarding the elapsed time during construction at the end of the complete tunnel excavation (Inc 25) and at the end of surface loading (Inc 65). The lining extrados is located at 0.0 m and the lining inrados is situated at a cross-sectional distance of 0.2 m. At the end of invert excavation in Inc 25, the linear elastic model (LE) predicts a linear stress distribution over the cross section that leads to large bending of the invert. The non-linear run simulating shotcrete behaviour at 28 days (NL) follows almost the same curve, except that the non-linearity leads to a reduced compressive stress at the lining extrados. As expected, the HME approach shows a much lower bending due to its relatively low constant stiffness compared to the run LE. Stresses are remarkably reduced for the time-dependent runs TPM 1, 5 and 9, where no bending of the invert is predicted and the mechanical behaviour is governed mainly by hoop compression. Run TPM 1 simulates a very young shotcrete and therefore stiffness and strength are at a low level. This leads to a constant compressive stress of -2.5 MPa. The shotcrete of the analyses TPM 5 and 9 is slightly older due to the elapsed time during excavation and compressive stresses rise up to -4.9 MPa and -5.6 MPa respectively. However, during the placing of the surface surcharge from Inc 26 to 65, the loading direction is changed and the bending of the invert is reversed, as can be seen in Fig. 8.51. Although heavily loaded, all analyses still predict compressive stresses over the whole lining cross section, which range from -6.0 MPa to -8.6 MPa for the linear elastic model (LE). The non-linear plasticity of the hardened shotcrete at 28 days (NL) has a minor effect at the lining intrados leading to a smaller stress of -4.7 MPa. One interesting fact is that the time-dependent analyses TPM 1, 5 and 9 show a very similar bending as run NL, since the curves appear to be almost parallel to each other, but differ in magnitude of the compressive stress. This indicates that for those time-runs, the compressive hoop stress is reduced for young shotcrete (TPM 1), but bending remains constant with cement hydration. The missing time-runs simulating the longitudinal distance between the bench and invert face by adopting a certain amount of elapsed time $\Delta t$ in Inc 13, are not included in these two figures since there is obviously no effect on the invert behaviour, which is installed in Inc 14.

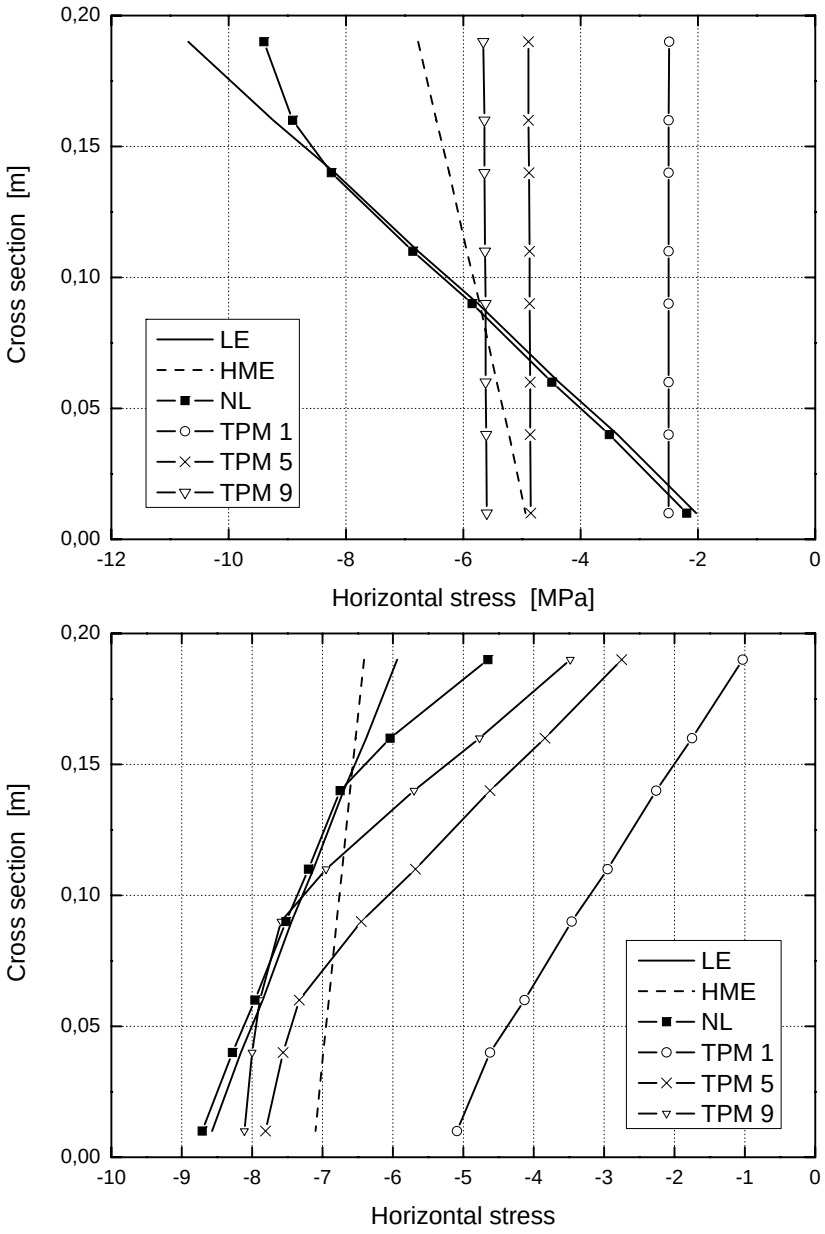



Figure 8.51: Horizontal hoop stresses in tunnel invert for various time-runs at the end of invert excavation (Inc 25, top) and end of surface loading (Inc 65, bottom)

The horizontal stresses in the centre of the temporary invert at the end of bench excavation (Inc 12) are presented in Fig. 8.52. The soil below this temporary support element pushes the temporary invert upwards leading to large bending of the cross section when applying a linear elastic model (LE). Tensile stresses at the intrados (0.15 m) are of a value of 3.5 MPa and slightly above the tensile strength of hardened shotcrete (3.0 MPa). Compressive stresses at the extrados (0.0 m) rise up to -9.1 MPa. Both stress values are slightly reduced when including non-linear plasticity of the shotcrete in run NL. The bending is significantly decreased when simulating shotcrete behaviour with the HME approach, where no tensile stresses are predicted and the compressive stresses vary from -2.0 to almost -4.0 MPa. Once

again, the time dependent runs TPM 1, 5 and 9 indicate that the mechanical behaviour of the temporary invert is governed mainly by hoop compression with little bending of the cross section. Due to the early age material properties of the shotcrete compressive stresses develop at a low level ranging from -1.4 MPa (TPM 1) to -3.9 MPa (TPM 9).

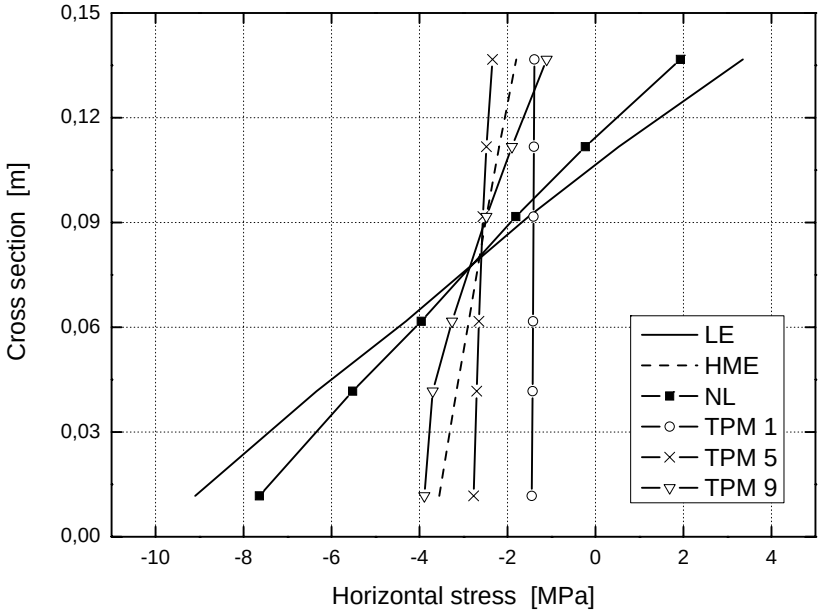



Figure 8.52: Horizontal hoop stresses in temporary invert for various time-runs at the end of bench excavation (Inc 12)

The adopted construction process of excavation Type 2 implies that the upper shotcrete shell of the tunnel for the bench is of an older age than the lower shell and experiences therefore a different mechanical behaviour due to the advanced progress of cement hydration within the shotcrete. When looking at the stress distribution in the tunnel crown at the completion of tunnel excavation (Inc 25), the elapsed time $\Delta t$ at the intermediate construction stage in Inc 13 seems to have an impact on the stresses that are generated due to the soil excavation, as can be seen in Fig. 8.53 to 8.55. In these figures, the lining intrados is located at 0.0 m, whereas the lining extrados is situated at a 0.2 m. From Fig. 8.53 it can be observed that the runs HME and TPM 1 predict a relatively low bending of the cross section, where stresses vary in between -2.0 and -4.0 MPa for TPM 1 and -2.4 to 5.6 MPa for the HME approach. The situation is very different for runs TPM 2, 3, and 4, which already show a very stiff lining behaviour due to the advanced shotcrete age. These analyses appear to approach the result from the linear elastic model (LE), introducing tensile stresses at the lining extrados ranging from 0.6 to 1.6 MPa. Differences are slightly larger at the lining intrados, where compressive stresses lie between -7.1 and -9.8 MPa.

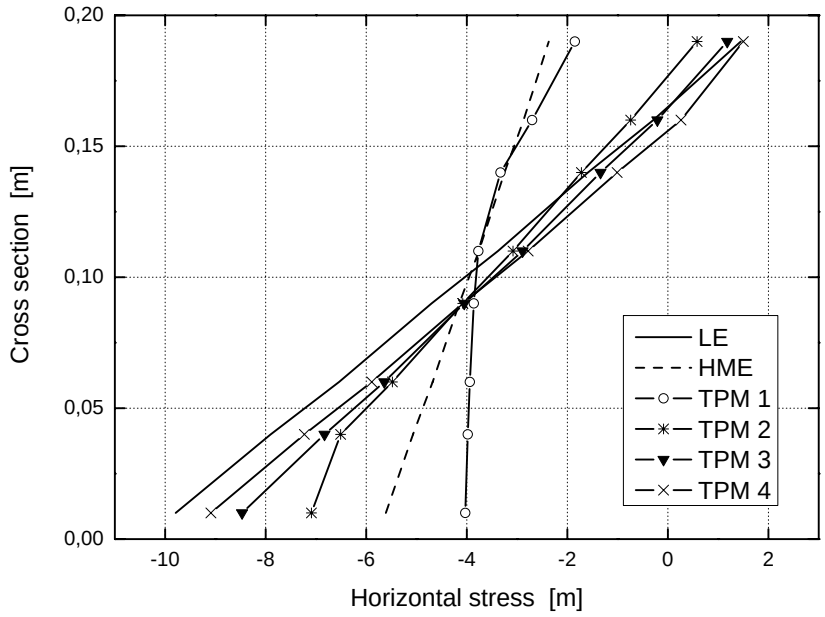



Figure 8.53: Horizontal hoop stresses in tunnel crown for time-runs TPM 1 to 4 at the end of invert excavation (Inc 25)

This effect of the difference in shotcrete age becomes slightly less pronounced for the time-dependent runs TPM 5 to 8, as can be seen in Fig. 8.54. Similar to the previous case, runs TPM 5 and HME are relatively close together predicting slight bending of the tunnel crown. However, stresses from the analyses TPM 6, 7 and 8 locate themselves in between the linear elastic model (LE) and the HME approach, showing compressive stresses over the whole lining cross section. Consequently no cracking at the lining extrados can be expected.

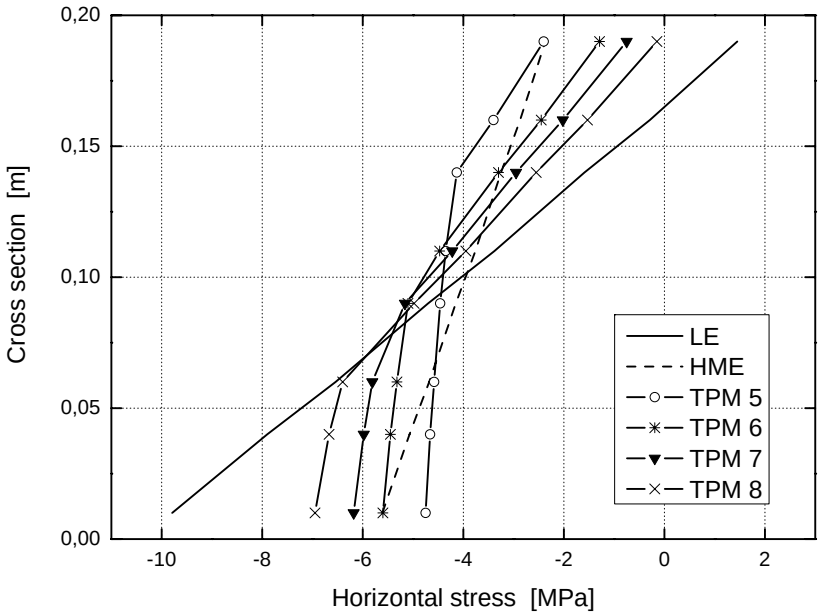



Figure 8.54: Horizontal hoop stresses in tunnel crown for time-runs TPM 5 to 8 at the end of invert excavation (Inc 25)

Finally, in Fig. 8.55 the horizontal stress predictions at the tunnel crown for runs TPM 9 to 12 are presented and compared to the simple models LE and HME. In the upper half of the cross section (0.1 to 0.2 m), elastic behaviour seems to be the governing factor of the mechanical behaviour since the stress distribution curves for all time runs tend to be parallel to the linear elastic model (LE). Cracking at the lining extrados is likely to happen upon further loading since tensile stresses start to develop for runs TPM 11 and 12. At the lining intrados, the non-linear behaviour of shotcrete during plastic deformation seems to be dominant and compressive stresses vary from -6.0 MPa (TPM 9) to -7.2 MPa (TPM 12). It appears, that for a more advanced age of shotcrete at the end of bench excavation, i.e. 24 hours for runs TPM 9 to 12, the influence of the elapsed time $\Delta t$ in Inc 13, simulating the longitudinal distance between bench and invert face, diminishes. A relatively stiff tunnel lining can lead to cracking at the lining extrados of the tunnel crown during excavation of the tunnel.

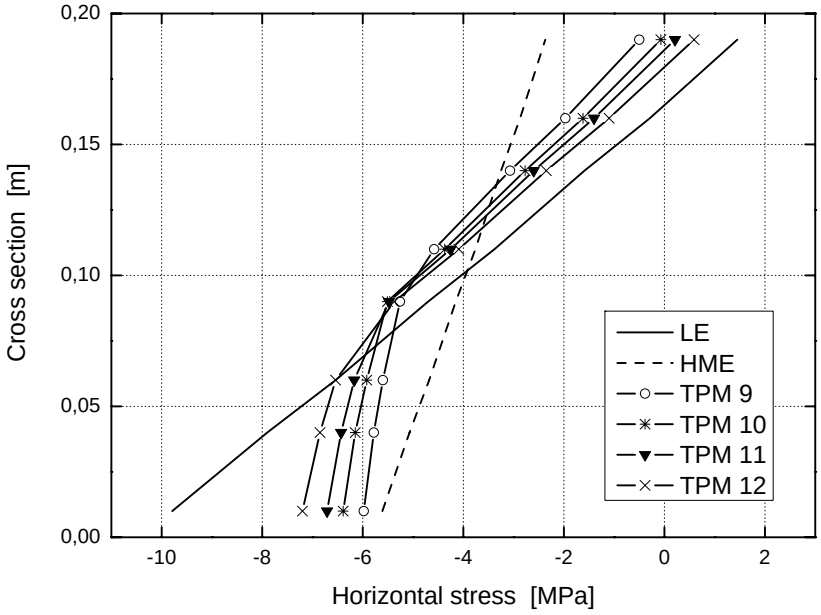



Figure 8.55: Horizontal hoop stresses in tunnel crown for time-runs TPM 9 to 12 at the end of invert excavation (Inc 25)

The influence of the increase of stiffness and strength with time on the mechanical lining behaviour of excavation Type 2 was investigated for the tunnel invert at the end of surface loading (Inc 65), as illustrated in Fig. 8.56. Run TPM 7 serves as a reference run and results are compared with three different runs with various stiffness and strength developments. Run STRENGTH 1 ($s = 0.1$) predicts almost identical compressive stresses as run TPM 7 at the lining extrados (0.0 m) of up to -7.9 MPa. The bending of run STRENGTH 5, having a stiffness and strength reduced by 25 %, appears to be very similar to the one obtained by run TPM 7. The largest difference in stresses is observed for run STRENGTH 3, where a cement parameter $s = 0.4$ simulates a retarded increase in stiffness and strength. At the lining extrados compressive stresses rise up to -5.0 Mpa, whereas at the lining intrados (0.2 m)

stresses of -0.9 MPa can be expected. However, when comparing these results with run TPM 7, it can be concluded that the major difference is the decreased hoop stress and bending seems to be unchanged. All runs show exclusively compressive behaviour and there is no risk of shotcrete cracking due to any tensile stresses.

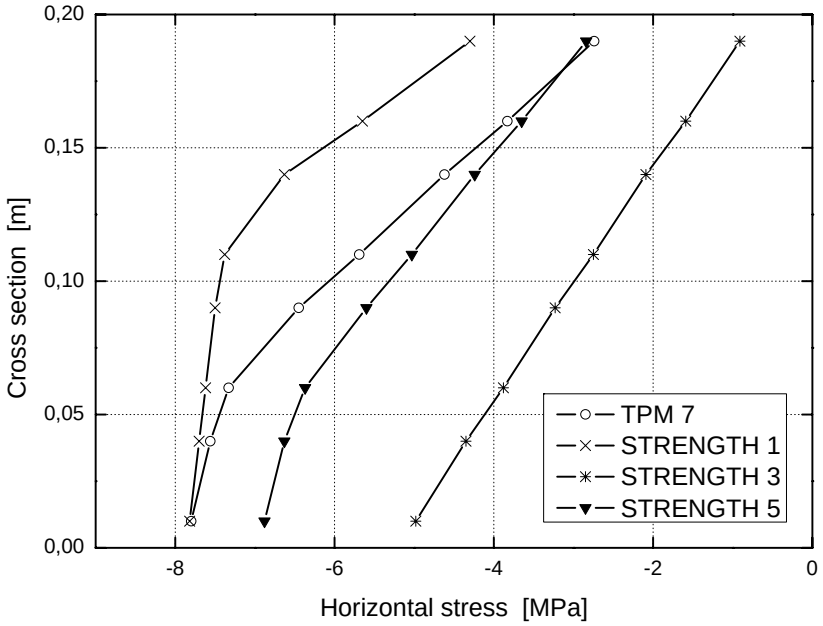



Figure 8.56: Horizontal hoop stresses in tunnel invert for various developments of stiffness and strength at the end of surface loading (Inc 65)

When analysing the tunnel construction with different admissible strain levels of the young shotcrete, it can be seen that results of runs STRAIN 3 and 4 are very similar to those of reference run TPM 7. In Fig. 8.57 the horizontal stresses at the tunnel crown are plotted at the end of surface loading in Inc 65. For all runs tensile stresses are generated at the tunnel intrados (0.0 m) that might lead to cracking and tensile strain softening of the crown. At the lining extrados (0.2 m), the compressive stresses vary between -7.4 and -9.0 MPa. No major change in hoop stress or bending of the cross section can be identified.

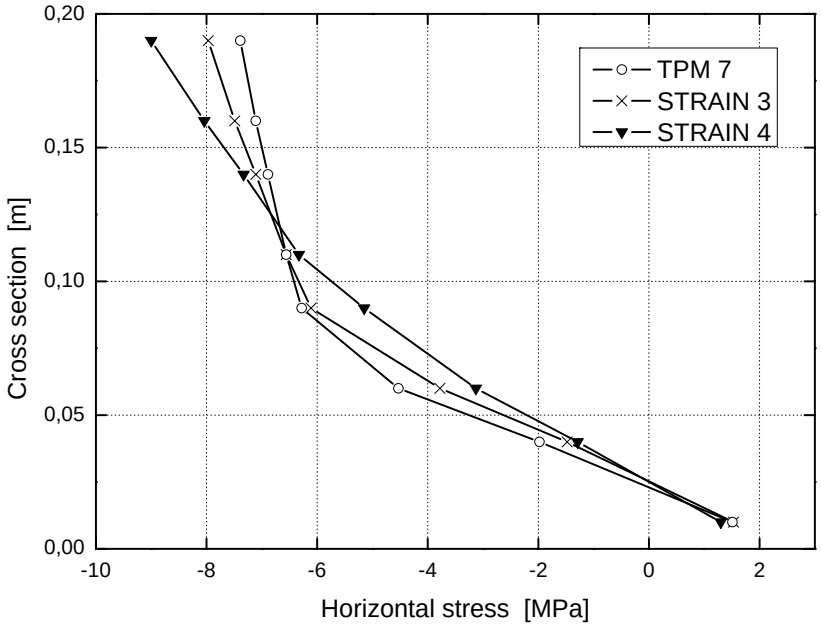



Figure 8.57: Horizontal hoop stresses in tunnel crown for various shotcrete deformabilty at the end of surface loading (Inc 65)

The influence of creep, shrinkage and hydration temperature of early age shotcrete on the mechanical behaviour of the lining is shown in Fig. 8.58 and 8.59, where the results 28 days after completion of the surface loading (Inc 100) are compared with reference run TPM 7 (Inc 65). In Fig. 8.58 the horizontal stresses in the tunnel crown are illustrated. It can be seen that the stresses for the run CREEP reduce slightly on both the lining intrados (0.0 m) and the lining extrados (0.2 m), giving values of 0.3 and -6.9 MPa respectively. This difference on the lining extrados is even more pronounced for run SHRINKAGE, where the compressive stresses decrease to -6.4 MPa. When combining all three effects (i.e. creep, shrinkage and hydration temperature) together in run C+SH+T, the bending of the tunnel crown is reduced in such a way, that even compressive stresses of -0.60 MPa occur at the lining intrados, preventing therefore the risk of cracking.

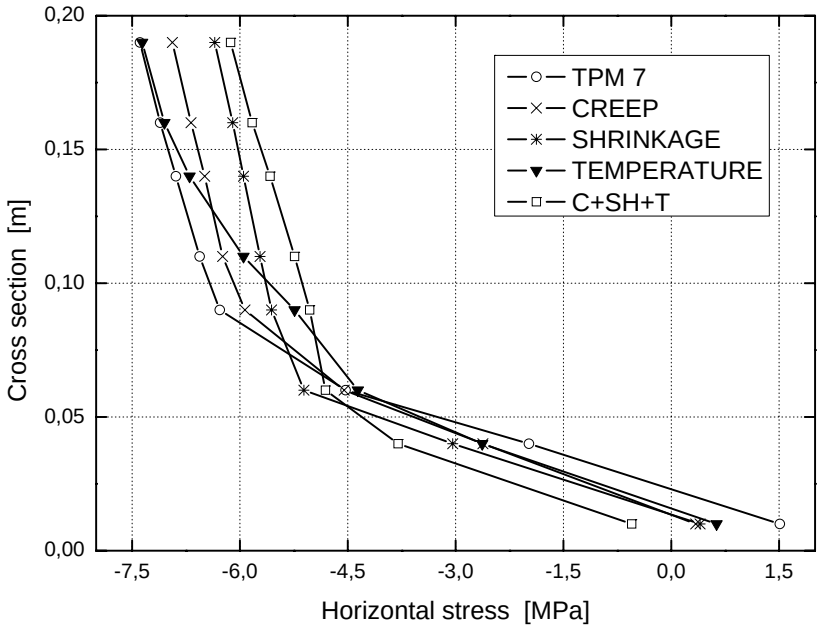



Figure 8.58: Horizontal hoop stresses in tunnel crown for analysis of creep, shrinkage and hydration temperature

Differences in the obtained stresses are of a similar magnitude for the horizontal stresses in the tunnel invert, as can be seen in Fig. 8.59. For this cross section of the tunnel lining, the run CREEP shows the biggest reduction in compressive stresses at the lining intrados (0.2 m) taking a value of -3.5 MPa. Results are almost unchanged for runs C+SH+T and TEMPERATURE compared to reference run TPM 7 (around -2.7 MPa). The compressive stresses at the lining intrados (0.0 m) vary from -6.9 to -7.8 MPa for all runs, with the run CREEP predicting the smallest bending of the cross section.

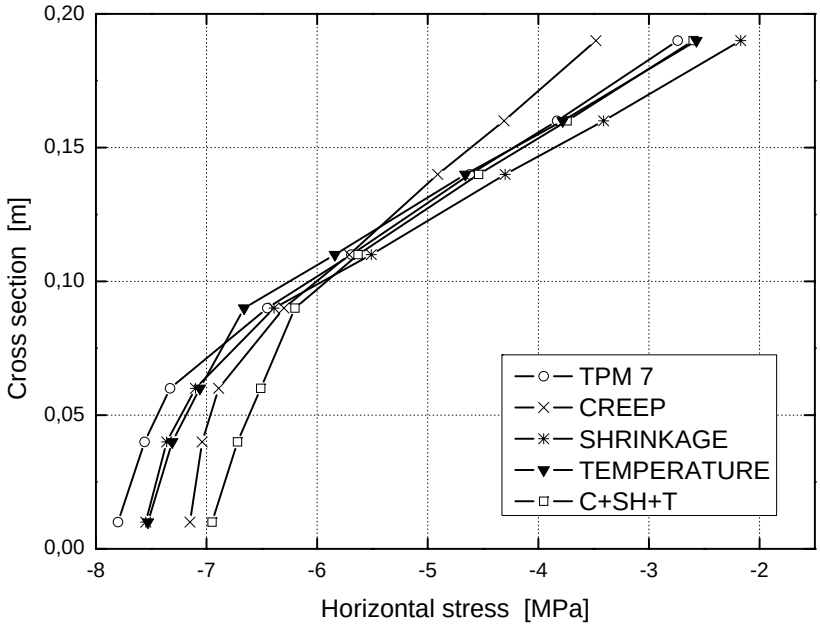



Figure 8.59: Horizontal hoop stresses in tunnel invert for analysis of creep, shrinkage and hydration temperature

The connection point of the temporary invert to the tunnel lining is of great importance regarding the stability of the excavated bench of the tunnel at an intermediate construction stage. From a numerical point of view, this connection area represents a zone where convergence problems could be expected because of the corners of the geometry (see Fig. 8.16) and since large changes in stresses can be expected.

The following Tab. 8.26 summarises the maximum tensile stress $\sigma_1$ and the maximum compressive stress $\sigma_3$ in this connection area for the different constitutive models for shotcrete. It can be seen immediately that the large maximum tensile stress of 25.5 MPa, predicted by the linear elastic model (LE), is unrealistic and would not occur in reality. An improvement in model predictions is achieved by adopting the HME approach with a reduced constant lining stiffness. However, the obtained tensile stress of 10.9 MPa still exceeds the tensile strength of 3.0 MPa of hardened shotcrete at 28 days, which is the limit stress for the non-linear plasticity model (NL). Incorporating the time-dependent behaviour of shotcrete in runs TPM 1, 5 and 9 leads to relatively low tensile stresses ranging from 0.3 to 1.3 MPa, since for these runs the shotcrete stiffness and strength are not fully developed yet. The same conclusion applies to the maximum compressive stresses, that are relatively large (-41.9 MPa) for the linear elastic model (LE) and are reduced by including non-linear plasticity (-30.5 MPa) or by adopting the HME approach (-22.0 MPa). For the time-dependent runs these stresses vary between -4.4 and -14.2 MPa. Retarding and reducing the increase in stiffness and strength (runs STRENGTH 3 and 5) leads to slightly reduced maximum tensile and maximum compressive stresses. The opposite effect has been noticed when changing the shotcrete deformabilty to a very brittle material behaviour (runs STRAIN 3 and 4), where the maximum compressive

stresses are increased up to -14.3 and -15.0 MPa compared to run TPM 7 (which equals TPM 5).

| Run | Maximum $\sigma_1$ (MPa) | Minimum $\sigma_3$ (MPa) |
|---|---|---|
| Linear elastic (LE) | + 25.5 | - 41.9 |
| HME | + 10.9 | - 22.0 |
| Non-linear (NL) | + 3.0 | - 30.5 |
| TPM 1 | + 0.3 | - 4.4 |
| TPM 5 | + 0.8 | - 10.1 |
| TPM 9 | + 1.3 | - 14.2 |
| STRENGTH 1 | + 1.6 | - 15.8 |
| STRENGTH 3 | + 0.2 | - 4.0 |
| STRENGTH 5 | + 0.6 | - 8.3 |
| STRAIN 3 | + 0.8 | - 14.3 |
| STRAIN 4 | + 0.8 | - 15.0 |

Table 8.26: Minimum and maximum principal stresses occurring in the intersection of the temporary invert with the tunnel lining at end of bench excavation (Inc 12)

The maximum stress levels (or utilisation factors) that occur at the intrados of the tunnel crown and invert in the course of tunnel excavation and surface loading are listed in the following Tab. 8.27 and will be discussed here briefly. From the results it can be concluded, that non-linear plasticity of shotcrete at early ages plays an important role in the mechanical behaviour of the shotcrete shell. For very young shotcrete, represented by runs TPM 1 to 7, the compressive stress levels range from $\rho_c = 0.28$ to $\rho_c = 0.53$ at the tunnel crown and from $\rho_c = 0.46$ to $\rho_c = 0.70$ at the tunnel invert. For these runs the compressive yield surface controls the material response during the formation of plastic deformation. However, when the cement hydration within the shotcrete is progressed at later ages (TPM 8 to 14), the behaviour of the lining intrados at the tunnel crown becomes tensile and the utilization factor rises quickly up to $\rho_t = 0.84$ which is already close to peak. In contrary, the stress states at the lining intrados of the tunnel invert remain compressive and the stress levels reduce to $\rho_c = 0.34$, since the compressive peak surface has moved away in stress space with time due to the advanced strength levels at later shotcrete ages. When applying an accelerated increase in stiffness and strength for run STRENGTH 1 ($s = 0.1$), the stress state at the tunnel crown does not show any plastic deformation and remains in the elastic area below the compressive yield surface. At the lining intrados of the tunnel invert the stress level is reduced to $\rho_c = 0.29$ compared to $\rho_c = 0.46$ for reference run TPM 7. The

utilization factor rises again in the case of a retarded development of stiffness and strength for run STRENGTH 3 ($s = 0.4$) and STRENGTH 5 (reduced stiffness and strength by 25 %). Maximum stress levels can reach $\rho_c = 0.58$ for the tunnel crown and $\rho_c = 0.80$ for the tunnel invert. A similar trend is observed when the early age shotcrete deformability is changed to a very brittle or even constant development of peak strains with time. For run STRAIN 4, the obtained utilization factor of the lining intrados at the tunnel invert goes up to $\rho_c = 0.62$ compared to $\rho_c = 0.46$ for reference run TPM 7.

| Run | Intrados crown | Intrados invert |
|---|---|---|
| | $\rho_c$ | $\rho_c$ |
| | (-) | (-) |
| Non-linear (NL) | elastic | 0.30 |
| TPM 1 | 0.53 | 0.70 |
| TPM 2 | 0.51 | 0.70 |
| TPM 3 | 0.50 | 0.70 |
| TPM 4 | 0.48 | 0.70 |
| TPM 5 | 0.29 | 0.46 |
| TPM 6 | 0.28 | 0.46 |
| TPM 7 | 0.28 | 0.46 |
| TPM 8 | $\rho_t = 0.82$ | 0.46 |
| TPM 9 | $\rho_t = 0.81$ | 0.34 |
| TPM 10 | $\rho_t = 0.82$ | 0.34 |
| TPM 11 | $\rho_t = 0.83$ | 0.34 |
| TPM 12 | $\rho_t = 0.83$ | 0.34 |
| STRENGTH 1 | elastic | 0.29 |
| STRENGTH 3 | 0.58 | 0.80 |
| STRENGTH 5 | 0.34 | 0.54 |
| STRAIN 3 | 0.31 | 0.53 |
| STRAIN 4 | 0.37 | 0.62 |

Table 8.27: Utilisation factor of lining intrados at tunnel crown and invert for excavation Type 2 ($K_o = 1.5$)

#### 8.7.2.3 Excavation Type 3

For a detailed understanding of the staged tunnel construction according to excavation Type 3, the figures presented in this section illustrate the hoop stresses within the tunnel lining

for various types of analyses at different construction and loading stages. As in the previous case of excavation Type 2, a constant $K_o$-profile of 1.5 was adopted.

In Fig. 8.60 to 8.62 the distributions of the vertical hoop stresses in the left tunnel sidewall are illustrated for several analyses investigating the influence of the elapsed time during excavation of the tunnel and surface loading. The lining extrados is located at 0.0 m, whereas the lining intrados is situated at a cross-sectional distance of 0.2 m. From Fig. 8.60 it can be observed, that at the end of surface loading in Inc 65 the linear elastic model (LE) predicts large bending of the cross section with tensile stresses at the lining extrados of 2.0 MPa and compressive stresses rising up to -17.1 MPa at the lining intrados. Due to the softer material behaviour of the HME approach, the bending is significantly reduced and the mechanical behaviour of the tunnel shell is mainly governed by compressive stresses across the section, ranging from -4.7 to -9.8 MPa. At this final stage of construction, non-linear plasticity of hardened shotcrete at 28 days (NL) seems to play an important rule, reducing mainly the compressive stresses at the lining intrados (-12.6 MPa) compared to the LE model. Results from run TPM 1 show the typical mechanical behaviour of very young shotcrete, where almost no bending of the cross section is obtained due to the low stiffness at early ages. Compressive stresses vary from -6.0 to -7.2 MPa. Runs TPM 2 to 4, which are controlled by the intermediate elapsed time at Inc 13, represent a transition from the HME approach to the linear elastic model. With an increasing amount of elapsed time in Inc 13, the material behaviour of shotcrete becomes stiffer and therefore a significant bending is introduced in the left tunnel sidewall, leading to critical tensile stresses at the tunnel extrados, ranging from 0.4 to 1.9 MPa.

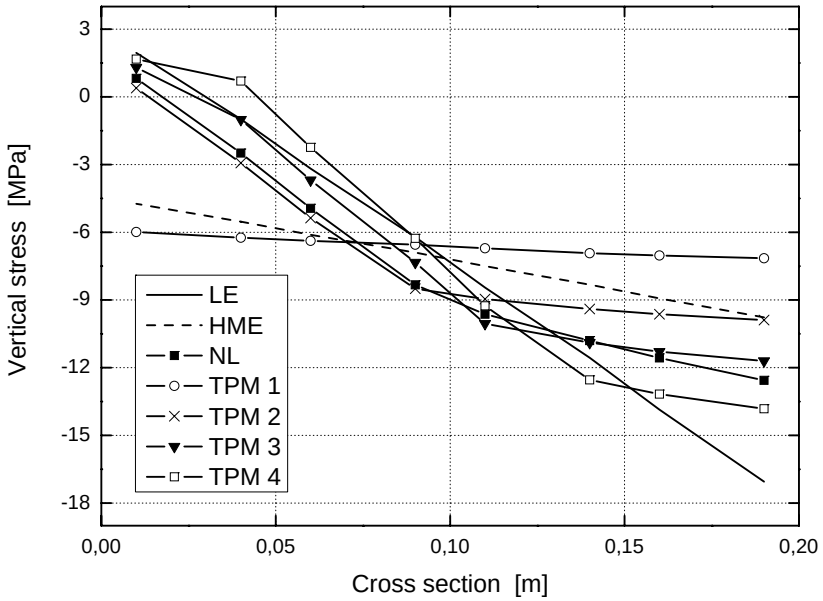



Figure 8.60: Vertical hoop stresses in left sidewall for time-runs TPM 1 to 4 at the end of surface loading (Inc 65)

A slightly different situation can be observed in Fig. 8.61, where the time-runs TPM 5 to 8 predict a very similar behaviour of the left tunnel sidewall. Stress distributions for all runs are located exclusively in the area of compressive stresses, showing very little differences at the lining intrados (-7.8 to -9.5 MPa). The stress distribution becomes more non-linear towards the extrados of the lining, where compressive stresses range from -1.7 to -6.6 MPa. It can be concluded, that the HME approach represents a fairly good approximation to these time-dependent runs, where bending of the cross section is much smaller compared to the linear elastic model (LE). The difference through the elapsed time in Inc 13 seems not so pronounced as in the previous case for runs TPM 1 to 4.

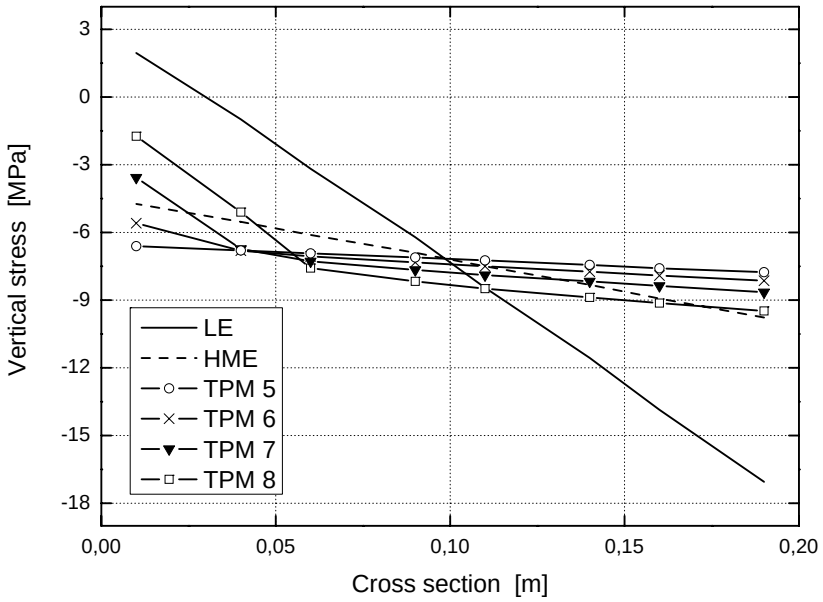



Figure 8.61: Vertical hoop stresses in left sidewall for time-runs TPM 5 to 8 at the end of surface loading (Inc 65)

By comparing Fig. 8.62 with Fig. 8.61 it can be seen that the compressive stresses at the lining intrados hardly change at all for runs TPM 9 to 12 and are located around -9.0 MPa. However, due to the older age of the shotcrete for these runs, the behaviour on the lining extrados becomes more brittle and stresses tend to move towards the tensile stress region. The smallest compressive stresses are obtained for run TPM 12 (-2.3 MPa), where the shotcrete of the left tunnel shell is the oldest with an age of 120 h.

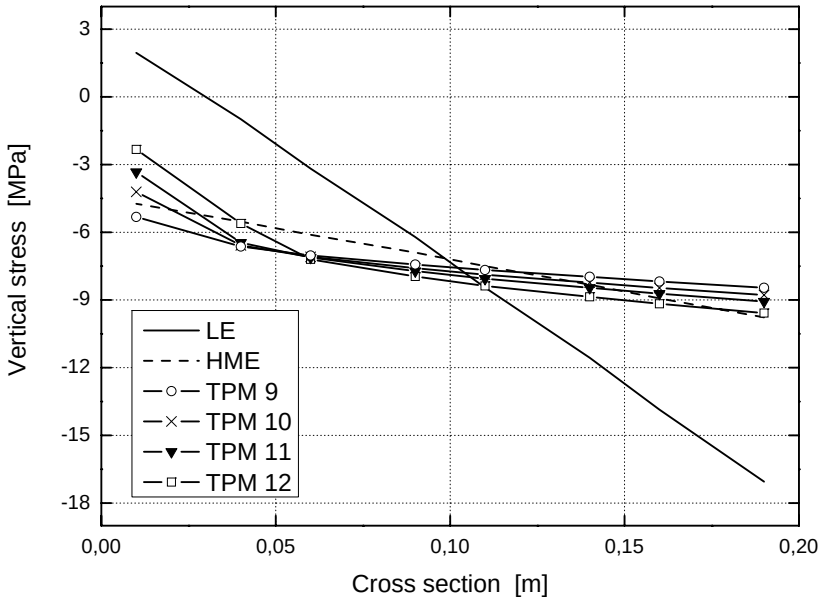



Figure 8.62: Vertical hoop stresses in left sidewall for time-runs TPM 9 to 12 at the end of surface loading (Inc 65)

Fig. 8.63 depicts the vertical stress distribution within the temporary sidewall at the end of the left side gallery excavation in Inc 12. High horizontal stresses in the surrounding ground ($K_o = 1.5$) push this temporary support element to the left towards the centre of the tunnel, introducing high tensile stresses at the intrados of the sidewall (0.0 m) reaching 7.4 MPa for the linear elastic model (LE). Compressive stresses at the sidewall extrados (0.15 m) rise up to -12.9 MPa. When adopting the HME approach, this large bending is reduced significantly and represents a fairly good approximation for the obtained curves from the time-dependent runs TPM 1, 5 and 9. Particularly runs TPM 1 and 5 do not show any bending of the temporary sidewall and the governing behaviour is hoop compression at relatively low stresses of -1.5 MPa for TPM 1 and -2.8 MPa for TPM 5. Due to the slightly progressed shotcrete age of run TPM 9 (24 h at the end of left side gallery excavation) a somewhat stiffer behaviour can be expected introducing a little bending. The non-linear plasticity model for hardened shotcrete at 28 days (NL) appears to be an average result with compressive stresses of -8.7 MPa. Tensile stresses go up to 2.5 MPa. Since they are already relatively close to the tensile capacity of hardened shotcrete (3.0 MPa), there is a potential risk of cracking at the intrados of the temporary sidewall.

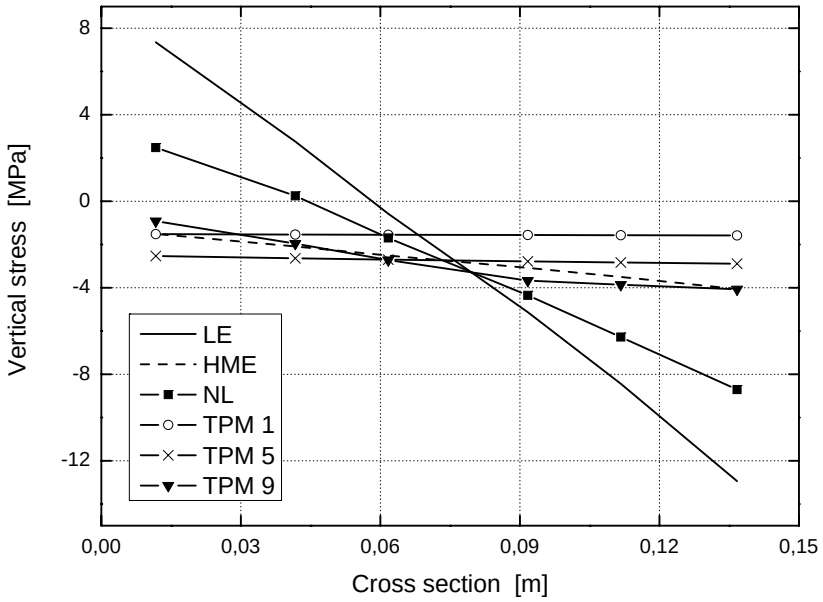



Figure 8.63: Vertical hoop stresses in temporary sidewall at the end of excavation of the left side gallery (Inc 12)

Fig. 8.64 and 8.65 show the vertical stresses in the right tunnel sidewall at the end of excavation in Inc 25 and at the end of surface loading in Inc 65. The lining intrados is located at 0.0 m and the lining extrados at a cross-sectional distance of 0.2 m. One interesting fact that can be observed from these figures is, that at the end of tunnel excavation the bending predicted by all applied constitutive models, even the linear elastic model (LE), is relatively small. Furthermore, although high initial horizontal stresses are anticipated ($K_o = 1.5$), the bending direction seems not to change for this particular cross section during the phase of surface loading, unlike the behaviour observed for excavation Type 1 and 2. Results from runs TPM 1, 5 and 9 show low compressive stresses with hoop compression as the main mechanical behaviour of the tunnel shell even when heavily loaded in Inc 65. During the phase of surface loading from Inc 25 to 65, the bending obtained from the linear elastic model (LE) appears to increase enormously, leading to tensile stresses at the lining extrados of 2.1 MPa and compressive stresses at the lining intrados of -17.2 MPa. These stresses are reduced by incorporating non-linear plasticity for hardened shotcrete at 28 days (NL).

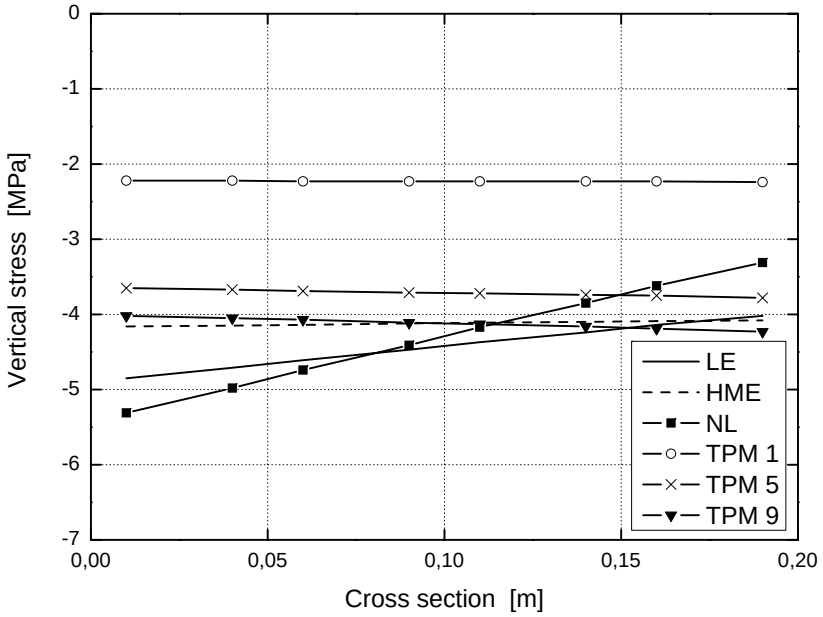



Figure 8.64: Vertical hoop stresses in right tunnel sidewall at the end of tunnel excavation (Inc 25)

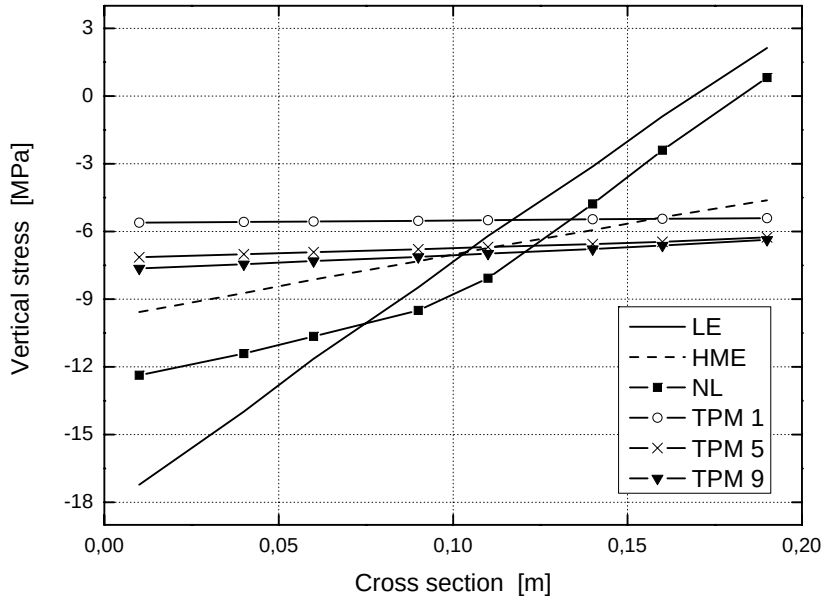



Figure 8.65: Vertical hoop stresses in right tunnel sidewall at the end of surface loading (Inc 65)

The influence of the increase in shotcrete stiffness and strength with time on the stress generation in the tunnel lining for excavation Type 3 can be studied in Fig. 8.66. The vertical stresses in the right tunnel sidewall are plotted at the end of surface loading in Inc 65 and results are compared with reference run TPM 7. It can be seen, that assuming a stiffer behaviour of the shotcrete for run STRENGTH 1 ($s = 0.1$) results in a slight increase of

the bending of the cross section, where stresses at the lining intrados (0.0 m) increase up to -7.8 MPa and reduce to -6.0 MPa at the lining extrados. Runs STRENGTH 3 and 5 simulate a softer lining behaviour through a retarded and reduced increase in stiffness and strength with time. Their results indicate that the bending of the right tunnel sidewall remains almost unchanged, since the curves appear to be almost parallel to each other. However, there is a noticeable difference for the hoop compression that occurs in the cross section, which is significantly reduced for run STRENGTH 3 ($s = 0.4$). Run STRENGTH 5, representing a reduction of the shotcrete stiffness and strength of 25 %, leads to a small reduction in compressive stresses on both the lining intrados and extrados, ranging from -6.1 to -6.7 MPa.

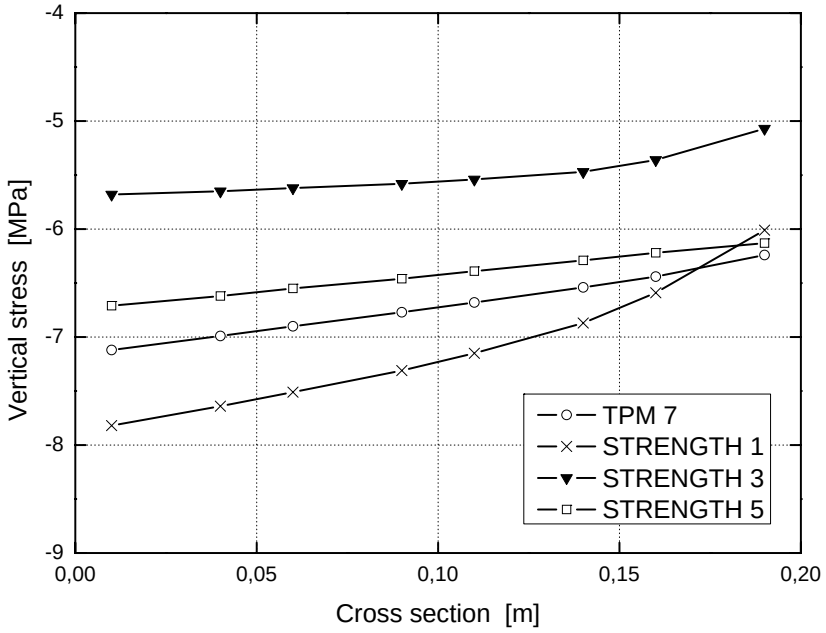



Figure 8.66: Vertical hoop stresses in right sidewall at the end of surface loading (Inc 65) for various developments of stiffness and strength

The application of different shotcrete deformabilities at early ages has been analysed in runs STRAIN 3 and 4, which represent a more brittle mechanical behaviour of shotcrete than reference run TPM 7. Fig. 8.67 shows the results for the vertical stress distribution at the left tunnel sidewall at the end of surface loading in Inc 65. As a general trend, it can be observed that reduced peak strains for both compression and tension lead to an increase in bending of the cross section. Run STRAIN 4, representing a low constant possible straining level of the uniaxial stress-strain curve for shotcrete, predicts small tensile stresses at the lining extrados (0.0 m) of 0.2 MPa. However, on the lining intrados (0.2 m) the compressive stresses increase from -8.7 MPa for run TPM 7 up to -13.0 MPa. Run STRAIN 4, governed by a sharp decrease in peak strains with time, can be seen to give an intermediate stress distribution, where stresses remain compressive at the lining extrados (-1.8 MPa), but rise to -10.1 MPa at the lining intrados.

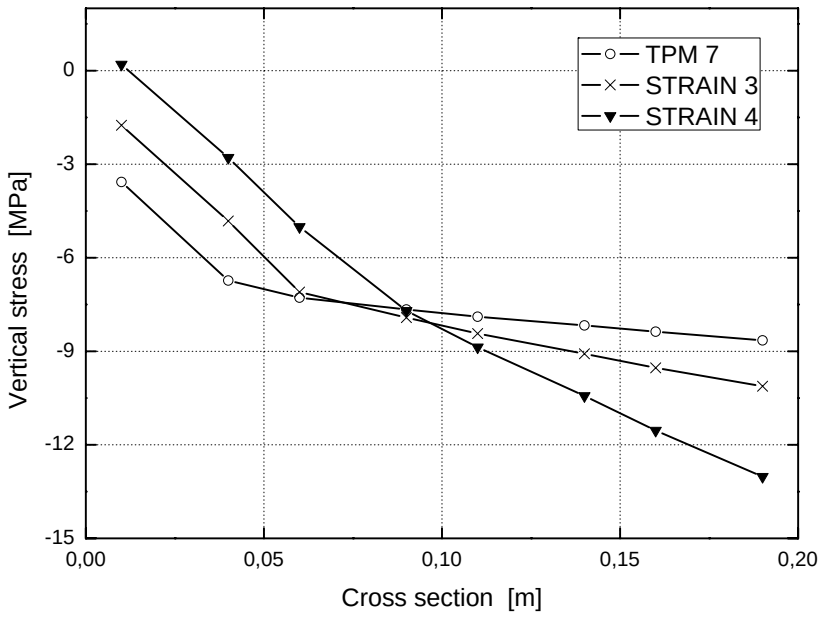



Figure 8.67: Vertical hoop stresses in left sidewall at the end of surface loading (Inc 25) for various shotcrete deformabilities

Fig. 8.68 and 8.69 investigate the influence of creep, shrinkage and hydration temperature of young shotcrete on the generated stress distributions within the tunnel lining. Fig. 8.68 plots the vertical stresses in the left tunnel sidewall at 28 days after the end of surface loading (Inc 100) and compares the results with reference run TPM 7 (Inc 65). It can be observed, that very little change occurs when incorporating creep of shotcrete, with the analysis giving a very similar stress distribution pattern as for run TPM 7. Shrinkage increases the compressive stresses at the lining extrados (0.0 m) from -3.6 MPa for run TPM 7 up to -5.1 MPa. On the contrary, at the lining intrados (0.2 m) run SHRINKAGE predicts slightly reduced compressive stresses of -8.4 MPa. Run TEMPERATURE tends to follow an almost linear stress distribution across the lining cross section with compressive stresses of -4.5 MPa at the lining extrados and relatively large stresses of -9.1 MPa at the lining intrados. These results are very close to those from run C+SH+T. The incorporation of all the time-dependent effects of creep, shrinkage and hydration temperature leads to a fairly linear stress distribution for the left tunnel sidewall.

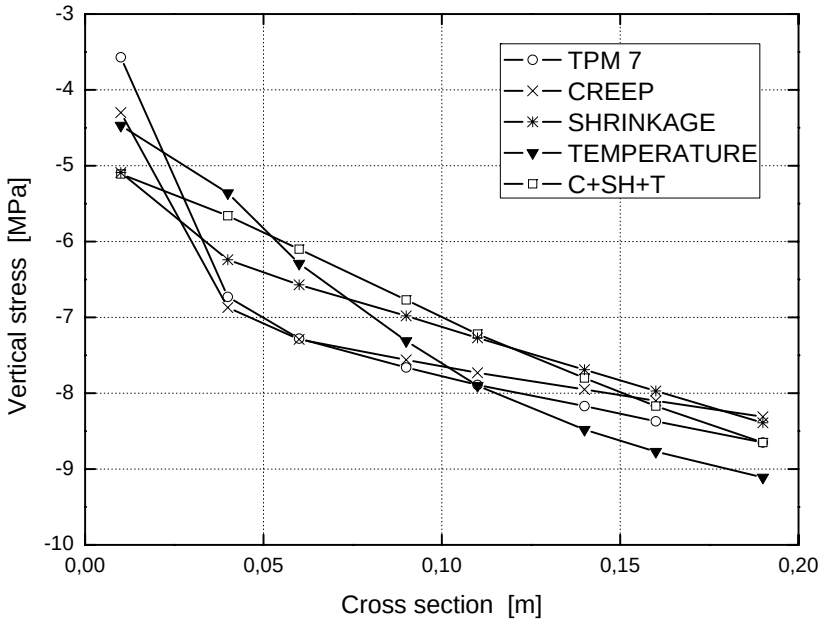



Figure 8.68: Vertical hoop stresses in left tunnel sidewall for analysis of creep, shrinkage and hydration temperature (Inc 100)

In Fig. 8.69 the vertical stresses in the right tunnel sidewall are illustrated at Inc 100. It can be seen, that there are only minor differences in the obtained stress results for the investigated runs taking into account creep, shrinkage and hydration temperature compared to reference run TPM 7. At the lining intrados (0.0 m) compressive stresses range from -7.1 MPa (SHRINKAGE) to -7.3 MPa (TEMPERATURE) and from -5.6 MPa (C+SH+T) to -6.3 MPa (CREEP). In this particular case, the bending of the cross section is slightly increased for run C+SH+T, compared to reference run TPM 7.

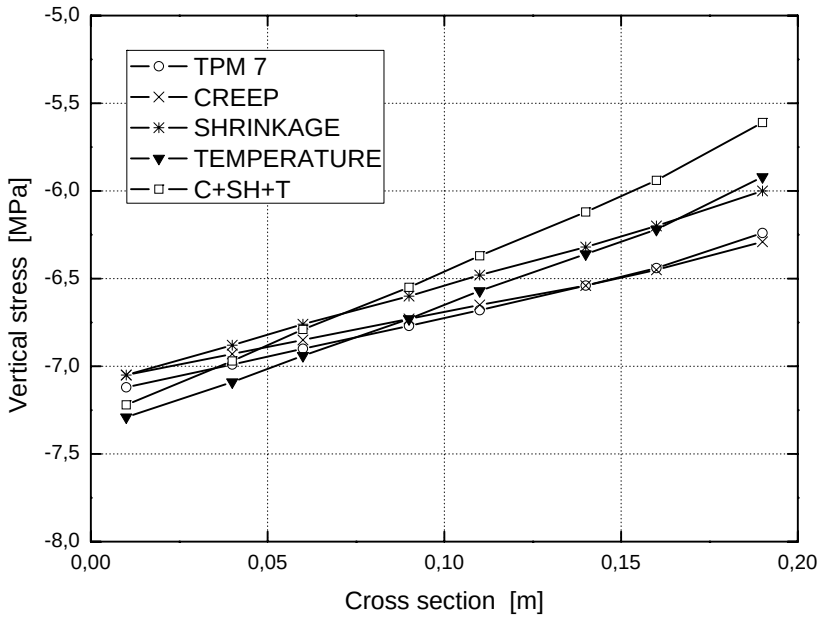



Figure 8.69: Vertical hoop stresses in right tunnel sidewall for analysis of creep, shrinkage and hydration temperature (Inc 100)

Similar to the analysis of excavation Type 2, the connection of the temporary sidewall to the tunnel lining was of special interest regarding the generated stresses due to excavation of the left side gallery. Tab. 8.28 summarises the results for the maximum principal stress $\sigma_1$ and the minimum principal stress $\sigma_3$ that occur in this top intersection area near the tunnel crown for all the analyses carried out. Firstly it is noted, that the linear elastic model predicts unrealistic high tensile stresses of up to 41.1 MPa. These stresses are reduced by adopting the softer HME approach, but the stresses still exceed the tensile capacity of hardened shotcrete at 28 days, as indicated for run NL (3.0 MPa). Runs TPM 1, 5 and 9 represent young shotcrete with low developed strengths and therefore, the tensile stresses are reduced significantly ranging from 0.3 to 1.3 MPa. The same observation can be made when retarding or reducing the development of the shotcrete stiffness and strength for runs STRENGTH 3 and 5. Tensile stresses remain unchanged for runs STRAIN 3 and 5, but compressive stresses increase slightly compared to reference run TPM 7 (-12.9 MPa). The compressive stress of -63.2 MPa predicted by the linear elastic model exceeds as well the adopted uniaxial compressive strength of -30 MPa. However, it should be mentioned that for a triaxial stress state such high compressive stresses for concrete and shotcrete are possible to achieve. A fact which is taken into account by the compressive yield surface of the presented constitutive model for shotcrete in the previous Chapter 7.

| Run | Maximum $\sigma_1$ (MPa) | Minimum $\sigma_3$ (MPa) |
|---|---|---|
| Linear elastic (LE) | + 41.1 | - 63.2 |
| HME | + 18.1 | - 32.3 |
| Non-linear (NL) | + 3.0 | - 29.7 |
| TPM 1 | + 0.3 | - 4.9 |
| TPM 5 | + 0.8 | - 12.9 |
| TPM 9 | + 1.3 | - 19.3 |
| STRENGTH 1 | + 1.6 | - 21.6 |
| STRENGTH 3 | + 0.2 | - 4.8 |
| STRENGTH 5 | + 0.6 | - 10.4 |
| STRAIN 3 | + 0.8 | - 16.1 |
| STRAIN 4 | + 0.8 | - 17.2 |

Table 8.28: Minimum and maximum principal stresses occurring in the top intersection of the temporary sidewall with the tunnel lining at end of left side gallery excavation (Inc 12)

Finally, Tab. 8.29 contains information about the maximum utilisation factors (or stress levels) that occur in the lining intrados of the left and right tunnel sidewall throughout the whole construction process. It can be seen, that for very young shotcrete (TPM 1), the stress level is mainly of a compressive nature reaching levels of up to $\rho_c = 0.67$ for the left sidewall and $\rho_c = 0.74$ for the right sidewall. These utilization factors tend to decrease with increasing age of the shotcrete during the analysis (TPM 2 to 12) and appear to stabilize at a relatively low level of around $\rho_c = 0.32$ to $\rho_c = 0.34$ for both cross sections. The maximum utilisation factor was achieved for run STRENGTH 3, where the increase in stiffness and strength is retarded by the cement parameter $s = 0.4$. Stress levels rise up to $\rho_c = 0.70$ for the left sidewall and $\rho_c = 0.82$ for the right sidewall. A faster development of stiffness and strength, as simulated in run STRENGTH 1 ($s = 0.1$), leads to a slightly reduced stress level for both cross sections ($\rho_c = 0.31$) compared to reference run TPM 7. Another conclusion that can be drawn is, that a reduced deformability of shotcrete at early ages implies an increased stress level as predicted by runs STRAIN 3 and 4. For the intrados of the right sidewall, the utilization factor rises up to $\rho_c = 0.64$ for run STRAIN 4. Finally, as already highlighted in the previous section for excavation Type 2, the connection of the temporary sidewall to the tunnel lining near the crown, is a heavily loaded zone, where cracking and crushing of the shotcrete is dominating the mechanical behaviour. This results in utilisation factors for both compression and tension that have a value of unity, indicating the occurance of strain softening.

| Run | Intrados left sidewall | Intrados right sidewall |
|---|---|---|
| | $\rho_c$ | $\rho_c$ |
| | (-) | (-) |
| Non-linear (NL) | 0.32 | 0.32 |
| TPM 1 | 0.67 | 0.74 |
| TPM 2 | 0.60 | 0.74 |
| TPM 3 | 0.59 | 0.74 |
| TPM 4 | 0.58 | 0.73 |
| TPM 5 | 0.38 | 0.43 |
| TPM 6 | 0.37 | 0.43 |
| TPM 7 | 0.35 | 0.43 |
| TPM 8 | 0.35 | 0.43 |
| TPM 9 | 0.32 | 0.34 |
| TPM 10 | 0.32 | 0.34 |
| TPM 11 | 0.32 | 0.34 |
| TPM 12 | 0.32 | 0.34 |
| STRENGTH 1 | 0.31 | 0.31 |
| STRENGTH 3 | 0.70 | 0.82 |
| STRENGTH 5 | 0.43 | 0.28 |
| STRAIN 3 | 0.42 | 0.51 |
| STRAIN 4 | 0.56 | 0.64 |

Table 8.29: Utilisation factor of lining intrados at left and right tunnel sidewall for excavation Type 3 ($K_o = 1.5$)

### 8.7.3 Lining displacements

#### 8.7.3.1 Excavation Type 1

Fig. 8.70 shows the development of the vertical displacements of the lining intrados at the tunnel crown during the whole construction process starting at lining installation (Inc 3) until the end of surface loading (Inc 50) adopting a $K_o$-profile of 0.5. Furthermore, the results from various constitutive models for simulating shotcrete behaviour are included. It can be seen that all runs indicate a negative movement of the crown towards the centre of the tunnel during the excavation process. This vertical displacement is very small for the linear elastic model (LE) with a value of -1.5 mm. The HME approach predicts a vertical displacement four times larger at -6.1 mm. The run TPM 1, where the shotcrete has just an

age of 2 h at the end of excavation, results in an extremely large lining displacement of up to -155.8 mm due to the low stiffness of the shotcrete at the early age. However, these vertical displacements reduce relatively quickly with increasing shotcrete age, showing values within a range of -77.6 to -5.8 mm for runs TPM 2 to 6. For runs TPM 7 to TPM 14 no significant change in vertical displacement with shotcrete age can be noted, with values close to the LE and HME approach. No difference has been obtained by including non-linear plasticity of the hardened shotcrete at 28 days (NL) meaning that with the full shotcrete stiffness the tunnel lining behaves mainly elastically. If the loading of the tunnel shell is continued by placing the surface surcharge from Inc 11 to Inc 50, the vertical displacements of the crown increase further, resulting in a final value of -105.9 mm for the linear elastic model (LE). Here again, the HME approach predicts a slightly larger value of -126.9 mm due to the lower constant stiffness of the lining. The model predictions of run TPM 1 reach a vertical crown displacement of -284.0 mm, followed by -195.3 mm for TPM 2. One interesting fact is, that all the displacement curves appear to be almost parallel to each other during the surface loading phase which indicates that the loading-displacement ratio must be more or less equal for all performed runs. Therefore the material properties of the young shotcrete age have a significant influence on the deformational behaviour of the tunnel lining particularly during tunnel excavation.

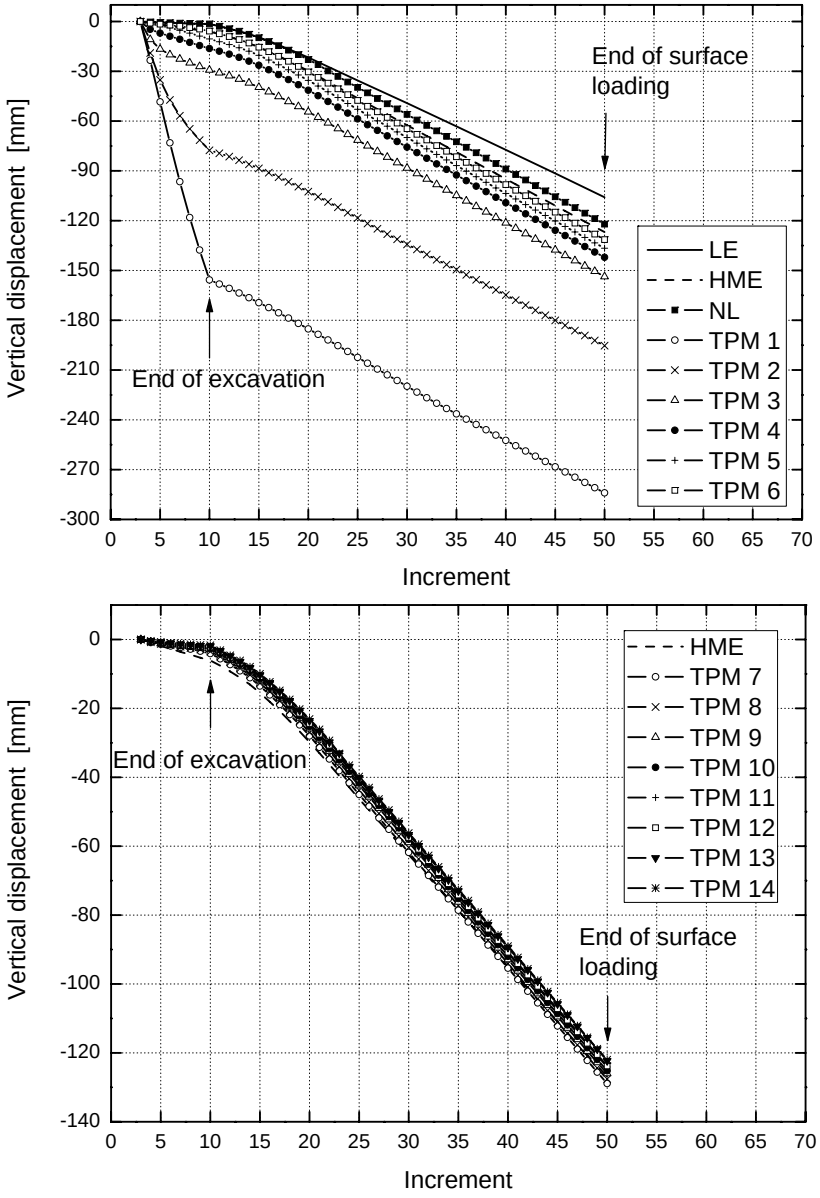



Figure 8.70: Vertical crown displacement for various time runs adopting $K_o = 0.5$ (Excavation Type 1)

The displacement pattern is of a similar nature for the behaviour of the lining intrados at the tunnel invert, as can be seen in Fig. 8.71. During excavation of the tunnel the lining tends to move inwards resulting in positive displacement values from Inc 3 to 10 adopting a $K_o$-profile of 0.5. In this graph, the influence of the development of stiffness and strength of the shotcrete on the vertical invert displacement was studied by performing six different runs (STRENGTH 1 to 6) and comparing results with the reference run TPM 6. The vertical displacement of TPM 6 reaches a value of 15.8 mm at the end of excavation. The run STRENGTH 1, which represents a stiffer tunnel lining by applying a cement parameter $s = 0.1$, shows a slightly reduced displacement of 14.5 mm. The retarded increase in shotcrete stiffness of run STRENGTH 4 ($s = 0.5$) leads to a large heave of the invert moving

up 30.5 mm. A reduction of the lining stiffness of 25 % (STRENGTH 5) leads to a displacement of 18.1 mm, whereas run STRENGTH 6 has a 41 % higher displacement (22.3 mm) than run TPM 6. When the surface surcharge is placed on top the tunnel is pushed further into the ground and the vertical invert displacements reduce for all analyses. Here again, the displacement curves tend to follow a parallel pattern resulting in a more or less constant loading-displacement ratio where the lining stiffness does not play an important role anymore. The final displacement values are in the range of -12.5 mm (for run STRENGTH 1) and 1.5 mm (for run STRENGTH 4).

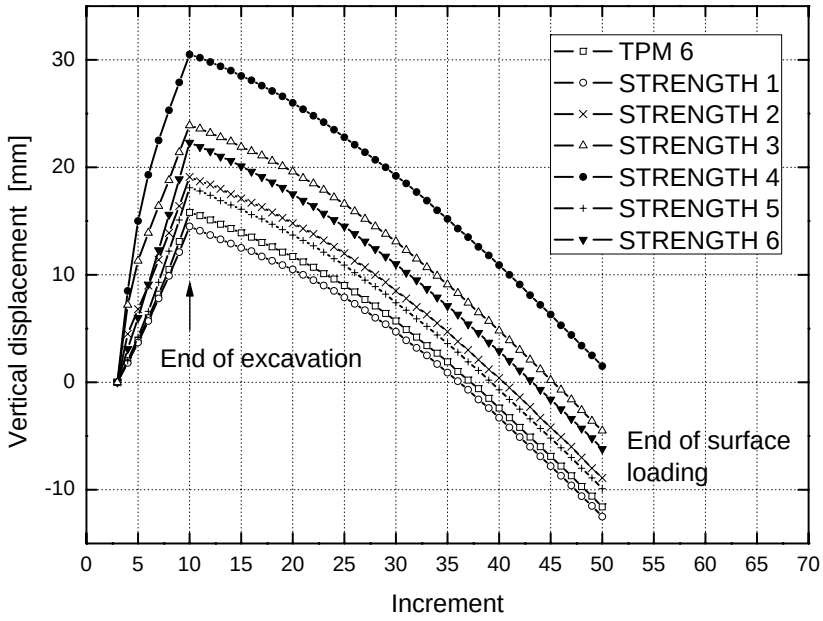



Figure 8.71: Vertical invert displacement for variation in development of stiffness and strength with $K_o = 0.5$

Another investigation focused on the impact of the shotcrete deformability on the vertical displacement of the lining intrados at the tunnel crown adopting a $K_o$-profile of 0.5, as illustrated in Fig. 8.72. No significant difference can be distuingished during the first loading phase of the tunnel in the course of excavation (Inc 3 to 10). However, the difference becomes a bit more pronounced during the surcharge loading with final values ranging from -134.3 mm for run STRAIN 1, representing a relatively high deformability of shotcrete at early ages, to -123.8 mm for run STRAIN 4, where the deformability is kept at a constant low level.

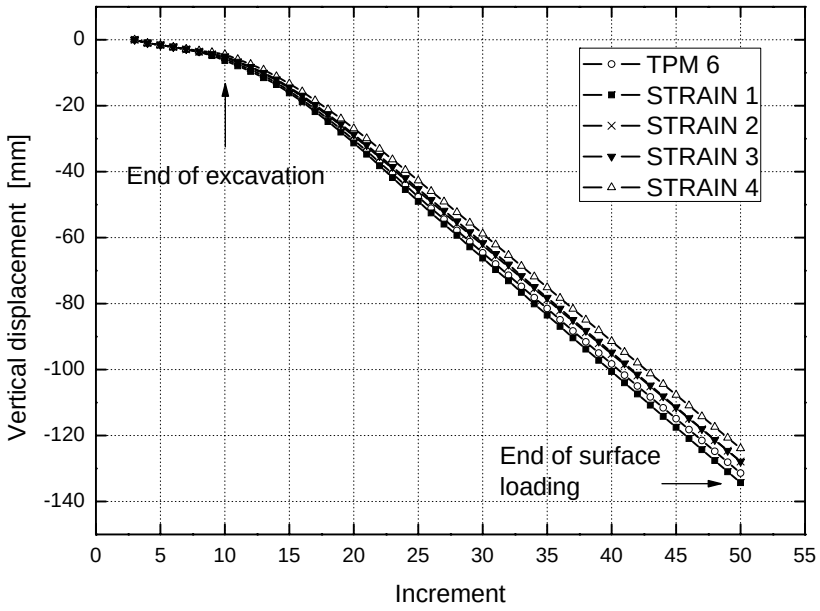



Figure 8.72: Vertical crown displacement for variation in shotcrete deformability with $K_o = 0.5$

Tab. 8.30 summarizes the vertical and horizontal displacements of various points on the lining intrados for different analyses concerning creep, shrinkage and hydration temperature (Inc 100) and compares the results with reference run TPM 6 (Inc 50). According to these results, the vertical crown displacements are increased for all analyses, but the inclusion of creep shows the smallest impact. Taking into account all the time-dependent aspects in run C+SH+T, leads to the largest absolute displacement of -139.2 mm. This trend is the opposite for the horizontal sidewall and vertical invert displacements, which tend do decrease compared to reference run TPM 6.

| Displacement | TPM 6 | CREEP | SHRINKAGE | TEMPERATURE | C+SH+T |
|---|---|---|---|---|---|
| Crown - $v$ (mm) | -131.4 | -132.5 | -136.8 | -132.9 | -139.2 |
| Sidewall - $u$ (mm) | 50.7 | 50.5 | 47.9 | 49.4 | 46.3 |
| Invert - $v$ (mm) | -11.6 | -11.2 | -9.6 | -10.6 | -8.5 |

Table 8.30: Lining displacements of performed analyses for creep, shrinkage and hydration temperature adopting $K_o = 0.5$

Fig. 8.73 shows the development of the horizontal displacements of the lining intrados at the right sidewall of the tunnel during the excavation and surface loading phase from Inc 5 to Inc 50 for an adopted $K_o$-profile of 1.5. Due to the high horizontal stresses all the illustrated time runs indicate a movement of the right sidewall towards the centre of the tunnel during the excavation phase. At the end of tunnel excavation (Inc 10), the linear elastic model (LE) predicts a horizontal displacement of -6.0 mm, which is the same for the non-linear time-

independent run (NL). The predictions from the HME approach are very similar to the LE run although the lining stiffness is much smaller, showing a horizontal movement of -8.0 mm. Here again, the largest horizontal displacement is predicted by the time-dependent run TPM 1, where the shotcrete is very young. Displacements reach up to -52.6 mm at Inc 10. With ageing of the shotcrete these displacements reduce significantly, having a value of -32.7 mm for run TPM 2 and -9.3 mm for run TPM 5. As illustrated in the figure, for the time runs TPM 7 to 14 there is no significant difference in the horizontal displacements due to the fact that the lining stiffness had developed to a relatively high level. On the onset of the surface loading, the general movement of the tunnel at the right sidewall is outwards and horizontal displacements tend to become positive again around Inc 30 to 40. At the final stage of the construction sequence the linear elastic model (LE) predicts horizontal movements of 10.1 mm, whereas run TPM 1 still shows a negative value of -43.7 mm.

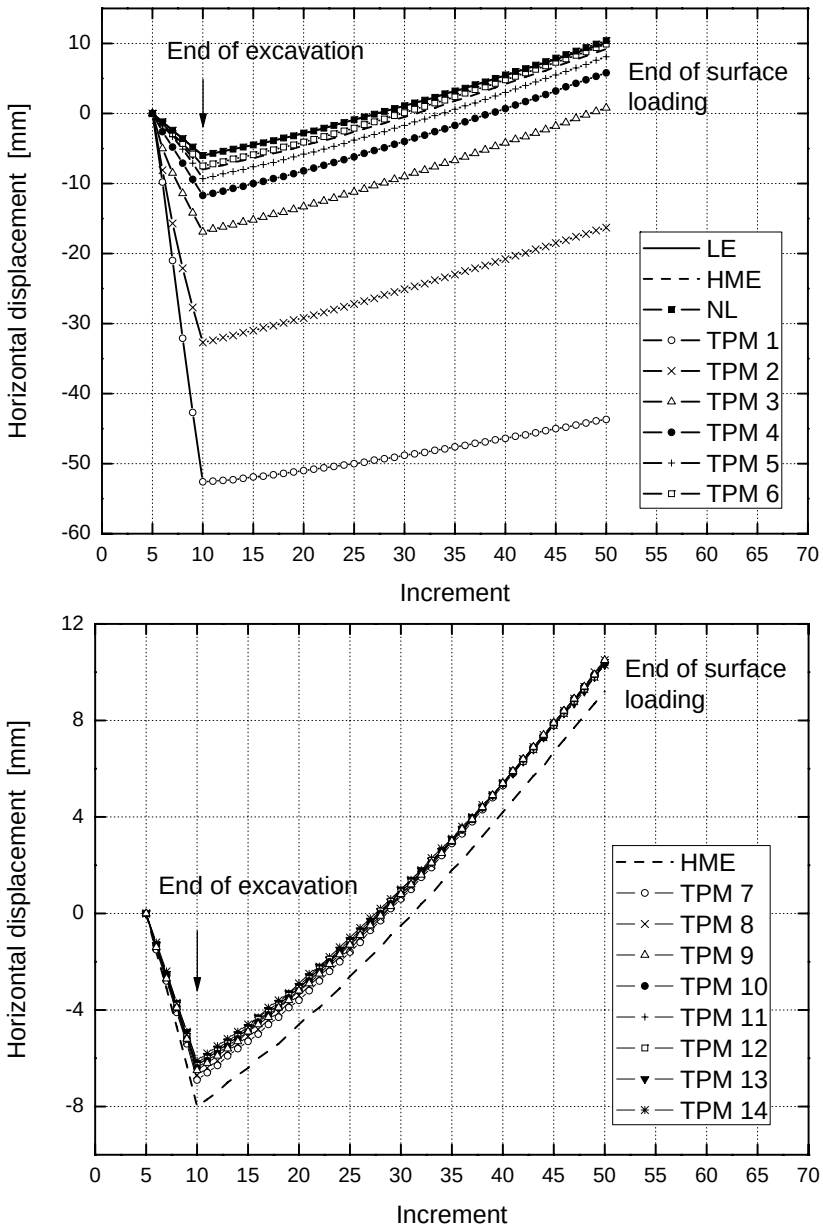



Figure 8.73: Horizontal displacement of right tunnel sidewall for various time runs adopting $K_o = 1.5$

As explained earlier, the development of the lining stiffness has a big influence on the deformational behaviour of the tunnel shell, as can be seen in Fig. 8.74. For a retarded increase in stiffness, represented by runs STRENGTH 3 and 4 ($s = 0.4$ and $s = 0.5$), the horizontal displacements of the lining intrados of the right sidewall increase up to -23.2 mm at the end of excavation in Inc 10 and are therefore 2 to 3 times larger than for the reference run TPM 6 (-7.5 mm). By reducing the stiffness and strength of the shotcrete by 25 and 50 %, horizontal displacements increase up to -9.7 and -14.6 mm respetcively. After placing the surface surcharge during Inc 11 to 50, the horizontal displacements of the right sidewall become positive for all investigated runs apart from run STRENGTH 4. These displacements

are in the range of 0.9 to 10.6 mm (STRENGTH 1).

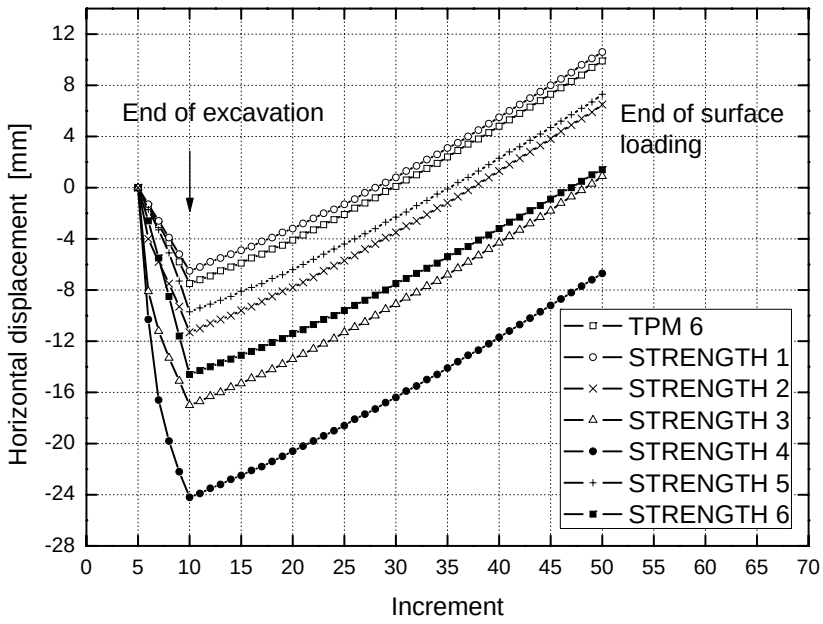



Figure 8.74: Horizontal sidewall displacement for variation in development of stiffness and strength with $K_o = 1.5$

A slight difference in the vertical displacements of the tunnel invert can be identified when applying different shotcrete deformabilities, as can be seen in Fig. 8.75. When adopting a $K_o$-profile of 1.5, a very small upwards movement of the tunnel invert can be expected for all performed analyses. Reference run TPM 6 shows a value of 0.7 mm at the end of excavation. For runs STRAIN 1 to 4 this value varies from 0.3 to 0.9 mm depending on the adopted development of peak strains representing either relatively soft or very brittle material behaviour regarding the possible strain levels of the shotcrete. This displacement range seems to keep constant during the surface loading phase, where the tunnel is pushed downwards. At the end of the construction process in Inc 50, the vertical invert displacements show negative values ranging from -6.0 to -5.3 mm.

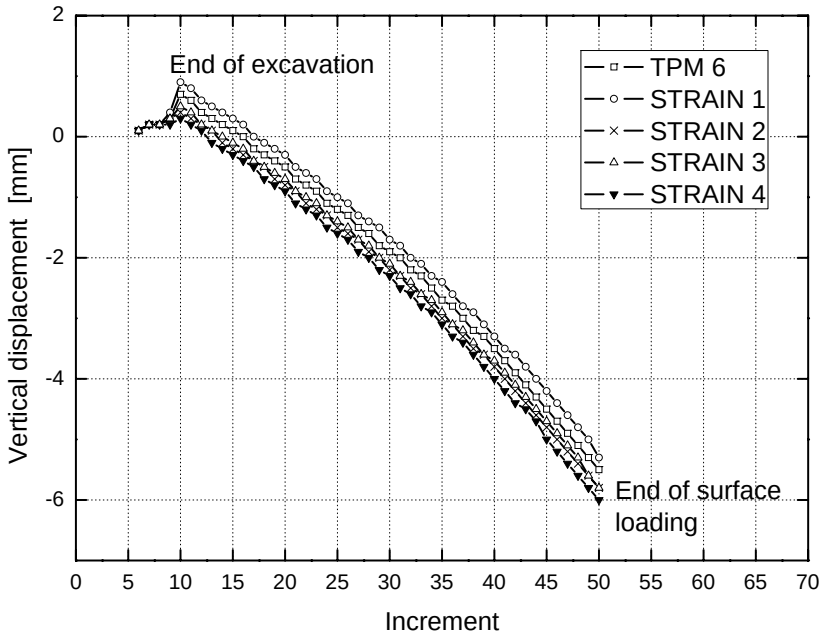



Figure 8.75: Vertical invert displacement for variation in shotcrete deformability with $K_o = 1.5$

In Tab. 8.31 the vertical and horizontal lining displacements of the tunnel crown, sidewall and invert are listed for the performed analyses which take into account creep, shrinkage and hydration temperature of the shotcrete, adopting a $K_o$-profile of 1.5. For the run C+SH+T a significant impact of these time-dependent aspects can be identified for the vertical displacements of the tunnel invert, which are reduced by 50 %. As in the case of $K_o = 0.5$, creep surprisingly seems to be of minor importance.

| Displacement | TPM 6 | CREEP | SHRINKAGE | TEMPERATURE | C+SH+T |
|---|---|---|---|---|---|
| Crown - $v$ (mm) | -34.7 | -35.4 | -40.1 | -36.9 | -42.9 |
| Sidewall - $u$ (mm) | 9.9 | 9.7 | 7.0 | 8.4 | 5.4 |
| Invert - $v$ (mm) | -5.5 | -5.3 | -3.9 | -4.5 | -2.7 |

Table 8.31: Lining displacements of performed analyses for creep, shrinkage and hydration temperature adopting $K_o = 1.5$

In Fig. 8.76 a comparison of different lining displacements for both $K_o$-profiles are presented, in order to show the effect of the initial stress conditions on the deformational behaviour of the tunnel lining. Run TPM 6 serves as a reference run and displacements are plotted for the intrados of the tunnel crown and the right sidewall. At the end of excavation in Inc 10, the vertical crown displacement for $K_o = 0.5$ shows a value of -5.8 mm, whereas for $K_o = 1.5$ the tunnel crown moves upwards resulting in a displacement of 9.5 mm. However, at the end of the surface loading in Inc 50 this effect is even more pronounced, with a difference in displacements of 97 mm, although both types of analyses predict negative values

meaning that the tunnel was pushed into the ground when placing the surface surcharge. A similar mechanism can be identified for the horizontal displacements of the right sidewall of the tunnel. In the case of $K_o = 0.5$, this movement goes up to 6.1 mm. The movement is contrary for $K_o = 1.5$, where the sidewall moves -7.5 mm towards the centre of the tunnel due to the high horizontal stresses in the ground. After loading the tunnel from the surface a total difference in horizontal displacements of 41 mm is indicated.

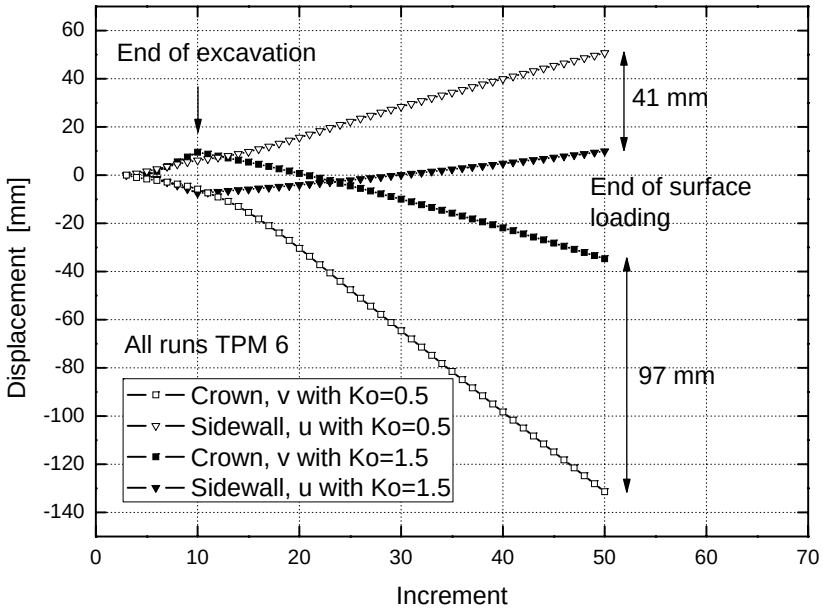



Figure 8.76: Comparison of vertical crown displacements $v$ and horizontal sidewall displacements $u$ for both $K_o$-profiles for time run TPM 6

#### 8.7.3.2 Excavation Type 2

The development of the vertical displacement of the lining intrados at the tunnel crown is shown for excavation Type 2 in Fig. 8.77, starting at the installation of the upper shell in Inc 7. Furthermore, the results from various time runs are compared with the linear elastic (LE) and HME approach. It can be seen that during the excavation of the bench, the tunnel crown tends to move downwards towards the centre of the tunnel showing negative displacement values for all runs. The runs LE, HME, TPM 5 and 9 predict displacements that are very close together of about -10.0 mm. However, run TPM 1 with its low stiffness of the young shotcrete, predicts movements of up to -29.2 mm. This trend of deformation is reversed during the excavation of the invert region of the tunnel from Inc 14 to 25, where the tunnel crown starts to move upwards resulting in a positive displacement of about 10 mm for the linear elastic run (LE). This crown movement is not so pronounced for run TPM 1, which still shows a negative displacement of -23.2 mm at the end of the complete tunnel excavation in Inc 25. The HME approach and run TPM 5 predict almost the same displacement value of about 5.7 mm. When the surface surcharge is applied from Inc 26 to Inc 65, the whole tunnel is pushed into the ground and therefore displacements start to reduce again. Run

TPM 1 shows relatively large crown displacements of -70.2 mm, since the stiffness is still at a very low level. The model predictions of the remaining analyses vary from -30.0 mm for the linear elastic model (LE) to -40.7 mm for run TPM 5. Here again, it appears that the load-displacement ratio during the surface loading phase seems to be of a similar magnitude for all the performed runs since the curves show a parallel position to each other.

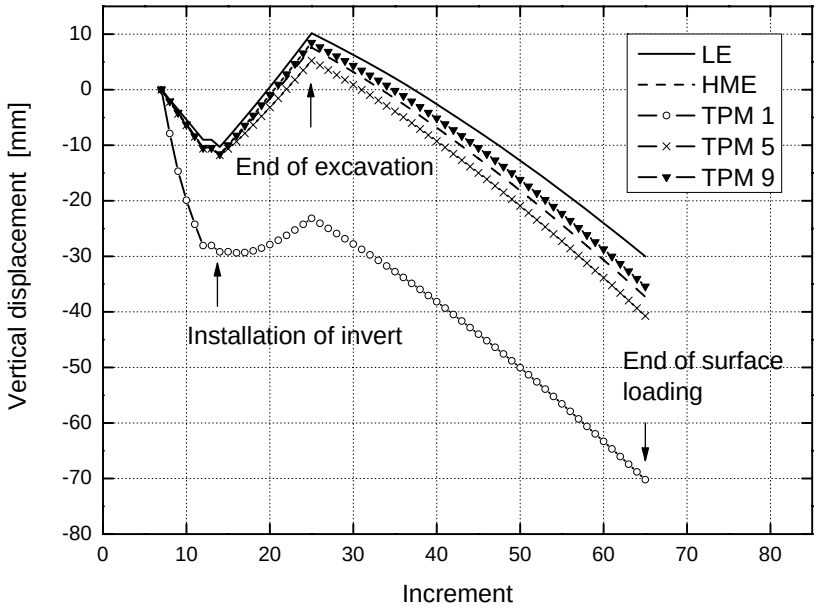



Figure 8.77: Vertical crown displacement for various time runs adopting $K_o = 1.5$

To study the effect of the difference in age of shotcrete of the upper and lower tunnel shell on the displacement behaviour, results for the time runs TPM 1 to 4 are plotted in Fig. 8.78. During the excavation of the tunnel from Inc 7 to 25 no significant difference is obtained. However, during the loading phase of the tunnel from the surface surcharge, a slight difference in vertical crown displacements with a maximum value of 4.4 mm can be identified. All curves for the time-dependent model remain far below the linear elastic model (LE) and the HME approach, as already discussed for the previous figure.

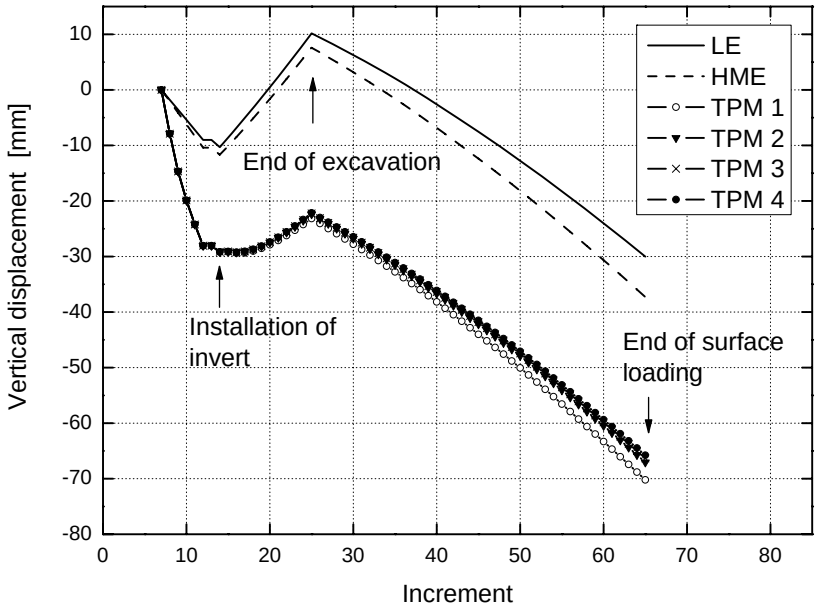



Figure 8.78: Vertical crown displacement for runs TPM 1 to 4 adopting $K_o = 1.5$

Fig. 8.79 illustrates the development of the horizontal displacements of the lining intrados at the intersection point of the tunnel shell with the temporary invert (see also Fig. 8.17). Here a different mechanism is obtained for time run TPM 1 due to the low stiffness of the young shotcrete. The intersection point tends to move towards the centre of the tunnel, resulting in a negative displacement of -3.4 mm at the end of the bench excavation in Inc 12. Conversely, the linear elastic model (LE), the HME approach and the time runs TPM 5 and 9 predict a positive movement of this point to the right with a maximum value of 5.5 mm for run TPM 9. During excavation of the tunnel invert from Inc 14 to 25, all models indicate a negative increase in horizontal displacements leading to movement towards the inside of the tunnel. The linear elastic model (LE) shows a value of -13.8 mm and the HME approach -16.9 mm in Inc 25. Here again, the run TPM 1 shows the largest displacement value of -32.8 mm. When placing the surface surcharge, the tunnel lining intrados starts to move to the right again with a maximum final displacement of 2.1 mm for the linear elastic model (LE), almost zero displacement (0.4 mm) for the HME approach and -17.4 mm for run TPM 1. The analyses TPM 5 and 9 show final displacements which are very close to zero (-1.3 and 1.3 mm respectively).

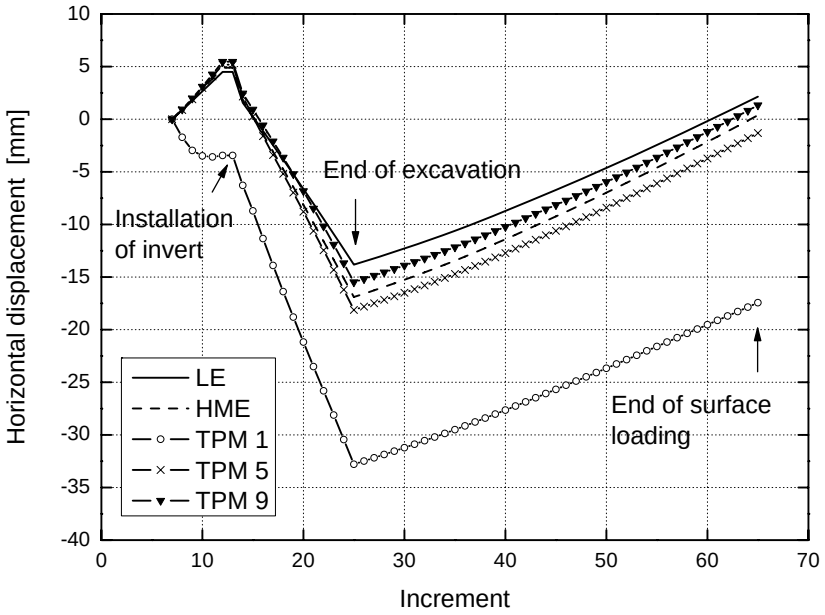



Figure 8.79: Horizontal displacement at the intersection of temporary invert with tunnel lining for various time runs adopting $K_o = 1.5$

As shown in Fig. 8.80, a small difference in the displacement curves can be identified for runs TPM 1 to 4 during the surface loading of the tunnel. Similar to the case for the vertical crown displacement, these differences lie in the range of 1.0 to 4.0 mm.

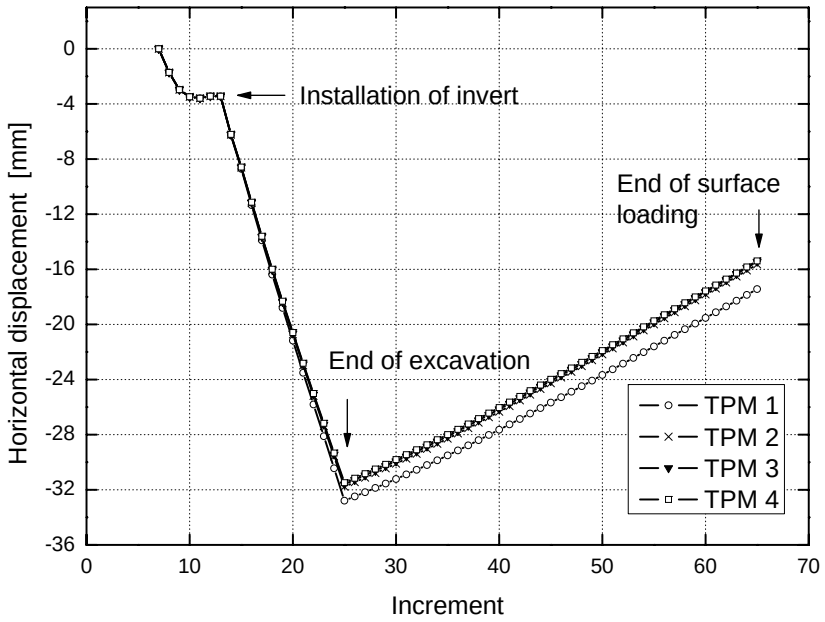



Figure 8.80: Horizontal sidewall displacement for runs TPM 1 to 4 adopting $K_o = 1.5$

The impact of the development of the shotcrete stiffness and strength with time on the deformational behaviour of the tunnel lining for excavation Type 2 can be studied in Fig. 8.81, where results for the vertical displacement of the lining intrados at the tunnel crown are

plotted. Run STRENGTH 1 has a slightly stiffer material response of the shotcrete due to its cement parameter $s = 0.1$. Vertical movements seem to be very close to those from the reference run TPM 7, with a maximum difference of 3.6 mm at the end of the complete tunnel excavation in Inc 25. Run STRENGTH 3 simulates a retarded increase in stiffness and strength ($s = 0.4$) and therefore displacements remain negative at Inc 25 with a value of -25.7 mm. A reduction in the shotcrete stiffness of 25 % leads to a softer lining behaviour, where the crown displacements at the end of excavation are almost zero (0.4 mm). However, during the construction phase of surface loading, the tunnel crown moves down vertically towards the centre of the tunnel resulting in negative displacements which lie in the range of -33.4 (STRENGTH 1) to -69.3 mm (STRENGTH 3).

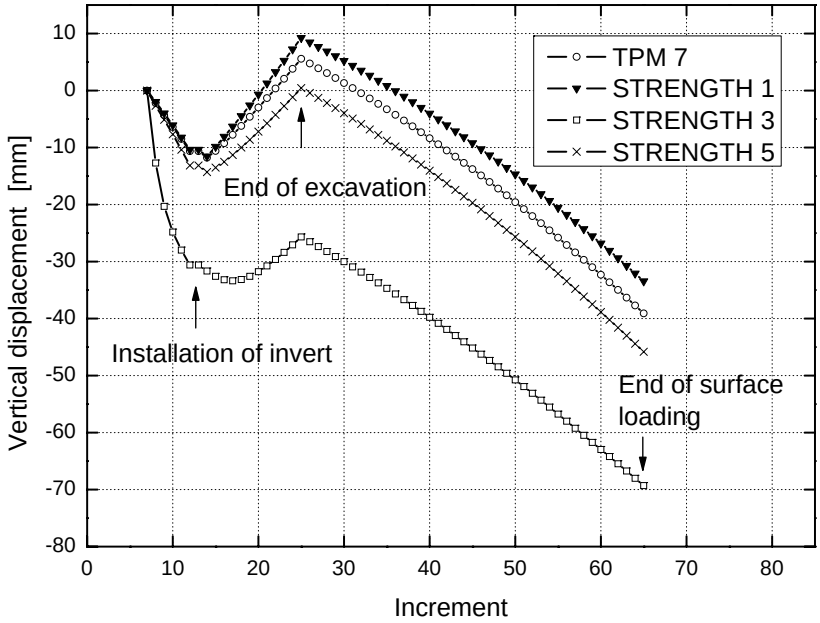



Figure 8.81: Vertical crown displacement for various developments of stiffness and strength adopting $K_o = 1.5$

Tab. 8.32 summarises the lining displacements of various points at the lining intrados at 28 days after the end of surface loading (Inc 100), taking into account creep, shrinkage and hydration temperature of the shotcrete. Results for run CREEP are very close to the ones from reference run TPM 7. An increase of about 3 to 5 mm can be expected for the tunnel crown and sidewall when considering shrinkage of shotcrete (run SHRINKAGE). However, for this run the invert displacement is reduced by 1.4 mm. A similar picture is obtained when investigating the effect of hydration temperature on the deformational behaviour of the lining (run TEMPERATURE). For the tunnel crown and sidewall an increase of about 1 to 2 mm has been calculated. The reduction for the lining displacement of the invert reaches 0.5 mm and is therefore negligible. In general, the biggest difference in lining displacement can be expected when coupling all the three time-dependent mechanisms in run C+SH+T. The vertical crown displacement reaches a value of 46.1 mm, which is 7 mm larger than for

run TPM 7. At the tunnel sidewall, the horizontal displacement increases from 0.7 to 4.8 mm. Once again, the vertical displacement of the lining invert is reduced by 2.2 mm taking a final value of 4.4 mm.

| Displacement | TPM 7 | CREEP | SHRINKAGE | TEMPERATURE | C+SH+T |
|---|---|---|---|---|---|
| Crown - $v$ (mm) | -39.1 | -39.8 | -44.4 | -40.4 | -46.1 |
| Sidewall - $u$ (mm) | -0.7 | -1.0 | -3.7 | -1.8 | -4.8 |
| Invert - $v$ (mm) | -6.6 | -6.4 | -5.2 | -6.1 | -4.4 |

Table 8.32: Lining displacements of performed analyses for creep, shrinkage and hydration temperature

For completeness, the vertical displacement of the temporary invert, which is installed in Inc 7, should be discussed here briefly. Tab. 8.33 summarises the results for the performed analyses with different constitutive behaviour for shotcrete. For the stiff linear elastic model (LE) the maximum displacements at the end of the bench excavation (Inc 12) are the smallest with 14.0 mm, followed by the non-linear approach (NL) with a value of 15.0 mm. Runs TPM 1 and STRENGTH 3 represent a very soft lining behaviour with a low stiffness and therefore displacements increase up to 20.1 mm. The shotcrete deformability (runs STRAIN 3 and 4) seems to have a minor influence on the behaviour of the temporary invert, compared to their reference run TPM 7 (15.6 mm).

| Run | Maximum vertical displacement $v$ of temporary invert (mm) |
|---|---|
| Linear elastic (LE) | + 14.0 |
| HME | + 15.5 |
| Non-linear (NL) | + 15.0 |
| TPM 1 | + 19.6 |
| TPM 5 | + 16.0 |
| TPM 9 | + 15.5 |
| STRENGTH 1 | + 15.4 |
| STRENGTH 3 | + 20.1 |
| STRENGTH 5 | + 16.6 |
| STRAIN 3 | + 15.7 |
| STRAIN 4 | + 15.8 |

Table 8.33: Maximum vertical displacement $v$ of temporary invert at the end of bench excavation (Inc 12)

#### 8.7.3.3 Excavation Type 3

In Fig. 8.82 the development of the horizontal displacements of the lining intrados at the left tunnel sidewall are shown for various analyses comparing simple elastic models with sophisticated time-dependent approaches. All runs have in common that during the excavation of the left side gallery the lining intrados is moving to the right towards the centre of the tunnel resulting in positive deformations. As expected, the stiff linear elastic model (LE) predicts the smallest displacement with a value of 14.4 mm in Inc 12. The HME approach is slightly softer and leads to a displacement of 16.4 mm. Including non-linearity of hardened shotcrete at 28 days makes a difference of about 1.6 mm, resulting in a total displacement of 16.0 mm. However, the time-dependent run TPM 1 shows a relatively large lining movement of up to 31.1 mm, governed by the low stiffness of the shotcrete during excavation. Runs TPM 9 tends to follow a similar behaviour as the HME approach, whereas TPM 5 predicts a slightly larger displacement of 18.0 mm. During the excavation of the right side gallery, this mechanism is reversed with the tunnel lining moving to the left and displacements reducing for all runs. In Inc 25 the linear elastic model results in a horizontal displacement of just 5.6 mm, whereas, the value for run TPM 1 is 25.8 mm. When loaded from the surface during Inc 26 to 66, the loading-displacement curves for all runs tend to be parallel to each other leading to a negative displacement of about -11.0 mm for runs LE, HME, NL and TPM 9. TPM 5 has a slightly smaller displacement in Inc 65 with a value of -8.5 mm. Run TPM

1 predicts positive displacement after placing the surface surcharge and leads to a horizontal movement of 8.2 mm. As noted in the previous case of excavation Type 2, the elapsed time $\Delta t$ in Inc 13, simulating the longitudinal distance between the left and right tunnel face and therefore different shotcrete ages of the tunnel shell, is of minor importance to the deformational behaviour of the lining and results vary within $\pm 4.0$ mm.

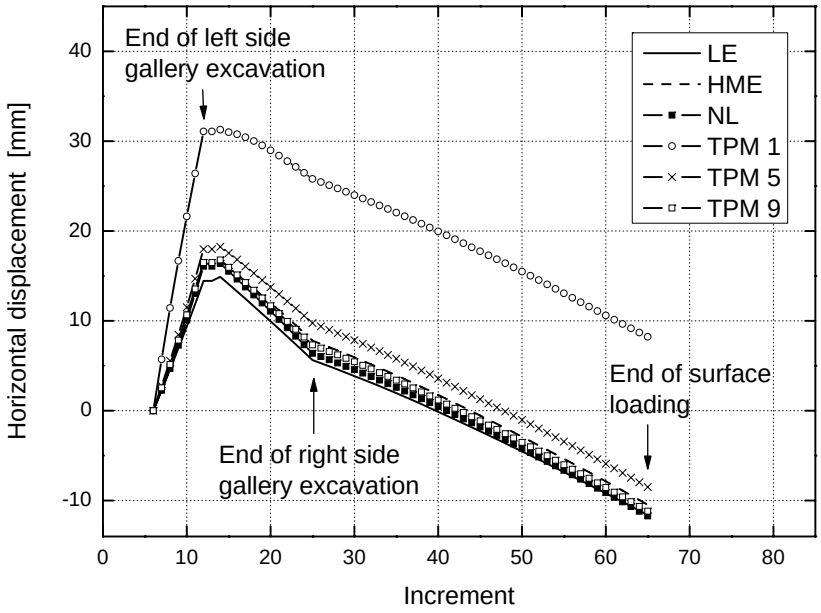



Figure 8.82: Horizontal displacements of left sidewall

Fig. 8.83 illustrates the development of the horizontal displacements of the lining intrados at the right tunnel sidewall, starting at the installation of the right shell in Inc 14. An interesting fact is that all runs, apart from run TPM 1, predict a positive lining movement to the right, where the linear elastic model (LE) and the HME approach show an almost identical displacement pattern, with a value of 5.2 to 5.6 mm in Inc 25 and 21.5 to 22.4 mm at the end of surface loading in Inc 65. Non-linear behaviour of hardened shotcrete (NL) leads to a larger displacement of 7.4 mm in Inc 25 and 24.5 mm in Inc 65. The displacement curve for run TPM 5 represents a somewhat softer lining behaviour. However, the deformational mechanism for run TPM 1 appears to be different than for the other analyses. During the excavation of the right side gallery, the right sidewall tends to move to the left towards the centre of the tunnel leading to a horizontal displacement of -16.0 mm at the end of excavation (Inc 25). During the surface loading the lining is pushed to the right again compensating almost all the previous deformation and resulting in a total displacement of 0.25 mm in Inc 65.

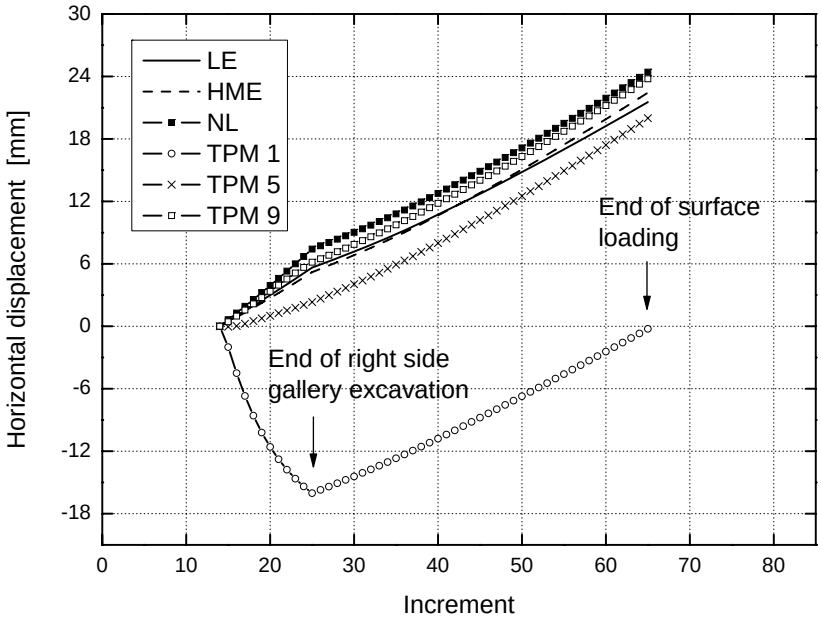



Figure 8.83: Horizontal displacements of right sidewall

The vertical displacements of the top intersection point of the temporary sidewall with the tunnel lining (see Fig. 8.17) during the course of excavation and surface loading are plotted in Fig. 8.84. As in the previous case in Fig. 8.83, almost all model predictions show a positive upwards movement of this particular point during the excavation of the left side gallery. However, this movement is the opposite for run TPM 1, which has a vertical displacement of -5.1 mm in Inc 12. The linear elastic model and the HME approach predict very similar results with 12.2 and 13.5 mm respectively. The largest displacement is obtained by the non-linear model (NL) with a value of 15.1 mm. Displacement values for TPM 5 and 9 lie in the range of 13.7 to 15.0 mm. During the excavation of the right side gallery, the upper part of the tunnel shell tends to move downwards towards the centre of the tunnel, where displacement values are located within -4.7 (NL) and -12.7 mm (TPM 5). Displacements according to run TPM 1 increase up to -42.6 mm. During the surface loading phase, these displacements increase further as the tunnel is pushed into the ground. In Inc 65 the linear elastic model (LE) predicts a vertical lining displacement of -44.1 mm and the HME approach -53.8 mm. The time-dependent runs TPM 5 and 9 show values of -57.4 and -51.4 mm respectively. The low lining stiffness of TPM 1 leads to the largest displacement value of -86.3 mm.

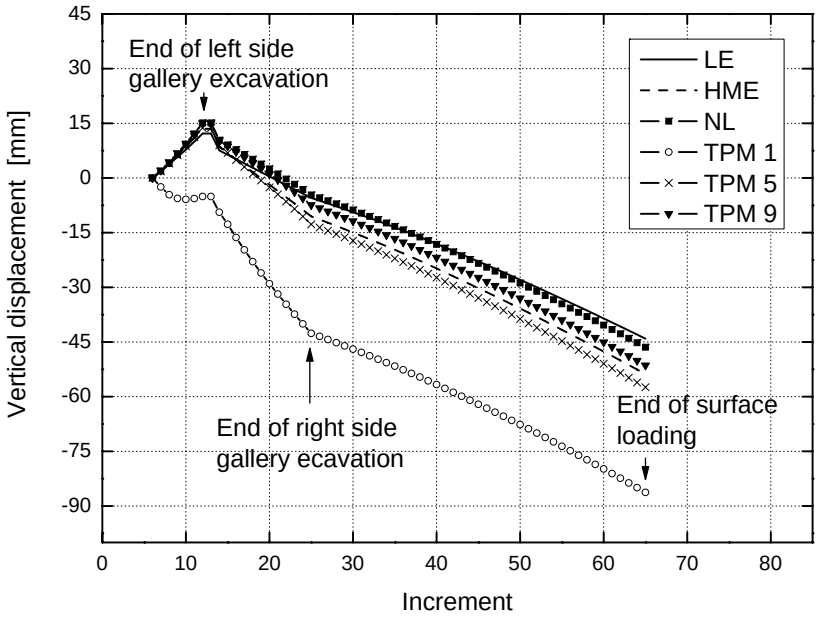



Figure 8.84: Vertical displacement of intersection point of temporary sidewall with tunnel lining

Fig. 8.85 investigates the influence of the development of the shotcrete stiffness and strength on the vertical displacements of the lining intrados located at the top intersection point between the temporary sidewall and the tunnel shell. It can be seen that run STRENGTH 3, with its retarded increase in stiffness ($s = 0.4$), shows a similar behaviour as run TPM 1 in Fig. 8.84. Reference run TPM 7, STRENGTH 1 and 5 tend to move upwards during the first excavation for the left side gallery leading to vertical displacements between 10.6 and 15.4 mm in Inc 12. At this stage of construction, STRENGTH 3 predicts a negative value of -9.8 mm. When excavation of the right side gallery is continued, the lining point moves vertically downwards for all the analyses. During the surface loading this movement is continued in the negative direction, leading to -49.4 mm for the slightly stiffer run STRENGTH 1 ($s = 0.1$) in Inc 65. The reduction of the stiffness by 25 % results in a vertical displacement that is 12 % larger (-62.2 mm) than the one from reference run TPM 7 (-55.4 mm) at the end of surface loading.

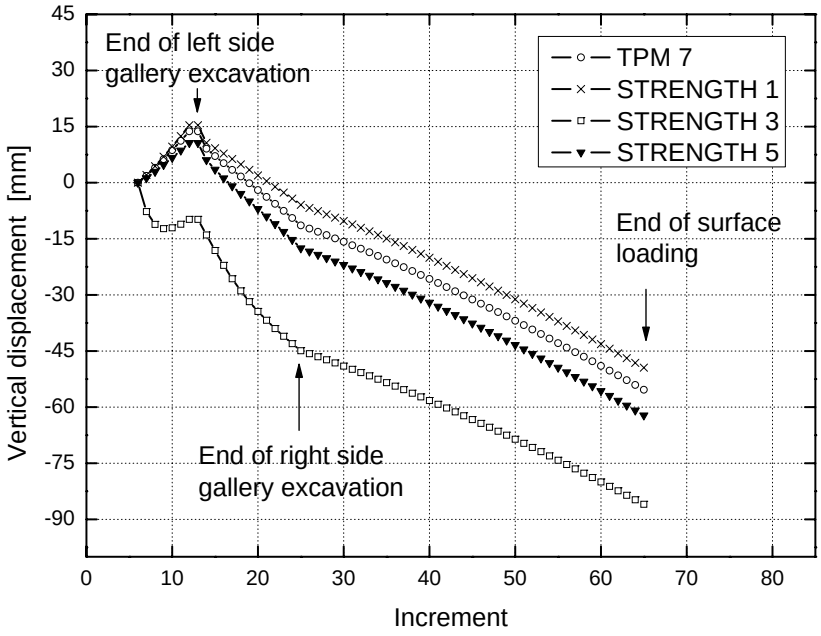



Figure 8.85: Vertical displacement of intersection point of temporary sidewall with tunnel lining for variousn developments of stiffness and strength

The aim of Fig. 8.86 is to show briefly the effect of the shotcrete deformability on the horizontal displacements of the lining intrados of the left tunnel sidewall. During the excavation of the left side gallery, no significant difference in the analyses is noticeable. Run TPM 7 shows a vertical displacement of 18.0 mm, whereas run STRAIN 4, representing a constant low peak strain, predicts a displacement of 16.9 mm. This difference becomes slightly more pronounced during the excavation of the right side gallery and the surface loading leading to a maximum difference of 1.4 mm in Inc 65.

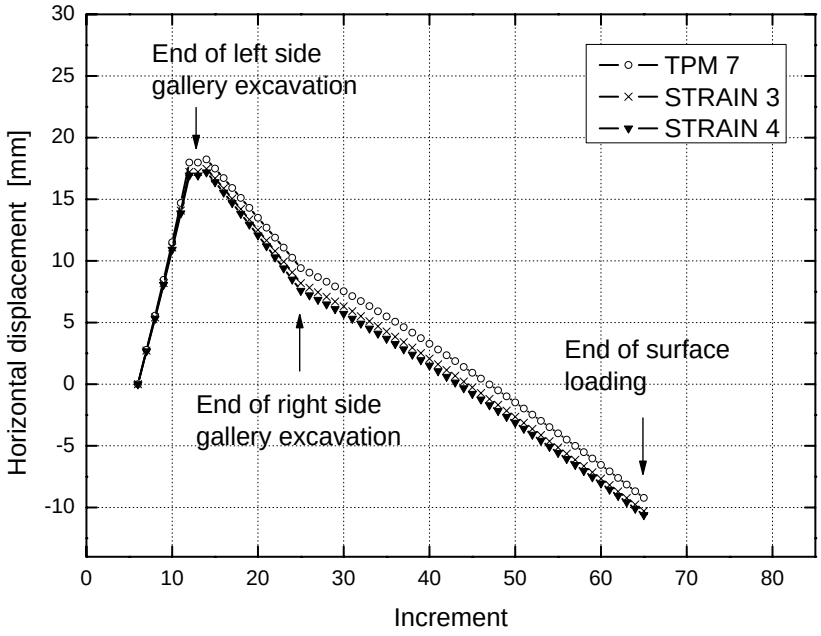



Figure 8.86: Horizontal displacement of left sidewall for various shotcrete deformabilities

Tab. 8.34 provides some information about the effect of creep, shrinkage and hydration temperature of the shotcrete on the lining displacement at various points of the tunnel shell. Results at 28 days after the end of surface loading (Inc 100) are compared with reference run TPM 7 (Inc 65). Surprisingly, the results taking into account creep of the young shotcrete show very little difference compared to run TPM 7. When considering shrinkage, the horizontal displacements at the left and right tunnel sidewall are reduced by 2.6 and 2.4 mm respectively. The vertical crown displacement is slightly larger, taking a value of 60.4 mm. The influence of hydration temperature on the deformational lining behaviour is slightly less pronounced. Horizontal displacements at both sidewalls reduce by roughly 1 mm and vertical displacements increase by 1.5 mm for the tunnel crown. Here again, the incorporation of all the three time-dependent mechanisms, i.e. creep, shrinkage and hydration temperature (run C+SH+T), has a bigger impact on the displacements for all the three points. At the left and right sidewall these displacements are reduced by 3.6 mm. An increase of 7.1 mm is predicted for the vertical displacement at the tunnel crown.

| Displacement | TPM 7 | CREEP | SHRINKAGE | TEMP. | C+SH+T |
|---|---|---|---|---|---|
| Left sidewall - $u$ (mm) | -9.2 | -9.0 | -6.6 | -8.2 | -5.4 |
| Right sidewall - $u$ (mm) | 19.9 | 19.7 | 17.5 | 19.1 | 16.3 |
| Crown - $v$ (mm) | -55.4 | -56.1 | -60.4 | -56.9 | -62.5 |

Table 8.34: Lining displacements of performed analyses for creep, shrinkage and hydration temperature

Finally, Tab. 8.35 contains a summary regarding the maximum horizontal displacement $u$ at the centre of the temporary sidewall at the intermediate construction stage Inc 12. The obtained values range from -29.0 (LE) to -45.0 mm (STRENGTH 3).

| Run | Maximum horizontal displacement $u$ of temporary sidewall (mm) |
|---|---|
| Linear elastic (LE) | - 29.0 |
| HME | - 32.9 |
| Non-linear (NL) | - 32.3 |
| TPM 1 | - 43.8 |
| TPM 5 | - 35.3 |
| TPM 9 | - 34.0 |
| STRENGTH 1 | - 33.6 |
| STRENGTH 3 | - 45.0 |
| STRENGTH 5 | - 36.8 |
| STRAIN 3 | - 34.9 |
| STRAIN 4 | - 34.5 |

Table 8.35: Maximum horizontal displacement $u$ at the centre of the temporary sidewall at the end of the left side gallery excavation (Inc 12)

### 8.7.4 Soil stresses

Tunnel excavation leads to subsurface movements and rearrangement of stresses in the ground adjacent to the tunnel. These changes in effective stresses and pore water pressures will be discussed in detail in the course of this section for excavation Type 1, adopting both $K_o$-profiles. Furthermore, results will be shown for two sets of analyses, where the mechanical behaviour of the lining is of crucial importance: the linear elastic model LE, representing a very stiff shotcrete shell, and run TPM 1, where the behaviour of the tunnel lining is mainly governed by the material properties of very young shotcrete.

Fig. 8.87 shows the contours of horizontal effective stresses in the ground near the tunnel opening at the end of excavation (Inc 10) for the linear elastic model LE (top) and run TPM 1 (bottom), assuming $K_o = 0.5$. For the linear elastic approach, horizontal stresses near the tunnel crown rise up to -130 kPa (compared to -82 kPa for the initial stress state), which is almost the same value as for the tunnel sidewalls (-140 kPa). Near the invert of the tunnel effective stresses increase up to -200 kPa. Due to the large displacement of the lining for run TPM 1, the stress conditions after excavation are different. Effective horizontal stresses at

the tunnel crown and invert increase significantly showing values of -650 kPa. A similar value of -580 kPa is obtained for the tunnel sidewall, compared to -102 kPa for the initial stress conditions.

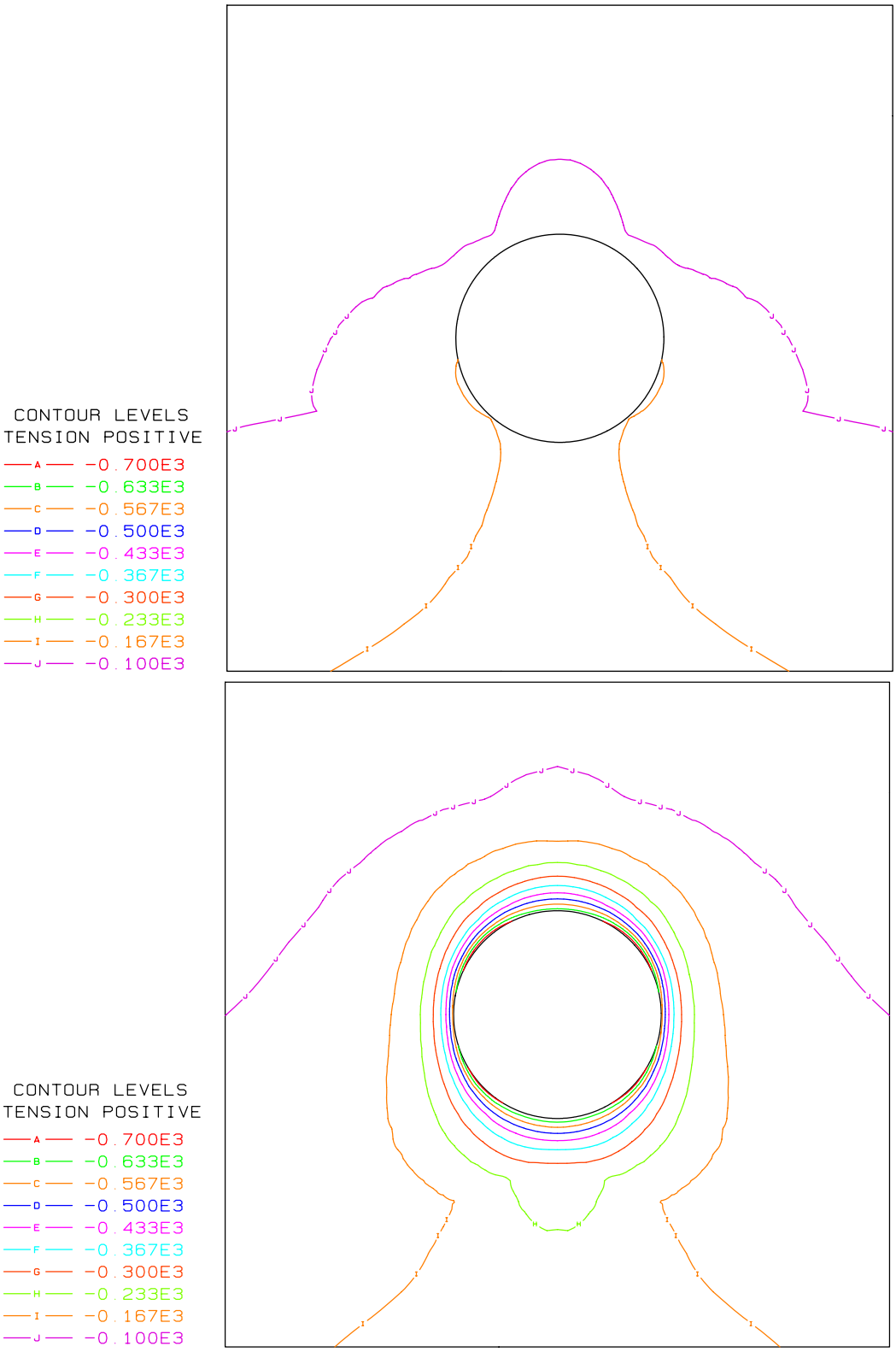



Figure 8.87: Effective horizontal stresses in ground after excavation of tunnel (Inc 10) for linear elastic model (top) and run TPM 1 (bottom) adopting $K_o = 0.5$

In Fig. 8.88 the contours of the vertical effective stresses in the ground after tunnel excavation (Inc 10) are illustrated for both lining models. For the linear elastic model LE (top), the vertical stresses near the tunnel crown reduce to -110 kPa compared to an initial vertical stress of -163 kPa. A similar reduction is achieved for the tunnel invert, with a vertical effective stress of -180 kPa after excavation. As expected, the stresses near the tunnel sidewalls show an increase from -204 kPa up to -380 kPa. Once again, the stress rearrangement for run TPM 1 is highly influenced by the large displacements of the lining due to the soft behaviour of shotcrete at early ages. Vertical effective stresses go up to -260 kPa for the tunnel crown and invert. A high stress value is obtained for the tunnel sidewalls reaching almost -1300 kPa, with the soil being close to failure.

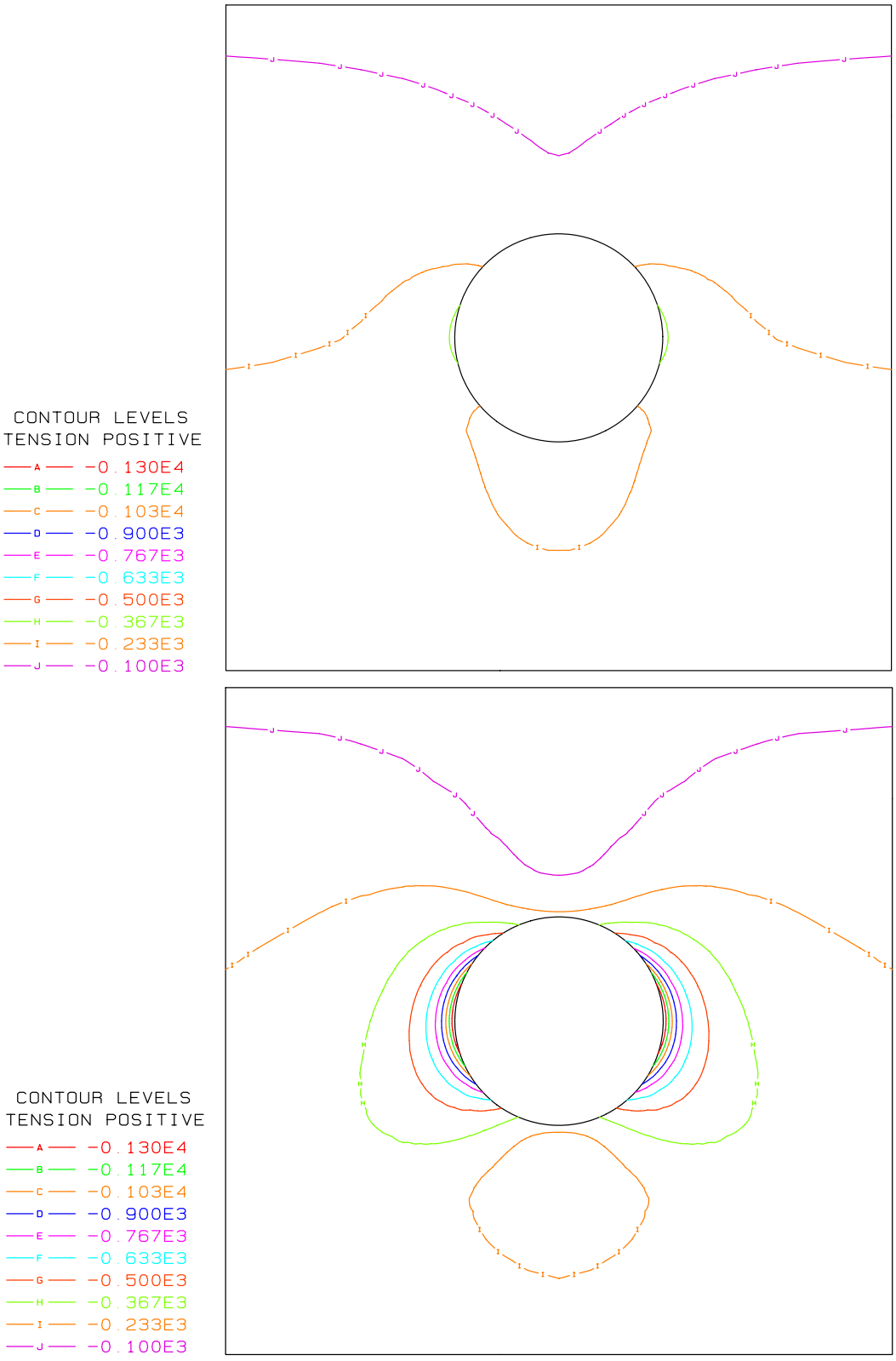



Figure 8.88: Effective vertical stresses in ground after excavation of tunnel (Inc 10) for linear elastic model LE (top) and run TPM 1 (bottom) adopting $K_o = 0.5$

The contours of the sub-accumulated pore water pressures induced by tunnel excavation (i.e. the pore water pressures at Inc 0 subtracted from the pore water pressures at Inc 10) are plotted for the linear elastic lining model LE (top) and run TPM 1 (bottom) in Fig. 8.89, assuming $K_o = 0.5$. It can be observed that due to the inwards movement of the tunnel lining, positive changes in pore water pressures (i.e. suctions) are induced into the ground in the close vicinity of the tunnel. This pressure change is of about 50 kPa near the tunnel crown assuming linear elastic shotcrete behaviour (LE) and 162 kPa for the tunnel invert. An intermediate pressure change of 105 kPa can be expected in the vicinity of the tunnel sidewall. The results from run TPM 1 show in general a similar trend as the LE approach by introducing positive changes in pore water pressures in the ground due to the movement of the tunnel lining. However, since these lining movements are relatively large, the changes in pore water pressure are of a much larger magnitude and appear to be unrealistic. Near the tunnel crown a pressure change of 380 kPa is predicted by run TPM 1, which is a similar value as for the tunnel invert (400 kPa). However, in the ground near the tunnel sidewall a larger change in pore water pressure of 690 kPa is obtained for run TPM 1. As can be seen in Fig. 8.89, these larges pressure changes reduce quickly within the first 2 to 4 metres of distance from the tunnel opening and tend to stabilise to a smaller value of about 70 kPa.

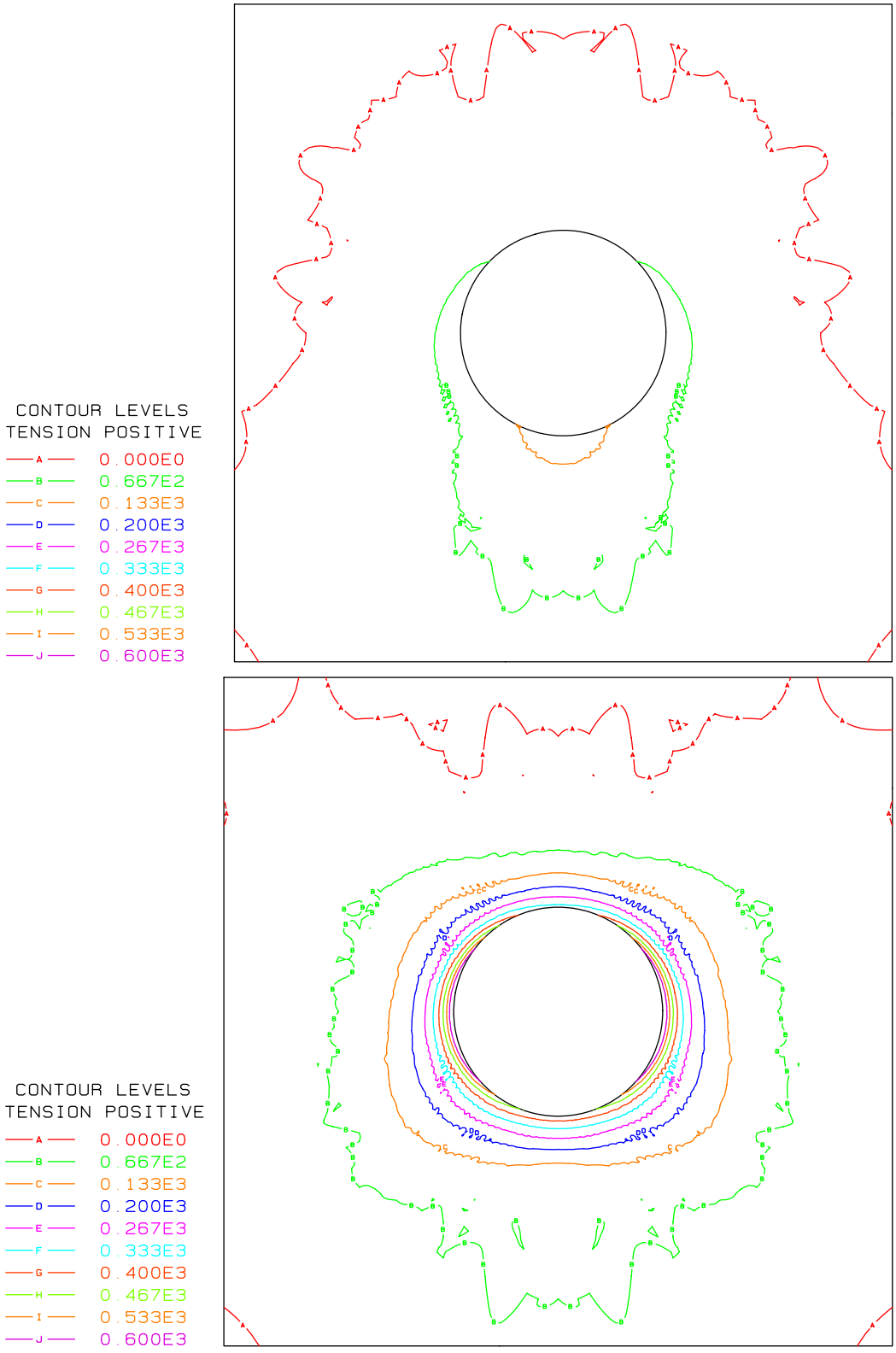



Figure 8.89: Sub-accumulated pore water pressures in ground after excavation of tunnel (Inc 10) for linear elastic model (top) and run TPM 1 (bottom) adopting $K_o = 0.5$

Fig. 8.90 contains the contours of the horizontal effective stresses at the end of tunnel excavation (Inc 10) for the linear elastic model LE (top) and run TPM 1 (bottom), adopting a $K_o$-profile of 1.5. Applying a relatively stiff lining behaviour in the linear elastic approach LE leads to an increased horizontal effective stress in the ground near the tunnel crown of -510 kPa. In contrast, the horizontal stresses near the tunnel sidewall are reduced to -190 kPa compared to -306 kPa for the initial stress state before excavation. Results show an increase in horizontal stresses near the tunnel invert with a predicted value of -610 kPa, compared to an initial stress of -368 kPa. Ground stresses are of a much larger magnitude when simulating the tunnel lining with very young shotcrete in run TPM 1. For the tunnel crown, the horizontal effective stresses rise up to -1150 kPa and to -1300 kPa in the vicinity of the tunnel invert. Furthermore, run TPM 1 predicts an increase in horizontal stresses for the tunnel sidewall with a value of -420 kPa after excavation in Inc 10.

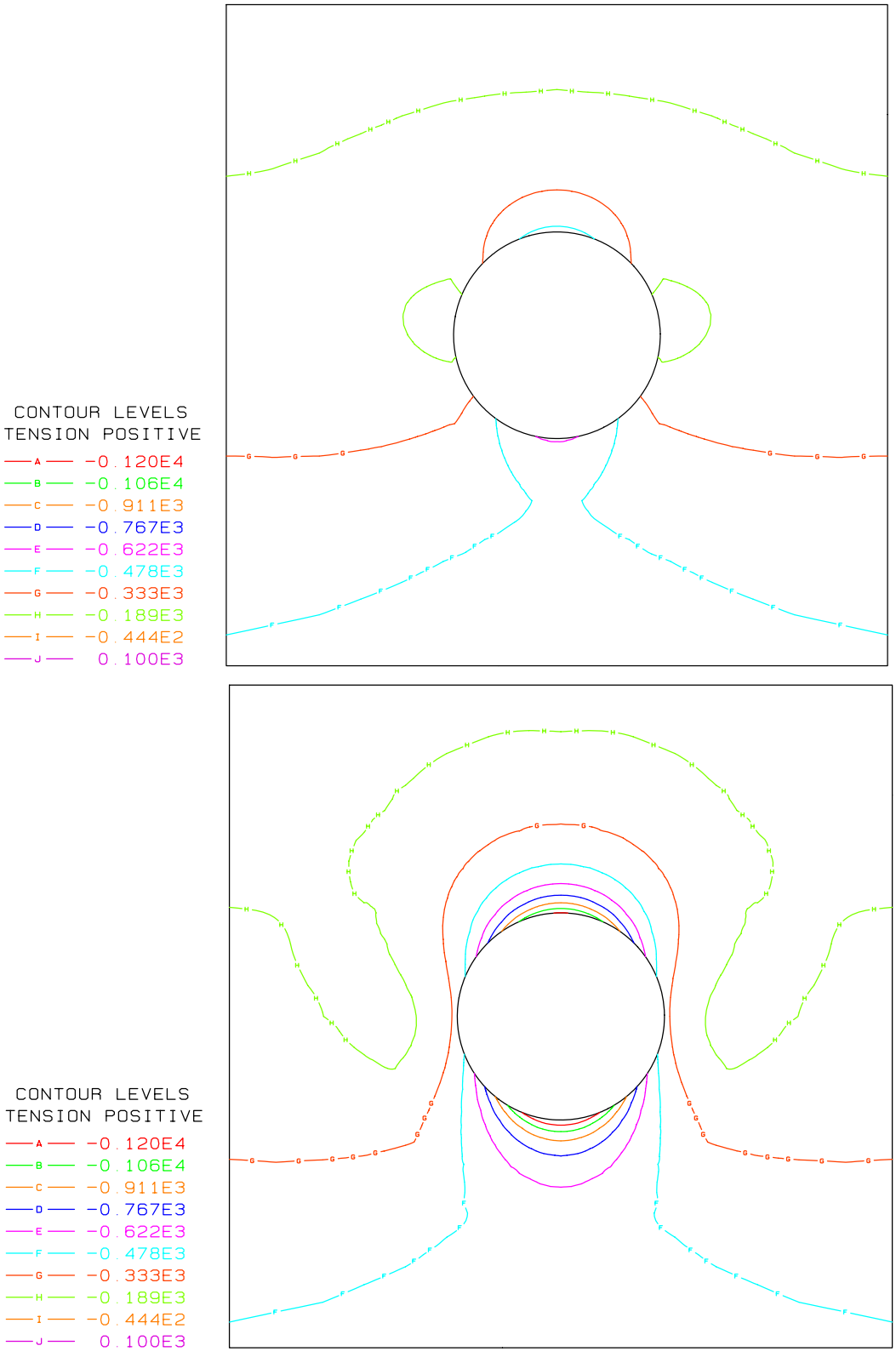



Figure 8.90: Effective horizontal stresses in ground after excavation of tunnel (Inc 10) for linear elastic model (top) and run TPM 1 (bottom) adopting $K_o = 1.5$

The contours of the vertical effective stresses for $K_o = 1.5$ are illustrated in Fig. 8.91. In the case of modelling the tunnel lining linear elastic (LE), the vertical stresses near the tunnel crown increase somewhat from -163 kPa for the initial stress conditions to -200 kPa at the end of excavation. A slightly smaller increase occurs at the tunnel invert, where vertical effective stresses of -260 kPa are predicted. At the tunnel sidewall, these stresses reach a value of -350 kPa. Stress conditions are significantly different for run TPM 1 caused by the extensive lining movement at early shotcrete ages. Near to the tunnel crown the vertical effective stresses increase up to -460 kPa. A similar stress rise occurs for the tunnel invert with a stress value of -550 kPa at the end of excavation. A substantial increase in vertical effective stresses with run TPM 1 occurs adjacent to the tunnel sidewall, reaching a value of -910 kPa.

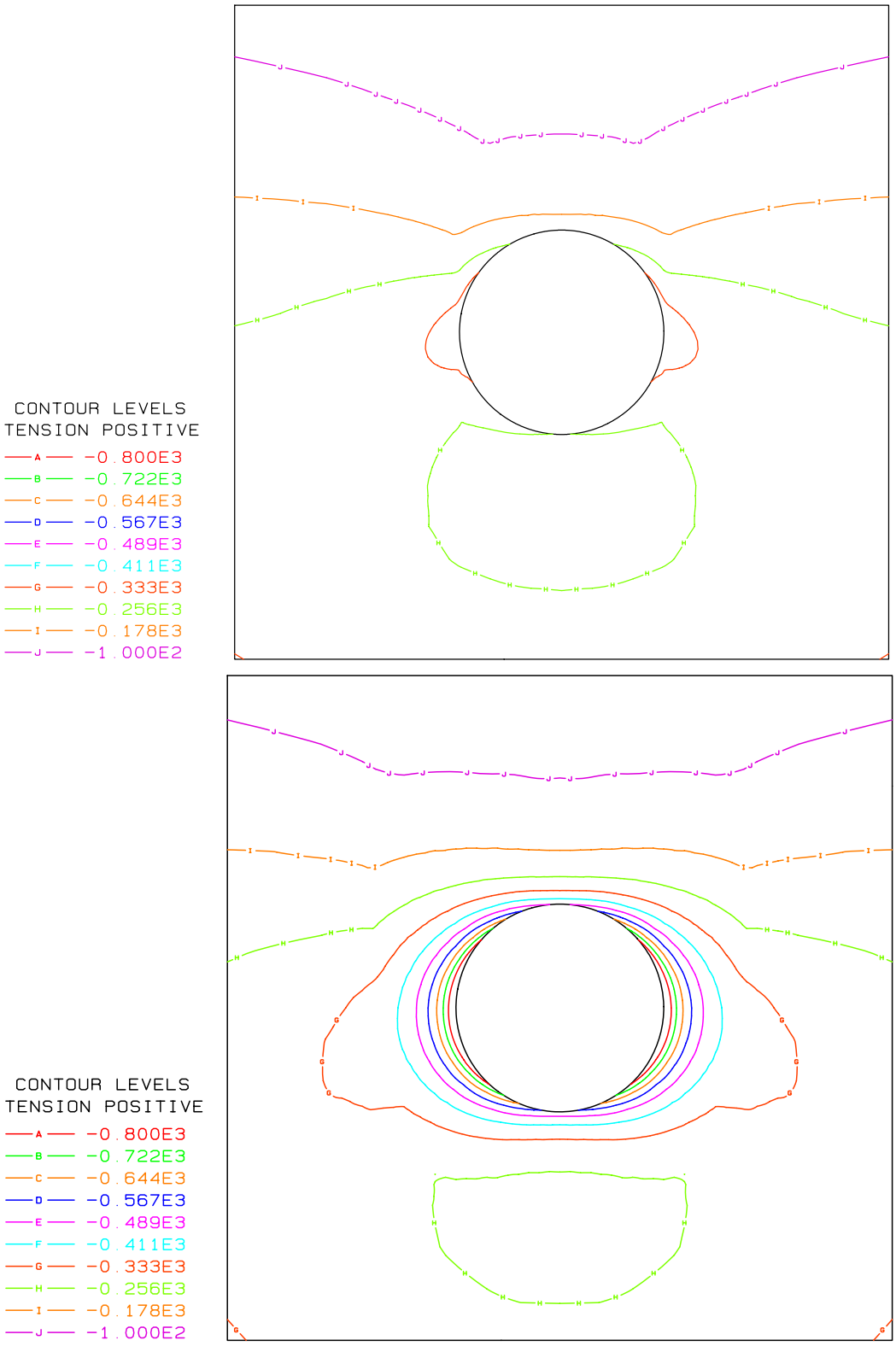



Figure 8.91: Effective vertical stresses in ground after excavation of tunnel (Inc 10) for linear elastic model LE (top) and run TPM 1 (bottom) adopting $K_o = 1.5$

Finally, the changes in pore water pressures in the ground from Inc 0 to Inc 10, adopting $K_o = 1.5$, are depicted in Fig. 8.92. Once more, the contours of the sub-accumulated pore water pressures for the linear elastic lining model (top) are compared with results from run TPM 1 (bottom). As in the previous case of $K_0 = 0.5$, positive changes in the pore water pressures (i.e. suctions) in the ground near the tunnel opening are to be expected due to the inwards movement of the tunnel lining. Applying the linear elastic model (LE) leads to a pressure change of 150 kPa for the tunnel crown and 120 kPa for the tunnel sidewalls. Near the invert of the tunnel these changes are larger in magnitude and reach a value of 230 kPa. A dramatic change in pore water pressure was obtained for run TPM 1. Near the tunnel crown the pressure change rises up to 540 kPa and 460 kPa for the tunnel sidewall. However, an extreme value was predicted for the pore water pressures in the vicinity of the tunnel invert. A positive pressure change of up to 700 kPa is introduced to the ground. In general, this high induced suctions tend to decrease with increasing distance from the tunnel opening and stabilise to a more realistic value of 50 kPa.

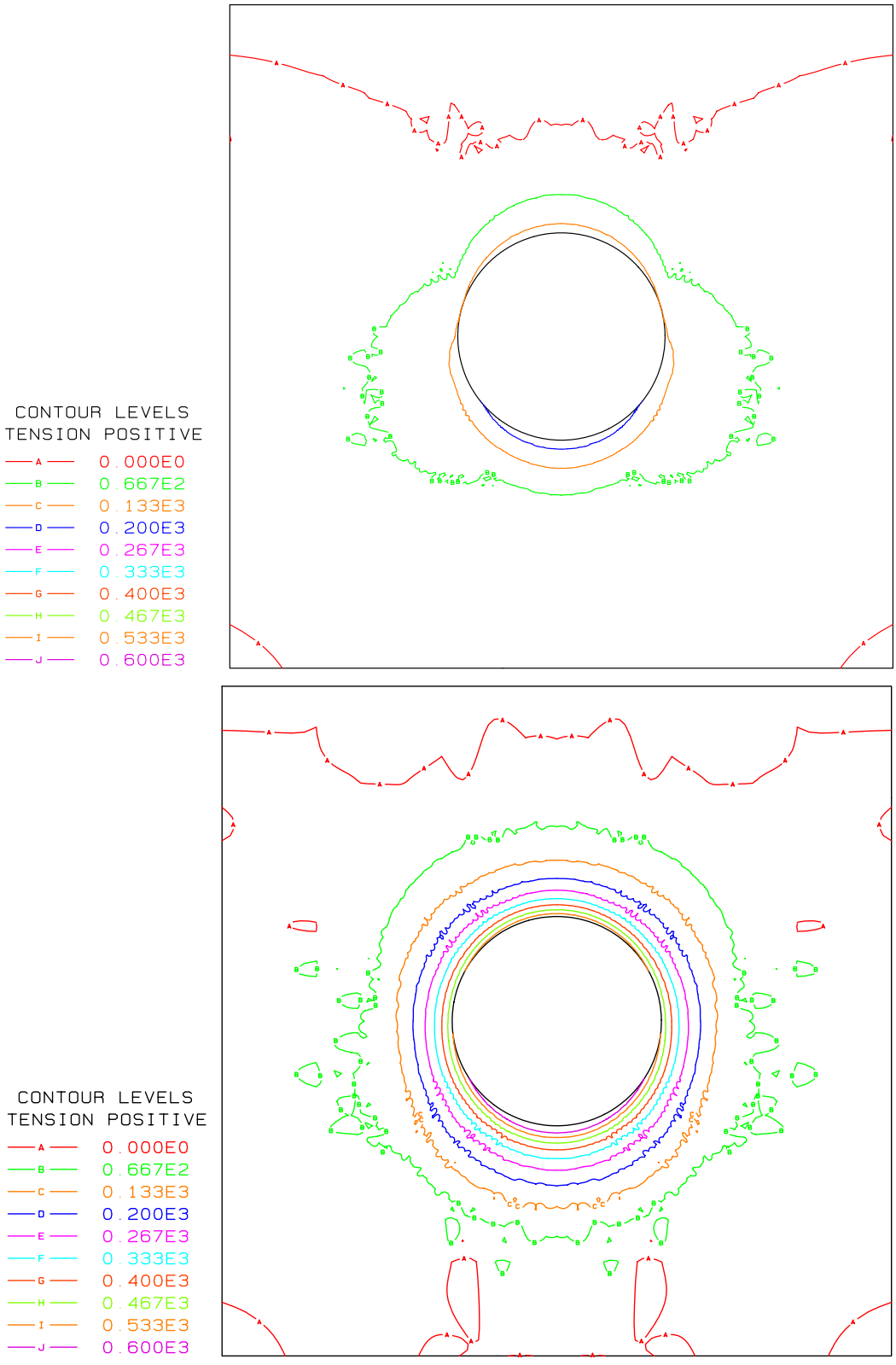



Figure 8.92: Sub-accumulated pore water pressures in ground after excavation of tunnel (Inc 10) for linear elastic model (top) and run TPM 1 (bottom) adopting $K_o = 1.5$

From these observations it can be concluded that the deformational behaviour of the tunnel lining highly affects the rearrangement of stresses and pore water pressures in the ground in the vicinity of the excavated tunnel. Since the movement of a tunnel shell is strongly influenced by the material properties of the early age shotcrete, the elapsed time during tunnel construction plays an important role. However, it was shown that for very young shotcrete and quick loading conditions (run TPM 1) quite unrealistic stresses and pore water pressure changes were predicted as a consequence of the associated high volume loss. For further analyses it is therefore recommended, to simulate this interaction between soil and tunnel lining in a more sophisticated way in 3D (and probably with the use of interface elements) in order to predict realistic results regarding the effective stresses and pore water pressures in the ground.

## 8.8 Summary

This chapter presented results of the 2D finite element analyses of a typical tunnel to be excavated under undrained conditions in London Clay. In this investigation, the mechanical behaviour of the installed shotcrete tunnel lining was of special interest and therefore the newly developed constitutive model for sprayed concrete, presented in Chapter 7, was adopted to simulate the complex material behaviour of shotcrete. Results from these analyses were compared with much simpler approaches for the simulation of sprayed concrete that are still state-of-the-art in engineering practice, i.e. linear elastic material behaviour and the Hypothetical Modulus of Elasticity (HME). Furthermore, the simulation of tunnel excavation followed three different excavation schemes (full face, bench-invert and sidewall drift), each of them leading to different stress generations within the tunnel lining. Construction of a possible structure above the tunnel was considered by applying some surface surcharge, which results in heavy loading of the tunnel shell. The following aspects were adressed in the extensive parametric study performed:

- In the case of full face excavation of the tunnel two $K_o$-profiles with a value of 0.5 and 1.5 have been adopted leading to different initial stress conditions in the soil before the start of excavation. It was shown, how this difference influences the mechanical behaviour of the tunnel lining.

- Two different types of shotcrete have been adopted: plain shotcrete in the case of full face excavation and steel-fibre reinforced sprayed concrete for staged tunnel excavation. The difference in material behaviour is accounted for by a modification of the tensile post-peak behaviour of each individual shotcrete type.

- Material parameters for young shotcrete were taken from various experimental data available in the open literature. This model calibration involved the realistic representation of the increase in stiffness and strength and the development of shotcrete deformability with time.

- The elapsed time during tunnel excavation and surface loading, and therefore the loading rate of the shotcrete, was one of the main parameters to be investigated. In the calculations, shotcrete ages at the end of the complete construction process ranged from only 2 hours up to 2 months, simulating the transition from fast to slow construction.

- The model parameters were varied in a controlled manner in order to capture the large scatter usually present in most of the experimental data for young shotcrete. Furthermore, an attempt was made to account for uncertainties regarding the material quality of shotcrete that can often be encountered in engineering practice.

- Additional analyses focusing on creep, shrinkage and hydration temperature induced deformation of sprayed concrete have been carried out for all of the three excavation types. Unfortunately, material parameters for these calculations had to be estimated from the very limited amount of experimental data available in the literature.

- The mechanical behaviour of the tunnel lining has been analysed extensively by discussing in detail the obtained results with respect to stress distributions within the shotcrete shell for selected cross sections, the maximum utilization factor (= stress level) during construction as a measure of safety against failure and the displacements of particular points on the lining intrados.

- Possible damage to adjacent buildings and surface structures due to tunnel excavation has been investigated by studying the predicted surface settlement troughs and the volume loss obtained at the end of excavation.

- Stress rearrangements and changes in pore water pressures in the ground as a consequence of tunnel construction have been discussed for the soil immediately adjacent to the tunnel and the interaction problem of soil-lining has been addressed.

# Chapter 9

# Summary and conclusions

## 9.1 Introduction

The main aim of this research project was to obtain a better understanding of NATM tunnelling in soft ground conditions by applying the finite element method, with a particular focus on the time-dependent, mechanical behaviour of the shotcrete tunnel lining. Therefore, it was necessary at first to perform an extensive literature review in order to study the fundamental characteristics of shotcrete and how material properties influence its behaviour. The next step in the research involved the choice of a proper constitutive model for sprayed concrete for a realistic description of the mechanical behaviour in multiaxial loading conditions. The methodology followed was to choose a well-known failure criterion that is capable of capturing the important features of the material response of hardened concrete, the Chen & Chen (1975) concrete model. This model was then improved by adopting two independent yield surfaces for compression and tension and introducing time-dependent material parameters for stiffness, strength and deformability. Furthermore, the model accounts for the complex aspects of creep, shrinkage and hydration temperature of the cement paste at early ages. Although published data for young shotcrete covering a complete set of tests is very hard to find in the literature, it was possible to calibrate the model in a reasonable and satisfactory way. The developed constitutive model for shotcrete was implemented into the Imperial College Finite Element Program (ICFEP) adopting robust numerical algorithms and was successfully used in the numerical analysis of different tunnel excavations in London Clay. The main conclusions that can be drawn from this research project are summarised in the following sections.

## 9.2 General remarks

A basic knowledge about material technology, installation techniques and the main mechanical characterstics of shotcrete are of great importance for a detailed understanding of the behaviour of shotcrete in tunnelling. Based on current literature the following key facts can

be summarised:

- Sprayed concrete is one of the main support elements for tunnels driven according to the principles of the New Austrian Tunnelling Method (NATM). Directly after excavation, shotcrete is sprayed at high pressure onto the tunnel walls providing temporary stability to the opening. It is usually reinforced with conventional wire mesh or lattice girders, but there is a tendency towards the innovative use of steel-fibres as reinforcement for mechanical, practical and economical reasons.

- Shotcrete can be seen as a special type of concrete since casting and compacting are performed in one single step. As any conventional cast concrete, shotcrete consists of cement, aggregates and water. Each of these components has an important impact on the mechanical behaviour of the shotcrete and has to be addressed in a proper mix design. Additives such as accelerators, plasticisers and silica fume are commonly used to change certain material properties, but they have to be treated with care.

- For the installation of shotcrete two different techniques exist - the dry-mix and the wet-mix process. Both technologies differ significantly in material preparation, each of them having its advantages and disadvantages. However, the tendency in tunnelling is clearly towards the wet-mix process due to its better control of the shotcrete quality (in particular of the water-cement ratio).

- The spraying technique is of great importance for achieving good material quality and this requires excellent skills and training of the nozzle-operator. Rebound of shotcrete is not only an economical loss but influences as well the mechanical behaviour of the material. It leads to a slightly richer cement mix of the in-situ material and this has to be taken into account in the mix design.

- Testing of young sprayed concrete at early ages is a difficult task to perform and no commonly agreed techniques exist in the literature. Usually, shotcrete samples are taken from the tunnel lining or are sprayed into boxes under field conditions, where the compressive strength of the material is the main parameter of interest in the design. For fresh shotcrete penetration needles and pull-out tests are often used to estimate the compressive strength of the material at early ages of cement hydration.

- Hardened shotcrete in uniaxial compression and tension shows a highly non-linear material behaviour, where crushing and cracking of the concrete govern the post-peak behaviour. Increased compressive strengths can be expected for concrete in biaxial and triaxial loading conditions, leading to smooth yield and failure surfaces. From the available data in the literature it is difficult to quantify any anisotropy of shotcrete that might be expected due to the spraying process.

- Shotcrete at early ages shows a relatively plastic and ductile material response with low stiffness and strength. Furthermore, higher strain limits can be achieved due to the

increased deformability of shotcrete at early stages of cement hydration. With curing time, material behaviour becomes more and more brittle associated with an increase in stiffness and strength. However, compressive and tensile strains at peak and failure strengths reduce during cement hydration. The effect of compressive preloading of shotcrete samples at early ages on the development of the compressive strength at later stages is not clear. In the literature both types of results can be found, i.e. an increase and a reduction in the strength values.

- Creep and relaxation are important aspects in shotcrete behaviour related to "time", depending on various factors, such as loading age, stress level, temperature, moisture conditions and concrete composition. It is believed that creep in tunneling leads to a reduction in the expected lining stresses and is therefore of a beneficial nature. Deformations of young shotcrete that occur due to shrinkage and increased hydration temperature might be important to consider in a realistic tunnel lining design, since these two phenomena can lead to cracking of the shotcrete shell. Their origin lies within the cement paste of the concrete and can be addressed in the mix design.

- A large number of empirical models based on experimental data exist for modelling concrete taking into account the non-linear material behaviour before peak. However, one big drawback is, that these models focus mainly on uniaxial stress conditions in compression and tension and are difficult to use in a numerical analysis. Nonetheless, simple concrete models have been developed within the framework of elasto-plasticity that are capable of reproducing the main characteristics of the material behaviour in multiaxial loading conditions. One of these models is the Chen & Chen (1975) concrete model, where the material behaviour in compression and tension is governed by two yield surfaces. At the onset of plastic deformation these two surfaces move together simultaneously in the principal stress space and isotropic strain-hardening controls the material behaviour before reaching peak.

- Cracking of concrete in tension is a relatively difficult phenomenon to model, since in reality it is a highly discrete and localized problem that occurs in a concrete structure. For simulating cracking in a numerical analysis two different approaches exist, i e. the discrete and the smeared crack model. However, when treating cracking of concrete within the framework of continuum mechanics, severe problems that are usually associated with strain-softening materials arise. A simple approach based on fracture energy was presented to avoid spurious mesh dependency of the results obtained in this thesis.

- No well accepted framework exists in the literature for the modelling of concrete creep and in particular for young shotcrete at early ages, which is a very creep active medium. Apart from some basic mathematical functions, in most of the cases, a combination of rheological units serves for the calculation of creep deformation in concrete structures (Kelvin-, Maxwell- and Burger-model). By establishing complex viscosity and stiffness

functions it is possible to fit model predictions to uniaxial compressive test data. However, very limited information is available for the extension of creep to 3D or how to deal with creep of concrete in tensile stress conditions.

- Three simple models for predicting shrinkage deformation of concrete have been presented. They are all based mainly on experimental data and take into account factors such as relative humidity, concrete strength in compression, geometry of the structure to be investigated and concrete composition. The modelling of the increase in temperature due to cement hydration in hardening concrete or shotcrete is a complex process mostly performed for the analysis of relatively thick concrete structures. Little information is available in the literature on how to incorporate these temperature effects in a constitutive model for the practical analysis of shotcrete tunnel shells.

## 9.3 A constitutive model for shotcrete

The constitutive model for sprayed concrete developed in this research project is formulated within the framework of elasto-plasticity and is generalised for the three-dimensional stress space. Crack formation of the shotcrete under tensile stresses is taken into account by applying the smeared crack concept and therefore cracks are treated as plastic strains. Two independent yield surfaces govern the mechanical behaviour under compression and tension and are described mathematically with the geotechnical stress invariants $p$, $J$ and $\theta$. These yield surfaces expand and contract during loading, which is controlled by non-linear plastic strain hardening and softening in the post peak regime, following normalised uniaxial stress-strain curves. This normalisation is performed in terms of the peak plastic strains and strengths since the material properties of the shotcrete are gradually changing with time. In order to avoid the strong mesh dependency typical for strain softening materials, the softening parameters are related to the element size by applying a fracture energy concept. With the help of a characteristic length of the finite element and the tensile and compressive fracture energy it is ensured, that the same amount of energy is released within the element upon complete crack opening or crushing.

As mentioned earlier, the main material parameters governing stiffness and strength are time-dependent and vary according to well established equations taken from widely accepted concrete standards. Making the compressive and tensile strain limits of the hardening/softening curves time-dependent accounts for the fact, that shotcrete at early ages appears to have the ability to withstand large strains without being completely damaged. Furthermore, the model takes into account that young shotcrete at early ages is a very creep active material. A uniaxial creep law, based on a Newton dashpot and including a time-dependent function for the shotcrete viscosity, was extended for the three-dimensional stress and strain space by assuming a creep plastic potential. Shrinkage of sprayed concrete represents a certain risk for early age cracking and is considered within the developed constitutive

model. Its mathematical formulation is given according to a standard shrinkage law taken from the American concrete code. Finally, the model formulation includes temperature induced deformations that occur due to the increase in temperature during cement hydration. In a series of numerical tests on a single element it was shown that the model is capable of reproducing various types of experimental tests such as uniaxial stress-strain curves in compression at various shotcrete ages, creep tests or shrinkage measurements.

## 9.4 Conclusions from tunnel analyses

A typical tunnel construction in London Clay (undrained conditions) following three different excavation schemes has been simulated within this thesis. The focus was on the mechanical and time-dependent behaviour of the shotcrete shell, which was modelled with the newly developed constitutive model for sprayed concrete. The obtained results were then compared with much simpler approaches for modelling the tunnel lining behaviour (linear elastic and HME). The following conclusions can be drawn:

- The overall system behaviour during tunnel construction and surface loading strongly depends on the initial stress conditions in the ground before excavation. Therefore, the adoption of a correct $K_o$-profile is of crucial importance as it controls the deformation of the tunnel lining and the predicted surface settlements. With a $K_o$ value greater than 1, typical for overconsolidated clays, the tunnel lining tends to oval to the vertical during excavation, but the bending direction changes during the surcharge loading. As a consequence, a relatively large amount of elastic deformation is introduced in the shotcrete shell since the stress path is reversed and travels through the elastic area of the adopted yield surfaces.

- The factor "time" plays a key role in tunnel construction and should be considered realistically in a finite element analysis. The loading rate of the shotcrete is controlled by the elapsed time during excavation and surface loading, leading to a complex stress-strain history within the tunnel lining. From a numerical point of view it is important to investigate how plastic strain hardening and softening of the material occurs in combination with the development of the shotcrete parameters with time. It can be concluded that the proper choice of a hardening parameter for a time-dependent material such as shotcrete is of crucial importance.

- Surface settlements and volume loss seem to be highly influenced by the constitutive model adopted for simulating the tunnel lining. The stiffness of the shotcrete shell is one of the main parameters that controls the surface settlement behaviour. Sprayed concrete at early ages represents a very soft material and hence the predicted surface settlements can increase resulting in a volume loss that is above a certain target value. However, with increasing shotcrete age the developed stiffness is sufficient to reduce

surface settlements to an acceptable limit. A rapid ring-closure in the case of staged tunnel construction should be aimed for as highlighted in the literature.

- Regarding the stress distribution within the lining it can be concluded that young shotcrete does not develop any appreciable bending stiffness and the overall mechanical behaviour is governed mainly by hoop compression. This fact is particularly pronounced for the full face excavation, where the lining acts as a perfect ring without any imperfections or geometrical irregularities. Furthermore, the absolute values of these compressive stress states are at a relatively low level, since the strength of the shotcrete has not fully developed at early stages of cement hydration. However, with increasing curing time (or elapsed time during construction), the material behaviour becomes more and more brittle and significant bending will be introduced. This can lead to cracking (tensile softening) of the shotcrete shell when heavily loaded.

- It was observed that plasticity of the shotcrete plays an important role when modelling young shotcrete. Already during the first increments of excavation most of the Gauss points across a lining section touch the current yield surface and plastic deformations are introduced. Plasticity becomes much less pronounced for older shotcrete, occuring mainly under heavy surface loading conditions.

- The formulation of normalised hardening parameters allows the stress level (or utilization factor) of a particular Gauss point to be established relatively easily. When tunnel construction is performed fast, relatively high compressive stress levels have been observed in all the analyses, being close to peak or even slightly beyond. However, with increasing time during excavation and loading these stress levels reduce significantly to a fairly low level. Some of the observed mechanisms of behaviour of the tunnel lining were such, that a switch from a compressive to a tensile stress state took place, which causes a risk of cracking.

- Non-linearity of the stress-strain behaviour of the young shotcrete represents an important factor when simulating tunnel construction. Particularly the non-linear hardening in compression and the tensile softening are of great importance. However, when modelling the tunnel lining with the material properties of hardened shotcrete at 28 days, almost no difference has been observed during excavation when comparing results with the linear elastic approach. The difference is more pronounced after placing the surface loading when tensile cracking was introduced in some of the tunnel cross sections due to the heaviy loading conditions.

- When performing a staged tunnel construction the connections between the tunnel lining and some temporary structures such as invert or sidewall are critical areas from the numerical point of view. Sharp corners and irregular shapes introduce high stresses and can be seen as weak points of the structural system. Compressive crushing and tensile cracking has to be expected with utilization factors far beyond peak. The associated

problems with such weak zones could be avoided or at least improved by a smooth transition or corner rounding.

- Modelling the tunnel lining as a linear elastic material with the stiffness of hardened shotcrete at 28 days overpredicts stresses that develop during loading and unrealistic high bending moments are introduced. Furthermore, the obtained lining deformations are very small and do not represent realistic values. Therefore, it is highly recommended not to adopt a linear elastic constitutive behaviour for shotcrete when the focus of the analysis is mainly on the tunnel lining behaviour. Assuming a reduced lining stiffness as in the HME approach is a huge improvement. It was shown, that with an appropriate reduction in the Young's modulus results tend to give a relatively good approximation of the overall system behaviour compared to more sophisticated models. However, it is this particular estimation of the stiffness reduction that has to be treated with caution, since it is purely based on experience. When analysing complex structures and geometries the HME approach will still overpredict stresses in the lining.

- The analyses carried out indicate, that for shotcrete at early ages, large differences can be expected regarding the lining displacements, where the stiffness of the material is a governing factor. In some cases these differences were pronounced such, that during excavation of the tunnel a completely different system behaviour was observed, when modelling a very young shotcrete response.

- The development of shotcrete stiffness and strength with time has been investigated in this thesis by performing a parametric study. It was shown, that variations in the development of these material properties highly influence the obtained results. A slower increase in stiffness and strength with time results in larger surface settlements, lower lining stresses but higher stress levels and larger lining displacements particularly during excavation of the tunnel.

- The shotcrete deformability at early ages has been analysed by adopting different developments of the plastic strain limits with time both in compression and tension. Results indicated that shotcrete deformability at early ages has a minor impact on the settlement behaviour. In contrast, some major differences in the stress distributions and stress levels have been obtained, with the main conclusion that a reduced straining capacity can increase the risk of cracking significantly due to the brittle material response.

- The consideration of creep and relaxation of the sprayed concrete has the ability to reduce stresses and bending moments in the tunnel lining. However, this reduction was much less than expected and less than that usually emphasised in the literature. One reason might be the choice of the adopted creep parameters. It is therefore recommended to investigate the influence of creep on the tunnel lining behaviour further by applying different sets of creep parameters and varying the elapsed time during tunnel

construction. From the performed analyses it was not possible to detect new mechanical mechanisms that might be caused by creep.

- Small changes in the predicted surface settlement troughs have been detected when considering the hydration temperature of the cement paste. An expansion of the lining during the first 10 to 12 hours after installation causes a relatively small reduction of the volume loss. For some cross sections of the lining a slightly increased bending has been observed when taking into account the temperature induced deformation. The reason for this is supposed to be the brittle material behaviour as a consequence of the cooling phase after reaching the peak temperature rise.

- Some minor differences have been observed in the results when accounting for shrinkage of the shotcrete, causing cracking in some particular cases. However, the elapsed time for these tunnel runs might not have been sufficient to reveal the complete impact of the decrease in volume on the behaviour of the tunnel lining. Shrinkage of shotcrete can be considered as a long-term problem and further investigations should be performed on this topic.

- Due to the high volume loss occuring during tunnel construction with very young shotcrete unrealistic high stress rearrangements in the soil and relatively high suctions in the pore water pressures were introduced.

- Finally, it can be concluded that the consideration of the material response of young shotcrete during the first 2 to 3 days after installation is a key element when simulating tunnel construction. During this time, the overall system behaviour is exclusively governed by the material properties of the young shotcrete. The combination of external loading and the transition from a ductile to a brittle type of material controls the development of stresses and displacements in the tunnel lining. Shotcrete behaviour in tunnelling can be regarded as a highly non-linear and complex problem being influenced by many factors.

## 9.5 Recommendations for future research

Shotcrete technology and its application in tunnel construction is a very innovative and challenging field of research. Enormous improvements have been made over the last few years with respect to the constituent materials, quality control, installation techniques and equipment. Nowadays, safe construction of shotcrete tunnel linings can be achieved with well trained workmen who are aware of the involved difficulties and their possible consequences. However, in a tunnelling project some uncertainties regarding varying ground conditions or unexpected loading scenarios of the lining will always exist, which can lead to critical system behaviour and even failure of the structure. It is the purpose of an appropriate design procedure to account for such situations and guarantee safety of the tunnel at all construction

stages. As highlighted throughout this thesis, advanced constitutive modelling of shotcrete was usually missing in the past and the design of a shotcrete shell was mainly based on the experience of the tunnel engineers. Furthermore, from the extensive literature review it can be observed that there is a large gap between experimental testing and numerical modelling of the material behaviour of sprayed concrete. Therefore, from the authors point of view, the following aspects and ideas should be taken into account for future research on the topic of shotcrete in tunnelling:

- For design purposes, experimental testing of shotcrete should be carried out in accordance with a particular constitutive model following a predefined testing scheme in such a way, that the necessary model parameters can be determined reliably from the obtained test results. For a correct modelling it is of crucial importance to calibrate a constitutive model using a complete set of tests for one specific type of shotcrete.

- In the past, testing of shotcrete has usually been restricted to uniaxial compression tests. This stress range should be extended in order to investigate the material behaviour under various loading conditions, such as biaxial or triaxial stress paths. Furthermore, the focus of these tests should be on the early age stages of cement hydration in order to capture the complete development of material properties up to an age of 28 days.

- Very little information is available in the literature about the tensile capacity of sprayed concrete due to various testing difficulties. However, it must be noted that these tensile material properties can be of great importance for a tunnel lining design, since cracking of the shotcrete should be avoided.

- The large scatter in almost any available shotcrete test data due to the large number of influencing factors represents a huge problem for a realistic calibration of appropriate model parameters. Future research should therefore shift its focus on new innovative testing methods that are already in use in other scientific fields (i.e. fibre optics, ultrasound, laser technology, etc.), since material science in general is a very interdisciplinary field. Collaboration with different areas of engineering or science could have a fruitful outcome for further experimental work on early age shotcrete.

- The current design philosophy for tunnel construction has to open up to new ideas and scientific trends. With respect to the design of a tunnel lining, it is not enough to guarantee safety of a structure by applying an approach that is almost entirely based on experience, since experience can lead to fatal errors. Simple design methods based on linear elasticity are easy to use and have their warranty indeed, but engineers should know their limits and should be aware of when there is the need for a more sophisticated constitutive model. The realistic modelling of shotcrete behaviour gives room for more developments and progress and will enable engineers to validate the simpler approaches.

- No claim is made for the entire completeness of the new constitutive model for shotcrete presented within this thesis. Several simplifications and problems remain unsolved,

such as the question of the correct hardening parameter for the realistic description of material behaviour for various loading conditions with respect to time. The applied normalisation of the principal plastic strains $\varepsilon_1$ and $\varepsilon_3$ is a first step in the right direction, but further progress has to be made on this topic.

- The generalisation of creep deformation into 3D with the help of a creep plastic potential is a powerful way of modelling creep. However, the obtained creep deformations have to be validated against experimental data in order to consider possible changes of the involved potential functions.

- One of the drawbacks of the current constitutive model for shotcrete is the use of solid elements for the simulation of the tunnel lining, which requires an extreme mesh refinement in order to obtain reasonable results for stress distributions across the lining thickness. Obviously, certain computational limitations exist and therefore, it might be better to focus in the future more on the development of advanced beam elements including time-dependent material behaviour.

- Due to time limitations all the analyses within this thesis were performed in 2D. However, it is recommended for the future to perform full 3D analyses in order to capture the complete process of stress rearrangements and deformations both in the soil and the tunnel lining close to the tunnel face in a realistic way.

- Finally, when analysing tunnel construction with the finite element method it is important to investigate extreme cases that might happen in reality. Case histories have proven that failures of tunnel linings occur mostly due to unexpected ground conditions, abnormalities in material quality, construction defects and irregular geometries. Analysing simple circular tunnels without imperfections in 2D will not detect critical stages during tunnel advance. The finite element method is a powerful tool for investigating different types of tunnel failures and this potential should be utilised.

# Appendix

Volume loss and maximum surface settlement for excavation Type 1 and $K_o = 0.5$

| Run | Volume loss $V_L$ (%) | Maximum settlement $\delta$ (mm) |
|---|---|---|
| Linear elastic (LE) | 1.48 | 21.3 |
| HME | 1.57 | 23.0 |
| Non-linear (NL) | 1.48 | 21.3 |
| TPM 1 | 5.63 | 81.9 |
| TPM 2 | 3.65 | 54.5 |
| TPM 3 | 2.26 | 33.3 |
| TPM 4 | 1.87 | 27.4 |
| TPM 5 | 1.70 | 25.0 |
| TPM 6 | 1.56 | 23.0 |
| TPM 7 | 1.51 | 22.2 |
| TPM 8 | 1.50 | 22.0 |
| TPM 9 | 1.50 | 21.8 |
| TPM 10 | 1.49 | 21.7 |
| TPM 11 | 1.49 | 21.5 |
| TPM 12 | 1.48 | 21.5 |
| TPM 13 | 1.48 | 21.3 |
| TPM 14 | 1.48 | 21.3 |
| STRENGTH 1 | 1.49 | 21.7 |
| STRENGTH 2 | 1.86 | 27.4 |
| STRENGTH 3 | 2.33 | 34.7 |
| STRENGTH 4 | 2.95 | 44.1 |
| STRENGTH 5 | 1.72 | 25.3 |
| STRENGTH 6 | 2.07 | 30.3 |
| STRAIN 1 | 1.58 | 23.2 |
| STRAIN 2 | 1.54 | 22.7 |
| STRAIN 3 | 1.54 | 22.6 |
| STRAIN 4 | 1.52 | 22.3 |
| CREEP (C) | 1.56 | 23.0 |
| SHRINKAGE (SH) | 1.57 | 23.1 |
| TEMPERATURE (T) | 1.53 | 22.6 |
| C + SH + T | 1.55 | 22.9 |

Volume loss and maximum surface settlement for excavation Type 1 and $K_o = 1.5$

| Run | Volume loss $V_L$ (%) | Maximum settlement $\delta$ (mm) |
|---|---|---|
| Linear elastic (LE) | 1.52 | 14.1 |
| HME | 1.61 | 14.9 |
| Non-linear (NL) | 1.52 | 14.1 |
| TPM 1 | 3.84 | 38.5 |
| TPM 2 | 2.87 | 29.5 |
| TPM 3 | 2.07 | 20.4 |
| TPM 4 | 1.79 | 17.1 |
| TPM 5 | 1.67 | 15.4 |
| TPM 6 | 1.58 | 14.4 |
| TPM 7 | 1.55 | 14.2 |
| TPM 8 | 1.54 | 14.2 |
| TPM 9 | 1.54 | 14.1 |
| TPM 10 | 1.53 | 14.1 |
| TPM 11 | 1.53 | 14.1 |
| TPM 12 | 1.53 | 14.1 |
| TPM 13 | 1.53 | 14.1 |
| TPM 14 | 1.53 | 14.1 |
| STRENGTH 1 | 1.54 | 14.1 |
| STRENGTH 2 | 1.78 | 16.8 |
| STRENGTH 3 | 2.08 | 20.4 |
| STRENGTH 4 | 2.46 | 24.8 |
| STRENGTH 5 | 1.69 | 15.7 |
| STRENGTH 6 | 1.95 | 19.0 |
| STRAIN 1 | 1.58 | 14.5 |
| STRAIN 2 | 1.57 | 14.4 |
| STRAIN 3 | 1.57 | 14.4 |
| STRAIN 4 | 1.56 | 14.3 |
| CREEP (C) | 1.58 | 14.5 |
| SHRINKAGE (SH) | 1.59 | 14.6 |
| TEMPERATURE (T) | 1.55 | 14.0 |
| C + SH + T | 1.57 | 14.3 |

# References


Abdel-Jawad, Y. & Haddad, R. (1992), 'Effect of early overloading of concrete on strength at later ages', *Cement and Concrete Research* **22**, pp. 927–936.

ACI 209R (1992), *Prediction of creep, shrinkage and temperature effects in concrete structures*, ACI Committee 209.

Aldrian, W. (1991), Beitrag zum Materialverhalten von früh belastetem Spritzbeton, PhD thesis, University for Mining and Metallurgy, Leoben, Austria.

Alkhiami, H. (1995), Ein Näherungsverfahren zur Abschätzung einer Spritzbetonkalottenschale auf der Grundlage von in-situ Messungen, PhD thesis, Technical University Hannover, Germany.

Armelin, H. & Banthia, N. (1998), 'Mechanics of aggregate rebound in shotcrete - Part I', *Materials and Structures* **31**, pp. 91–98.

Arsland, H. & Sture, S. (2008), 'Finite element simulation of localization in granular materials by micropolar continuum approach', *Computers and Geotechnics* **35**, pp. 548–562.

ASCCT - Austrian Society for Concrete- and Construction Technology (2004), *Guideline sprayed concrete*, Csöngei GmbH.

Atrushi, D. (2003), Tensile and compressive creep of early-age concrete: testing and modelling, PhD thesis, Norwegian University of Science and Technology, Trondheim, Norway.

Attard, M. & Setunge, S. (1996), 'Stress-strain relationship of confined and unconfined concrete', *ACI Materials Journal* **93**(5), pp. 432–442.

Austin, S. & Robins, P. (1995), *Sprayed concrete - properties, design and application*, Whittles Publishing.

Aydan, O., Sezaki, M. & Kawamoto, T. (1992), Mechanical and numerical modelling of shotcrete, *in* Pande & Pietruszczak, eds, 'Numerical Models in Geomechanics', pp. 757–764.

Babu, R., Benipal, G. & Singh, A. (2005), 'Constitutive modelling of concrete: an overview', *Asian Journal of Civil Engineering (Building and Housing)* **6**(4), pp. 211–247.

Balmer, G. (1949), Shearing strength of concrete under high triaxial stress - computation of Mohr's envelope as a curve, Technical Report SP-23, Structural Research Laboratory, Branch of Design and Construction, Denver.

Banthia, N., Trottier, J., Wood, D. & Beaupré, D. (1992), 'Influence of fibre geometry on steel fibre reinforced dry-mix shotcrete', *Concrete International* **14**(5), pp. 24–28.

Barros, J. & Figuieiras, J. (1999), 'Flexural behaviour of SFRC: testing and modelling', *Journal of Materials in Civil Engineering* **11**, pp. 331–339.

Barton, N., Lien, R. & Lunde, J. (1974), 'Engineering classification of rock masses for the design of tunnel support', *Rock Mechanics* **6**(4), pp. 189–239.

Bažant, Z. & Baweja, S. (1995), *Creep and shrinkage prediction model for analysis and design of concrete structures: Model B3*, a report submitted to ACI Committee 209.

Bićanić, N. & Pearce, C. (1996), 'Computational aspects of a softening plasticity model for plain concrete', *Mechanics of Cohesive-Frictional Materials* **1**, pp. 75–94.

Bićanić, N., Pearce, C. & Owen, D. (1994), Failure predictions of concrete like materials using softening Hoffman plasticity model, *in* 'Euro-C 1994 International Conference, Computer Modelling of Concrete Structures', pp. 185–198.

Bieniawski, Z. (1994), *Rock mechanics design in mining and tunnelling*, Balkema, Rotterdam.

Bischoff, P. & Paixao, R. (2004), 'Tension stiffening and cracking of concrete reinforced with glass fibre reinforced polymer (GFRP) bars', *Canadian Journal of Civil Engineering* **31**, pp. 579–588.

Bockhold, J. (2005), Modellbildung und numerische Analyse nichtlinearer Kriechprozesse in Stahlbetonkonstruktionen unter Schädigungsaspekten, PhD thesis, Ruhr-University Bochum, Germany.

Bosnjak, D. (2000), Self-induced cracking problems in hardening concrete structures, PhD thesis, Norwegian University of Science and Technology, Trondheim.

Brameshuber, W. & Hilsdorf, H. (1989), Development of strength and deformability of very young concrete, *in* Shah & Swartz, eds, 'Fracture of Concrete and Rock', pp. 409–421.

Byfors, J. (1980), Plain concrete at early ages, Technical report, Swedish Cement and Concrete Research Institute.

Camps, G., Turatsinze, A., Sellier, A., Escadeillas, G. & Bourbon, X. (2008), 'Steel-fibre reinforcement and hydration coupled effects on concrete tensile behaviour', *Engineering Fracture Mechanics* **75**, pp. 5207–5216.

Carlson, R. (1937), 'A simple method for the computation of temperatures in concrete structures', *ACI Journal* **34**, pp. 89–102.

CEB-FIP Model Code (1990), *Design Code - Comite Euro-International du Beton*, Thomas Telford, London.

Cendón, D., Gálvez, J., Elices, M. & Planas, J. (2000), 'Modelling the fracture of concrete under mixed loading', *International Journal of Fracture* **103**, pp. 293–310.

Chang, Y. (1994), Tunnel support with shotcrete in weak rock - A rock mechanics study, PhD thesis, Royal Institute of Technology, Stockholm, Sweden.

Chen, A. & Chen, W. (1975), 'Constitutive relations for concrete', *Journal of the Engineering Mechanics Division, ASCE* **101**(4), pp. 465–481.

Chen, W. (1982), *Plasticity in reinforced concrete*, McGraw-Hill Book Company.

Clayton, C., Hope, V., Heymann, G., van der Berg, J. & Bica, A. (2000), 'Instrumentation for monitoring sprayed concrete lined soft ground tunnels', *Proceedings of the Institution of Civil Engineers, Geotechnical Engineering* **143**(July), pp. 119–130.

Clayton, C., van der Berg, J., Heymann, G., Bica, A. & Hope, V. (2002), 'The performance of pressure cells for sprayed concrete linings', *Géotechnique* **52**(2), pp. 107–115.

Clayton, C., van der Berg, J. & Thomas, A. (2006), 'Monitoring and displacements at Heathrow Express Terminal 4 station tunnels', *Géotechnique* **56**(5), pp. 323–334.

Cornejo-Malm, G. (1995), Spritzbeton und seine Eigenschaften - Schwinden von Spritzbeton, Technical report, Institut für Bauplanung und Baubetrieb, ETH Zürich, Switzerland.

Davis, R., Davis, H. & Hamilton, J. (1934), 'Plastic flow of concrete under sustained stress', *ASTM Proceedings* **34**(2), pp. 354–386.

De Borst, R. (1987), 'Computation of post-bifurcation and post-failure behaviour of strain-softening solids', *Computers & Structures* **25**(2), pp. 211–224.

De Borst, R. (2002), 'Fracture in quasi-brittle materials: a review of continuum damage-based approaches', *Engineering Fracture Mechanics* **69**, pp. 95–112.

De Borst, R., Remmers, J., Needleman, A. & Abellan, M. (2004), 'Discrete vs. smeared crack models for concrete failure: bridging the gap', *International Journal for Numerical and Analytical Methods in Geomechanics* **28**, pp. 583–607.

De Borst, R. & van den Boogaard, A. (1994), 'Finite-element modelling of deformation and cracking in early-age concrete', *Journal of Engineering Mechanics* **120**(12), pp. 2519–2534.

De Schutter, G. (1999), 'Extension towards early age concrete of CEB-FIP Model Code 1990 stress-strain relation for short-term compressive loading', *ACI Materials Journal* **96**(1), pp. 95–100.

De Schutter, G. & Taerwe, L. (1997), 'Fracture energy of concrete at early ages', *Materials and Structures* **30**, pp. 67–71.

Desayi, P. & Krishnan, S. (1964), 'Equation for the stress-strain curve of concrete', *ACI Journal* **61**(22), pp. 345–350.

Ding, Y. (1998), Technologische Eigenschaften von jungem Stahlfaserbeton und Stahlfaserspritzbeton, PhD thesis, University of Innsbruck, Austria.

Ding, Y. & Kusterle, W. (1999), 'Comparative study of steel-fibre reinforced concrete and steel mesh-reinforced concrete at early ages in panel tests', *Cement and Concrete Research* **29**, pp. 1827–1834.

Ding, Y. & Kusterle, W. (2000), 'Compressive stress-strain relationship of steel fibre-reinforced concrete at early ages', *Cement and Concrete Research* **30**, pp. 1573–1579.

Duddeck, H. & Erdmann, J. (1982), Structural design models for tunnels, *in* 'Tunnelling '82, Institute of Mining and Metallurgy, London', pp. 83–91.

Duddeck, H. & Erdmann, J. (1985), 'On structural design models for tunnels in soft soil', *Underground Space* **9**, pp. 246–259.

Duvaut, G. & Lions, J. (1972), *Les inequations en mechanique et en physique*, Dunod, Paris.

Dvorkin, E., Cuitiño, A. & Gioia, G. (1989), 'A concrete material model based on non-associated plasticity and fracture', *Engineering Computations* **6**, pp. 281–294.

Ebead, U. & Marzouk, H. (2005), 'Tension-stiffening model for FRP-strengthened RC concrete two-way slabs', *Materials and Structures* **38**, pp. 193–200.

Eddie, C. & Neumann, C. (2003), 'LaserShell leads the way for SCL tunnels', *Tunnels & Tunnelling International* (June), pp. 38–42.

Eddie, C., Neumann, C. & Jäger, J. (2009), Innovative permanent shotcrete tunnel linings in London Clay, *in* Kusterle, ed., 'Internationale Spritzbetontagung, Alpbach, Austria', pp. 1–40.

EFNARC (1996), *European specification for sprayed concrete*.

Eierle, B. & Schikora, K. (1999), 'Computational modelling of concrete at early ages', *Diana World* **2**.

Einstein, H. & Schwartz, W. (1979), 'Simplified analysis for tunnel supports', *Journal of Geotechnical Engineers, ASCE* .

EN 1992-1-1 (2004), *Eurocode 2: Design of concrete structures - Part 1-1: General rules and rules for buildings*, European Committee for Standardization.

Engelbreth, K. (1961), 'Beregning av tunnel eller rør med sirkulaert tverrsnitt gjennom homogen jordmasse', *Teknisk Ukeblad* **108**, pp. 625–627.

England, G. & Illston, J. (1965), 'Methods of computing stress in concrete from a history of measured strain', *Civil Engineering and Public Works Review* **60**(1,2,3), pp. 513–517, 692–694,846–847.

Feenstra, P. (1993), Computational aspects of biaxial stress in plain and reinforced concrete, PhD thesis, Delft University, Netherlands.

Fields, K. & Bischoff, P. (2004), 'Tension stiffening and cracking of high-strength reinforced concrete tension members', *ACI Structural Journal* **101**(4), pp. 447–456.

Fischnaller, G. (1992), Untersuchungen zum Verformungsverhalten von jungem Spritzbeton im Tunnelbau, Grundlagen und Versuche, Master's thesis, University of Innsbruck, Austria.

Flügge, W. (1967), *Viscoelasticity*, Blaisdell Publishing Company.

Frantziskonis, G., Desai, C. & Somasundaram, S. (1986), 'Constitutive model for non-associative behaviour', *Journal of the Engineering Mechanics Division, ASCE* **112**, pp. 932–946.

Franzen, T. (1992), 'Shotcrete for underground support: a state-of-the-art report with focus on steel-fibre reinforcement', *Tunnelling and Underground Space Technology* **7**(4), pp. 383–391.

Freiesleben Hansen, P. & Pederson, E. (1977), 'Måleinstrument til kontrol af betons hærdning', *Nordisk Betong* **21**, pp. 21–25.

Galler, R. (1997), Shotcrete - realistic modelling for the purpose of economical tunnel design, *in* Yuan, ed., 'Computer Methods and Advances in Geomechanics', pp. 1383–1387.

Garboczi, E. & Bentz, D. (1992), Computer-based models of the micro structure and properties of cement-based materials, *in* 'Proceedings of the 9th International Conference on the Chemistry of Cement', Vol. VI, pp. 3–15.

Gardner, N. & Lockman, M. (2001), 'Design provisions for drying shrinkage and creep of normal-strength concrete', *ACI Materials Journal* **98**(2), pp. 159–167.

Gasparre, A. (2005), Advanced laboratory characterisation of London Clay, PhD thesis, Imperial College, London, UK.

Gilbert, R. & Warner, R. (1978), 'Tension stiffening in reinforced concrete slabs', *Journal of the Structural Division, ASCE* **104**, pp. 1885–1899.

Girmscheid, G. (2000), *Baubetrieb und Bauverfahren im Tunnelbau*, Ernst & Sohn.

Golser, J. (1999), Behaviour of early-age shotcrete, *in* T. Celestino & H. Parker, eds, 'Shotcrete for Underground Support VIII, Sao Paulo, Brazil', pp. 83–92.

Golser, J., Rabensteiner, K., Sigl, O. & Aldrian, W. (1990), Materialgesetz für Spritzbeton, Straßenforschung 696, Technical report, Bundesministerium für Wirtschaftliche Angelegenheiten, Austria.

Golser, J., Schubert, P. & Rabensteiner, K. (1989), A new concept for evaluation of loading in shotcrete linings, *in* 'International Congress on Progress and Innovation in Tunnelling', pp. 79–85.

Gopalakrishnan, K., Neville, A. & Ghali, A. (1969), 'Creep Poisson's ratio of concrete under multiaxial compression', *ACI Journal* **66**, pp. 1008–1020.

Grassl, P., Lundgren, K. & Gyltoft, K. (2002), 'Concrete in compression: A plasticity theory with novel hardening law', *International Journal of Solids and Structures* **39**(20), pp. 5205–5223.

Graziani, A., Boldini, D. & Ribacchi, R. (2005), 'Practical estimate of deformations and stress relief factors for deep tunnels supported by shotcrete', *Rock Mechanics and Rock Engineering* **38**(5), pp. 345–372.

Gullan, G. (1975), 'Shotcrete for tunnel linings', *Tunnels and Tunnelling* **7**(9), pp. 37–47.

Gutsch, A. & Rostásy, F. (1994), Young concrete under high tensile stresses - creep, relaxation and cracking, *in* Springenschmid, ed., 'Thermal Cracking in Concrete at Early Ages', pp. 111–118.

Hafez, N. (1995), Post-failure modelling of three-dimensional shotcrete lining for tunnelling, PhD thesis, University of Innsbruck, Austria.

Hagihara, S., Masuda, Y. & Nakamura, S. (2002), Creep behaviour of high-strength concrete at early age, *in* '6th International Symposium on High Strength/High Performance Concrete'.

Han, D. & Chen, W. (1986), 'Strain space plasticity formulation for hardening-softening materials with elastoplastic coupling', *International Journal of Solids and Structures* **22**, pp. 935–950.

Haufe, A. (2001), Dreidimensionale Simulation bewehrter Flächentragwerke aus Beton mit der Plastizitätstheorie, PhD thesis, Universit Stuttgart, Germany.

Hauggaard, A., Damkilde, L., Freisleben Hansen, P., Pederson, E. & Nielsen, A. (1997), Hetek - control of early age cracking in concrete - phase 4 and 5: Material modelling, continuum approach, Technical report, Ministry of Transport, Denmark.

Hellmich, C., Sercombe, J., Ulm, F. & H.A., M. (2000), 'Modelling of early-age creep of shotcrete. II: Application to tunnelling', *Journal of Engineering Mechanics* **126**(3), pp. 292–299.

Hellmich, C., Ulm, F. & Mang, H. (1999*a*), 'Multisurface chemoplasticity. I: Material model for shotcrete', *Journal of Engineering Mechanics* **125**(6), pp. 692–701.

Hellmich, C., Ulm, F. & Mang, H. (1999*b*), 'Multisurface chemoplasticity. II: Numerical studies on NATM tunneling', *Journal of Engineering Mechanics* **125**(6), pp. 702–713.

Hesser, J. (2000), Zum Einfluß unterschiedlicher Spritzbetonqualitäten auf das Tragverhalten tiefliegender Gesteinsstrecken - Laborative Untersuchungen und numerische Analysen, PhD thesis, Technical University Clausthal, Germany.

Hilar, M., Thomas, A. & Falkner, L. (2005), 'The latest innovation in sprayed concrete lining - the LaserShell method', *Tunel (Magazine of the Czech Tunnelling Committee and the Slovak Tunnelling Committee ITA/AITES)* **4**, pp. 11–19.

Hillerborg, A. (1985), Determination and significance of the fracture toughness of steel fibre concrete, *in* Shah & Skarendahl, eds, 'Steel Fibre Concrete, US-Sweden joint seminar'.

Hillerborg, A., Modéer, M. & Petersson, P. (1976), 'Analysis of crack formation and crack growth in concrete by means of fracture mechanics and finite elements', *Cement and Concrete Research* **6**, pp. 773–782.

Hills, D. (1982), 'Site-produced sprayed concrete', *Concrete* **16**(12), pp. 44–50.

Hoek, E. (2007), 'Integration of geotechnical and structural design in weak rock tunnels', *RocNews* (Spring), pp. 1–15.

Hofstetter, G., Simo, J. & Taylor, R. (1993), 'A modified cap model: closest point solution algorithms', *Computers & Structures* **46**, pp. 203–214.

Holt, E. (2001), Early age autogeneous shrinkage of concrete, Technical Report 446, Technical Research Centre of Finland.

Houst, Y. (1997), Carbonation shrinkage of hydrated cement paste, *in* '4th CANMET/ACI International Conference on Durability of Concrete, Ottawa, Canada', pp. 481–491.

HSE (2000), The collapse of NATM tunnels at Heathrow Airport, Technical report, Health and Safety Executive.

HSE - Health & Saftey Executive (1996), *Safety of the New Austrian Tunnelling Method (NATM) Tunnels*, HSE Books, Sudbury.

Huber, F. (2006), Nichtlineare dreidimensionale Modellierung von Beton- und Stahlbetontragwerken, PhD thesis, Universit Stuttgart, Germany.

Huber, H. (1991), Untersuchungen zum Verformungsverhalten von jungem Spritzbeton im Tunnelbau, Master's thesis, University of Innsbruck, Austria.

Huo, X. & Wong, L. (2006), 'Experimental study of early-age behaviour of high performance concrete deck slabs under different curing methods', *Construction and Building Materials* **20**, pp. 1049–1056.

ÖIAV (1980), Neue Österreichische Tunnelbaumethode, Definition und Grundsätze, Technical Report Heft 74, Österreichischer Ingenieur- und Architektenverein.

ICE - Institution of Civil Engineers (1996), *Sprayed concrete linings (NATM) for tunnels in soft ground*, Thomas Telford, London.

ICE - Institution of Civil Engineers (2004), *Tunnel lining design guide*, Thomas Telford, London.

Illston, J. (1965), 'The creep of concrete under uniaxial tension', *Magazine of Concrete Research* **17**(51), pp. 77–84.

Jardine, R., Potts, D., Fourie, A. & Burland, J. (1986), 'Studies of the influence of non-linear stress-strain charactersitics in soil-structure interaction', *Géotechnique* **36**(3), pp. 377–396.

Jodl, H. & Kusterle, W. (1998), Experiences with austrian sprayed concrete technology in tunnelling, *in* Bergdahl & Nordmark, eds, 'Underground Construction in Modern Infrastructure', pp. 367–373.

Jones, B. (2007), Design of SCL tunnels in soft ground using Eurocodes, *in* Eberhardsteiner, ed., 'ECCOMAS Thematic Conference on Computational Methods in Tunnelling (EURO:TUN 2007)', pp. 1–12.

Jones, B., Thomas, A., Hsu, Y. & Hilar, M. (2008), 'Evaluation of innovative sprayed-concrete-lined tunnelling', *Proceedings of the Institution of Civil Engineers, Geotechnical Engineering* **161**, pp. 137–149.

Jones, B., Thomas, A. & Stärk, A. (2005), The importance of stress measurement in a holistic sprayed concrete tunnel design process, *in* Chambery, ed., 'Int. Congress on Tunnelling for a Sustainable Europe, Lyon'.

Karakus, M. (2007), 'Appraising the methods accounting for 3D tunnelling effects in 2D plane strain FE analysis', *Tunnelling and Underground Space Technology* **22**(1), pp. 47–56.

Karakus, M. & Fowell, R. (2003), 'Effects of different tunnel face advance excavation on the settlement by FEM', *Tunnelling and Underground Space Technology* **18**, pp. 513–523.

Karakus, M. & Fowell, R. (2004), An insight into the New Austrian Tunnelling Method (NATM), *in* 'ROCKMEC - VII$^{\text{th}}$ Regional Rock Mechanics Symposium, Sivas, Turkey'.

Karrer, J. (1986), Spritzbeton im Tunnelbau: Technologie, Festigkeitsentwicklung, Tragverhalten, Master's thesis, University for Mining and Metallurgy, Leoben, Austria.

Kasai, Y., Yokoyama, K. & Matsui, I. (1971), Tensile properties of early-age concrete, *in* 'Proc. of the International Conference on Mechanical Behaviour of Materials', pp. 288–299.

Kavvadas, M. (2003), Monitoring and modelling ground deformations during tunnelling, *in* '11$^{\text{th}}$ Int. Symposium on Deformation Measurements, Santorini, Greece', pp. 371–390.

Kazemi, M., Fazileh, F. & Ebrahiminezhad (2007), 'Cohesive crack model and fracture energy of steel-fibre-reinforced-concrete notched cylindrical specimens', *Journal of Materials in Civil Engineering* **19**(10), pp. 884–890.

Kienberger, G. (1999), Einschaliger Tunnelbau - Einfluß des zeitabhängigen Materialverhaltens auf die Ausbaubeanspruchung, PhD thesis, University for Mining and Metallurgy, Leoben, Austria.

König, G. & Duda, H. (1991), Basic concept for using concrete tensile strength, *in* 'IABSE Colloquium on Structural Concrete', pp. 605–621.

Kobler, H. (1966), Dry-mix coarse-aggregate shotcrete as underground support, *in* ACI, ed., 'Shotcreting (SP-14)', pp. 33–58.

Kolymbas, D. (1998), *Geotechnik - Tunnelbau und Tunnelmechanik*, Springer.

Kooiman (2000), Modelling steel fibre reinforced concrete for structural design, PhD thesis, Delft University of Technology, Netherlands.

Kotsovos, M. & Newman, J. (1978), 'Generalized stress-strain relations for concrete', *Journal of the Engineering Mechanics Division, ASCE* **104**(4), pp. 845–857.

Kropik, C. & Mang, H. (1995), 'Computational mechanics of the excavation of tunnels', *Engineering Computations* **13**(7), pp. 49–69.

Kützing, L. (2000), *Tragfähigkeitsermittlung stahlfaserverstärkter Betone*, B.G. Teubner.

Kupfer, H. & Gerstle, K. (1973), 'Behaviour of concrete under biaxial stresses', *Journal of the Engineering Mechanics Division, ASCE* **99**(4), pp. 853–866.

Kusterle, W. (1985), Frühfestigkeiten des Spritzbetons, *in* Lukas, ed., 'Internationale Fachtagung Spritzbetontechnologie', pp. 35–38.

Kusterle, W. (1999), Comparison of shrinkage behaviour and creep properties under different compressive stress levels for wet mix sprayed concrete from ten hours up to two weeks, Technical report, Morgan Tunnelling.

Kusterle, W. & Lukas, W. (1990), Spritzbeton hoher Güte für die einschalige Spritzbetonbauweise, *in* 'Tagungsband der 3. Int. Fachtagung Spritzbeton-Technologie, Innsbruck, Austria', pp. 29–40.

Kusterle, W. & Lukas, W. (1993), Single-shell shotcrete method, *in* Wood & Morgan, eds, 'Shotcrete for Underground Support VI, Canada', pp. 118–129.

Kuttner, C. (1989), Numerische Simulation einer Druckmeßdose, eingebaut in einen Spritzbetonkörper, Master's thesis, University for Mining and Metallurgy, Leoben, Austria.

Kuwajima, F. M. (1999), Early age properties of shotcrete, *in* T. Celestino & H. Parker, eds, 'Shotcrete for Underground Support VIII, Sao Paulo, Brazil', pp. 153–173.

Labahn, O. (1982), *Ratgeber für Zementingenieure*, Bauverlag.

Lackner, R., Hellmich, C. & Mang, H. (2002), 'Constitutive modelling of cementitious materials in the framework of chemoplasticity', *International Journal for Numerical Methods in Engineering* **53**, pp. 2357–2388.

Lackner, R., Macht, J. & Mang, H. (2006), 'Hybrid analysis method for on-line quantification of stress states in tunnel shells', *Computer Methods in Applied Mechanics and Engineering* **195**, pp. 5361–5376.

Lackner, R. & Mang, H. (2000), Material modelling and computational strategies in the analysis of concrete shells, *in* 'ECCOMAS European Congress on Computational Methods in Applied Sciences and Engineering', pp. 1–23.

Lackner, R. & Mang, H. (2003), 'Cracking in shotcrete tunnel shells', *Engineering Fracture Mechanics* **70**, pp. 1047–1068.

Lackner, R. & Mang, H. (2004), 'Chemoplastic material model for the simulation of early-age cracking: From the constitutive law to numerical analyses of massive concrete structures', *Cement & Concrete Composites* **26**, pp. 551–562.

Lu, J., Lin, G., Wang, Z. & Xiao, S. (2004), 'Reduction of compressive strength of concrete due to triaxial compressive loading history', *Magazine of Concrete Research* **56**(3), pp. 139–149.

Malmberg, B. (1977), Steel fibre reinforced concrete under free and restrained shrinkage, Technical report, Fiberbetong, Nordforsks projektkommitte för FRC-material, Sweden.

Malmgrem, L., Nordlund, E. & Rolund, S. (2005), 'Adhesion strength and shrinkage of shotcrete', *Tunnelling and Underground Space Technology* **20**, pp. 33–48.

Matsuo, S., Matsuoka, S., Masuda, A. & Yanagi, H. (1995), A study on approximation method of tension softening curve of steel fibre reinforced concrete, *in* Wittmann, ed., 'Second

International Conference on Fracture Mechanics of Concrete Structures (FRAMCOS II)', pp. 745–754.

Mehta, P. & Monteiro, P. (1985), *Concrete - Structure, Properties and Materials*.

Meschke, G. (1996), 'Consideration of aging of shotcrete in the context of a 3-D viscoplastic material model', *International Journal for Numerical Methods in Engineering* **39**, pp. 3123–3143.

Meschke, G., Kropik, C. & Mang, H. (1996), 'Numerical analysis of tunnel linings by means of a viscoplastic material model for shotcrete', *International Journal for Numerical Methods in Engineering* **39**, pp. 3145–3162.

Meschke, G., Lackner, R. & H.A., M. (1998), 'An isotropic elastoplastic-damage model for plain concrete', *International Journal for Numerical Methods in Engineering* **42**, pp. 703–727.

Müller, L. (1990), 'Removing misconceptions an the New Austrian Tunnelling Method', *Tunnels & Tunnelling* (Special Issue), pp. 15–18.

Müller, L. & Fecker, E. (1978), Grundgedanken und Grundsätze der Neuen Österreichischen Tunnelbauweise. Grundlagen und Anwendung der Felsmechanik, *in* 'Felsmechanik Kolloquium Karlsruhe', pp. 247–262.

Möller, S., Vermeer, P. & Marcher, T. (2004), NATM-tunnelling in softening stiff clays and weak rocks, *in* 'Proceedings of the 9th Symposium on Numerical Models in Geomechanics (NUMOG IX), Ottawa, Canada', pp. 404–413.

Mosler, J. & Meschke, G. (2004), 'Embedded crack vs. smeared crack models: a comparison of elementwise discontinuous crack path approaches with emphasis on mesh bias', *Computer Methods in Applied Mechanics and Engineering* **193**, pp. 3351–3375.

Moussa, A. M. (1993), Finite element modelling of shotcrete in tunnelling, PhD thesis, University of Innsbruck, Austria.

Muir Wood, A. (1975), 'The circular tunnel in elastic ground', *Géotechnique* **25**(1), pp. 115–127.

Nayal, R. & Rasheed, H. (2006), 'Tension stiffening model for concrete beams reinforced with steel and FRP bars', *Journal of Materials in Civil Engineering* **18**(6), pp. 831–841.

Nelissen, L. (1972), 'Biaxial testing of normal concrete', *Heron* **18**(1).

Neubert, B. & Manns, W. (1993), Mechanical-technological properties of shotcrete with accelerating admixtures, *in* 'International Symposium on Sprayed Concrete, Norwegian Concrete Association', pp. 258–270.

Neville, A. (1970), *Creep of Concrete: Plain, Reinforced and Prestressed*, North Holland Publishing Company, Amsterdam.

Neville, A. (1981), *Properties of concrete*, Longman Scientific & Technical.

Oliver, J. (1989), 'A consistent characteristic length for smeared cracking models', *International Journal for Numerical Methods in Engineering* **28**, pp. 461–474.

Oluokun, F., Burdette, E. & Deatherage, J. (1991*a*), 'Elastic modulus, Poisson's ratio and compressive strength relationships at early ages', *ACI Materials Journal* **88**(1), pp. 3–10.

Oluokun, F., Burdette, E. & Deatherage, J. (1991*b*), 'Splitting tensile strength and compressive strength relationship at early ages', *ACI Materials Journal* **88**, pp. 115–121.

Onate, E., Oller, S., Oliver, J. & Lubliner, J. (1988), 'A constitutive model for cracking of concrete based on the incremental theory of plasticity', *Engineering Computations* **5**, pp. 309–319.

Oreste, P. (2003), 'Analysis of structural interaction in tunnels using the convergence-confinement approach', *Tunnelling and Underground Space Technology* **18**, pp. 347–363.

Outterside, J. (2003), Sprayed concrete tunnel liners, Technical report, Department of Engineering Science, Oxford University.

Pamin, J. K. (1994), Gradient-dependent plasticity in numerical simulation of localization phenomena, PhD thesis, Delft University of Technology, Netherlands.

Panet, M. & Guenot, A. (1982), Analysis of convergence behind the face of a tunnel, *in* 'Tunnelling '82, Institute of Mining and Metallurgy, London', pp. 197–203.

Parker, H., Fernandez-Delgado, G. & Lorig, L. (1977), A practical new approach to rebound loss, *in* ACI, ed., 'Shotcrete for Ground Support (SP-54)', pp. 149–187.

Parrott, L. (1978), Effect of loading at early age upon creep and relaxation of concrete, Technical Report UK5, RILEM Committee 42-CEA.

Peterson, A. (1989), Geostatische Untersuchungen für tiefliegende Regionalbahnen am Beispiel Hannover, Technical report, University of Hannover, Germany.

Pölling, R. (2000), Eine praxisnahe, schädigungsorientierte Materialbeschreibung von Stahlbeton für Strukturanalysen, PhD thesis, Ruhr-University Bochum, Germany.

Popovics, S. (1970), 'A review of stress-strain relationships for concrete', *ACI Journal* **67**(14), pp. 243–248.

Potts, D. & Zdravković, L. (1999), *Finite element analysis in geotechnical engineering - Theory*, Thomas Telford, London.

Potts, D. & Zdravković, L. (2001), *Finite element analysis in geotechnical engineering - Application*, Thomas Telford, London.

Powell, D., Sigl, O. & Beveridge, J. (1997), Heathrow express - design and performance of platform tunnels at Terminal 4, *in* 'Tunnelling '97', pp. 565–593.

Probst, B. (1999), Entwicklung einer Langzeitdruckversuchsanlage für den Baustellenbetrieb zur Bestimmung des Materialverhaltens von jungem Spritzbeton, Master's thesis, University for Mining and Metallurgy, Leoben, Austria.

Pöttler, R. (1985), 'Ideeller Elastizitätsmodul zur Abschätzung der Spritzebetonbeanspruchung bei Felshohlraumbauten', *Felsbau* **3**(3), pp. 136–139.

Pöttler, R. (1990), 'Time-dependent rock-shotcrete interaction - a numerical shortcut', *Computers and Geotechnics* **9**, pp. 149–169.

Pöttler, R. (1993), To the limits of shotcrete linings, *in* Wood & Morgan, eds, 'Shotcrete for Underground Support VI, Niagara-on-the-Lake, Canada', pp. 83–90.

Pöttler, R. & Klapperich, H. (1999), Single-shelled shotcrete lining aspects and application in Central Europe, *in* Celestino & Parker, eds, 'Shotcrete for Underground Support VIII, Sao Paulo, Brasil', pp. 174–192.

Pöttler, R. & Schweiger, H. (1999), Single-shell permanent lining reflections from the structural point of view, *in* Celestino & Parker, eds, 'Shotcrete for Underground Support VIII, Sao Paulo, Brasil', pp. 57–66.

Rabcewicz, L. (1964), 'The New Austrian Tunnelling Method', *Water Power* (Nov.), pp. 453–457.

Rabensteiner, K. (1988), 'Research project on the constitutive behaviour of shotcrete (personal communication with Schubert P.)'.

Rathmair, F. (1997), Numerische Simulation des Langzeitverhaltens von Spritzbeton und Salzgestein mit der im FE-Programm Abaqus implementierten Routine, Master's thesis, University for Mining and Metallurgy, Leoben, Austria.

Reinhardt, H., Blaaunwendraad, J. & Jongedijk, J. (1982), Temperature development in concrete structures taking account of the state dependent properties, *in* 'International Conference of Concrete at Early Ages'.

RILEM (1998), Prevention of thermal cracking in concrete at early ages, Technical Report 15.

Rokahr, R. B. & Lux, K. H. (1987), 'Einfluß des rheologischen Verhaltens des Spritzbetons auf den Ausbauwiderstand', *Felsbau* **5**(1), pp. 11–18.

Rokahr, R., Zachow, R. & Zander-Schiebenhöfer, D. (2005), Calculation of the stress intensity index of a sprayed concrete lining, *in* E. . Solak, ed., 'Underground Space Use: Analysis of the Past and Lessons for the Future', pp. 985–989.

Ross, A. (1937), 'Concrete creep data', *The Structural Engineer* **15**(8), pp. 314–326.

Rots, J. (1988), Computational modelling of concrete fracture, PhD thesis, Delft University of Technology, Netherlands.

Rowe, R., Lo, K. & Kack, K. (1983), 'A method of estimating surface settlement above shallow tunnels constructed in soft ground', *Canadian Geotechnical Journal* **20**, pp. 11–22.

Ryan, T. (1975), 'Steel fibres in gunite: an appraisal', *Tunnels and Tunnelling* **7**(7), pp. 74–75.

Sargin, M. (1968), Stress-strain relationship for concrete and the analysis of structural concrete sections, PhD thesis, University of Waterloo, Ontario, Canada.

Sauer, G. (1988), 'Further insights into the NATM', *Tunnels & Tunnelling* (July), pp. 35–39.

Sauer, G., Gall, V., Bauer, E. & Dietmaier, P. (1994), Design of tunnel concrete linings using capacity limit curves, *in* Siriwardane & Zaman, eds, 'Computer Methods and Advances in Geomechanics', pp. 2621–2626.

SCA - Sprayed Concrete Association (1999), *Introduction to sprayed concrete*.

Schubert, P. (1988), 'Beitrag zum rheologischen Verhalten von Spritzbeton', *Felsbau* **6**(3), pp. 150–153.

Schubert, W. & Grossauer, K. (2004), Evaluation and interpretation of displacements in tunnels, *in* '14$^{\text{th}}$ Int. Conference on Engineering Surveying, Zürich, Switzerland'.

Schulze, H. & Duddeck, H. (1964), 'Spannungen im schildvorgetriebenen Tunnel', *Beton und Stahlbetonbau* **59**, pp. 169–175.

Sercombe, J., Hellmich, C., Ulm, F. & Mang, H. (2000), 'Modelling of early-age creep of shotcrete. I: Model and model parameters', *Journal of Engineering Mechanics* **126**(3), pp. 284–291.

Sezaki, M., Kibe, T., Ichikawa, Y. & Kawamoto, T. (1989), 'An experimental study on the mechanical properties of shotcrete', *Journal of the Society of Materials Science, Japan* **38**, pp. 106–110.

Shank, J. (1935), The plastic flow of concrete, Technical Report 91, Engineering Experiment Station, Ohio State University.

Sloan, S. (1987), 'Substepping algorithms for numerical integration of elasto-plastic stress-strain relations', *International Journal for Numerical Methods in Engineering* **24**, pp. 893–911.

Smith, S., William, K., Gerstle, K. & Sture, S. (1989), 'Concrete over the top, or is there life after peak?', *ACI Materials Journal* **86**(5), pp. 491–497.

Stang, H. & Aarre, T. (1992), 'Evaluation of crack width in FRC with conventional reinforcement', *Cement and Concrete Composites* **14**, pp. 143–154.

Stelzer, G. & Golser, J. (2002), Investigations regarding geometrical imperfections of shotcrete linings - results from laboratory and from numerical calculations, *in* 'Spritzbeton-Technologie, Alpbach, Austria', pp. 105–111.

Strack, M. (2007), Modellbildung zum rissbreitenabhängigen Tragverhalten von Stahlfaserbeton unter Biegebeanspruchung, PhD thesis, Ruhr-University Bochum, Germany.

Straub, L. (1930), 'Plastic flow in concrete arches', *Proceedings of the American Society of Civil Engineers* **56**, pp. 49–114.

Swoboda, G. (1979), Finite element analysis of the New Austrian Tunnelling Method (NATM), *in* 'Proc. of the 3rd International Conference on Numerical Methods in Geomechanics, Aachen, Germany', pp. 581–586.

Swoboda, G. & Moussa, A. (1992), Numerical modelling of shotcrete in tunnelling, *in* Pande & Pietruszczak, eds, 'Numerical Models in Geomechanics', pp. 717–727.

Thomas, A. (2003), Numerical modelling of sprayed concrete lined (SCL) tunnels, PhD thesis, University of Southampton, UK.

Thomas, A. (2009), *Sprayed concrete lined tunnels*, Taylor and Francis.

Thomas, A., Legge, N. & Powell, D. (2004), The development of sprayed concrete lined (SCL) tunnelling in the UK, *in* Schubert, ed., '53rd Geomechanik Colloquium, Salzburg, Austria'.

Thomas, F. (1933), 'A conception of the creep of unreinforced concrete and an estimation of the limiting values', *The Structural Engineer* **11**(2), pp. 69–73.

Thomée, B. (2005), Physikalische nichtlineare Berechnung von Stahlfaserkonstruktionen, PhD thesis, Technical University Munich, Germany.

Timoshenko, S. & Goodier, J. (1951), *Theory of elasticity*, McGraw Hill, New York.

U.S. Bureau of Reclamation (1955), Investigation of creep in concrete: review of literature on creep in concrete, Technical Report 1, U.S. Army Engineer Waterways Experiment Station, Corps of Engineers, Vicksburg.

Vaishnav, R. & Kesler, C. (1961), Correlation of creep of concrete with its dynamic properties, Technical Report 603, University of Illinois.

van Mier, J., Reinhardt, H. & van der Vlugt, B. (1987), 'Ergebnisse dreiachsiger verformungsgesteuerter Belastungsversuche an Beton', *Bauingenieur* **62**, pp. 353–361.

Vermeer, P. & Brinkgreve, R. (1994), A new effective non-local strain-measure for softening plasticity, *in* V. Chambon, Desrues, ed., 'Localisation and Bifurcation Theory for Soils and Rocks', pp. 89–100.

Vermeer, P. & de Borst, R. (1984), 'Non-associated plasticity for soils, concrete and rock', *Heron* **29**(23), pp. 1–64.

Vonk, R. (1992), Softening of concrete loaded in compression, PhD thesis, Eindhoven University of Technology, Netherlands.

Walter, H. (1997), Application of a new shotcrete model in a 3-D FE-analysis of a tunnel excavation, *in* Pande & Pietruszczak, eds, 'Numerical Models in Geomechanics (NUMOG VI)', pp. 455–460.

Walter, H. (2003), Design of the shotcrete tunnel lining of a metro station - safety considerations, *in* 'Proceedings of the Euro-C Conference on Computational Modelling of Concrete Structures', pp. 855–865.

Watson, P., Warren, C., Eddie, C. & Jäger, J. (1999), CTRL north downs tunnel, *in* 'Tunnel Construction and Piling '99', pp. 301–323.

Weber, J. (1979), 'Empirische Formeln zur Beschreibung der Festigkeitsentwicklung und des E-Moduls von Beton', *Betonwerk- und Fertigteiltechnik* **12**, pp. 753–756.

Weigler, K. (1974), Junger Beton - Beanspruchung - Festigkeit - Verformung, Technical Report 20, Institut für Massivbau, University Darmstadt, Germany.

Wierig, H. (1971), 'Einige Beziehungen zwischen den Eigenschaften von "grünen" und "jungen" Betonen und denen des Festbetons', *Beton* **11+12**, pp. 445–490.

Wierig, H. & Gollasch, E. (1967), Untersuchung über das Verformungsverhalten von jungem Beton, Technical Report 47, University of Hannover.

Williams, I. (2008), 'Heathrow Terminal 5: tunnelled underground infrastructure', *Civil Engineering, Proceedings of ICE* **161**(May), pp. 30–37.

Wolfsier, J. & Morgan, D. (1993), 'Silica fume in shotcrete', *Concrete International* **15**(4), pp. 34–39.

Wolsiefer, J. & Morgan, D. (2003), 'Silica fume in shotcrete', *Shotcrete Magazine* **5**(1), pp. 28–33.

Woods, R. & Clayton, C. (1993), The application of CRISP finite element program to practical retaining wall problems, *in* 'ICE Conference on Retaining Structures, Cambridge', pp. 102–111.

Wu, W. & Roony, P. (2001), The role of numerical analysis in tunnel design, *in* D. Kolymbas, ed., 'Tunnelling Mechanics, Eurosummerschool, Innsbruck', pp. 87–168.

Yin, J. (1996), Untersuchungen zum zeitabhängigen Tragverhalten von tiefliegenden Hohlräumen im Fels mit Spritzbetonausbau, PhD thesis, Technical University Clausthal, Germany.

Zachow, R. (1995), Dimensionierung zweischaliger Tunnel im Fels auf Grundlage von in situ Messungen, PhD thesis, Technical University Hannover, Germany.

Zervos, A., Vardoulakis, I. & Papanastasiou, P. (2007), 'Influence of nonassociativity on localization and failure in geomechanics based on gradient plasticity', *International Journal of Geomechanics* **7**(1), pp. 63–74.

Zheng, H. (1989), Beanspruchungen des Tunnelausbaus bei zeitabhängigem Materialverhalten von Beton und Gebirge, PhD thesis, Technical University Braunschweig, Germany.